Fabrication, Thermophysical, and Mechanical Properties of Cermet and Cercer Fuel Composites for Nuclear Thermal Propulsion

A Dissertation Presented for

The Doctor of Philosophy

Degree

The University of Tennessee, Knoxville

Neal D. Gaffin

December 2022

© by Neal D. Gaffin, 2022
All Rights Reserved.

This work is dedicated first and foremost to my wife, Miquela. She has been a constant source of support and love throughout the entire degree. She has sacrificed so much to help me achieve my dreams.

This work is also dedicated to my children Zachary and Brynlee.

Acknowledgements

Thank you to my advisor, Dr. Steven Zinkle, who has mentored me throughout my entire graduate career. He has helped to not only have success in my research but to also grow and develop the skills that are necessary for my future success. Thank you to Dr. Kelsa Palomares and Dr. Justin Milner, who not only helped with my research, but also provided much needed mentor-ship at multiple points throughout my career. Thank you also to Dr. Lawrence Heilbronn who always took the time to meet with me to discuss a variety of nuclear space related topics. I acknowledge NASA Glenn Research Center and the NASA Space Nuclear Propulsion (SNP) project for sponsoring this work under Grant No. 80NSSC20K1434. Thank you to Dr. Caen Ang, who provided mentor-ship, technical expertise, and laboratory support, especially during the start of my doctoral research. Thank you to Dr. Timothy Ironman for aiding in experiments and providing advice for technical and research challenges. Thank you to Madison Vandergriff, Annie Berens, and Mason Phillips, excellent undergraduate research assistants who provided much needed laboratory assistance. Thank you to John Dunlap and Neal Evans for their excellent training and help with the SEM systems at IAMM. Thank you also to Michael Koehler for his assistance with Xray diffraction. Thank you to Michael Pagan, Qinyung Chen, William Ponder Peter Doyle, and Taylor Duffin, and Brian Ensign, fellow graduate students who helped with research and coursework. Thank you Tyler Gerzack, Hsin Wang, Stephanie Curlin, Richard Howard, and Dianne Ezell for providing access to equipment and expertise at ORNL. Thank you Dr. Lignell and Dr. Memmott, who both took the time to help

me discover a passion for research as an undergraduate student. Finally, thank you Pat Reardon, Ted Ball, Jeanne Ball, and Elena Guardincerri, my mentors at LANL. Thank you to everyone else who has helped me with my educational and professional pursuits.

Abstract

Nuclear thermal propulsion (NTP) utilizes nuclear fission to double the efficiency of in-space propulsion systems compared with traditional combustion rocket systems. NTP systems are limited primarily by the fuel material choice, due to the extreme conditions they will need to endure, including temperatures up to 3000 K, multiple thermal cycles with rapid heating and cooling, exposure to hot flowing hydrogen, large thermal gradients, and high neutron flux. Particle based fuels, namely ceramic-metallic (cermet) and ceramic-ceramic (cercer) composites are both promising fuel element material candidates for NTP. Given the high temperature nature, these materials are difficult to fabricate and very little thermophysical and mechanical property data exists. The fabrication of a cermet with a molybdenum-tungsten matrix and a cercer with a zirconium carbide matrix using surrogate fuel particles have been optimized utilizing spark plasma sintering to produce materials to greater than 97% theoretical density. Thermophysical properties including the coefficient of thermal expansion, thermal conductivity, and heat capacity were determined up to 1000 °C. Compression and notched bend bar tests up to 800 °C also provided information on the effect of the particles to the strength of the composites. From this data, predictive models were created to approximate the thermophysical and mechanical properties of fueled materials for use in NTP design.

Table of Contents

1 Introduction **1**

1.1 Background 1

1.2 NTP Operating Conditions and Material Requirements 2

1.3 NTP Fuel Manufacturing Techniques 7

1.4 Cermet and Cercer Fuel Forms 7

1.5 Research Objectives 10

2 Literature Review **12**

2.1 Legacy NTP Fuel Systems 12

2.1.1 Graphite (Rover/NERVA) 13

2.1.2 Refractory Metal Cermets 18

2.1.3 Carbides and Ceramic Matrix Fuels 25

2.2 Spark Plasma Sintering 31

2.2.1 SPS Background 31

2.2.2 Effect of Control Parameters 31

2.2.3 Sintering of Refractory Metals and Alloys 32

2.2.4 Sintering of Zirconium Carbide 48

2.2.5 Sintering of Refractory Composites and Cermets 59

2.3 Properties of Molybdenum and Tungsten 61

2.3.1 Crystal Structure of Molybdenum and Tungsten 61

2.3.2 Thermal Properties of Molybdenum and Tungsten 66

2.3.3 Mechanical Properties of Molybdenum and Tungsten 81
2.4 Properties of Zirconium Carbide 94
2.4.1 Crystal Structure of ZrC 94
2.4.2 Thermal Properties of Zirconium Carbide 97
2.4.3 Mechanical Properties of Zirconium Carbide 109
2.5 Properties of Surrogate and Fuel Ceramics 121
2.5.1 Properties of UO_2 and YSZ 121
2.5.2 Properties of UN and HfN 136
2.6 Properties of Metallic Alloys 146
2.7 Properties of Composite Materials 151
2.7.1 Heat Capacity 152
2.7.2 Thermal Conductivity 153
2.7.3 Coefficient of Thermal Expansion 154
2.7.4 Strength and Fracture Toughness 157

3 Methods **163**
3.1 Experimental Methods 163
3.1.1 Fabrication 163
3.1.2 Characterization 165
3.1.3 Thermophysical Property Measurements 166
3.1.4 Mechanical Testing 167
3.2 Sintering Analysis 172
3.2.1 Young and Cuttler Initial Stage Sintering 172
3.2.2 Master Sintering Curve 173

4 Results **176**
4.1 Fabrication 176
4.1.1 Initial Consolidation of Mo30W Matrix 176
4.1.2 Comparison of the Consolidation of Different Mo30W Powders 185
4.1.3 ZrC Matrix Optimization 200

4.1.4 Scaling and Optimum Sintering Conditions 210
4.1.5 Powder Coating 210
4.1.6 Fabrication of Cermet Materials 218
4.1.7 Fabrication of Cercer Materials 232
4.2 Thermophysical Properties 239
4.2.1 Coefficient of Thermal Expansion 244
4.2.2 Specific Heat Capacity 250
4.2.3 Thermal Conductivity 254
4.3 Mechanical Properties 259
4.3.1 Dynamic Modulus 259
4.3.2 Tensile Properties 259
4.3.3 Fracture Toughness 264

5 Discussion **277**
5.1 Fabrication 277
5.1.1 Mo30W Matrix 277
5.1.2 Comparison of the Consolidation of Different Mo30W Powders 286
5.1.3 Comparison of Sintering Analysis Techniques 290
5.1.4 Mo30W-HfN Secondary Phase Formation 292
5.1.5 Sintering Analysis for Cermet and Cercer 296
5.2 Thermophysical Properties 302
5.2.1 Coefficient of Thermal Expansion 302
5.2.2 Specific Heat Capacity 310
5.2.3 Thermal Conductivity 315
5.3 Mechanical Properties 324
5.3.1 Model of Modulii and Poisson's Ratio 324
5.3.2 Tensile Properties 324
5.3.3 Fracture Toughness 328

6 Conclusions **342**

6.1 Fabrication . . . 342

6.2 Thermophysical Properties . . . 345

6.3 Mechanical Properties . . . 346

6.4 General Conclusions . . . 347

7 Recommendations for Future Work **349**

Bibliography **351**

A Appendix A: Example Python Code for Sintering Analysis **382**

A.1 Young and Cuttler Initial Stage Sintering . . . 382

A.2 Master Sintering Curve . . . 389

B Appendix B: Thermal-Shock Testing **395**

B.1 Background . . . 395

B.2 Introduction . . . 395

B.3 Results . . . 400

B.4 Discussion . . . 404

B.5 Conclusions . . . 410

C Appendix C: Additional Cermet and Cercer Composites **414**

C.1 Tungsten Coated YSZ . . . 414

C.2 Tungsten Carbide . . . 416

C.3 Surrogate BISO . . . 420

C.4 Power T . . . 428

Vita **431**

List of Tables

1.1 A few relevant properties for composite NTP fuel forms. Mo, W, and Mo30W melting point were determined from [1]. Thermal neutron absorption cross-sections were taken from [2]. 9

2.1 Summary of fuel element materials [3]. 15

2.2 Summary of GE 710 program issues and solutions as summarized by Smith [4]. 21

2.3 Sintering conditions, relative density, and hardness of ZrC fabricated using reactive SPS [5]. 53

2.4 Sintering conditions for W/HfO_2 cermet powders by Tucker et al. [6]. 62

2.5 Fitting parameters for thermal expansion of Mo and W determined by Suh et al. [7]. 76

2.6 Zerilli and Armstrong model parameters for Mo and W determined by Škoro et al. [8]. 87

2.7 Tensile properties of pure Mo tested at 973, 1273, and 1623 K [9]. . . 91

2.8 Typical elastic properties of ZrC at room-temperature compiled by Jackson and Lee [10]. 110

2.9 Room temperature mechanical properties of hot pressed ZrC as reported by Korklan et al. [11] and Feng et al. [12]. 117

2.10 A summary of material properties for UO_2 and YSZ taken from a. [13], b. [14], c. [15], d. [16], e. [17], f. [18], g. [19], h. [20], i. [21], j. [22], k. [23], l. [24], m. [25], and n. [26]. 125

2.11 Fitting parameters for the heat capacity for UO_2 [21]. 126
2.12 Room temperature mechanical properties of UN, HfN and Hf_3N_4. Data was taken from a. [27], b. [28], c. [29], d. [30], e. [31], f. [32], g. [33], h. [34], i. [35], j. [36], k. [37], and l. [38]. 137
2.13 Fitting parameters for the semi-empirical specific heat capacity for UN determined by [39]. 140
2.14 A values for different dispersed particle geometries for the Lewis and Nielsen Semi-Theoretical Model. 155
2.15 ϕ_m values for different geometries for the Lewis and Nielsen Semi-Theoretical Model 155

3.1 Powders, suppliers, particle sizes, and measured densities for the feedstock materials used in cermet fabrication. 164
3.2 Summary of physical properties tested, equipment and techniques used along with the ASTM standard and the tested temperature range. . . 168

4.1 Sintering parameters and density and hardness results for the chemical reduction Mo30W powder taken from [40]. 180
4.2 Elemental Analysis of the four different as received Mo30W powders (wt%). 188
4.3 Characteristics of the four pre-alloyed Mo30W powders. 190
4.4 Final sintering densities, hardness, and open porosity for the powders sintered at 1600°C and 30 MPa for 15 minutes. 191
4.5 Onset and peak displacement temperatures for the CR, BM, and GA Mo30W powders. 198
4.6 Summary of important properties for the as received Stanford Advanced ZrC powder. 201
4.7 Optimum sintering conditions and resultant properties for Mo30W and ZrC matrix materials. 211

4.8 Ideal, envelope, and theoretical densities for the Mo30W cermets fabricated using SPS. 219
4.9 Determined optimum SPS sintering conditions for the Mo30W cermets. 234
4.10 Ideal, envelope, and theoretical densities for the ZrC cercers fabricated using SPS. 242
4.11 Grain size and sample nomenclature for the pure matrix Mo30W and ZrC test samples. The grain size presented for the cermet and cercer materials is the matrix grain size. 242
4.12 Fitting parameters for the CTE of the different cermet and cercer materials. 253
4.13 Empirical Einstein temperature (θ_E) and specific heat capacity constants determined as a fit. Literature values for YSZ [41], and UN [39] are also included. 255
4.14 Room temperature properties of ZrC and Mo30W. 260
4.15 Fitting parameters for Young's modulus, the sheer modulus, and Poisson's ratio for Mo30W and ZrC. 260
4.16 Room temperature tensile properties for wrought W, small grained Mo30W (Mo30W-Sm), and medium grained Mo30W (Mo30W-Md). e_u is the uniform elongation, e_t is the total elongation, YS is the yield strength at 0.02% offset, and UTS is the ultimate tensile strength. . . 265

5.1 Results from linear regression to fit the Hall-Petch relationship for pure Mo, pure W, and Mo30W taken from [40]. 280
5.2 Measured apparent activation energy (nQ) and calculated Q_B grain boundary activation energy and Q_v, volume diffusion limited activation energy. 287
5.3 Apparent activation energies for sintering for the Mo30W and ZrC powders using the Young and Cutler and Master Sintering Curve models. 291

5.4 Apparent activation energies for the cermet materials determined from initial sintering curve analysis. 297
5.5 Apparent activation energies for the cercer materials determined from initial sintering curve analysis. 301
5.6 Calculated YS from Tabor relationship compared to tensile YS for wrought W and as sintered Mo30W small and medium grain size. . . 325
5.7 P values and estimated probability of statistical significance that the room temperature fracture toughness of the cermet and cercer composite materials vary from the pure matrix materials, using the student t-test. 330

B.1 Summary of existing NTP testbeds with the maximum temperature (Max T), flowing hydrogen availability (H_2), and irradiation testing (Irrad) indicated. 397
B.2 Test samples and sintered densities with "C" and "TS" representing samples for characterization and thermal shock testing, respectively. The density of the sintered materials is presented as percent theoretical density (% TD). 399
B.3 Summary of thermal shock testing using SPS. 402

C.1 Sintering conditions and density of the ZrC-WC cercer composites. . 417
C.2 Results of EDS point scan of the BISO paricle. 422

List of Figures

1.1 Schematic of NERVA derived liquid hydrogen NTR engine [42]. . . . 3

1.2 Approximate ISP of an NTP system using H_2 propellant as a function of chamber temperature using Equation 1.1. 5

2.1 Estimated maximum operating conditions for different NTP fuel core materials using data taken from Bhattacharyya [3]. 14

2.2 Diagrams of the 4 tested Rover/NERVA fuel forms taken from Bhattacharyya [3]. 15

2.3 Corrosion rates for various Rover/NERVA fuel forms, illustrating mid-band corrosion [3]. 16

2.4 W-UO_2 fuel elements manufacture by ANL taken from Bhattacharyya [3]. 24

2.5 Mass loss data for ANL W cermet tests at 2500°C taken from Bhattacharyya [3]. 26

2.6 Derived Cermet operating limit from GE710 and ANL experiments taken from Bhattacharyya [3]. 27

2.7 Candidate fuel forms for the USSR CIS program taken from Byattacharyya et al. [3]. 29

2.8 Final porosity and microstructure of ZrC sintered at 600 °C/min to a maximum temperature of a) 2300, b) 2500, c) 2700, and d) 2900 °C, taken from Lanin [43]. 30

2.9 Illustrations for the sintering of a powder compact with a. the initial green body, b. after stage I, c. after stage II., and d. after stage III, taken from Derlet [44]. 33
2.10 Illustration of different mass transport mechanisms during powder consolidation, taken from Derlet [44]. 34
2.11 Densification behavior of pure molybdenum using SPS compared to isothermal sintering using traditional methods taken from [45]. 36
2.12 Normalized grain growth comparing different sintering techniques taken from [45]. 37
2.13 SEM micrographs of pure Mo sintered at 67 MPa using SPS taken from [45]. 38
2.14 Corrected piston travel vs. sintering time for different heating rates at an applied pressure of 67 MPa taken from [45]. 39
2.15 Relative density and hardness of the as sintered Mo for a) various temperatures with a constant hold time of 5 minutes, and b) for various hold times at a constant temperature of 1850°C taken from [46]. . . . 41
2.16 a) the microstructure of pure Mo consolidated using SPS, b) a histogram of the grain size for a sample sintered at 1850°C, c) the average grain size with respect to temperature, and d) the average grain size with respect to time taken from [46]. 42
2.17 Micrographs of pure W powder prior to consolidation taken from [47]. 43
2.18 a) Relative density of W consolidate with SPS with respect to temperature, and b) the relative density for three runs at 60 MPa during sintering [47]. 43
2.19 a) Grain growth with respect to sintering time at 1700 and 1800°C, and b-e), grain coarsening of W microstructure with increasing sintering time taken from [48]. 45
2.20 Densities of mechanically alloyed and pure elemental mixing of Mo and W powders sintered for 6 hours at various temperatures taken from [49]. 46

2.21 An SEM micrograph of the sintered Mo30W alloy taken from [49]. . . 47
2.22 Relative density versus sintering temperature for Mo-30wt % W 1) sintered in using SPS, and 2) sintered in hydrogen taken from [50]. . . 49
2.23 Relative density versus sintering temperature for 1) Mo-10weight % W, 2) Mo-20weight % W, and 3) Mo-30weight%, and pure W taken from [50]. 50
2.24 Hardness variation with sintering temperature for 1) Mo-10wt% W, 2) Mo-20wt% W, and 3) Mo-30wt% W taken from Batienkov et al. [50]. 51
2.25 Micrographs of unspecified Mo-W alloys sintered at a) 1400°C, b) 1600°C, and c) 1800°C taken from Batienkov et al. [50]. 52
2.26 SPS densification curves of ZrC powder as received and for various ball-milling times taken from [51]. 55
2.27 Microstructure of ZrC consolidated using SPS at 2100°C for 3 minutes with an applied pressure of 65 MPa [52]. 56
2.28 Relative density of various ZrC samples produced by SPS and HP under a variety of different conditions taken from Wei et al. [53]. . . . 57
2.29 Densification curves of the hot-pressed ZrC (blue) and SPS ZrC at 1600°C for 60 minutes at 55 MPa taken from Wei et al. [53]. 58
2.30 SEM image of W coated spherical HfO_2 particles taken from Tucker et al. [54]. 60
2.31 SEM micrographs of the polished surface of the W/HfO_2 at a) 40 x and b) 150 x [6]. 63
2.32 W-UO_2 cermets sintered using HIP with a 60vol% fuel loading for angular UO_2 prepared without any powder coating prepared using the binding agent technique developed by Tucker et al. [6]. 64
2.33 W-UO_2 cermets sintered using HIP with a 60vol% fuel loading for spherical UO_2 prepared using the binding agent technique developed by Tucker et al. [6]. 65
2.34 The Mo-W binary phase diagram taken from [1]. 67

2.35 Coefficients of thermal expansion of Mo, W, Ta, and Nb as compiled by Martienssen and Warlimont [55]. 67
2.36 Thermal expansion of Mo and Ta determined from two heating and cooling cycles by Rasor and McClelland [56]. 68
2.37 Thermal expansion of Mo from 1100 to 2100 K, calculated using the change in lattice parameter determined from XRD taken from Edwards et al. [57]. 70
2.38 Volume CTE of pure Mo up to the melting point as compiled by Bodryakov et al. [58]. 71
2.39 Volume CTE of pure W up to the melting point as compiled by Bodryakov et al. [58]. 72
2.40 Molar volume thermal expansion of pure tungsten up to the melting point determined from XRD as measured by Dubrovinsky and Saxena [59]. 73
2.41 Linear thermal expansion of Mo and W determined from push rod dilatometry and XRD compiled by Suh et al. [7]. The dark circles represent values collected using push rod dilatometry by Suh et al. [7], the open circles were calculated from XRD by Waseda et al. [60], the solid line was determined by XRD from Demarquay [61], and the line broken line with dot was determined by XRD from Worthing [62]. . . 74
2.42 Thermal conductivity of Mo, W, Ta, and Nb as compiled by Martienssen and Warlimont [55]. 76
2.43 Thermal conductivity of Mo above 2300 K [63]. 77
2.44 Thermal conductivity of W above 2300 K [63]. 77
2.45 Specific heat capacity of Mo, W, Ta, and Nb as compiled by Martienssen and Warlimont [55]. 78
2.46 Heat capacity of pure Mo up to the melting point from 24 sources compiled by Bodryakov [58]. 79

2.47 Heat capacity of pure W up to the melting point from 24 sources compiled by Bodryakov [64]. 80
2.48 a) Vapor pressure and b) evaporation rate of Mo, W, Ta, and Nb as compiled by Martienssen and Warlimont [55]. 82
2.49 Young's modulus of Mo, W, Ta, and Nb as compiled by Martienssen and Warlimont [55], taken from Tietz and Wilson [65]. 83
2.50 The elastic modulus at elevated temperature for polycrystalline and single crystal W taken from Robinson et al. [66]. 84
2.51 Vickers hardness of W (open triangles) measured by Mutoh et al. [67]. 85
2.52 Tensile strength with respect to test temperature for Mo30W and other Mo alloys [68]. 87
2.53 Mechanical properties of W at elevated temperatures (sample 1) including a) the ultimate tensile strength and b) the yield strength taken from [69]. 88
2.54 a) Elongation and b) compression of pure W (1) and other W alloys (2 and 3) from 773 to 2773 K taken from [69]. 88
2.55 High temperature yield strength data of pure Mo (left) and pure W (right) fitted to the Zerilli and Armstrong BCC plastic deformation model by Škoro et al. [8]. 89
2.56 Yield strength (blue) and total elongation (orange) of pure tungsten tensile tested from room temperature to 1000°C [70]. 91
2.57 Total absorbed energy with respect to test temperature for pure Mo (open circle) determined by Hiraoka et al. [71]. 92
2.58 Yield strength determined from the impact test with respect to test temperature for pure Mo (open circle) determined by Hiraoka et al. [71]. 92
2.59 Temperature dependence of K_{IC} fracture toughness (left) and J_{IC} fracture toughness (right) for pure tungsten (open triangles) and some W-rhenium alloys from Mutoh et al. [67]. 93

2.60 Fractographs collected by Mutoh et al. for W and two W-rhenium alloys for samples fractured up to 1600°C [67]. 95
2.61 Fracture toughness K_Q of pure W and other tungsten alloys up to 800°C [72]. 95
2.62 Zr-C binary phase diagram as assessed by Fernandez-Guillermet [73] and compiled by Jackson and Lee [10]. 96
2.63 Heat capacity of ZrC for various stoichiometries up to 3000°C as compiled by Jackson and Lee [10]. 98
2.64 Specific heat capacity of ZrC as a function of temperature as compiled by Katoh et al. [74]. 99
2.65 Thermal conductivity of ZrC at various stoichiometries as a function of temperature, compiled by Jackson and Lee [10]. 101
2.66 Thermal conductivity of ZrC at room temperature as a function of C/Zr ratio compiled by Jackson and Lee [10]. 103
2.67 Linear coefficient of thermal expansion (CTE) of ZrC with respect to temperature compiled by Jackson and Lee [10]. 104
2.68 CTE of ZrC at 1273 K with respect to the C/Zr ratio compiled by Jackson and Lee [10]. 105
2.69 Thermal expansion and CTE, for two high stoichiometric ZrC powders with measured free carbon compiled by Katoh et al. [74]. 106
2.70 Vapor pressures of C and Zr as a function of temperature as compiled by Jackson and Lee [10]. 107
2.71 Langmuir evaporation rate of ZrC for different stoichiometric ratios at various temperatures as compiled by Jackson and Lee [10]. 108
2.72 Young's Modulus of ZrC as a function of temperature compiled by Jackson and Lee [10]. 110
2.73 Young's modulus at room temperature as a function of the C/Zr ratio compiled by Jackson and Lee [10]. 111

2.74 Indentation hardness of ZrC as a function of temperature, compiled by Jackson and Lee [10]. 112
2.75 Room temperature hardness of ZrC as a function of the C/Zr ratio compiled by Jackson and Lee [10]. 113
2.76 Indentation hardness of single crystal ZrC with respect to test temperature compiled by Katoh et al. [74]. 114
2.77 Variation of indentation hardness of ZrC with respect to the C/Zr ratio including hypo-stoichiometric carbon compiled by Katoh et al. [74]. . 115
2.78 Ultimate Tensile strength of ZrC with various stoichiometries as a function of temperature compiled by Jackson and Lee [10]. 117
2.79 Bend strength of ZrC with respect to temperature, compiled by Jackson and Lee [10]. 118
2.80 Flexural strength of ZrC (open diamonds) along with other transition metal carbides compiled by Demirskyi et al. [75]. [10]. 119
2.81 Compressive yield stress of $ZrC_{0.94}$ from 1200 to 1800°C taken from Darolia and Archbold [76]. 120
2.82 Uranium oxygen phase diagram taken from [17]. 122
2.83 ZrO_2 – $YO_{1.5}$ phase diagram [60] taken from [14]. 123
2.84 Dynamic elastic modulus of YSZ compared with transformation-toughened ZrO_2 [20]. 125
2.85 Heat capacity of UO_2 (solid blue line) from Fink et al. [21], of 7.76 x 10^{-2} mole fraction YSZ (orange line) from Tojo et al. [22], and of 3 mole percent YSZ (green squares) and 8 mole percent YSZ (yellow squares) from Sasaki et al. [77]. 126
2.86 Heat capacity of solid YSZ with various compositions compiled by Xiwen et al. [41]. 127
2.87 Heat capacity of solid UO_2 compiled by Fink et al. [21]. 128
2.88 Heat capacity of UO_2 with the lines representing various models, and the open circles and crosses representing data from Grønvold et al. [78]. 129

2.89 Heat capacity of UO_2 from various sources compiled by Naito et al. [79]. 130
2.90 Thermal conductivity of fully dense UO_2 to 370°C (blue line) [25], a model for UO_2 up to 3000°C (yellow line) , and YSZ samples of 3 (orange squares) and 8 mol % (green circles) YSZ up to 1000°C [26]. . 132
2.91 Thermal diffusivity of UO_2 up to the melting point, taken from [80]. The values at lower temperatures (blue squares) were measured using a laser-flash apparatus (LAF) and the higher temperatures points (blue circles) were measured using continuous wave laser-heating apparatus (CLASH). 133
2.92 Coefficient of thermal expansion for UO_2 [23], and for YSZ of various molar percentages [24]. 134
2.93 Thermal expansion of stoichiometric UO_2 from various sources, compiled by Martin et al. [81]. 135
2.94 Uranium-nitrogen phase diagram taken from [82]. 137
2.95 Hafnium-nitrogen phase diagram taken from [83]. 138
2.96 Computed HfN heat capacity taken from [35]. 140
2.97 High temperature heat capacity taken from [28]. 141
2.98 Thermal conductivity of $HfN_{0.92}$ (blue) [38] and of UN (green) [37]. . 142
2.99 Thermal conductivity of uranium nitride from various studies compiled by Muta et al. [34]. 143
2.100 Unit thermal expansion of $HfN_{0.92}$ (blue) [38], UN (orange) [34], and UN (green) [84]. 144
2.101 Young's modulus of UN with respect to porosity compiled by Muta et al. [34]. 145
2.102 a) and b) SEM images of the indents on the UN samples, c) microhardness of the different materials, and d) the calculated fracture toughness taken from Yang et al. [85]. 147
2.103 CTE versus temperature for Ni, NiCr, NiRe and NiMo binary alloys taken from Pavlovic et al. [86]. 148

2.104Average CTE from 40 to 600°C for Pd-Co alloy as a function of Ag concentration taken from Asoka et al. [87]. 149
2.105Average CTE from 40 to 600°C for Pd-Co alloy as a function of Co concentration taken from Asoka et al. [87]. 150
2.106CTE of W-UO_2 cermets (60vol%) taken from the GE-710 program compared with pure W and pure UO_2 [88]. 156
2.107CTE of stainless-steel-UO_2 cermets from o to 63.5% volume loadings with the Turner and Blackburn models [89]. 158
2.108Fracture toughness of Al_2O_3 with ZrO_2 microspheres dispersed at volume loadings from 0 to 20 % taken from [90]. 160

3.1 The LABOX-675-FC used to consolidate all powders at UTK. 164
3.2 Instron 5900 10 kN loadframe with attached ATR furnace. 169
3.3 SENB from four-point bend testing schematic. 171

4.1 SEM micrograph of the chemical reduction powder taken from [40]. . 177
4.2 Temperature (solid line) and displacement (dashed line) profiles for SPS run to 1600°C with a heating rate of 100°C/min taken from [40]. 178
4.3 EDS map of the as sintered Mo30W material with an insert at higher magnification and resolution taken from [40]. 178
4.4 Densification of the chemical reduction Mo30W powder through SPS by varying a) hold temperature, b) set pressure, and c) hold time at 1600°C for 30 MPa. taken from [40]. 181
4.5 SEM micrographs of Mo30W solidified at 30 MPa at 1400, 1500, 1600, and 1700°C with a hold time of 5 minutes taken from [40]. 183
4.6 Grain size for sintered Mo30W with respect to a) hold temperature and b) sintering pressure taken from [40]. 184
4.7 The grain size aspect ratio a) with respect to set pressure and b) with respect to the hold temperature taken from [40]. 184

4.8 Vickers hardness a) with respect to hold temperature for 10 and 30 MPa and b) cross-sectional hardness with respect to pressure at hold temperatures of 1400, 1500, and 1600°C taken from [40]. 186
4.9 Particle size distribution for the four Mo30W powders. 190
4.10 SEM micrographs of a) the CR (b) BM, c) GA (-325 mesh), and d), GA (-635 mesh) powders. 191
4.11 Powder XRD diffraction patterns for the a) CR, b) BM, c) GA (-325), and d) GA (-635) Mo30W powders. 192
4.12 Backscatter electron images of the etched microstructure of consolidated a) CR, b) BM, c) GA (-325), and d) GA (-635) Mo30W samples sintered at 1600°C and 30 MPa for 15 minutes. 194
4.13 Particle size distribution (solid line) and grain size histograms (filled blue) for the a) CR b) BM c) GA (-325 mesh), and d), GA (-635 mesh) Mo30W powders sintered at 1600°C and 30 MPa for 15 minutes. . . . 195
4.14 Particle size distribution (solid line) and grain size histograms (filled blue) for the a) CR b) BM c) GA (-325 mesh), and d), GA (-635 mesh) Mo30W powders sintered at 1600°C and 30 MPa for 15 minutes. . . . 196
4.15 Corrected displacement rate of the four powders with respect to temperature. Two runs were used for both the CR and BM powders. 198
4.16 Normalized density of Mo30W powder compacts with respect to sintering temperature. 199
4.17 SEM image of the Stanford Advanced ZrC powder 201
4.18 XRD spectra of the as received Stanford Advanced ZrC powder. The ZrC crystal planes are labeled in black, and the only visibly carbon plane is listed in blue. 202
4.19 Lattice parameter of ZrC as a function of the C/Zr ratio as determined by Equation 2.6. The lattice parameter of 4.962 nm equates to a C/Zr ratio of 0.77. 203

4.20 Mass (red curve) and temperature profile (blue dotted line) from the TGA of the ZrC powder up to 1200°C. 203
4.21 SPS vacuum curves for the ZrC powder as a function of temperature for the 1) roughing pump, 2) argon purge, and 3) turbo pump. 205
4.22 Density as a function of sintering temperature for the three different vacuum systems. 206
4.23 Plot of theoretical density (red triangles) and Vickers hardness (blue diamonds) with respect to sintering time for the ZrC powder consolidated using SPS at 1750°C with an applied pressure of 30 MPa. . . . 207
4.24 SEM images of the grain structure of ZrC powder consolidated using SPS at 1750°C with an applied pressure of 30 MPa from 0 to 90 minutes. 208
4.25 Relative density of ZrC prepared by SPS from this study compared with ZrC sintered using SPS and HP taken from Wei et al. [53] . . . 209
4.26 A sintered 40 mm diameter puck of Mo30W. 212
4.27 A sintered 40 mm diameter puck of ZrC. 213
4.28 Surrogate particles coated in the matrix material utilizing the two developed powder coating processes. a. Mo30W coated YSZ, b. Mo30W coated angular HfN, c. Mo30W coated spherical HfN, d. ZrC coated YSZ, e. ZrC coated angular HfN, f. ZrC coated spherical HfN 215
4.29 Attempted coating of spherical HfN particles with the ZrC powder. . 217
4.30 SEM micrographs of the polished cross-sections of Mo30W a. 50vol-YSZ, b. 50vol-HfN (angular), and c. 50vol-HfN (spherical). 219
4.31 XRD spectra for a) Mo30W-70vol-YSZ, b) Mo30W-70vol-HfN-angular, and Mo30W-70vol-HfN-spherical. Mo30W crystal planes are labeled in blue. 220
4.32 SEM image and EDS maps of a Mo30W-40vol-YSZ cermet. 222
4.33 Graphic of a YSZ particle before sintering (left) and after sintering (right) illustrating the particle deformation. 223

4.34 SEM images of the sintered microstructures of Mo30W-YSZ cermets at volume loadings ranging from 30 to 90 % taken at 200X magnification. 224
4.35 SEM images of the sintered microstructures of Mo30W-YSZ cermets at volume loadings ranging from 30 to 90 % taken at 2000X magnification. 225
4.36 Spherical YSZ cermet density with respect to volume loading. 226
4.37 Calculated Mo30W matrix density from the spherical YSZ cermets with respect to volume loading. 226
4.38 EDS map of Mo30W-50vol-HfN cermet sintered at 1600°C and 30 MPa for 15 min. 228
4.39 SEM images of the sintered microstructures of Mo30W-HfN cermets at volume loadings ranging from 30 to 90 % taken at 200X magnification. 229
4.40 SEM images of the sintered microstructures of Mo30W-HfN cermets at volume loadings ranging from 30 to 90 % taken at 2000X magnification. 230
4.41 Angular HfN Cermet density with respect to volume loading. 231
4.42 Calculated Mo30W matrix density from the angular HfN cermets with respect to volume loading. 231
4.43 SEM images of the Mo30W-50vol-HfN (spherical cermet sintered at 1600°C and 30 MPa for 15 minutes. 233
4.44 EDS map of the Mo30W-50vol-HfN (spherical cermet sintered at 1600°C and 30 MPa for 15 minutes. 233
4.45 SEM image and EDS map of the polished cross-sections for ZrC-50vol-YSZ sintered at 1900°C and 30 MPa for 10 minutes. The loss of oxygen is not apparent, but carburization can be seen at the interface and the cracks. 234
4.46 SEM images of the polished cross-sections for ZrC-50vol-YSZ sintered at a) 1900°C and 30 MPa for 10 minutes, b) 1800°C and 30 MPa for 20 minutes, and c) 1800°C and 30 MPa but with a slowed cooling rate of -33°C per minute. 236

4.47 SEM images of the polished cross-sections for ZrC-50vol-HfN sintered at 1800°C and 30 MPa for 20 minutes. 236
4.48 SEM images of the polished cross-sections for ZrC-70vol-HfN sintered at 2000°C and 30 MPa for 20 minutes. Three phases are visible, ZrC (darkest), HfN (lightest), and a Hf,Zr-C,N (medium tone). 237
4.49 XRD spectra for the as sintered Zr,Hf-C,N carbonitride (black), ZrC (red), and HfN (blue). 238
4.50 SEM images of the polished cross-sections for ZrC-20vol-HfN sintered at 1850°C and 30 MPa for 10 minutes taken at two different magnifications. 240
4.51 EDS map of the ZrC-20vol-HfN sintered at 1850°C and 30 MPa for 10 minutes 241
4.52 XRD spectra for a) ZrC-20vol-YSZ, b) ZrC-20vol-HfN-Angular, and c) ZrC-20vol-HfN-Spherical. ZrC crystal planes are labeled in blue. . . . 243
4.53 XRD spectra for Mo30W taken every 50°C up to 1200°C. An insert provides a closer look at the [220] peak. As the temperature increases, the intensity increases and the 2θ shifts decreases. 245
4.54 $\Delta a/a_0$ versus temperature for Mo30W for both an as polished sample and a stress-relieved sample. 246
4.55 Calculated CTE of Mo30W, Mo, and W up to 1400°C. 247
4.56 XRD spectra for ZrC taken at 600, 650, 700, 750, 800, and 1200°C. . 248
4.57 CTE of ZrC with the blue line from this study, the orange line from [74], the green line from Leipold & Nielsen, and red diamonds from Bukatov et al. 249
4.58 $\Delta L/L_0$ from dilatometry data for all the materials tested. 251
4.59 CTE for a) Mo30W and b) Mo30W-YSZ cermets, c) Mo30W-HfN cermets, and d) pure HfN determined from push rod dilatometry. The CTE results from high temperature XRD were also included for pure Mo30W. 252

4.60 CTE for a) ZrC and b) ZrC-HfN cercers determined from push rod dilatometry. The CTE results from high temperature XRD were also included for pure ZrC. 252
4.61 Specific heat capacity determined using calorimetry for a. Mo30W, b. ZrC, C. HfN, d. Mo30W-YSZ cermets, e. Mo30W-HfN cermets, and f. ZrC-HfN Cercer. 253
4.62 Thermal diffusivity from RT to 600°C for a) pure Mo30W for the medium and large grain sized material, b) for the Mo30W-YSZ cermets, and c) for the Mo30W-HfN (angular) cermets. The solid lines with diamond points represent the points taken during heating and the dotted lines and circles represent the points taken during cooling. The standard deviation from the three runs taken at each temperature is also included. 255
4.63 Thermal diffusivity from RT to 600°C for a) pure ZrC for the medium and small grain sized material and b) for the ZrC-HfN angular cermets. The solid lines with diamond points represent the points taken during heating and the dotted lines and circles represent the points taken during cooling. The standard deviation from the three runs taken at each temperature is also included. 257
4.64 Thermal conductivity from RT to 700°C for the large grained (34.9 µm) and medium grained (12.8 µm) Mo30W, compared to that of pure Mo and W [55]. 257
4.65 a) Electrical diffusivity and b) Seebeck coefficient for Mo30W and ZrC measured from 50 to 450°C. The dotted lines represent the measurements taken during the cooling of the specimens. 258
4.66 Elastic modulus, shear modulus, and Poisson's ratio for as SPS Mo30W. The dotted lines are the linear models determined from linear regression. 261

4.67 Elastic modulus, shear modulus, and Poisson's ratio for as SPS ZrC. The dotted lines are the linear models determined from linear regression. 262
4.68 Tensile stress strain curves for the Mo30W Small grained Mo30W. The red curves are for samples tested at 20°C, the offset blue curve is for the sample tested at 400°C, and the offset green curve is for the sample tested at 800°C. 263
4.69 Tensile stress strain curves for the Mo30W Small grained Mo30W. The red curves are for samples tested at 20°C and the offset green curve is for the sample tested at 800°C. 265
4.70 Fracture surfaces for Mo30W tensile specimens tested at room temperature. 266
4.71 The UTS for Mo30W small grain size (blue diamonds) and medium grain size (red triangles) tested at room temperature, 400, and 800°C. 267
4.72 Room temperature fracture toughness determined using SENB for a) Mo30W, Mo30W-YSZ cermets, Mo30W-HfN (angular) cermets, HfN, and YSZ taken from literature and b) ZrC, ZrC-HfN cercers, and HfN. 268
4.73 SEM fractographs of the Mo30W matrix SENB samples tested at 25, 400, and 800°C. 269
4.74 SEM fractographs of the ZrC matrix SENB samples tested at 25, 400, and 800°C. 271
4.75 Room temperature SEM (80% secondary electron and 20% backscatter electron) fractographs of the Mo30W cermets with angular HfN and spherical YSZ particles. 272
4.76 Room temperature SEM (50% secondary electron and 50% backscatter electron) fractographs of the ZrC cercer with angular HfN particles. . 272
4.77 Fracture toughness determined using SENB for a) Mo30W and b) ZrC from 25 to 800°C. 274
4.78 Fracture toughness determined using SENB for Mo30W surrogate cermets at 25, 400, and 800°C. 275

5.1 Vickers hardness a) Vickers hardness versus average grain size for various densities and b) calculated yield strength verse square root of grain size for the Hall-Petch relationship for the sintered chemical reduction powder taken from [40]. 278
5.2 SEM micrographs and a plot of the square of grain size of the sintered Mo30W at 1600°C and 30 MPa for 0.5, 5, 30, and 90 minutes and the linear relationship between the grain size squared and time taken from [40]. 282
5.3 Hardness (inverted red triangles) and grain size (blue diamonds) as a function of sintering time for the chemical reduction Mo30W sintered at 1600°C and 30 MPa. The hardness and grain growth models have also been included, taken from [40]. 284
5.4 Histogram of grain size for Mo30W sintered at 1600°C and 30 MPa for 0.5, 5, 30, and 90 minutes taken from [40]. 284
5.5 Plots of $\ln\left(\frac{d(\Delta L/L_0)/L_0}{dT}\right)$ versus inverse temperature for initial stage sintering of the Mo30W powders. 287
5.6 a) Mean square residuals for Mo30W and b) the collapsed normalized densification curves with Ψ models. 291
5.7 EDS line scan of the MoW-HfN cermet crossing the newly formed interfacial region. 293
5.8 XRD Spectra for the Mo30W-50vol-HfN cermet fitted using a modified Rietveld refinement. 294
5.9 Phase diagram for the Mo-HfN system taken from [91]. 295
5.10 Plots of $\ln\left(\frac{d(\Delta L/L_0)/L_0}{dT}\right)$ versus inverse temperature for initial bulk sintering stage of the Mo30W powders. 297
5.11 Plots of $\ln\left(\frac{d(\Delta L/L_0)/L_0}{dT}\right)$ versus inverse temperature for the initial stage sintering of the CR Mo30W and the cermet materials for volume loadings of 50 and 70%. 298

5.12 Plots of $\ln\left(\frac{d(\Delta L/L_0)/L_0}{dT}\right)$ versus inverse temperature for initial bulk sintering stage of the Mo30W powders. 300
5.13 Plots of $\ln\left(\frac{d(\Delta L/L_0)/L_0}{dT}\right)$ versus inverse temperature for the initial stage sintering of the ZrC and the cercer materials for volume loadings of 10 and 20%. 300
5.14 CTE of Mo30W (medium and large grain size), pure Mo and pure W, taken from Martienssen and Warlimont [55], and the predicted CTE using the Blackburn model. 303
5.15 CTE model fits as a function of volume loading for Mo30W-HfN cermet at 100, 200, 500, and 1000°C. 304
5.16 Mo30W-70vol-HfN (angular) CTE fit to the model derived by Tummalla et al. 305
5.17 CTE model fits as a function of volume loading for Mo30W-YSZ cermet at 50 and 70 vol% at 100, 200, 500, and 1000°C. 306
5.18 Range of predicted Mo30W-YSZ (spherical) CTE using the ROM model as an upper bound and the model derived by Tumala et al. as the lower bound. 308
5.19 Predicted CTE for Mo30W cermets with a) 50 and 70 vol% UO_2 and b) 50 and 70vol% UN. CTE data for UO_2 and UN were taken from Fink et al. [21] and Hayes et al. [92], respectively. The range provided for the predicted UO_2 cermets were bound by the ROM and the model by Tummala et al. The value for the UN cermet was predicted by Tummala et al. [93]. 308
5.20 CTE model fits as a function of volume loading for ZrC-HfN cercer at 100, 200, 500, and 1000°C. 309
5.21 Specific heat capacity of Mo30W compared with pure Mo and W. The ROM model for heat capacity is also plotted. The data for Mo and W comes from [55]. 311

5.22 Specific heat capacity of Mo30W, Mo30W-50vol-YSZ, Mo30W-70vol-YSZ, and YSZ taken from [41]. The ROM models for 50 and 70vol% were also included. 312
5.23 Specific heat capacity of Mo30W, Mo30W-50vol-HfN, Mo30W-70vol-HfN, and HfN. The ROM models for 50 and 70vol% were also included. 313
5.24 Specific heat capacity of ZrC, ZrC-10vol-HfN, ZrC-20vol-HfN, and HfN. The ROM models for 10 and 20vol% were also included. 314
5.25 Predicted heat capacity for a) Mo30W-YSZ cermets, b) Mo30W-HfN cermets, c) ZrC-YSZ cercers, and d) ZrC-HfN cercers. The reference matrix and fuel particle heat capacities are also provided. The UO_2 and UN values were taken from [21] and [39]. 316
5.26 Calculated Lorenz number for Mo30W up to 600°C. 317
5.27 a) through e) the thermal conductivity of Mo30W fitted to Equation 2.20 from 50 to 700°C and f) the relationship between the k value and temperature. 318
5.28 Model fits for the thermal conductivity of the Mo30W-YSZ composites at 100, 200, 400, and 600°C. The upper and lower bounds are represented by the ROM and IROM models, respectively. 320
5.29 Model fits for the thermal conductivity of the a) Mo30W-YSZ and b) Mo30W-HfN cermet composites from 30 to 600°C. The Mo30W-YSZ cermets are fit to the Lewis and Nielsen semi-theoretical model and the Mo30W-HfN is fit to the geometric mean model. 320
5.30 Model fits for the thermal conductivity of the Mo30W-HfN composites at 100, 200, 400, and 600°C. The upper and lower bounds are represented by the ROM and IROM models, respectively. 321
5.31 Predicted thermal conductivity for a) Mo30W-UO_2 and b) Mo30W-UN cermet composites at 50 and 70 vol% from 30 to 600°C. The Mo30W-UO_2 cermet uses Lewis and Nielsen semi-theoretical model and the Mo30W-UN cermet uses the geometric mean model. 323

5.32 Model fits for the thermal conductivity of the ZrC-HfN composites at 100, 200, 400, and 600°C. The upper and lower bounds are represented by the ROM and IROM models, respectively. 323
5.33 Thermal conductivity of the ZrC-HfN angular cercer fit to the ROM model for 10 and 20 % volume loadings. 325
5.34 Predicted thermal conductivity for ZrC-UN cercer composites at 10 and 20 vol% from 30 to 600°C using the series ROM model. 326
5.35 Range of Young's Modulus for a) Mo30W-UO_2, b) Mo30W-UN, and c) ZrC-UN composites as a function of volume loading. The maximum value is the series or ROM model and the minimal value is the parallel or IROM model. 327
5.36 Plot of Fracture toughness versus $d^{-1/2}$ for the Mo30W samples tested at room temperature. 330
5.37 Room temperature fracture toughness of Mo30W with angular HfN cermets fit to various models. 332
5.38 Predicted fracture toughness for Mo30W-UN cermets using the modified simple model. The ROM and IROM model is also included. . . . 334
5.39 Composite backscatter (20%) and secondary electron (80%) SEM micrographs of the fracture surfaces for the Mo30W-YSZ cermet samples with the highest and lowest fracture toughness. As fracture toughness increases, more particles sheared as opposed to debonded. . 335
5.40 Sheared YSZ contribution to fracture toughness of Mo30W-YSZ cermets as a function of the number of sheared particles. The blue diamonds are data taken from the Mo30W-50vol-YSZ and the green circles are data taken from the Mo30W-70vol-YSZ cermets. 336
5.41 Fitted range for the room temperature fracture toughness of Mo30W-YSZ cermets as a function of volume loading. The lower limit is an area reduced model, while the upper limit takes into account the shearing of YSZ particles. 338

5.42 K_{IC} ROM and IROM models fit to the ZrC-HfN cercers tested at room temperature. . . . 339
5.43 Predicted K_{IC} for ZrC-UN cercer at room temperature using the ROM and IROM models. . . . 341

B.1 Thermal shock test setup with graphite insulation. . . . 401
B.2 Backscatter SEM image and EDS maps of the Mo30W-40vol-YSZ, Mo30W-40vol-HfN ZrC-40vol-YSZ, and ZrC-50vol-HfN cross-sections prior to testing. . . . 403
B.3 Diffraction patterns for a) Mo30W-40vol-YSZ, b) Mo30W-40vol-HfN, c) ZrC-40vol-YSZ, and d) ZrC-50vol-HfN. . . . 405
B.4 Temperature (left) and pressure (right) profiles for a) Mo30W-40vol-YSZ, b) Mo30W-40vol-HfN, c) ZrC-40vol-YSZ, and d) ZrC-50vol-HfN. 405
B.5 Images of Mo30W-40vol-YSZ before (left) and after (right) thermal shock testing. . . . 407
B.6 XRD spectra of melted material (blue), Mo2C (red), and Mo30W (orange). . . . 408
B.7 Phase diagram of the Mo-C binary system [94]. . . . 408
B.8 Images of Mo30W-40vol-HfN before (left) and after (right) thermal shock testing. . . . 409
B.9 Images of ZrC-40vol-YSZ before (left) and after (right) thermal shock testing. . . . 411
B.10 Images of ZrC-50vol-HfN before (left) and after (right) thermal shock testing. . . . 412

C.1 Optical images (top) and SEM images (bottom) of the W coated YSZ. 415
C.2 SEM images of the W coated YSZ. . . . 417
C.3 Mo30W cermets with 70 vol% W coated YSZ particles. . . . 417
C.4 SEM images of the as received spherical WC powder. . . . 418
C.5 SEM image of ZrC-50vol-WC sintered at 1850 °C for 10 min. . . . 418

C.6 SEM image of ZrC-50vol-WC sintered at 1900 °C for 20 min. 419
C.7 SEM image of ZrC-20vol-WC sintered at 1850 °C for 5 min. 421
C.8 SEM image of a sectioned BISO particle used for the EDS point scan. 421
C.9 Optical image of the polished Mo30W-50vol-BISO. 422
C.10 SEM images of the polished cross-section of Mo30W-50vol-BISO. . . 423
C.11 Optical image of the polished ZrC-50vol-BISO. 425
C.12 Optical image of the polished ZrC-50vol-BISO. 426
C.13 SEM images of the polished cross-section of ZrC-30vol-BISO. 426
C.14 SEM images of the polished cross-section of ZrC-30vol-BISO. 427
C.15 XRD spectra of the ZrC-30vol-BISO. 427
C.16 Optical image of 6 different ZrC-HfN "T" composites. 429
C.17 Colorized SEM image of a ZrC-HfN "Power T" composite. 430

Nomenclature

°C	Degrees Celsius
a.u.	Arbitrary units
ANL	Argonne National Laboratory
Ar	Argon
BM	Ball-milling or ball-milled
C	Carbon
C_P	Specific heat capacity
cercer	ceramic-ceramic fuel
cermet	ceramic-metallic fuel
CR	Chemical Reduction
CTE	Coefficient of Thermal Expanison
DBTT	Ductile to brittle transition temperature
DC	Direct Current
DM	Dynamic modulus
e_t	Total elongation

e_u	Uniform elongation
EDS	Energy Dispersive XRay Spectroscopy
GA	Gas Atomized
H_2	Hydrogen
HALEU	High assay low enriched uranium
HEU	High enriched uranium
HfN	Hafnium nitride
HIP	Hot Isostatic Pressing
HP	Hot Pressing
HTXRD	High temperature XRay diffraction
IAMM	Institute for Advanced Materials & Manufacturing
IROM	Inverse Rule of mixtures
K	Kelvin
LSM	Least Squares Method
min	minute(s)
MiNES	Materials in Nuclear Energy Systems
Mo	Molybdenum
Mo30W	Molybdenum 30 weight percent tungsten
NASA	National Aeronautics and Space Administration
NETS	Nuclear and Emerging Technologies in Space

NTP	Nuclear Thermal Propulsion
ODS	Oxide dispersion strengthened
ORNL	Oak Ridge National Laboratory
PECS	Pulsed electric current sintering
PID	Proportional integral differential controller
ROM	Rule of mixtures
RT	Room Temperature
s	second(s)
SAM	Stanford Advanced Materials
SEM	Scanning electron microscopy
SENB	Single-Edge Notched Bending
SNP	Space Nuclear Propulsion
SPS	Spark Plasma Sintering
TC	Thermal Conductivity
TD	Theoretical Density
TD	Theoretical density
TD	Thermal Diffusivity
TGA	Thermogravimetric Analysis
TMS	The Minerals, Metals, and Materials Society
UC	Uranium carbide

UN	Uranium nitride
UO_2	uranium dioxide
UTK	The University of Tennessee – Knoxville
UTK	The University of Tennessee–Knoxville
W	Tungsten
XRD	X-ray diffraction
YSZ	Yttria stabilized zirconium
Zr	zirconium
ZrC	Zirconium carbide
ZrO_2	zirconium dioxide

Chapter 1

Introduction

1.1 Background

Over the past seventy years, nuclear thermal propulsion (NTP) has been examined as an alternative to chemical rockets for in space propulsion, especially for crewed missions. Currently, there is significant interest in developing an NTP system for use for a crewed mission to Mars. One of the greatest challenges in developing these systems is to identify fuel and matrix materials that are capable of withstanding the extremely detrimental environment related to NTP. Several different materials have been considered for use in NTP with varying levels of success. Any material that will be used will have to be rigorously tested under a variety of extreme conditions that are highly detrimental to most materials. Additionally, the thermophysical properties of these materials up to just below their melting points need to be well understood in order to ensure a safe and functioning design. Moreover, current NASA designs call for the use of high assay low enriched uranium (HALEU) in place of high enriched uranium (HEU) [95].

This thesis will discuss the fundamental synthesis and testing of two different NTP particle composite fuel forms. In both options, the fuel will be a high temperature ceramic (UO_2, UN or UC/UC_2) that may or may not be encased in a "BISO" or

"TRISO"-style containment, which is then suspended in a high temperature matrix. One of the composite fuel systems is a refractory metal matrix with a ceramic particulate fuel known as a ceramic-metallic (cermet) fuel. The matrix will consist of a molybdenum (Mo)–tungsten (W) alloy. The other composite fuel form is a ceramic matrix and ceramic particulate fuel form known as a ceramic-ceramic (cercer) fuel, with zirconium carbide (ZrC) acting as the matrix material. To ease in fabrication and testing, a variety of non-radioactive oxide and nitride fuel surrogate particles were used in place of the uranium-based fuels.

1.2 NTP Operating Conditions and Material Requirements

Nuclear thermal propulsion (NTP) is an in-space propulsion system with good promise for crewed missions to Mars [96, 97, 98]. A solid core NTP system generates thrust in a similar matter to chemical propulsion. The primary difference is that the power is derived using nuclear fission as opposed to traditional combustion. In its simplest form, NTP consists of a nuclear reactor core, turbopump system, and nozzle, as shown in Figure 1.1. Heat is generated in the reactor core, and cryogenic hydrogen (H_2) stored in tanks is pumped into the reactor and heated. The heated hydrogen is then expelled from the reactor and expanded out of a nozzle to generate thrust. Rocket efficiency can be described using specific impulse (Isp) that takes into account both energy and mass of the system/fuel. The higher the Isp, the more efficient the propulsion system. Efficiency of the system is directly related to the outlet temperature of the hydrogen, with a greater efficiency as temperature increases. This maximum temperature is limited by the fuel core materials due to melting point and hydrogen compatibility considerations.

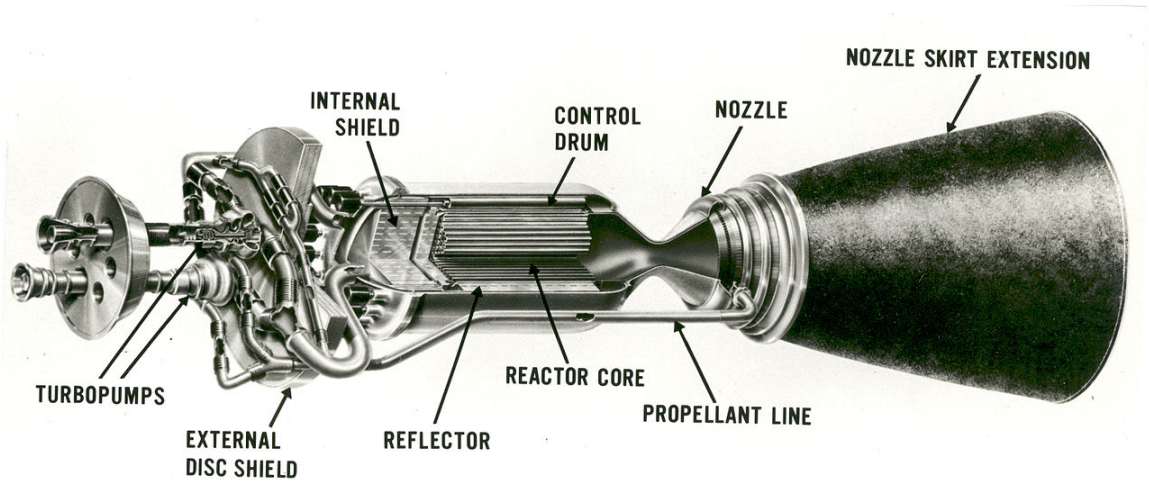


Figure 1.1: Schematic of NERVA derived liquid hydrogen NTR engine [42].

The efficiency of rocket engines is measured using Isp. This is a measure of how efficiently the propellant is used to generate thrust. A simplified equation that is often used that depends solely on the thermodynamic properties of the propellant and on the chamber temperature is presented in Equation 1.1 [99].

$$Isp = \frac{1}{g_c}\sqrt{\frac{2\gamma}{\gamma - 1}\frac{R}{M_W}T_c\left[1 - \left(\frac{P_e}{P_c}\right)^{\frac{\gamma-1}{\gamma}}\right]} \tag{1.1}$$

where g_c is a conversion factor, γ is the ratio of constant pressure heat capacity to constant volume heat capacity, R is the universal gas constant, M_W is the molecular weight of the propellant, T_C is the chamber temperature, P_e is the exit pressure and P_c is the chamber pressure. Using H_2 as the propellant, the approximate Isp as a function of chamber temperature is shown in Figure 1.2. Current design goals for reference NTP systems is 900 s, which corresponds to a maximum chamber temperature of 2700 K [95, 100]. Current chemical engines typically have an Isp around 450 s, which is half of the set goal for NTP.

The combination of high thrust and Isp allows for larger mission abort windows, increased cargo and science capacity, and a decrease in total launch mass. More importantly, NTP can shorten Mars transit times. Current opposition-class missions will last between 160 and 180 days [101]. Shortening transit times is especially important for crewed missions, as deep space provides an inhospitable environment to humans from the exposure to microgravity and cosmic radiation. However, achieving these high Isp values requires the hydrogen outlet temperatures to be $\geq$ 2700 K, which places severe temperature and hydrogen corrosion demands on the core matrix and fuel materials.

Between 1955 and 1972, the nuclear engine for rocket vehicle application (NERVA)/Rover program designed, built, and tested twenty full-scale reactors [101]. These reactors focused primarily on UC_2 particles suspended in a graphite matrix, but also tested a (U,Zr)C, graphite composite and a (U,Zr)C solid solution fuel elements. The fuel element geometry consisted of solid sections with coolant channels for the H_2

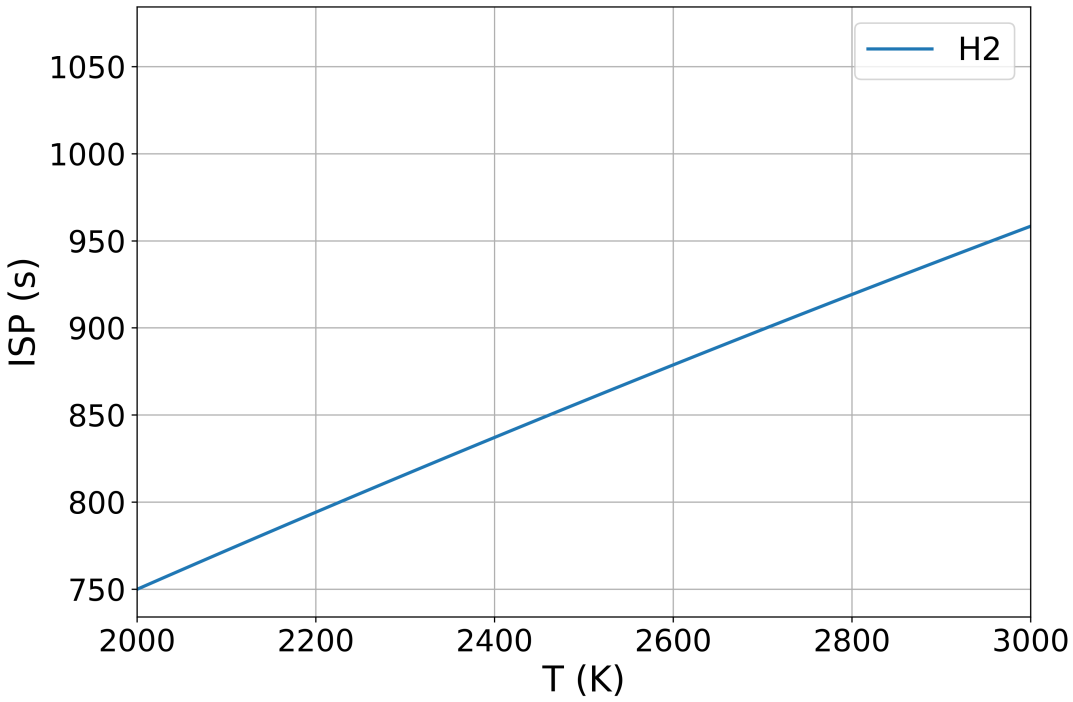


Figure 1.2: Approximate ISP of an NTP system using H_2 propellant as a function of chamber temperature using Equation 1.1.

flow. The SNTP program looked at a particle bed reactor (PBR) with UC_2 particles coated with a layer of low density graphite, a layer of high density graphite, and an outer ZrC layer in a TRISO-like manner. The Russian CIS program analyzed coated ternary carbides consisting of uranium, zirconium, and niobium, typically in a twisted ribbon geometry. Finally, both the US and Soviet Union tested ceramic oxide fuel particles (UO_2 suspended in a refractory metal matrix, called cermet fuels [3].

NTP creates a very difficult environment for all materials involved, especially those in the fuel core. The fuel element has to endure the harshest environment, with exposure to hot hydrogen, irradiation, temperatures up to 3000 K, thermal transients, and large thermal stresses. Moreover, current opposition mission designs call for multiple burns for acceleration and deceleration as well as course corrections totaling 3 hours of total run time [102]. The fuel has to be capable of surviving this environment [103]. The desired attributes of NTP fuel materials are provided in the following list.

1. High temperature compatibility (2500 – 3000+ K)
2. Low neutron absorption cross-section
3. High thermal conductivity
4. Compatibility with hot flowing hydrogen
5. Compatibility with uranium compound (UO_2 or UN)
6. Machinability/Fabricability
7. Resistance to radiation over a wide range of temperatures
8. Resistance to thermal shock during startup and shutdown

1.3 NTP Fuel Manufacturing Techniques

High temperature materials, namely refractory metals and refractory carbides (a ceramic consisting of a binary mixture of a refractory metal and carbon) are more difficult to fabricate due to their high melting point and difficulty in machining. By applying a significant pressure, powder can be consolidated into a solid material at temperatures below the melting point, such as with Hot Isostatic Pressing (HIP). Pulsed electric current sintering (PECS) also known as spark plasma sintering (SPS) is another technique to consolidate powders into solid materials [104]. SPS uses a pulsed direct current (DC) to heat the powder. With an applied uniaxial load, the powder will consolidate. SPS is able to fabricate materials at lower temperatures, applied pressures, and for shorter times compared with other powder consolidation techniques. Additionally, SPS allows for the fabrication of more complicated geometries. Finally, SPS can allow for greater control on final sintered material properties compared with other similar techniques. Further discussion into the benefits of SPS are discussed later in Chapter 2.

1.4 Cermet and Cercer Fuel Forms

Cermet fuels have high promise as the fuel core for solid nuclear thermal rockets [101]. Cermets consist of ceramic fuel particles made from either uranium dioxide (UO_2) or uranium nitride (UN) randomly dispersed in a refractory metal matrix. Cermets have the potential to survive the harsh environment of the NTP fuel core because of their fission product retention, resistance to thermal shock, hydrogen compatibility, corrosion resistance, high thermal conductivity, and high temperature strength [98, 105]. Currently, Mo and W are two of the best candidates due to their hydrogen compatibility, high melting points, high thermal conductivity, and availability [106, 107].

While both Mo and W cermets have been considered, both materials have issues with current programs. Ideally, a cermet fuel core utilizing pure W would produce the highest Isp with a large factor of safety, due to the high melting point of W of 3,422 °C. However, W is incredibly dense, and would increase the mass and corresponding launch costs from Earth. Additionally, with the current interest to switch from HEU to HALEU for a variety of logistic and safeguards and security considerations, the high parasitic thermal neutron absorption of W creates a neutronics issue [108, 100]. Mo has much lower parasitic neutron absorption and has been considered as a replacement for the W metal matrix [109, 110, 98]. However, for the current desired Isp of at least 900s, pure Mo has too low of a melting point (2623 °C) to provide the desired margin of safety. Mo30W offers a compromise of melting point with good neutronic properties and is the cermet matrix that will be considered for this study. Table 1.1 contains a summary of a few relevant properties for the refractory matrix materials previously discussed [111].

Cercer fuel forms are also being considered. Ceramic fuels have potential advantages compared to refractory metal-based fuels, particularly due to an increase in melting point of the matrix material. Additionally, ceramic fuels have the potential for improved neutronics and hydrogen resistance. Both the US NTP program and Russian CIS programs focused heavily on the development of ceramic based fuels. The Russian CIS program especially reported success in producing, shaping, and testing of mixed carbide [3]. The current program is focusing heavily on zirconium carbide (ZrC) as the matrix material, due to its high melting point, low neutron absorption cross-section, and high thermal conductivity for a ceramic material [112, 113]. Oxide, nitride, and carbide fuel particles are being considered, as well as a solid solution carbide and carbonitride. Properties of ZrC are also summarized in Table 1.1.

Table 1.1: A few relevant properties for composite NTP fuel forms. Mo, W, and Mo30W melting point were determined from [1]. Thermal neutron absorption cross-sections were taken from [2].

Property	Mo	W	Mo30W	ZrC
Melting Point (°C)	2623	3422	2740	3530
Thermal Neutron Absorption Cross-section (barn)*	2.51	18.4	5.42	0.1
Thermal Conductivity (W/mK)	142	175	∼60	6 - 12

1.5 Research Objectives

The primary objective for this research is to lay the groundwork for the development of two particle based fuel forms for NTP, the cermet and the cercer. Surrogate particles were used in place of uranium containing particles to allow for the use of equipment not compatible with radiological material. The experimental aspect of this work focused on three primary areas, listed below.

1. Fabrication of surrogate cermet and cercer composites
2. Thermophysical property measurements
3. Mechanical testing

The first stage was to optimize and understand the fabrication of the cermet and cercer materials using SPS. Extensive sintering studies were first conducted to understand the densification of the pure matrix materials. Then a new powder coating technique was developed, and finally, the sintering of the cermet and cercer composites was optimized.

The material properties of the cermet and cercer materials need to be understood and well documented, to aid in the design of NTP systems. Currently, NASA is completing a material property handbook to document these different properties. The coefficient of thermal expansion (CTE), specific heat capacity (C_P), thermal diffusivity (TD), and dynamic modulus (DM) will all be determined for the matrix materials and the cermet and cercer composites. For the equipment available, these properties were measured from room temperature up to 1000 °C.

The final experimental aspect of this thesis is mechanical properties testing up to 800 °C. These include tensile testing (for the pure metal matrix), compression, and single edge notched bending (SENB).

This thesis focuses primarily on understanding the effect that the surrogate particles have on the sintering and thermophysical properties of the cermet and cercer. Two different hypotheses, which are listed below, were tested.

1. The surrogate particles will aid in the sintering of the matrix material.

2. The surrogate particles will affect the thermophysical properties predictably with relation to the particle geometry and volume loading.

In discussing the sintering of the cermet and cercers, a majority of the consolidation will occur in the matrix powders, as the surrogate particles are already mostly densified. Ideally, the particles will be completely surrounded by the matrix material and will not touch each other. Constant Rate Heating (CRH) experiments tested the densification mechanism of the matrix materials both with and without the surrogate particles, resulting in apparent activation energies for sintering. From this understanding, ideal sintering conditions can be predicted for cermet and cercers with actual uranium ceramic particles loaded.

For the second hypothesis, thermophysical property data was collected through thermal properties testing, hardness, tensile, compression, and SENB testing. Different volume loadings were tested for each surrogate particle material and geometry. From these experiments, the effect of particle loading and geometry were understood and used as a predictive model to determine properties for uranium containing compounds of various fuel loadings.

The final goal of this thesis is to first understand how the composite materials sinter and to understand how the different types of surrogate particles affect the thermophysical and mechanical properties of the composites. From this information, predictive models will be made that predict the different properties for composites with uranium ceramic particles in place of the surrogate particles.

Chapter 2

Literature Review

An extensive literature review was conducted to understand different material options for NTP. Legacy NTP materials were first considered. A review was also conducted on the sintering of refractory metals, carbides, and composite materials using SPS. Additionally, the thermal and mechanical properties of zirconium carbide and molybdenum and tungsten were also reviewed. Different surrogate materials were also compared to their uranium-based analogs. Finally, existing models for the thermophysical and mechanical properties of particle composites were also examined.

2.1 Legacy NTP Fuel Systems

There are three primary options for NTP materials. The first is carbon-based materials. These include graphite, carbon-composite, and mixed carbide fuels; for all of these carbon-based materials, a robust impermeable surface coating is required to inhibit hydrogen reactions with carbon. These carbon-based fuel systems experienced some limited success in the Rover/NERVA program, but the inherent incompatibility with hydrogen make them a less desirable selection. Another option is the ceramic metallic (cermet) fuel, consisting of ceramic fuel particles suspended in a refractory metal matrix. These materials were tested heavily in the laboratory scale, but a full-scale system was never built and tested. The estimated maximum

operating conditions are illustrated in Figure 2.1, but these ranges, especially for the mixed carbide, are extrapolated based on limiting testing and therefore have large uncertainties [3].

Only three basic classes of materials have melting points high enough to be considered for use in an NTP fuel core. These include graphite, refractory metals, and carbides/ceramics. All three material options have been tested to some extent through various programs starting in the 1950's [103]. Table 2.1. includes a summary of the major NTP fuel element programs for the US and USSR/Russia.

2.1.1 Graphite (Rover/NERVA)

The Rover/NERVA program, which began in 1955, represented the largest effort to develop NTP. The program developed several different fuel forms and led to the building and testing of 20 full-scale NTP systems [3, 98, 3, 114]. The primary fuel form of interest for Rover/NERVA was carbide fuel particles suspended in a graphite matrix [98, 115].

Rover/NERVA developed four different fuel forms as shown in Figure 2.2. The first form consisted of uranium carbide (UC_2) particles dispersed in a graphite matrix, known as bead loaded graphite. The surface exposed to hydrogen was coated with NbC. The failure resulted from cracks forming due to both the build up of fission gas as well as a local decrease in thermal conductivity [3, 116].

Pyrolytic carbon coating on the fuel particles was also later used to prevent fissile fuel loss and better hold the UC_2 in the graphite matrix [3]. It was also used to prevent the oxidation of the UC_2 kernels during processing and fabrication [42].

Post operation analysis of the fuel elements found significant mass loss in both the mid-band region (or the center of the fuel element where temperatures are not at the maximum) and near the nozzle chamber where temperatures were the hottest, as illustrated in the top curve of Figure 2.3 [3, 114].

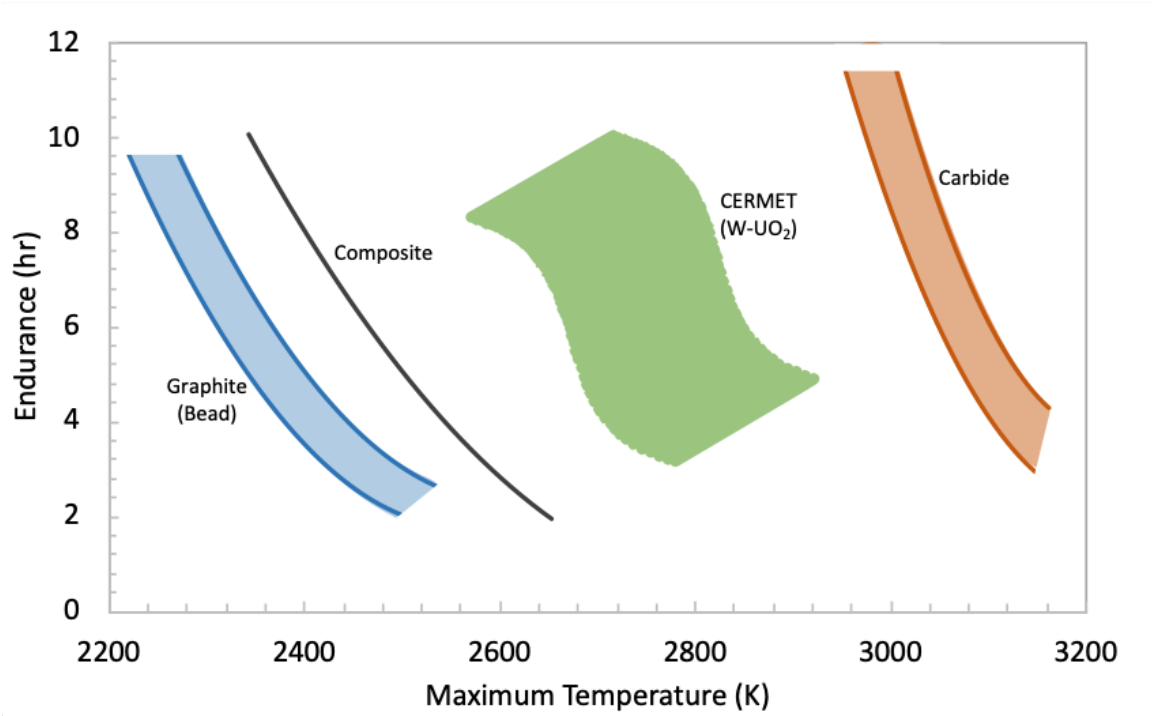


Figure 2.1: Estimated maximum operating conditions for different NTP fuel core materials using data taken from Bhattacharyya [3].

Table 2.1: Summary of fuel element materials [3].

Program	Fuel Composition	Fuel Geometry
Rover/NERVA	UC_2 in graphite (U,Zr) C, graphite composite (U,Zr) C, solid solution	Solid prismatic rod elements with coolant channels
SNTP (PBR)	Coated UC_2 Binary, ternary carbides	Particle
CIS (USSR)	Coated (U, Zr, Nb) C (Other ternary carbides) Carbonitrides	Twisted Ribbon
Cermet	UO_2 in W	Solid blocks with cooling channels

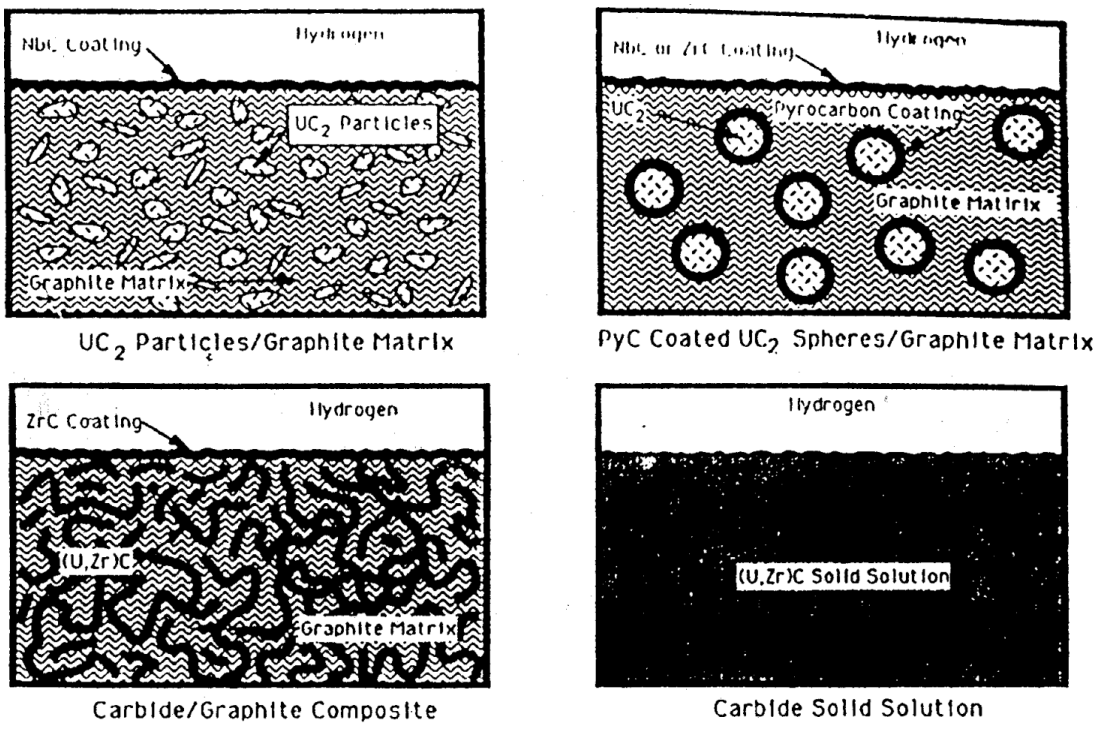


Figure 2.2: Diagrams of the 4 tested Rover/NERVA fuel forms taken from Bhattacharyya [3].

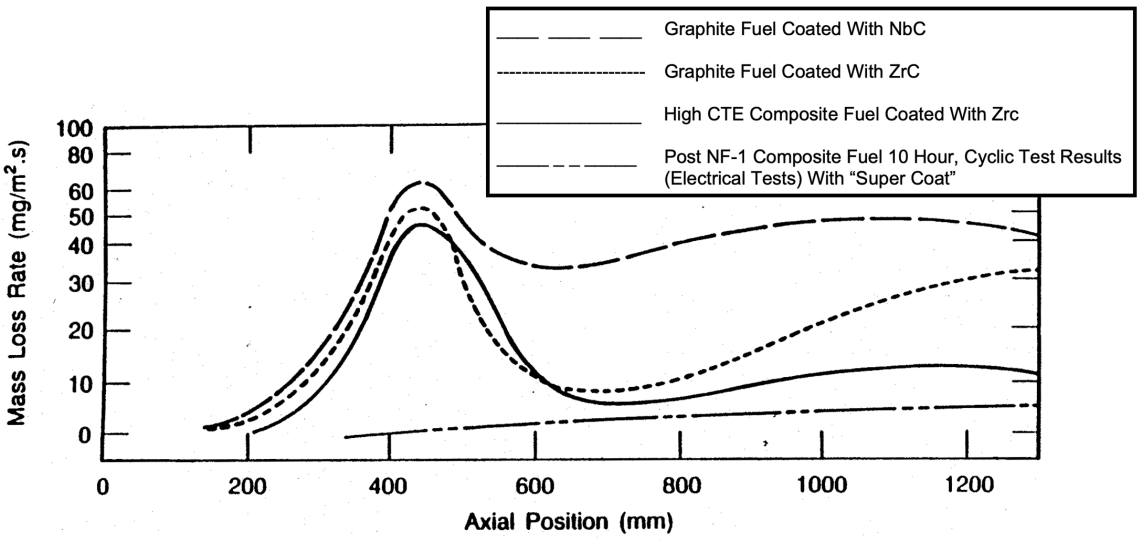


Figure 2.3: Corrosion rates for various Rover/NERVA fuel forms, illustrating mid-band corrosion [3].

Mid-band corrosion for Rover/NERVA fuels were one of the most significant materials challenges. It was found to have several causes. First, it resulted from cracking of the coating caused by the mismatch in the coefficient of thermal expansion between the NbC coating (7 x 10^{-6} K^{-1}) compared to the graphite (3 x 10^{-6} K^{-1}) [3]. Second, most materials experience a transition from brittle to ductile deformation at a certain temperature. In the mid-band region, just above the center line, a vast majority of the coating is still operating in the brittle regime where it is more prove to cracking under thermal stresses. At higher temperatures, the coating is more ductile and resistant to cracking. The third cause of mid-band corrosion was the high-power density and neutron flux in that region of the core. This resulted in the highest fuel element temperature gradients, which resulted in large thermal stresses. Also, since the high power density was correlated to the high neutron flux and fission rate, the highest levels of irradiation damage to the fuel elements occurred in this region [117]. The result of the cracking was exposure of the graphite matrix to hydrogen and significant corrosion [3, 114].

Mid-band corrosion for the Rover bead loaded graphite systems was mitigated by switching from NbC cladding to zirconium carbide (ZrC) cladding. The ZrC not only had a slightly better CTE match with the graphite, but also prevent fission product diffusion that resulted in embrittlement. The result of the cladding change can be seen in Figure 2.3. Not only did the ZrC cladding perform a little better in the mid-band region, but it also performed significantly better in the high temperature region. Still, corrosion was higher than desired.

Graphite as a fuel form had several additional advantages, as listed below [103].

1. Weak neutron absorption
2. Good neutron moderation
3. Good high temperature compressive strength
4. High thermal conductivity

5. Good compatibility with uranium ceramics

6. Low density (reduced reactor mass)

However, despite these advantages, the inherent incompatibility of the graphite with the hot flowing hydrogen leads to an inherently unsafe design completely dependent upon the cladding material.

Based on the test data from the Rover/NERVA program, NTP endurance (or the maximum expected time and temperature each fuel element material was expected to last) lifetimes with given operating temperatures were approximated. Figure 2.1 illustrates these conclusions.

2.1.2 Refractory Metal Cermets

Ceramic Metallic (cermet) fuel form consists of ceramic fuel particles, namely uranium dioxide (UO_2) or uranium nitride (UN) suspended in a refractory metal matrix. Refractory metals refer to the d block metallic elements of tungsten, molybdenum, niobium, tantalum, and rhenium, which are characterized by their high melting point and resistance to wear. Cermets were considered a viable option for NTP systems due to their fission product retention, resistance to thermal shock, hydrogen compatibility, corrosion resistance, high thermal conductivity, and high strength [106, 98, 105].

The use of refractory materials for nuclear power applications was first considered in the 1940's. Two programs tested cermets in the 1960's. Cermet fuels were tested in both the GE-710 and the Argonne National Laboratory (ANL) programs [118, 119]. Both focused primarily on tungsten (W) UO_2 cermets. W was chosen for the matrix due to its high melting point. Tantalum (Ta) and molybdenum (Mo) were also considered, but known oxygen migration in Ta and the lower melting point of Mo excluded these materials from the initial program [120].

The two programs had four major outcomes. The first was the optimization of fabrication of UO_2 and UN based cermet fuels. These fuels underwent both steady-state and thermal cycling non-nuclear hot H_2 testing to temperatures up to 3000 K.

Steady state irradiation tests occurred up to 2000 K and up to U burnups of 1.6 a/o. Finally, transient nuclear testing occurred with heating rates up to 16000 K/s and temperatures of 2900 K [3]. The programs were canceled before any prototypic cermet NTP reactors could be built and tested.

One limit for interparticle spacing between the cermets is associated with potential fission fragment damage to the metal matrix. 60 vol% UO_2 seems to be a good balance between high fuel load and interparticle spacing. Cermet fuel particles are typically around 100 µm in diameter. This size is large enough to also minimize the fission fragment damage to the metal matrix without causing a temperature spike in the fuel particle (due to the low thermal conductivity of the particle in relation to the metal matrix). Porosity is also introduced to the cermet to allow for fission gas retention, though due to the relatively low burnup of an NTP system, this is a smaller concern [121].

The GE-710 program ran from 1962 to 1968 as an offshoot to the aircraft nuclear propulsion program. The program originally called for an NTP system that could operate at 2750 K for 100 thermal cycles to a longer lived system that could operate for 10,000 hours in the range of 2000-2250 K range [118]. The program considered both closed cycle systems for power generation and open cycle systems for propulsion [122]. Due to the focus on long life systems, testing occurred at temperatures between 2000 – 2250 K. Even though these temperatures are low for NTP requirements, information on failure mechanisms were determined [3, 107].

Most of the early work was spent on fuel fabrication. Powder metallurgy processes along with sintering were used to fabricate the UO_2 cermet hexagonal wafers for both W and Mo matrix.

The GE-710 program included several out-of-pile thermal cycling and life tests [118]. W-25Re clad (W-UO_2-ThO_2) cermets were exposed to hot flowing hydrogen at 3270 K for one hour, 3180 K for three hours, and 3070 K for ten hours for two cycles. These results yielded no leaking and no apparent macroscopic failure. Another test with the same material at 2865 K for 50 hours found the same result. W-UO_2-ThO_2

cermets with W-Re-Mo clad were also tested for up to 51 cycles for over 500 hours from 2420 to 530 K and also found no leaks. Early hot hydrogen testing saw difficulties with U precipitation due to lack of stoichiometric control of the UO_2. The addition of the ThO_2 added stoichiometric stability and demonstrated success [3, 118]. The mechanism of U precipitation will be discussed in the fissile fuel section.

Post-test microstructural characterization occurred for all of these tests. The W-25Re clad (W-UO_2-ThO_2) cermets were found to be exceptionally stable up to 3270 K. At 3270 K a few samples experienced loss of bonding for the fuel-cladding. Further examination did not find any melting of the UO_2 fuel, but did find fuel deposition at the cladding interface. Due to the high volatility of UO_2 at 3270 K, it was able to transport via the vapor phase to the interface. Examination of the cladding did not find any porosity. It was still single phase, though it experienced grain growth typical of high temperature annealing. Cracking was found in the fuel component of all the specimens tested, but this may have been caused by the sectioning of the samples that took place after the tests. Pulse-echo inspection before the sectioning found no issues of incomplete bonding to the surface.

The GE-710 program performed three different steady-state irradiation experiments. They occurred at the ETR at INEL, and the Low Intensity Test Reactor (LITR) and Oak Ridge Research Reactor (ORR) at Oak Ridge National Laboratory (ORNL). W and W-Re matrix cermets with 60 volume% (vol%) ThO_2 stabilized UO_2 were tested with Ta, Ta-10W, W-30Re-30Mo and W-25Re-3Mo cladding. From the hydrogen and irradiation testing of the cermet fuel elements, several failure mechanisms were determined and resolved. Table 2.2 summarizes these mechanisms [4].

In the first experiment, all of the Ta clad samples experienced leaking. The leaks were caused by the formation of sub-stoichiometric UO_2. Free uranium was then able to penetrate the cladding wall during subsequent thermal cycling. The mechanism for this loss is described in the fissile fuel section. Since the issue only occurred in the Ta cladded alloys, it was discovered that Ta is relatively transparent to oxygen at

Table 2.2: Summary of GE 710 program issues and solutions as summarized by Smith [4].

Fuel Failure Mode	Mechanism	Solution
Loss of oxygen	Ta cladding oxygen transparency	Used W instead
Volumetric expansion and cracking	Coefficient of thermal expansion mismatch	Used W alloyed with Re and Mo-Re
Void formation	Insufficient autoclaving	W alloys to improve ductility
Fission product release	Building up pressure, dislocation weakness	Sinter to 84% theoretical density
Vaporization of Mo in cladding	Vapor pressure of Mo significant above 2470 K	Problem not solved

high temperatures and became embrittled with the oxygen. The removal of Ta from the cladding resolved this issue [3, 118, 4].

Another failure mechanism was cracking of the W-UO_2 fuel matrix caused by the volume expansion of the UO_2 particles after significant thermal cycling. This volume expansion was caused by the thermal coefficient mismatch between W and UO_2 at high temperatures. After multiple thermal cycles, the fuel particles begin to pull apart from the W matrix. One tested solution was to alloy tungsten with Re or with Mo-Re to better match CTEs. Another was to use UN instead of UO_2. Once again, this occurred after significant thermal cycling, greater than expected for a crewed NTP mission [3].

Another observed issue was the formation of voids between the cermet fuel and the alloy "can" cladding during fabrication and early operation. This was caused by difficulties in getting a good seal between the two components. It was resolved using electron beam welding and would likely be easily resolved today due to advances in high temperature materials manufacturing [3].

Several samples experienced fission product damage and release after 4000 hours of operation between 1870 and 2270 K. This release occurred in samples sintered to 95% or higher theoretical density. Fission product damage to the cermet and eventually to cladding material is caused by accumulated buildup of pressure, lattice stresses, and dislocation weaknesses inherent in fuel materials under irradiation. The fission products could then diffuse out of the sample or would cause embrittlement. To resolve this issue, samples were sintered to 84% theoretical density. The internal porosity present in these low-density sintered products created sinks for the fission products to diffuse to without the buildup of stresses in the cermets. Testing of the 84% theoretical density cermets saw a factor of 10 increase in allowable burnup [3].

Yet another fuel failure mode occurred after 4000 to 7500 hours operating at 1870-2270 K when fission products were released in specimens sintered to 95% or greater theoretical density. Fission product damage to the cermet/clad led to the formation of small surface blisters that were caused by the accumulated buildup of pressure,

lattice stress inherent in the fuel materials under irradiation. To resolve this issue, samples were sintered to only 84% theoretical density to avoid stresses above the tungsten matrix capacity at high temperatures. This led to the samples surviving a burnup a factor of 10 greater than saw failure with the highly sintered samples [3].

For most of the fuel failure modes discussed previously and listed in Table 2.2, solutions were developed that resolved the problem. It is important to note that a majority of the issues occurred in testing to burnups significantly higher than what would be expected for a crewed NTP mission. Overall, the GE 710 program proved the viability of cermets for use in NTP. Unfortunately, the program ended before any prototypical systems could be built and tested.

Another cermet based NTP program was conducted at Argonne National Laboratory (ANL) between 1960 and 1966. W matrix cermets with gadolinia stabilized UO_2 fuel were the primary cermets tested. Samples were tested in out of pile hydrogen loops and in-pile pulse testing [3].

Despite difficulties in manufacturing refractory metals, namely tungsten, the ANL program was able to manufacture numerous samples using powder metallurgy processes and cold isostatic pressing followed by sintering at 1950 K. Cladding was deposited in the cooling channels using chemical vapor deposition. Large samples were successfully manufactured up to 50 cm long as shown in Figure 2.4.

Like with the GE 710 program, several out-of-pile thermal cycling tests were performed. W-UO_2 cermets were tested in hot flowing hydrogen up to 2770 K. Only minimal fuel loss was observed for up to 45 hours and 180 cycles. In pile testing occurred in the TREAT reactor at INL. The highest temperature reached was 3023 K with a ramp rate of 16,000 K/s. Only one failure occurred during these tests that was later attributed to issues with manufacturing. One specimen in particular survived eight transients at high temperature with a peak temperature of 2900 K.

Samples were tested to higher burnups and more thermal cycles than would ever be used in an NTP mission. They found that both the W and W-Re-Mo based cermets would contain fission products until burnup significantly higher than would

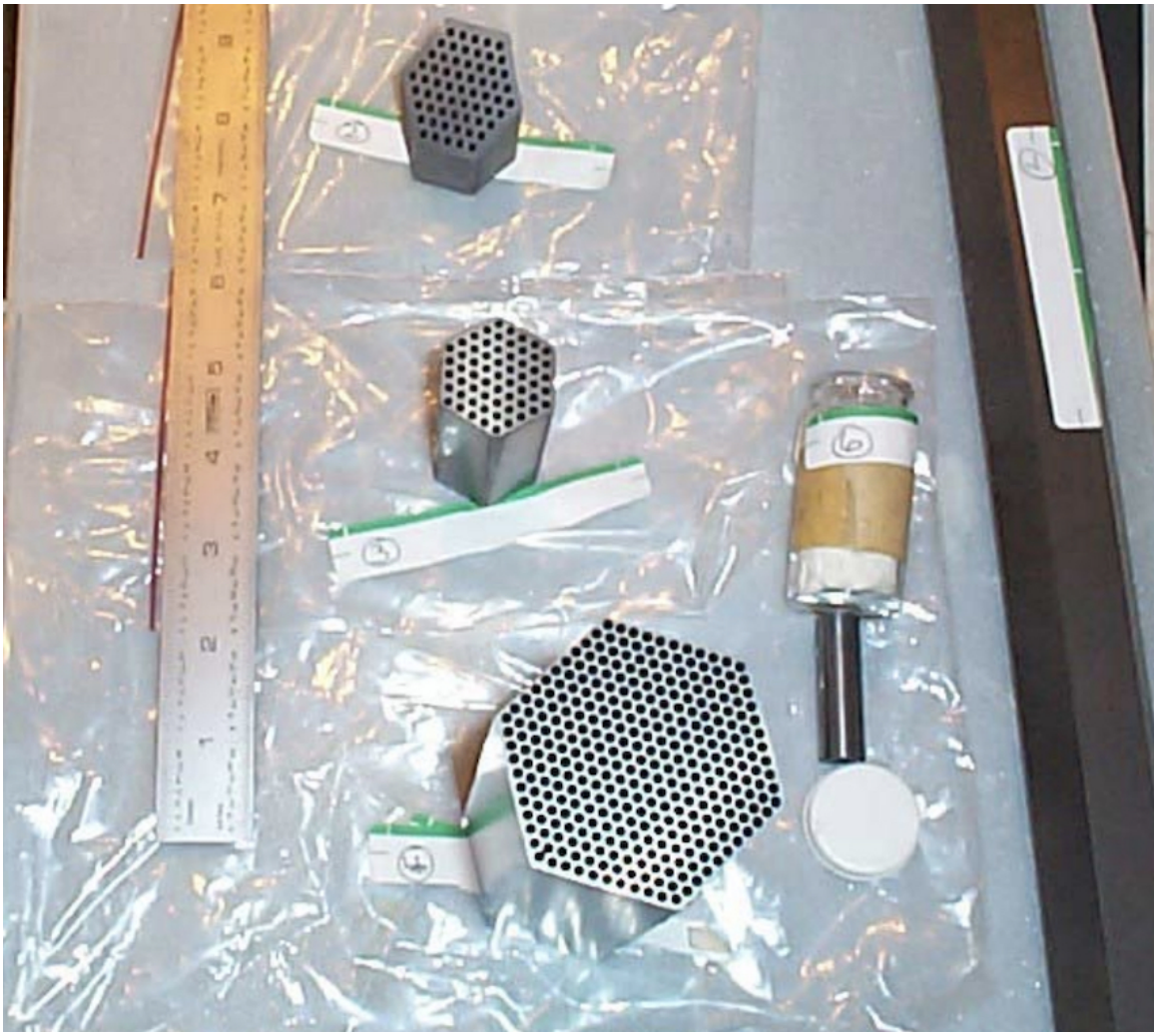


Figure 2.4: W-UO_2 fuel elements manufacture by ANL taken from Bhattacharyya [3].

be used in an NTP mission. Also, during hydrogen thermal cycling, it was found that the samples would experience less than 1.0 % fuel loss up to around 200 cycles equating to 50 hours at temperature as seen in Figure 2.5 [3].

Combining the data and lessons learned from the GE 710 and ANL programs, suggested operating conditions for W based cermet fuel were determined as shown in Figure 2.6.

The final results of the GE-710 program focused primarily on longer lifetime, lower temperature systems. Because of this, efforts were made to improve matrix ductility to handle significant thermal cycling and to improve the cladding-matrix interface. Moreover, by increasing the porosity of the matrix material, more void space was available to hold fission products released from the high burn up of the fuel. Current designs will not require high burn up of the fuel and will require significantly less thermal cycling (4-5). For this reason, the desired microstructural properties of current systems will differ. The matrix will still need to contain the uranium ceramic particles in the matrix and withstand the thermal stresses generated from CTE mismatch.

The primary failure mechanisms in the ANL programs resulted in issues with fabrication, compared to failure of higher quality test specimens. It was determined that the fabrication of the samples into near net shape was beneficial to prevent needed machining and potential weakening of the materials.

2.1.3 Carbides and Ceramic Matrix Fuels

In addition to the prismatic graphite fuel, the Rover/NERVA program attempted to to further improve corrosion resistance by considering two other fuel forms, tested in the NERVA NF-1 system [114]. A carbide/graphite composite and the carbide solid solution form both used uranium zirconium carbides as seen in the bottom two images in Figure 2.2 [114]. The composite consisted of (U, Zr) C-graphite composite fuel elements with a carbide volume fraction of 30-35%. These had significantly higher

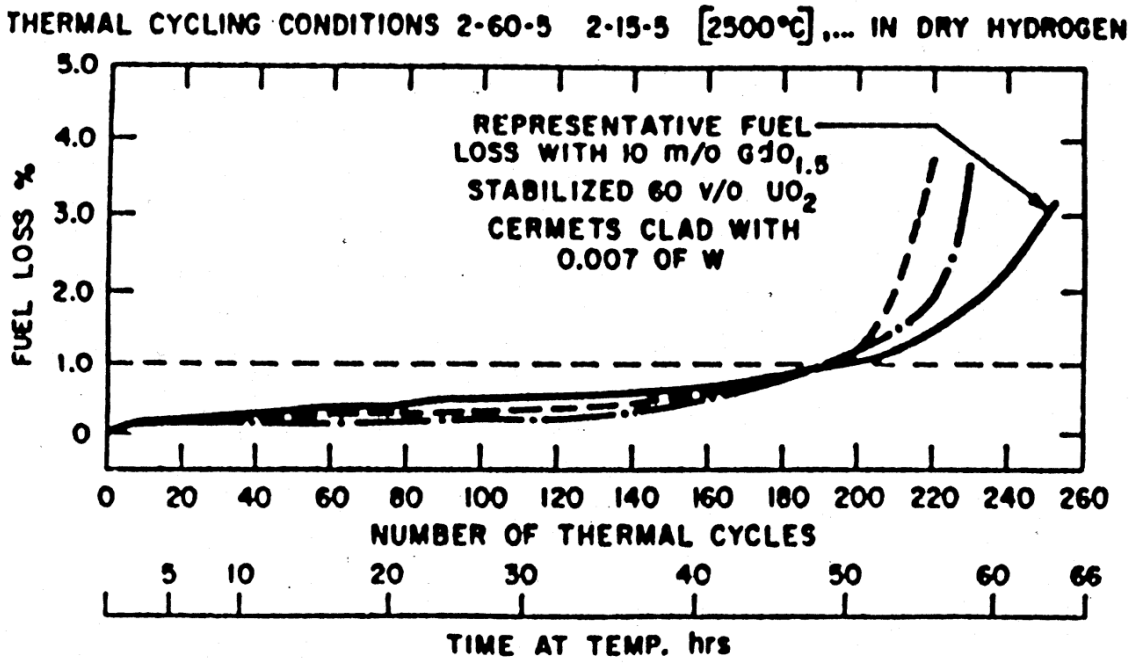


Figure 2.5: Mass loss data for ANL W cermet tests at 2500°C taken from Bhattacharyya [3].

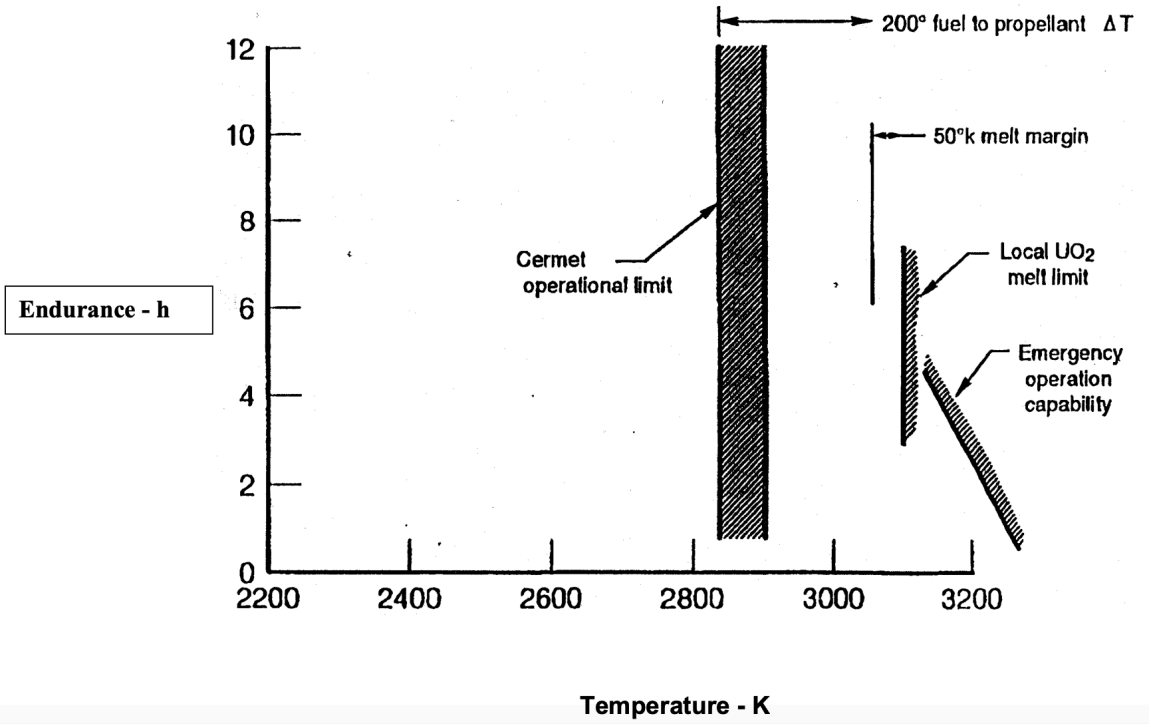


Figure 2.6: Derived Cermet operating limit from GE710 and ANL experiments taken from Bhattacharyya [3].

thermal expansion coefficients that closely matched the ZrC cladding. It improved corrosion resistance in both the mid-band and high temperature regions with the graphite bead fuels as seen in Figure 2.5., though still suffered significant mass loss in the mad-band region. The composite also experienced inferior irradiation resistance as it began to breakdown under the intense flux [42, 123].

The Carbide element utilized single phase (U, Zr) C fuel. This material had the highest melting point and therefore the highest potential for NTP. It was introduced late in the NERVA program, so it experienced only limited development [42, 114]. Analysis of the NF-1 experiments did yield significant corrosion and serious cracking, however, it was postulated that the issues were exacerbated due to poor manufacturing of the fuel elements [114].

Both the US and the USSR considered solid solution carbide and ceramic matrix fuels for NTP. The USSR CIS program considered carbides, carbonitrides, and cermet carbonitrides [3]. A summary of the tested fuels as well as the maximum operating temperature is summarized in Figure 2.7.

Ceramics are known for their difficulty in processing and machining, primarily due to their high operating temperature. The processing of ceramic materials was described by Lanin et al. was described to follow 5 steps [124]. The first two focus on powder synthesis and preparation, followed by the formation of the green body, then high temperature sintering. The final step involves process quality. The sintering stage is one of the most crucial steps for the development of high quality NTP materials [43]. The final properties of ZrC are heavily dependent on the porosity, which in turn is dependent upon the sintering conditions.

High speed sintering was used to produce ZrC from a powder green body [43]. Fast heating (600 °C/min) and temperatures above 2300 °C were used to achieve samples with porosity below 7%. Figure 2.8 contains the microstructure of ZrC consolidated using several high-speed sintering runs. At lower maximum temperatures, the porosity remained high, but the grain size was kept low at (7 µm for 2500 °C). In order to reduce the porosity, the sintering temperature was raised to 2900 °C, resulting in

Table 3.3.1
Candidate Fuels Listed by CIS

Fuel Type		Uranium Content (density g/cm^3)	Maximum Operating Temperature, K	Technology Status
Carbides	(U, Zr) C,C (U, Zr) C (U, Zr, Nb) C (U, Zr, Ta) C	≤ 2.5	2500 3300 3500 3700	Highest Intermediate
Carbonitrides	(U, Zr) C,N	6-8	3100	
Cermet (carbonitride)	(U, Zr) C,N-W	≤ 6.5	2900	Lowest

Intermediate

Figure 2.7: Candidate fuel forms for the USSR CIS program taken from Byattacharyya et al. [3].

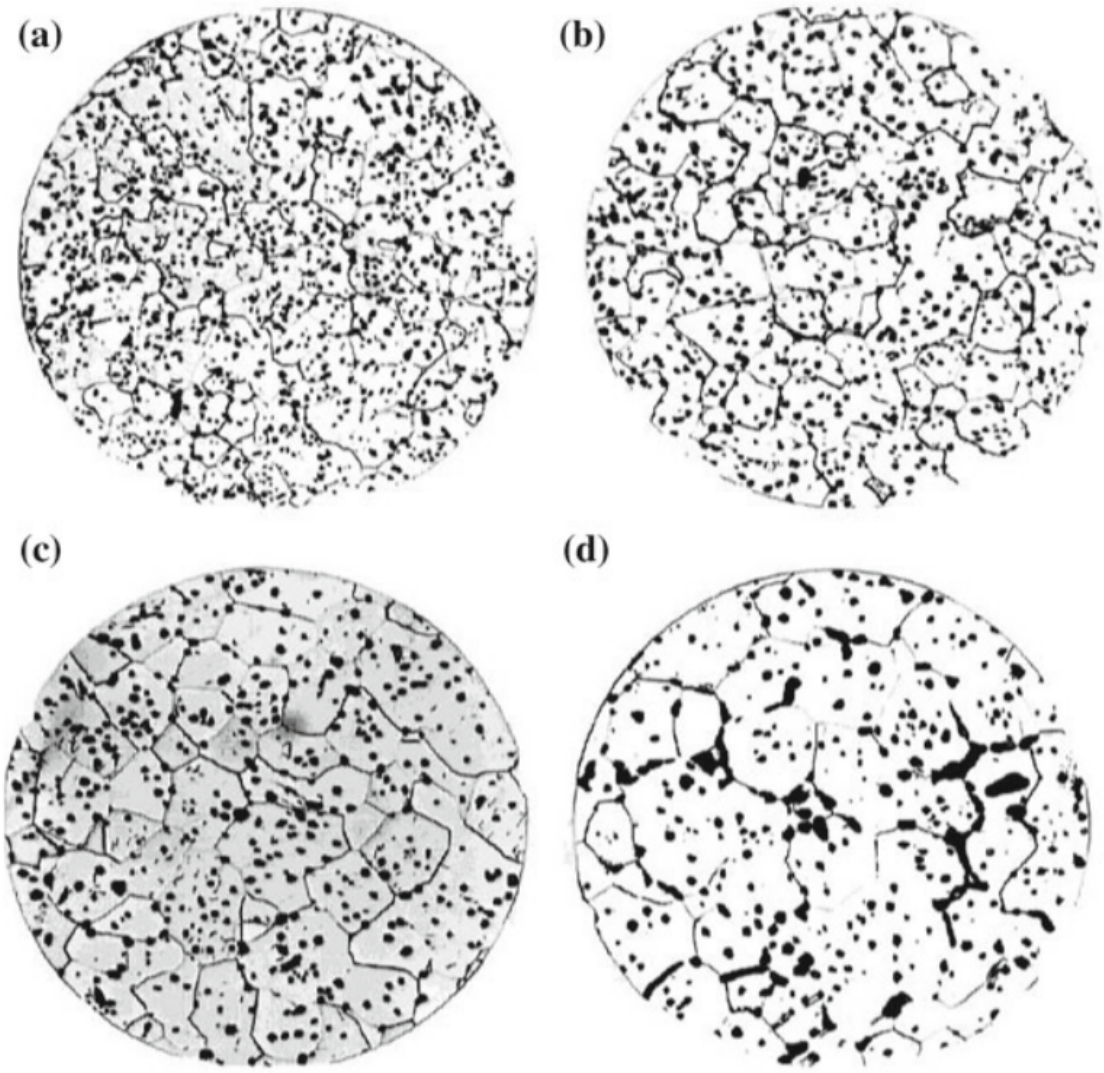


Figure 2.8: Final porosity and microstructure of ZrC sintered at 600 °C/min to a maximum temperature of a) 2300, b) 2500, c) 2700, and d) 2900 °C, taken from Lanin [43].

a 30 µm grain size, despite the short sintering time. While low porosity ZrC was achieved, the equipment needed to produce these high temperatures is rare. Other methods of powder consolidation will need to be applied.

2.2 Spark Plasma Sintering

2.2.1 SPS Background

SPS is an alternative sintering process that uses an electric current to aid in the sintering processes. It is also known as the Field Assisted Sintering Technique (FAST) and Pulsed Electric Current Sintering (PECS). Compared with traditional sintering techniques, such as hot pressing, a lower applied pressure, lower maximum hold temperature, and shorter sintering times are required. This leads to improved mechanical properties [104]. SPS allows for greater control over the microstructural development of the material undergoing sintering. In order to sinter a sample using SPS, a powder is first loaded into a graphite die, which is then placed in a vacuum chamber. Hydraulic rams exert an uniaxial pressure and the sample is heated when a pulsed DC current is run through the sample utilizing Joule heating.

The electric field created during SPS operations increases diffusion mass transfer within the material in question [104]. Asoka-Kumar et al. proposed that the field increases the vacancy concentration in the material, which then acts to increase diffusion [87]. Munir et al. experimented further using positron annihilation spectroscopy to show that the application of a DC current could decrease the activation energy for defect mobility by 24 % [104]. This accounts for the reduced sintering time and temperature requirements using SPS.

2.2.2 Effect of Control Parameters

Another benefit to using SPS is the increased control over a variety of parameters. Firstly, particle selection, namely size, geometry, and purity, and sample preparation

can have a significant effect on the final sintered material. During SPS, the heating rate, applied pressure, maximum hold temperature, hold time at maximum temperature, and vacuum/atmosphere can all play a role in the consolidation of the powder.

Sintering occurs in three different stages, initial, intermediate, and final. The initial stage starts when adjacent particles begin to bond and form interconnected necks. The intermediate stage represents the maximum densification and is where the porous and solid stage become interconnected. The final stage of sintering the solid stage becomes completed interconnected and the pores begin to close. A majority of the microstructural evolution occurs during this final stage [125]. Figure 2.9 illustrates these different sintering stages.

The sintering process is dependent upon the mass transport of the material during the deformation process. Several diffusion mechanisms will play a role, though, typically one will dominate for a specific material under different sintering conditions [126]. Figure 2.10 illustrates the different diffusion mechanisms responsible for driving sintering.

2.2.3 Sintering of Refractory Metals and Alloys

SPS is a useful method for the sintering of high temperature materials, such as refractory metals and alloys. Both molybdenum and tungsten powders have been consolidated using SPS [45, 47, 46]. A wide range of sintering conditions and powder types have been analyzed. When compared with more traditional sintering techniques, materials sintered using SPS showed comparable or higher density with lower applied pressures and shorter sintering times. A selection of these experiments will be discussed.

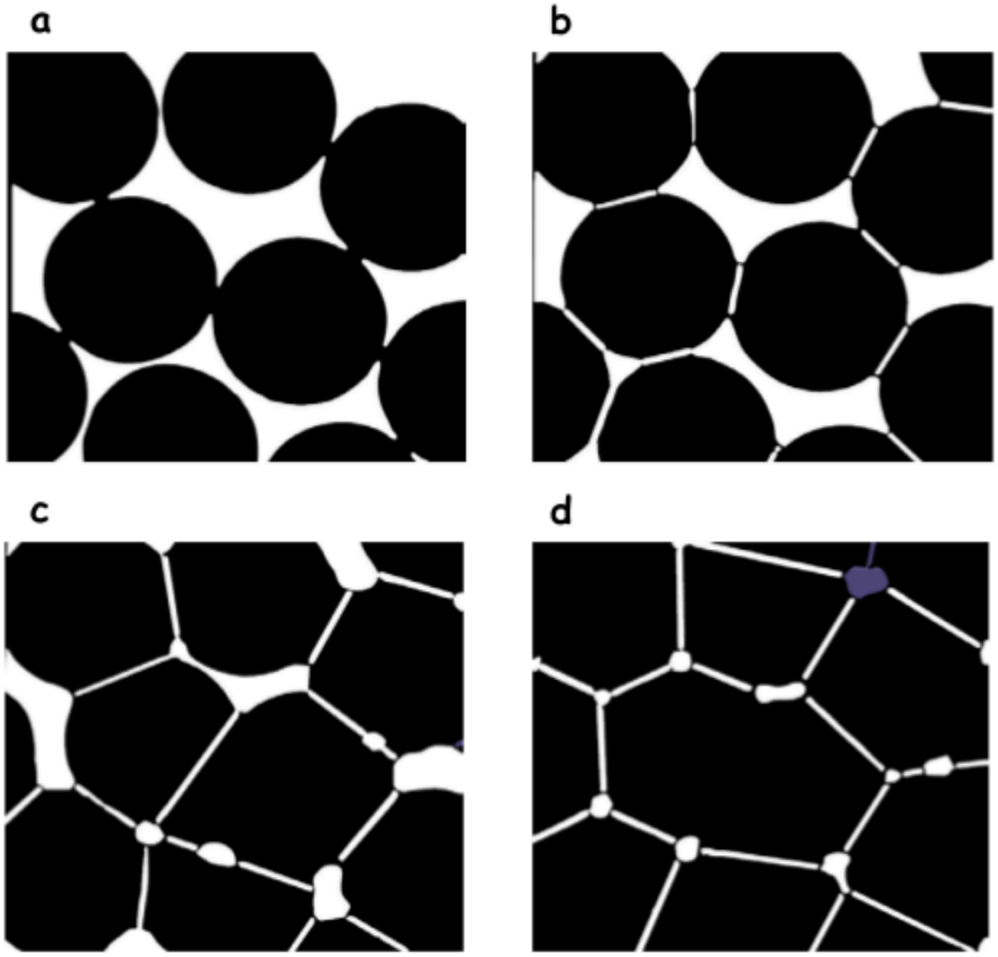


Figure 2.9: Illustrations for the sintering of a powder compact with a. the initial green body, b. after stage I, c. after stage II., and d. after stage III, taken from Derlet [44].

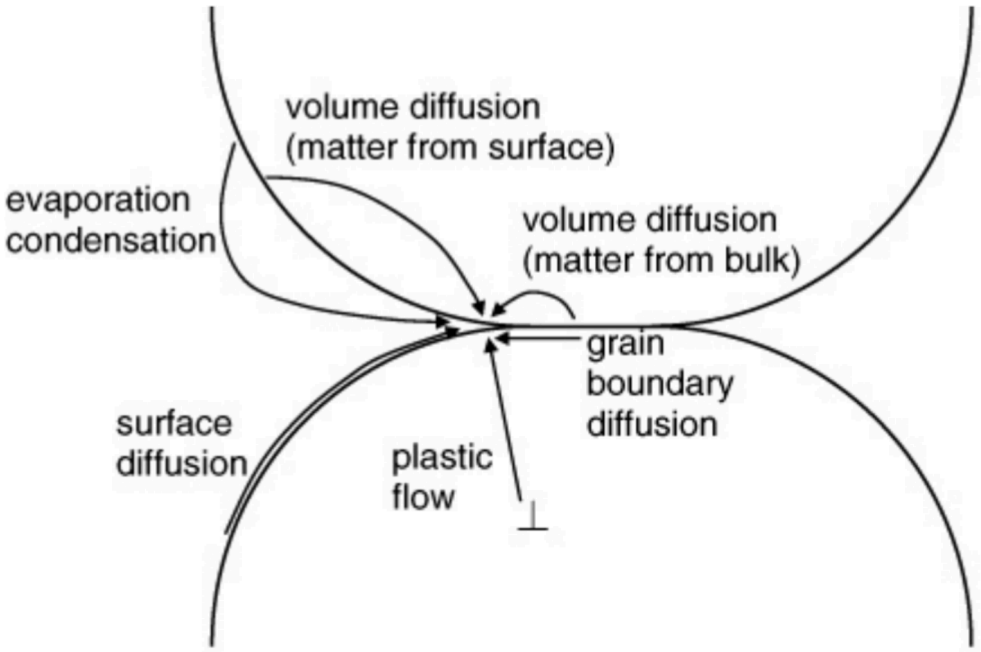


Figure 2.10: Illustration of different mass transport mechanisms during powder consolidation, taken from Derlet [44].

Since the alloy of interest is primarily Mo, prior studies of the sintering of pure Mo are of relevance. One study by Ohser-Wiedemann et al. used powder with 3-5 µm particle diameters [45]. Applied pressures of 29, 57, and 67 MPa, sintering temperatures between 850 and 2000°C, and heating rates from 130 to 360 K/min were all examined. Densification results from this study are shown in Figure 2.11. The sintering was conducted using SPS and compared with isothermal sintering. Below 1400°C, samples experienced relatively low densification, even at higher pressures. Above 1400°C, densities reached 90 % for all pressures.

According to the data in Figure 2.11, there is very little difference in density between the 57 and 67 MPa applied pressure. There is a noticeable decrease in density for the 29 MPa pressures. The grain size increases exponentially with temperature, as would be expected, for a hold time of three minutes. There was also a noticeable decrease in grain growth for the SPS fabricated samples compared with the isothermal sintering samples, as seen in the right plot of Figure 2.12. The microstructure of the sintered Mo is captured in micrographs in Figure 2.13. At lower temperatures, below 1400°C, significant porosity remains after sintering. Above 1400°C, the open porosity closes. Grain growth also increases drastically above 1600°C, with little increase in density.

This study found that most of the shrinkage and consolidation occurs during the rapid heating, or stage II sintering. Instead of using the standard three stage sintering model, Ohser-Wiedemann et al. used a 4 stage sintering model laid out by Zhaohui et al., where an additional rearrangement stage was added prior to stage I sintering [127]. this includes the first three stages of sintering. Very little densification occurred during the final stage and isothermal hold. These stages are illustrated in the corrected piston travel of the sintering of Mo in Figure 2.14. This study did not look at the effect of vacuum pressure on the final density.

Another study by Mouawad et al. looked at the consolidation of Mo using SPS with the primary goal of achieving a fully densified matrix [46]. Pressure was held constant at 67 MPa. They also used a rapid heating rate of 700 K/min for all sintering

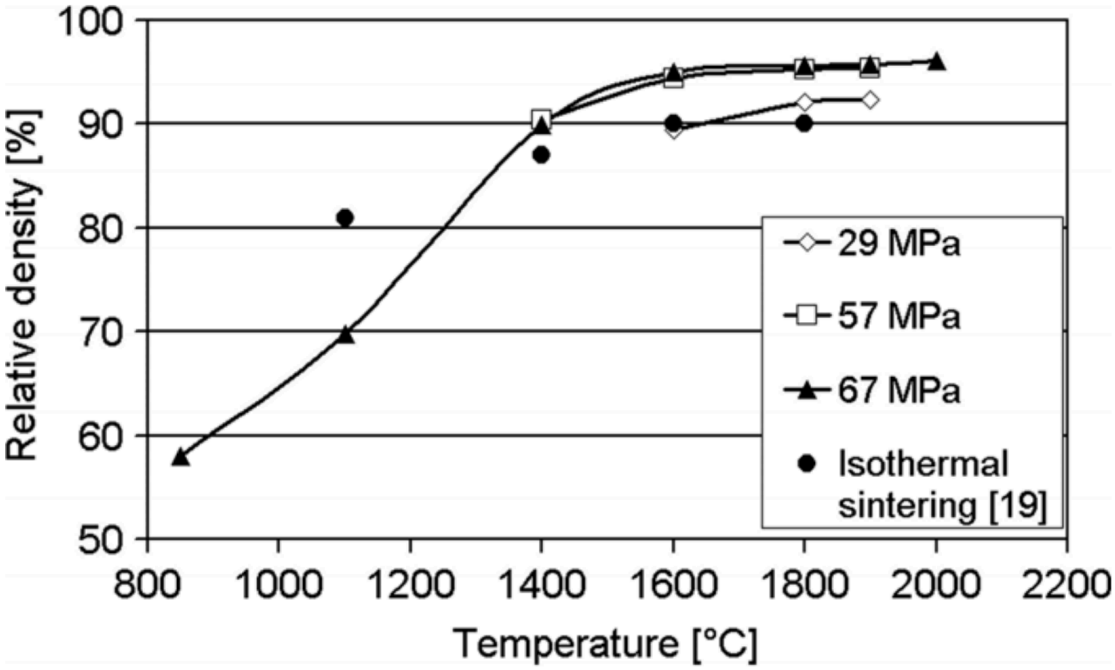


Figure 2.11: Densification behavior of pure molybdenum using SPS compared to isothermal sintering using traditional methods taken from [45].

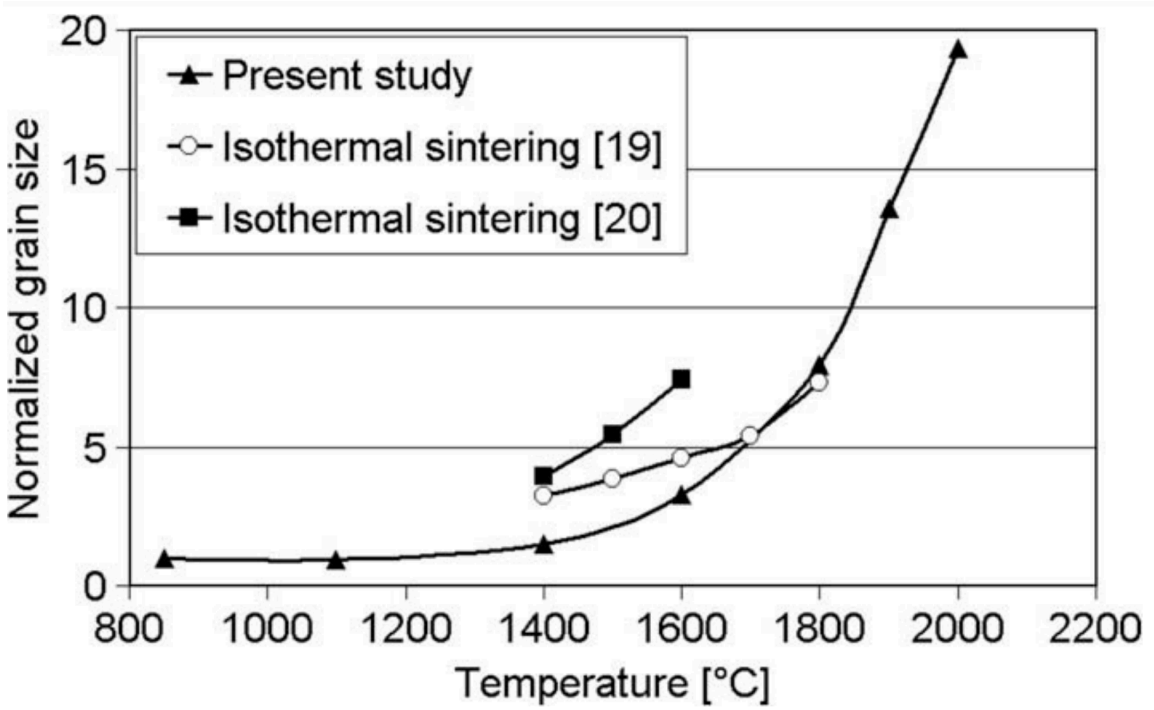


Figure 2.12: Normalized grain growth comparing different sintering techniques taken from [45].

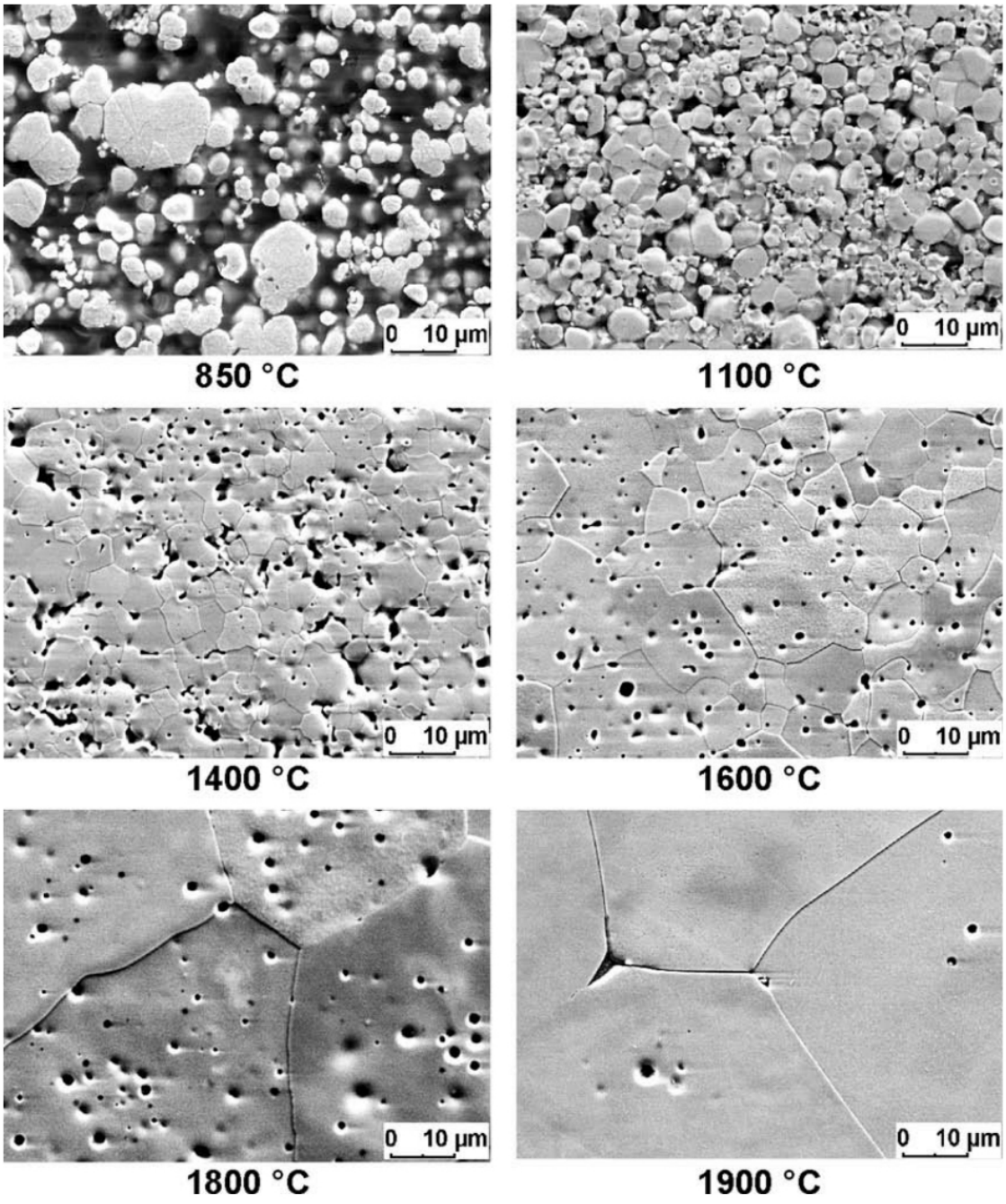


Figure 2.13: SEM micrographs of pure Mo sintered at 67 MPa using SPS taken from [45].

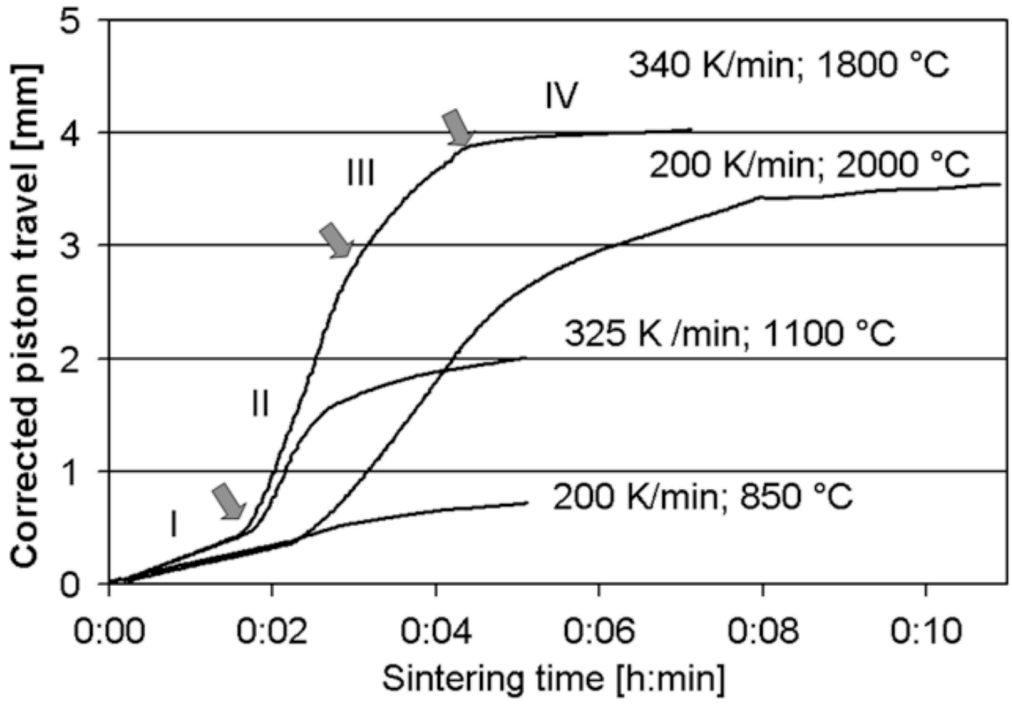


Figure 2.14: Corrected piston travel vs. sintering time for different heating rates at an applied pressure of 67 MPa taken from [45].

conditions. The maximum hold temperature was varied from 1200 to 1950°C and hold times at maximum temperature from 5 to 30 minutes. Figure 2.15 a. contains the relative density of the final sintered samples with respect to temperature. As expected, the final relative density increases with increasing temperature. However, above 1550°C the increase in density becomes relatively small. Interestingly, they reported no decrease in hardness with increasing temperature, as would be expected for a material with an increasing grain size. Figure 2.15 b. illustrates the effect of hold temperature on the final sample density. Increasing the time increases the density, but after 10 minutes the increase begins to diminish rapidly. Once again, the reported hardness values did not exhibit the expected decrease with increasing grain size.

Mouawad et al. examined the microstructure of each sintered sample. An example microstructure is presented in Figure 2.16 a. with a histogram presented in Figure 2.16 b. The grain size follows a Gaussian distribution, as would be expected. Figure 2.16 c. presents an exponential relationship of grain size with temperature. Finally, Figure 2.16 d. presents a linear relationship of increasing grain size with time. Generally, grain growth is not linear with respect to time. In all likelihood, this data would fit better to a second or third order exponential. In the end, they reported achieving near 100 % theoretical density with a hold temperature of 1850°C, an uniaxial pressure of 67 MPa, and a hold time of 30 minutes.

Pure W has also been consolidated using SPS. One study by Lee et al. studied the densification mechanism of a pure tungsten powder [47]. The powder, shown in Figure 2.17, was between 1 and 12 µm, with a tendency to form into agglomerates. The powder was consolidated using SPS with 60 and 120 MPa of applied pressure, at 1600 to 1800°C maximum temperature, up to 120-minute hold times, with a heating rate of 100°C/min. The effect of temperature and time on the final sintered density of the W samples is presented in Figure 2.18 a. For shorter sintering times, below 6 minutes, there is an increase in density with increasing temperature, however, for

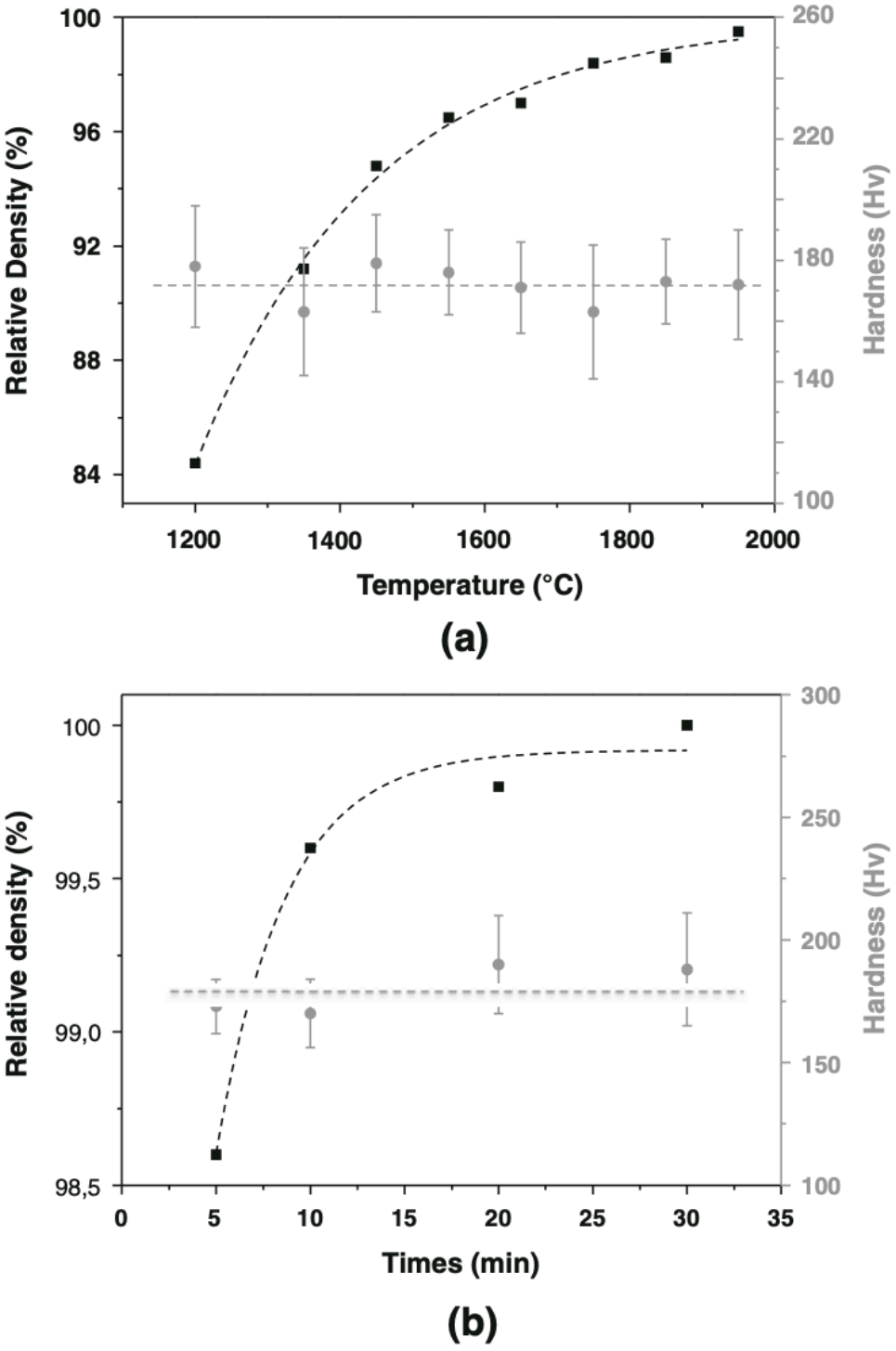


Figure 2.15: Relative density and hardness of the as sintered Mo for a) various temperatures with a constant hold time of 5 minutes, and b) for various hold times at a constant temperature of 1850°C taken from [46].

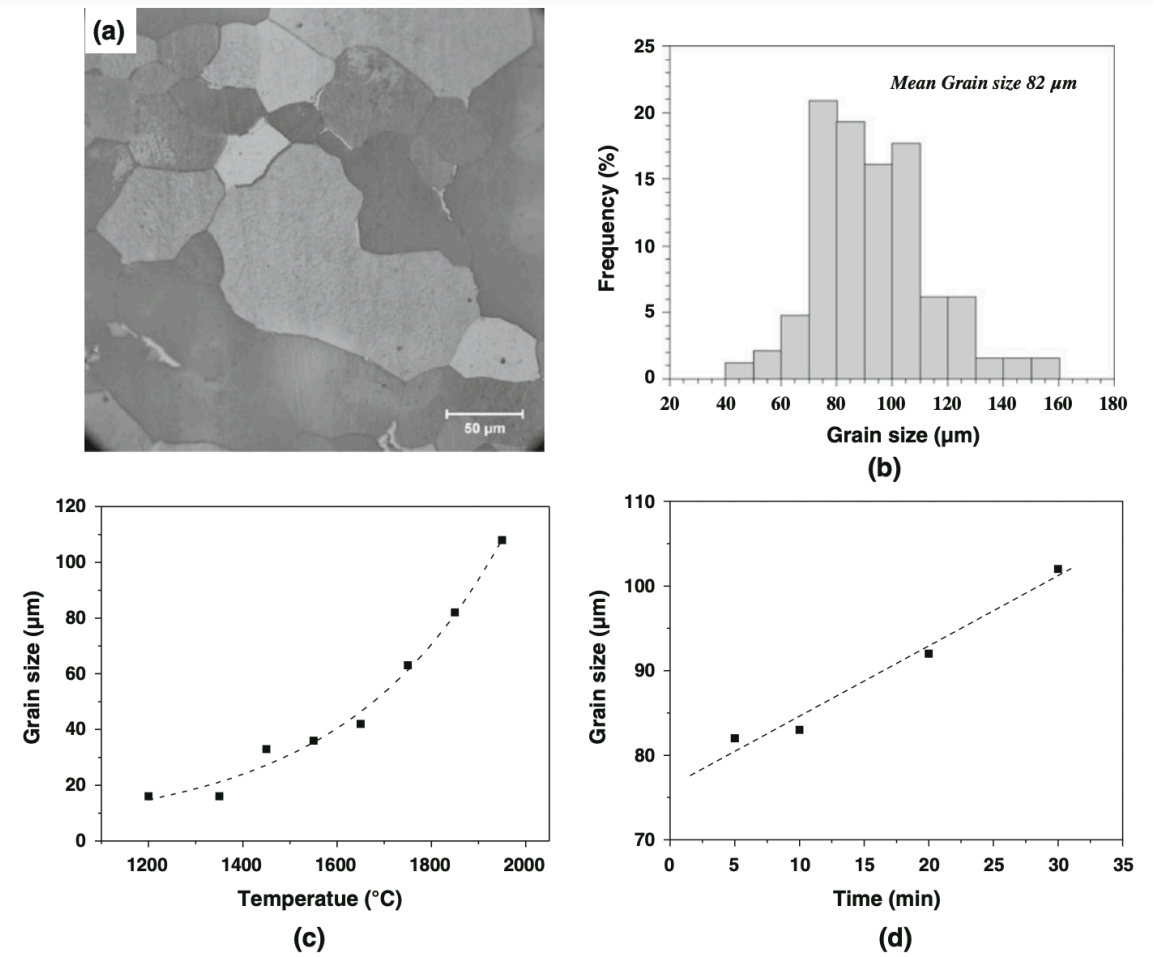


Figure 2.16: a) the microstructure of pure Mo consolidated using SPS, b) a histogram of the grain size for a sample sintered at 1850°C, c) the average grain size with respect to temperature, and d) the average grain size with respect to time taken from [46].

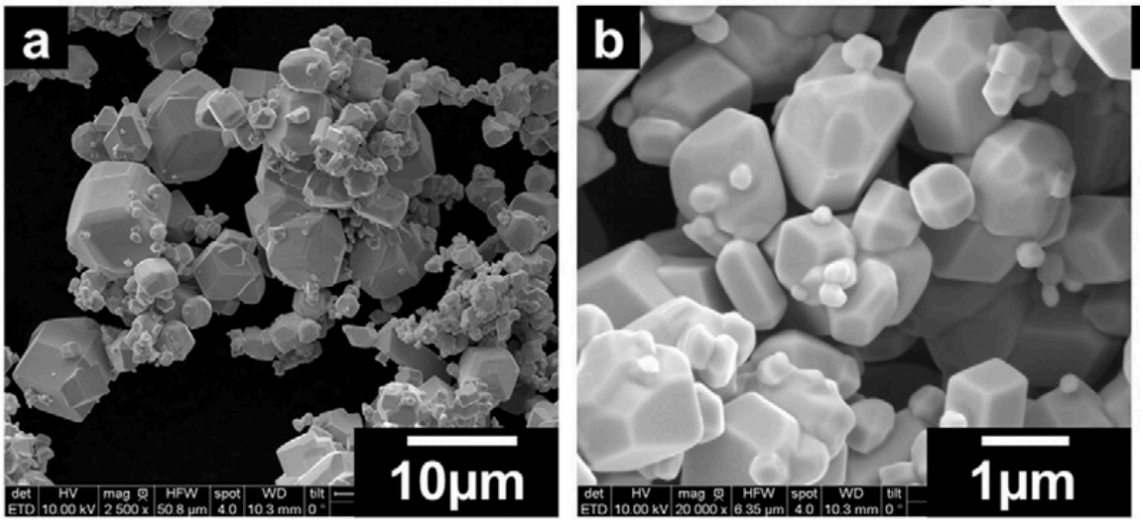


Figure 2.17: Micrographs of pure W powder prior to consolidation taken from [47].

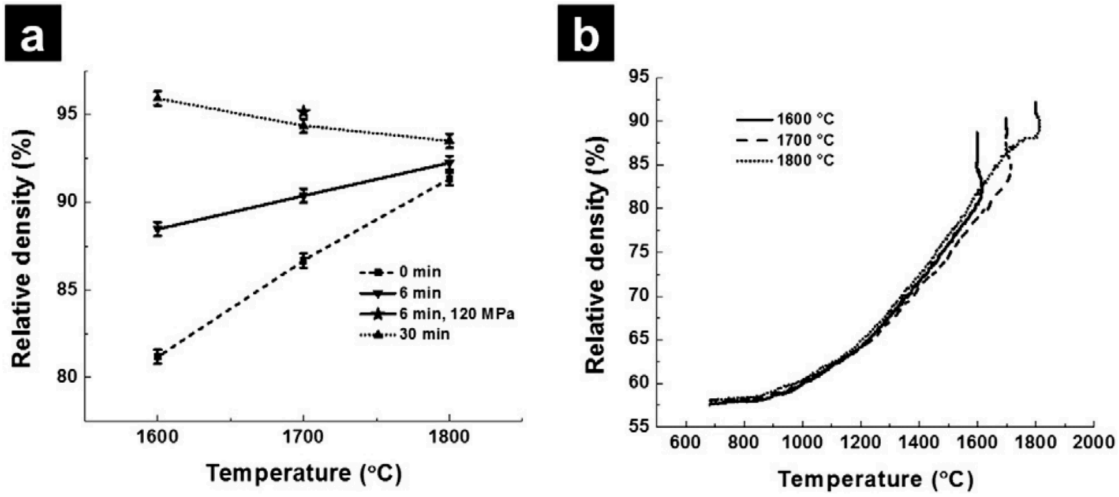


Figure 2.18: a) Relative density of W consolidate with SPS with respect to temperature, and b) the relative density for three runs at 60 MPa during sintering [47].

hold times of 30 minutes, the final relative density actually decreases with increasing temperature.

Figure 2.19 contains the grain growth kinetics for tungsten sintered at 1700 and 1800°C. Grain growth with respect to time follows the following exponential equation [48].

$$D^S - D_0^S = kt \tag{2.1}$$

where D is the average grain size, D_0, is the starting grain size, S is the grain growth exponent, k is a constant dependent upon the applied pressure and sintering temperature, and t is the time. Increasing the temperature decreases the grain growth exponent.

Lee et al. treated the sintering of W using SPS as a creep deformation mechanism [47]. Fitting the consolidation data, a strain rate sensitivity of 0.39 was calculated, with a sintering activation energy between 412 and 433 kJ/mol obtained. This is much higher than the calculated activation energy of pure Mo. However, powder size also plays a role in this value.

A few recent studies have looked at the consolidation of Mo-W alloys, including Mo30W. Chakraborty et al. created two different Mo30W pre-alloyed powders through a mechanical alloying technique and by simply mixing a Mo and W powder [49]. The powders were consolidated using traditional hot sintering technique between 600 and 1500°C for 6 hours in a reducing atmosphere. The highest reported density was 99 % of theoretical, though the value used for the theoretical density was not provided. Figure 2.20 contains the densification results for the two different powders over the tested temperature range. Below 900°C, the mixed powder achieved a higher sintered density, but above 900°C, the mechanically alloyed material achieved the higher final density. This is likely due to the difference in powder size and geometry between the two types of powders. Figure 2.21 contains an SEM micrograph of the sintered material.

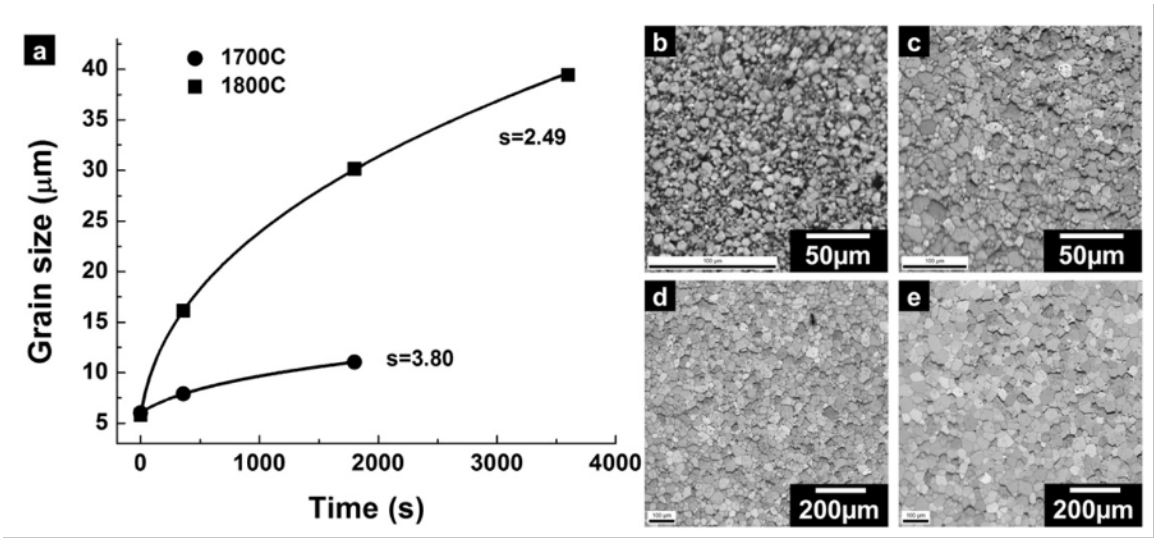


Figure 2.19: a) Grain growth with respect to sintering time at 1700 and 1800°C, and b-e), grain coarsening of W microstructure with increasing sintering time taken from [48].

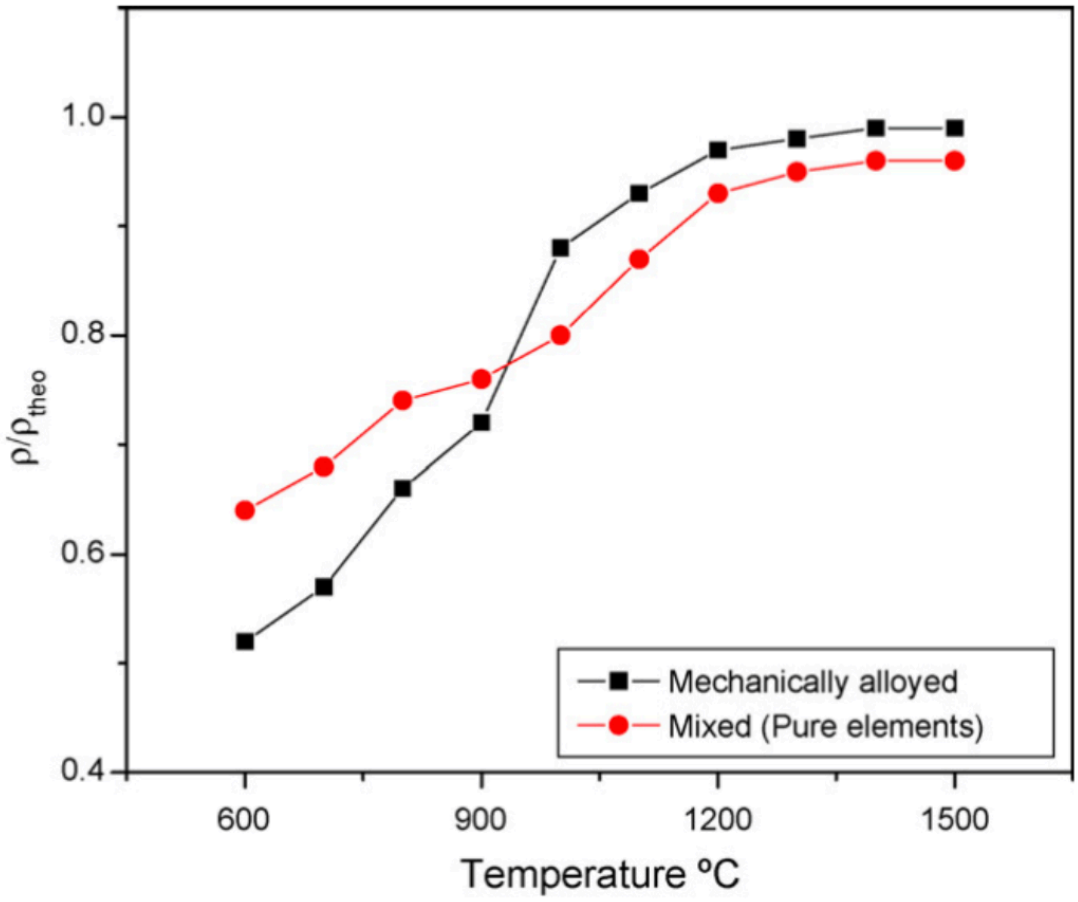


Figure 2.20: Densities of mechanically alloyed and pure elemental mixing of Mo and W powders sintered for 6 hours at various temperatures taken from [49].

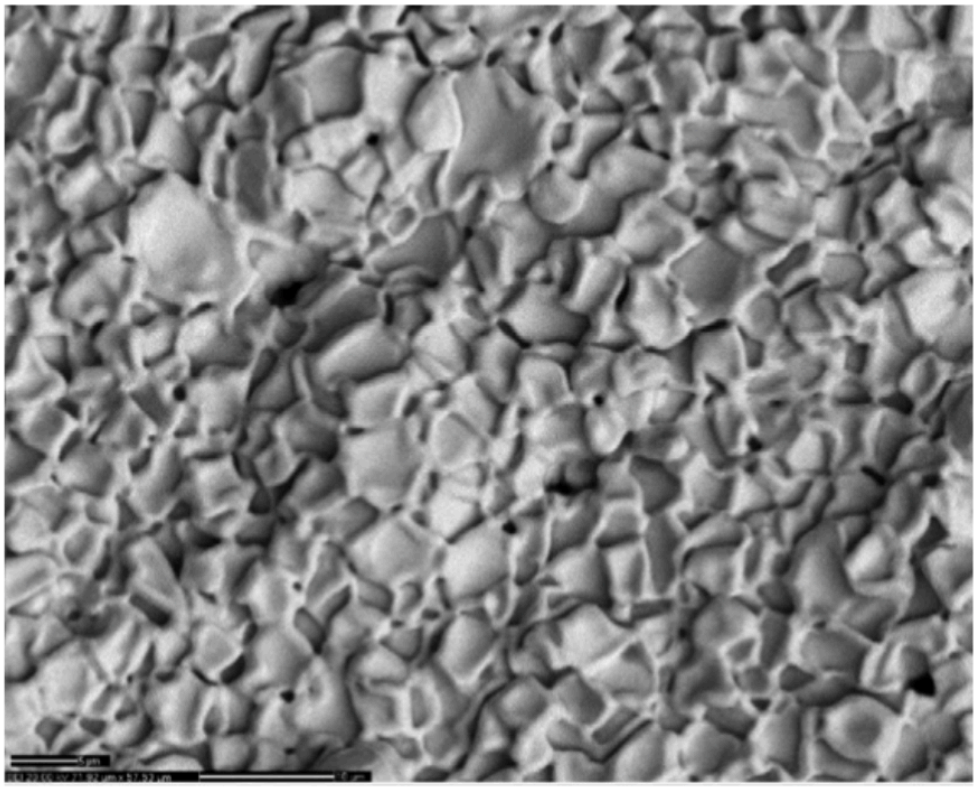


Figure 2.21: An SEM micrograph of the sintered Mo30W alloy taken from [49].

Another study conducted by Batienkov et al. sintered three different Mo-W alloys, with 10, 20, and 30 wt% W, using SPS [50]. The powders were prepared using a ball milling technique, directly combing pure Mo and W powder. The powders were consolidated from 35 to 50 MPa at 1000 to 1950°C with heating rates of 50 to 150°C/min and hold times of 3 to 30 minutes. Figure 2.22 compares the sintering of Mo30W using SPS and hot pressing in hydrogen. SPS shows a considerable improvement with at the same temperatures with respect to the traditional sintering. The relative density of the three materials consolidated using SPS is shown in Figure 2.23. The most interesting trend was the decrease in final density with increasing tungsten content. This is likely due to tungsten requiring a higher temperature to deform more rapidly. The highest reported density of Mo30W was 96% TD with a sintering temperature of 1850°C and a pressure of 50 MPa.

The hardness of the final materials is presented in Figure 2.24. The materials followed an increase in hardness with increasing sintering temperature. This increase is likely due to a decrease in porosity with increasing sintering temperature. Finally, Figure 2.25 contains micrographs of the final sintered material. Even at the higher sintering temperatures, the microstructure has relatively high porosity. There are also significant oxide inclusions between the grain boundaries.

2.2.4 Sintering of Zirconium Carbide

ZrC, like other carbides, is a difficult material to produce. SPS has proven its potential in fabricating ZrC from powder. One study, conducted by Sun et al., used reactive SPS to produce solid ZrC [5]. The material was formed by first mixing zirconia (ZrO_2) powder with carbon black and then heating the powder mixture to allow the carbothermal reduction to occur. This releases oxygen and leaves behind near stoichiometric ZrC. The powder was then sintered using SPS. Three different sintering conditions were tested, as shown in Table 2.3. All samples used a heating rate of

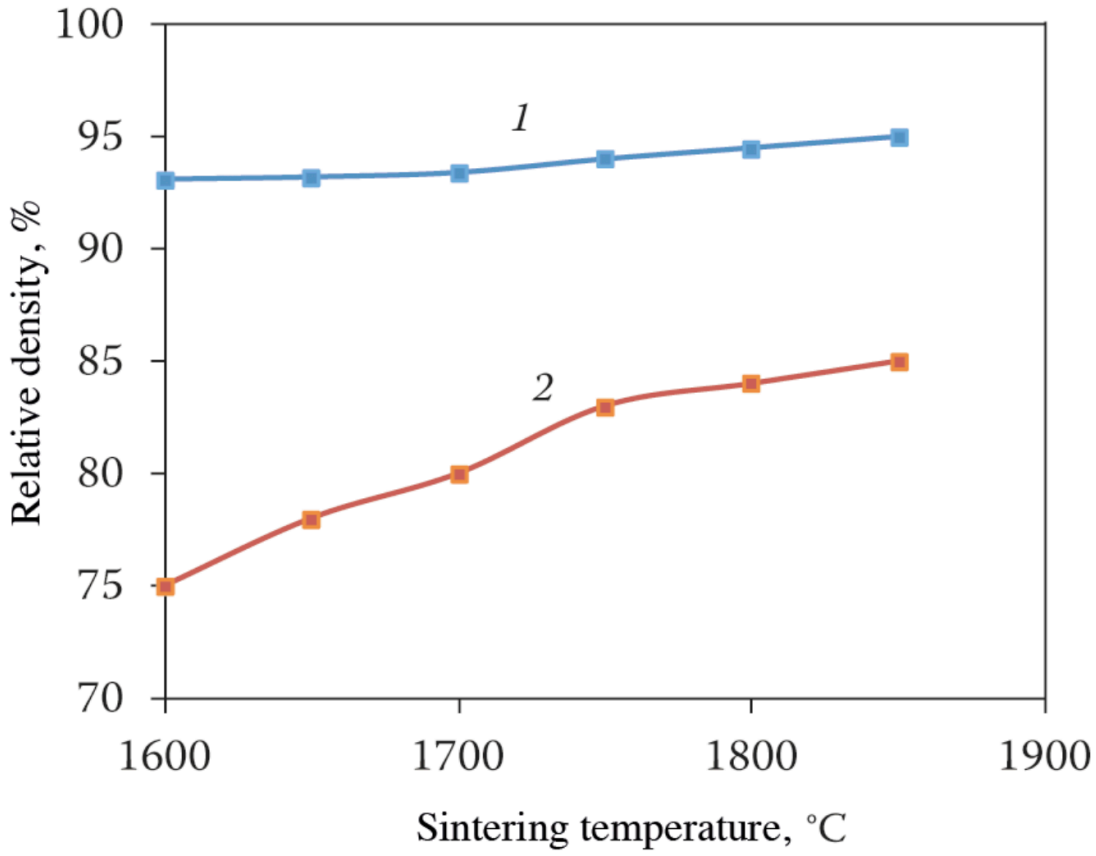


Figure 2.22: Relative density versus sintering temperature for Mo-30wt % W 1) sintered in using SPS, and 2) sintered in hydrogen taken from [50].

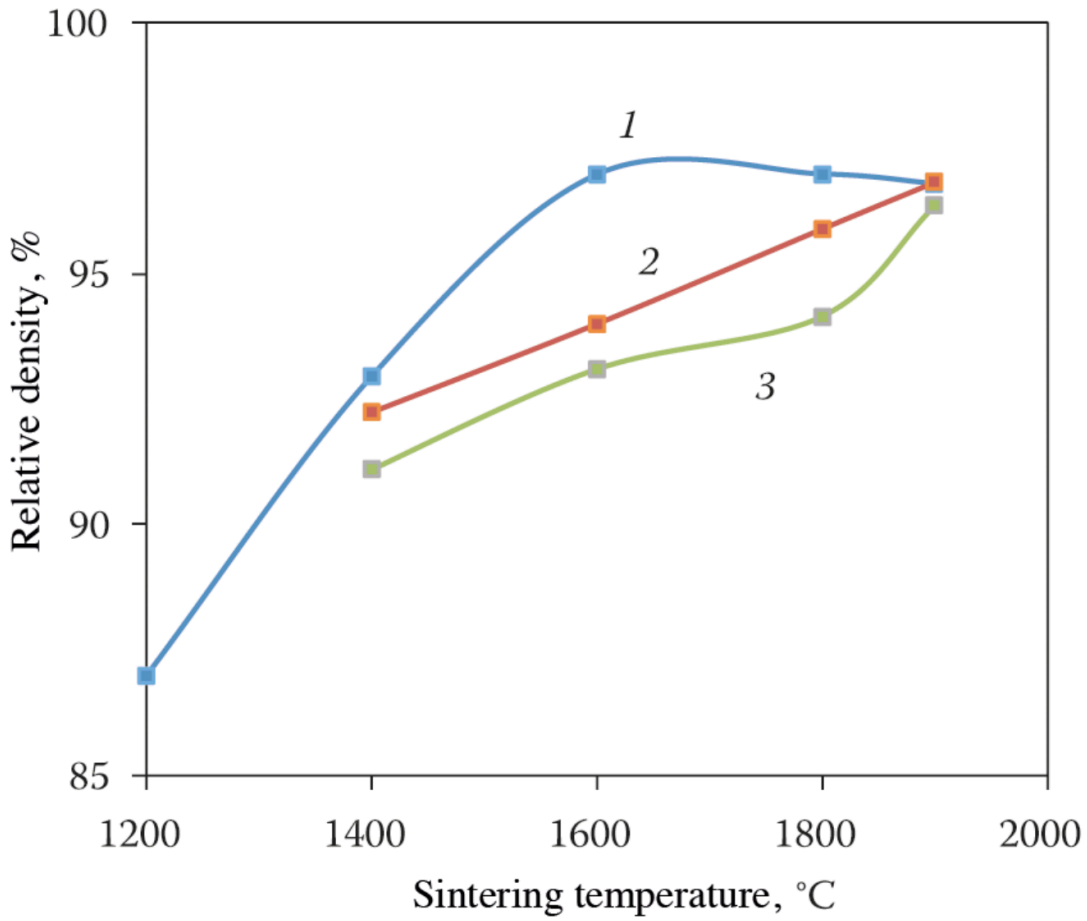


Figure 2.23: Relative density versus sintering temperature for 1) Mo-10weight % W, 2) Mo-20weight % W, and 3) Mo-30weight%, and pure W taken from [50].

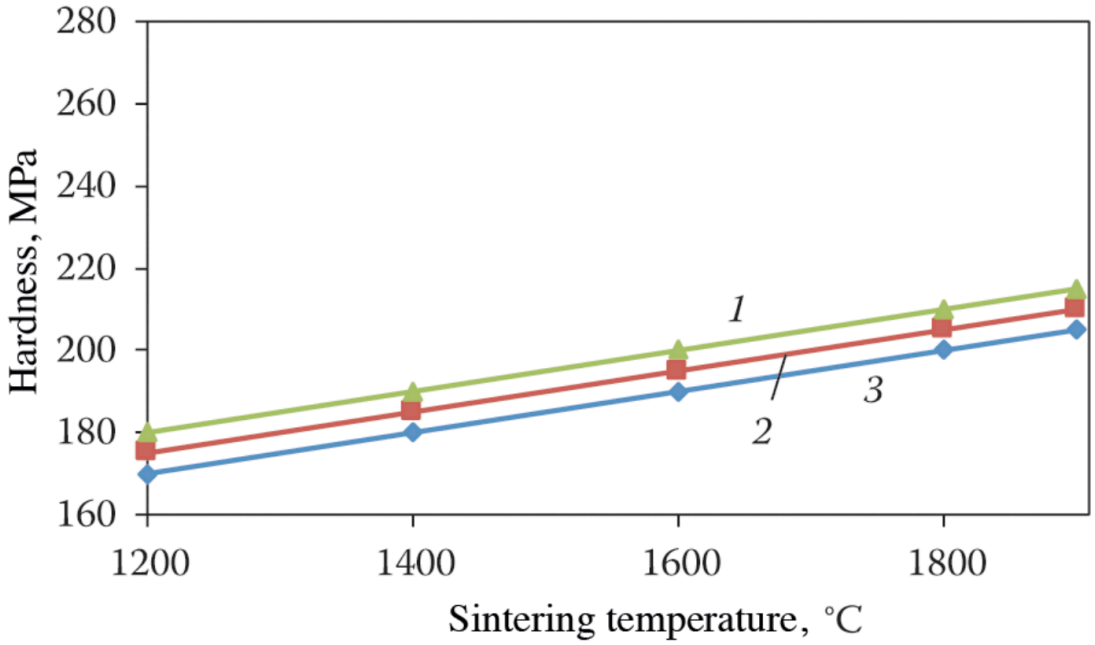


Figure 2.24: Hardness variation with sintering temperature for 1) Mo-10wt% W, 2) Mo-20wt% W, and 3) Mo-30wt% W taken from Batienkov et al. [50].

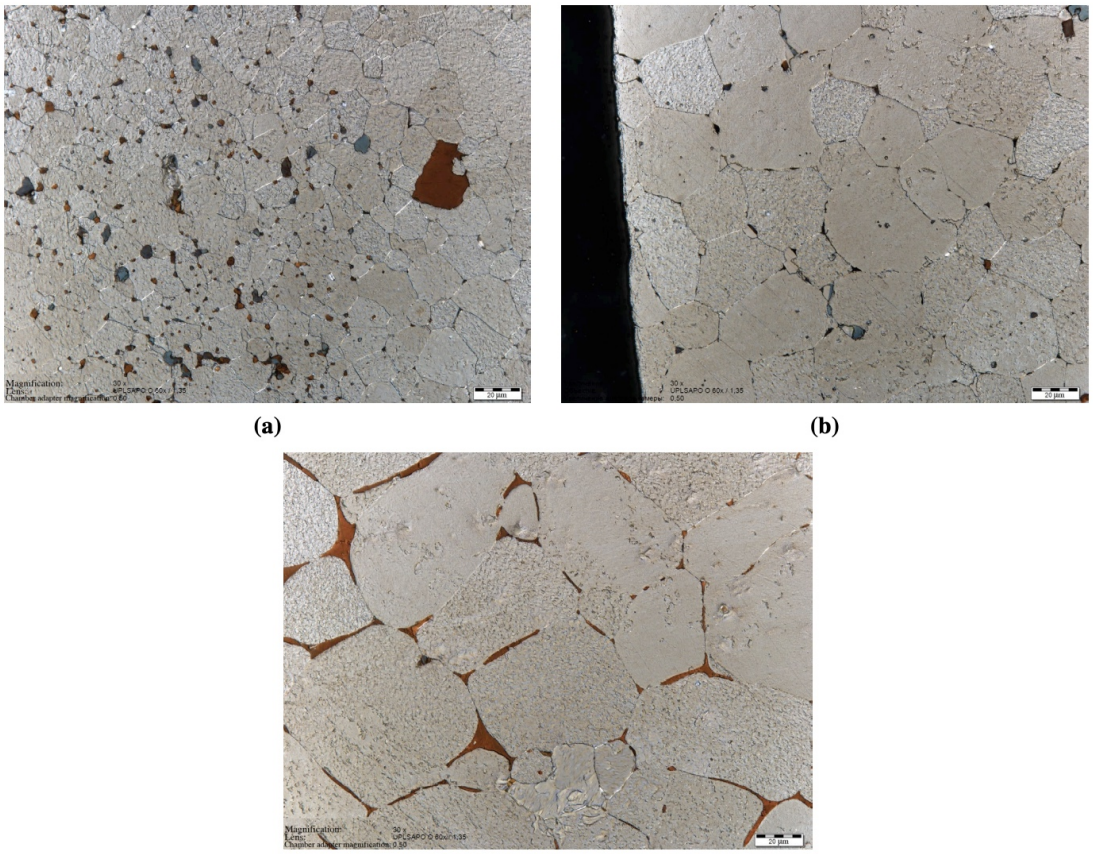


Figure 2.25: Micrographs of unspecified Mo-W alloys sintered at a) 1400°C, b) 1600°C, and c) 1800°C taken from Batienkov et al. [50].

Table 2.3: Sintering conditions, relative density, and hardness of ZrC fabricated using reactive SPS [5].

Hold temperature (°C)	Hold time (minutes)	Applied pressure (MPa)	Relative density (%)	Hardness (HV_{10}, GPa)
1750	5	5	46.9	N/A
1850	10	60	85.3	9.1 ± 1.4
1900	10	60	96.1	16.3 ± 1.6

100°C/min. The highest density achieved was 96.1 % that of theoretical, by sintering at 1900°C for 10 minutes at 60 MPa.

Another study by Núñez-Gonzélez et al. looked at the fabrication of ZrC using SPS and the effect of high energy ball milling [51]. High energy ball milling was used to reduce crystalline size and improve sintering of ZrC. The ball-milling primarily reduced the crystalline size. Ball-milling times from 1 to 180 minutes were investigated. As illustrated in Figure 2.26, the characteristic sintering temperature is reduced with increasing ball-milling time (reduction in crystalline size). A shift of almost 300°C was observed comparing the as received material for the material ball-milled for 180 minutes.

Another study by Sciti et al. reported a sintered density of 99 % relative density using SPS [52] [16]. Commercially available ZrC powder, with an average size of 3.8 µm, was cleaned in ethanol and ball-milled for 1 hour. The material was sintered using SPS with a 3-minute hold at 2100°C and an uniaxial applied pressure of 65 MPa. The average grain size 13 ± 1 µm. Densification began at around 1650°C, with the maximum densification rate occurring above 2000°C. The final microstructure is shown below in Figure 2.27. The darker specks were identified as free carbon, which was said to make up 2% of the total volume. No other information on the stoichiometry of the ZrC was provided.

Another more comprehensive study was conducted by Wei et al., which looked at densification kinetics, grain growth, and the thermal properties of ZrC [53]. Commercially available powder with an average particle size of 1 µm was acquired and characterized. A wide range of sintering conditions were tested. These results are summarized in Figure 2.28. The highest density achieved was around 98% with a 24-minute hold at 1700°C, with an applied pressure of 60 MPa. The SPS runs were compared to a single hot pressing (HP) conducted at 55 MPa and 1900°C for 60 minutes. SPS was able to increase the densification kinetics of the ZrC compared with the HP technique, as seen in Figure 2.29. Finally, the SPS produced a more uniform microstructure with much lower porosity.

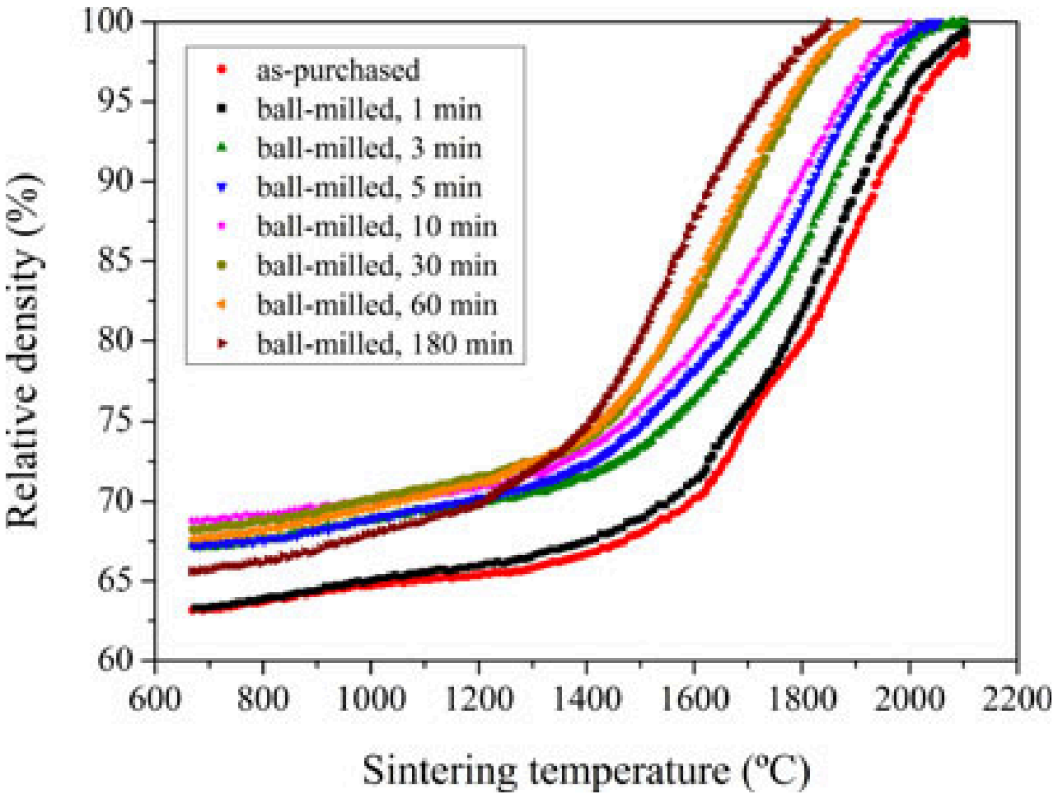


Figure 2.26: SPS densification curves of ZrC powder as received and for various ball-milling times taken from [51].

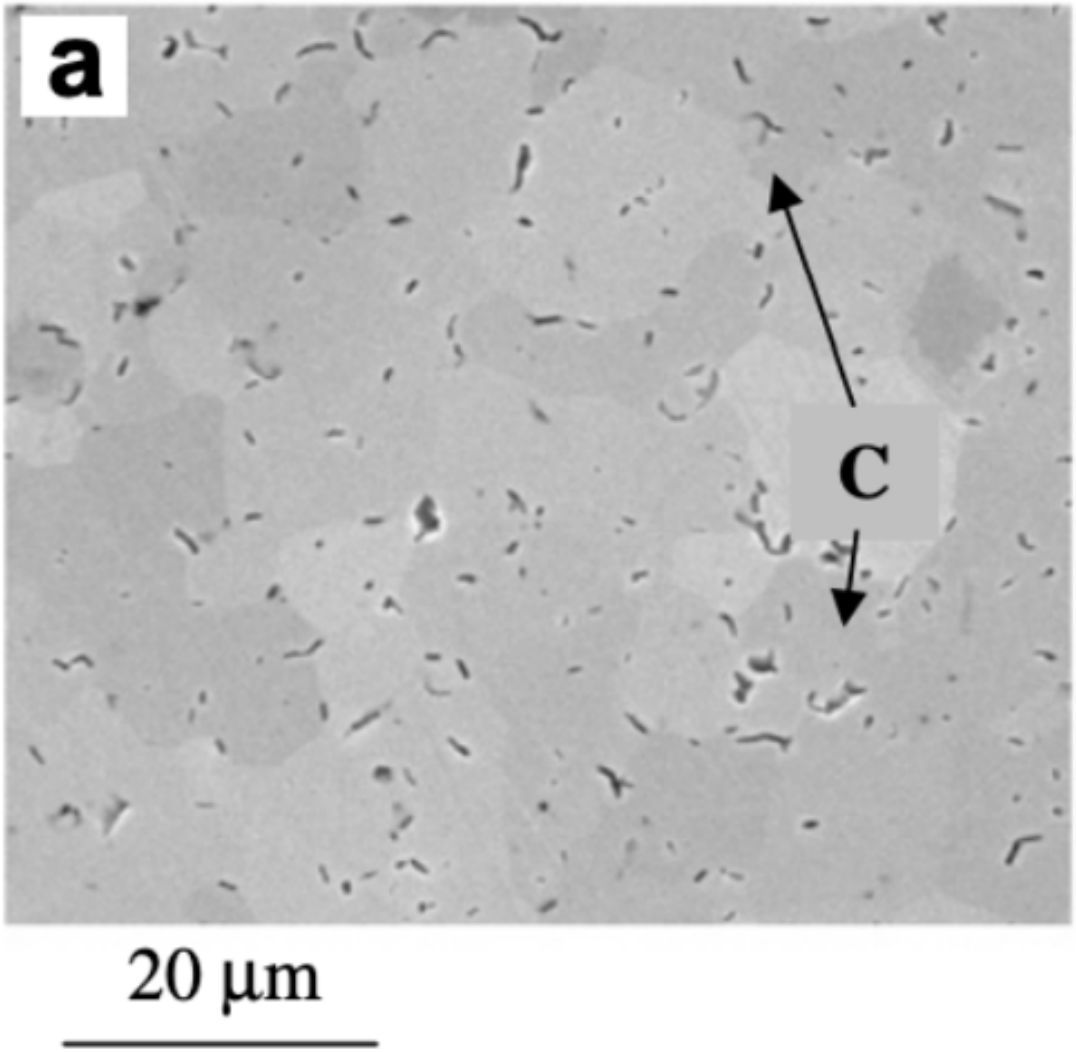


Figure 2.27: Microstructure of ZrC consolidated using SPS at 2100°C for 3 minutes with an applied pressure of 65 MPa [52].

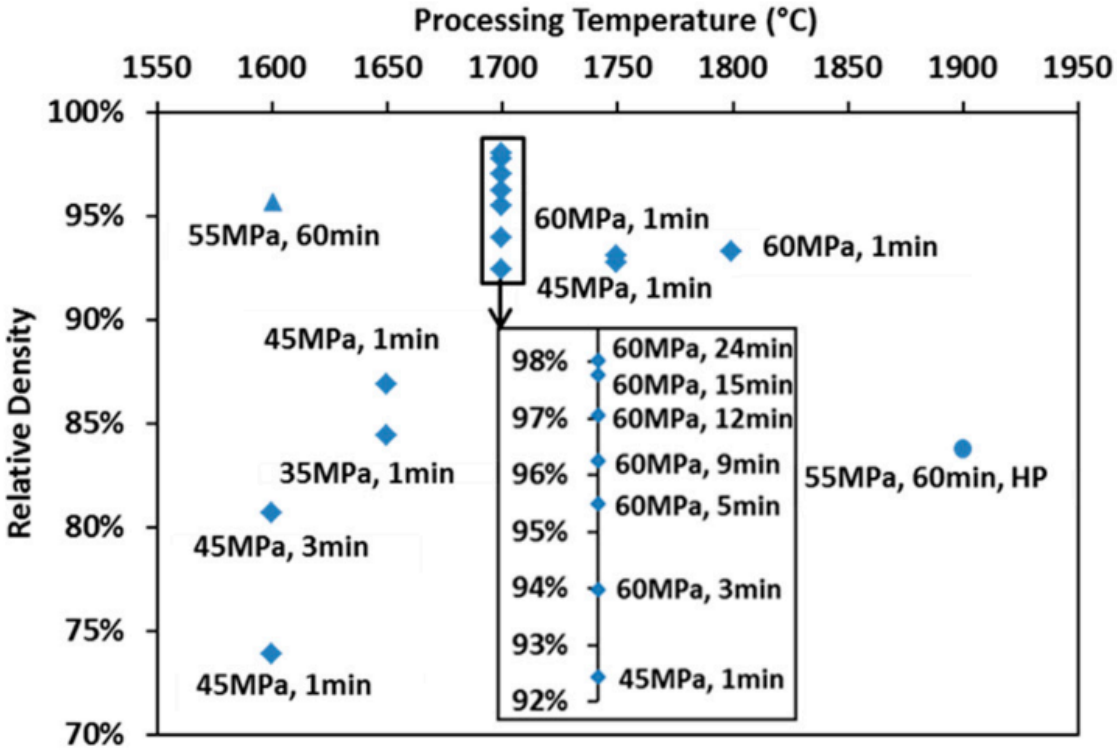


Figure 2.28: Relative density of various ZrC samples produced by SPS and HP under a variety of different conditions taken from Wei et al. [53].

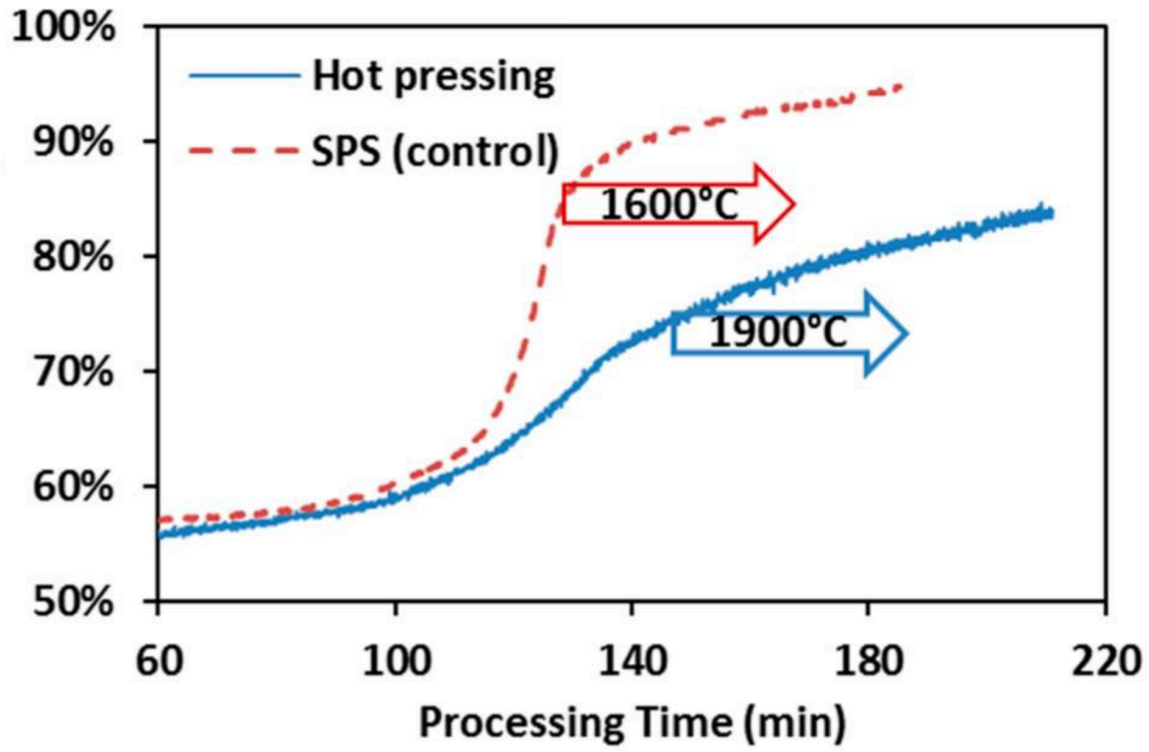


Figure 2.29: Densification curves of the hot-pressed ZrC (blue) and SPS ZrC at 1600°C for 60 minutes at 55 MPa taken from Wei et al. [53].

2.2.5 Sintering of Refractory Composites and Cermets

One of the earliest studies on using SPS to produce cermets was conducted by O'Brien et al. [128]. W with 25 weight percent rhenium (Re) matrix with 50 volume % UO_2 particles was produced. A 99.95% pure W powder 0.6-0.99 µm, a Re powder less than 20 µm, and depleted UO_2 powder 3 µm in size were mixed mechanically using ball milling. The powder was sintered using a heating rate of 100°C/min, with a hold temperature and time of 1500°C and 20 minutes, respectively. The sintered samples reached 97.9 % theoretical density, with good interface between the W-Re matrix and the UO_2.

Tucker et al. developed a powder coating method in order to produce tungsten based cermet materials with minimal particle interconnectivity and high final density [54]. Initially, 250 µm diameter spherical hafnium oxide (HfO_2) was used as a surrogate for UO_2. A volume loading of 60 percent was used for the initial testing. It became apparent that a binding agent was necessary to coat the oxide particles in the matrix material. After testing several binding agents, it was discovered that the Polyethylene homopolymer, AC-617A, produced the best results, as seen in Figure 2.30. The powder coating method used involved first milling the binder using alumina balls for 30 minutes in a Turbula mixer. Next, the tungsten, HfO_2, and binder were all mixed for 30 minutes in the Turbula to uniformly disperse the binder. Binding amounts from 0.25 to 1.0 wt% were tested. The powder mixture was then stirred on a hot plate for 5 minutes at 5°C above the drop point of the powder (101°C). It was found that 0.5 wt% binder produced the optimal coating on the particles. A lower percentage of binding agent did not uniformly coat the HfO_2 particles in tungsten, while a higher percentage caused significant clumping of the tungsten particles.

Once the powder coating method was optimized, the powder was sintered using SPS. The uniaxial pressure was fixed at 50 MPa. The sintering temperature varied from 1400 to 1700°C and the sintering time ranged from 5 to 20 minutes. The density of the final samples was measured using Archimedes technique. The results of these

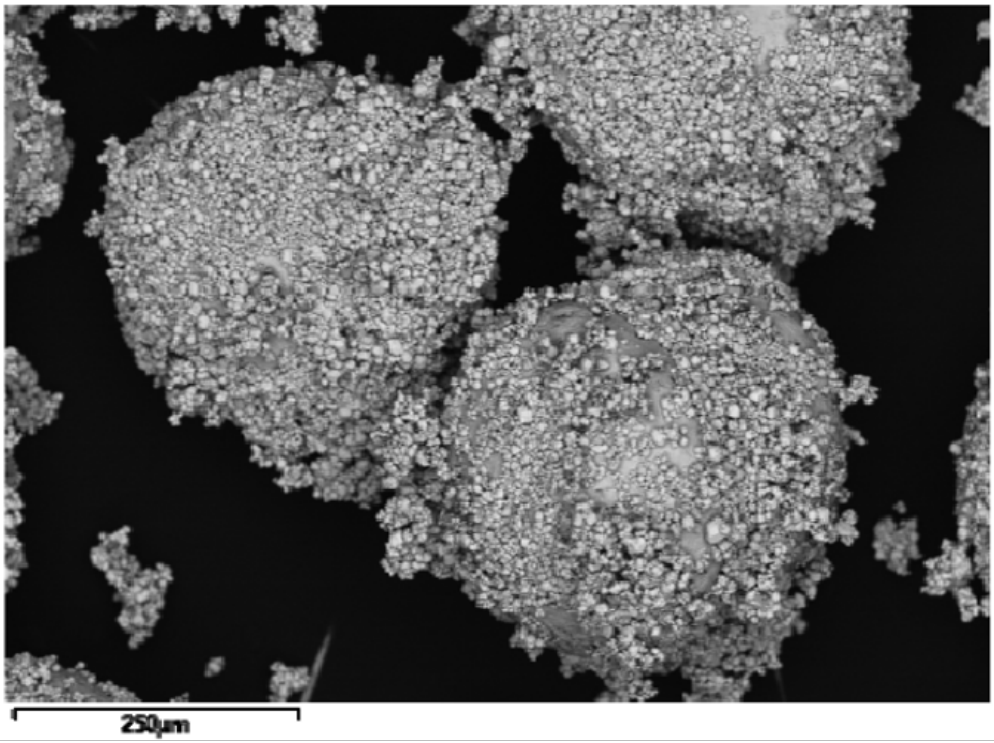


Figure 2.30: SEM image of W coated spherical HfO_2 particles taken from Tucker et al. [54].

sintering experiments are presented in Table 2.4. The highest achieved density was 96 percent theoretical, by sintering at 1700°C for 20 minutes. Density increased with both increasing sintering density and sintering time. Figure 2.31 contains an SEM image of the polished surface. Very little porosity was observed in the matrix. More importantly, the particles were fairly evenly spaced.

This powder coating technique was also applied to the sintering of spherical and angular depleted UO_2 based cermets. The W-UO_2 cermets were sintered using hot isostatic pressing (HIP). The material was pressed at 1800°C with an uniaxial force of 27,000 psi for 4 hours. As a control, angular UO_2 was also used without any powder coating prior to sintering. SEM micrographs of polished surfaces are shown in Figure 2.32 for the angular UO_2 cermets and in Figure 2.33 for the spherical UO_2 cermets. The angular powder was not well dispersed and significant matrix porosity in the W was observed. While the spherical W-UO_2 cermet still had porosity in the tungsten matrix, the particles were found to be much more evenly dispersed. It was also found that SPS produced a higher density in the matrix compared with HIP.

The technique developed by Tucker et al. has been used to produce Mo and W based surrogate cermets with spherical YSZ used in place of UO_2 [109]. Recently, Cureton et al. used a similar methodology to produce Mo matrix UO_2 cermets [110].

2.3 Properties of Molybdenum and Tungsten

2.3.1 Crystal Structure of Molybdenum and Tungsten

Current studies have been looking at replacing the W metal matrix with pure Mo and Mo alloys [109, 110, 98]. However, pure Mo has too low a melting point to achieve the desired ISP. A compromise is to use an alloy of Mo with 30 weight percent W (Mo30W) to balance the parasitic neutron absorption cross-section with a higher melting point.

Table 2.4: Sintering conditions for W/HfO_2 cermet powders by Tucker et al. [6].

Sintering temperature (°C)	Sintering time (min)	Theoretical Density (%)
1400	5	82
1500	5	85
1500	20	91
1600	20	93
1700	20	96

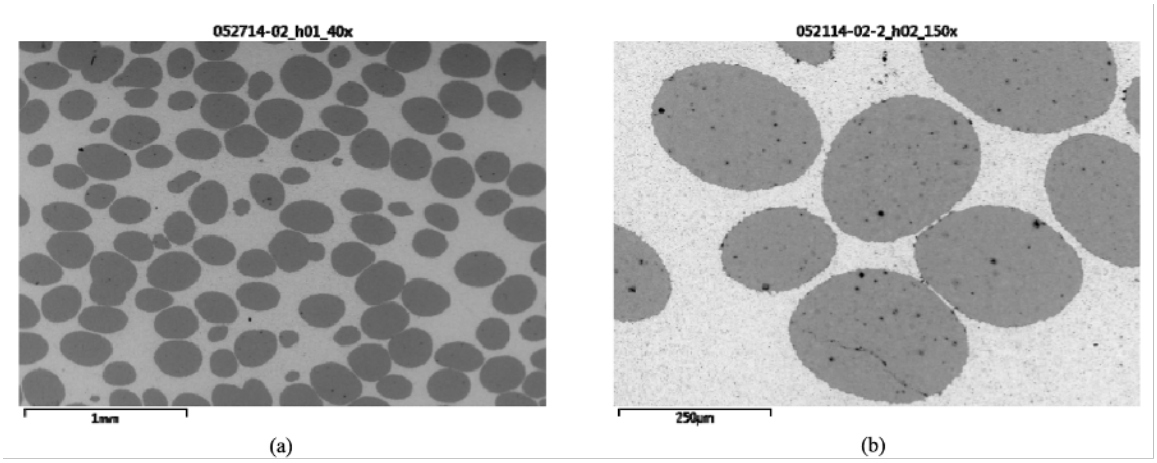


Figure 2.31: SEM micrographs of the polished surface of the W/HfO $_2$ at a) 40 x and b) 150 x [6].

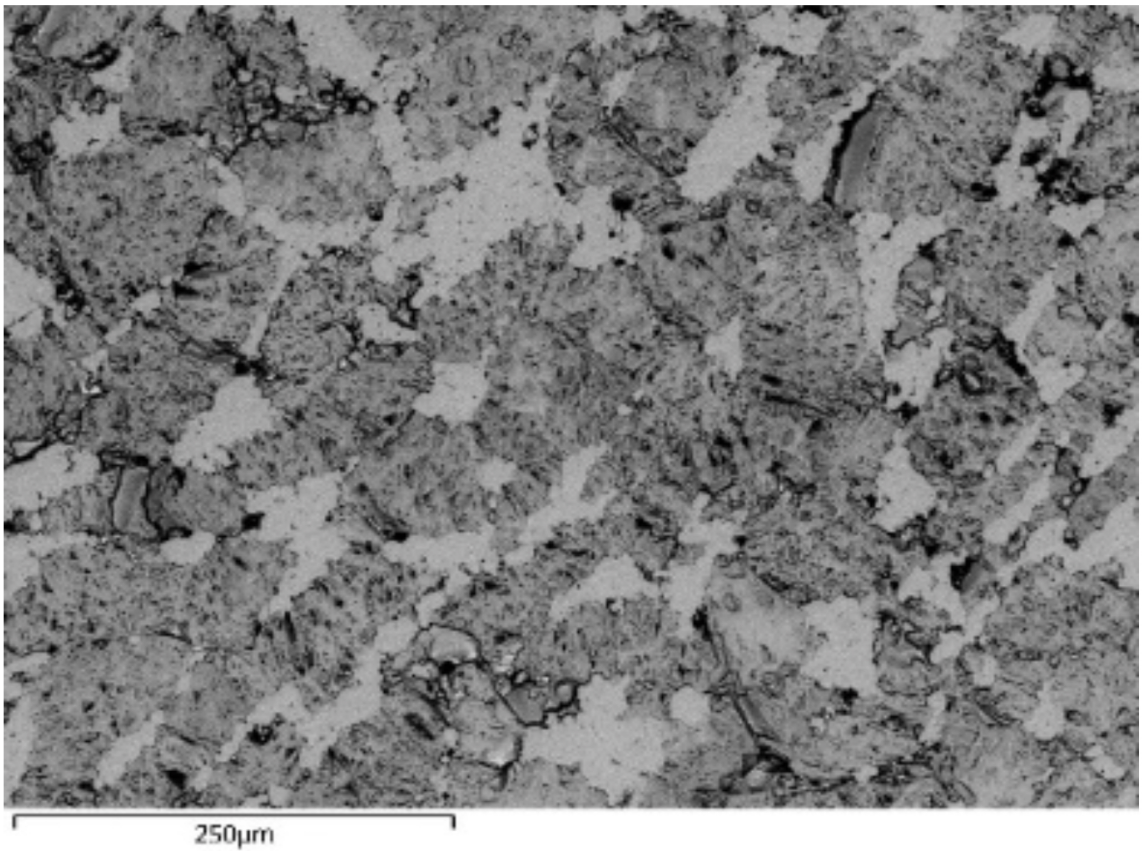


Figure 2.32: W-UO_2 cermets sintered using HIP with a 60vol% fuel loading for angular UO_2 prepared without any powder coating prepared using the binding agent technique developed by Tucker et al. [6].

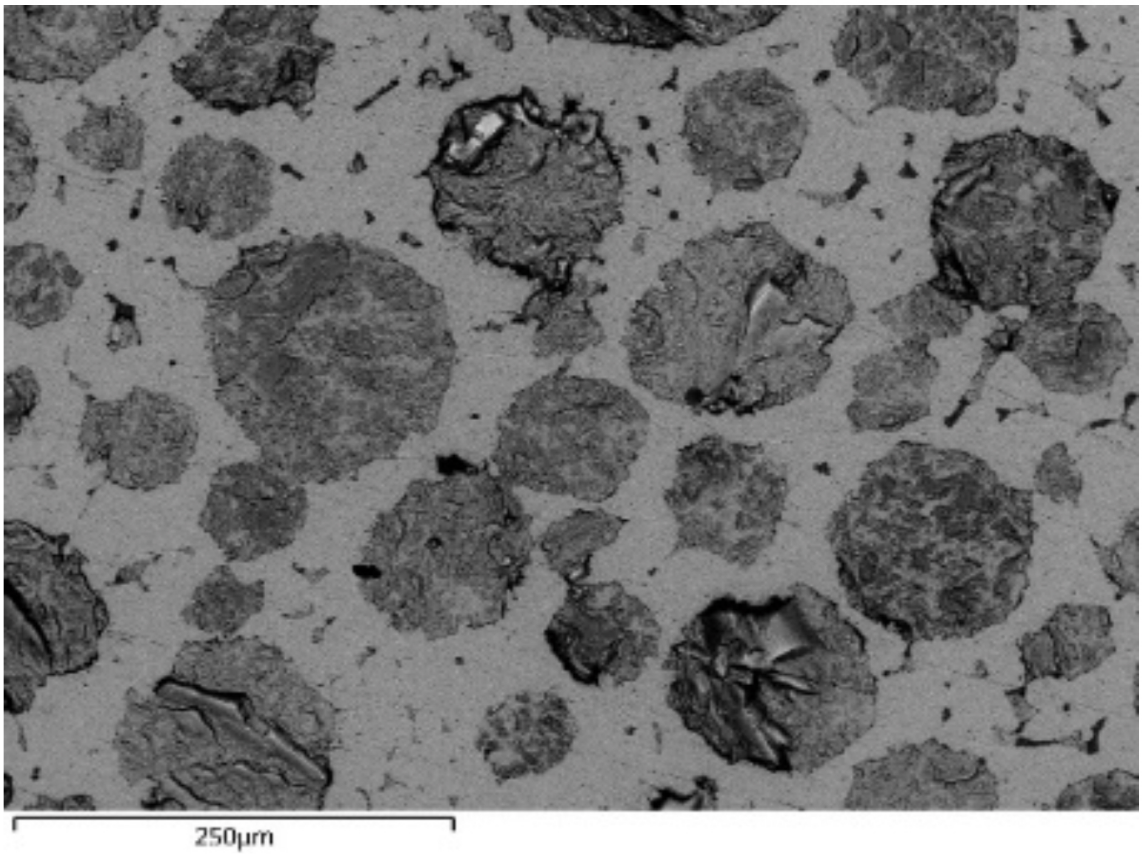


Figure 2.33: W-UO_2 cermets sintered using HIP with a 60vol% fuel loading for spherical UO_2 prepared using the binding agent technique developed by Tucker et al. [6].

Both Mo and W have a BCC crystal structure. They also have similar lattice parameters of around 0.315 nm for Mo and 0.316 nm for W. Because of their similarities in crystal structure, Mo and W form a solid solution when alloyed together, as seen in Figure 2.34. The ideal density and lattice parameter's calculated from Vegard's Law [129] for Mo30W are 11.889 g/cm^3 and 0.315 nm, respectively. The theoretical melting point is 2816°C, determined from the solid–solid+liquid two phase boundary.

2.3.2 Thermal Properties of Molybdenum and Tungsten

There is very little thermophysical data available for Mo30W. However, there is significant data available for pure Mo and W.

Martienssen and Warlimont compared the CTE of Mo and W, along with niobium (Nb) and tantalum (Ta) as seen in Figure 2.35. W has the lowest CTE, with Mo having a CTE roughly 25 % greater than that of W. This experiment only tested CTE to a value of 1500°C, and higher temperature CTE data is needed.

Lower temperature thermal expansion of both Mo and W (<300 K) were tested by Nix and MacNair and fit to Grueneisen plots [130]. Temperatures below 300 K are expected before startup, but after the first operation, the system is expected to be kept at a higher temperature than ambient space due to the decay heat in the core.

One study by Rasor and McClelland measured the thermal expansion of pure molybdenum by heating a sample in a carbon-tube furnace, then measuring the distance between two fiducial marks on the specimen [56]. The results are plotted in Figure 2.36. Two heating and cooling cycles were conducted on the samples. They observed a small permanent elongation from the initial heating, but saw very little change between the two heating and cooling cycles. From this experiment, they were able to fit the data to an equation for the coefficient of thermal linear expansion, as

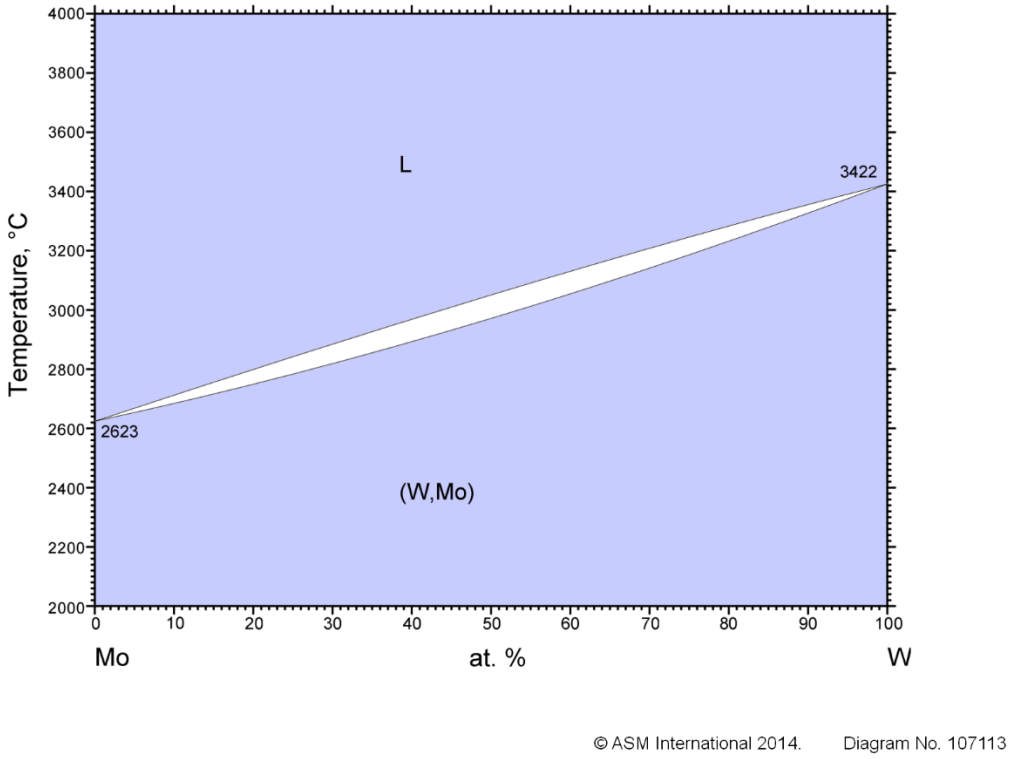


Figure 2.34: The Mo-W binary phase diagram taken from [1].

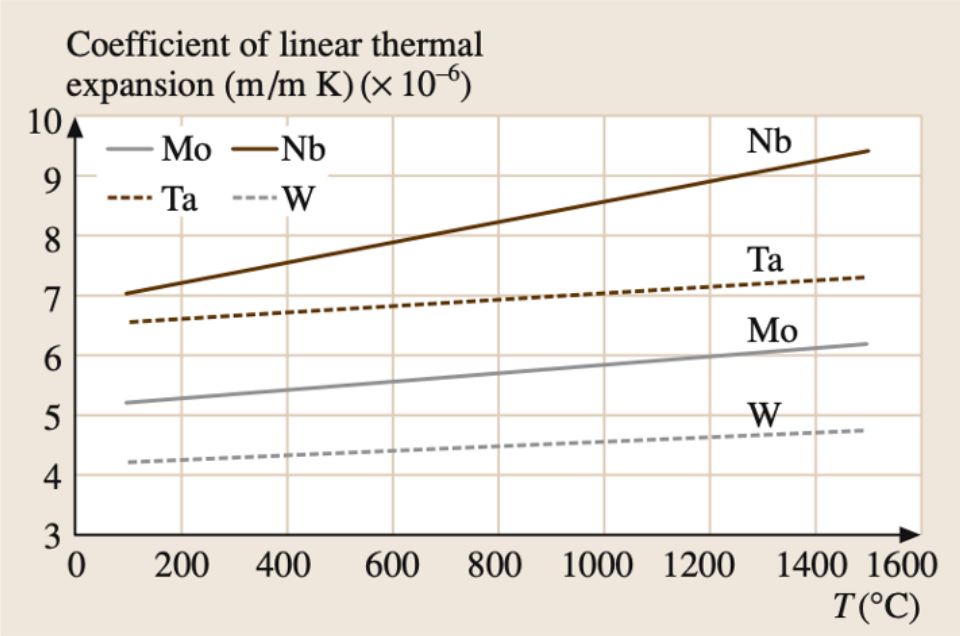


Figure 2.35: Coefficients of thermal expansion of Mo, W, Ta, and Nb as compiled by Martienssen and Warlimont [55].

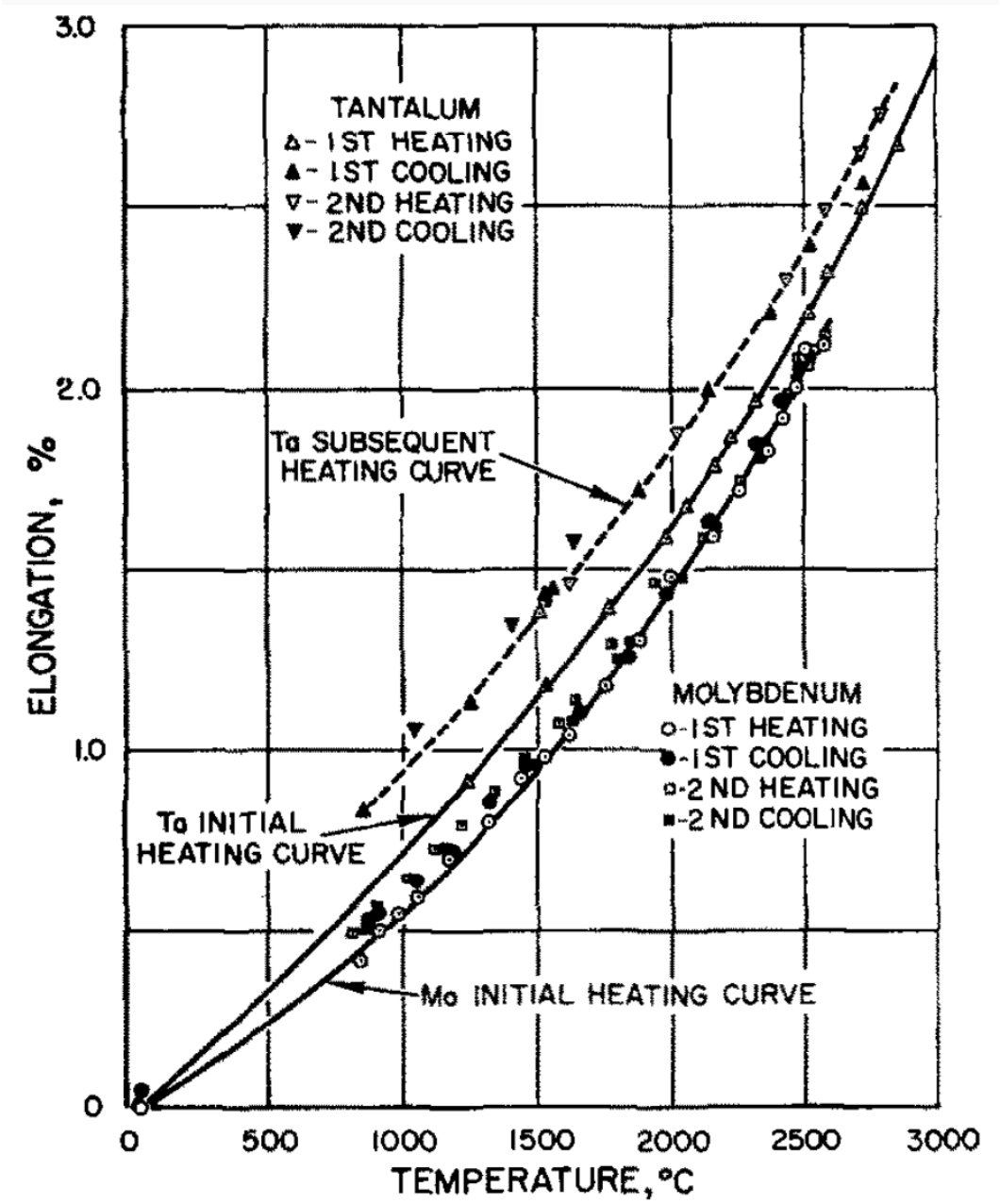


FIG. 1. Thermal expansion of molybdenum and tantalum.

Figure 2.36: Thermal expansion of Mo and Ta determined from two heating and cooling cycles by Rasor and McClelland [56].

shown in Equation 2.2, where α represents the linear CTE and T_e is the difference between the test and reference temperatures, which was 20°C in this case.

$$\alpha = 2.95 \times 10^{-6} + 4 \times 10^{-9} T_e^2 \tag{2.2}$$

Thermal Expansion of pure Mo was also calculated from X-ray diffraction (XRD) up to 2100 K [57]. Compared with the data in Figure **??**, the thermal expansion from XRD matched well with the thermal expansion calculated using a dilatometer, as seen in Figure 2.37.

Bodryakov compiled data from 23 different CTE experiments on pure Mo ranging from 0 K to the melting point, as seen in Figure 2.38 [58]. From 0 K to room temperature, there is a sharp increase in the volume expansion followed by a linear regime up to roughly 2000 K. Above 2000 K, there appears to be an increasing rate in the volume expansion up to the melting point. Below 2000 K, there is very good fit among all the data, considering the CTE was measured from a variety of techniques. Above 2000 K, the data spread increases, but the trend is the same.

Bodryakov also compiled data from 25 different CTE experiments on pure W ranging from 0 K to the melting point, as seen in Figure 2.39 [64]. The general trend matched that of pure Mo, but is lower in magnitude for similar temperatures. Also, the same trend of the data spread increasing at higher temperatures, especially above 3000 K, was observed.

Dubrovinsky and Saxena tested the thermal expansion of pure W up to the melting point using XRD [59]. The lattice parameter was determined at different temperature ranges from room temperature up to above 3500 K. The volume thermal expansion is shown in Figure 2.40. It exhibited a good fit with push rod dilatometer measurements.

Suh et al. compared the thermal expansion of pure Mo and W determined from push rod dilatometry and XRD experiments, as seen in Figure 2.41 [7]. The XRD experiments were able to test the materials up to above 2600 K. Suh et al. found good agreement with the two experimental test methods. Suh et al. then fit the data

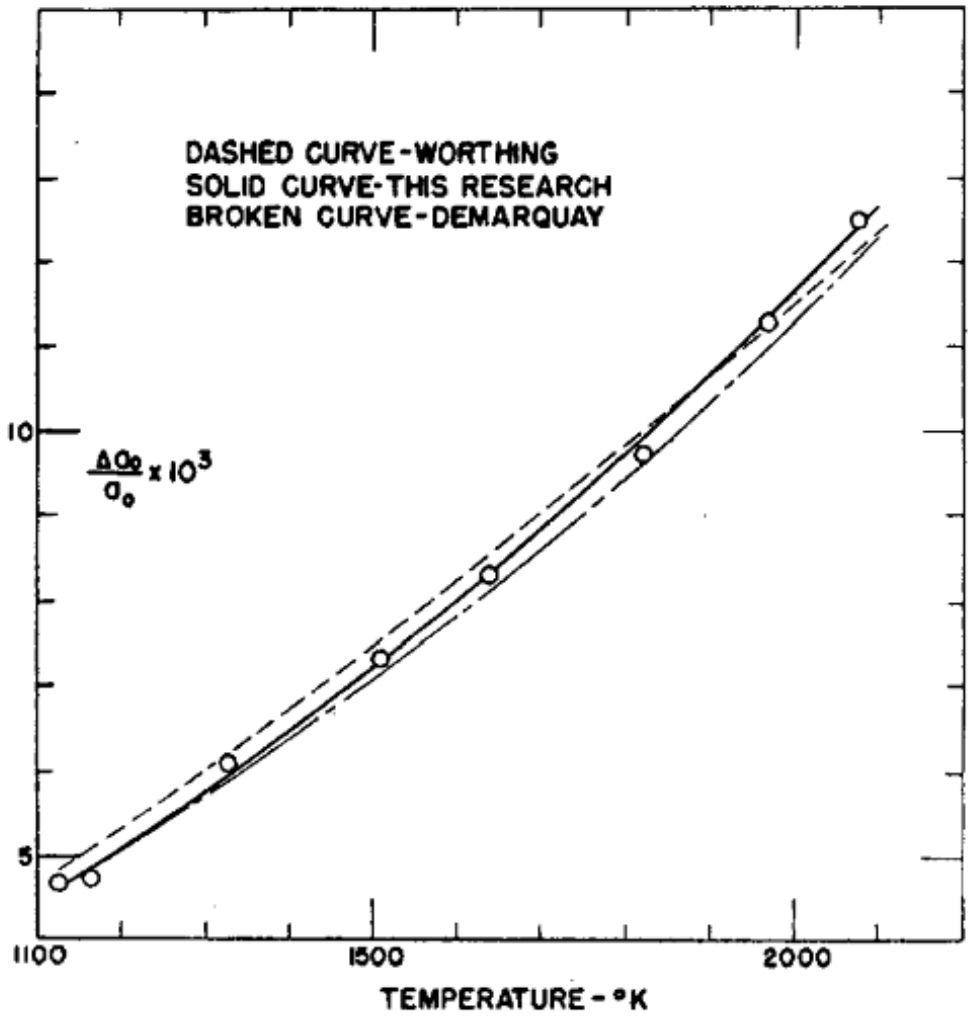


Figure 2.37: Thermal expansion of Mo from 1100 to 2100 K, calculated using the change in lattice parameter determined from XRD taken from Edwards et al. [57].

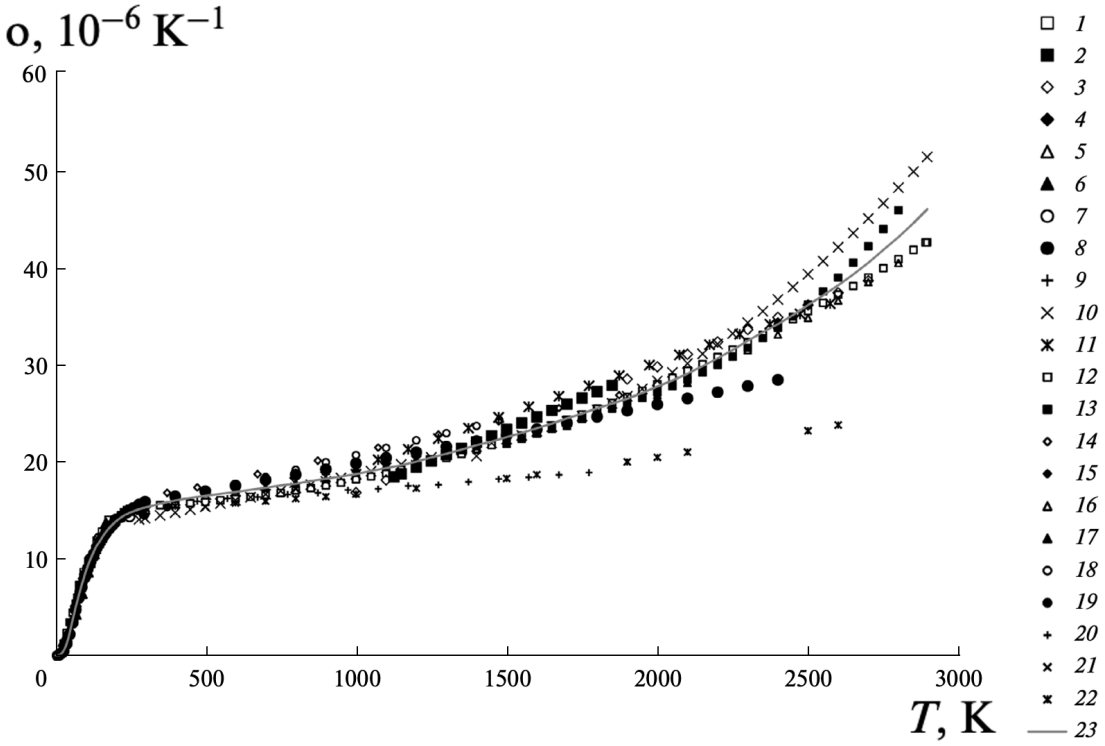


Figure 2.38: Volume CTE of pure Mo up to the melting point as compiled by Bodryakov et al. [58].

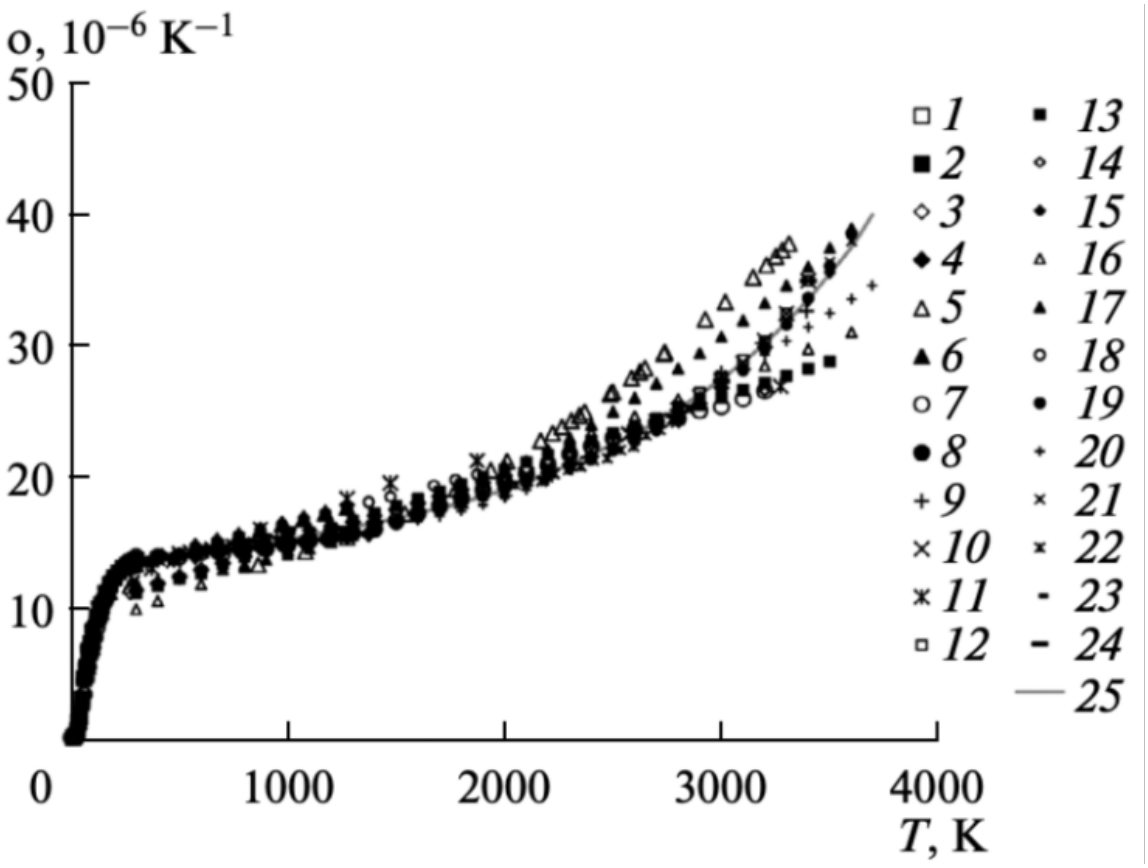


Figure 2.39: Volume CTE of pure W up to the melting point as compiled by Bodryakov et al. [58].

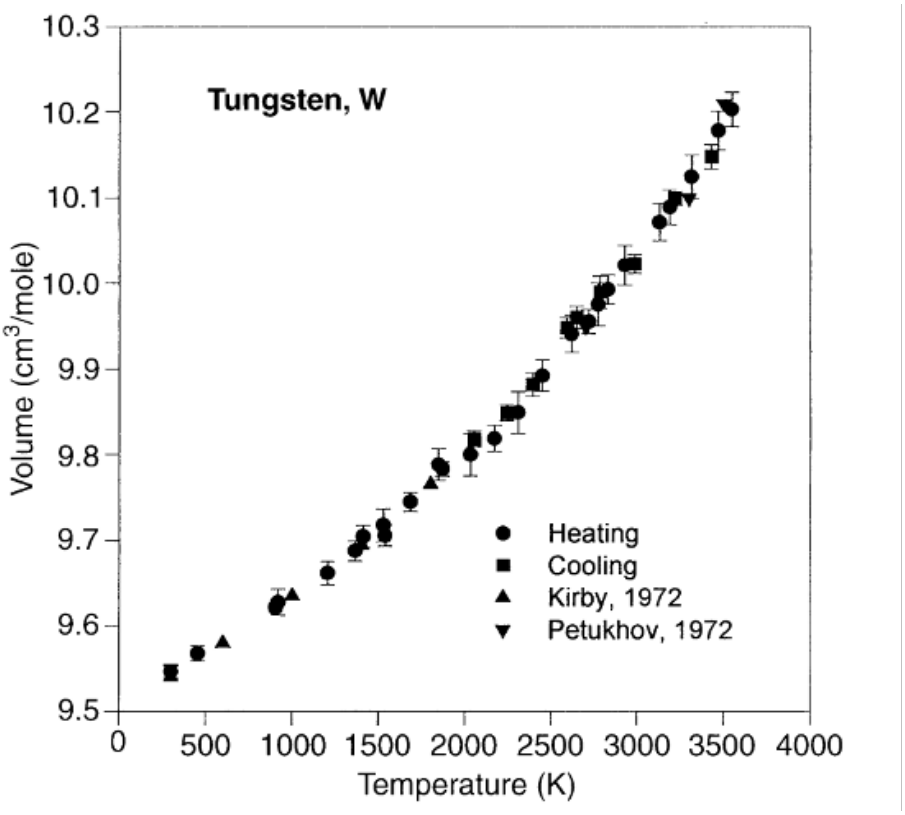


Figure 2.40: Molar volume thermal expansion of pure tungsten up to the melting point determined from XRD as measured by Dubrovinsky and Saxena [59].

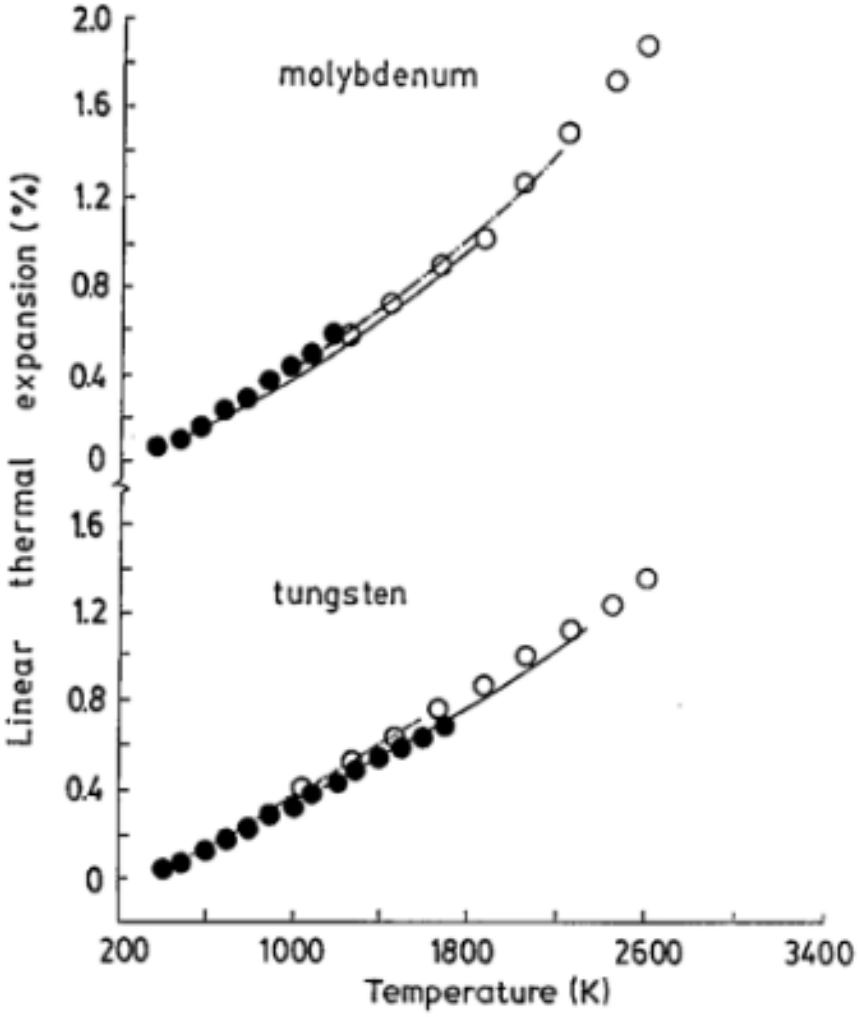


Figure 2.41: Linear thermal expansion of Mo and W determined from push rod dilatometry and XRD compiled by Suh et al. [7]. The dark circles represent values collected using push rod dilatometry by Suh et al. [7], the open circles were calculated from XRD by Waseda et al. [60], the solid line was determined by XRD from Demarquay [61], and the line broken line with dot was determined by XRD from Worthing [62].

to a second order equation to model the linear expansion and compare the two test methods. Equation 2.3 contains the model, where A_1 and A_2 are constants listed in Table 2.5, and T is the temperature in K.

$$\frac{\Delta L}{L_0} = A_1(T - 293) + A_2(T - 293)^2 \tag{2.3}$$

Martienssen and Warlimont also compiled thermal conductivity data of Mo, W, Ta and Nb as seen in Figure 2.42 [55]. The data for Mo and W was acquired from 100°C up to 1300°C. W had a higher thermal conductivity than Mo over the tested range, and both materials saw a decrease in thermal conductivity with increasing temperature.

Allen et al. tested the thermal conductivity of pure Mo and W above 2300 K [63] [32]. These high temperature measurements are shown in Figure 2.43 for pure Mo and Figure 2.44 for pure W.

Martienssen and Warlimont also compiled specific heat capacity data for Mo, W, Ta and Nb as seen in Figure 2.45 [55]. The heat capacity shows the greatest disparage between Mo and W, compared with the other thermal properties of interest. Mo has almost double the specific heat capacity of W over the tested range of 100 to 1400°C. This is likely due to the fact that W is about twice as dense as Mo. The value for both metals increases with increasing temperature.

Bodryakov compiled heat molar heat capacity data from a variety of sources up to the melting point of pure Mo [58] and pure W [64]. As with other metals, the heat capacity of Mo and W increases with increasing temperature. Below 300 K, the heat capacity increases rapidly, then levels off. From 300 to around 2200 K, the increase in heat capacity is linear with temperature. Above 2200 K, the increase in heat capacity with regard to temperature moves from a linear relationship to a second order relationship. The heat capacity as a function of temperature for pure Mo is shown in Figure 2.46 and for pure W in Figure 2.47. For pure W, the spread increases rapidly above 3200 K between the various sources.

Table 2.5: Fitting parameters for thermal expansion of Mo and W determined by Suh et al. [7].

	Method	A_1	A_2	Range (K)
Mo	Dilatometer	5.08×10^{-6}	1.41×10^{-9}	293 to 1200
	XRD	3.91×10^{-6}	1.81×10^{-9}	298 to 2614
W	Dilatometer	4.97×10^{-6}	3.16×10^{-11}	293 to 1700
	XRD	5.37×10^{-6}	1.81×10^{-10}	298 to 2621

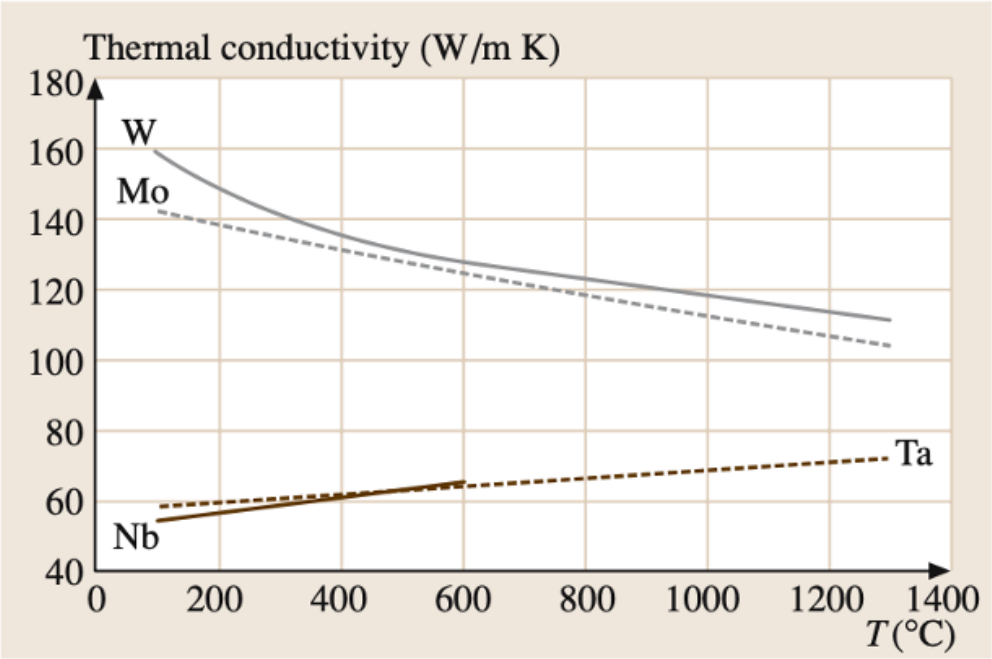


Figure 2.42: Thermal conductivity of Mo, W, Ta, and Nb as compiled by Martienssen and Warlimont [55].

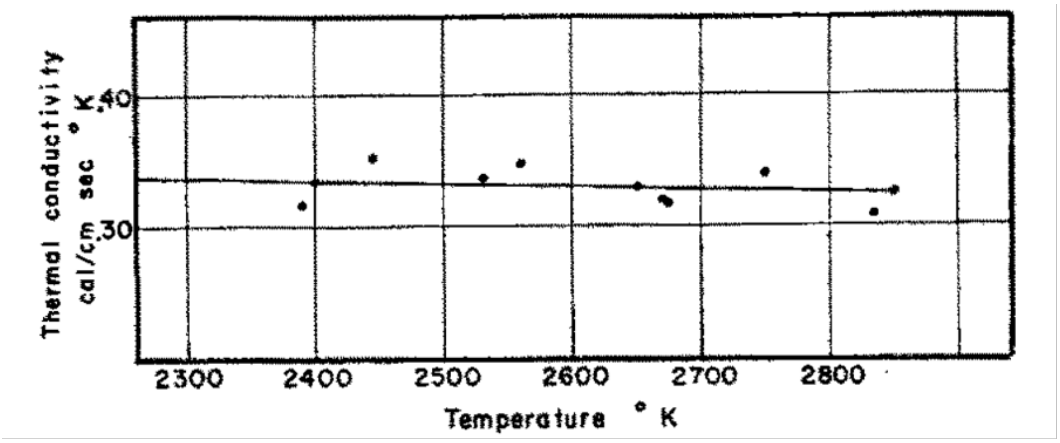


Figure 2.43: Thermal conductivity of Mo above 2300 K [63].

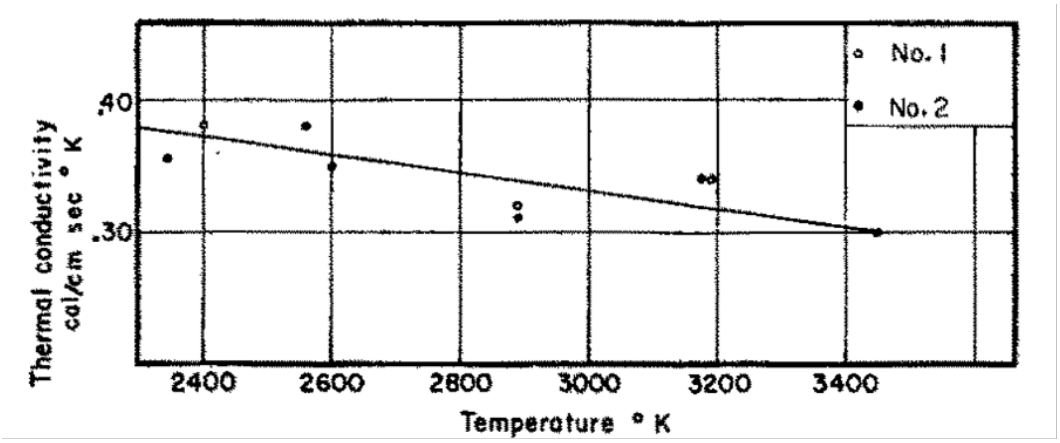


Figure 2.44: Thermal conductivity of W above 2300 K [63].

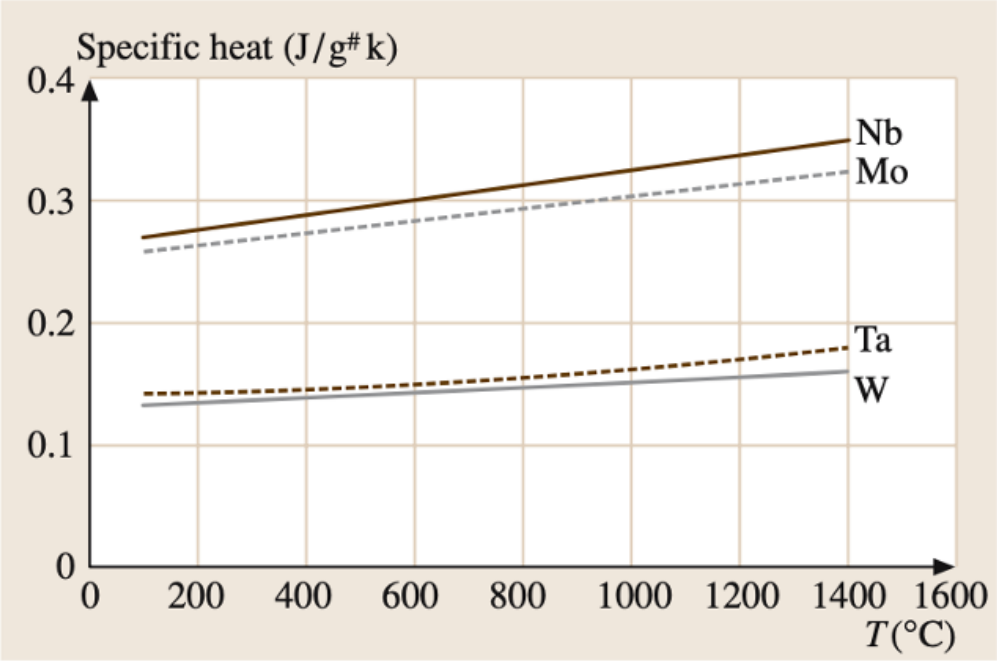


Figure 2.45: Specific heat capacity of Mo, W, Ta, and Nb as compiled by Martienssen and Warlimont [55].

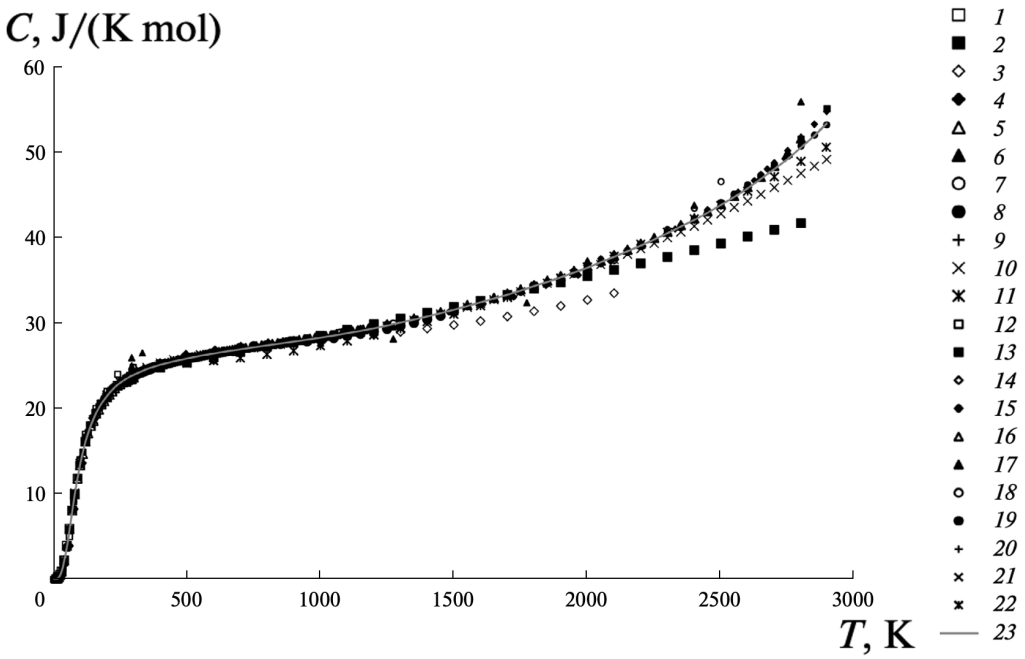


Figure 2.46: Heat capacity of pure Mo up to the melting point from 24 sources compiled by Bodryakov [58].

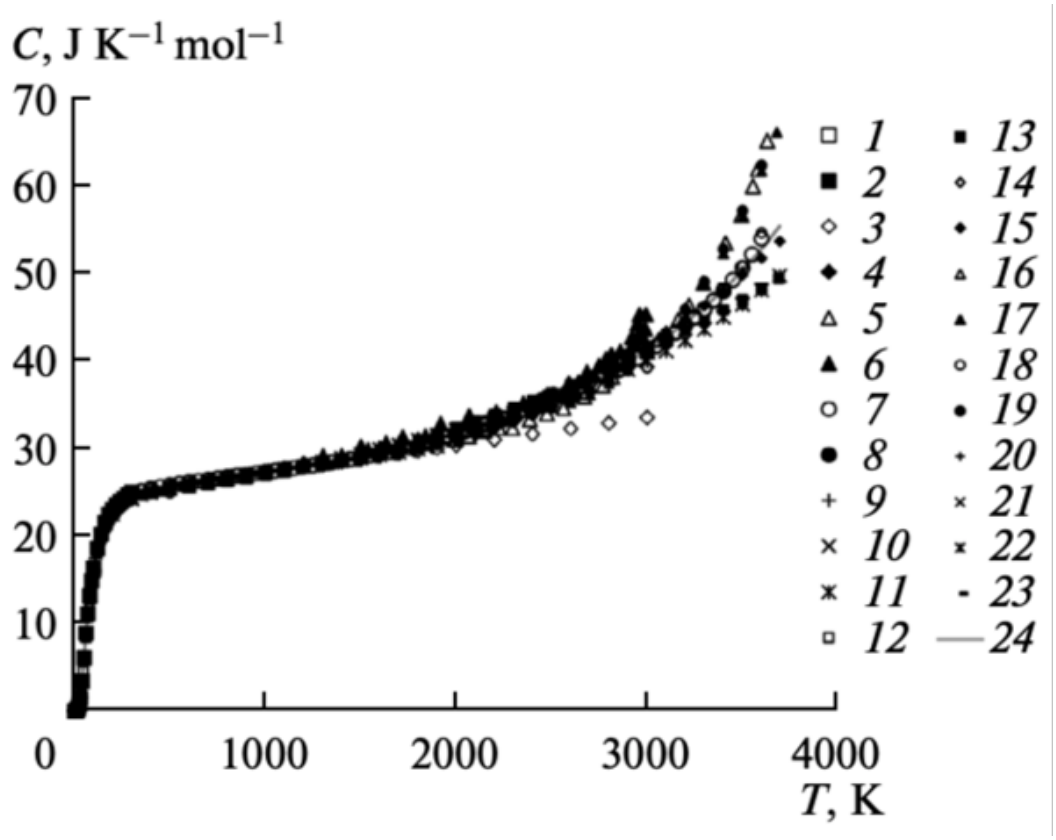


Figure 2.47: Heat capacity of pure W up to the melting point from 24 sources compiled by Bodryakov [64].

Martienssen and Warlimont also compiled vapor pressure and evaporation rate data up to 2900°C for Mo, W, Ta and Nb as seen in Figure 2.48 [55]. Over the range of 1500 to 2400°C, Mo has a much higher vapor pressure than W, by almost five orders of magnitude. Correspondingly, the evaporation rate of Mo over the same range is five orders of magnitude greater than that of tungsten.

The thermophysical properties of the pure refractory elements can provide a good estimate for the expected properties of the alloy.

2.3.3 Mechanical Properties of Molybdenum and Tungsten

Young's modulus for most metals decreases with increasing temperature, i.e., the material becomes less stiff. Martienssen and Warlimont [55] compiled modulus data for both Mo and W from Tietz and Wilson [65] and plotted it in Figure 2.49. The modulus of W is typically between 75 and 100 GPa higher than that of Mo. Figure 2.50 contains the modulus of W up to 3000°C for a single crystal and up to 2000°C for a poly crystal. Above 2000°C, Young's modulus begins to decrease more rapidly. Depending on the material, the modulus of pure W has been observed to decrease to as little as one third of the room temperature value near the melting point.

The hardness of BCC metals is a good indicator for the strength of a material. The well understood Tabor relationship for BCC metals, $H(GPa) = 3\sigma_Y$, correlates the yield strength with the measured hardness [131]. Mutoh et al. collected hardness data for pure W at elevated temperatures [67]. Up to around 1100°C, W experiences a slight decrease in hardness with increasing temperature, as seen in Figure 2.51. At 1100°C, W experiences a significant drop in hardness to roughly 80% the value at room temperature. This material was not recrystallized, as W normally is prior to use in various applications. This drop likely reflects a decrease in the dislocation density above the recrystallization temperature.

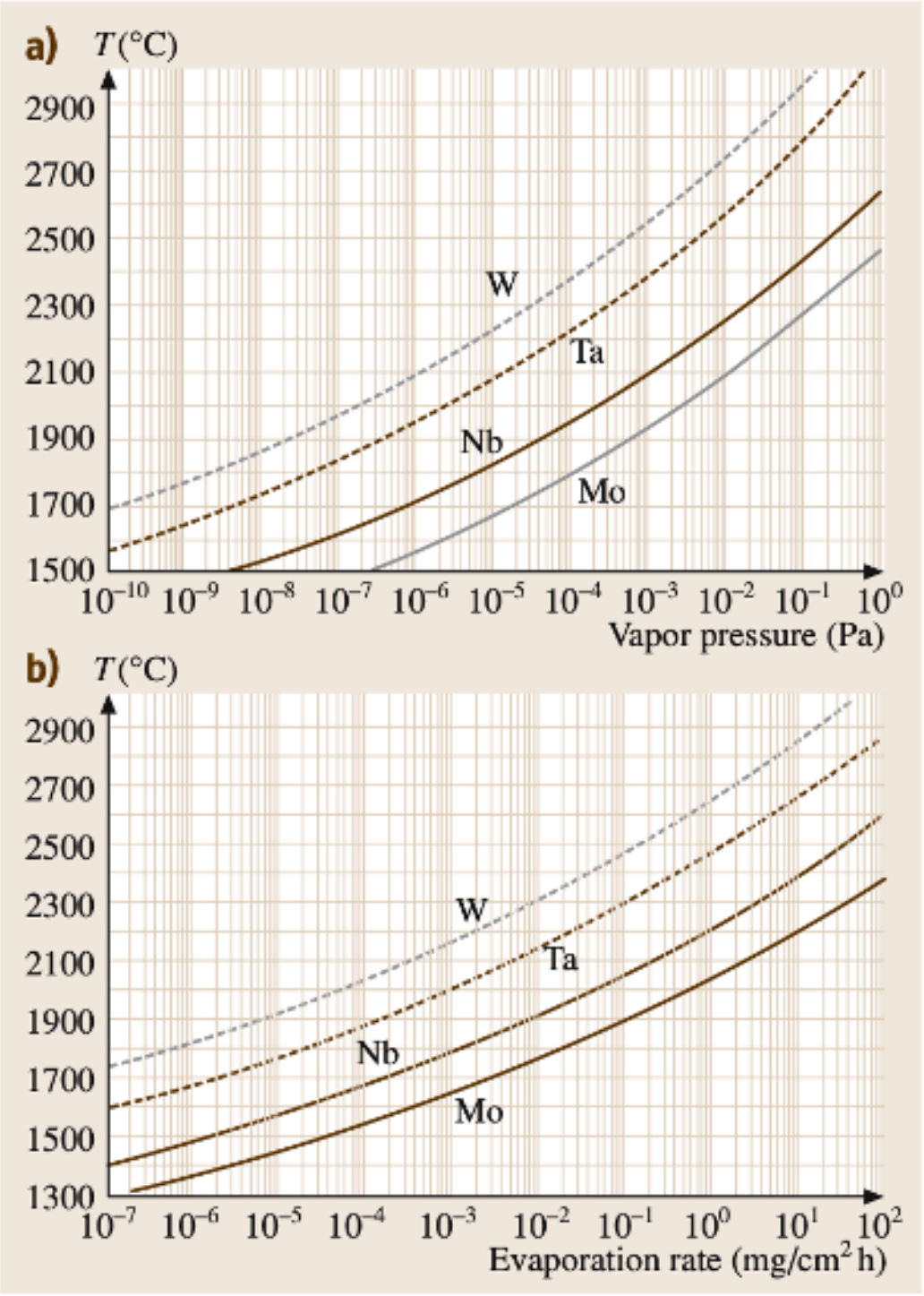


Figure 2.48: a) Vapor pressure and b) evaporation rate of Mo, W, Ta, and Nb as compiled by Martienssen and Warlimont [55].

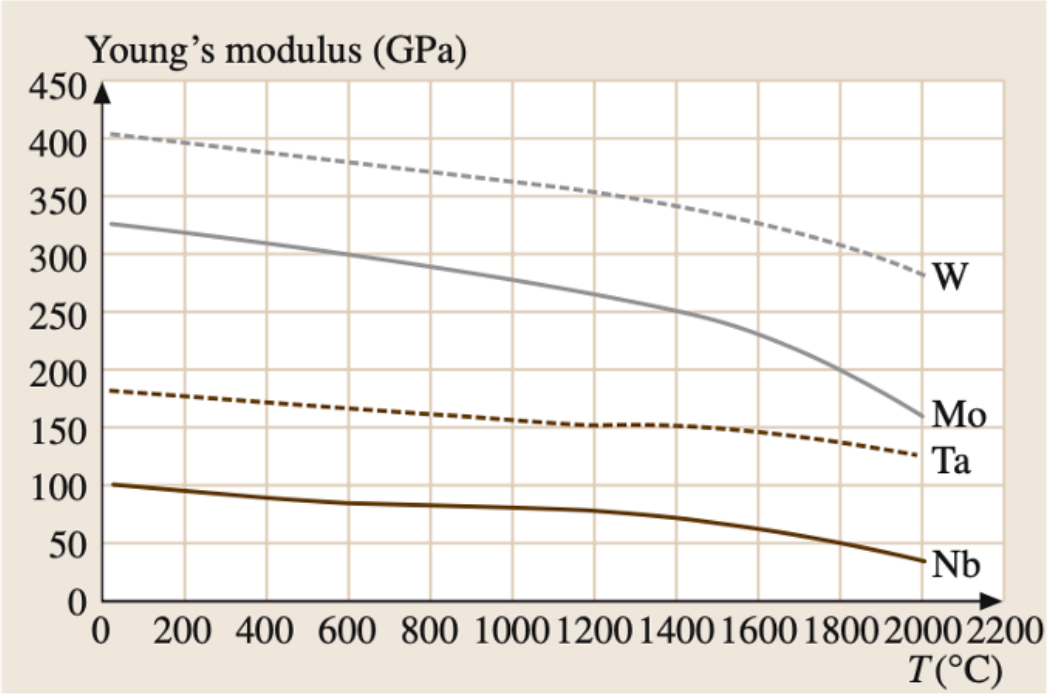


Figure 2.49: Young's modulus of Mo, W, Ta, and Nb as compiled by Martienssen and Warlimont [55], taken from Tietz and Wilson [65].

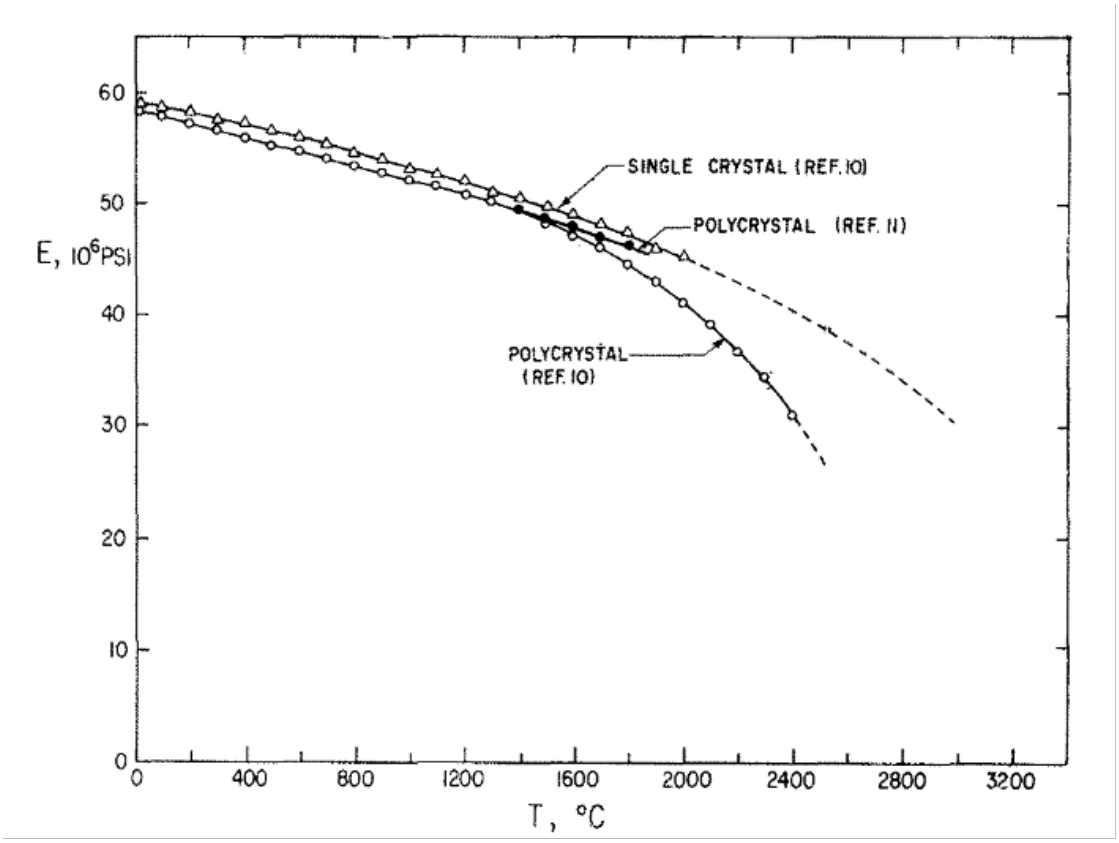


Figure 2.50: The elastic modulus at elevated temperature for polycrystalline and single crystal W taken from Robinson et al. [66].

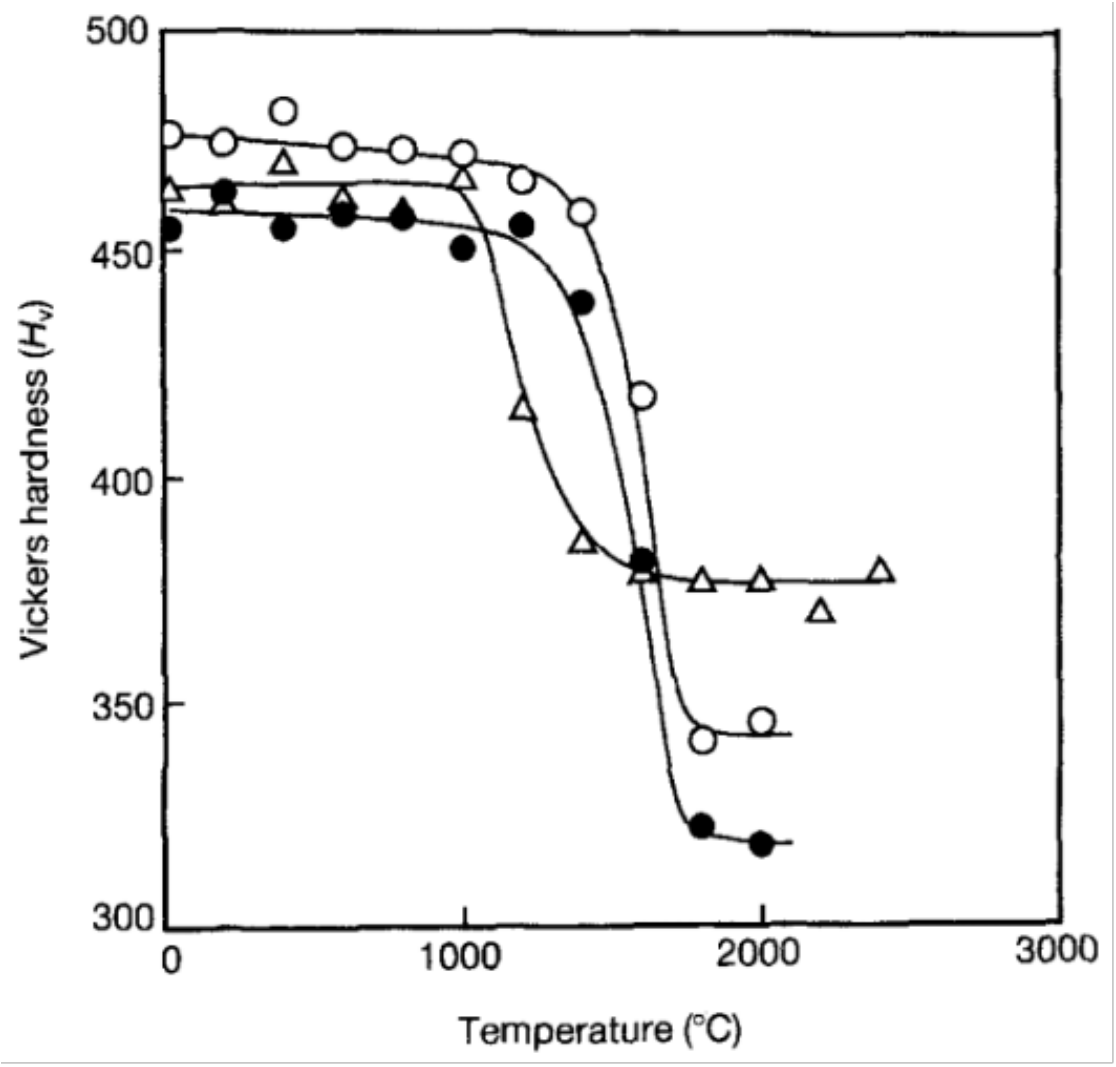


Figure 2.51: Vickers hardness of W (open triangles) measured by Mutoh et al. [67].

One study conducted in the 1970's by Burman, produced some initial tensile data for pure Mo, Mo30W, and TZM (another Mo based alloy) [68]. At the time Mo30W was being used in pump equipment for molten Zinc. Figure 2.52 contains the tensile strength of Mo30W up to 1200°C. Compared with pure Mo, Mo30W exhibits a slightly higher tensile strength, resulting from the solid solution strengthening. At 1100°C, pure Mo experiences a greater decrease in tensile strength with increasing temperature, but Mo30W does not. This is likely due to the W increasing the recrystallization temperature.

The tensile properties of pure W are summarized well in Figure 2.53 and Figure 2.54 up to 2773 K [69]. Both the ultimate tensile strength (UTS) and yield strength (YS) decrease with increasing test temperature. Above 2000 K, the decrease levels off and becomes less noticeable. The uniform elongation of pure W spikes at around 2000 K, while the compression spikes at the lower temperature of 1273 K.

Škoro et al. used Mo and W wires 0.5 and 0.8 mm in diameter to test for high temperature yield strength [8]. The metals were pressed, sintered, forged, then drawn with the W also undergoing stress relief at 400°C. The wires were heated then subject to high stresses by using a fast high current wire pulse until yielding or bending. This technique alloyed for testing the yield strength of Mo up to 2400 K and W up to 2700 K. These data are presented in Figure 2.55. The data was fit to the model presented by Zerilli and Armstrong [132], which is a constitutive equation for the flow stress of BCC metals.

$$\sigma = C_1 \exp\left(-C_2 T + C_3 T \ln \dot{\epsilon}\right) + C_4 + C_5 \epsilon^n + k d^{-1/2} \tag{2.4}$$

where T is the temperature, ϵ is the strain, $\dot{\epsilon}$ is the strain rate, d is the average grain size, and C_1, C_2, C_3, C_4,C_5, n, and k are all constant material parameters. Skoro et al. did not measure the grain size of the samples, so they combined the $k_d^{-1/2}$ with the C_4 constant as seen in Equation 2.5. These parameters were experimentally determined by Skoro et al. and are presented in Table 2.6.

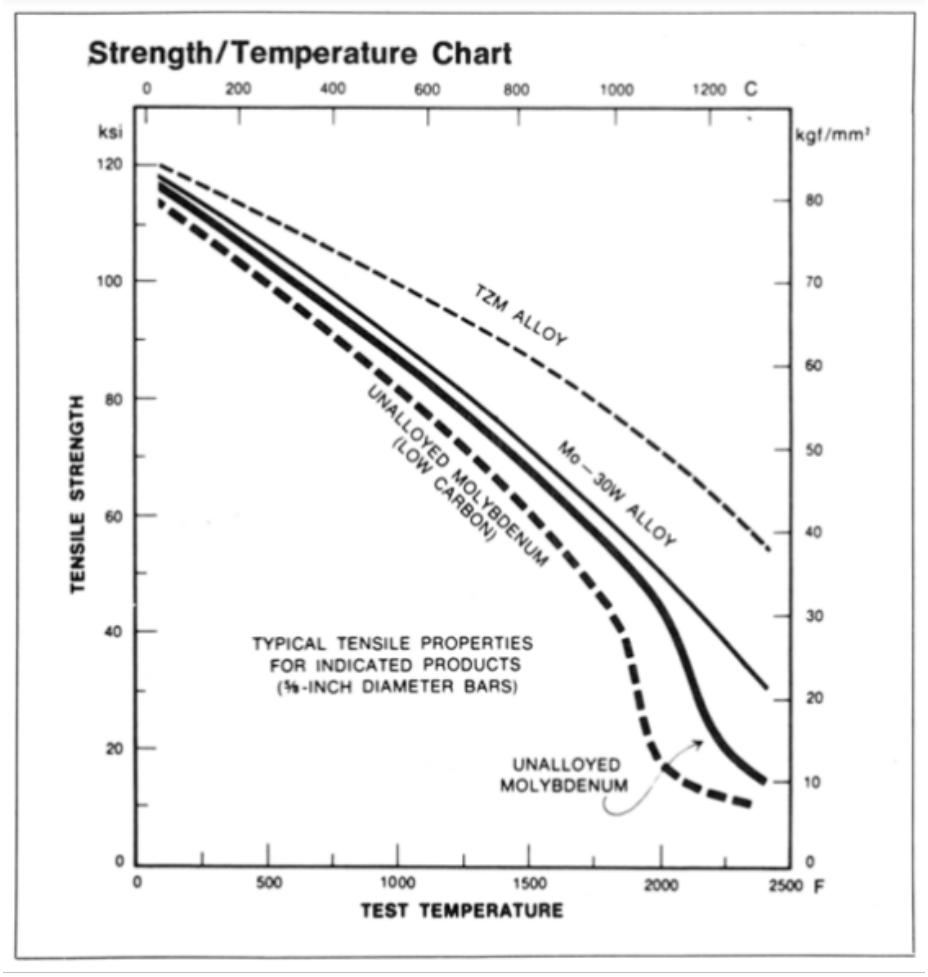


Figure 2.52: Tensile strength with respect to test temperature for Mo30W and other Mo alloys [68].

Table 2.6: Zerilli and Armstrong model parameters for Mo and W determined by Škoro et al. [8].

Parameter	Molybdenum (Mo)	Tungsten (W)
C_1 (MPa)	2259 ± 149	4711 ± 261
C_2 (K-1)	(5.01 ± 0.05) x 10^{-3}	(5.97 ± 0.28) x 10^{-3}
C_3 (K-1)	(5.05 ± 0.07) x 10^{-4}	(6.24 ± 0.42) x 10^{-4}
C_4 (MPa)	22 ± 5	94 ± 8
C_5 (MPa)	158 ± 42	133 ± 20
n	0.59 ± 0.10	0.51 ± 0.07

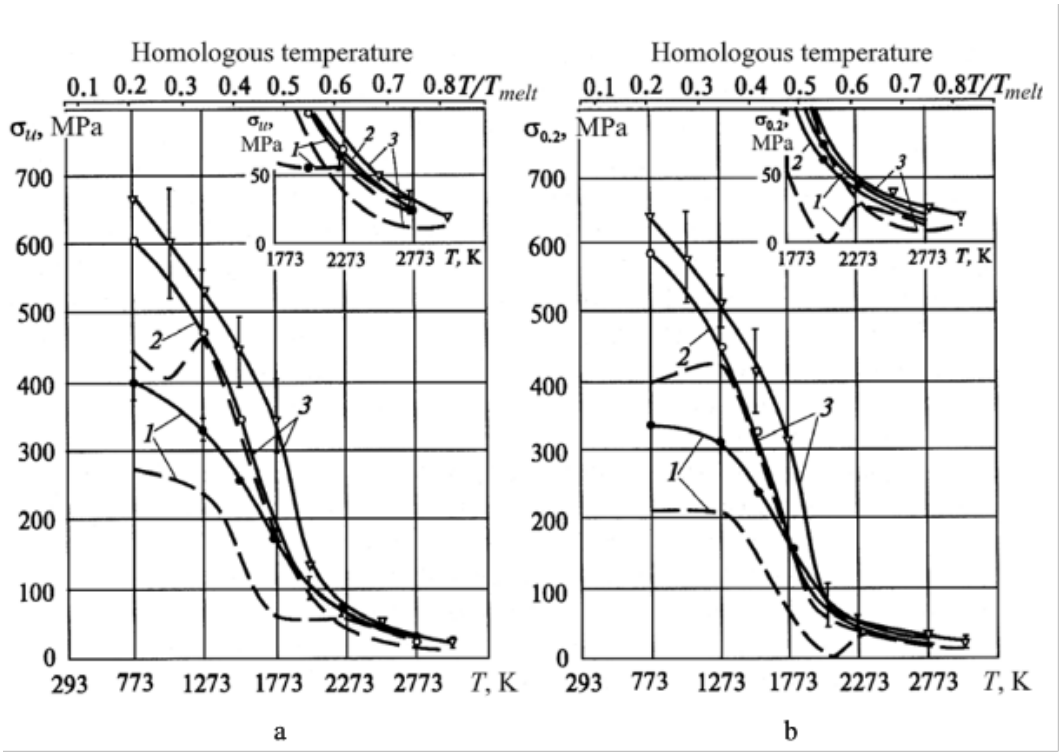


Figure 2.53: Mechanical properties of W at elevated temperatures (sample 1) including a) the ultimate tensile strength and b) the yield strength taken from [69].

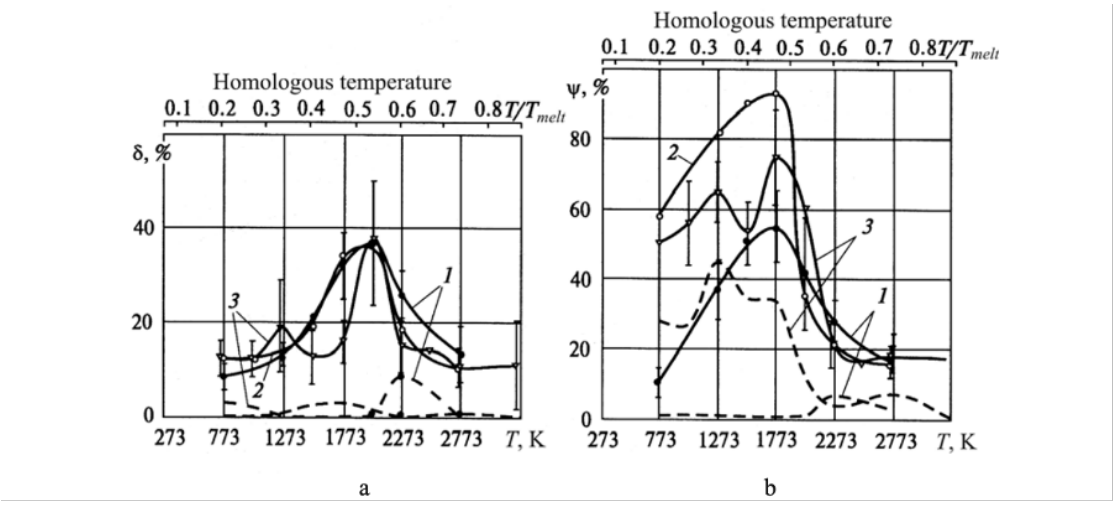


Figure 2.54: a) Elongation and b) compression of pure W (1) and other W alloys (2 and 3) from 773 to 2773 K taken from [69].

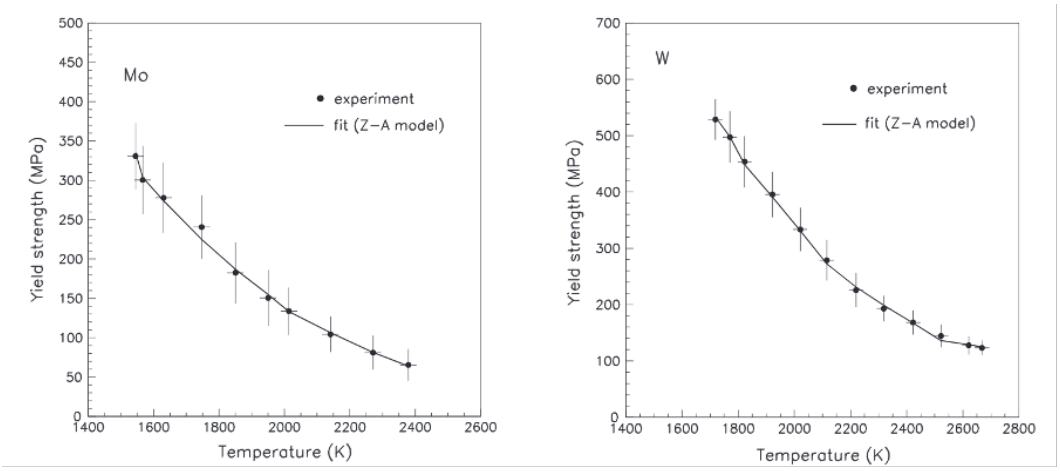


Figure 2.55: High temperature yield strength data of pure Mo (left) and pure W (right) fitted to the Zerilli and Armstrong BCC plastic deformation model by Škoro et al. [8].

$$\sigma = C_1 \exp\left(-C_2 T + C_3 T \ln \dot{\epsilon}\right) + C_4 + C_5 \epsilon^n \tag{2.5}$$

Wang et al. tensile tested 10 mm diameter specimens of pure Mo at 973, 1273, and 1623 K as part of a recrystallization study on pure Mo and Mo with dopants [9]. The results are presented in Table 2.7. The pure Mo samples experienced a decrease in yield and ultimate tensile strengths with increasing temperature. Using total elongation and reduction in are as measures of ductility, there was a slight increase in ductility from 973 to 1273 K, followed by a significant decline in ductility at 1623 K, where the material lost a considerable amount of strength. It appears only one sample was tested at each temperature, so no error information was provided to collaborate the increase in ductility from 973 to 1273 K.

Steichen et al. conducted tensile testing on pure tungsten from room temperature to 1000°C [70]. Figure 2.56 contains the yield strength and total elongation measured as part of this experiment. Steichen et al. also calculated a DBTT of around 65°C for tungsten, which seems low. Tensile DBTT is typically lower than the DBTT determined from impact and fracture tests, which will be discussed later.

Hiraoka et al. determined the DBTT for pure Mo by using impact and static bend tests [71]. The impact test determined a DBTT temperature of 375 K, while the static bend tests produced a DBTT of 200 K. The total absorbed energy with respect to test temperature for pure Mo is shown in Figure 2.57. The DBTT is represented by the drastic increase in total absorbed energy, from almost nothing to around 300 mJ. The yield strength determined from the impact testing is presented in Figure 2.58. The YS decreases with increasing temperature for pure Mo.

The DBTT for pure W was determined from fracture toughness testing by Mutoh et al. [67]. Two different fracture toughness tests were utilized. K_{IC} was used at lower temperatures and J_{IC} was used at higher temperatures. Figure 2.59 contains the fracture toughness of pure W with K_{IC} values up to 800°C, and JIC values up

Table 2.7: Tensile properties of pure Mo tested at 973, 1273, and 1623 K [9].

Properties	973 K	1273 K	1623 K
Yield Strength (MPa)	136	76	44
Ultimate Tensile Strength (MPa)	293	258	53
Total Elongation (%)	16	18	13
Reduction in Area (%)	86	94	31

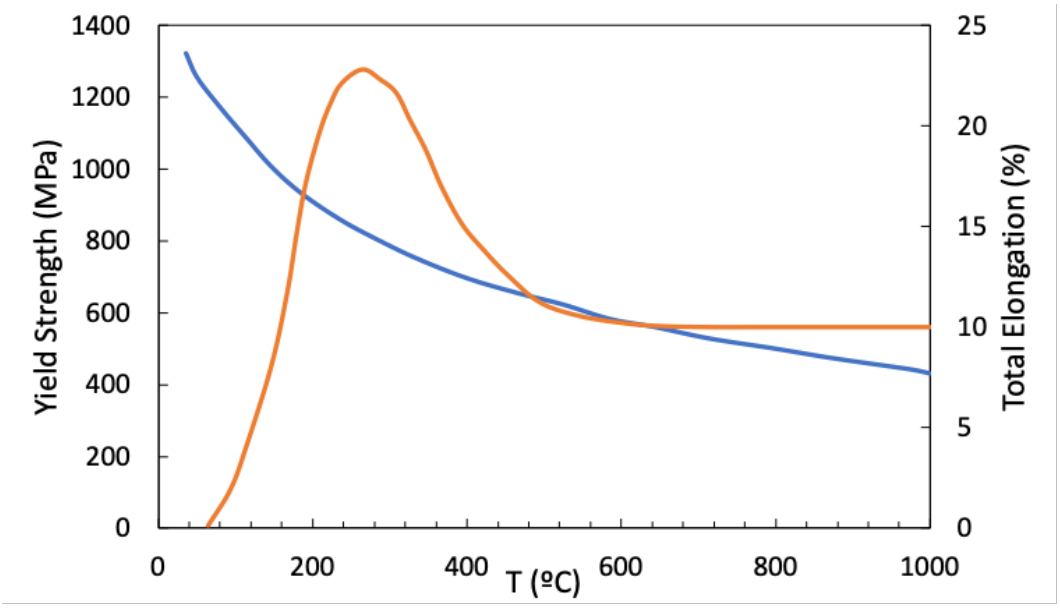


Figure 2.56: Yield strength (blue) and total elongation (orange) of pure tungsten tensile tested from room temperature to 1000°C [70].

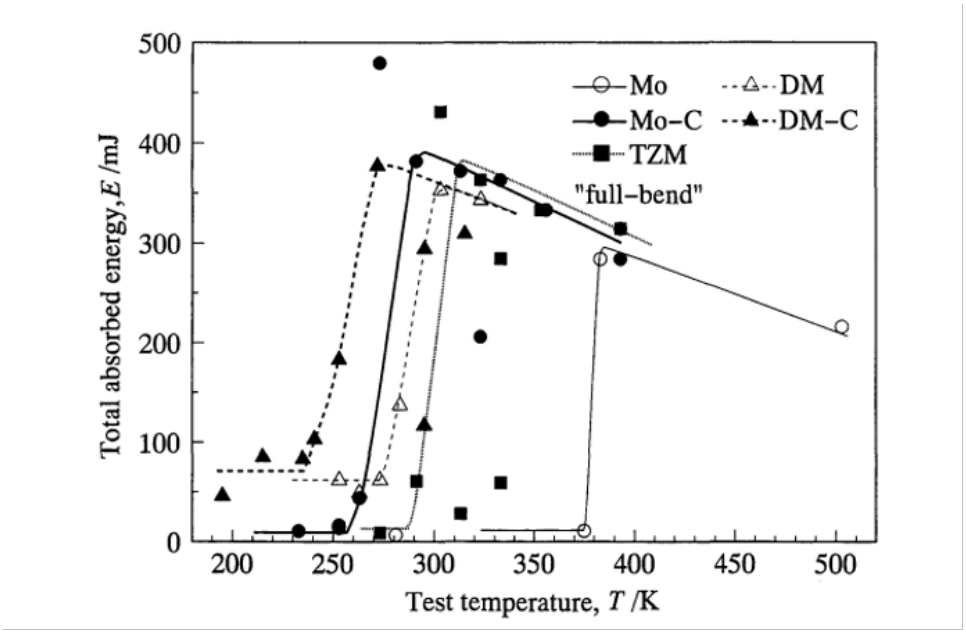


Figure 2.57: Total absorbed energy with respect to test temperature for pure Mo (open circle) determined by Hiraoka et al. [71].

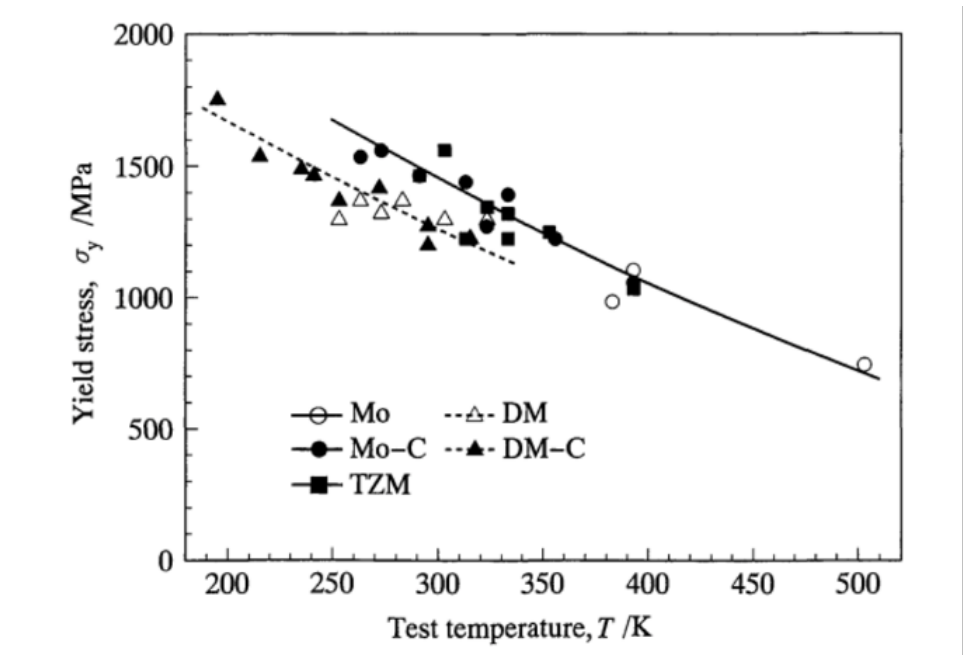


Figure 2.58: Yield strength determined from the impact test with respect to test temperature for pure Mo (open circle) determined by Hiraoka et al. [71].

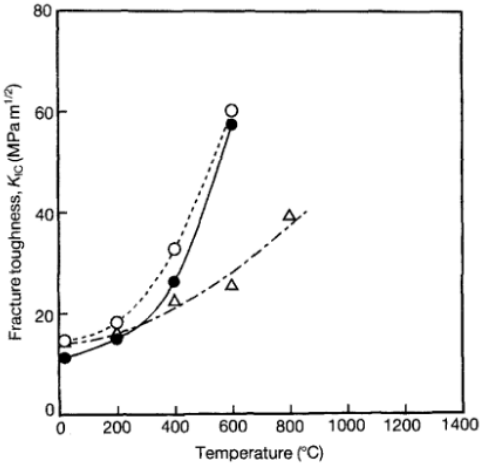


Figure 7 Temperature dependency of K_{IC} values for (△) W, (●) W–5 Re, and (○) W–10 Re.

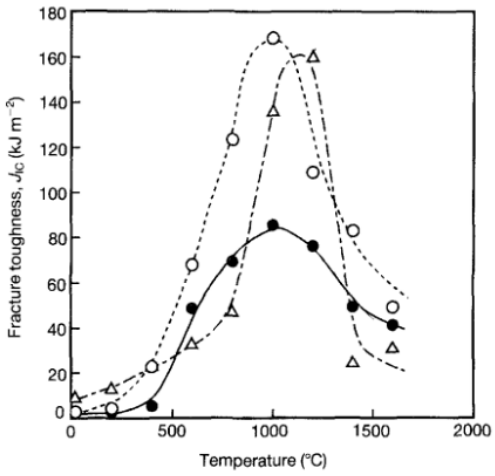


Figure 8 Temperature dependency of J_{IC} values for (△) W, (●) W–5 Re, and (○) W–10 Re.

Figure 2.59: Temperature dependence of K_{IC} fracture toughness (left) and J_{IC} fracture toughness (right) for pure tungsten (open triangles) and some W-rhenium alloys from Mutoh et al. [67].

to 1600°C. From this, the DBTT was determined to be 900°C. Fractographs of the fractured samples are shown in Figure 2.60.

Gludovatz et al. collected the fracture toughness through three different methods, 3-point bending, double cantilever beam, and compact tension specimens [72]. K_Q fracture toughness values of W and three other W alloys are presented in Figure 2.61. The fracture toughness of pure tungsten is relatively low below 400°C, but there is a significant increase in fracture toughness at 800°C.

2.4 Properties of Zirconium Carbide

Zirconium carbide (ZrC) is a great candidate for the matrix material for a solid fuel element for NTP. Its high melting point, high strength, high thermal conductivity, and excellent neutronic properties all make it a good candidate for NTP [10].

2.4.1 Crystal Structure of ZrC

ZrC is a refractory ceramic with only one stable cubic phase. This stable phase is an FCC B1 (NaCl-type) symmetry with an Fm3m space group. The ZrC phase is stable from around 0.36 to 0.5 atomic percent carbon, as seen in Figure 2.62, with the highest melting point existing for $ZrC_{0.85}$. The melting point is around 3700 K. Two types of bonds exist in the ZrC crystal lattice, namely the Zr-Zr metallic bonds and the C-Zr covalent/ionic metal to carbon bonds [133]. Most ZrC feedstocks currently available are sub stoichiometric and contain free carbon impurity [134]. This can have a significant effect on the thermal and mechanical properties of the material.

All of the properties of ZrC are heavily dependent upon the stoichiometry. The stoichiometry of ZrC is typically specified by the carbon to zirconium (C/Zr) ratio, with a value of one representing perfectly stoichiometric ZrC. Jackson and Lee developed a model that predicts the lattice parameter as a function of the C/Zr

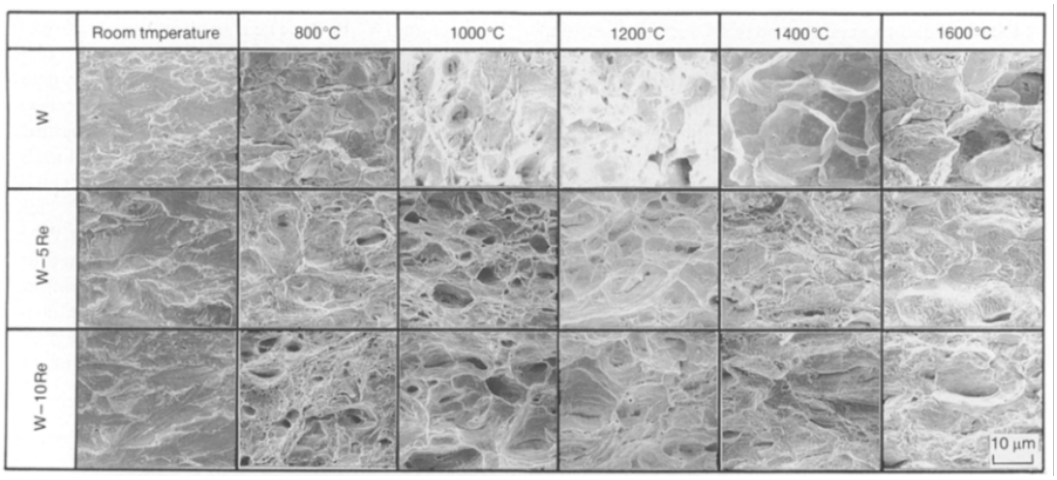


Figure 2.60: Fractographs collected by Mutoh et al. for W and two W-rhenium alloys for samples fractured up to 1600°C [67].

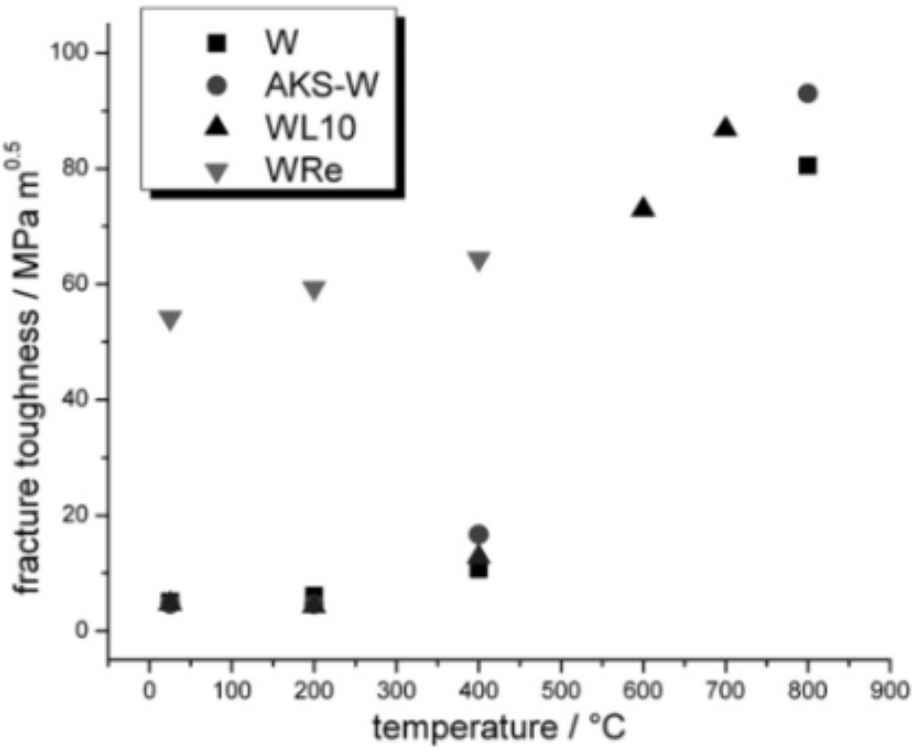


Figure 2.61: Fracture toughness K_Q of pure W and other tungsten alloys up to 800°C [72].

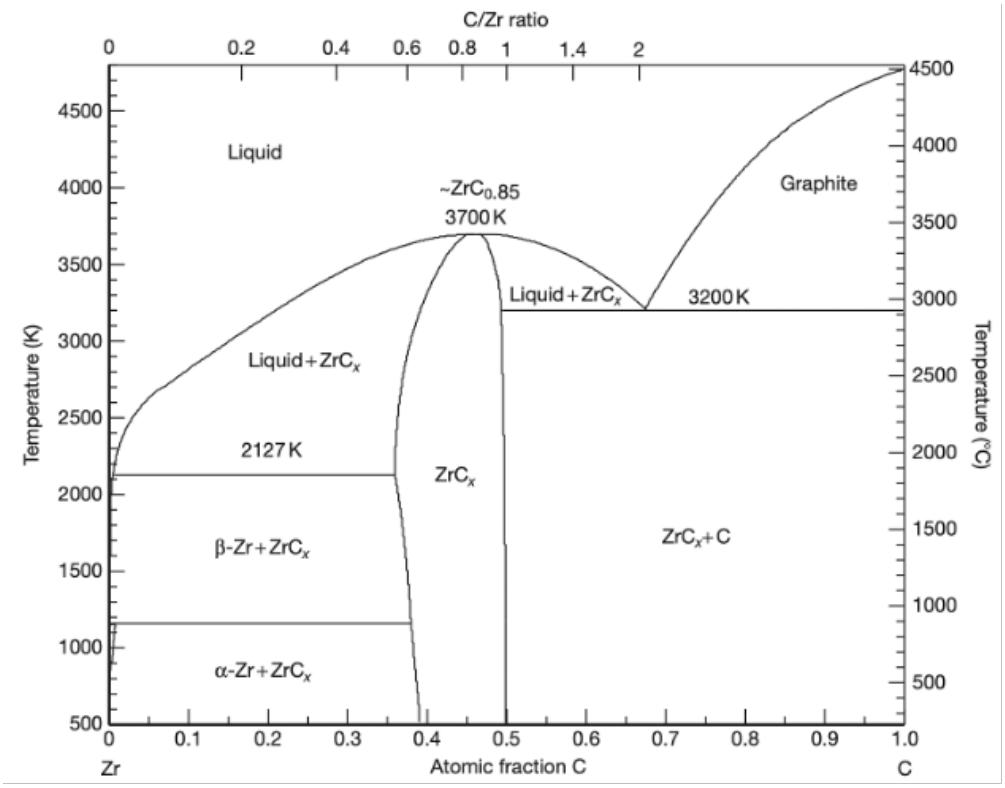


Figure 2.62: Zr-C binary phase diagram as assessed by Fernandez-Guillermet [73] and compiled by Jackson and Lee [10].

ratio and the oxygen nitrogen (ON) impurity content, as seen in Equation 2.6, where x is the C/Zr ration and y is the (ON) fraction [135].

$$a_{ZrC_x(ON)_y} = 4.5621 - 0.2080x^2 + 0.3418x - 0.80y(1-x) \tag{2.6}$$

2.4.2 Thermal Properties of Zirconium Carbide

As with the refractory materials, the thermal properties of greatest interest for the design of cercer NTP systems are heat capacity, thermal conductivity and diffusivity, thermal expansion, and vapor pressure. Not only do the thermal properties of ZrC depend the temperature of the material, but they also depend on the stoichiometry of the material. Porosity and free carbon can also affect the properties of ZrC.

The heat capacity of ZrC with various stoichiometries have been measured using a variety of techniques up to 3000 K. Several of these experiments were compiled by Jackson and Lee and are shown in Figure 2.63 [10]. Below room temperature, the heat capacity drops off pretty rapidly. From room temperature to 2700 K, there is only a slight increase in heat capacity for most stoichiometries. Katoh et al. took similar data and used it to plot the specific heat capacity and then also fit an equation for the heat capacity as a function of temperature as shown in Figure 2.64 [74].

From the different experiments, Katoh et al. developed four models for the specific heat capacity of ZrC for four different C/Zr ratios, with value of 0.69, 0.76, 0.96 and 0.99. Equation 2.7 through Equation 2.11 contain these models [53]. Equation 2.11 is shown in Figure 2.64 overlayed with the data.

$$C_p(ZrC_{0.69}) = 8.057 + 1.928 \times 10^{-3}T + \frac{7.623 \times 10^9 \exp\left(\frac{-31.4\times10^3}{T}\right)}{T^2} \tag{2.7}$$

$$C_p(ZrC_{0.76}) = 7.762 + 2.348 \times 10^{-3}T + \frac{33.11 \times 10^9 \exp\left(\frac{-19.9\times10^3}{T}\right)}{T^2} \tag{2.8}$$

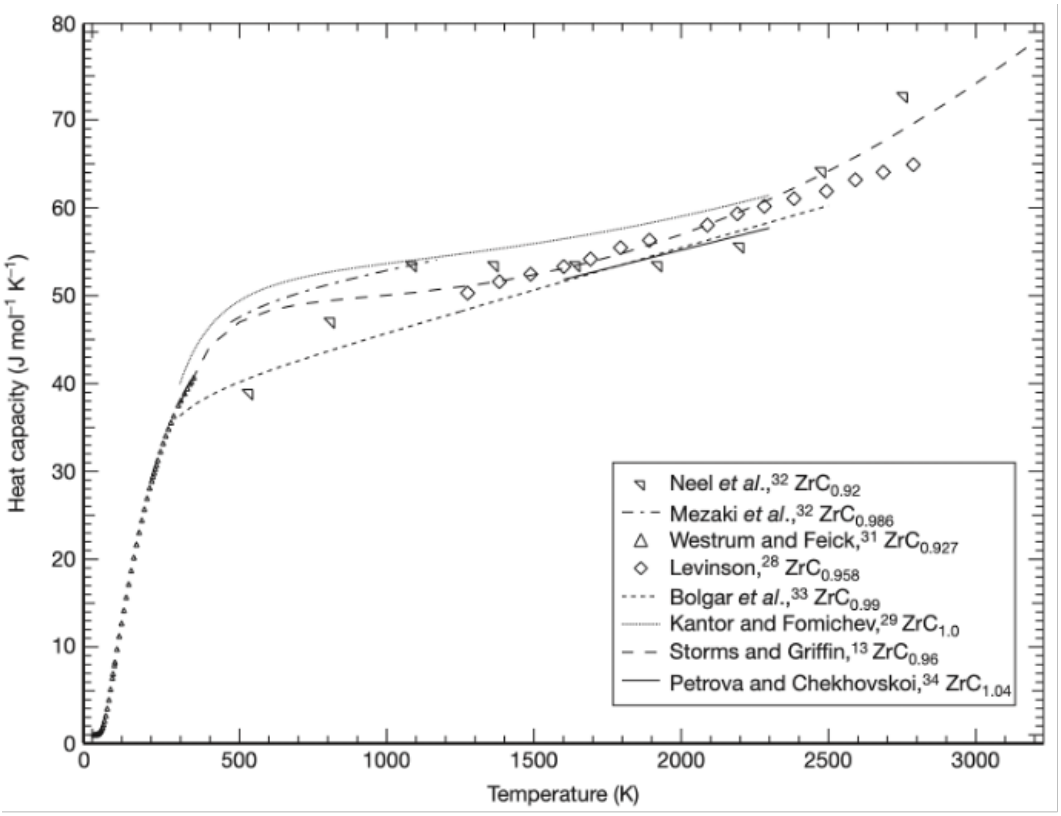


Figure 2.63: Heat capacity of ZrC for various stoichiometries up to 3000°C as compiled by Jackson and Lee [10].

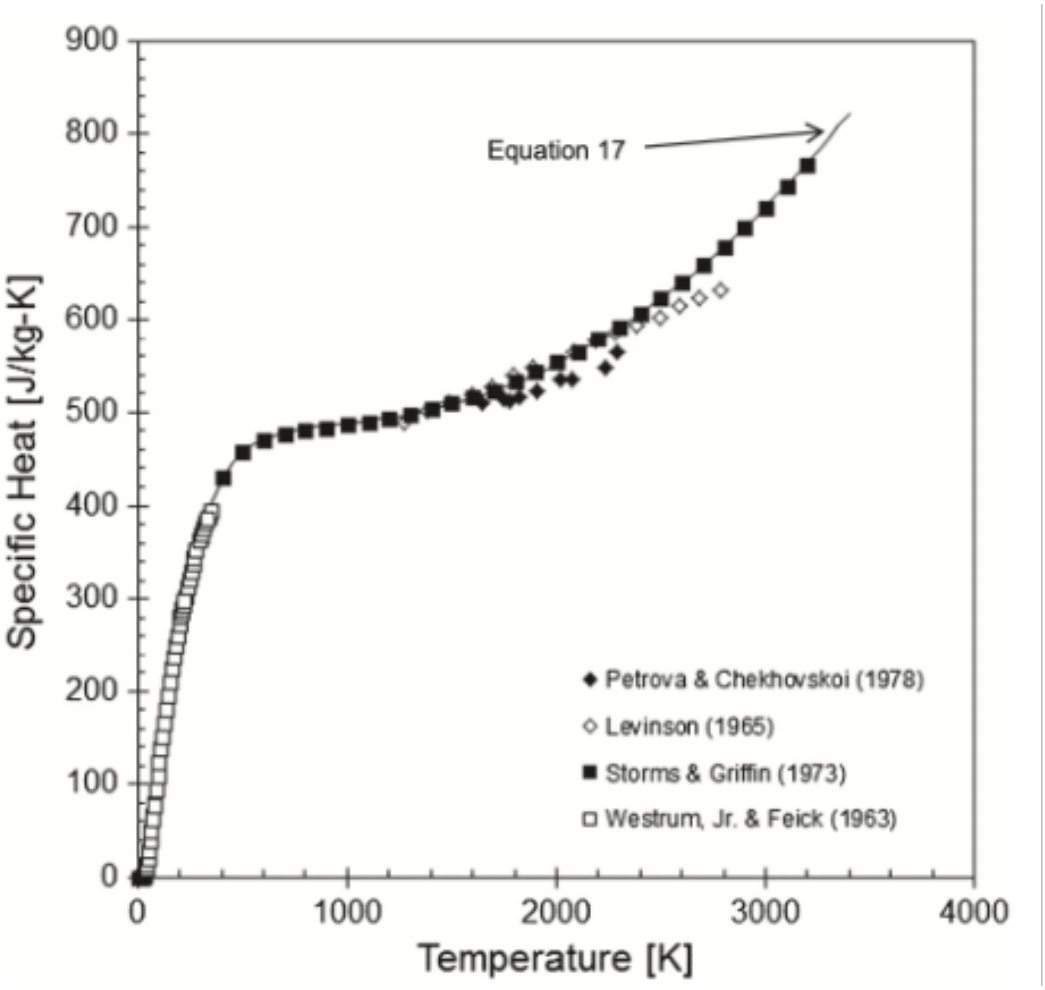


Figure 2.64: Specific heat capacity of ZrC as a function of temperature as compiled by Katoh et al. [74].

$$C_p(ZrC_0.96) = 8.71 + 2.28 \times 10^{-3}T + \frac{70.65 \times 10^5}{T^2} \tag{2.9}$$

$$C_p(ZrC_0.99) = 7.33 + 3.32 \times 10^{-3}T \tag{2.10}$$

$$C_p(ZrC_0.96) = 8.71 + 2.28 \times 10^{-3}T + \frac{70.65 \times 10^5}{T^2} \tag{2.11}$$

The effect of the C/Zr ratio on heat capacity can be seen in Figure 2.63. The heat capacity at room temperature from C/Zr ratios from 0.6 to 1.0 show an increase in heat capacity as the C/Zr ratio increases. While the ratio does affect the heat capacity, the effect is minimal, less than 15 percent for the entire range. Figure 2.64 contains the specific heat capacity of ZrC as a function of the C/Zr ratio, as compiled by Katoh et al. Katoh et al. proposed a model for the room temperature specific heat capacity as a function of the C/Zr ratio which is presented as Equation 2.12 [74].

$$C_p = 373.2 - 355.6x + 686.0x^2 - 334.3x^3 (0.65 < x < 1.0) \tag{2.12}$$

The thermal conductivity of the matrix material is very important, as a significant amount of heat will need to be conducted throughout the NTP fuel element. A higher thermal conductivity can prevent the formation of hot spots and help the material heat up and cool off during the rapid thermal transients proposed for NTP. The thermal conductivity (k) and diffusivity (α) are related by the following equation:

$$k = \alpha \rho C_p \tag{2.13}$$

where ρ is the density in kg/m^3 and C_P is the specific heat capacity in J/kgK. As the temperature increases, the thermal conductivity also increases. This is likely due to the large contribution of conduction band electrons to thermal conductivity, along with the high phonon conductivity common in most ceramics [74]. Figure 2.65

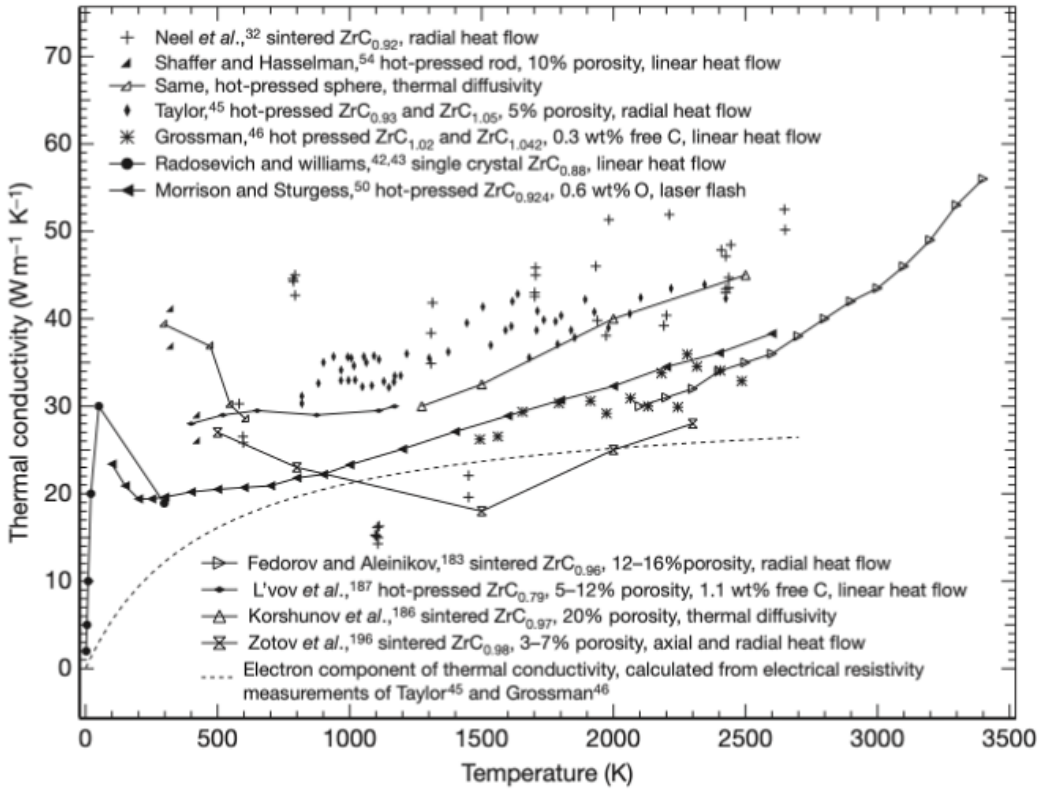


Figure 2.65: Thermal conductivity of ZrC at various stoichiometries as a function of temperature, compiled by Jackson and Lee [10].

contains thermal conductivity data of ZrC of various stoichiometries as a function of temperature. Once again, it becomes apparent that the stoichiometry of the ZrC plays a significant effect in the thermal conductivity of the material. Figure 2.66 illustrates this effect by comparing the thermal conductivity for C/Zr ratios from 0.6 to 1.0 at room temperature. The thermal conductivity of ZrC increases as the C/Zr ratio increases, with the highest thermal conductivity at room temperature for stoichiometric ZrC being around 45 W/mK. Once the C/Zr ratio drops below 0.9, the thermal conductivity at room temperature drops by a factor of 4. This is a major impact and suggests that near-stoichiometric material will be required for an NTP system.

As with most metals and ceramics, ZrC has an increasing coefficient of thermal expansion with increasing temperature. This property depends more heavily on the porosity of the material compared with the C/Zr ratio. Figure 2.67 contains the CTE data for several ZrC materials with different stoichiometries and porosities up to 3000°C. The maximum measured CTE is $10 \times 10^{-6} K^{-1}$ for $ZrC_{0.946}$ sintered and tested at 2800°C. The effect of C/Zr ratio on the CTE is illustrated in Figure 2.68. There appears to be a slight decrease in CTE at 1273 K with increasing C/Zr ratio up to a value of 1. Most ZrC feedstocks have free carbon. The effect of free carbon on CTE was analyzed in two different studies. As shown in Figure 2.69, free carbon up to 0.5 weight percent has almost no effect on the thermal expansion of ZrC.

The vapor pressure and evaporation rates of ZrC are also important for NTP systems. The vapor pressure of ZrC, shown in Figure 2.70, follows an Arrhenius relationship. The evaporation rate, shown in Figure 2.71, also follows and Arrhenius relationship. Given the short operating time of the NTP system, these values should not cause significant concern against using ZrC as a matrix material.

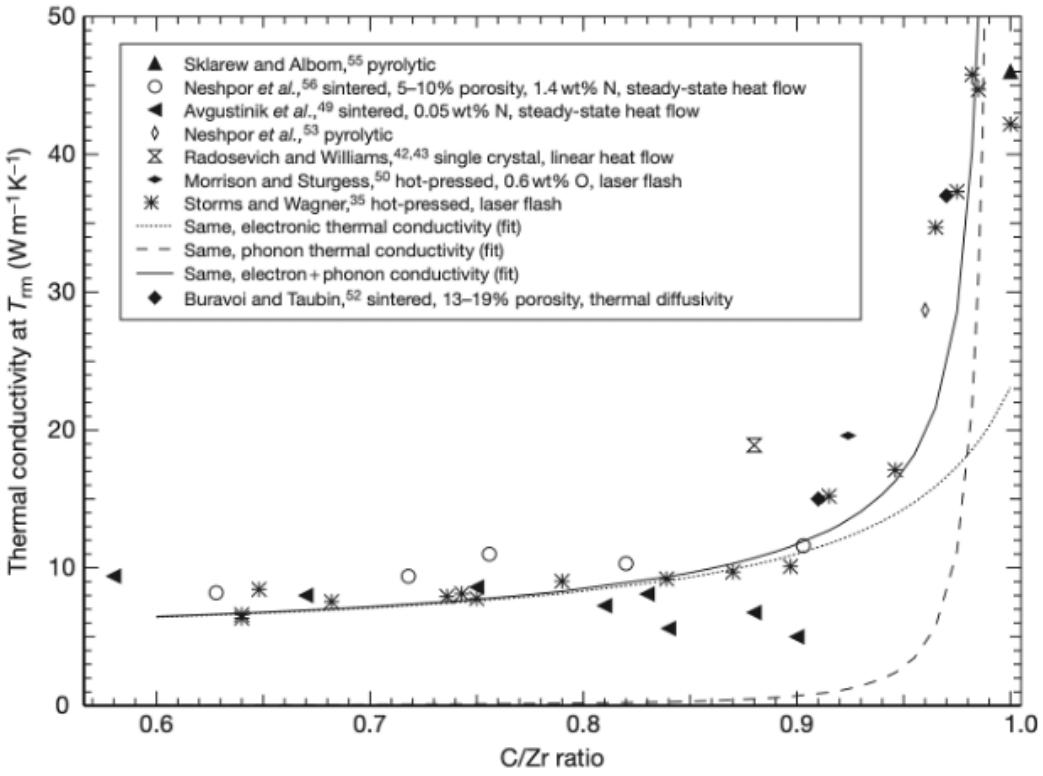


Figure 2.66: Thermal conductivity of ZrC at room temperature as a function of C/Zr ratio compiled by Jackson and Lee [10].

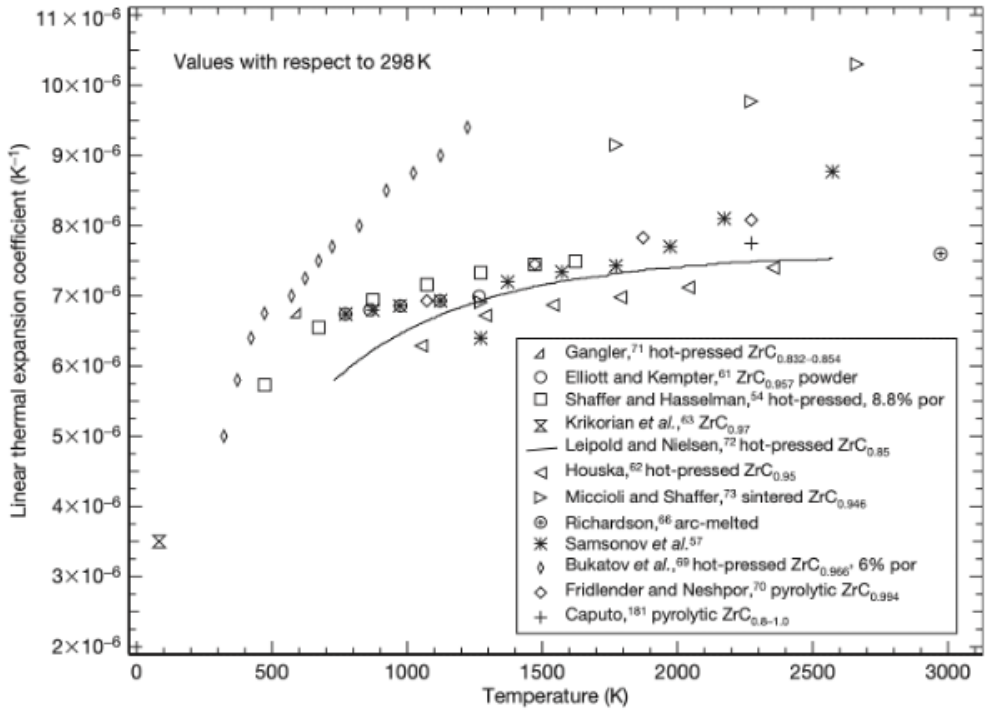


Figure 2.67: Linear coefficient of thermal expansion (CTE) of ZrC with respect to temperature compiled by Jackson and Lee [10].

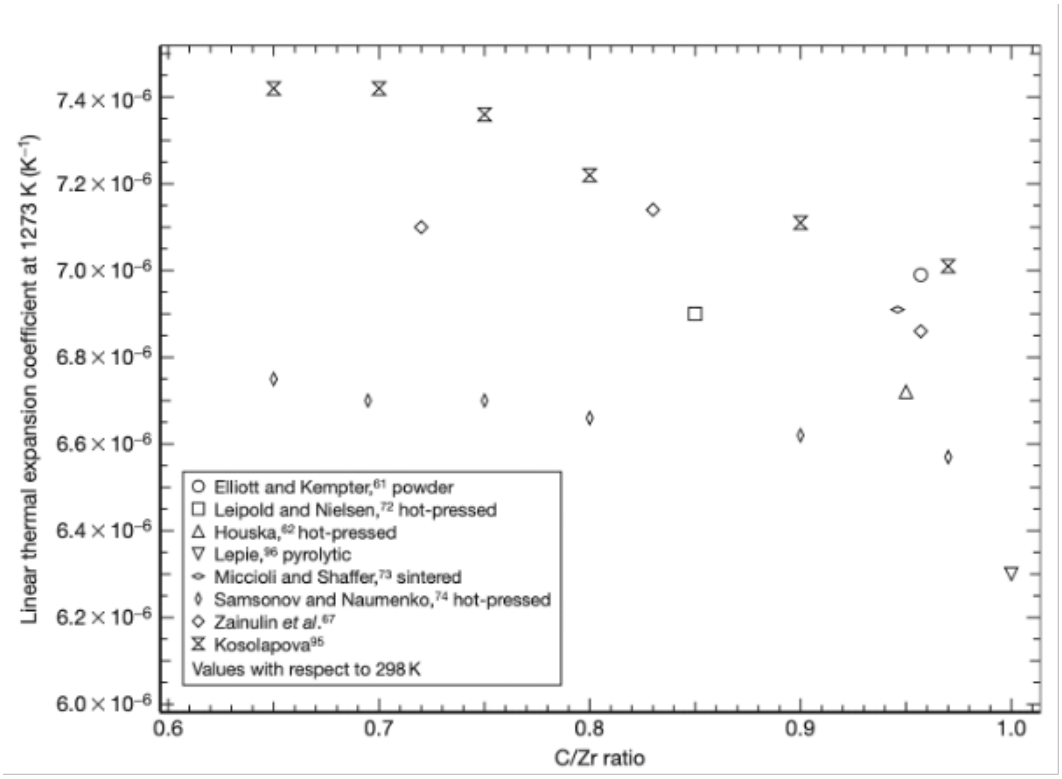


Figure 2.68: CTE of ZrC at 1273 K with respect to the C/Zr ratio compiled by Jackson and Lee [10].

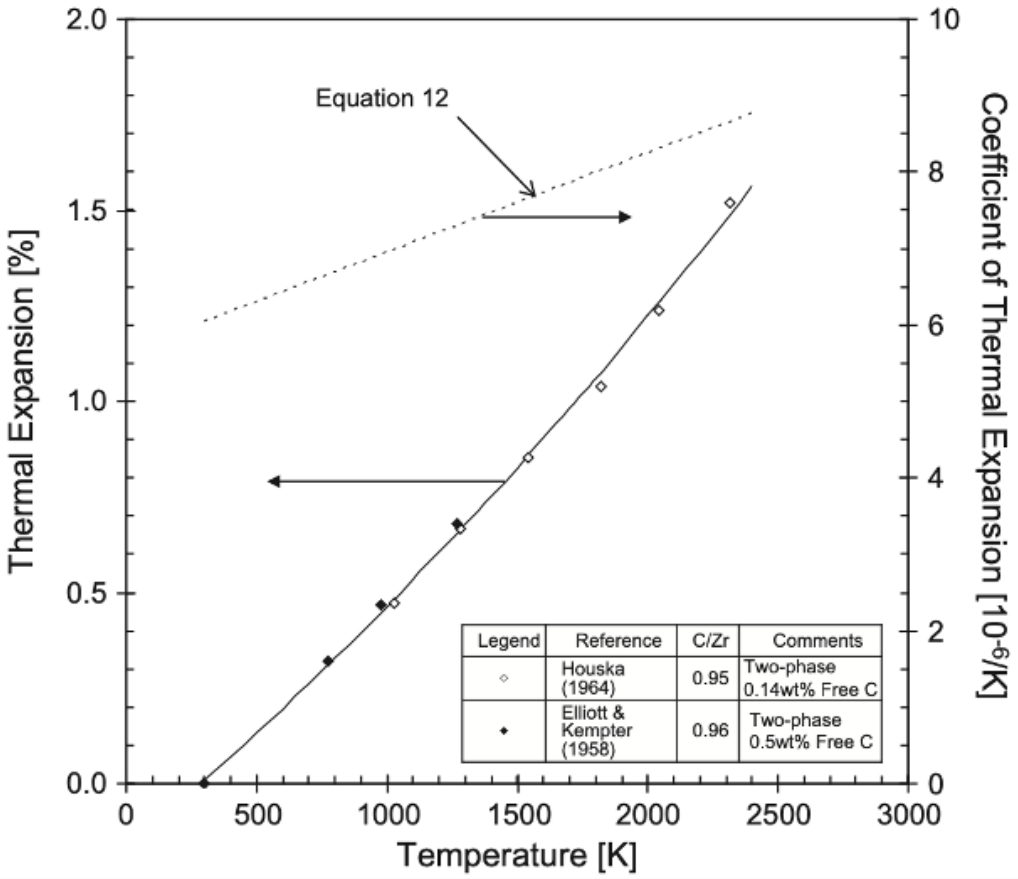


Figure 2.69: Thermal expansion and CTE, for two high stoichiometric ZrC powders with measured free carbon compiled by Katoh et al. [74].

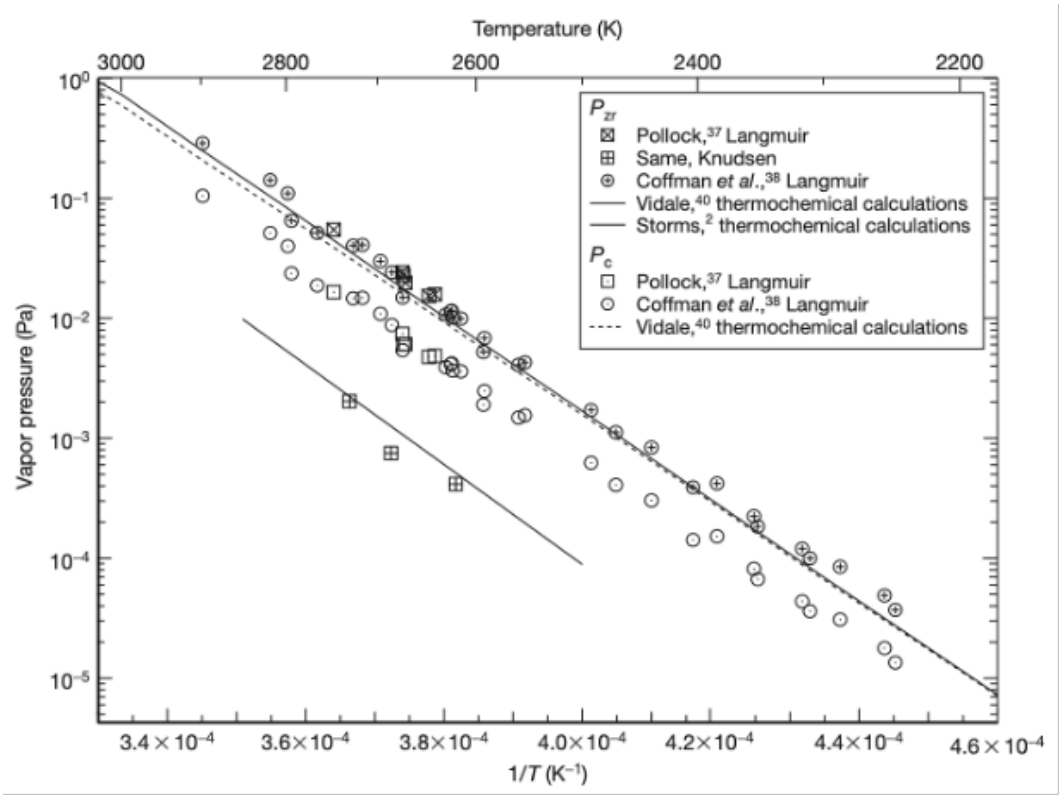


Figure 2.70: Vapor pressures of C and Zr as a function of temperature as compiled by Jackson and Lee [10].

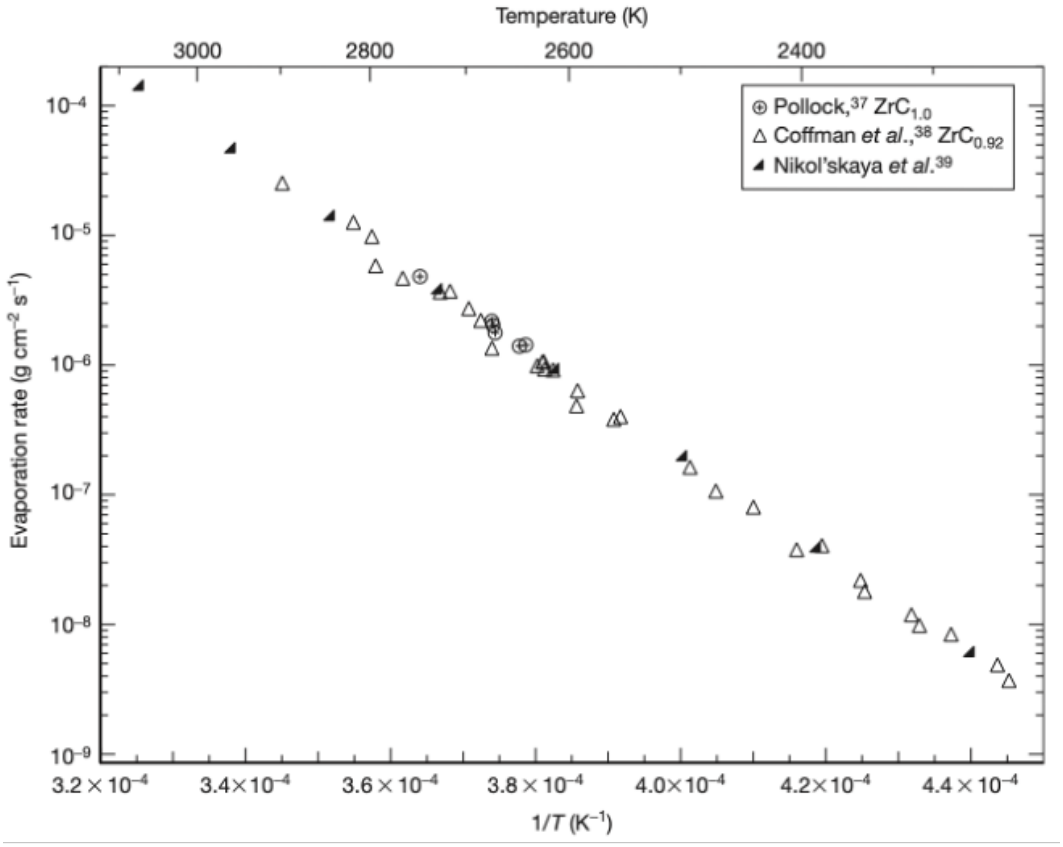


Figure 2.71: Langmuir evaporation rate of ZrC for different stoichiometric ratios at various temperatures as compiled by Jackson and Lee [10].

2.4.3 Mechanical Properties of Zirconium Carbide

Zirconium carbide shares similar mechanical properties to most metallic carbides. Room temperature elastic properties for stoichiometric ZrC as summarized by Jackson and Lee [10] can be found in Table 2.8.

Like the thermal properties, the elastic moduli depend on the temperature and the C/Zr ratio. As seen in Figure 2.72, as the temperature increases, the value of Young's modulus decreases. The change is roughly linear until around 2250 K, where there appears to be a more significant drop. More higher temperature data is needed to confirm this result. Figure 2.73 illustrates the effect of the C/Zr ratio on Young's modulus. As the ratio decreases, so too does the value of the modulus. This change is less severe than that caused by the elevated temperature.

Hardness can be a good measure of strength in a material. The hardness of ZrC decreases dramatically with increasing temperature. As seen in Figure 2.74, the loss of strength is pretty apparent above 1000 K, with the loss saturated at 1400 K. The C/Zr ratio seems to have less of an impact on the hardness, but still a noticeable one. As the C/Zr ratio falls, so too does the hardness, but much less dramatically, as show in Figure 2.75. Hardness also depends heavily on the porosity, which was not reported in the figure. Since the porosity will vary depending on the material fabrication techniques, this likely accounts for the observed spread in the hardness.

Katoh et al. provided a more in-depth review of hardness of ZrC by looking at single crystals with specific orientations and including hypo-stoichiometric ZrC [74]. As seen in Figure 2.76, there is not much effect in the hardness of ZrC based on the crystallographic plane and direction tested. This is especially true above 1000 K. Figure 2.77 illustrates the affect stoichiometry has on room temperature hardness. Below a C/Zr value of 1, there is an increasing hardness with increasing ratio, until there is a drop off at a value of 0.8. Since this represents data from a single study, this is likely the case, at least for the specific material tested. Above a C/Zr ratio of

Property	Value
C_{11} (GPa)	468.2 to 472
C_{12} (GPa)	98.7 to 99.7
C_{44} (GPa)	157.3 to 159.3
Young's modulus (GPa)	398 ± 20
Shear modulus (GPa)	167 ± 5
Bulk modulus (GPa)	229 ± 25
Poisson's ratio	0.197 ± 0.023

Table 2.8: Typical elastic properties of ZrC at room-temperature compiled by Jackson and Lee [10].

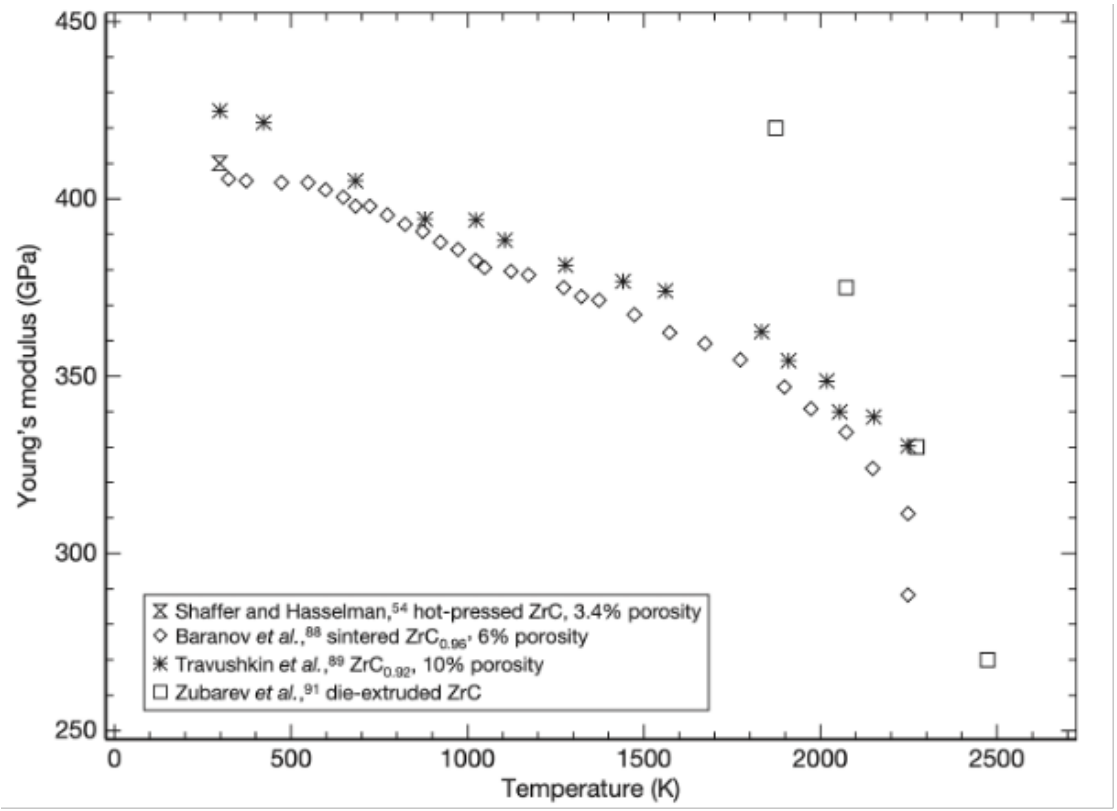


Figure 2.72: Young's Modulus of ZrC as a function of temperature compiled by Jackson and Lee [10].

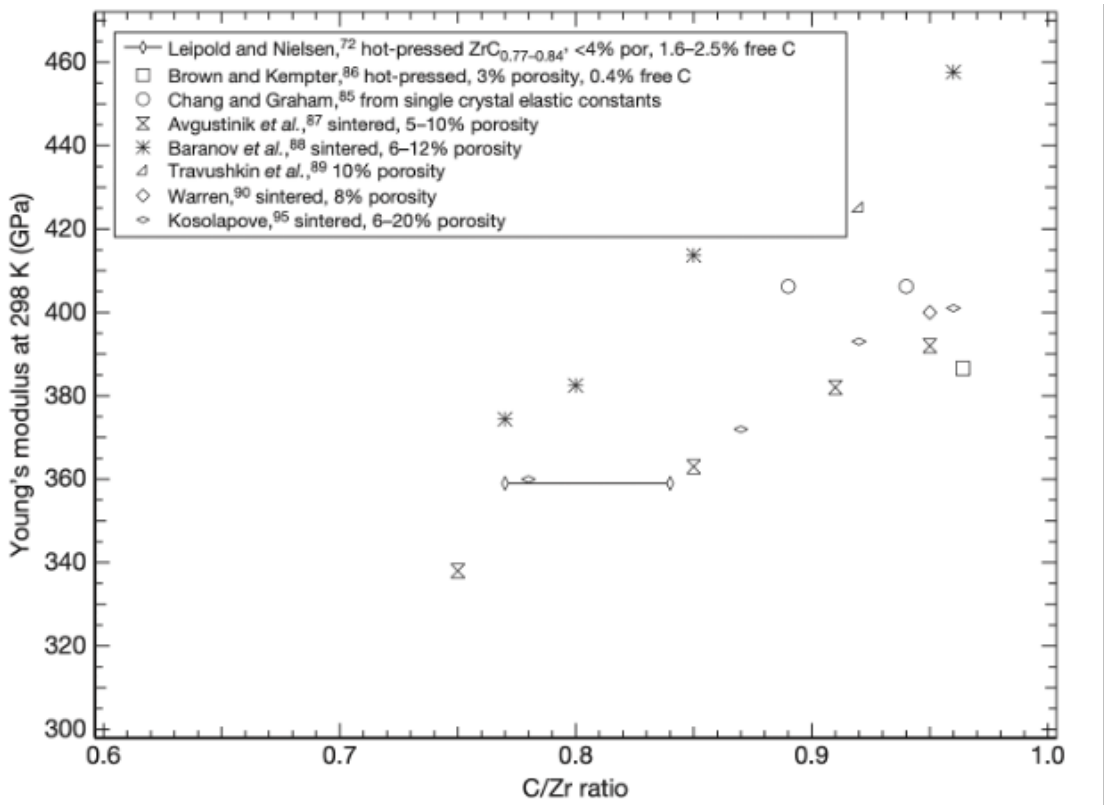


Figure 2.73: Young's modulus at room temperature as a function of the C/Zr ratio compiled by Jackson and Lee [10].

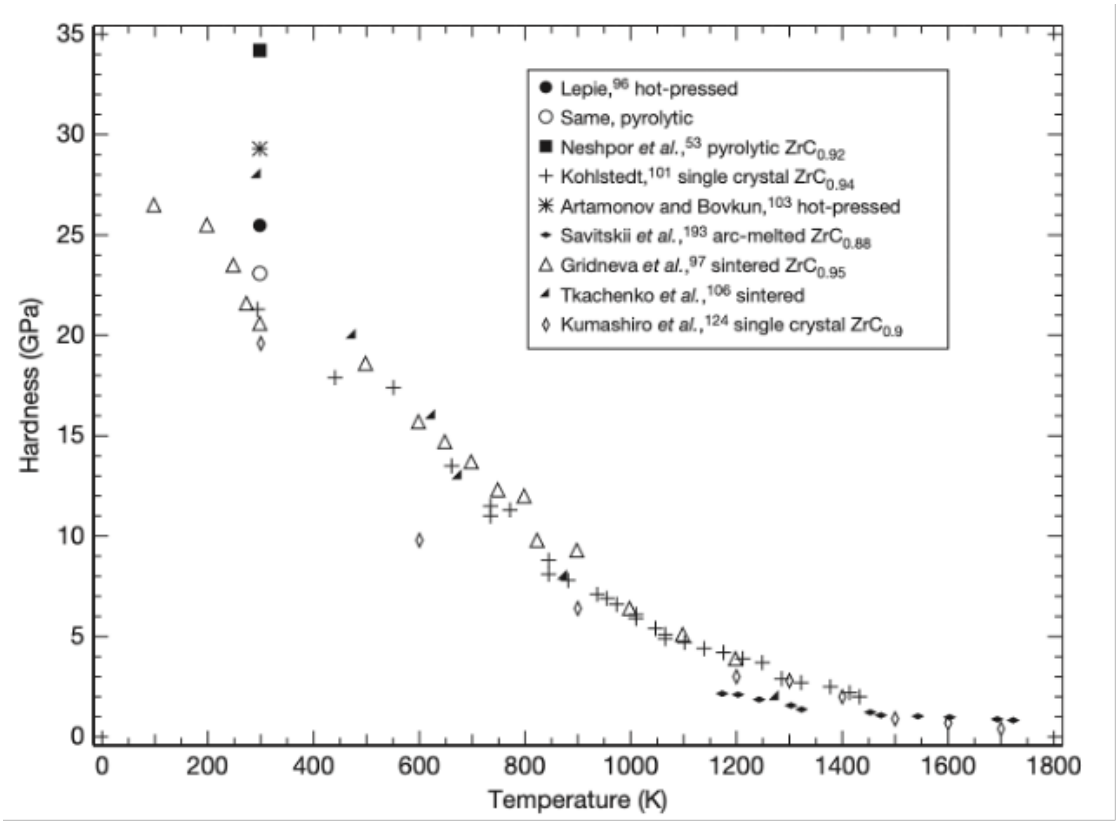


Figure 2.74: Indentation hardness of ZrC as a function of temperature, compiled by Jackson and Lee [10].

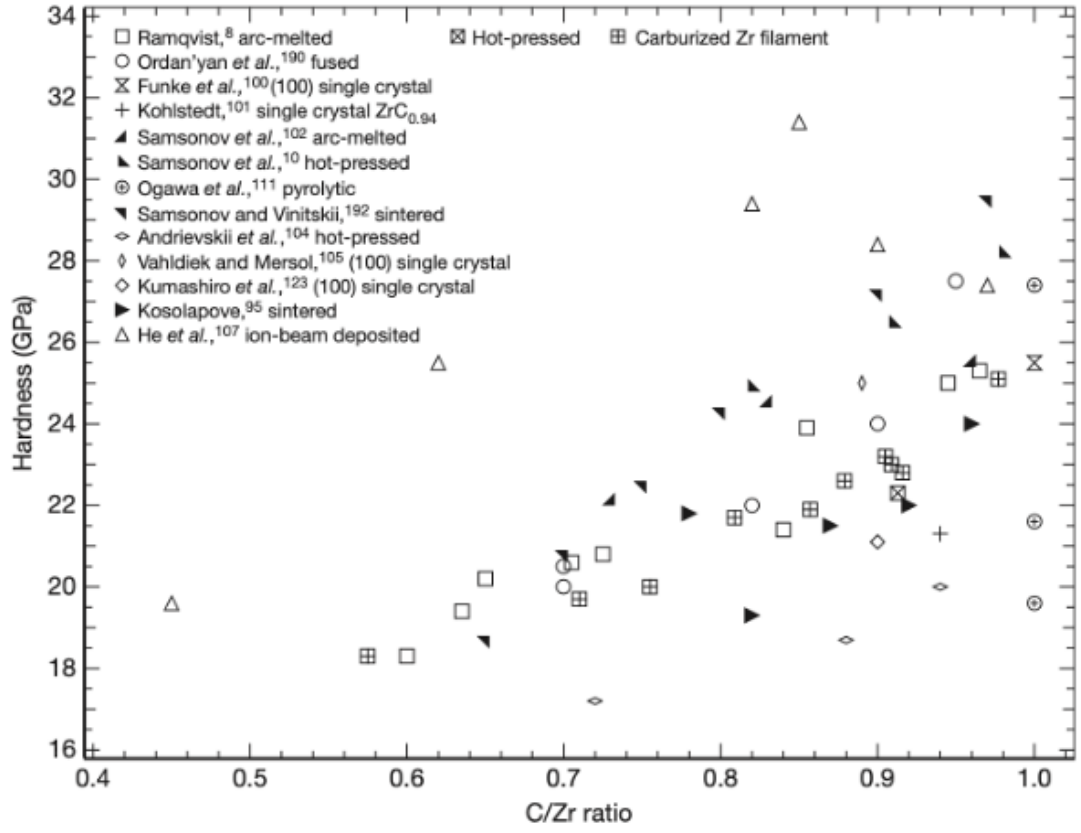


Figure 2.75: Room temperature hardness of ZrC as a function of the C/Zr ratio compiled by Jackson and Lee [10].

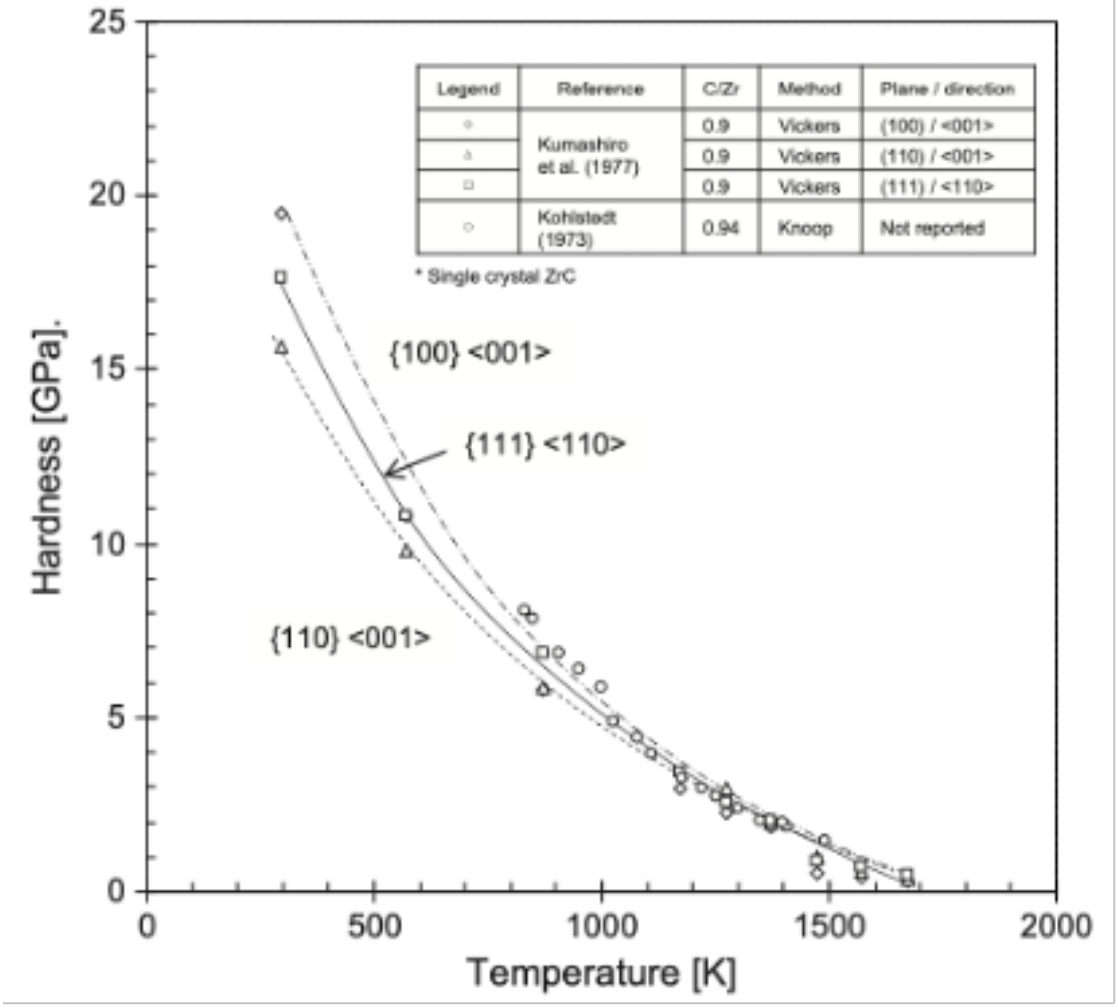


Figure 2.76: Indentation hardness of single crystal ZrC with respect to test temperature compiled by Katoh et al. [74].

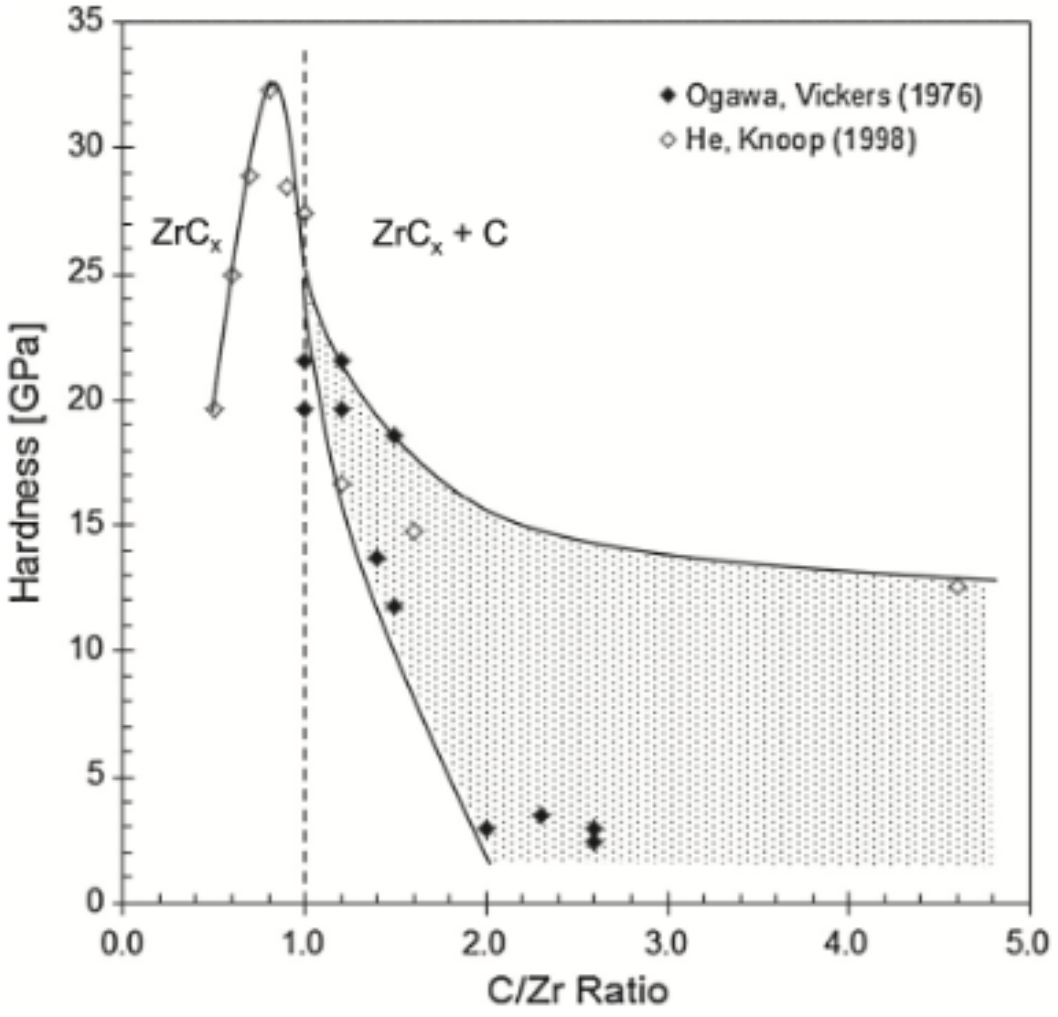


Figure 2.77: Variation of indentation hardness of ZrC with respect to the C/Zr ratio including hypo-stoichiometric carbon compiled by Katoh et al. [74].

1.0, where a second phase of free carbon is present, the hardness drops of drastically, as would be expected.

While hardness is a convenient test to gauge mechanical properties, more information can be inferred from larger scale mechanical testing. Figure 2.78 and Figure 2.79 contain the ultimate tensile strength (UTS) of ZrC and the bend strength of ZrC with respect to temperature, respectively, as compiled by Jackson and Lee [10]. The UTS depends heavily on the C/Zr ratio, the porosity, and the free carbon. Near stoichiometric ZrC appears to increase in strength with temperature until around 2300 K, at which point the strength begins to diminish rapidly. Other materials appear to have ultimate tensile strengths which decrease with increasing temperature. The data from the bend bar tests appears even more convoluted. Several materials experienced an increase in bend strength at moderate temperatures, while others experienced a steady decrease in bend strength with increasing temperature. Even at room temperature, the bend strength varied from around 100 to 300 MPa. The sample with the highest reported bend strength was pyrolytic $ZrC_{1.03}$, suggesting that a small amount of free carbon may help the mechanical properties of ZrC.

Another study by Demirskyi et al. compared the flexural strength of ZrC along to other transition metal carbides [75]. The tests were conducted to abover 2400°C, as shown in Figure 2.80. Once again, the strength did not increase until above 1600°C, after which it dropped off again.

Compression testing is typically conducted on ceramics and other brittle materials to quantify strength values. Darolia and Archbold compression testing from 1200 to 1800°C [76] as seen in Figure 2.81. Over this range, the compressive strength decreases linearly with increasing temperatures.

Two studies looked at the room temperature mechanical properties of hot pressed ZrC. These properties are listed in Table 2.9. Korklan et al. tested the mechanical properties $ZrC_{0.92}$ at room temperature [11]. The material was hot pressed using a step method starting at 1600°C and with a maximum temperature of 2150°C for 35 minutes with a uniaxial pressure of 32 MPa. Fracture toughness tests were

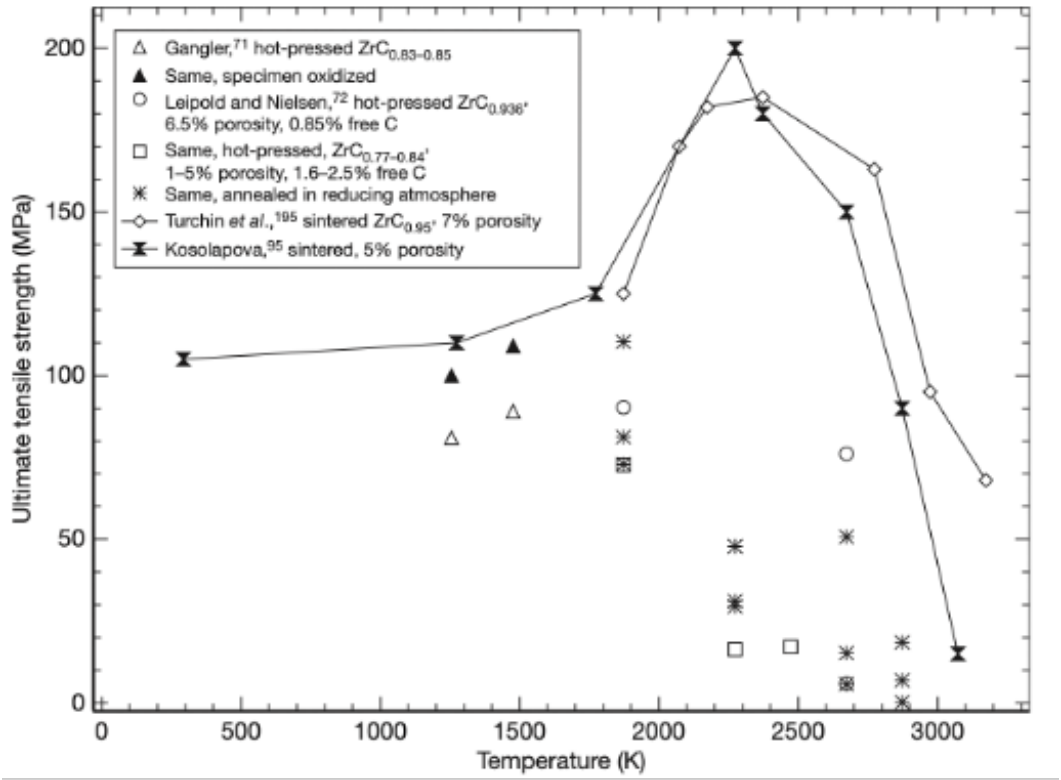


Figure 2.78: Ultimate Tensile strength of ZrC with various stoichiometries as a function of temperature compiled by Jackson and Lee [10].

Table 2.9: Room temperature mechanical properties of hot pressed ZrC as reported by Korklan et al. [11] and Feng et al. [12].

Source	Korklan et al.	Feng et al.
Composition	$ZrC_{0.92}$	Not Given
Relative Density (%)	95.9	96.8
Grain Size (µm)	2.7 ± 1.4	0.6 ± 0.3
Young's Modulus (GPa)	397 ± 13	405
Shear Modulus (GPa)	161 ± 4	N/A
Hardness (GPa)	17.0 – 19.5	18.6 ± 0.8
Flexural Strength (MPa)	362 ± 46	310 ± 10
Fracture Toughness (MPa $m^{1/2}$)	2.9 ± 0.1	2.35 ± 0.20

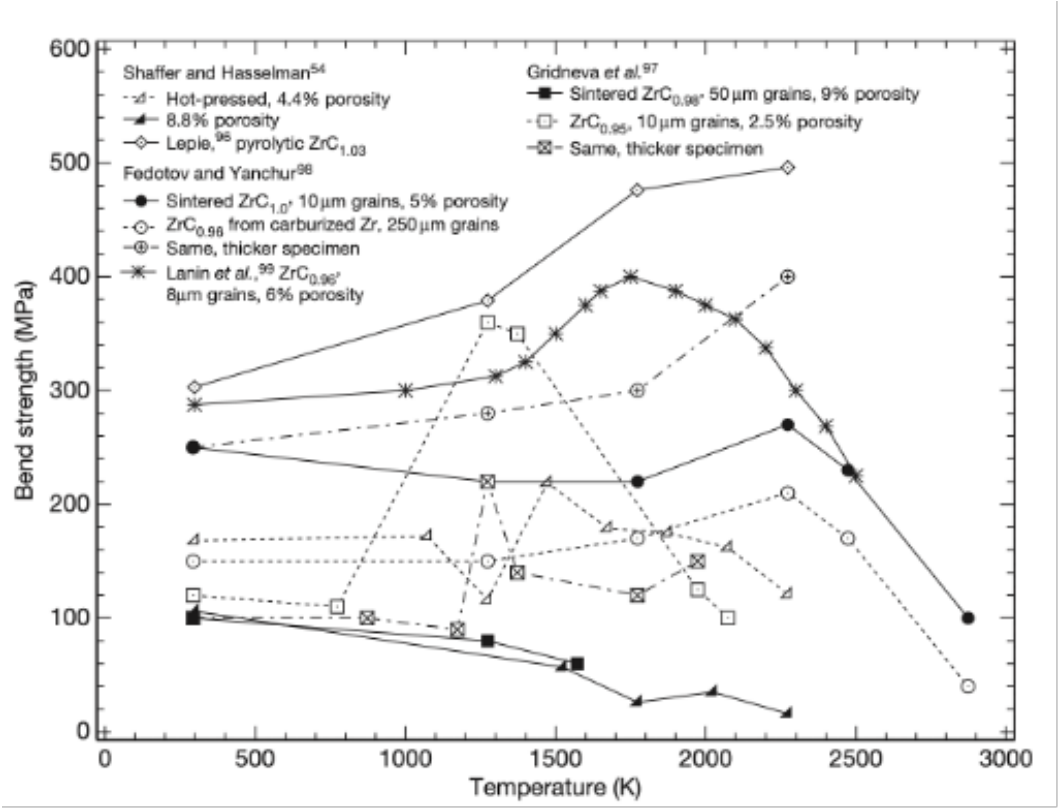


Figure 2.79: Bend strength of ZrC with respect to temperature, compiled by Jackson and Lee [10].

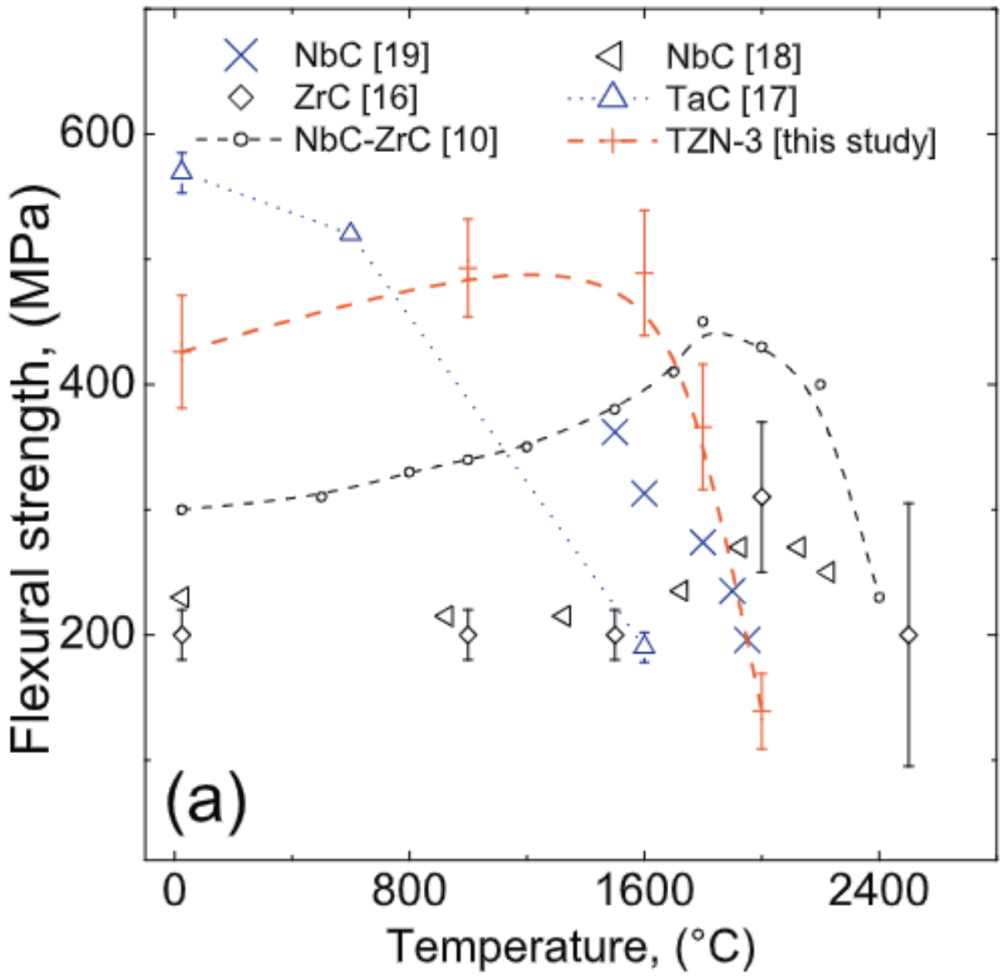


Figure 2.80: Flexural strength of ZrC (open diamonds) along with other transition metal carbides compiled by Demirskyi et al. [75]. [10].

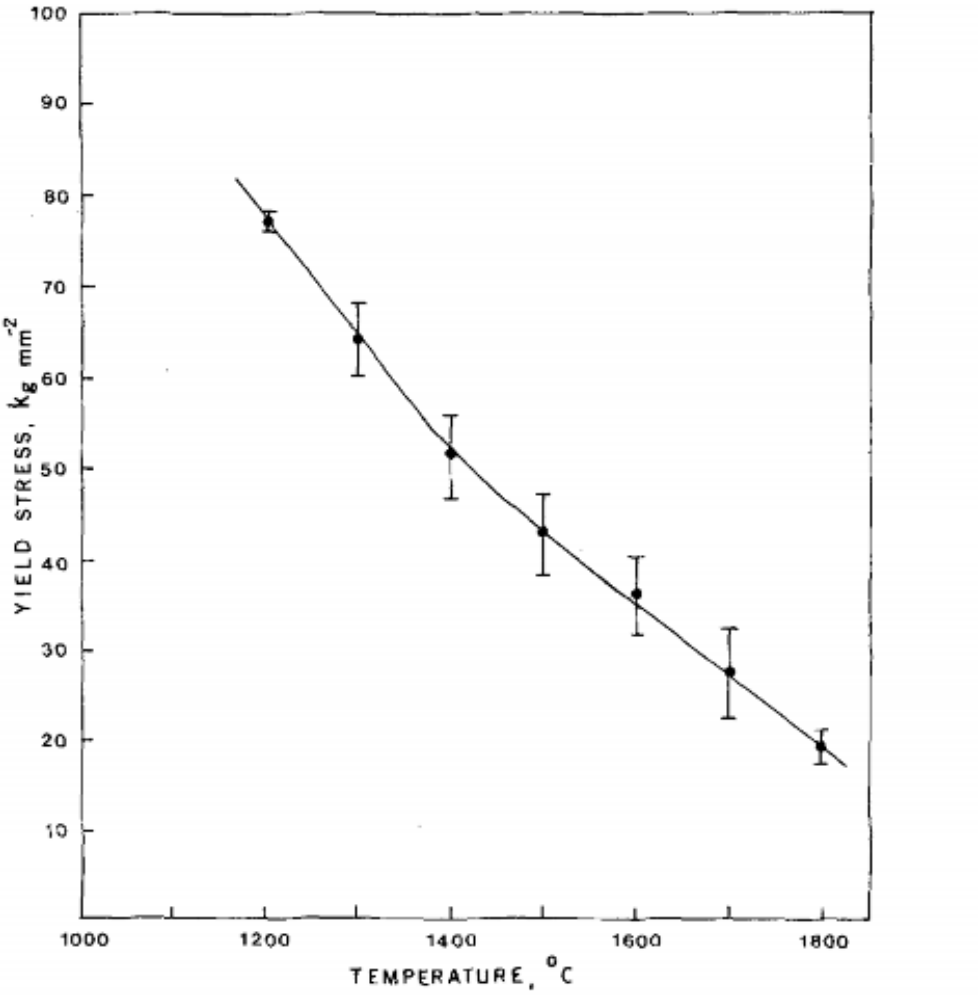


Figure 2.81: Compressive yield stress of $ZrC_{0.94}$ from 1200 to 1800°C taken from Darolia and Archbold [76].

conducted using a chevron notched bend bar test. Feng et al. also looked at the room temperature mechanical properties of ZrC [12]. These samples were hot pressed at 1900°C and 32 MPa for 1 hour. The final stoichiometry of the ZrC was not reported in the article. Feng et al. also tested the fracture toughness of the ZrC material. Short type-B bars (24 mm x 4 mm x 3 mm) were prenotched using a Vicker's indenter to a load of 5 kg. This notch acted as the crack propagation site. The samples were then tested using a four-point bending apparatus. The fracture toughness was determined from Equation 2.14, where ν_V^R is a geometric constant, E is the Young's modulus (GPa), H is the Vicker's hardness (GPa), σ is the four-point bending strength (MPa), and P is the indentation load (N).

$$K_{IC} = \nu_V^R \left(\frac{E}{H}\right)^{\frac{1}{8}} \left(\sigma P^{\frac{1][3}{]}}\right)^{\frac{3}{4}} \tag{2.14}$$

2.5 Properties of Surrogate and Fuel Ceramics

As discussed previously, to simplify the fabrication and testing of the sintered materials, non-radioactive surrogate ceramic particles were used. Currently, the three fuel forms of interest are uranium dioxide (UO_2) and uranium nitride (UN).

2.5.1 Properties of UO_2 and YSZ

Uranium dioxide (UO_2) is the most common fuel form for commercial nuclear reactors. Its properties are well understood. Yttria stabilized zirconia (YSZ) has been used as a surrogate for UO_2 for a variety of different research applications, mostly pertaining to NTP [109, 136, 137]. The phase diagram of the uranium-oxygen system is presented in Figure 2.82. At room temperature, zirconia (ZrO_2) exists in the monoclinic crystal structure. The addition of yttria, allows for the cubic phase to become stable at room temperature, as seen in Figure 2.83 [14].

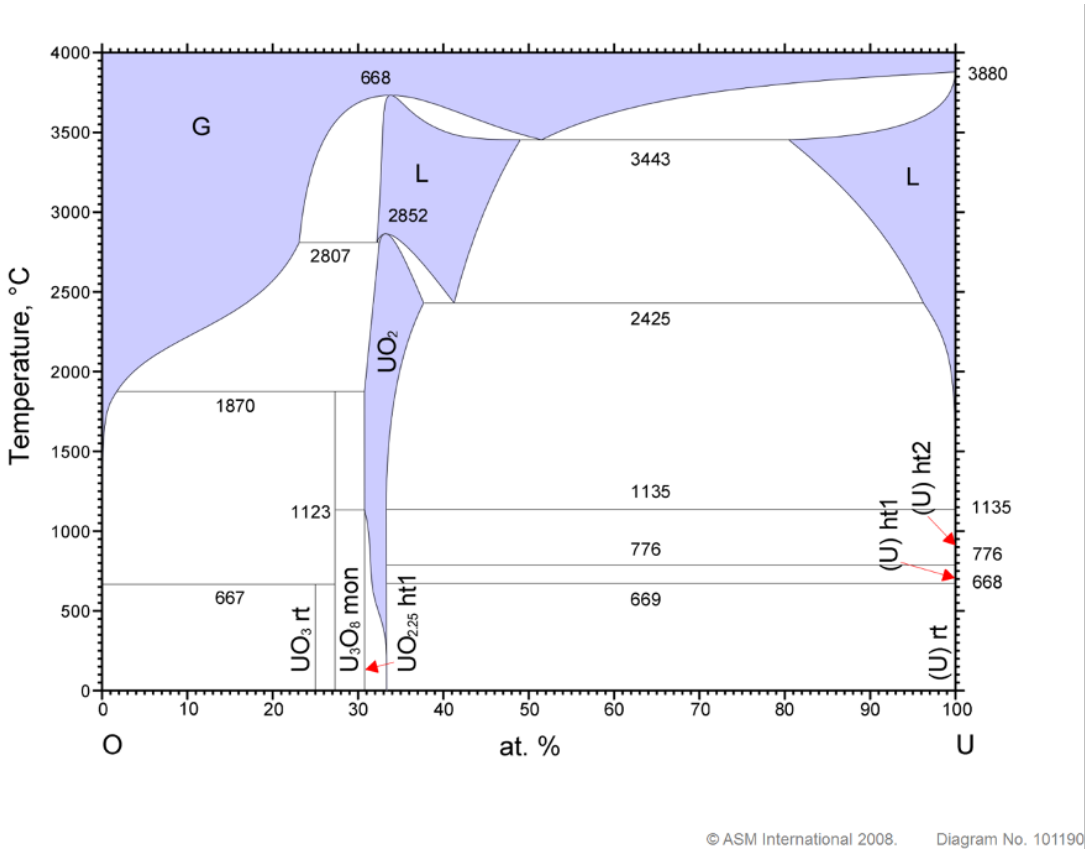


Figure 2.82: Uranium oxygen phase diagram taken from [17].

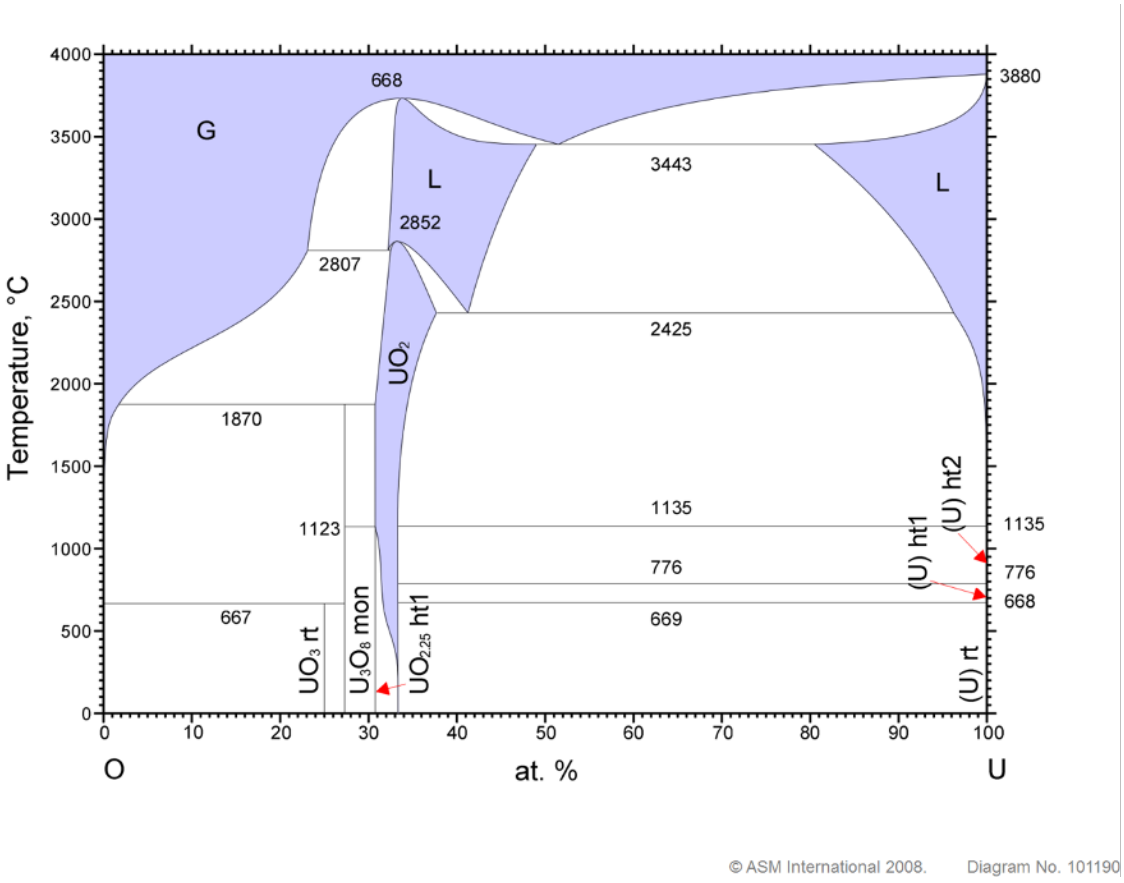


Figure 2.83: ZrO_2 – $YO_{1.5}$ phase diagram [60] taken from [14].

Table 2.10 contains a summary of room temperature properties for UO_2 and YSZ. Several properties are quite similar, such as the crystal structure, Young's modulus, and Poisson's ratio. The CTE for both materials is also similar at room temperature. The primary differences between UO_2 and YSZ are the density and thermal conductivity between the two materials.

Figure 2.84 summarizes the temperature dependence of the dynamic elastic modulus of YSZ compared with pure ZrO_2. There is very limited data available for the modulus of UO_2 at elevated temperatures.

Given the data available, the heat capacity of YSZ matches that of UO_2 fairly well over a large yttria concentration up to 1500 K, as seen in Figure 2.85. The heat capacity of YSZ also depends on yttria content. This variation in YSZ heat capacity can be seen in Figure 2.86 [41]. As the YSZ content increases, the specific heat capacity decreases, while following the same trend. Above 1500 K, there is a lack of data available for YSZ.

The heat capacity for UO_2 can vary depending primarily on concentration and model used as seen in Figure 2.88. The heat capacity of UO_2 did not vary much with different material compositions, as shown in Figure 2.87 up to 3000 K. However, another source did show a much greater variation of CP with respect to composition above 2000 K for UO_2 as seen in Figure 2.89.

The heat capacity of UO_2 was fit to the semi-empirical model presented in Equation 2.15 [21].

$$C_P = C_1\left(\frac{\theta_E}{T}\right)^2 \frac{\exp\left(\theta_E/T\right)}{\left[\exp\left(\theta_E/T\right)-1\right]^2} + 2C_2T + \frac{C_3k}{T}\exp\left(-\frac{E_d}{kT}\right)\left(1+\frac{E_d}{kT}\right) \quad (2.15)$$

where θ_E is the Einstein temperature, E_a is the activation energy, k is Boltzmann's constant, and C_1, C_2, and C_3 are all constants determined from a nonlinear fit. The value of these constants is listed in Table 2.11. The first term is related to the phonons.

Table 2.10: A summary of material properties for UO_2 and YSZ taken from a. [13], b. [14], c. [15], d. [16], e. [17], f. [18], g. [19], h. [20], i. [21], j. [22], k. [23], l. [24], m. [25], and n. [26].

Properties	UO_2	YSZ
Crystal Structure	Cubic [a]	Cubic [b]
Lattice Parameter (Å)	5.473 [c]	5.143 – 5.152 [d]
Density (g/cm^3)	11.084 [a]	5.8 – 6.1 [d]
Melting Point (°C)	2852 [e]	>2600
Young's Modulus at 298 K (GPa)	220 ± 1 [g]	200-210 [h]
Poisson Ratio	0.324 [f]	0.3
Heat Capacity at 298 K (J/mol K)	63 [i]	55 [j]
Thermal Expansion at 298 K (x 10-6/°C)	8.9 [k]	7.2-8.7 [l]
Thermal Conductivity at 298 K (W/mK)	10.2 ± 1 [m]	1.7 – 3.1 [n]

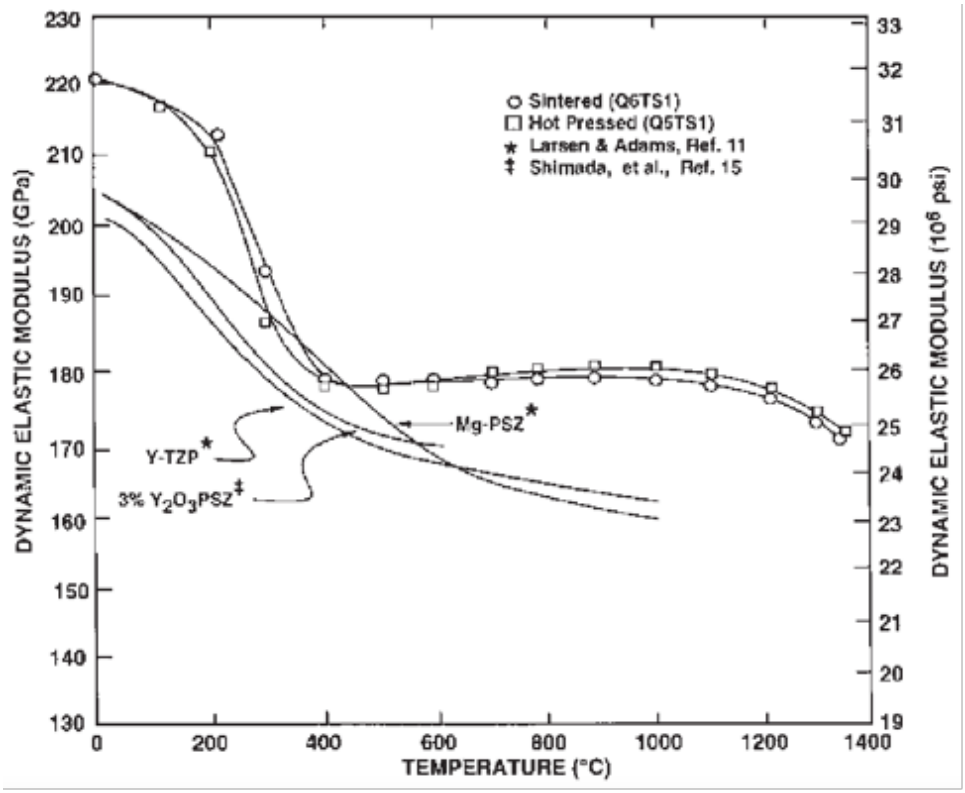


Figure 2.84: Dynamic elastic modulus of YSZ compared with transformation-toughened ZrO_2 [20].

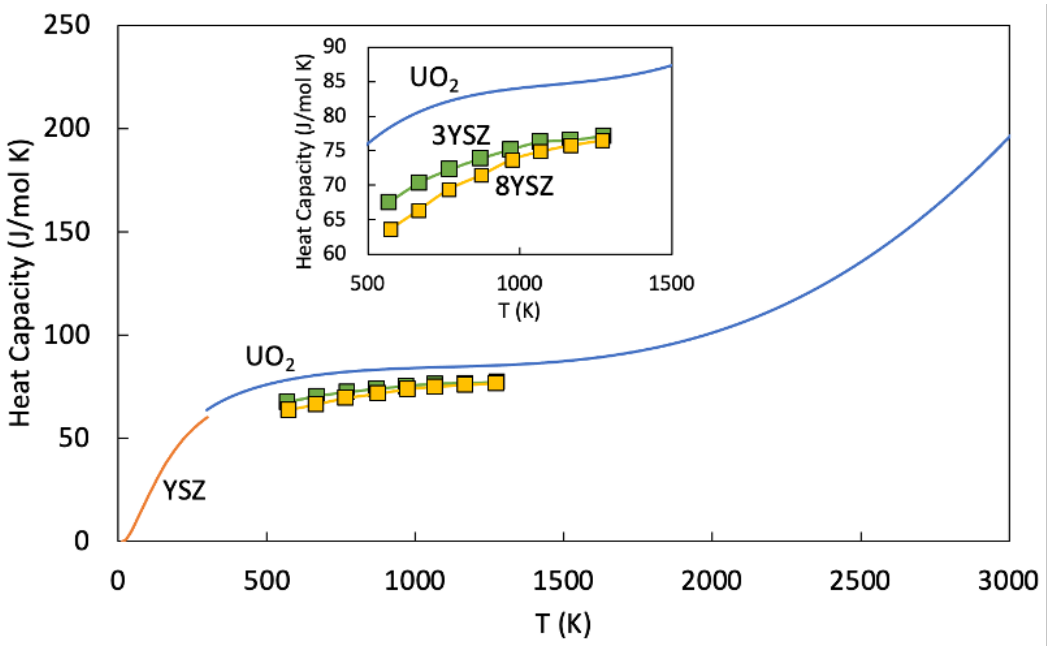


Figure 2.85: Heat capacity of UO_2 (solid blue line) from Fink et al. [21], of 7.76 x 10^{-2} mole fraction YSZ (orange line) from Tojo et al. [22], and of 3 mole percent YSZ (green squares) and 8 mole percent YSZ (yellow squares) from Sasaki et al. [77].

Table 2.11: Fitting parameters for the heat capacity for UO_2 [21].

Material	θ_E (K)	C_1 $(J/mol\ K)$	C_2 $(J/mol\ K^2)$	C_3 $(J/mol\ eV)$	E_a (eV)
UO_2	516.12	78.215	3.8609 x 10^{-3}	3.425 x 10^{8}	1.9105

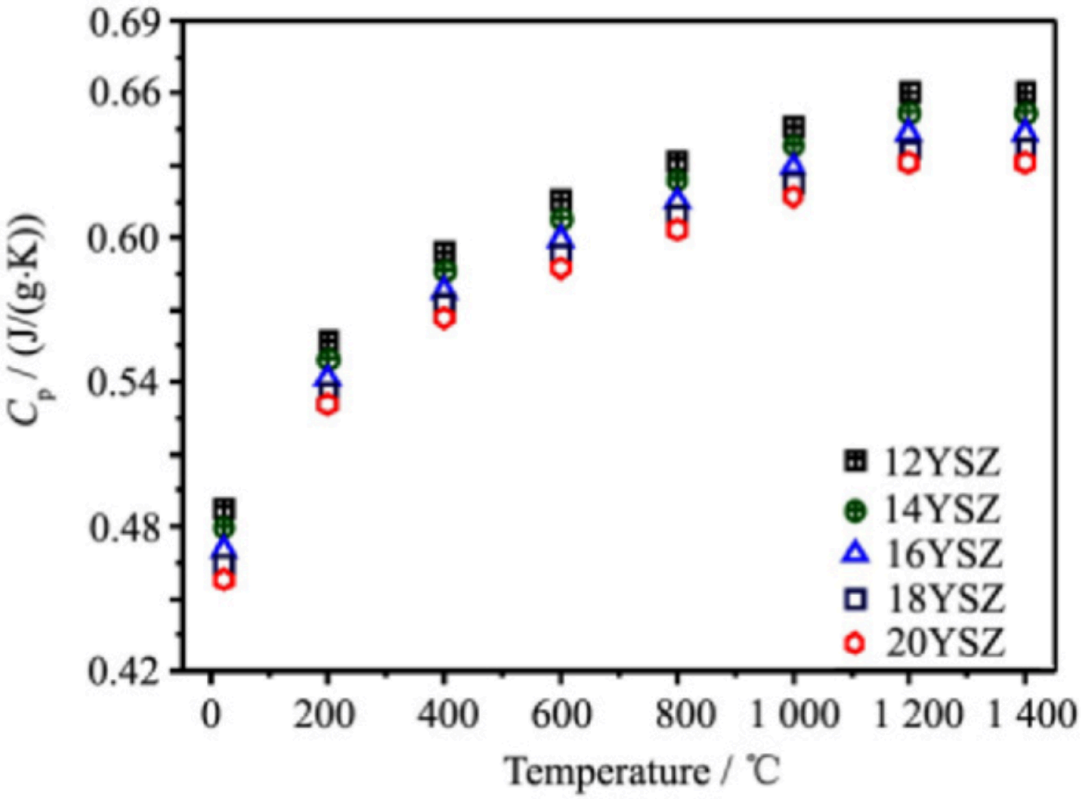


Figure 2.86: Heat capacity of solid YSZ with various compositions compiled by Xiwen et al. [41].

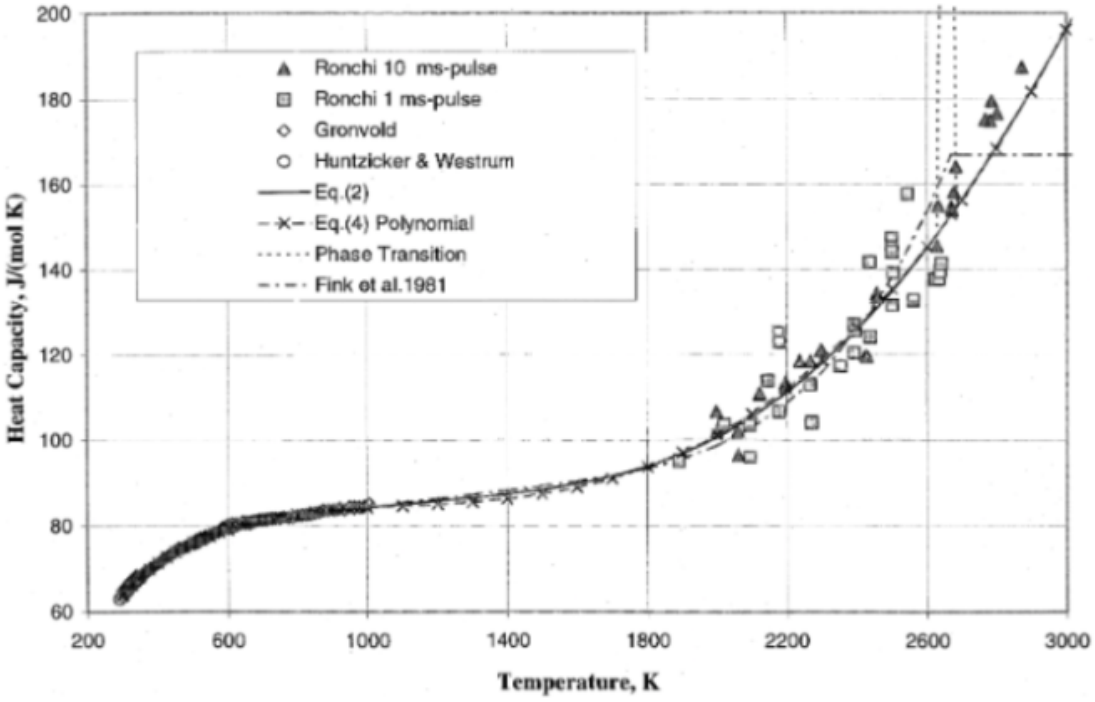


Figure 2.87: Heat capacity of solid UO_2 compiled by Fink et al. [21].

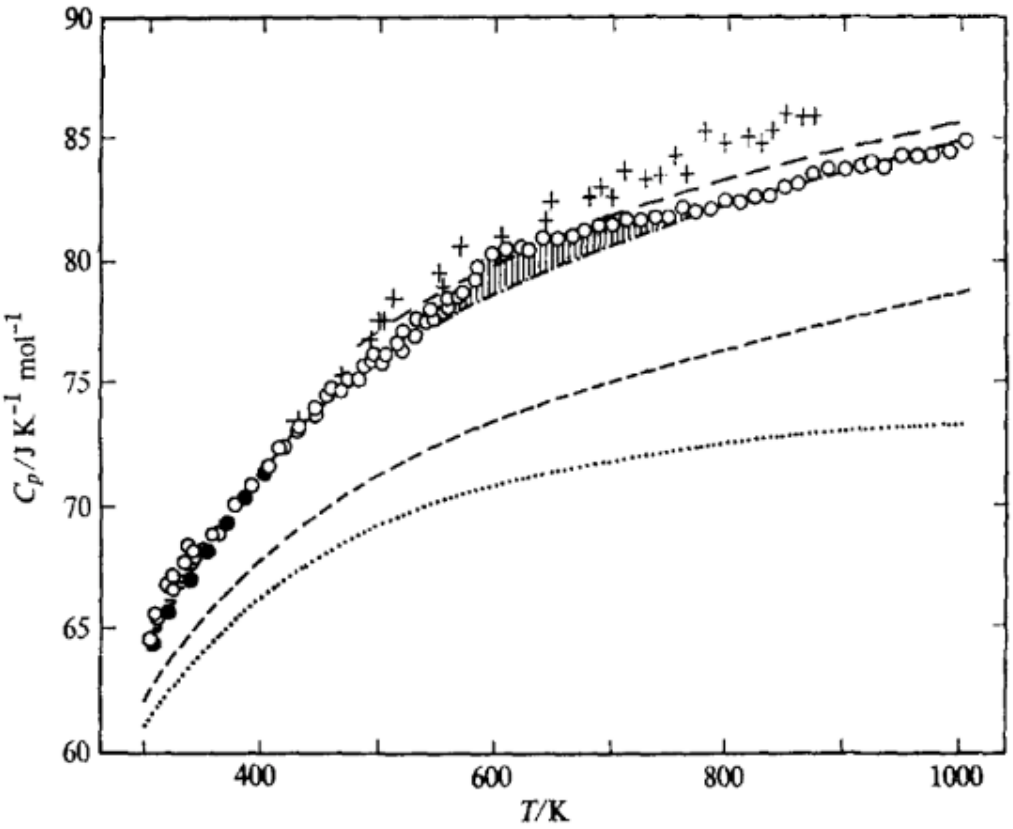


Figure 2.88: Heat capacity of UO_2 with the lines representing various models, and the open circles and crosses representing data from Grønvold et al. [78].

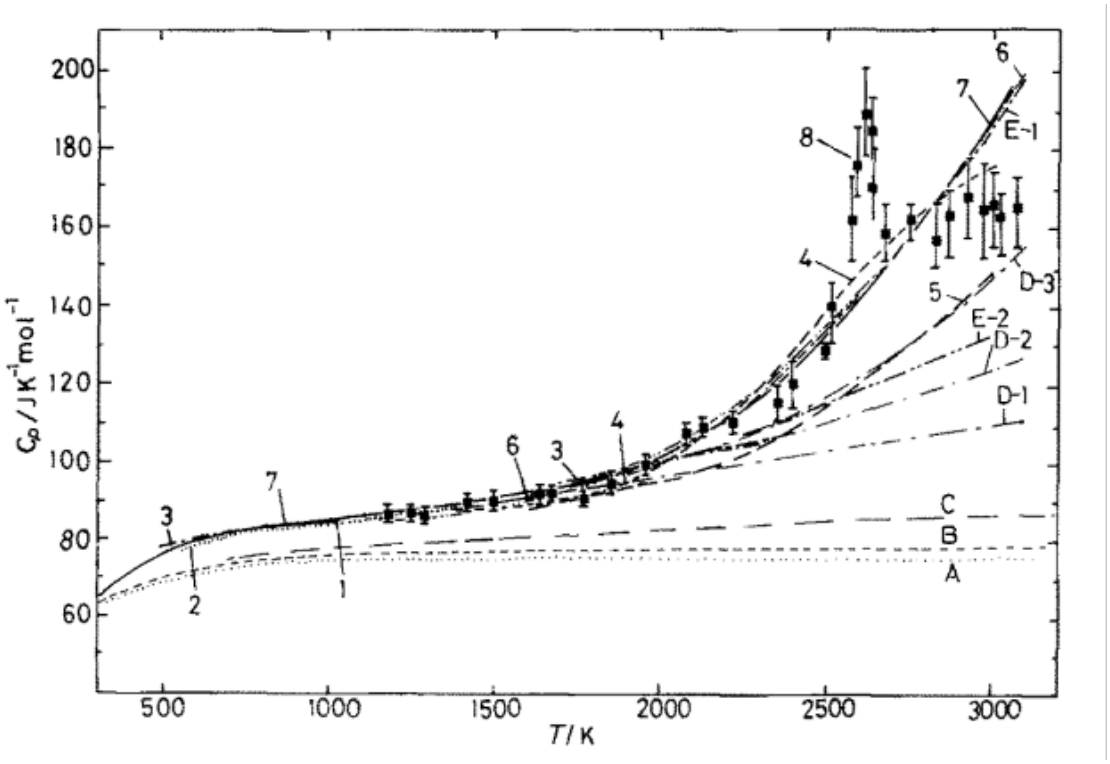


Figure 2.89: Heat capacity of UO_2 from various sources compiled by Naito et al. [79].

The second term takes into account the thermal expansion component of the heat capacity, and the last term relates to the electrons.

The thermal conductivity of UO_2 is significantly higher than YSZ, at least below 400°C as seen in Figure 2.90. Above 400°C, UO_2 appears to be trending down towards values more comparable to that of YSZ. Figure 2.91 contains the thermal diffusivity of UO_2 up to the melting point. Above 1600 K, the decrease in thermal diffusivity levels off. Fink et al. presented a model for the thermal conductivity of UO_2 up to the melting point [138]. This equation is presented in Equation 2.16.

$$\lambda_0(T) = \frac{115.8}{7.5408 + 17.692t + 3.6142t^2} + 7410.5t^{(-\frac{5}{2})} \exp\big(-\frac{-16.35}{t}\big) \tag{2.16}$$

Gibby also provided a model for the thermal conductivity of 96% density UO_2 which is presented in Equation 2.17 [139].

$$\lambda(T) = (0.00308 + 0.0002294T)^{-}1 \tag{2.17}$$

Thermal expansion is an important property, especially when considering the fabrication of cermets and cercer composites above 1600°C. As samples are heated, sintered, then cooled, mismatch between thermal expansion can cause cracking and significant stresses to be introduced into the cooled, solidified composite. Moreover, an NTP fuel element will need to endure multiple heating and cooling cycles to as high as 3000 °C without significant cracking or material loss. Ideally, the thermal expansion of the matrix and particle should be as close together as possible to minimize this effect. Moreover, the CTE of the surrogate particles needs to match that of the fuel particles to provide an accurate reference for sintering and testing of the surrogate composites. Figure 2.92 compares the CTE of YSZ from 3 to 10 mol% yttria with UO_2. There is a good match above 500 K. However, below 500 K UO_2 experiences a significantly lower CTE compared with YSZ. Additional thermal expansion data for UO_2 up to the melting point is presented in Figure 2.93.

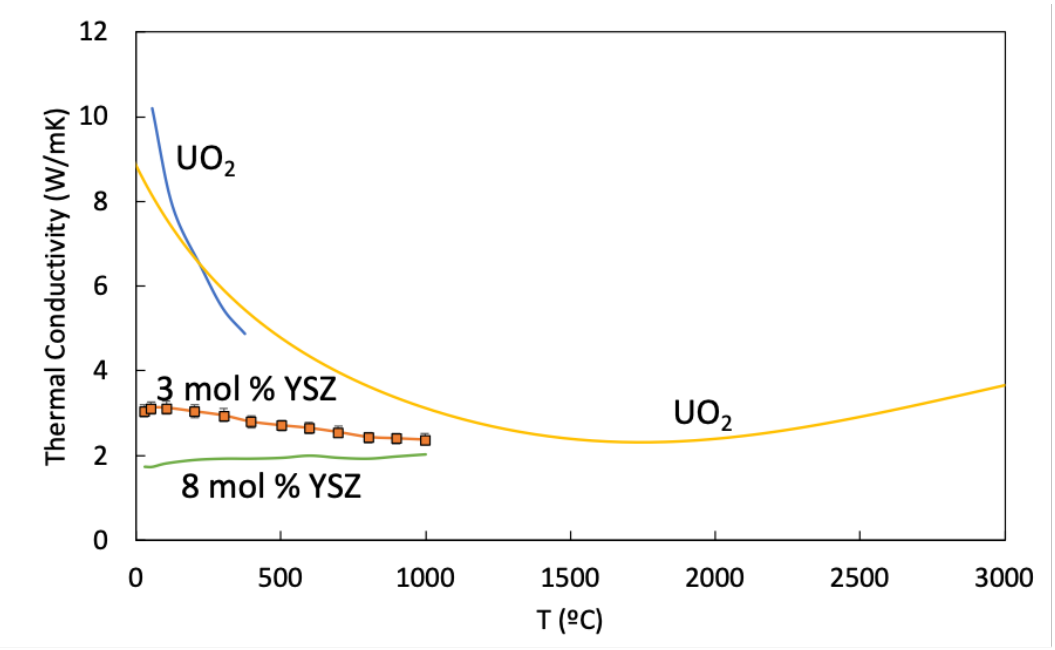


Figure 2.90: Thermal conductivity of fully dense UO_2 to 370°C (blue line) [25], a model for UO_2 up to 3000°C (yellow line) , and YSZ samples of 3 (orange squares) and 8 mol % (green circles) YSZ up to 1000°C [26].

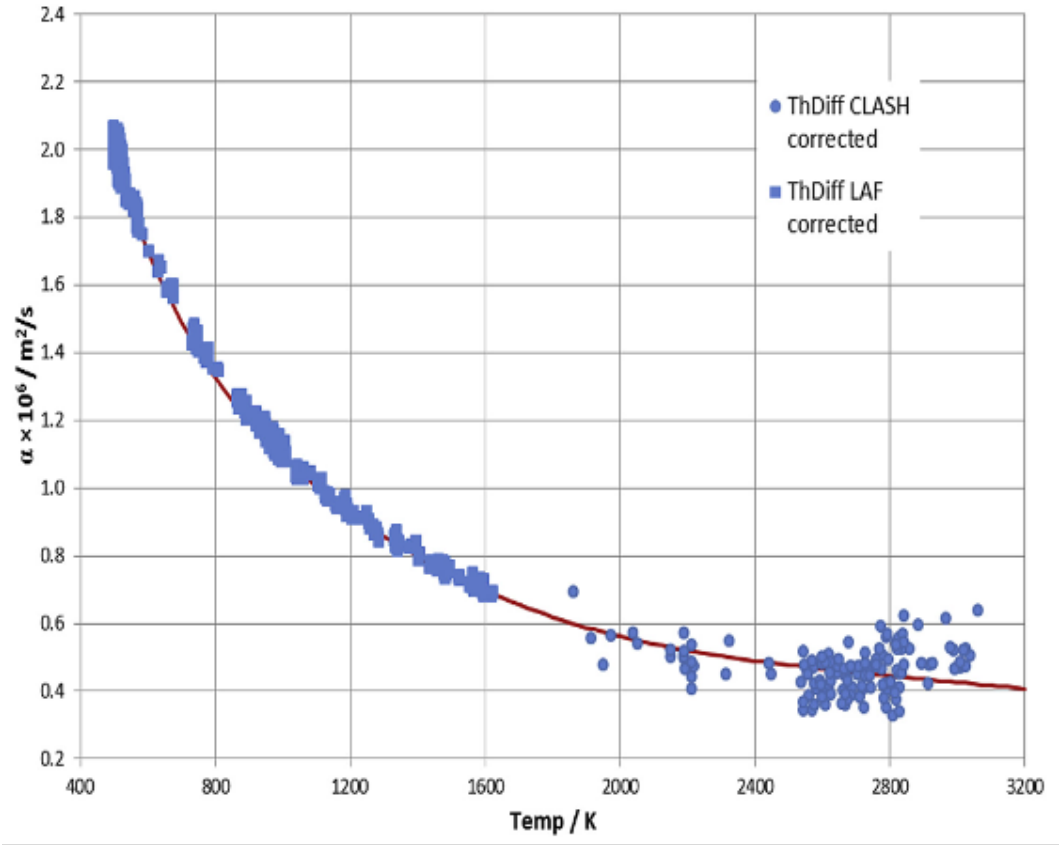


Figure 2.91: Thermal diffusivity of UO_2 up to the melting point, taken from [80]. The values at lower temperatures (blue squares) were measured using a laser-flash apparatus (LAF) and the higher temperatures points (blue circles) were measured using continuous wave laser-heating apparatus (CLASH).

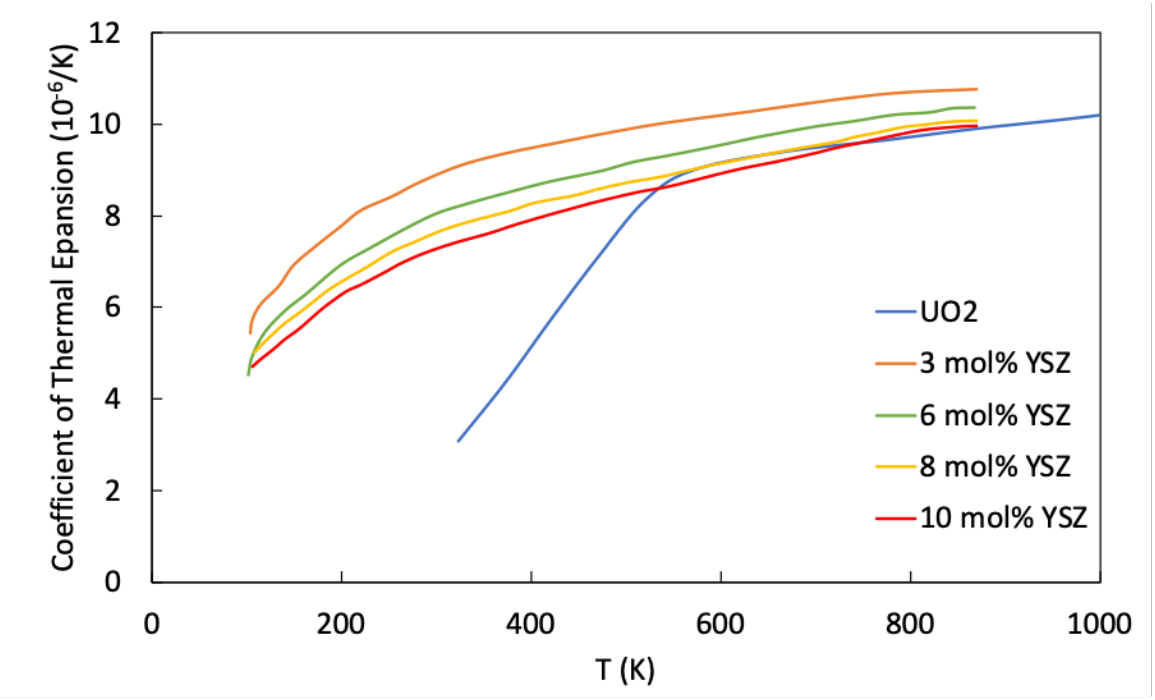


Figure 2.92: Coefficient of thermal expansion for UO_2 [23], and for YSZ of various molar percentages [24].

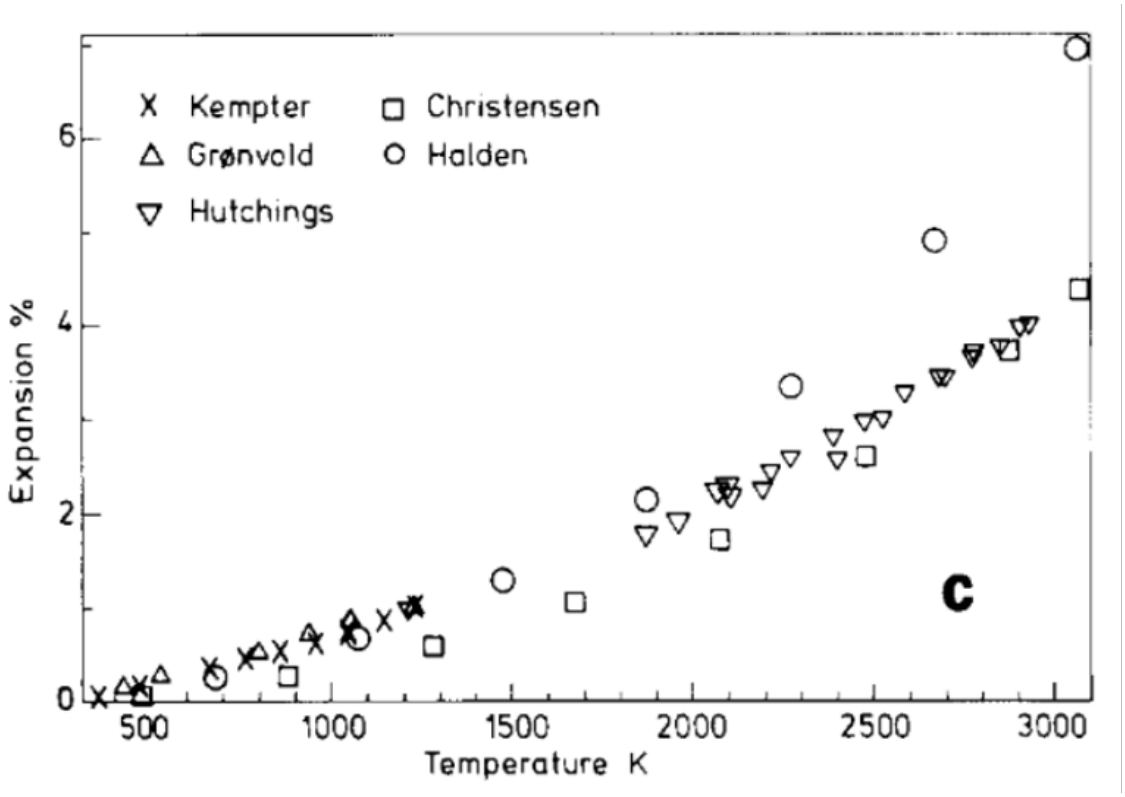


Figure 2.93: Thermal expansion of stoichiometric UO_2 from various sources, compiled by Martin et al. [81].

The fracture toughness of UO_2 has been measured using the indentation method by Novikov et al. [140]. The fracture toughness of pressed UO_2 is quite low. The measured values ranged from 1.26 to 2.09 MPa-$m^{1/2}$.

The yttria content effects the thermophysical properties of YSZ. The thermal expansion decreases with increasing yttria content up to 10% [24]. The heat capacity and thermal conductivity also decrease with increasing yttria content up to 20% [41]. Moreover, Young's modulus, fracture toughness, and tensile strength all decrease with increasing yttria content [141]. Overall, yttria has a negative impact on all the properties of interest.

2.5.2 Properties of UN and HfN

Uranium nitride (UN) is a promising fuel for NTP due to its similar melting point and higher uranium density compared with UO_2. UN is less understood than UO_2, since UO_2 has been heavily utilized as the primary fuel in commercial light water reactors. A major concern with UN is that it begins to dissociate at temperatures above 1800 K (generating low-melting metallic U) [142], so the stability of UN at NTP-relevant temperatures above 2700 K needs careful evaluation.

Hafnium nitride (HfN) was selected as the surrogate for UN. Stoichiometric UN is very similar to HfN, as seen in the room temperature properties summarized in Table 2.12. The crystallographic and elastic properties of both materials are very similar. Conversely, there is a significant difference in the thermal expansion and thermal conductivity of UN compared with HfN. In currently available commercial HfN powders, Hf_4N_3 can be a dominant phase present in the powder feedstock. For this reason, some properties of Hf_4N_3 were also included in the table. The phase diagrams of the uranium-nitrogen and hafnium-nitrogen systems are included in Figures 2.94 and 2.95, respectively.

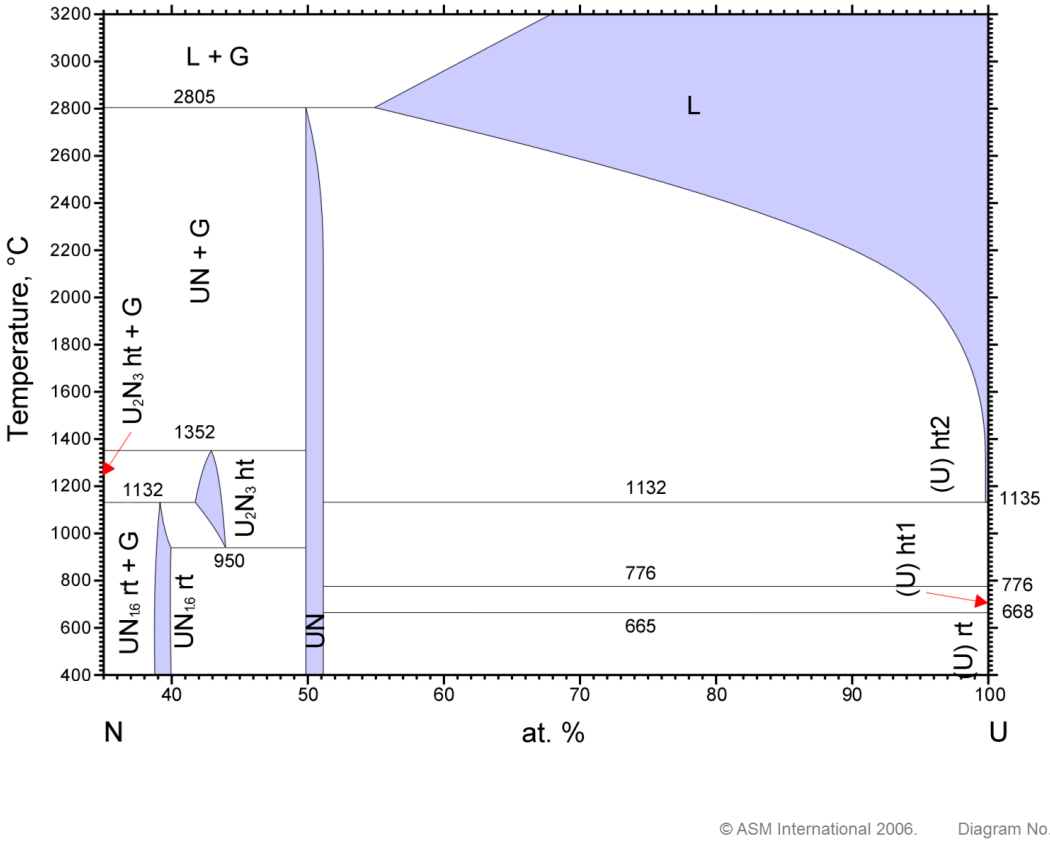
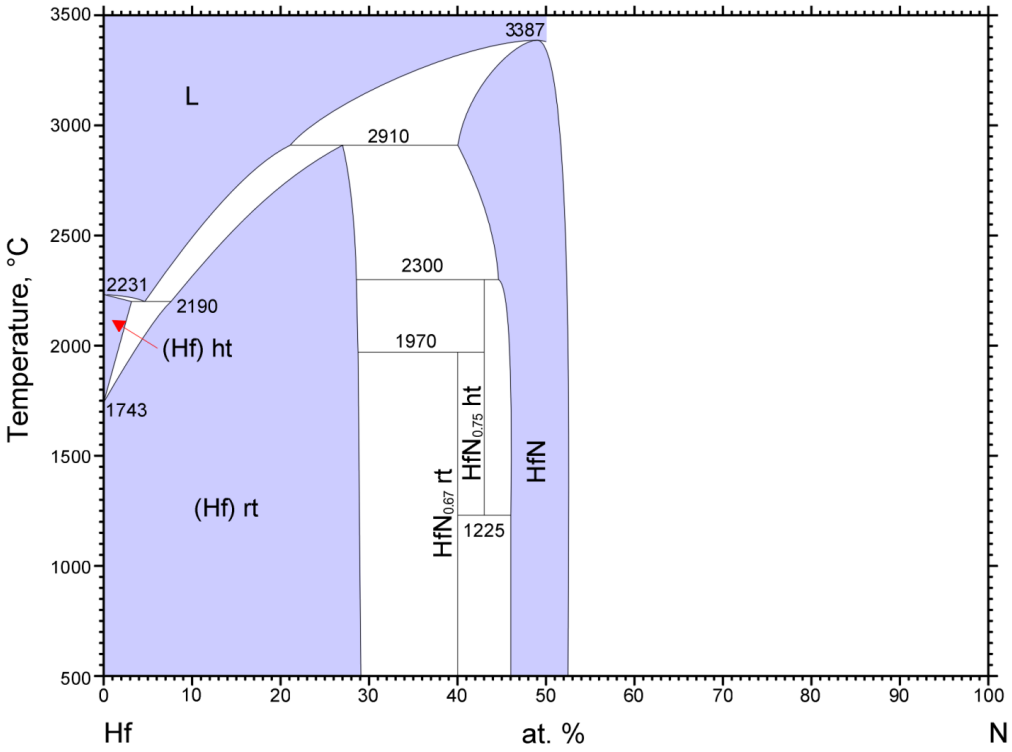


Figure 2.94: Uranium-nitrogen phase diagram taken from [82].

Table 2.12: Room temperature mechanical properties of UN, HfN and Hf_3N_4. Data was taken from a. [27], b. [28], c. [29], d. [30], e. [31], f. [32], g. [33], h. [34], i. [35], j. [36], k. [37], and l. [38].

Properties	UN	HfN	Hf3N4
Crystal Structure	Fm3m [a]	Fm3m [b]	-I42 [c]
Lattice Parameter (Å)	4.88 [d]	4.52 [b]	6.701(6) [e]
Density (g/cm^3)	14.32 [d]	13.83 [f]	13.058 [e]
Melting Point (°C)	3416 [g]	3387 [f]	N/A
Young's Modulus at 298 K (GPa)	200-250 [h]	266 [c]	260 [c]
Poisson Ratio	0.34 [c]	0.25 [c]	0.30 [c]
Heat Capacity at 298 K (J/mol K)	37.5 [i]	38.01 [f]	
Thermal Expansion at 298 K (x 10-6/°C)	7.5 [j]	6.5 [f]	
Thermal Conductivity at 298 K (W/mK)	12.7 [k]	14.9 [l]	



© ASM International 2006. Diagram No. 901275

Figure 2.95: Hafnium-nitrogen phase diagram taken from [83].

Heat capacity data at elevated temperatures for HfN is presented in Figure 2.96 and Figure 2.97. The increase in heat capacity from 800 K to 2000 K is roughly linear.

The heat capacity of UN was fit to a semi-emprical model shown in Equation 2.18 [39]

$$C_p(T) = a\left(\frac{\theta_E}{T}\right)^2 \frac{\exp\left(\theta_E/T\right)}{\left[\exp\left(\theta_E/T\right)-1\right]^2} + bT + \frac{c}{T^2}\exp\left(-\frac{d}{T}\right) \tag{2.18}$$

where C_p is the molar heat capacity, T is the absolute temperature, θ_E is the Einstein temperature for UN, and a, b, c, and d are all constants. This model is valid from 298 to 2800 K. The fitting parameters are presented in Table 2.13.

The thermal conductivity of UN and HfN match fairly well up to high temperatures. Figure 2.98 compares stoichiometric UN to slightly sub stoichiometric HfN. The thermal conductivity of HfN is higher than that of UN by 15% at 0°C. The difference increases with increasing temperature. Figure 2.99 contains additional thermal conductivity data for UN, illustrating how dependent this property is upon stoichiometry and sample porosity. The thermal conductivity decreases with increasing porosity and decreases with the addition of carbon and oxygen.

The thermal expansion of UN and HfN also matches fairly well up to 800°C, as seen in Figure 2.100. The higher temperature expansion of the two materials was determined using the change in lattice parameter with increasing temperature.

Young's modulus of nitrides is highly dependent upon the porosity of the material. Young's modulus as a function of porosity is shown in Figure 2.101. As porosity increases, the modulus decreases.

The fracture toughness of UN fabricated using SPS was measured using indentation hardness and crack length measurements by Yang et al. [85]. The model used is presented in Equation 2.19.

$$K_{IC} = \sigma\left(\frac{E}{H}\right)^{0.5}\left(\frac{P}{C^{1.5}}\right) \tag{2.19}$$

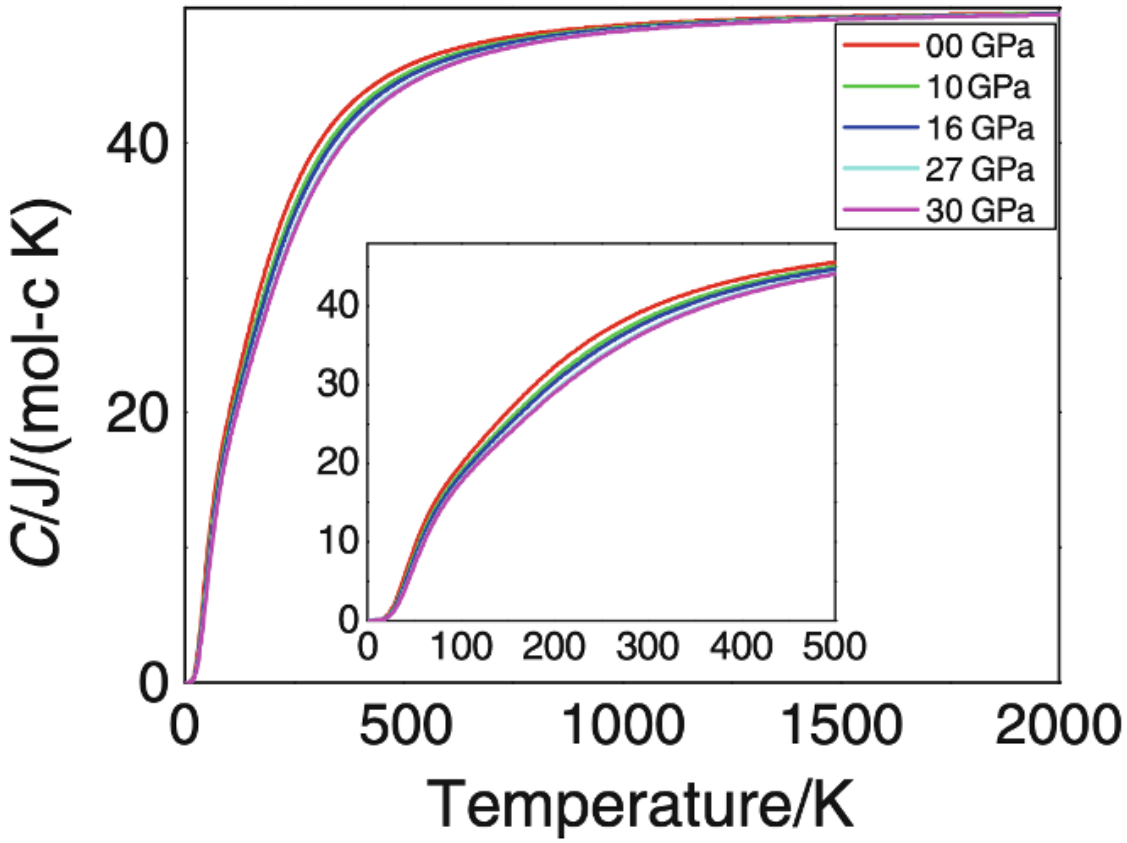


Figure 2.96: Computed HfN heat capacity taken from [35].

Table 2.13: Fitting parameters for the semi-empirical specific heat capacity for UN determined by [39].

Property	Value	Unit
θ_E	367.5	K
a	51.14	J/mol K
b	9.491×10^{-3}	J/mol K^2
c	2.642×10^{11}	J/mol K^3
d	18081	K

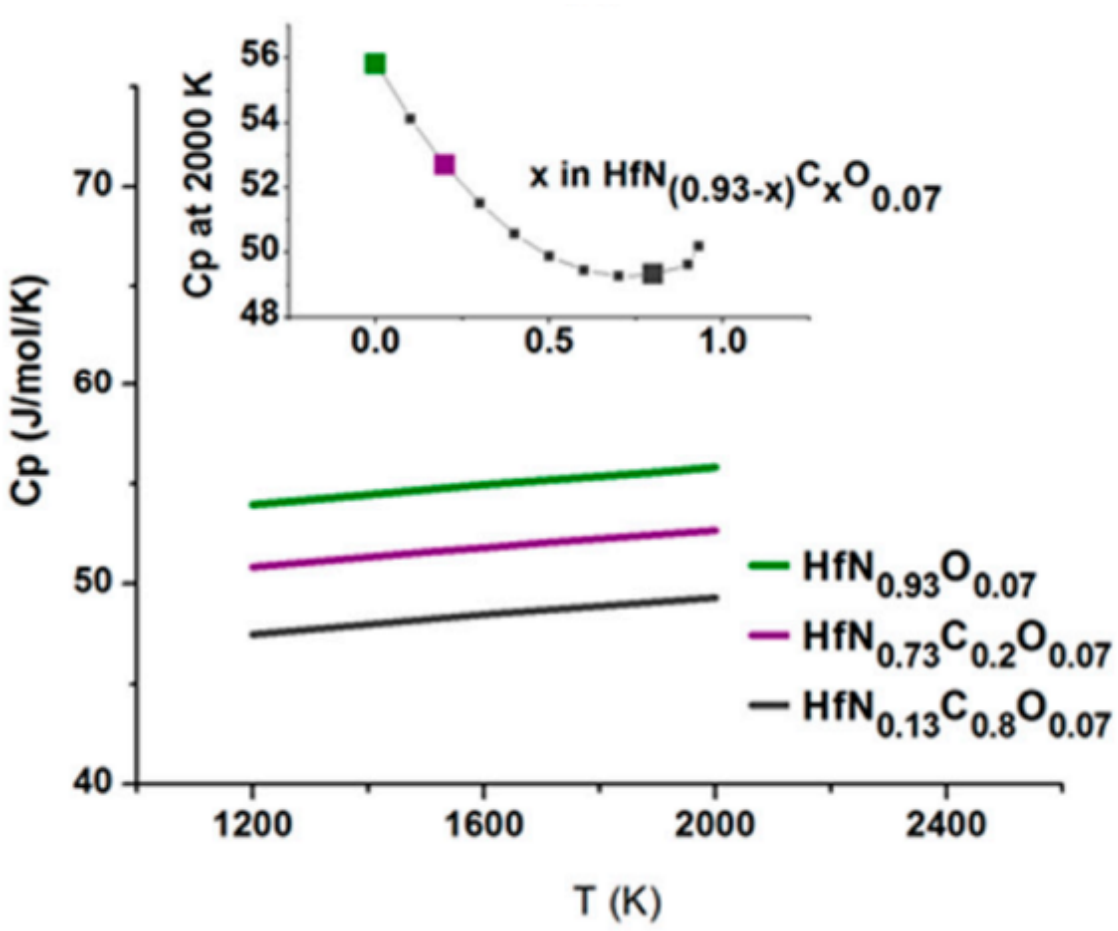


Figure 2.97: High temperature heat capacity taken from [28].

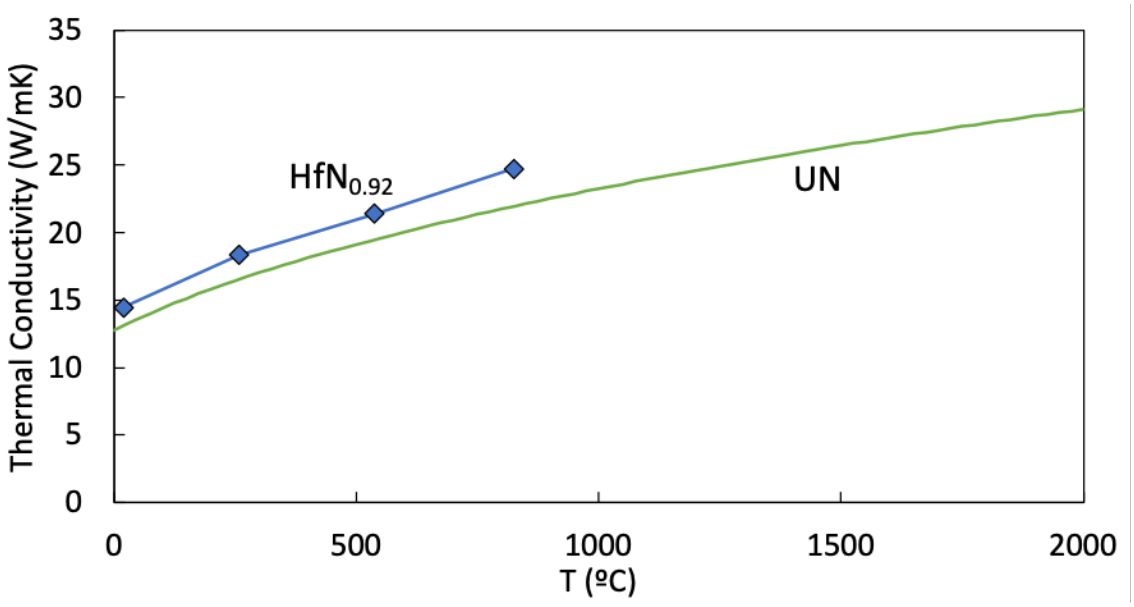


Figure 2.98: Thermal conductivity of HfN $_{0.92}$ (blue) [38] and of UN (green) [37].

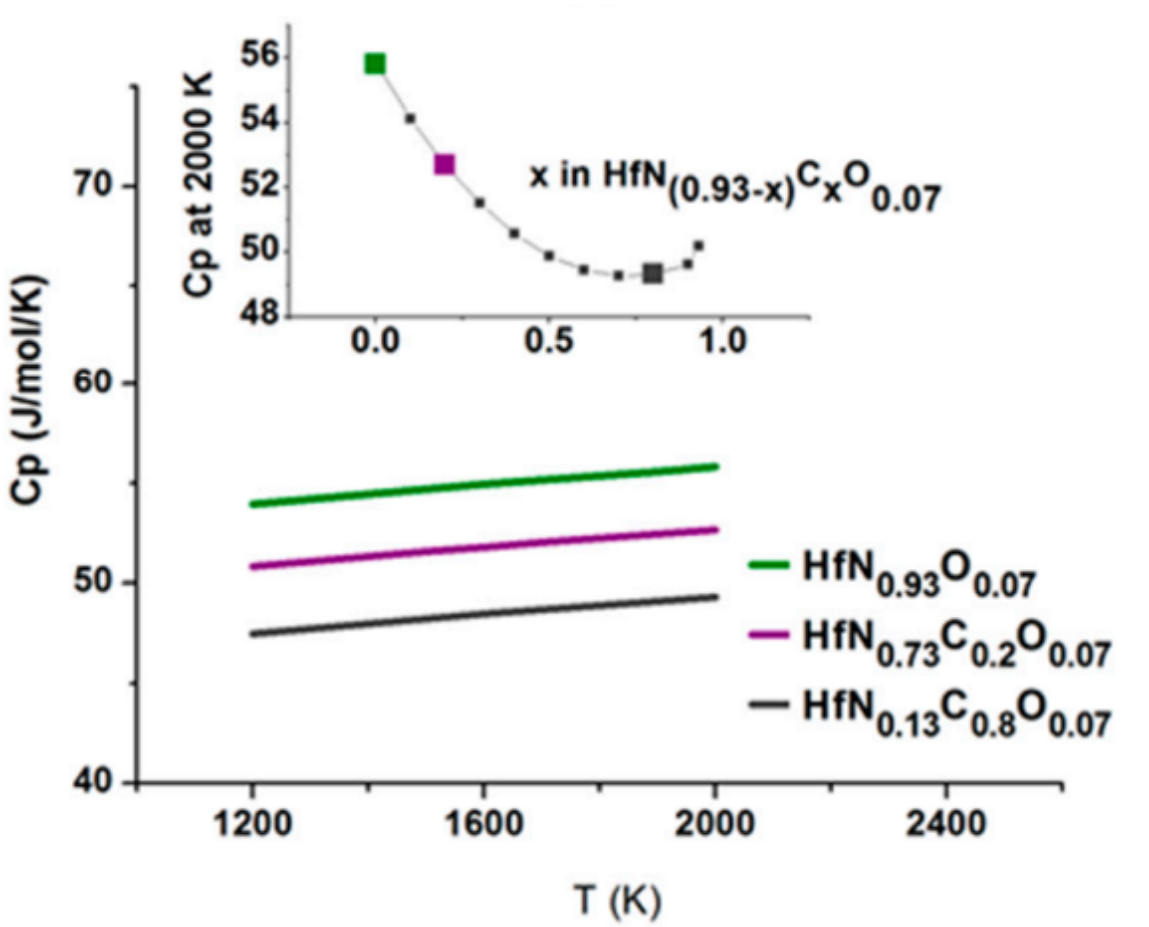


Figure 2.99: Thermal conductivity of uranium nitride from various studies compiled by Muta et al. [34].

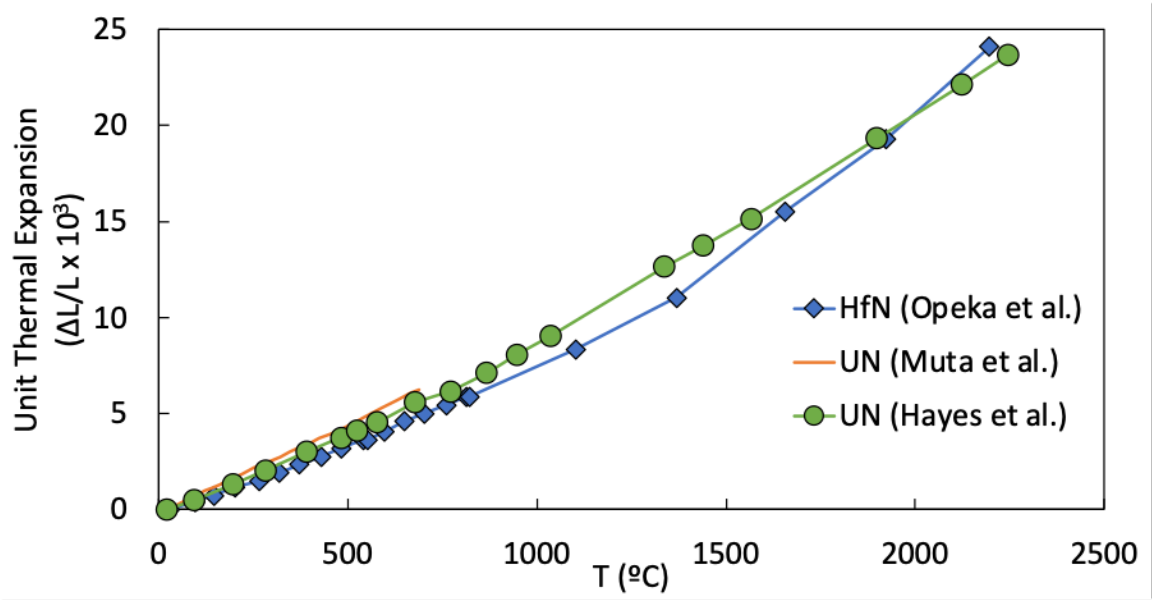


Figure 2.100: Unit thermal expansion of $HfN_{0.92}$ (blue) [38], UN (orange) [34], and UN (green) [84].

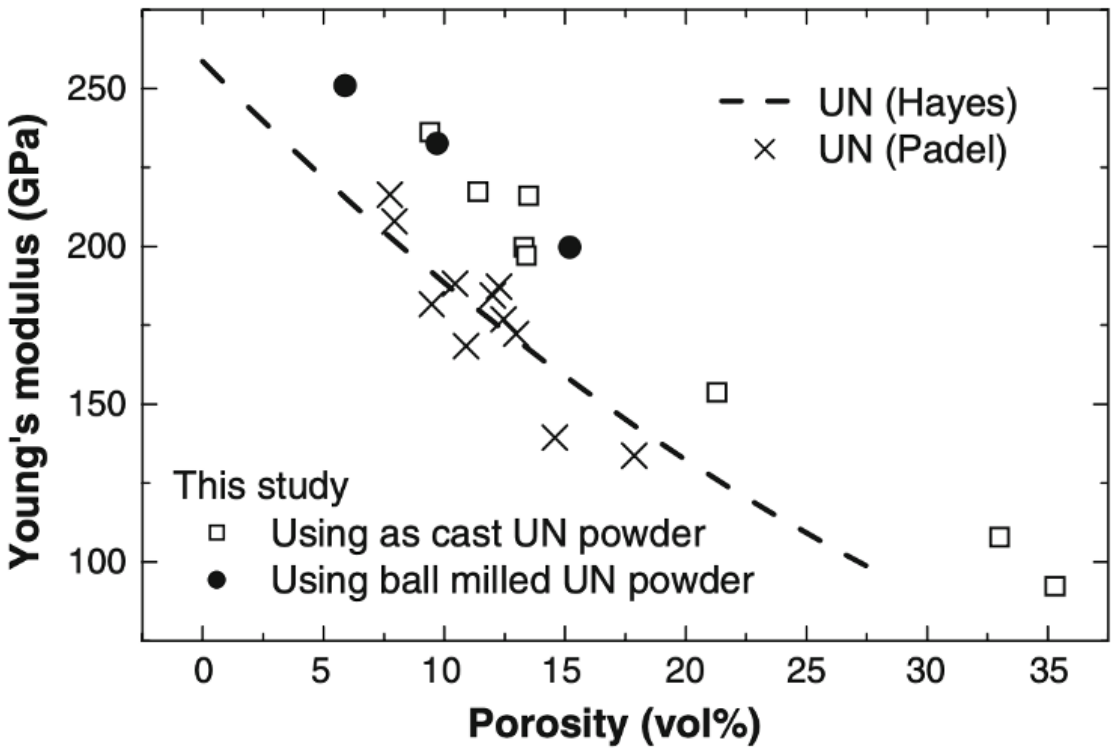


Figure 2.101: Young's modulus of UN with respect to porosity compiled by Muta et al. [34].

where E is the modulus, H is the hardness, P is the indentation load, and C is the crack length. Figure 2.102 contains SEM images of indents along with the micro hardness and indentation fracture toughness. The fracture toughness of the UN ranged from 2.5 to 3.3 MPa $m^{1/2}$.

2.6 Properties of Metallic Alloys

Mo30W is a binary metallic alloy. Binary alloys do not always follow simple rule of mixture (ROM) models for thermophysical and mechanical properties. Specific heat capacity is typically composition dependent. Both an increase and decrease in CTE have been observed as a result of creating a binary alloy. In one study, the CTE of binary alloys of Nickel with chromium, Mo, and rhenium were determined up to 650°C [86]. As seen in Figure 2.103, the CTE decreased with increasing alloy concentration.

In another study by Asoka et al., the binary alloy system of palladium (Pd) with silver (Ag), copper (Cu), and cobalt (Co) were examined [87]. While some of these materials did experience a phase change, they did not in the range of 40 to 600°C. The average CTE in the previously mentioned temperature range was determined over a range of alloying elemental compositions. These can be seen in Figure 2.104 for the Pd-Ag system and in Figure 2.105 for the Pd-Co system. For the Pd-Ag system, the CTE increased linearly with increasing Ag content, and for the Pd-Co system, there was a linear increase in CTE up to a composition of 25 wt %.

Another study tested various properties of binary Mo-W alloys [143]. At 1300 K, the thermal expansion coefficients for were measured at 6.05 and 5.19 x 10^{-6} K^{-1} for Mo and W respectively. An alloy of Mo with 62.5% W measured at the same temperature returned a value of 6.7 x 10^{-6} K^{-1}, higher than that of both the pure Mo and pure W.

For solid solution materials, most thermal properties do not follow a simple rule of mixtures. Instead, they tend to follow a more complex model. Nordheim developed a relationship for the electrical resistivity for binary alloys [144]. In his model, he

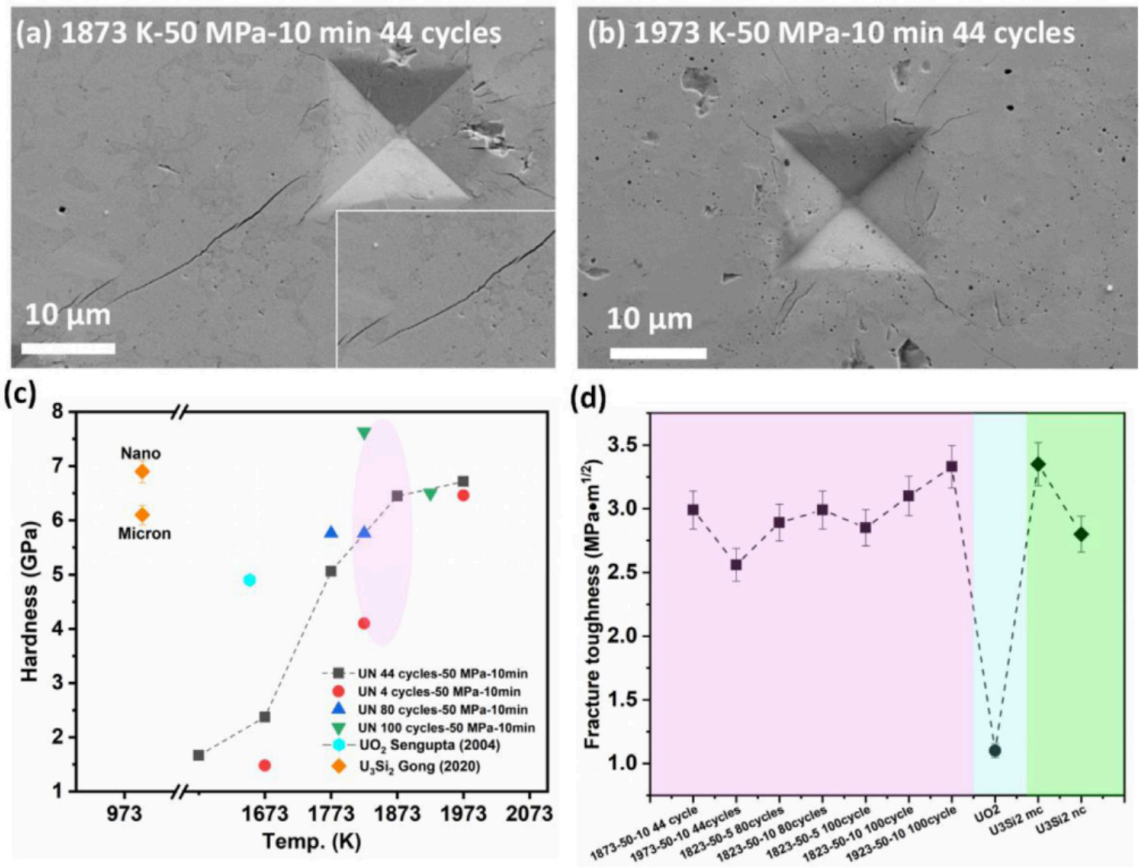


Figure 2.102: a) and b) SEM images of the indents on the UN samples, c) microhardness of the different materials, and d) the calculated fracture toughness taken from Yang et al. [85].

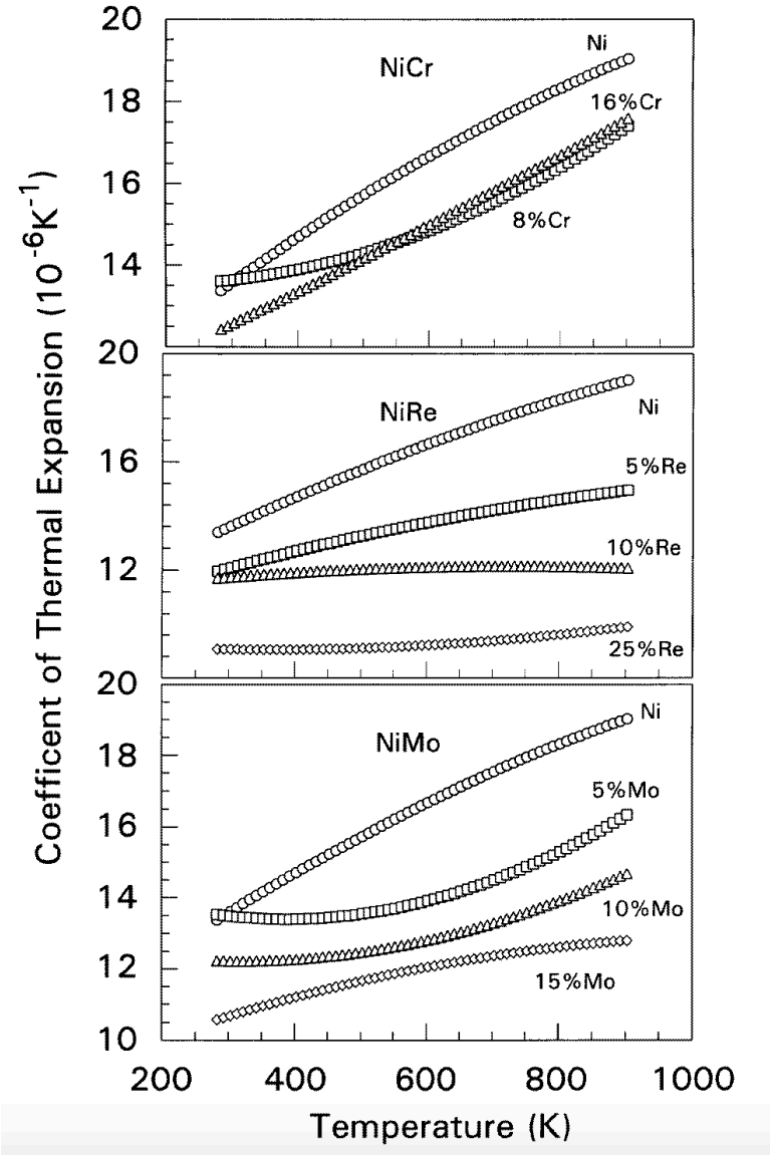


Figure 2.103: CTE versus temperature for Ni, NiCr, NiRe and NiMo binary alloys taken from Pavlovic et al. [86].

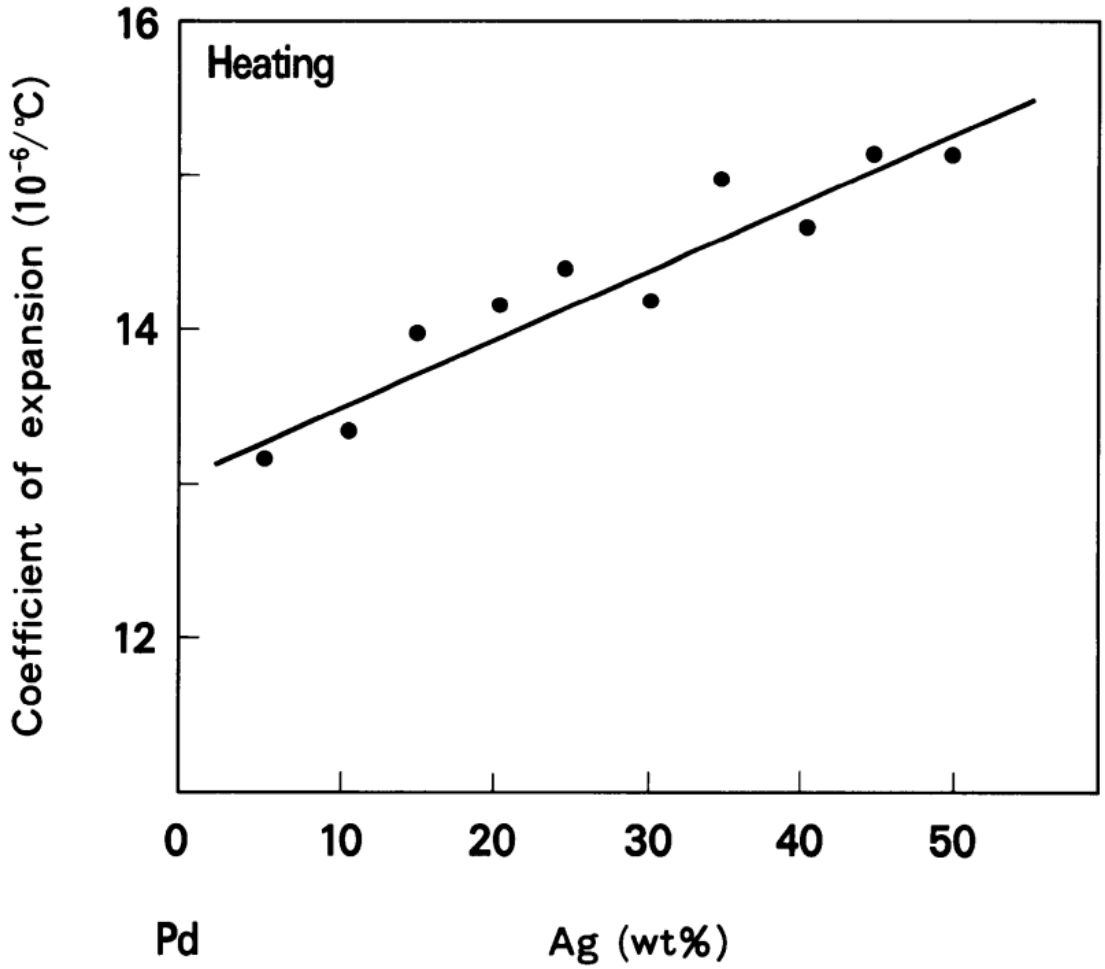


Figure 2.104: Average CTE from 40 to 600°C for Pd-Co alloy as a function of Ag concentration taken from Asoka et al. [87].

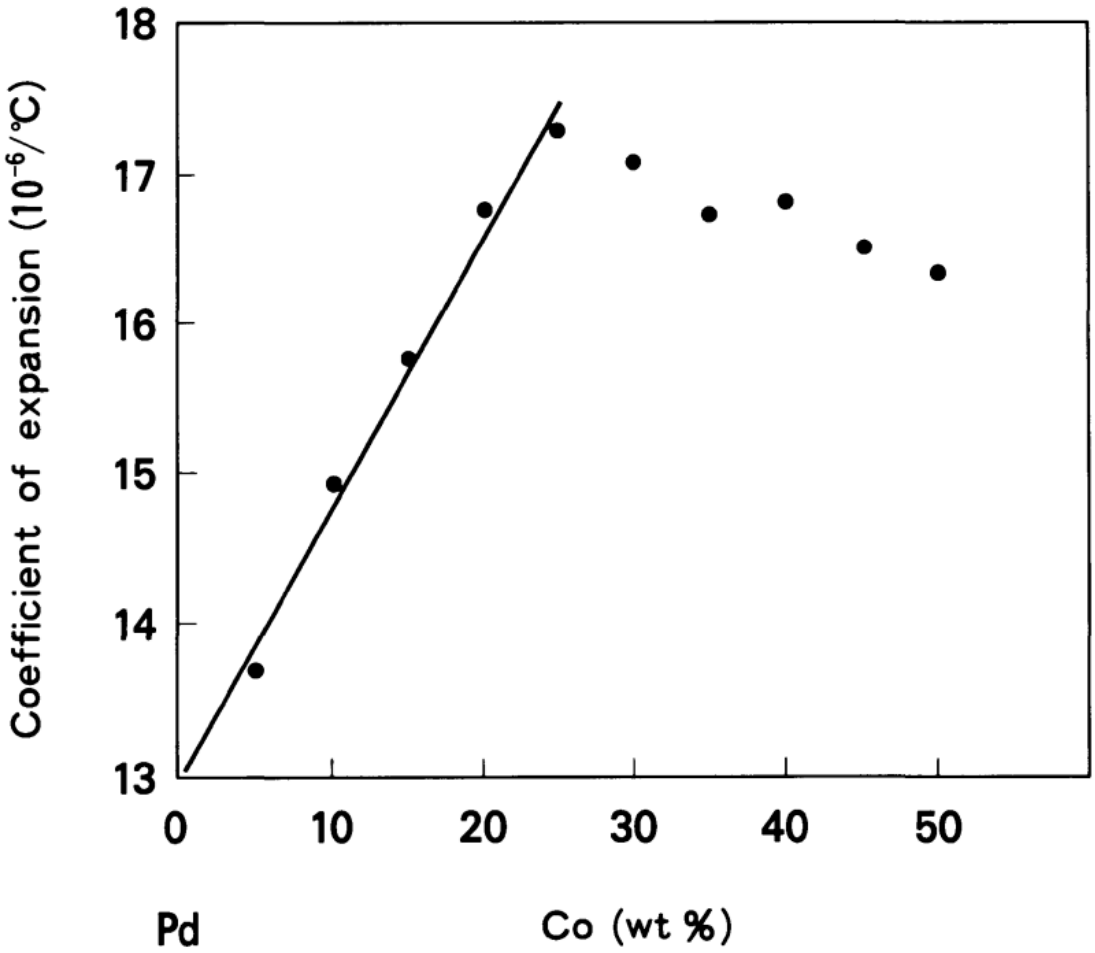


Figure 2.105: Average CTE from 40 to 600°C for Pd-Co alloy as a function of Co concentration taken from Asoka et al. [87].

determined the residual electrical resistivity was related to the concentration of the two alloying elements times a constant that is valid for all compositions, defined as Cx_Ax_B, with C being the constant and x_A and x_B being the volume fraction of the two alloying elements. Rudajevovét al. used the Wiedmann-Franz law (Equation 5.6) which states that the thermal conductivity is inversely proportional to the electrical resistivity [145]. Equation 2.20 contains this relationship for the thermal conductivity of a binary alloy.

$$\lambda_{SS} = \frac{1}{\frac{(1-x)}{\lambda_A} + \frac{x}{\lambda_B} + kx(1-x)} \tag{2.20}$$

λ_{SS} is the thermal conductivity of the solid solution material, λ_A is the thermal conductivity of the matrix atom, λ_A is the thermal conductivity of the solute atom, x is the composition of the solute, and k is a constant that depends on the alloy system. This model only works if the Lorenz number remains relatively constant over the temperature range in question.

The CTE of solid solution materials typically does not follow ROM models. Turner et al. developed a method for modeling the thermal expansion in reinforced plastics, as presented in Equation 2.21 [146].

$$\alpha_C = \frac{\alpha_m v_m K_m + \alpha_d v_d K_d}{v_m K_m + v_d K_m} \tag{2.21}$$

α_C is the CTE of the composite material, α_m and α_d are the CTE's, K_m and K_d are the bulk modulii, and v_m and v_d are the volume fractions of the matrix and discrete phases, respectively.

2.7 Properties of Composite Materials

The most common models for the physical properties of composite materials are the rule of mixture (ROM) models. These are often used to describe the modulus of composite materials, but can also describe other properties including strength, heat

capacity, thermal conductivity, and the coefficient of thermal expansion. In terms of yield strength, the Voigt model in Equation 2.22 [147] is the standard ROM and the inverse ROM is the Reuss model in Equation 2.23 [148].

$$\sigma_{eff} = f_p\sigma_p + f_m\sigma_m \tag{2.22}$$

$$\sigma_{eff} = \left(\frac{f_p}{\sigma_p} + \frac{f_m}{\sigma_m}\right)^{-1} \tag{2.23}$$

where σ_{eff} is the effective stress, σ_p is the particle stress, σ_m is the matrix stress, f_p is the volume fraction of particles, and f_m is the volume fraction of the matrix. These models will be useful in some cases, however, other most material properties will not follow these simple models.

2.7.1 Heat Capacity

Heat capacity is most likely to follow the more simple ROM models. In a review paper outlining criteria for selecting properties for composite materials, Ashby suggests that the heat capacity for composites follows the density normalized ROM model shown in Equation 2.24 [149].

$$\rho_c C_{P_c} = f_p\rho_p C_{P_p} + (1 - f_p)\rho_m C_{P_m} \tag{2.24}$$

C_{P_c}, C_{P_m}, and C_{P_p} are the specific heat capacities (in J/g K) and ρ_c, ρ_m, and ρ_p are the densities of the composite, matrix, and particulate/discrete phases, respectively. There will be a slight deviation from the straight rule of mixtures that results from the thermal expansion mismatch between the matrix and particle as the composite is heated. The mismatch creates local stresses that change the specific heat in the areas affected [150, 151]. Ashby considers this effect negligible. However, one study examined the heat capacity of Al_20_3-NiAl composites with varying volume loadings and found a noticeable deviation from the ROM model [152]. The deviation was at

a maximum at roughly a 50 vol% loading. They also noted an increase in deviation with increasing temperature, likely resulting from increased stresses induced by the thermal expansion mismatch.

2.7.2 Thermal Conductivity

Progelhof et al. reviewed several models for determining the thermal conductivity of composites [153]. The three simplest models consisted of a series model (similar to the Voigt model), a parallel model (similar to the Reuss model), and a geometric mean model, presented in Equations 2.25, 2.26, and 2.27, respectively.

Series Model

$$k_e = (1 - \phi)k_m + \phi(k_p) \tag{2.25}$$

Parallel Model

$$\frac{1}{k_e} = \frac{1 - \phi}{k_m} \frac{\phi}{k_p} \tag{2.26}$$

Geometric Mean Model

$$k_e = k_p^{\phi} k_m^{1-\phi} \tag{2.27}$$

For these three equations, k_e is the effective thermal conductivity of the composite, k_m is the thermal conductivity of the matrix phase, k_p is the thermal conductivity of the particulate or discrete phase, and ϕ is the volume fraction of the particle.

The Bruggeman theoretical model works for dilute suspensions of spheres in a homogeneous medium. It is defined in Equation 2.28 [154].

$$1 - \phi = \left(\frac{k_p - k_e}{k_p - k_m}\right)\left(\frac{k_m}{k_e}\right)^{1/3} \tag{2.28}$$

The Lewis and Nielsen Semi-Theoretical Model modified an existing model (Halpin-Tsai equation) to take into account the shape, orientation, and packing of particles suspended in a homogeneous matrix. The effective composite thermal conductivity is defined in Equation 2.29 [155, 156, 157].

$$k_e = k_m\left(\frac{1+AB\phi}{1-B\phi\psi}\right) \tag{2.29}$$

where A is a constant depending on the type of dispersed particle (seen in Table 2.14, B is given by

$$B = \frac{\frac{k_p}{k_m}-1}{\frac{k_p}{k_m}+A} \tag{2.30}$$

and ψ is given by

$$\psi = 1+\left(\frac{1-\phi_m}{\phi_m^2}\right)\phi \tag{2.31}$$

where ϕ_m is a constant that depends on the particle shape and geometry and is presented in Table 2.15. This model is not limited to dilute systems.

Another model is the Maxwell theoretical model that looks at randomly distributed and non-interacting spherical particles suspended in a homogeneous matrix, shown in Equation 2.32 [158].

$$k_e = k_m\left[.\frac{k_p+2k_m+2\phi(k_p-k_m)}{k_p+2k_m-\phi(k_p-k_m)}\right] \tag{2.32}$$

2.7.3 Coefficient of Thermal Expansion

The CTE of W-UO_2 cermets was measured as part of the GE-710 program [88]. Initial results found that for a 60 vol% cermet roughly followed the rule of mixtures, as seen in Figure 2.106. Efforts were made to reduce the CTE and they were able to significantly lower the CTE of the composite cermet.

Several models exist for CTE of composites. The Turner equation (Equation 2.21) previously mentioned has been used to fit the CTE for some binary models. When the Young's modulus of the two phases are similar, then the Turner model collapses to the ROM. The Blackburn equation has been used to model small amounts of a discrete phase dispersed in a homogeneous matrix, as seen in Equation 2.33 [89].

Table 2.14: A values for different dispersed particle geometries for the Lewis and Nielsen Semi-Theoretical Model.

Type of dispersed phase	Direction of heat flow	A
Spheres	Any	1.50
Randomly oriented rods Aspect ratio = 2	Any	1.58
Randomly oriented rods Aspect ratio = 4	Any	2.08

Table 2.15: ϕ_m values for different geometries for the Lewis and Nielsen Semi-Theoretical Model

Shape of Particle	Type of Packing	ϕ_m
Spheres	Hexagonal close	0.7405
Spheres	Face centered cubic	0.7405
Spheres	Body centered cubic	0.60
Spheres	Simple cubic	0.524
Spheres	Random close	0.637
Spheres	Random close	0.601
Rods or fibers	Uniaxial hexagonal close	0.907
Rods or fibers	Uniaxial simple close	0.785
Rods or fibers	Uniaxial random	0.82
Rods or fibers	Three dimensional random	0.52

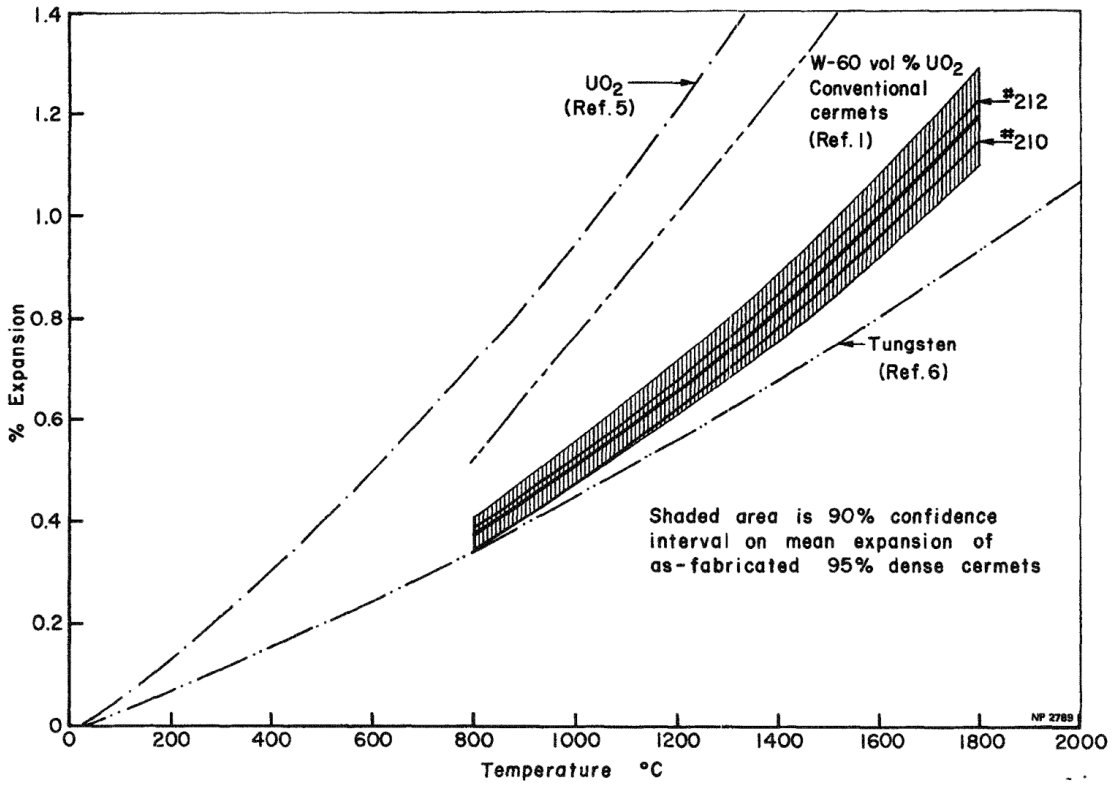


Figure 2.106: CTE of W-UO_2 cermets (60vol%) taken from the GE-710 program compared with pure W and pure UO_2 [88].

$$\alpha_c = \frac{\left[\alpha_1 + x_2(\alpha_2 - \alpha_1)\right]\frac{3}{2}(1-\sigma)}{\frac{1}{2}(1-\sigma_1) + x_2(1-2\sigma_2) + (1-x_2)(1-2\sigma_2)(E_1/E_2)} \tag{2.33}$$

for small amounts of material 1 dispersed in matrix 2. σ is Poisson's ratio. Both of these models were fit to stainless-steel-UO_2 cermets with spherical particles, as seen in Figure 2.107. Neither the Turner nor the Blackburn model fit well to this model. Instead, the CTE decreased linearly with increasing volume loading up to 63.5%, but to a lesser extent than the models predicted.

Another equation is the Kerner model [159] presented in Equation 2.34.

$$\alpha_C = \frac{[\alpha_d v_d K_d/(3K_d + 4G_m)] + [\alpha_m v_m K_m/(3K_m + 4G_m)]}{[v_d K_d/(3K_d + 4G_m)] + [v_m K_m/(3K_m + 4G_m)]} \tag{2.34}$$

Tummala and Friedberg [93, 160] created a model for CTE meant for use with binary composites with dilute amounts of spherical particles. This model took into account the physical interaction between the matrix and the particle. Equation 2.35 contains this equation.

$$\alpha_C = \alpha_m - V_p q(\alpha_m - \alpha_p) \tag{2.35}$$

where q is equal to Equation 2.36.

$$q = \frac{\frac{1+\nu_m}{2E_m}}{\frac{1+2\nu_m}{2E_m} + \frac{1-2\nu_p}{E_p}} \tag{2.36}$$

2.7.4 Strength and Fracture Toughness

The strength of any material, including composites, can be related to the porosity. Arthur et al. used the Knudsen porosity strength equation to relate the strength of stainless-steel-UO_2 cermets to the final material porosity [89, 161].

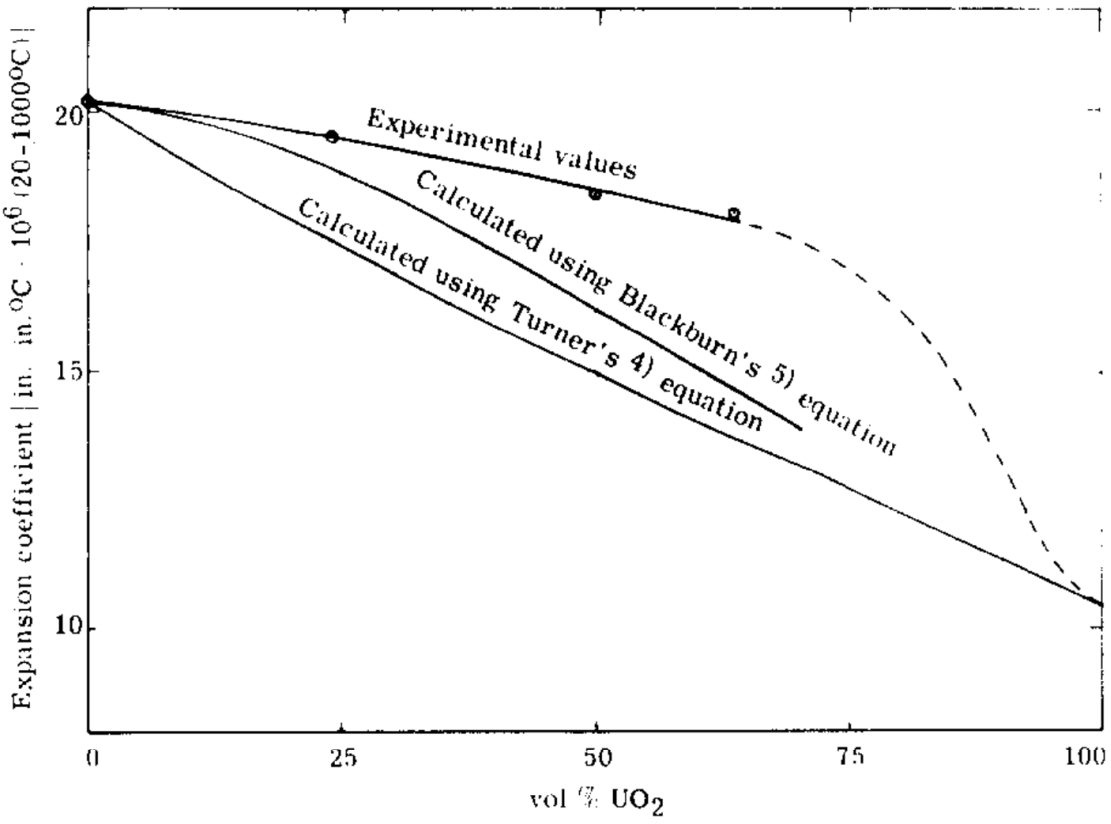


Figure 2.107: CTE of stainless-steel-UO_2 cermets from o to 63.5% volume loadings with the Turner and Blackburn models [89].

$$S = S_0 \exp(-bp) \tag{2.37}$$

where S is the ultimate tensile strength (UTS), S_0 is the strength of the fully densified material, b is a material constant that ranges from 4 to 9, and p is the final porosity. Knudsen proposed that the decrease in strength with increased porosity resulted from a reduced load-bearing cross-section, with the pores removed [161]. This law typically only works for a porosity below 20%, since above this value, other factors work to weaken the material.

When adding composite particles to a matrix material, the strength can both be improved and lost. In one study, 0.3 µm ZrO_2 spheres were added to an Al_2O_3 matrix. Volume loadings from 0 to 20 % were tested. At a volume loading of 15 %, the fracture toughness doubled, as seen in Figure 2.108. Claussen et al. theorized that the increase in fracture toughness resulted from many micro cracks formed in the matrix as a result of hot pressing with the particles [90]. These micro cracks were able to absorb energy and slow propagation of larger cracks, increasing the toughness. Above 15 vol%, the addition of more particles started to have a detrimental effect in the fracture toughness, as seen in Figure [90].

The strength of some composites is known to follow the simple rule of mixture models shown in Equations 2.38 and 2.38 [162, 163, 164].

$$\sigma_c = f_p \sigma_p + f_m \sigma_m \tag{2.38}$$

$$\sigma_c = \left(\frac{f_p}{\sigma_p} + f \frac{f_m}{\sigma_m} \right)^{-1} \tag{2.39}$$

σ_c is the strength of the composite and f and σ are the strength of the matrix, with the subscript m, and of the particle, with the subscript p. However, these models do not take into account any particle interactions with the matrix. They typically

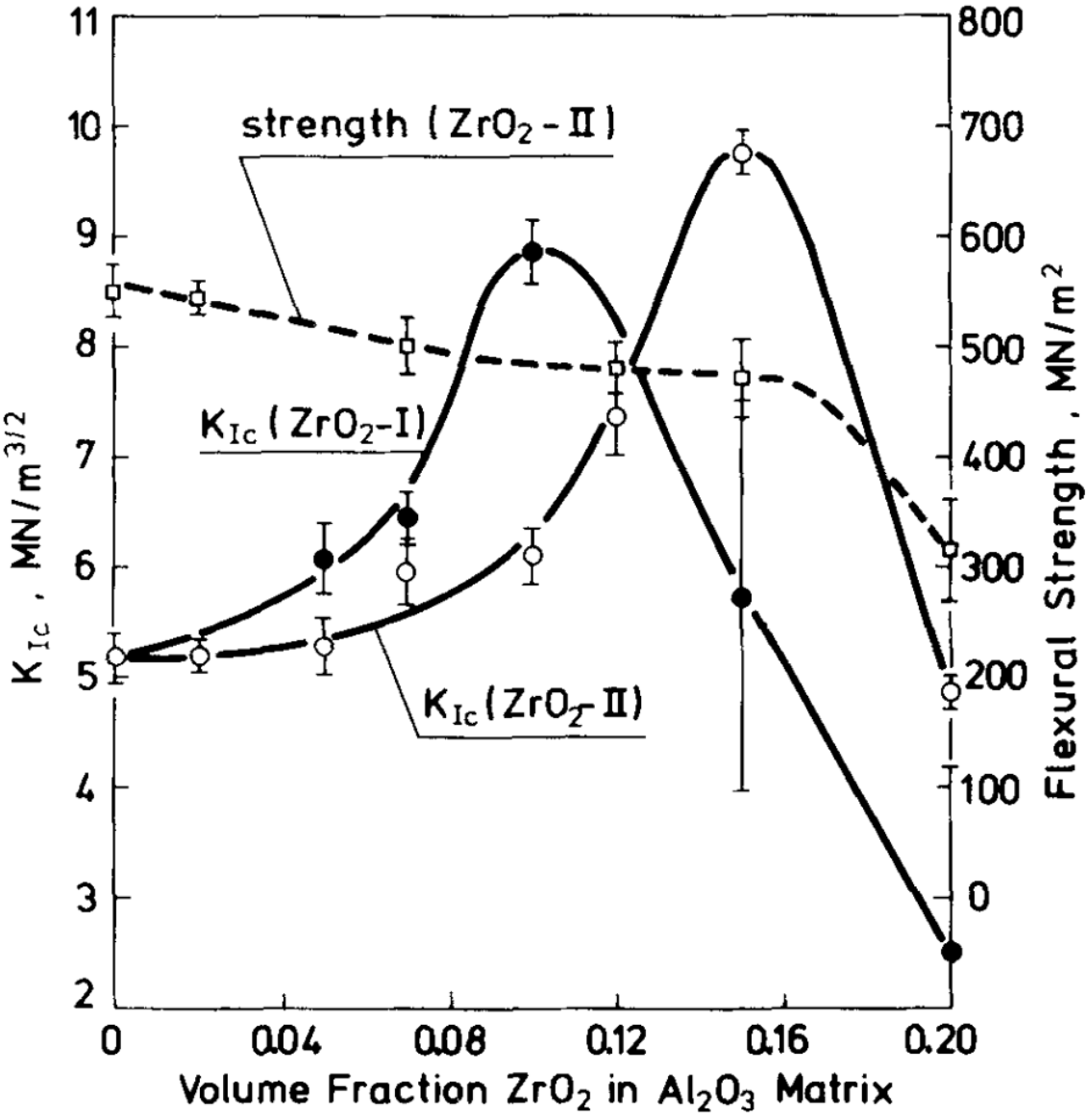


Figure 2.108: Fracture toughness of Al_2O_3 with ZrO_2 microspheres dispersed at volume loadings from 0 to 20 % taken from [90].

represent the upper and lower bounds for strength, with the ROM model being the upper and the inverse ROM model being the lower.

Another model assumes that the stress cannot be transferred to the discrete (particulate) phase and that the change in strength is due to the shrinkage of the effective cross-sectional area of the load-bearing matrix with the particles removed [165, 166, 167]. The equation is presented in Equation 2.40.

$$\sigma_c = \sigma_m(1 - v_p) \tag{2.40}$$

σ_c is the composite strength, σ_m is the matrix strength, and v_p is the particle volume fraction. This model is only valid in the case of no adhesion of the particle to the matrix. Studies have found that the linear nature of Equation 2.40 often oversimplifies the strength of composites. The equation was modified to include two constants a and b, which depend on the particle shape and their dispersion in the matrix [168, 169, 167].

$$\sigma_c = \sigma_m(1 - aV_p^b) \tag{2.41}$$

Leidner and Woodhams [170, 167] created a model that included the friction resulting from the particle matrix interface as well as residual pressure to produce Equation 2.42.

$$\sigma_c = 0.83pfV_p + k\sigma_m(1 - V_p) \tag{2.42}$$

p is the pressure, f is the particle-matrix friction coefficient, and k is a constant that represents the change in matrix strength as a result of the added particle.

For a very strong particle-matrix interface, the model by Pukanszky presented in Equation 2.43 is the best fit [171].

$$\sigma_c = \left[\frac{1 - V_p}{1 + 2.5V_p}\sigma_m\right] \exp\left(BV_p\right) \tag{2.43}$$

B is an empirically derived constant that depends on particle density, interfacial bond energy, and the particle surface area. For poorly bonded particles, B is equal to 0. The value increases as the particle-matrix bonding increases.

Additional strength and fracture toughness models are given in Fu et al. and in Rabiei et al. [167, 172]. For ceramic matrix composites, smaller and longer particles provide greater strengthening as opposed to larger, more angular particles. The maximum increase in strength that a ceramic-ceramic composite can attain is estimated to be about 2 [173]. Significant effort was made to improve the strength of ceramic materials by using small particles to strengthen and toughen the material [174, 175]. The fracture toughness for a particle reinforced ceramic matrix can be defined by Equation 2.44.

$$K_{IC} = K_0 + \Delta K_R + \alpha \Delta K_T \tag{2.44}$$

K_0 is the plain strain fracture toughness for the matrix material. α is the fraction of transgranular fracture on the surface of the composites, ΔK_T is the strengthening resulting from the change in fracture mechanism, and ΔK_R is the strengthening caused by the average residual stress in the matrix, which is defined in Equation 2.45 [176].

$$\Delta K_R = 2q[2(\lambda - d)/\pi]^{1/2}] \tag{2.45}$$

q is the average residual stress in the matrix and λ is the distance between the reinforcing particles defined by $\lambda = 1.085 \times d/(f_p)^{1/2}$. d is the average particle size and f_p is the volume loading of the particle. This model predicts an increase in overall toughness for low volume loadings.

Chapter 3

Methods

3.1 Experimental Methods

3.1.1 Fabrication

Two different matrix materials, Mo30W and ZrC, were used to fabricate the cermet and cercer composites using three different surrogate particles, namely spherical YSZ, angular HfN, and spherical HfN. All powders along with their suppliers, size distributions, and measured densities are presented in Table 3.1.

All materials were fabricated using powder consolidation using SPS. Powders were loaded into graphite foil lined graphite dies that were 13, 20, and 40 mm in diameter. A LABOX-675-FC, NJS Co. Ltd, shown in Figure 3.1, was used to consolidate all the powders. Pulsed electric current sintering (PECS) mode was used with the default 40:7 on:off DC pulse. Temperature was measured using a pyrometer and was controlled using a proportional integral and differential (PID) controller to alter the current and power output. Heating rates from 50 to 150 °C/min were used. The hold temperature ranged from 1400 to as high as 2100 °C. The uniaxially applied pressure ranged from 10 to 50 MPa. Both isothermal sintering and constant rate heating (CRH) were used to consolidate materials.

Table 3.1: Powders, suppliers, particle sizes, and measured densities for the feedstock materials used in cermet fabrication.

Powder	Supplier	Size Distribution (µm)	Measured density (g/cm^3)
CR Mo30W	HC Starck	14.40 ± 8.40	11.871
BM Mo30W	Rhenium Alloys	10.9	11.655
GA Mo30W	GA	16.1 & 30.5	11.881
ZrC	Stanford Advanced Materials	<5	6.011
Spherical YSZ	MSE Supplies	236.7 ± 52.1	6.033
Angular HfN	Stanford Advanced Materials	156.6 ± 52	12.787
Spherical HfN	Alfa Chemistry	172.1 ± 64.2	13.199



Figure 3.1: The LABOX-675-FC used to consolidate all powders at UTK.

3.1.2 Characterization

Most characterization was performed at the University of Tennessee Institute for Advanced Materials and Manufacturing (IAMM). X-ray Diffraction (XRD) was used to characterize both the as received powders and the sintered samples. XRD was performed on a Malvern PANalytical Empyrean diffractometer setup with a PIXcel3D area detector using a Cu-Kαradiation source from 20 to 90°. The powder was imaged using scanning electron microscopy (SEM). Energy Dispersive X-ray Spectroscopy (EDS) and X-ray Diffraction (XRD). EDS was performed using on a Zeiss Evo SEM with the Bruker XFlash 6 360 EDS system and ESPIRIT software. XRD was performed on a Malvern PANalytical Empyrean diffractometer setup with a PIXcel3D area detector using a Cu-Kαradiation source from 20 to 90°. The tap and green densities were also determined using stainless steel punches and a hydraulic press.

The densities of all the sintered Mo30W specimens were initially measured using the Archimedes density technique. The relative densities were calculated assuming the true density was that of the powder density of 11.871 g/cm^3. The sintered Mo30W specimens were sectioned and mounted in epoxy so that the cross-section and axial surface of each sample could be polished. Samples were ground using 68, 25, 15, and 9 µm grinding sheets. The samples were then mechanically polished using 6, 3, and 1 µm polycrystalline diamond solution. After polishing, the surfaces were etched using Murakami's reagent at room temperature. EDS and XRD analysis was conducted on several samples, both before and after etching.

The microstructure of each sample was examined using both optical microscopy and SEM. Grain size was determined using the mean linear intercept method with the aid of MATLAB software [177]. Vickers hardness was measured using a Wilson® Hardness TUKONTM 1102 tester with a load of 1 kilogram (kg). Prior to indentation, the samples were mechanically polished to a surface finish of 1 µm. 10 indents were conducted randomly for each sample with a dwell time of 10 s and both diagonals were measured.

3.1.3 Thermophysical Property Measurements

All samples used for both the thermophysical properties and for the mechanical tests were machined from 40 mm diameter by 10 to 11 mm tall disks of as sintered material. The pure Mo30W, and Mo30W-HfN (angular) materials were machined using wire EDM. The surfaces were then polished using diamond paper. The Mo30W-YSZ, Mo30W-HfN (spherical), ZrC, and all ZrC cercer materials were machined using diamond blades at BMS BOMAS Machine Specialties, Inc.

Young's Modulus, shear modulus, and Poisson's ratio were all determined using impulse excitation of vibration following ASTM E 1876 – 21. Properties were measured by the University of South Carolina. The coefficient of thermal expansion of the pure matrix materials were determined using high temperature X-ray diffraction (XRD) [57]. XRD was performed on a Malvern PANalytical Empyrean diffractometer setup with a PIXcel3D area detector using a Cu-Kαradiation source from 20 to 90°from room temperature to 1200 °C using an Ar-H_2 cover gas to prevent oxidation. Lattice parameters were determined using a modified Rietveld refinement. The lattice parameters for the annealed Mo30W were then converted into a change in length utilizing the formula $(a - a_0)/a_0$, where a is the lattice parameter at any given temperature and a_0 is the lattice parameter at 25 °C. This was then fit to a second order polynomial equation. By taking the derivative of this polynomial, a first order equation for the CTE of Mo30W was produced, following Equation 3.1.

$$\alpha = \frac{1}{L}\frac{dL}{dT} = \frac{1}{a_0}\frac{da}{dT} \tag{3.1}$$

The linear coefficient of thermal expansion for both matrix and composite materials was also determined using a Netzsch Dil 402 pushrod dilatometer following ASTM E228-17.

Specific heat capacity was determined using a Netzsch DSC 404 differential scanning calorimeter following ASTM E1269-11. The heat capacity of all materials

was fit to the semi-empirical model used to model the heat capacity of UN and YSZ, presented in Equation 2.18.

Thermal diffusivity was determined using a Netzsch Laser Flash Apparatus LFA 457 MicroFlash® following ASTM E-1461. The equipment used to measure the thermal properties and temperature ranges are presented in Table 3.2. The thermal conductivity of each material was calculated using Equation 2.13. The density was assumed constant over the measured temperature range, based off the measured room temperature value. The semi-empirical heat capacity model was also used to calculate the thermal conductivity.

3.1.4 Mechanical Testing

All mechanical testing was performed using an Instron 5900 10 kN static Load Cell (2850-10 kN). A 5 kN load cell was used for both the flexural and tension experiments. A custom ATR induction furnace was also used to heat the specimens to the desired test temperature, up to 800 °C. The furnace was water cooled and designed to be run in either a low vacuum (around 200 torr) or over pressurized in high purity Argon to 1140 torr to prevent oxidation. Given the high oxidation potential of the matrix materials, the over pressurized Argon proved to be the most successful at preventing surface oxidation. Three thermocouples, placed below, at, and above the sample, were used to control the PID programmable heating system. The furnace and attached furnace are shown in Figure 3.2.

Tensile tests were performed only for the pure metal matrix material, or the Mo30W. SS-3 dog bone tensile specimens were machined using wire EDM. Tensile testing followed ASTM E21-20 and ranged from room temperature to 800 °C.

Single edged notched bending (SENB) testing was used to determine the fracture toughness of the samples. While fracture toughness can be determined from 3 and 4-point bend-bar tests, the addition of a notch acts a crack propagation site and provides more accurate fracture toughness data for brittle materials. While the

Table 3.2: Summary of physical properties tested, equipment and techniques used along with the ASTM standard and the tested temperature range.

Physical Property	Equipment/ Technique	ASTM Standard	Temperature Range (°C)
Young's Modulus shear modulus, and Poisson's ratio	Impulse excitation of vibration	ASTM E 1876-21	RT – 800
Coefficient of Thermal Expansion	XRD	N/A	RT – 1200
Coefficient of Thermal Expansion	Netzsch Dil 402 pushrod dilatometer	ASTM E228-17	RT – 1000
Specific Heat Capacity	Netzsch DSC 404 differential scanning calorimeter	ASTM E1269-11	RT – 1000
Thermal Conductivity	Netzsch Laser Flash Apparatus LFA 457 MicroFlash	ASTM E-1461 ASTM E-1461	RT – 1000



Figure 3.2: Instron 5900 10 kN loadframe with attached ATR furnace.

most accurate fracture data are derived by fatiguing the crack site prior to testing, several studies have shown success in using simply a machined notch in the materials [178, 179, 180, 181], though it should be expected that a higher fracture toughness will be obtained with the SENB technique, compared with other methods [178, 182]. The fracture toughness from a SENB four-point bend test can be calculated using Equation 3.2 [178, 183].

$$K_{IC} = \sigma_f Y a^{1/2} \tag{3.2}$$

where K_{IC} is the fracture toughness, σ_f is the fracture strength in (MPa), a is the notch depth (m), and Y is a geometric factor given by the following equation:

$$Y = 1.99 - 2.47(a/w) + 12.97(a/w)^2 - 23.17(a/w)^3 + 24.80(a/w)^4 \tag{3.3}$$

with w defined as the sample width. The flexural stress for a 4-point bendbar is defined in Equation 3.4 [178].

$$\sigma = \frac{3F(L_0 - L_i)}{2Bw^2} \tag{3.4}$$

L_0 and L_i are the lengths of the inner and outer spans (m), B is the sample height, and F is the load at failure (N). Combining Equations 3.2 and 3.4 yields Equation 3.5, or the combined K_{IC} used to determine the fracture toughness of the SENB samples. Figure 3.3 provides the schematic for the 4-point SENB test with all labeled relevant dimensions.

$$K_{IC} = 3F_C\left(\frac{(L_0 - L_i)Y a^{(1/2)}}{2Bw^2}\right) \tag{3.5}$$

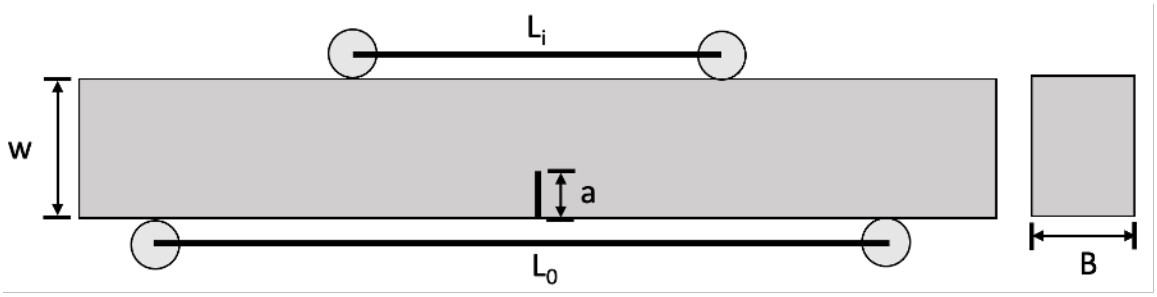


Figure 3.3: SENB from four-point bend testing schematic.

3.2 Sintering Analysis

3.2.1 Young and Cuttler Initial Stage Sintering

Two different approaches were used to analyze the sintering of the powders using SPS. Both utilized constant rate of heating (CRH) experiments. The first technique looks at the initial stage sintering and was developed by Young and Cuttler [126].

$$(\Delta L/L_0)^{2.06}\frac{d\Delta L/L_0}{dt} \cong 2.63\gamma\Omega D_v\frac{2.63\gamma\Omega D_v(\Delta L/L_0)^{1.03}}{kTa^3} + \frac{0.7\gamma\Omega bD_B}{kTa^4} \tag{3.6}$$

where $\Delta L = L_0 - L$ is the one-dimensional specimen shrinkage, L_0 is the initial specimen length prior to densification, γ is the surface energy, ω is the vacancy concentration, D_v is the volume diffusion, b is the effective grain-boundary width, D_B is the grain-boundary diffusion coefficient, t is the time, T is the absolute temperature, k is Boltzmann's constant, and a is the average particle radius. Typically, during sintering, one diffusion mechanism is dominant. The contribution of the other diffusion mechanism can therefore be ignored. The differential form of the equations for grain boundary diffusion dominant and volume diffusion dominant consolidation are presented in equations 3.7 and 3.8, respectively,

$$\frac{d\Delta L/L_0}{dt} \cong \left(\frac{2.14\gamma\Omega bD_{0B}RT}{ka^4cQ}\right)^{1/3}\left(\frac{Q}{3RT^2}\right)\exp\left(-\frac{Q}{3RT}\right) \tag{3.7}$$

$$\frac{d\Delta L/L_0}{dt} \cong \left(\frac{2.14\gamma\Omega D_{0v}RT}{ka^4cQ}\right)^{1/3}\left(\frac{Q}{2RT^2}\right)\exp\left(-\frac{Q}{2RT}\right) \tag{3.8}$$

with D_{0B} and D_{0v} as the coefficients for diffusion, c is the heating rate, R is the universal gas constant, and Q is the mechanism specific activation energy. While it is difficult to extract all the physical parameters from the shrinkage data, the apparent activation energy (nQ) can be determined with some level of accuracy [126]. This activation energy is independent of the dominant diffusion mechanism. By simplifying

equations 3.7 and 3.8, and combining all constants into a single term, equation 3.9 is generated as a practical approach for determining activation energies from CRH data.

$$T^m \frac{d\Delta L/L_0}{dt} \cong A^n \exp\Big(-\frac{nQ}{RT}\Big) \tag{3.9}$$

where A is a constant that includes all physical properties, m is a constant that is 5/3 for grain boundary diffusion and 3/2 for volume diffusion, and n is the mechanism dependent activation energy coefficient (1/3 for grain boundary diffusion and 1/2 for volume diffusion). Young and Cutler state that by plotting $\ln\left(T\frac{d(\Delta L/L_0}{dt}\right)$ versus inverse temperature, the slope of the line over the range of initial stage sintering will be the apparent activation energy [126].

3.2.2 Master Sintering Curve

The master sintering curve (MSC) is another model that fits all three sintering stages based on diffusion. Like previous models, it can be simplified to rely on a single diffusion mechanism, resulting in a single activation energy [184]. The MSC was developed by Hansen et al. to model the sintering of crystalline materials, and this multistaged sintering model is presented in Equation 3.10 [185]:

$$\frac{1}{\rho}\frac{d\rho}{dt} = \frac{3\gamma\Omega}{k_B T}\Big(\frac{\delta D_b \Gamma_b}{G^4} + \frac{D_v \Gamma_v}{G^3}\Big) \tag{3.10}$$

where ρ, is the relative density, $d\rho/dt$ is the densification rate, γ is the surface energy, ω is the molar volume, k_B is Boltzmann's constant, T is the absolute temperature, G is the grain size, δD_b is the diffusion coefficient for grain boundary diffusion, D_v is the volume diffusion coefficient, and Γ_b and Γ_v are a geometric scaling factors. This model is similar to the model derived by Young and Cutler, but it focuses on density data as opposed to shrinkage data. Like with the Young and Cutler method, one diffusion mechanism is assumed to be dominant, so Equation 3.10 simplifies to

$$\frac{1}{\rho}\frac{d\rho}{dt} = \frac{3\gamma\Omega}{k_B T}\left(\frac{D\Gamma}{G^n}\right) \tag{3.11}$$

where $D = D_0 \exp(-Q/RT)$ is the Arrhenius diffusion equation for either volume or grain boundary diffusion and where D_0 is the diffusion constant, Q is the activation energy, and R is the gas constant. Equation 3.11 can be rearranged to move all microstructural variables to the left-hand size, leaving only temperature dependent variables on the right-hand side.

$$\frac{k_B G^n}{3\rho\gamma\Omega\Gamma D_0}\frac{d\rho}{dt} = \frac{1}{T}\exp\left(-\frac{Q}{RT}\right) \tag{3.12}$$

Most of the constants on the left-hand side are unknown during sintering and are hard to measure. Integrating Equation 3.12 over the entire densification process leaves

$$\frac{k_B}{\gamma\Omega\Gamma D_0}\int_{\rho_0}^{\rho}\frac{\Big(G(\rho)\Big)^n}{3\rho\Gamma(\rho)}d\rho = \int_0^t \frac{1}{T}\exp\left(-\frac{Q}{RT}\right)dt = \Theta \tag{3.13}$$

where Θ is defined as the work of sintering. The mastering sintering curve is created by plotting Θ versus ρ. However, Q is unknown. In order to determine Q, an array of possible values are assumed and a value for Θ is calculated for each Q. A material needs to be sintered at using multiple heating rates to provide the needed data for this process. The mean residual square series of arbitrary values are assumed, then the mean residual square is calculated by

$$Mean\ Residual\ Square = \sqrt{\frac{1}{\rho_s\rho_0}\int_{\rho_0}^{\rho_s}\frac{\sum_{i=1}^{N}\left(\frac{\theta_i}{\theta_{avg}}-1\right)^2}{N}d\rho} \tag{3.14}$$

where N is the total number of data points obtained at various heating rates and sintered density, ρ_s is the final density, θ_i is the work of sintering for the ith experimental measurement, and $\theta_a vg$ is the average of all θ_i for any given Q. A more practical computational approach is to use a modified residuals method, where

prior to determining the residuals for a given Q, the densification data is normalized using a densification parameter [186], Ψ, where

$$\Psi = \frac{\rho - \rho_0}{1 - \rho_0} \tag{3.15}$$

The normalized densification data is then fit to a sigmoidal function with respect to θ [187, 188]:

$$\Psi = \frac{1}{1 + \exp\left(-\frac{\ln\theta - a}{b}\right)} \tag{3.16}$$

where a and b are fitting parameters. Once the density data for each heating rate is fit to Equation 3.16 using standard regression methods, the mean residual square can be calculated using Equation 3.14. This method can then be used to calculate an activation energy for sintering.

Chapter 4

Results

4.1 Fabrication

4.1.1 Initial Consolidation of Mo30W Matrix

Prior to fabricating the cermet materials, studies were conducted on the pure matrix materials, namely the Mo30W and the ZrC, to understand the optimal sintering conditions required. For the Mo30W, an initial study was conducted to understand the consolidation behavior of a single powder. The CR powder, which was a pre-alloyed Mo-W mixture prepared using chemical reduction, is shown in Figure 4.1. The powder XRD and EDS results confirmed that most of the powder was a solid solution of Mo and W, which is expected from the thermal equilibrium continuous solid solution phase behavior for the binary Mo-W system [1]. A few larger particles, around 10 to 15 µm in diameter, of pure Mo and W were found in the powder feedstock. XRD and EDS analysis were also used to determine how effectively the final sintered Mo30W was in solid solution. The X-ray spectra and an EDS maps of Mo30W samples sintered at 1600°C and 30 MPa for 15 minutes are shown in Figure 4.2 and Figure 4.3, respectively. The peak doublet observed in the spectra is caused by the $K_{\alpha 1}$ and $K_{\alpha 2}$ emissions from the copper source. The $K_{\alpha 1}$ diffraction patterns

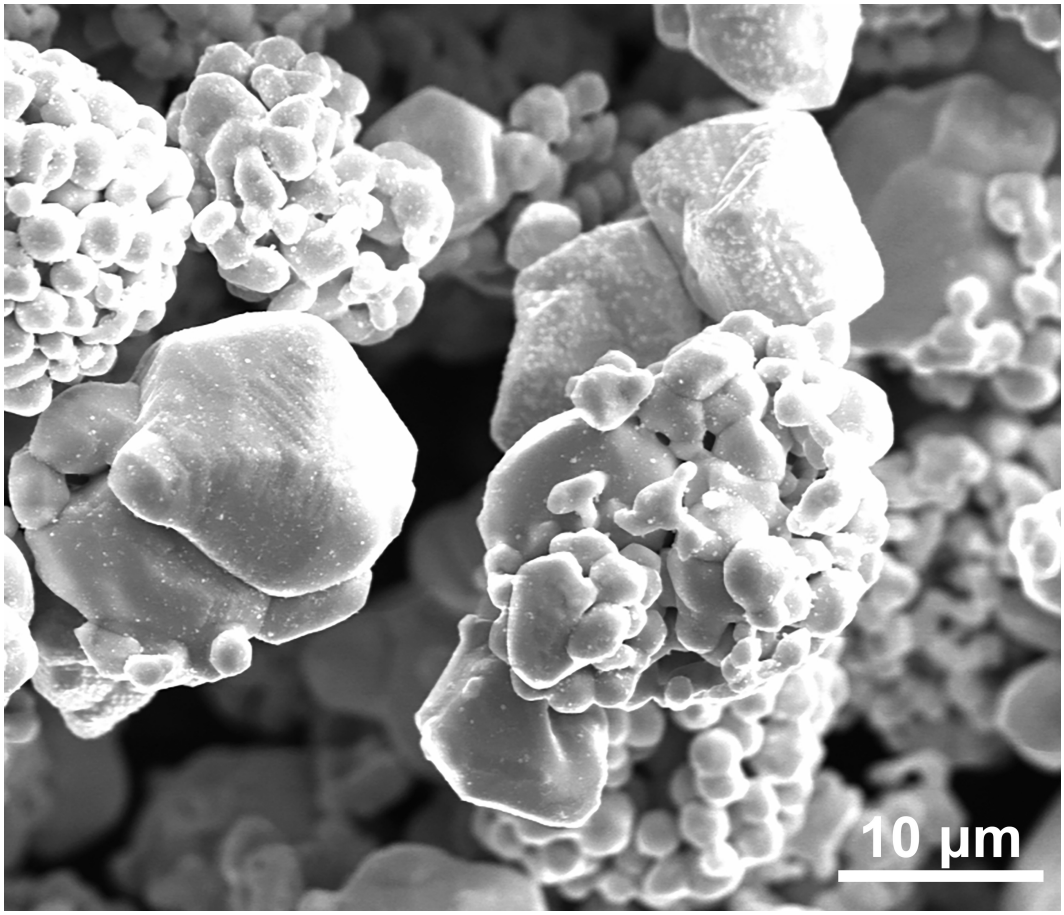


Figure 4.1: SEM micrograph of the chemical reduction powder taken from [40].

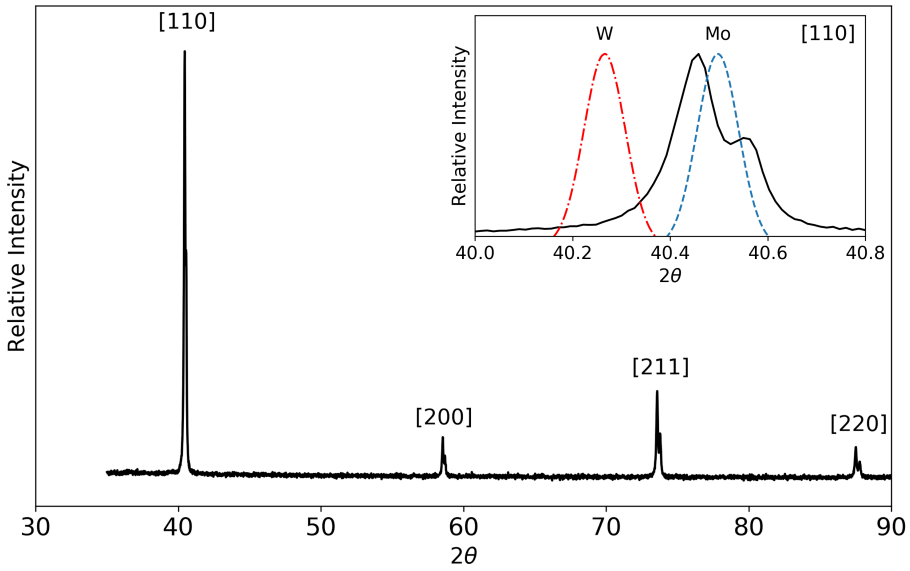


Figure 4.2: Temperature (solid line) and displacement (dashed line) profiles for SPS run to 1600°C with a heating rate of 100°C/min taken from [40].

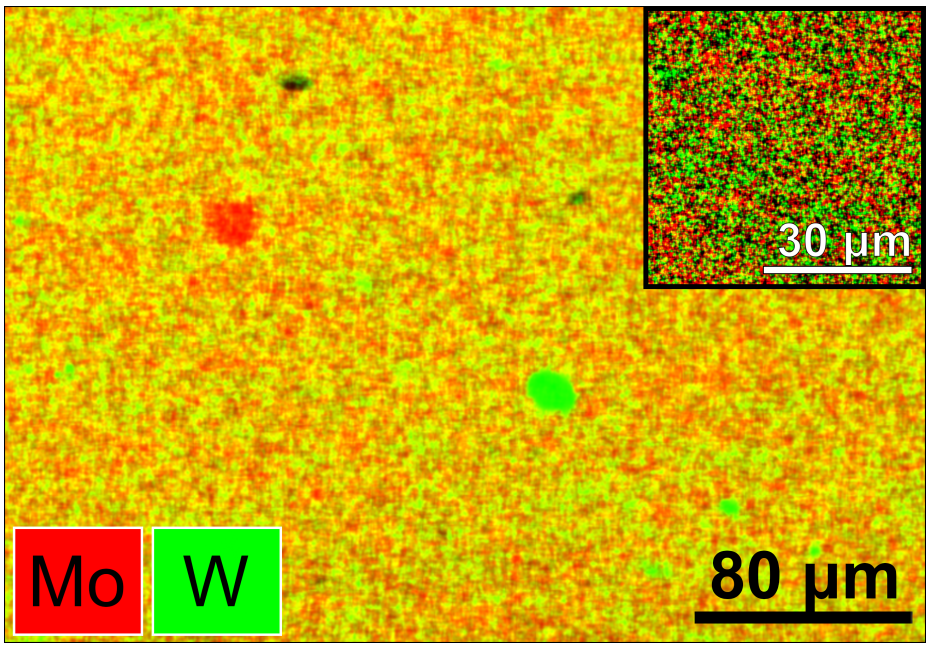


Figure 4.3: EDS map of the as sintered Mo30W material with an insert at higher magnification and resolution taken from [40].

of pure Mo and W at the [110] peak are shown in the inset image in Figure 4.2 for reference [189, 190].

The Mo30W $K_{\alpha 1}$ peak falls between that of pure Mo and W, tending closer to the pure Mo peak. The expected lattice parameter from Vegard's law using pure Mo and W is 3.149 nm, which is close to the 3.150 nm determined from the Rietveld refinement of the Mo30W alloy. From the EDS map, there appeared to only be a few areas that were enriched in Mo or W. These areas were found to be between 10 and 20 µm in diameter, corresponding to the pure Mo and W powder particles observed in the feedstock. The sintering temperatures and times tested in this study were not high and long enough for significant Mo and W interdiffusion to occur, based on tracer diffusion of W in Mo [191]. Due to the identical crystal structure and similar lattice parameters, the characteristic diffraction peaks for Mo and W are within less than one degree of each other. However, spectra for the sintered Mo30W produced narrow peaks between the two values, suggesting the material is mostly in solid solution

Eighteen total samples were sintered at various hold temperatures, pressures, and times. The conditions for sintering are listed in Table 4.1 along with the final sintered densities and indentation hardness. All samples resulted in greater than 88 % theoretical density. The results can be found in Table 4.1 and in Figure 4.4.

A theoretical density greater than 95 % was desired for the NTP reactor core application. Of the eighteen samples fabricated and tested, 13 samples reached a final density greater than 95 % theoretical density. Below 1600°C, temperature was found to have a strong effect on densification, whereas the temperature effect became weak at higher temperatures. The differences in density between sintering at 1600°C and 1700°C at all pressures were small. Applied pressure played a significant role in increasing the final sintered density, especially for the 1400 and 1500°C runs. All of the samples sintered at 50 MPa (1400-1700°C) achieved >97 % theoretical density. At 1600°C, the density increased linearly with applied pressure until 30 MPa was reached. Sintering at 50 MPa almost completely negated the effects of temperature over the 1400-1700°C test range. The highest density sample for this initial study

Table 4.1: Sintering parameters and density and hardness results for the chemical reduction Mo30W powder taken from [40].

Sample ID	Hold temp (°C)	Heat rate (K/min)	Set press. (MPa)	Hold time (min)	Final density (g/cm^3)	Relative density (%)	Hardness (HV_1)
1400-10	1400	100	10	5	10.54	88.8	240.4 ± 12.6
1500-10	1500	100	10	5	10.96	92.4	238.2 ± 4.1
1600-10	1600	100	10	5	11.16	94.0	246.0 ± 6.2
1600-20	1600	100	20	5	11.33	95.4	241.5 ± 5
1400-30	1400	100	30	5	10.62	89.4	263.3 ± 2.8
1500-30	1500	100	30	5	11.00	92.7	245.3 ± 7.7
1600-30	1600	100	30	5	11.46	96.6	242.0 ± 5.2
1700-30	1700	100	30	5	11.55	97.3	227.5 ± 3.8
1600-40	1600	100	40	5	11.51	96.9	231.8 ± 5.7
1700-40	1700	100	40	5	11.57	97.5	211.9 ± 7.8
1400-50	1400	100	50	5	11.55	97.3	246.6 ± 4.4
1500-50	1500	100	50	5	11.62	97.9	249.9 ± 5.3
1600-50	1600	100	50	5	11.59	97.6	233.0 ± 6.6
1700-50	1700	100	50	5	11.62	97.9	218.3 ± 6.4
1600-30-0.5	1600	100	30	0.5	11.39	96.0	260.1 ± 4.5
1600-30-15	1600	100	30	15	11.54	97.2	229.5 ± 5.3
1600-30-30	1600	100	30	30	11.57	97.5	223.9 ± 8.6
1600-30-90	1600	100	30	90	11.59	97.7	215.6 ± 6.1

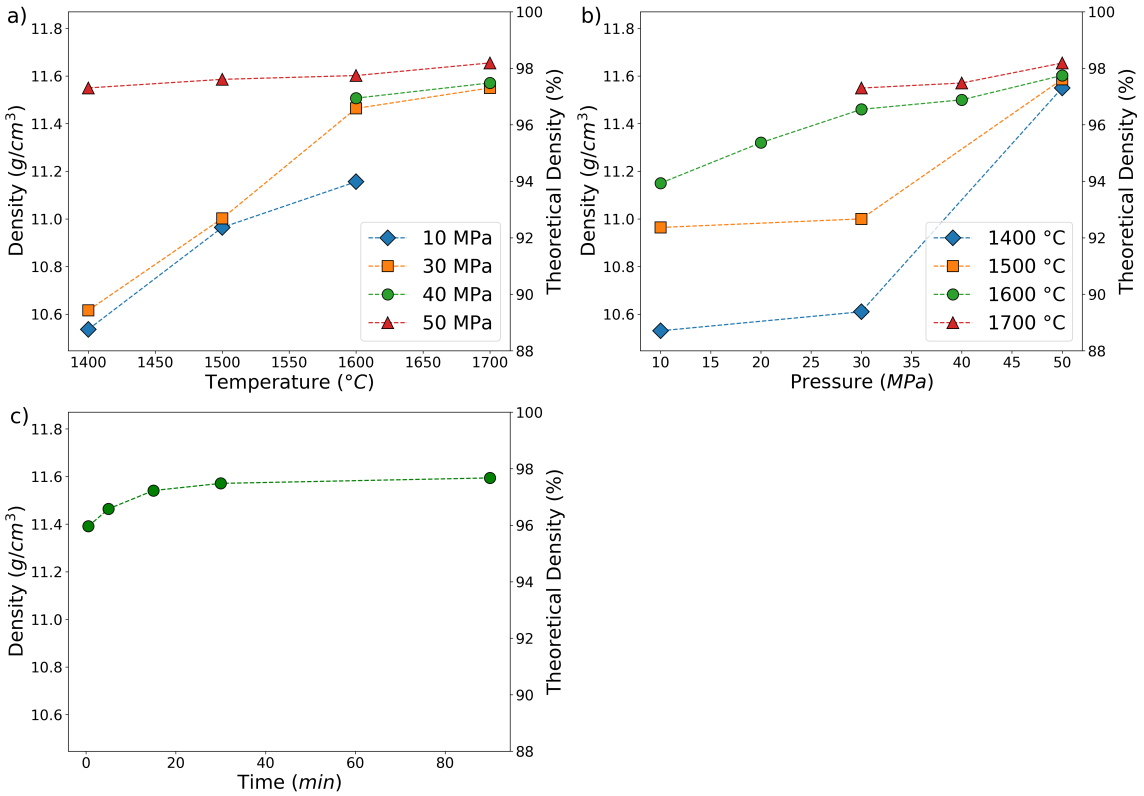


Figure 4.4: Densification of the chemical reduction Mo30W powder through SPS by varying a) hold temperature, b) set pressure, and c) hold time at 1600°C for 30 MPa. taken from [40].

(97.9 % theoretical density) was sintered at 1700°C and 50 MPa, corresponding to the highest tested temperature and pressure. The same density was also achieved in a specimen sintered at 1500°C and 50 MPa. Given the small change between the 1600°C and 1700°C runs, increasing the temperature will likely not have any major effect on density.

Mechanical properties of the sintered materials (hardness, strength, fracture toughness) can depend heavily on grain size. Figure 4.5 illustrates the general microstructure and grain growth associated with increasing hold temperature for a constant sintering time of 5 minutes. The average grain size is plotted with respect to hold temperature and pressure in Figure 4.6. Overall, the grain size varied from 2 to 25 µm for the different samples. Pressure had little effect on grain size. The grain size increased significantly with increasing sintering temperature for all applied pressures. The standard error of grain size also increases with temperature as there are a wider range of grain sizes formed as smaller grains are consolidated into larger ones. There is also a decrease in porosity as the sintering temperature increases. For the 1400 and 1500°C runs, the porosity is extensive in some regions and typically clustered at the grain boundaries. At 1600 and 1700°C, this porosity decreases rapidly. There is not much difference between the porosity of the 1600 and 1700°C samples.

Grain anisotropy was also examined in the sintered materials, as seen in Figure 4.7. This was primarily to study the effect of applied pressure on grain growth during sintering. The aspect ratio of interest is defined as the grain size along the axis of applied stress divided by the transverse (radial) grain size. These values were determined from the polished cross-sections of the samples. For most pressures and temperatures, the grain size aspect ratio appears to be nearly equiaxed, with all calculated values falling between 0.8 and 1.3. Moreover, there is no discernable trend in aspect ratios with the change in pressure or temperature. Even at the maximum examined pressure of 50 MPa, there was very little anisotropy over the temperature range tested. This suggests that the mechanical properties of the sintered materials are essentially isotropic.

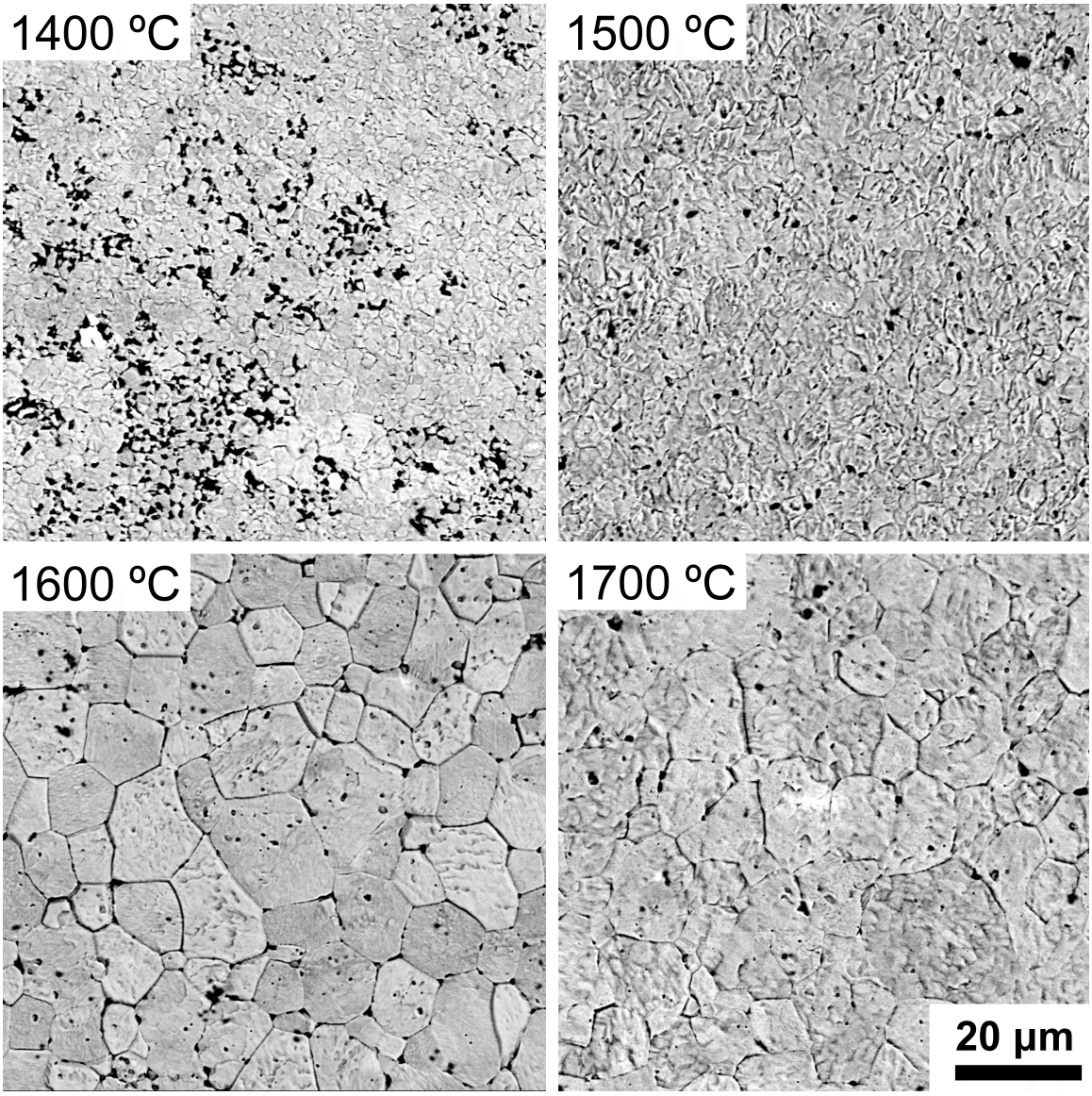


Figure 4.5: SEM micrographs of Mo30W solidified at 30 MPa at 1400, 1500, 1600, and 1700°C with a hold time of 5 minutes taken from [40].

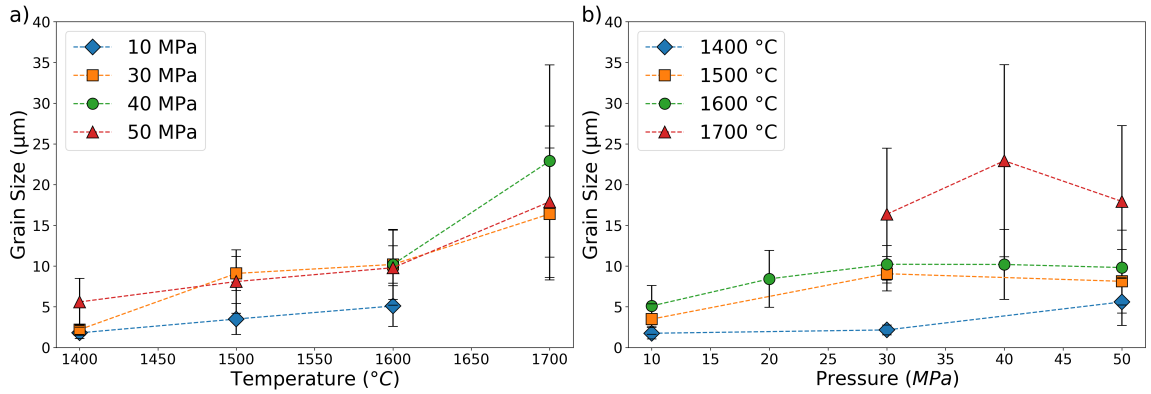


Figure 4.6: Grain size for sintered Mo30W with respect to a) hold temperature and b) sintering pressure taken from [40].

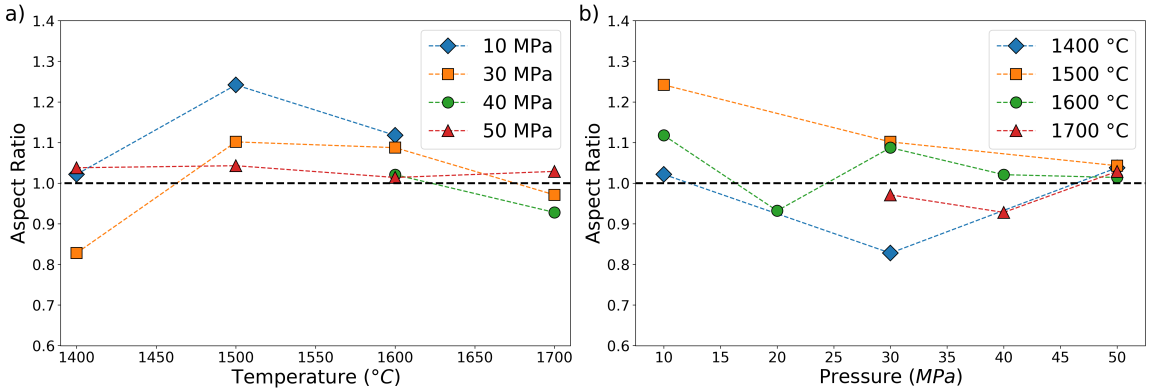


Figure 4.7: The grain size aspect ratio a) with respect to set pressure and b) with respect to the hold temperature taken from [40].

Hardness testing is a useful metric to determine the qualitative changes in strength of different materials. In general, there is a direct correlation between yield or ultimate strength and hardness of metals [131]. The hardness values of the sintered samples are plotted in Figure 4.8. While there is no discernible trend with respect to sintering pressure, there is a definitive decrease in hardness with increasing sintering temperature. While hardness does depend on density, it is also highly dependent upon the microstructure and grain size of the material. As illustrated previously in Figure 4.6, the average grain size increased with increasing hold temperature. The increasing grain size consequently decreased the hardness. The highest hardness occurred in the sample sintered at 1400°C and 30 MPa for 5 minutes. This corresponds to the smallest grain size that achieved greater than 90% theoretical density. The combination of high density and small grain size led to this material having the highest hardness value.

4.1.2 Comparison of the Consolidation of Different Mo30W Powders

Different Mo30W powders prepared using different techniques were available for the use as the matrix material for the cermet composites. It was unclear as to which powder was better for this application. One key consideration for powder selection was how well the material sintered without the addition of the ceramic particles. The powders differed in size and geometry. Powder geometry and size distribution affect powder sintering during consolidation with SPS and other sintering methods [192, 193, 194, 195]. The effect of Mo30W particle geometry and size distribution on sintering and sintered microstructures was characterized. Three different Mo30W powder feedstocks were selected for this experiment. Additionally, two different size distributions were also tested, totaling four tested materials. The final desired microstructure for NTP applications is a highly dense and homogeneous matrix with a fine-grained microstructure. The final microstructure and sintering mechanisms of each case were compared.

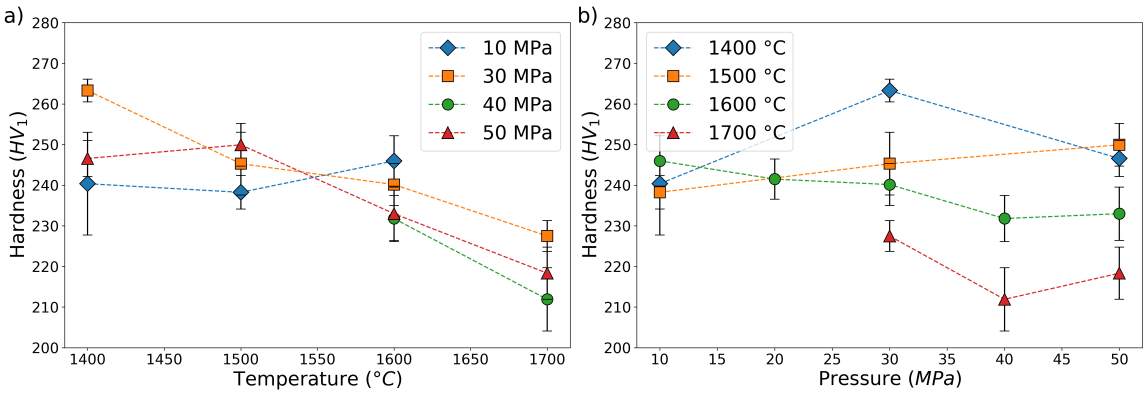


Figure 4.8: Vickers hardness a) with respect to hold temperature for 10 and 30 MPa and b) cross-sectional hardness with respect to pressure at hold temperatures of 1400, 1500, and 1600°C taken from [40].

Three different pre-alloyed Mo30W powders were supplied by NASA Glenn Research Center. All powders were intended to be pre-alloyed to the desired 30 wt% W with minimal added impurities. One powder was produced utilizing a chemical reduction (CR) technique to chemically alloy the materials in solution, which was discussed extensively in the previous section. Another technique utilized ball-milling (BM) of elemental Mo and W powders to produce the pre-alloyed material. The final powder was produced using a gas atomization process (GA). Mo30W electrodes were produced from extrusion of vacuum arc casted Mo30W. A plasma torch then melted the electrodes and the molten material was passed through a gas atomization nozzle to produce a spherical powder. In order to test the effect of size distribution as well as geometry, two different size distributions of the GA powder were tested, with a -325 mesh (<43 µm) and -635 mesh (<20 µm) utilized.

The powder size distribution (PSD) was determined by Laser Diffraction following ISO 13320 and chemical analysis was determined by ICP and LECO following ISO 17025. Both the PSD and chemical analysis were conducted by an analytical lab. The results of the elemental analysis are presented in Table 4.2. All three feedstocks showed high impurity contents. The BM impurities likely came from the milling media and previous milled materials. A high iron content was also noted. The CR and GA materials impurities resulted from the fabrication of other materials with the same equipment. The GA material had a large concentration of titanium impurity from previous material atomization processes. The GA material had the lowest oxygen content, which was an order of magnitude lower than that of the CR material. Moreover, the CR material had a lower oxygen content compared with the BM material. The ball-milling process is known to introduce oxygen into metallic materials [196, 197].

The instantaneous relative density of the powder compact during sintering, ρ (% theoretical), was calculated from the displacement data using Equation 4.1, where L_0 (mm) is the initial powder compact height, L (mm) is the instantaneous powder

Table 4.2: Elemental Analysis of the four different as received Mo30W powders (wt%).

Element	CR	BM	GA (-325)	GA (-635)
Mo	69.5	68.4	70.2	70.1
W	30.2	30.3	29.5	29.6
Al	-	-	0.012	0.016
C	<0.005	0.0054	0.004	0.026
Co	0.002	0.052	–	–
Cr	0.003	0.002	0.003	0.006
Cu	–	–	0.030	0.044
Fe	–	0.250	0.020	0.032
Mn	–	0.004	0.001	0.002
N	0.005	0.010	<0.001	<0.001
Ni	0.002	0.021	0.002	0.003
O	0.280	0.600	0.034	0.062
S	<0.001	<0.001	<0.001	<0.001
Sn	–	0.220	–	–
Ti	–	-	0.130	0.160
V	–	–	0.005	0.006
Zn	–	–	0.002	0.003
Zr	–	0.051	–	–

height, and ρ_0 (%) is the initial relative density determined using the final density and total sample displacement, assuming no change in diameter [198].

$$\rho = \frac{L_0}{L}\rho_0 \tag{4.1}$$

Particle size, density, and lattice parameters are presented in Table 4.3. The theoretical density was calculated from the tungsten content in the elemental analysis, listed in Table 4.2. The GA powders had lower tungsten contents, and thus lower calculated theoretical densities. The powder density for the CR and GA materials were all above 99% theoretical density. The BM materials had the lowest powder density resulting from higher powder porosity, but it was still greater than 97% theoretical.

The particle size distribution (PSD) of the powders is shown in Figure 4.9, with the average, and 10, 50, and 90 distribution volume percent listed in Table 4.3. The BM and GA powders all followed a logarithmic-normal size distribution, but the CR material exhibited a bimodal size distribution. The lower peak was the base fine MoW powder, with the larger distribution consisting of larger spherical agglomerates of the fine powder. SEM images of the powders are shown in Figure 4.10 at the same magnification. The GA powders are mostly spherical, while the BM material is quite angular. The CR material had the lowest tap and green densities, while the GA materials had the highest at around 70%. This is due to spherical particles having improved flowability compared with other particle geometries [199, 200].

The XRD peaks for each powder feedstock are presented in Figure 4.11. Given the similar crystal structure of Mo and W, the peaks of the two materials line up closely, with the peaks for MoW falling between them. Kα1 and Kα2 peak doublets are present in the CR and GA materials, but not in the BM material. The BM has the greatest peak broadening due to significant strain induced by the milling process.

The calculated densities, measured hardness, and average grain sizes of the sintered powders are listed in Table 4.4. Both the consolidated CR and BM powders

Table 4.3: Characteristics of the four pre-alloyed Mo30W powders.

Property	CR	BM	GA (-325)	GA (-635)
Particle Size (µm)				
D_{10}	2.21	3.24	14.9	10.1
D_{50}	6.51	9.45	31.4	16.4
D_{90}	45.0	21.8	51.7	25.5
D_{mean}	14.4	10.9	30.5	16.1
Density (g/cm^3)				
Theoretical	11.905	11.932	11.859	11.866
Powder	11.871	11.655	11.887	11.874
Tap	2.952	4.017	7.394	6.941
Green at 30 MPa	4.639	5.560	8.184	7.379
Lattice Parameter (nm)				
Rietveld Analysis	3.1504	3.1513	3.1509	3.1509
Error	5.0×10^{-6}	3.1×10^{-6}	1.2×10^{-6}	1.0×10^{-6}

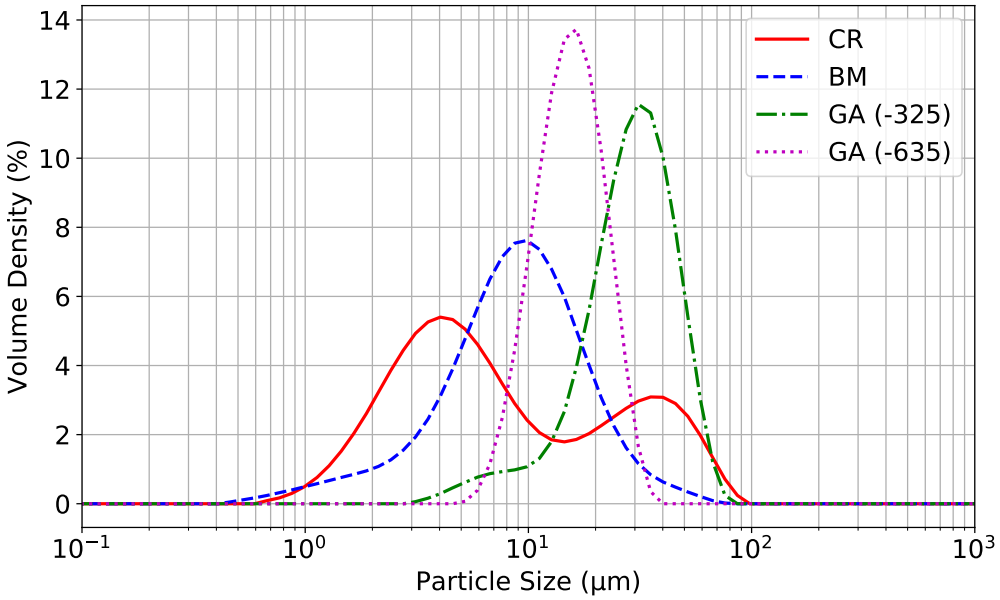


Figure 4.9: Particle size distribution for the four Mo30W powders.

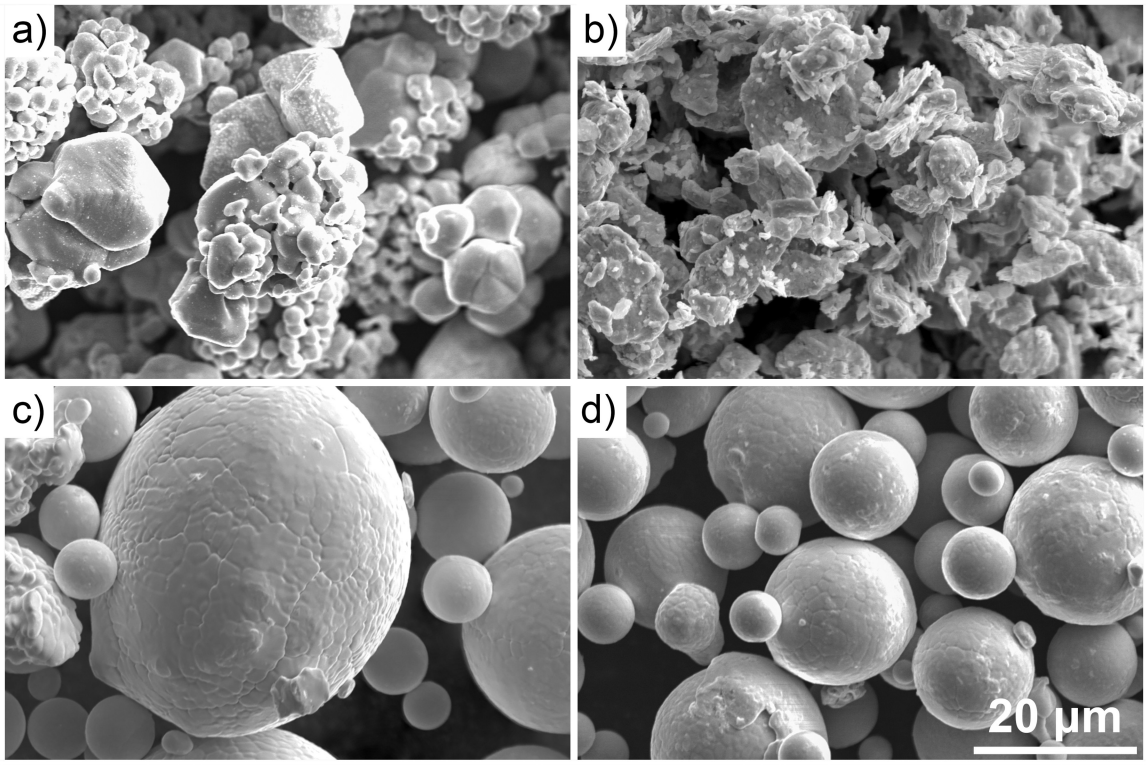


Figure 4.10: SEM micrographs of a) the CR (b) BM, c) GA (-325 mesh), and d), GA (-635 mesh) powders.

Table 4.4: Final sintering densities, hardness, and open porosity for the powders sintered at 1600°C and 30 MPa for 15 minutes.

Material	Final density (g/cm^3)	Final relative density (g/cm^3)	Average grain size (µm)	Indentation hardness (HV_1)
CR	11.644 ± 0.053	97.8	12.42 ± 6.93	242.0 ± 5.2
BM	11.401 ± 0.070	95.5	9.98 ± 4.92	223.1 ± 9.3
GA (-325)	10.745 ± 0.087	90.6	11.54 ± 7.52	136.6 ± 10.3
GA (-635)	10.523 ± 0.104	88.7	9.24 ± 4.75	135.9 ± 6.1

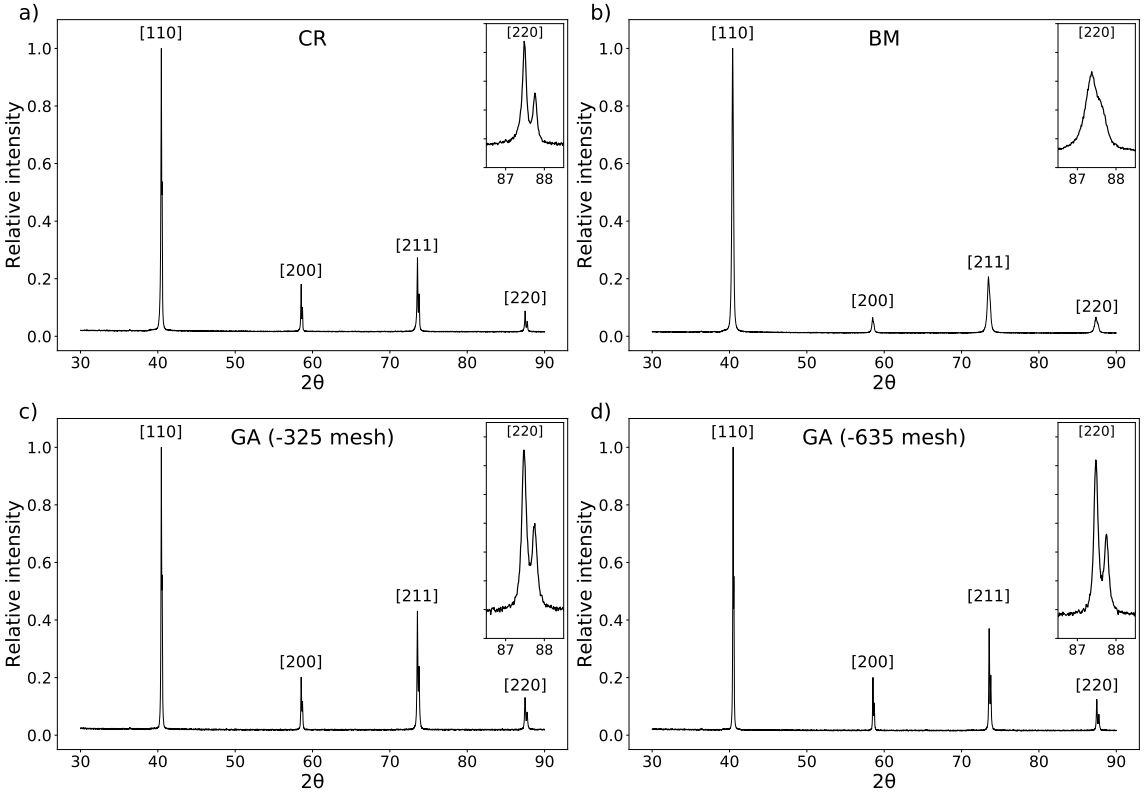


Figure 4.11: Powder XRD diffraction patterns for the a) CR, b) BM, c) GA (-325), and d) GA (-635) Mo30W powders.

reached a density greater than 95% theoretical. The consolidated GA powder feedstocks were both below 91% theoretical density. This is evident in the microstructure of the samples seen in Figure 4.12. Both the CR and BM materials formed a more traditional metallic polygon grain structure, while the GA powders formed a more spherical grain structure, matching the starting particle size and geometry. The sintered GA powders also had a much lower hardness compared to the CR and BM powders.

Figure 4.13 compares the starting PSD with the histograms of the final sintered grains for the four different powder feedstocks. The CR powder consolidated into a relatively uniform grain size, falling in-between the peaks of the bimodal distribution. The BM material grain size histogram matches the starting PSD, suggesting that the particles are only deforming during consolidation and that only minimal grain growth has occurred. Both GA material histograms fall below the starting PSD, suggesting that the spherical powders are multi-grained. The hardness of the sintered GA materials was significantly lower than the CR and BM materials. This is due to the pronounced intergranular porosity of the GA powders.

The sintering conditions of 1600°C and 30 MPa with a hold time of 15 minutes were sufficient to achieve optimized density and microstructure for the CR and BM materials. They were not sufficient for the GA powders to complete the bulk densification. A higher sintering temperature of applied pressure is required to produce a more highly densified material for the GA powders.

Figure 4.14 contains EBSD and EDS maps of the four different MoW consolidated powders. The CR and GA materials were found to be in solid solution, except for a few small areas enriched in either Mo or W. EDS analysis of the powders found several Mo and W enriched particles of similar sizes to those found in the CR and GA materials. Based on tracer diffusion of W in pure Mo, the sintering conditions of 1600°C for 15 minutes is not sufficient time to allow for any observable interdiffusion of Mo and W, let alone to form a complete solid solution, if the starting powder is not already in solid solution [201, 191]. Based on these tracer diffusion data, the

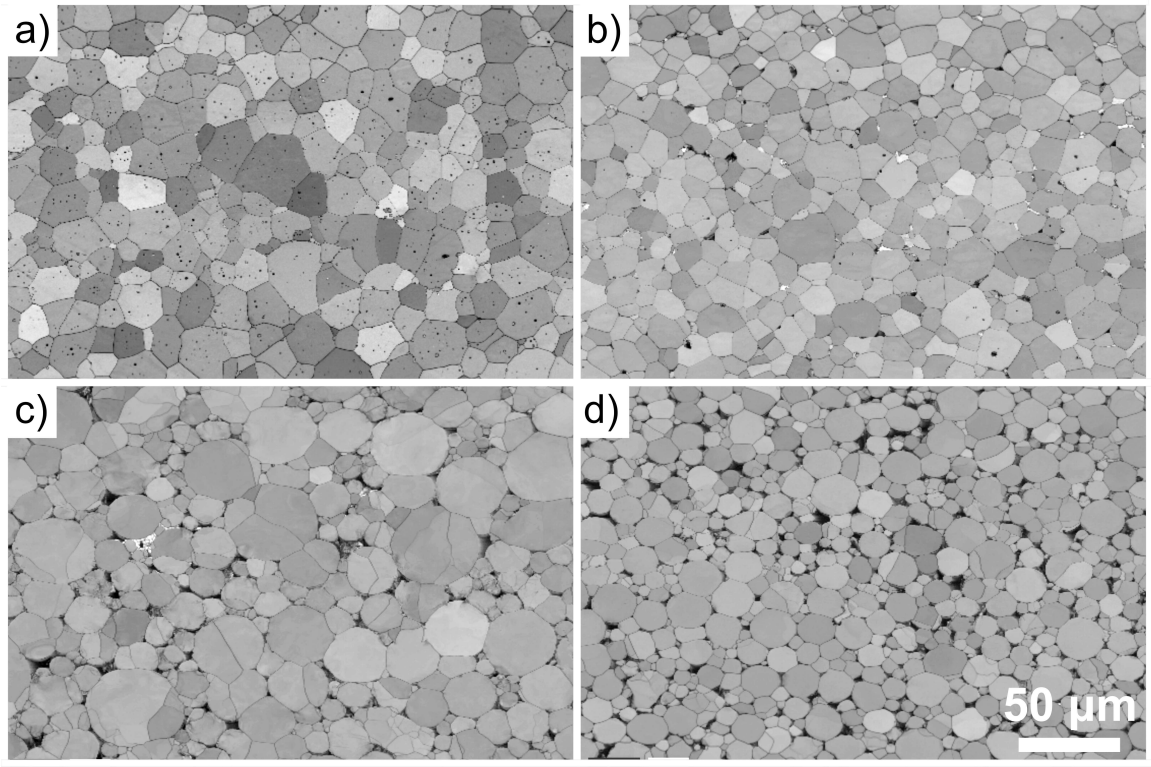


Figure 4.12: Backscatter electron images of the etched microstructure of consolidated a) CR, b) BM, c) GA (-325), and d) GA (-635) Mo30W samples sintered at 1600°C and 30 MPa for 15 minutes.

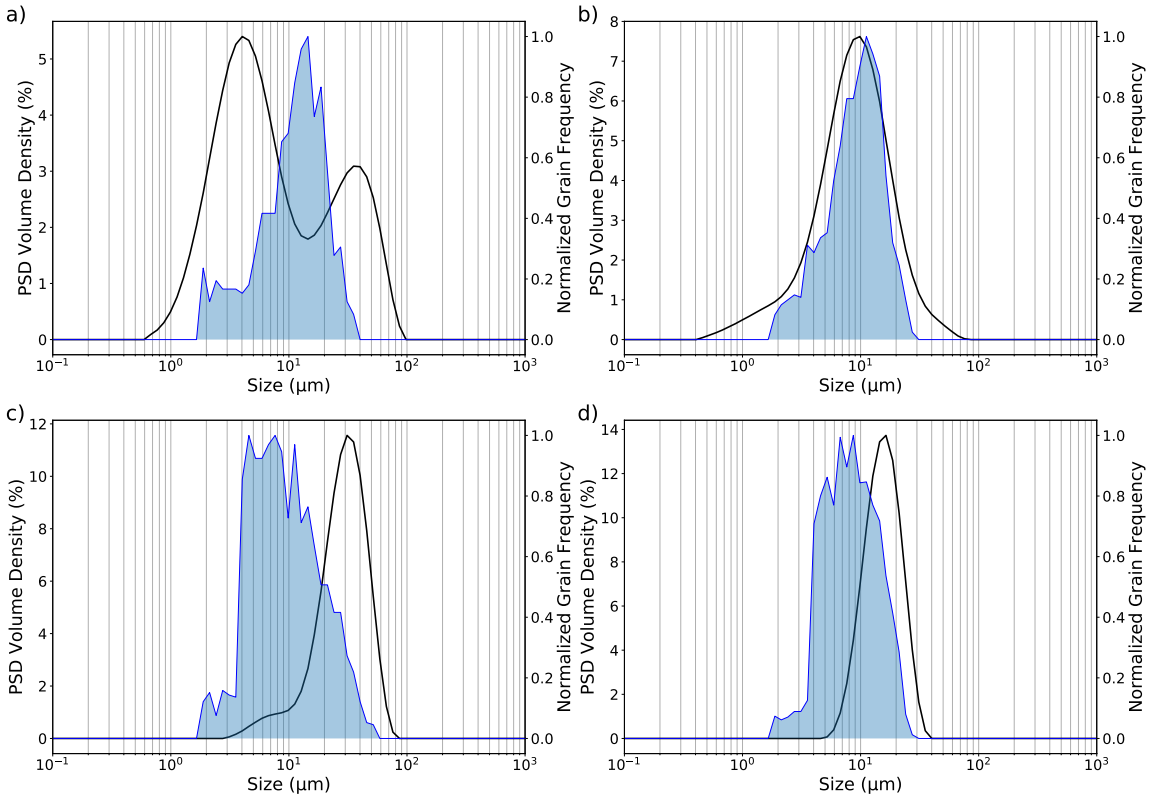


Figure 4.13: Particle size distribution (solid line) and grain size histograms (filled blue) for the a) CR b) BM c) GA (-325 mesh), and d), GA (-635 mesh) Mo30W powders sintered at 1600°C and 30 MPa for 15 minutes.

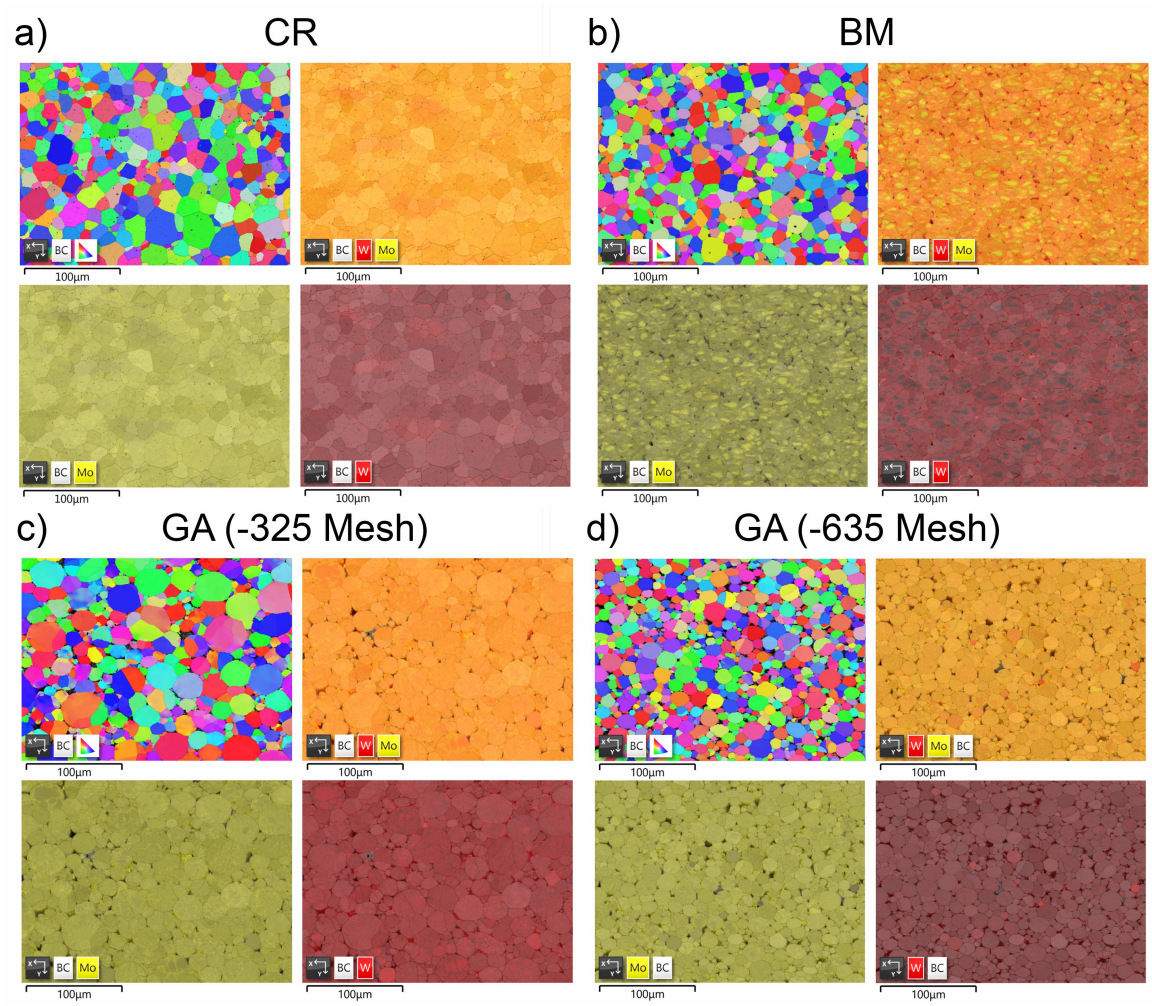


Figure 4.14: Particle size distribution (solid line) and grain size histograms (filled blue) for the a) CR b) BM c) GA (-325 mesh), and d), GA (-635 mesh) Mo30W powders sintered at 1600°C and 30 MPa for 15 minutes.

expected diffusion distance from $\sqrt{Dt}$ approximations for the sintering conditions is 0.001 µm. The BM material consists of three phases. Roughly 60% is a solid solution with Mo and W, and the other two phases consisting of either Mo or W rich phases. EDS analysis of the BM powders also showed that each particle was either Mo or W rich, with the compositions not consistent.

Figure 4.15 summarizes the piston travel corrected displacement rate of the four different powders as a function of temperature during constant heating rate sintering up to 1800°C. The differences in the maximum magnitude of densification rate can be attributed to different starting green body densities. The spherical geometry of the GA powders resulted in the highest starting green densities, requiring the least amount of densification to achieve the around 90 %. The CR material started at the lowest green density, thus requiring the most densification to achieve the final density, resulting in the highest magnitude densification rate.

The onset bulk densification temperature (defined by the displacement rate reaching 4 to 5% of the maximum value) and peak bulk densification temperatures (defined by zero value of the derivative of the displacement rate) are listed in Table 4.5. The BM material initiated stage I sintering at the lowest temperature. The BM material also had the lowest peak densification temperature, followed by the CR powder. Both GA powders exhibited similar densification curves, with the peak bulk densification occurring several hundred degrees above the CR and BM materials. Additionally, sintering of the GA powders occurred over a wider temperature range. The higher onset displacement temperatures further illustrate the greater temperature required to begin particle deformation during sintering.

Figure 4.16 contains a plot of the relative density, normalized to the theoretical density presented in Table 4.3, of the four different powders as a function of temperature during the 50°C/min. constant heating rate tests. The CR and BM materials both follow the standard "S" shaped sintering curve, with the inflection point corresponding to the maximum densification rate. The GA materials of both

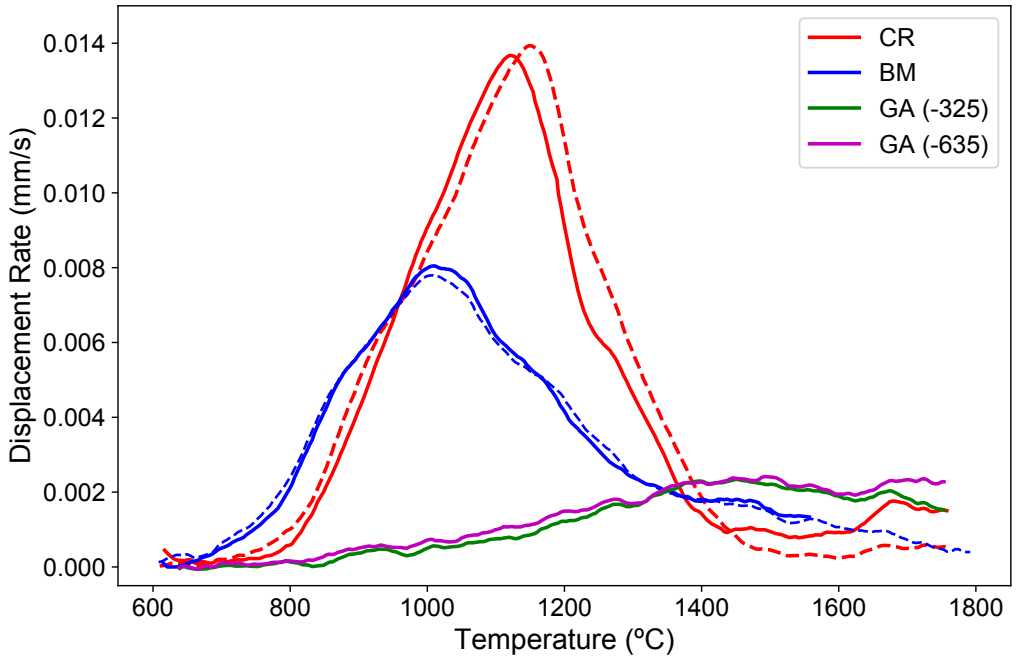


Figure 4.15: Corrected displacement rate of the four powders with respect to temperature. Two runs were used for both the CR and BM powders.

Table 4.5: Onset and peak displacement temperatures for the CR, BM, and GA Mo30W powders.

Material	Onset displacement temperature (°C)	Peak displacement rate (°C)
CR	780-800	1120-1140
BM	680-690	1010
GA (-325 Mesh)	850-860	1450
GA (-635 Mesh)	770-790	1490

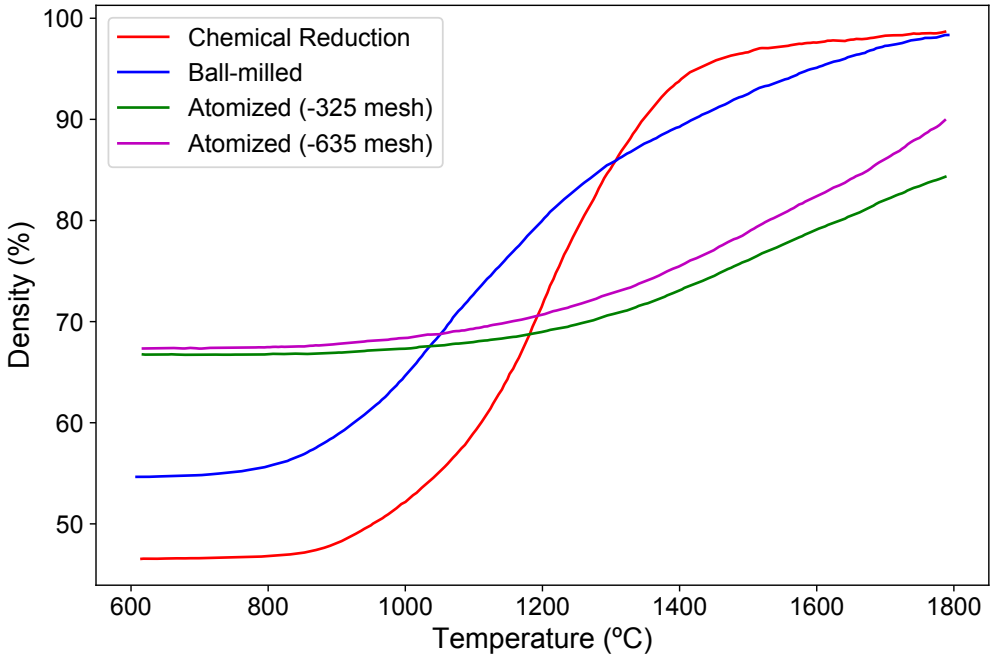


Figure 4.16: Normalized density of Mo30W powder compacts with respect to sintering temperature.

PSDs were still undergoing near-maximized bulk densification at 1800°C, with the inflection point not yet reached for the -635 mesh material.

4.1.3 ZrC Matrix Optimization

One ZrC powder was tested as part of this study. Some relevant properties are listed in Table 3.1. The powder, as seen in Figure 4.17, was an angular geometry $< 3\mu m$ in size. As discussed in Chapter 2, the properties of ZrC are heavily dependent upon the stoichiometry. A variety of methods were used to determine the C to Zr (C/Zr) ratio. Figure 4.18 contains the XRD spectra for the as received ZrC powder. A lattice parameter of 4.962 nm was determined using a modified Rietveld refinement. A pure C (0004) peak was observed at a $2\vartheta$of 21.6°. Using the Rietveld refinement, a free C amount of 2.2 wt% was determined. This number was then used to determine the lattice parameter as a function of the C/Zr ratio using Equation 2.6 developed by Jackson and Lee [135], which is shown in Figure 4.19. EDS was used to determine an approximate nitrogen and oxygen concentration of 0.056 atom%, which was needed for this model. By using this equation and the lattice parameter determined from the Rietveld refinement, a C/Zr ratio of 0.77 was determined.

The C/Zr ratio was confirmed using Thermogravimetric Analysis (TGA). The mass curves are shown in Figure 4.20. By compensating for the free C determined in the previous method, and by assuming the remaining oxide formation is ZrO_2, a C/Zr ratio of 0.80 was determined. This is similar to the value determined using XRD. All the properties are summarized in Table 4.6.

When fabricating composite materials, it is important to minimize the applied pressure to prevent excessive particle deformation or cracking during sintering. For this reason, 30 MPa was used as the maximum pressure for the initial ZrC sintering experiments. It is known that the sintering of ZrC powder is dependent on the vapor phase transport. For this reason, the effect of vacuum pressure on the densification of the material was examined. Three different vacuum systems were examined. The

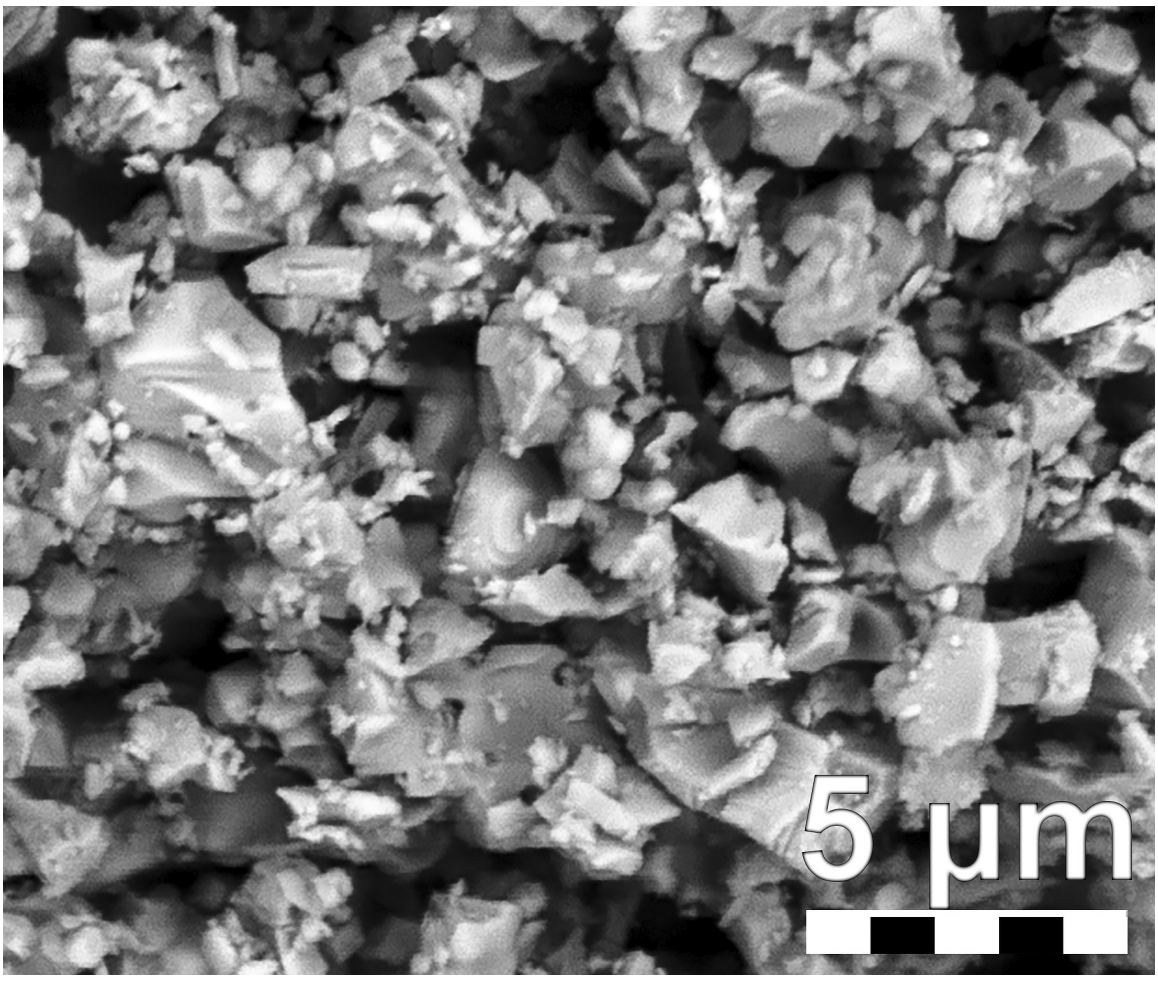


Figure 4.17: SEM image of the Stanford Advanced ZrC powder

.

Table 4.6: Summary of important properties for the as received Stanford Advanced ZrC powder.

Parameter	Method	Value
Free Carbon	XRD + EDS + SEM	2.2 (wt%)
ZrC Lattice Parameter	XRD + Refinement	4.962 (nm)
(O+N)/Zr atomic ratio	EDS	0.056
C/Zr Ratio	XRD + Model Fit	0.77
C/Zr Ratio	TGA	0.80

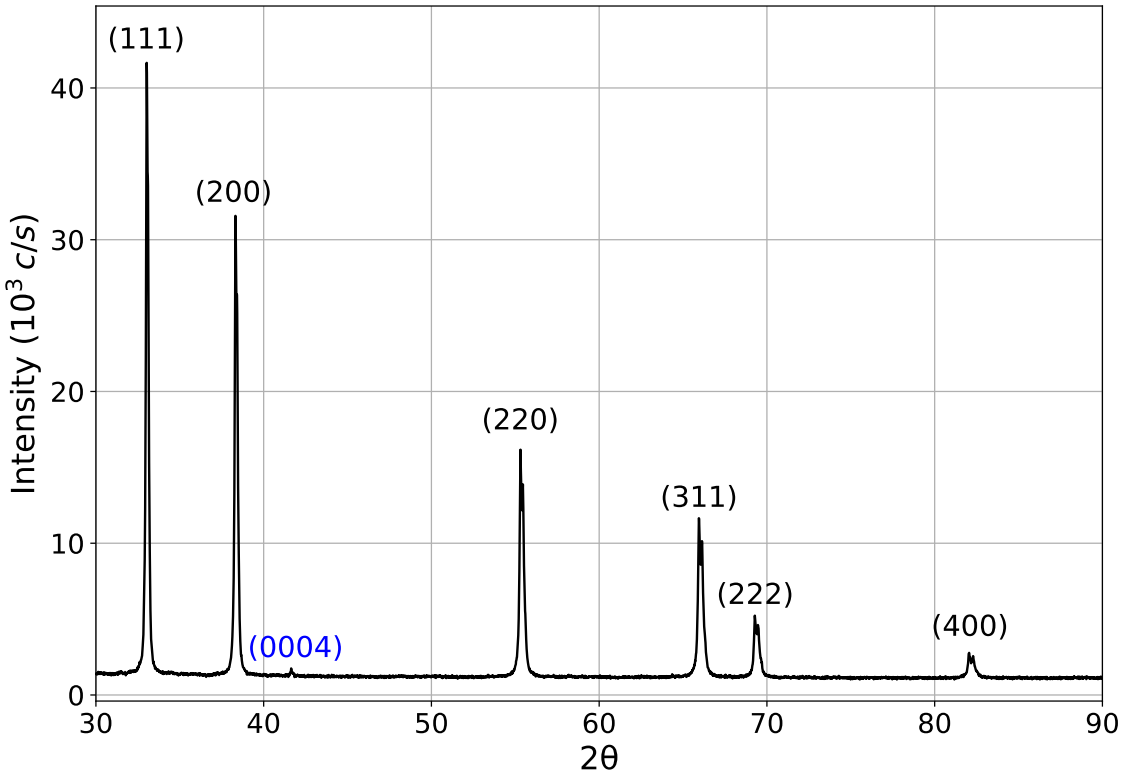


Figure 4.18: XRD spectra of the as received Stanford Advanced ZrC powder. The ZrC crystal planes are labeled in black, and the only visibly carbon plane is listed in blue.

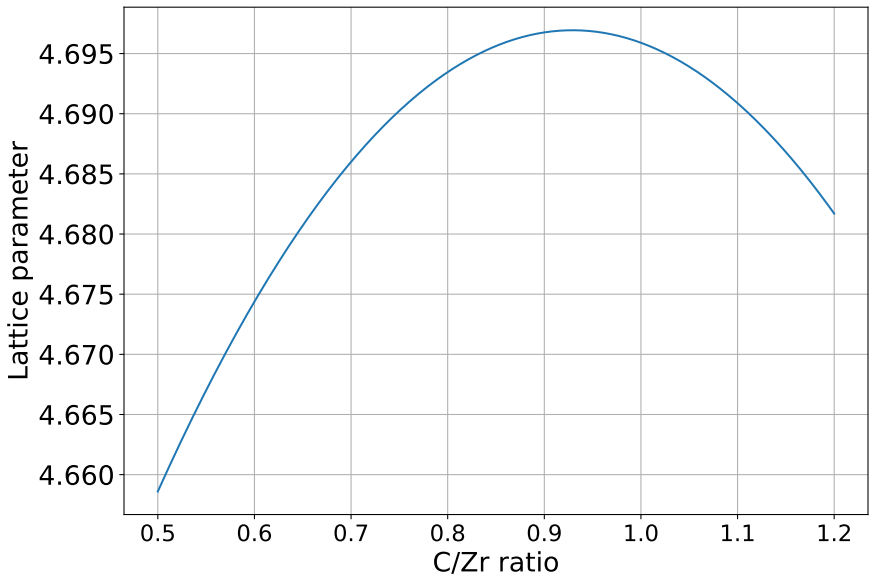


Figure 4.19: Lattice parameter of ZrC as a function of the C/Zr ratio as determined by Equation 2.6. The lattice parameter of 4.962 nm equates to a C/Zr ratio of 0.77.

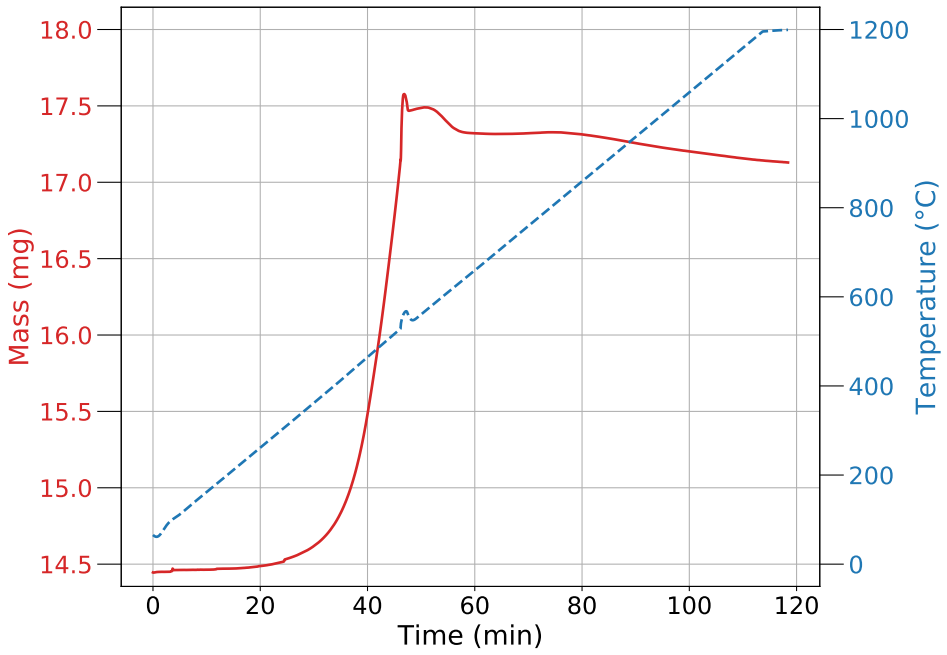


Figure 4.20: Mass (red curve) and temperature profile (blue dotted line) from the TGA of the ZrC powder up to 1200°C.

first was a simple roughing pump. The second used the roughing pump, but added an Ar purge to lower the oxygen partial pressure. The third system was using a turbo pump in series with the roughing pump. Typical vacuum pressure profiles observed in the sintering of ZrC are presented in Figure 4.21 with the three different systems. There was not a major difference in absolute vacuum pressure, especially between the Ar purge and roughing pump. The turbo pump did keep the pressure at about half that of the other two systems.

The density of the sintered powders for each of the different vacuum systems with respect to temperature is shown in Figure 4.22. All samples sintered to a theoretical density of 95% or greater. For any given temperature, the Ar purged samples experienced the least amount of densification. In order to achieve 99 % TD, a sintering temperature of 2100°C was required. The roughing pump produced ZrC samples 1 to 2 % higher in density compared with the Ar purging. The addition of the turbo pump increased the density to above 99 % TD even as low as 1800°C.

To determine the maximum time needed for sintering, a study was conducted to test the consolidation of ZrC using SPS at 1750°C. The turbo-pump was used as well as an applied pressure of 30 MPa. The density and hardness of the consolidated material is presented in Figure 4.23. As the time increases, so to does the final grain size, as seen in Figure 4.24. The density increased with sintering time until around 10 minutes. After 10 minutes, the porosity is closed off, and there is no further benefit to the final density at 1750°C. The hardness increased with increasing hold time, then leveled off after 10 minutes. This suggests the ZrC does not follow the Hall-Petch relationship like the Mo30W. Instead, the strength of the ZrC is directly dependent upon the porosity.

Figure 4.25 contains the density results of this study as well as some literature values for both HIP and SPS sintered ZrC taken from Wei et al. [53]. Wei et al. relied on a higher driving force from the applied pressure. For hot pressing, an uniaxial pressure of 65 MPa was used while for SPS, a pressure of 55 MPa was used.

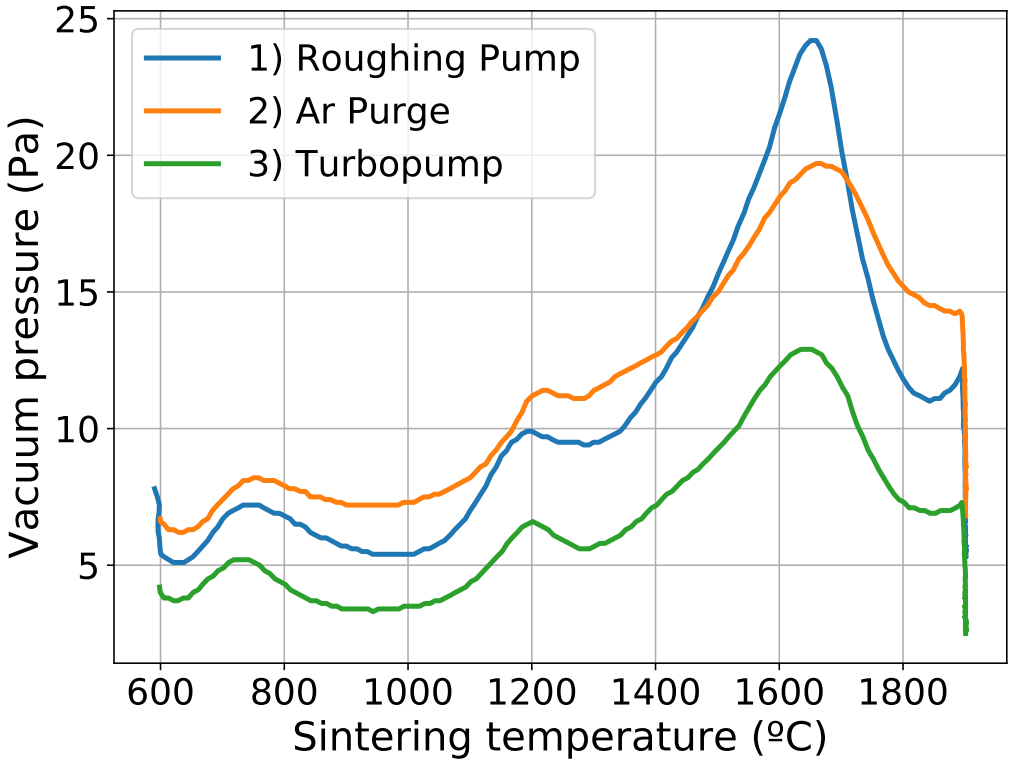


Figure 4.21: SPS vacuum curves for the ZrC powder as a function of temperature for the 1) roughing pump, 2) argon purge, and 3) turbo pump.

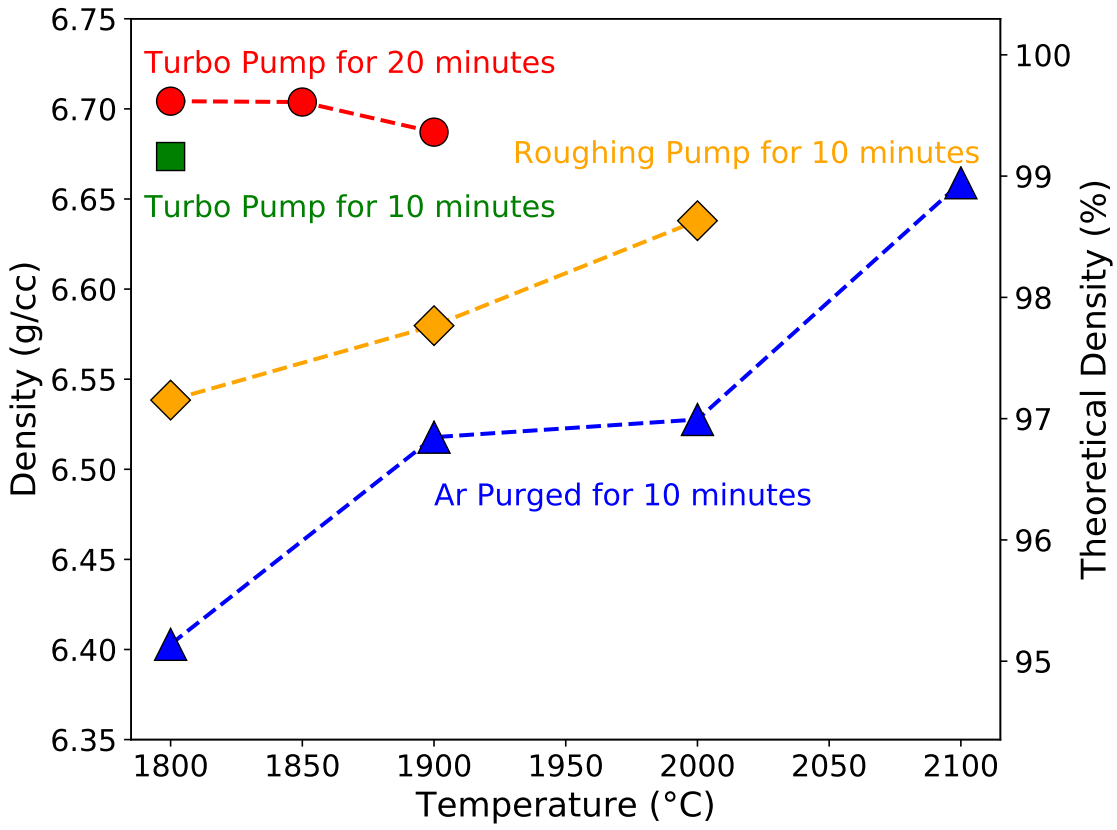


Figure 4.22: Density as a function of sintering temperature for the three different vacuum systems.

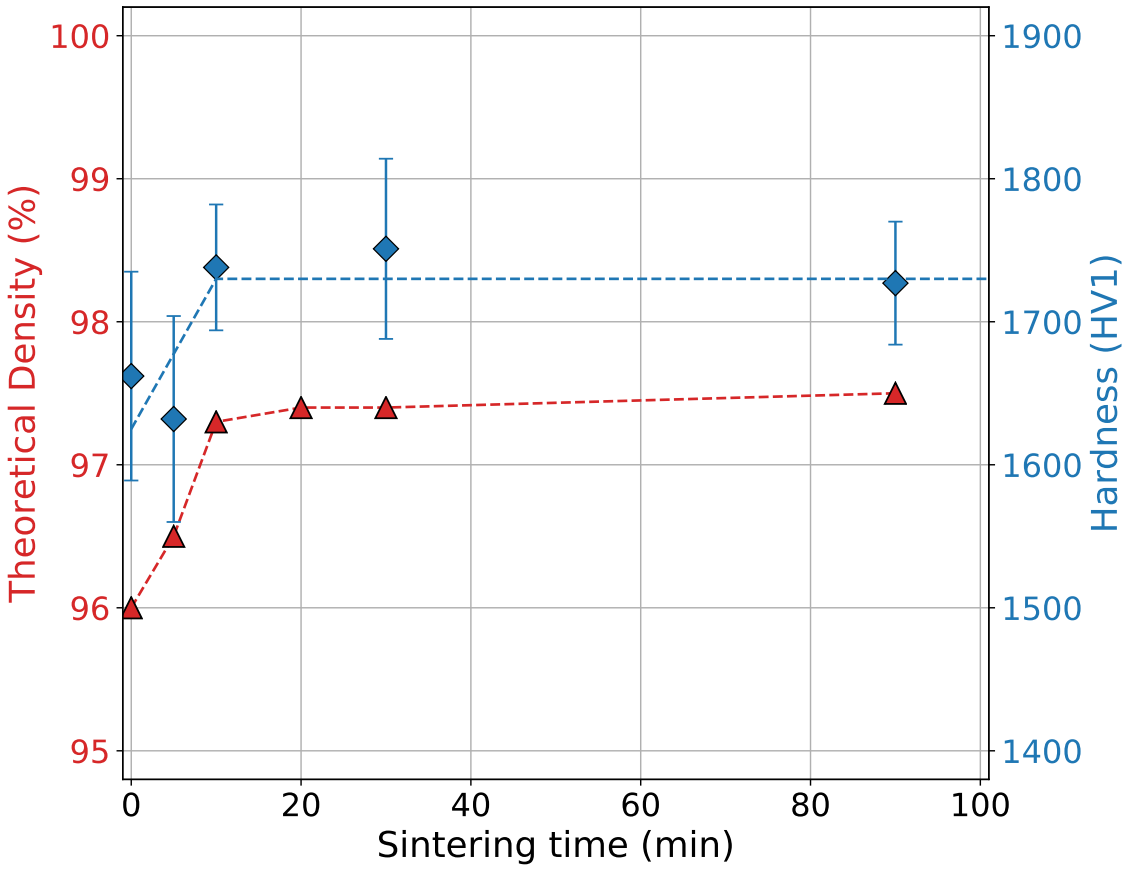


Figure 4.23: Plot of theoretical density (red triangles) and Vickers hardness (blue diamonds) with respect to sintering time for the ZrC powder consolidated using SPS at 1750°C with an applied pressure of 30 MPa.

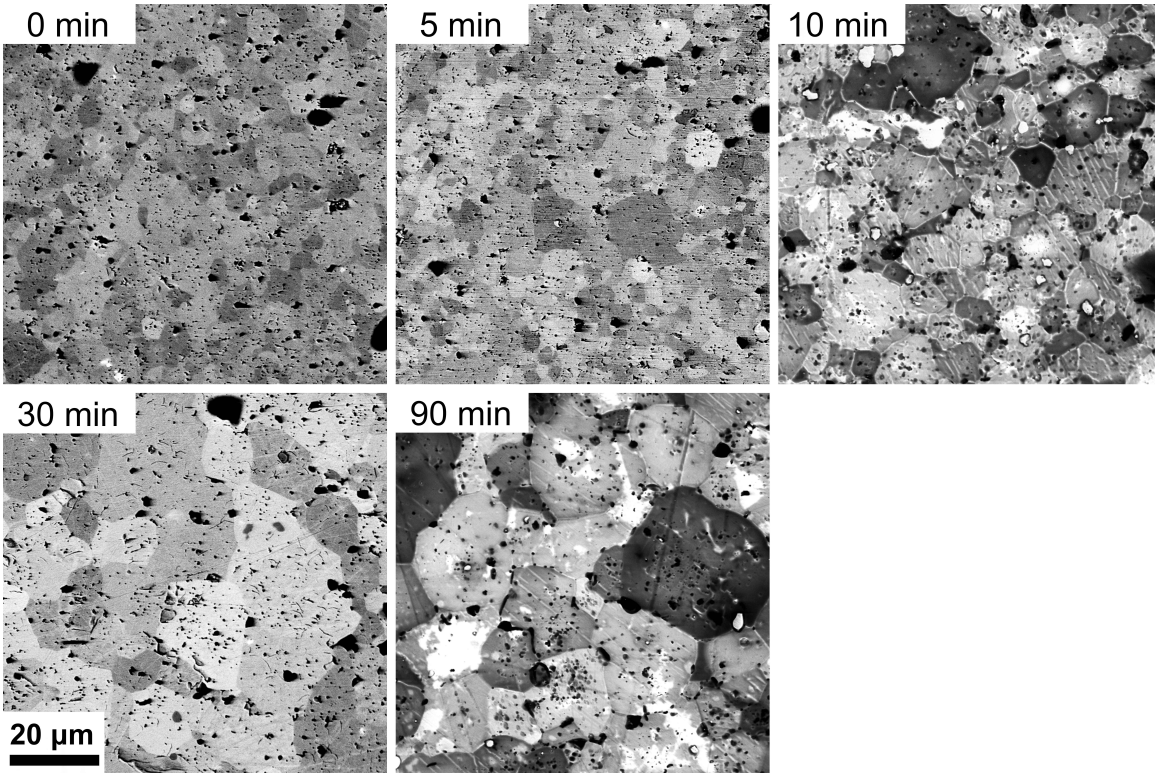


Figure 4.24: SEM images of the grain structure of ZrC powder consolidated using SPS at 1750°C with an applied pressure of 30 MPa from 0 to 90 minutes.

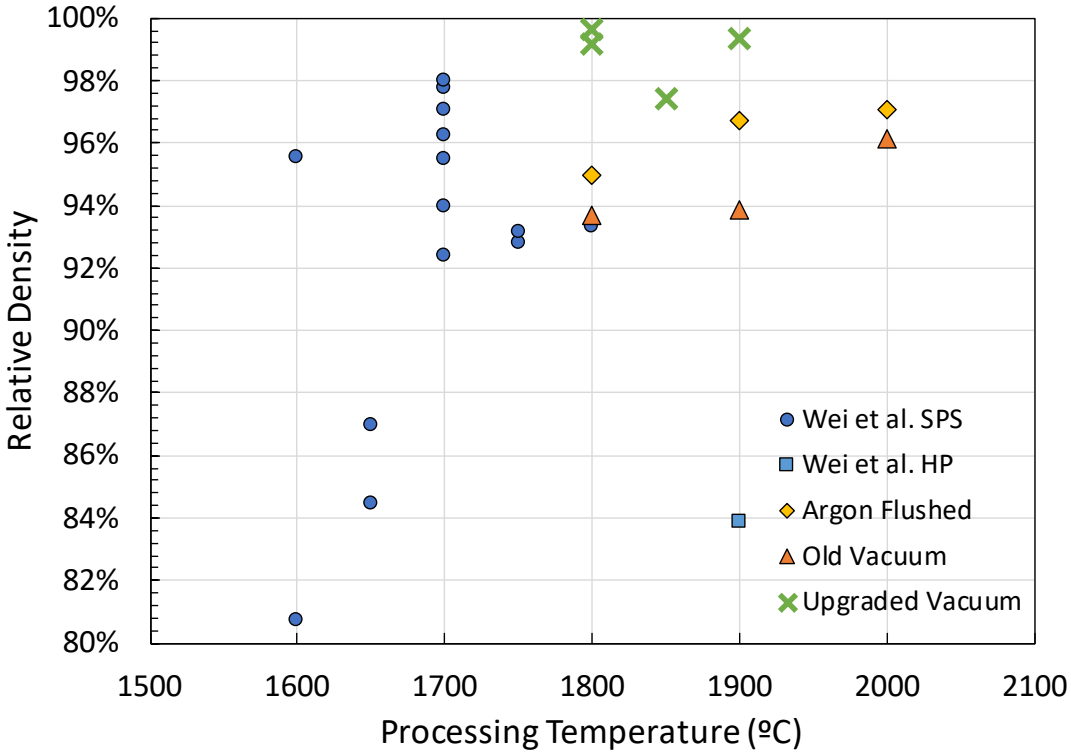


Figure 4.25: Relative density of ZrC prepared by SPS from this study compared with ZrC sintered using SPS and HP taken from Wei et al. [53]

For this study, the pressure was limited to 30 MPa. For this reason, a higher sintering temperature was needed to achieve the high density results of this study.

4.1.4 Scaling and Optimum Sintering Conditions

All the initial studies were conducted using 20 mm diameter graphite dies. An ideal set of sintering conditions was determined for each matrix material. As discussed previously, the goal was to achieve a highly densified matrix (>95% TD) without requiring too high a pressure that could potentially damage the surrogate particles during the fabrication of the cermet and cercer. The pressure was limited to 30 MPa. The other optimized sintering conditions are listed below in Table 4.7.

In order to produce enough material to machine sample specimens for the thermophysical and mechanical properties testing, larger samples needed to be sintered. A larger 40 mm graphite die was acquired and both Mo30W and ZrC samples were sintered at the conditions listed in Table 4.7. The final density of the larger samples decreased slightly compared with the 20 mm samples, however the density of both materials remained greater than 95 % theoretical. Figure 4.26 and 4.27 contain images of the 40 mm pure matrix materials sintered.

4.1.5 Powder Coating

In order to produce a two phase composite material with a homogeneous particle distribution, the particles need to be coated in the matrix material prior to sintering [54]. Two powder coating technique were developed to coat the particles in the matrix material prior to sintering. A binding agent was acquired from Honeywell called A-C® 617-A. This low density polyethylene homopolymer was found to be the best additive for the coating of spherical particles in a refractory metal matrix [54]. Mixing times and additive weight percents were all altered until the best process was developed. The optimized process for coating the spherical YSZ and angular HfN with both the

Table 4.7: Optimum sintering conditions and resultant properties for Mo30W and ZrC matrix materials.

Property	Mo30W	ZrC
Hold temp (°C)	1600	1850
Heating rate (°C/min)	100	100
Applied pressure (MPa)	30	30
Hold time (min)	15	10
Grain Size (µm)	12.42 ± 4.0	9.49 ± 5.7
Hardness (HV_1)	242.0 ± 5.2	1740 ± 44

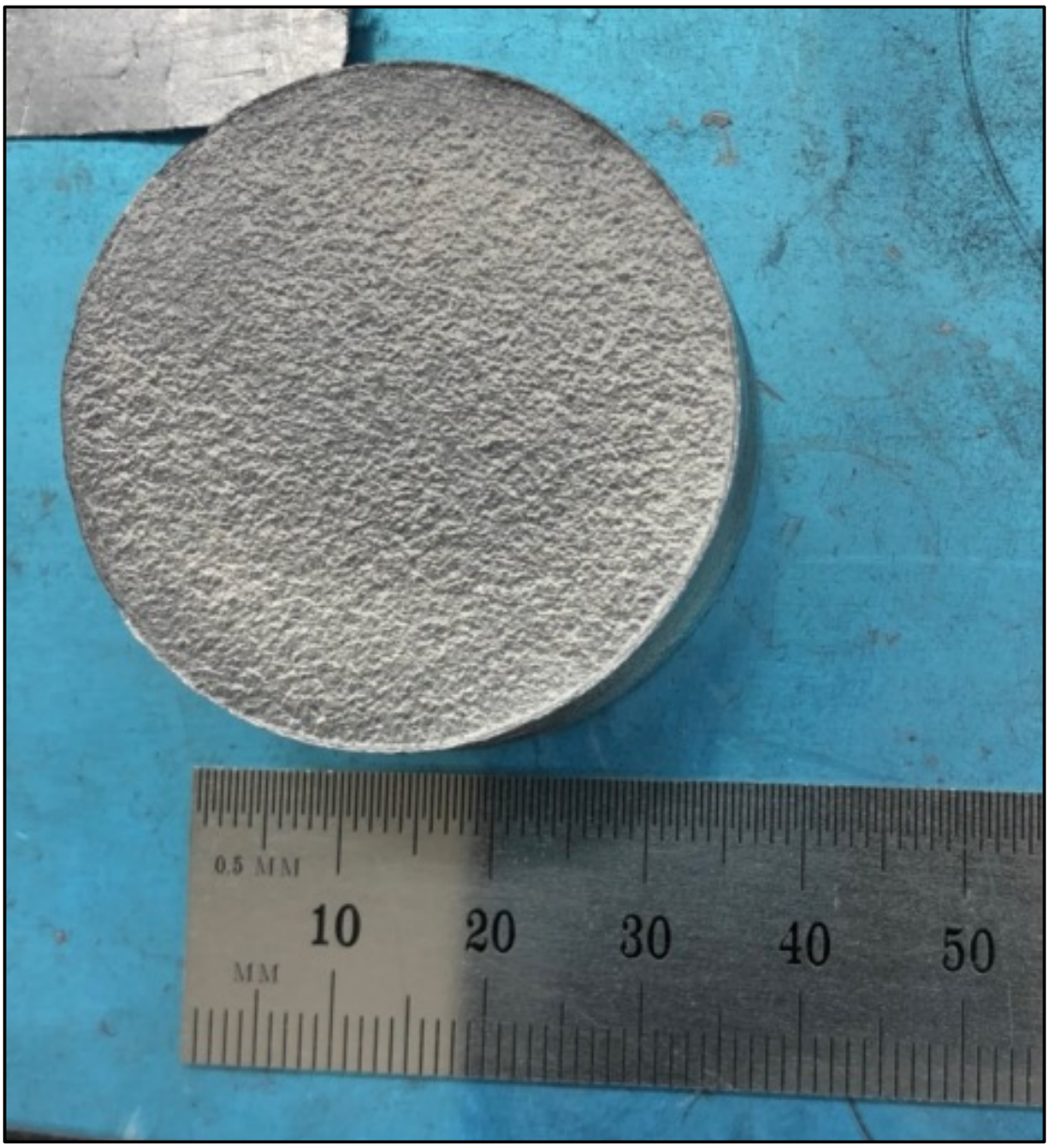


Figure 4.26: A sintered 40 mm diameter puck of Mo30W.



Figure 4.27: A sintered 40 mm diameter puck of ZrC.

CR Mo30W and the ZrC is listed below. The results of the optimized coating process can be seen in Figure 4.28.

1. Collect the matrix material powder, particles to be coated, and the A-C® 617A additive.
2. Collect and label two containers. One is for the matrix powder and the other is for the particles to be coated.
3. Measure out the desired matrix and surrogate materials and place into two separate containers.
4. Add 0.5 wt% of A-C® 617-A to the container with the matrix material.
5. Add 1.0 wt% of A-C® 617-A to the container with the surrogate material.
6. Mix both containers for 5 seconds at 1600 rpm. If a mixer is not available, a vortex mixer at a moderate to high setting for 10-15 seconds.
7. Remove the lids and place both containers in an oven at 85°C for 15 minutes.
8. Remove the sample from the oven and replace the lids. Place each material separately on the vortex mixer at a high speed and mix for 10 seconds.
9. Remove the lids and check for clumps, if any form, mix again for another 10 seconds.
10. While still warm, dump the contents of the surrogate container (surrogate material and A-C® 617 A) into the container with the matrix powder.
11. Replace the lid and mix on high for 10-15 seconds, depending on the amount of material in the container.
12. As the powder cools, the surrogate will now be coated by the matrix powder.

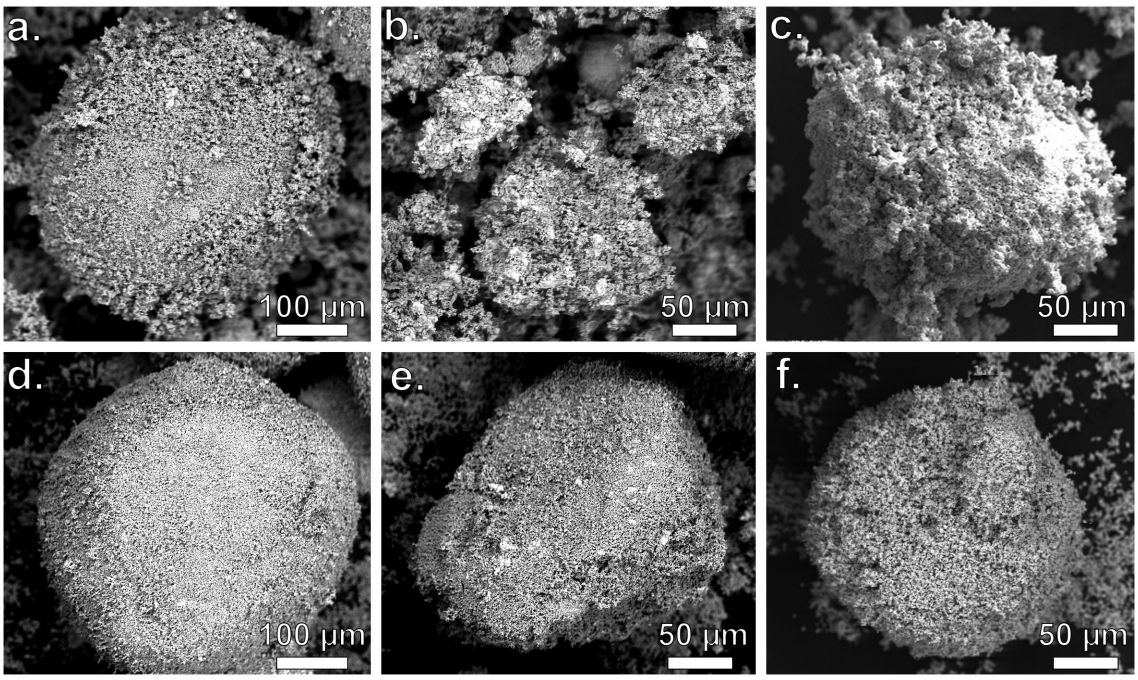


Figure 4.28: Surrogate particles coated in the matrix material utilizing the two developed powder coating processes. a. Mo30W coated YSZ, b. Mo30W coated angular HfN, c. Mo30W coated spherical HfN, d. ZrC coated YSZ, e. ZrC coated angular HfN, f. ZrC coated spherical HfN

While this process worked well for the spherical YSZ and angular HfN, it did not work well for the spherical HfN. As seen in Figure 4.29, the ZrC only partially coated each particle or did not coat at all. This is likely due to the smaller surface area and smoother surface of the spherical HfN particle compared with the spherical YSZ and the angular HfN particles. An updated coating approach was created to better coat the spherical HfN particle. Two changes were made. First, the matrix powder was added to the surrogate (in increments of 1/3 the total amount). The second change was rolling the surrogate in the matrix powder, instead of mixing using a vibration table. This resulted in a more uniform coating of the spherical HfN with the ZrC as seen in Figure 4.28 f. and with the Mo30W, as seen in Figure 4.28 c.

1. Collect the matrix material powder, particles to be coated, and the A-C® 617A Additive.

2. Collect and label two containers. One is for the matrix powder and the other is for the particles to be coated.

3. Measure out the desired matrix and surrogate materials and place into two separate containers.

4. Add 1.0 wt% of A-C® 617-A to the container with the matrix material.

5. Add 1.5 wt% of A-C® 617-A to the container with the surrogate material.

6. Mix both containers by swirling them (with the lids tightly closed) around (rolling motion) for at least 60 seconds. Use the vibration table on 9 for another 10 seconds.

7. Loosen the lids and place the containers in the oven at 85°C. Leave them in the oven for 20 minutes.

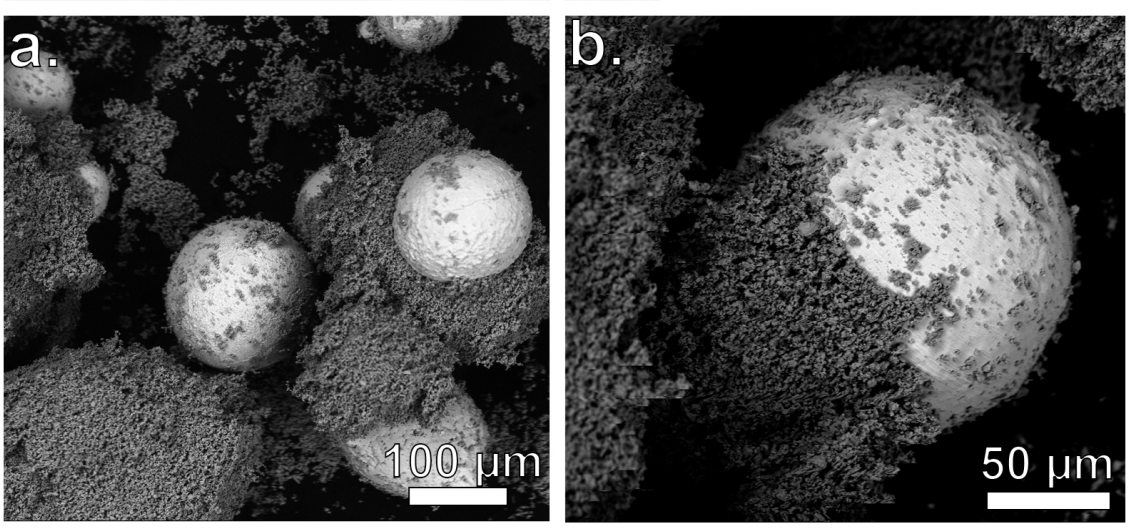


Figure 4.29: Attempted coating of spherical HfN particles with the ZrC powder.

8. While still hot remove the two containers. Take the container with the surrogate particles and pour 1/3 of the contents of the spherical HfN powder into jar with the matrix powder. Roll the material for several tens of seconds until an even coating starts to form.

9. Add the next 1/3 (approximately) and continue with the rolling step.

10. Add the final 1/3 and once again roll until even coating is observed.

4.1.6 Fabrication of Cermet Materials

For the Mo30W cermets with spherical YSZ and angular HfN particles, sintering conditions of 1600°C and 30 MPa with a hold time of 15 minutes were sufficient to produce materials with a high final matrix density. Volume loadings ranging from 30 to 90 vol% were also sintered.

For the Mo30W spherical YSZ and angular HfN composites, the sintering conditions of 1600°C and 30 MPa for 15 minutes were sufficient to sinter the materials to a high density ($>$ 89%). For the spherical HfN composites, increased matrix porosity ($>$ 14%) was observed under these conditions. These samples required a sintering temperature 1700°C. Table 4.8 contains the density data for the three different surrogate materials along for 50 and 70 % volume loadings. The theoretical densities were determined by measuring the powder densities of the Mo30W, YSZ, and HfN powders using gas pycnometry, then by using a role of mixtures to approximate the expected density. The density of the MoW-YSZ surrogates were above 98% theoretical for both 50 and 70vol%. The densities of the HfN cermets were generally lower and were less consistent. SEM images of the polished microstructure of the cermets, as seen in Figure 4.30, revealed a highly densified and low porosity matrix. The lack of high measured density in the samples resulted from high porosity in the starting HfN feedstock. After sintering, this porosity was still visible in the HfN particles, as seen in the SEM images in Figure 4.30. XRD spectra for 3 as sintered representative cermets is also included in Figure 4.31.

Table 4.8: Ideal, envelope, and theoretical densities for the Mo30W cermets fabricated using SPS.

Cermet material	Volume loading (%)	Ideal density (g/cm^3)	Envelope density (g/cm^3)	Theoretical density (%)
Mo30W-YSZ	50	8.952	8.78 ± 0.13	98.1
(spherical)	70	7.784	7.69 ± 0.10	98.8
Mo30W-HfN	50	12.294	10.92 ± 0.36	88.8
(angular)	70	12.463	11.42 ± 0.49	91.7
Mo30W-HfN	50	12.535	11.98 ± 0.80	95.6
(spherical)	70	12.800	10.44 ± 0.26	81.5

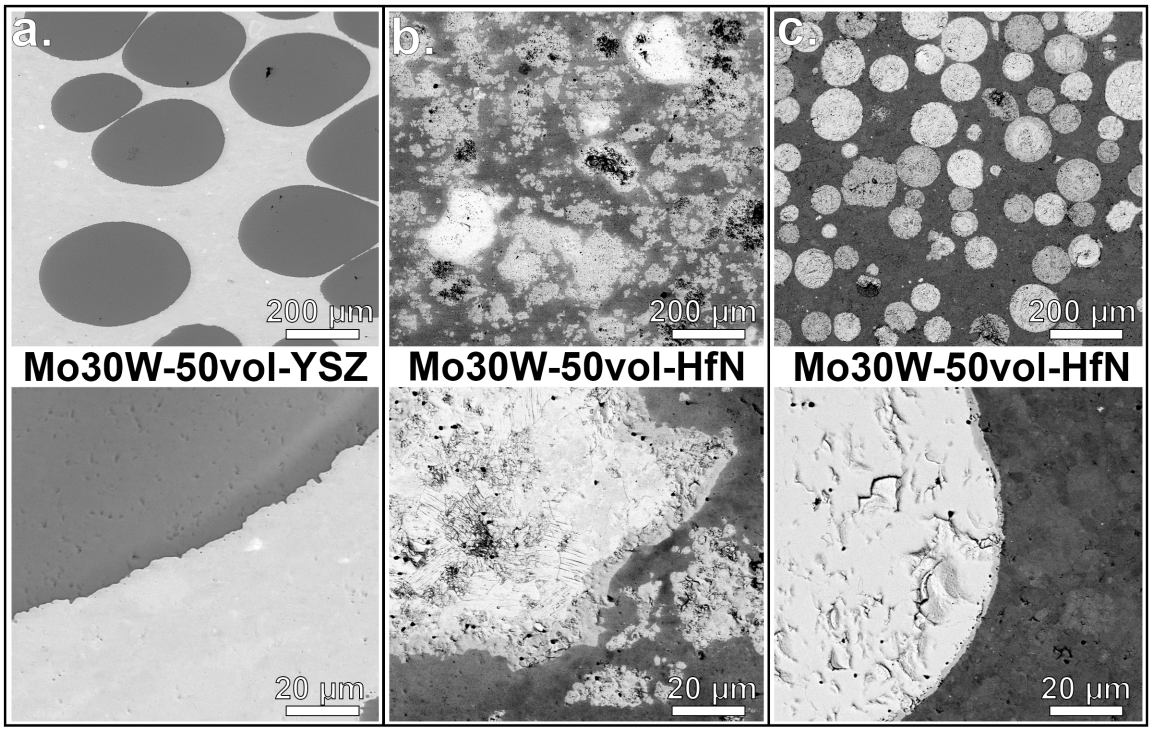


Figure 4.30: SEM micrographs of the polished cross-sections of Mo30W a. 50vol-YSZ, b. 50vol-HfN (angular), and c. 50vol-HfN (spherical).

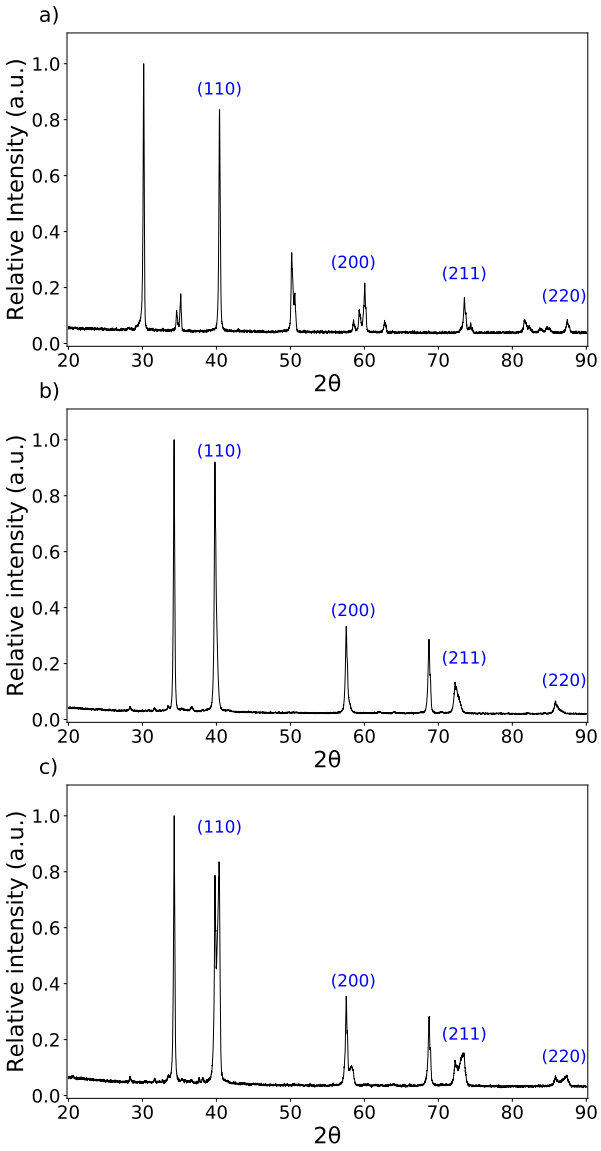


Figure 4.31: XRD spectra for a) Mo30W-70vol-YSZ, b) Mo30W-70vol-HfN-angular, and Mo30W-70vol-HfN-spherical. Mo30W crystal planes are labeled in blue.

The cermet samples with YSZ particles had excellent bonding with the Mo30W after sintering. Both Figure 4.30 a. and Figure 4.32 show excellent bonding at this interface. Only a small amount of increased porosity was observed as well. EDS maps of the cermet material are also included in Figure 4.32. While the particle and matrix had an excellent interface resulting from diffusion bonding, there is no preferential diffusion of Mo or W into YSZ or no preferential diffusion of Y, Zr, or O into the MoW evident. A small area of enriched W was observed in the Mo30W matrix, but this is due to some W rich powder regions in the starting CR feedstock powder.

YSZ particle deformation in the axial direction resulted from the applied uniaxial pressure during sintering and the shrinkage of the powder. The starting aspect ratio of the YSZ particles was 1.00 ± 0.06. Using sectioned samples, the aspect ratio of the YSZ particles (defined as the radial axis divided by the axial axis) was determined to be 1.56. This shrinkage during sintering is illustrated in Figure 4.33. In spite of this significant deformation, no cracks appeared in the matrix or YSZ particles.

A range of different volume loadings from 30 to 90% were tested to see how higher volume loadings affect the sintering and final microstructure of the composites. The SEM microstructure of these are shown in Figures 4.34 and 4.35. Particle deformation was observed to increase with increased volume loadings above 70 %. There was also a slight increase in porosity at the particle matrix interface. Finally, as the volume loading increased, the particle interconnectivity separation decreased with more particles touching, as a result of there no longer being sufficient matrix to coat all the particles.

The densities as a function of volume loading are plotted in Figure 4.36. There is a slight trend of increasing theoretical density with increasing volume loading, which appears to contradict the increased observed matrix porosity. The measured density of the YSZ particles were 6.033 g/cm^3, which corresponds to 99% theoretical density. Assuming no additional sintering of the YSZ, the matrix density can be extracted by subtracting out the density contribution from the YSZ. The Mo30W matrix density is plotted in Figure 4.37. Up to 60 vol%, there is no observed change in matrix density,

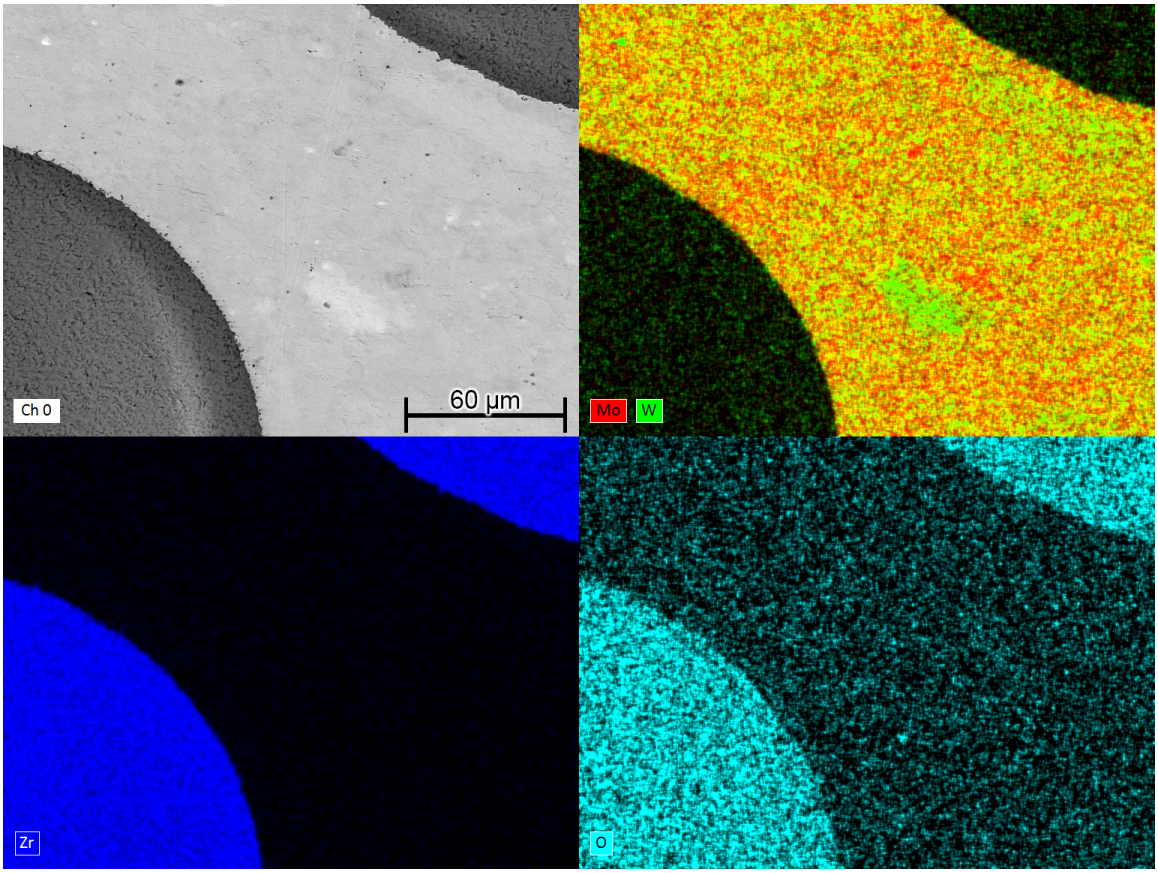


Figure 4.32: SEM image and EDS maps of a Mo30W-40vol-YSZ cermet.

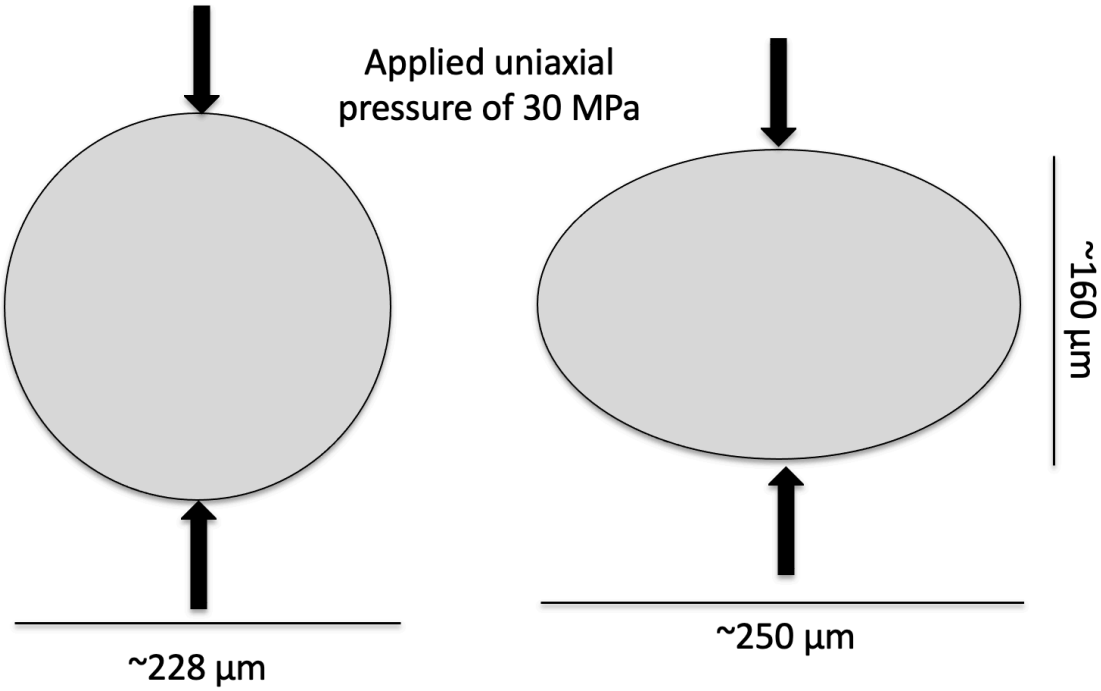


Figure 4.33: Graphic of a YSZ particle before sintering (left) and after sintering (right) illustrating the particle deformation.

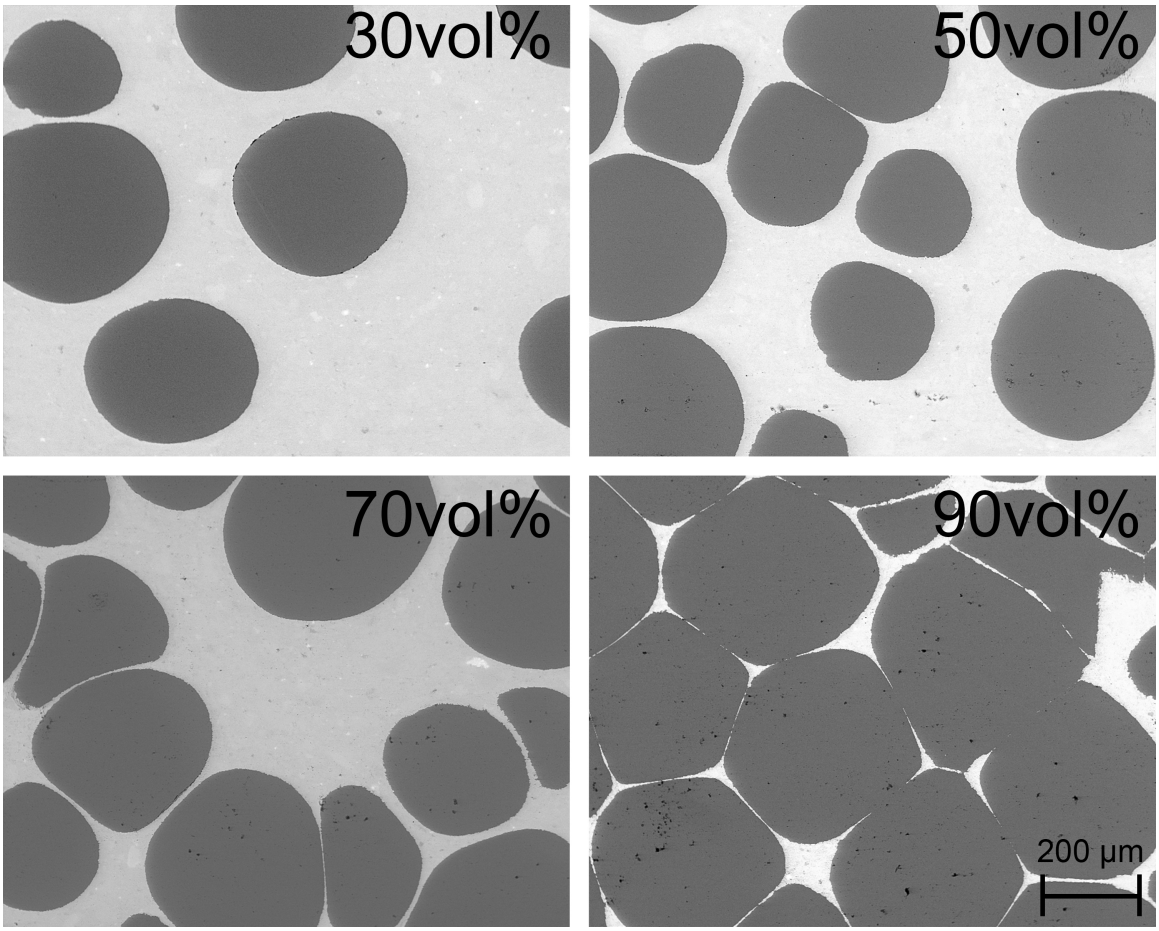


Figure 4.34: SEM images of the sintered microstructures of Mo30W-YSZ cermets at volume loadings ranging from 30 to 90 % taken at 200X magnification.

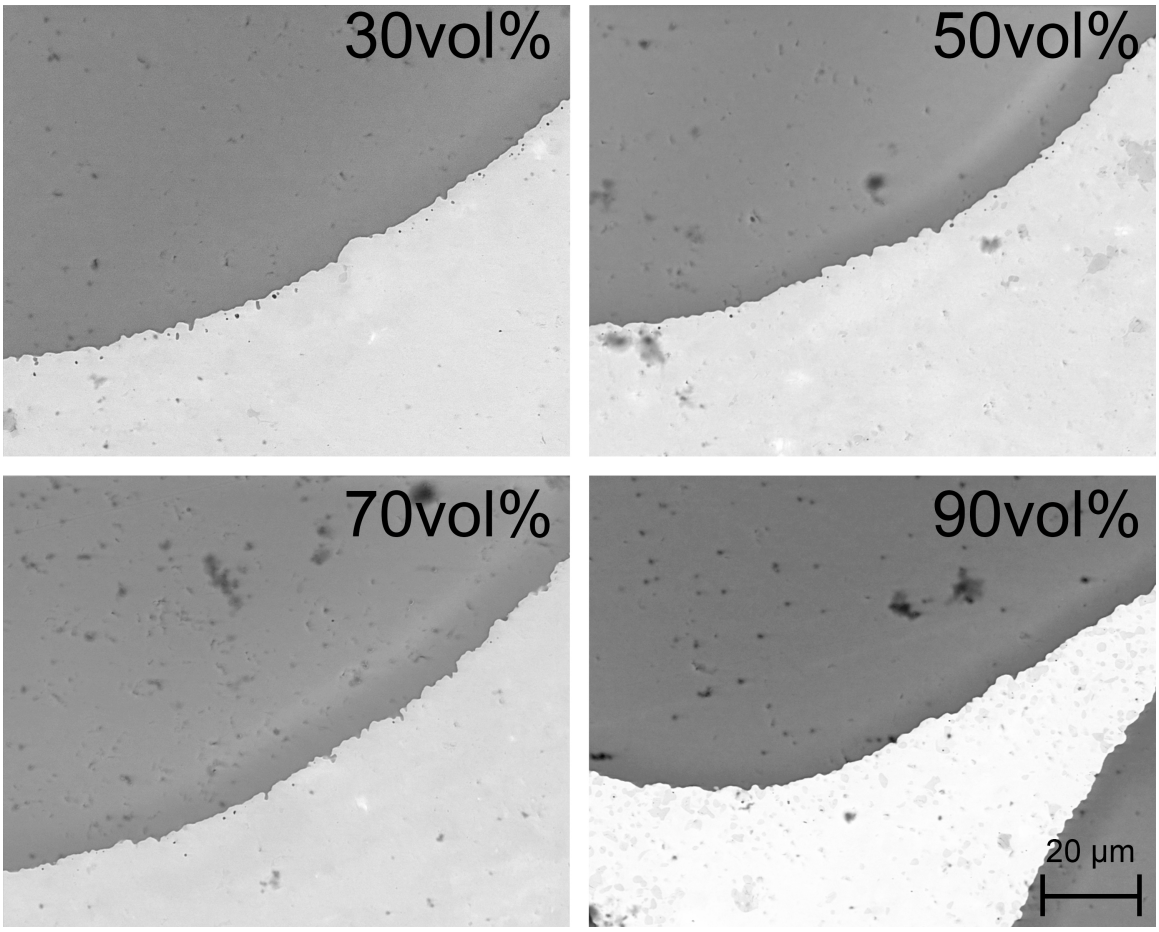


Figure 4.35: SEM images of the sintered microstructures of Mo30W-YSZ cermets at volume loadings ranging from 30 to 90 % taken at 2000X magnification.

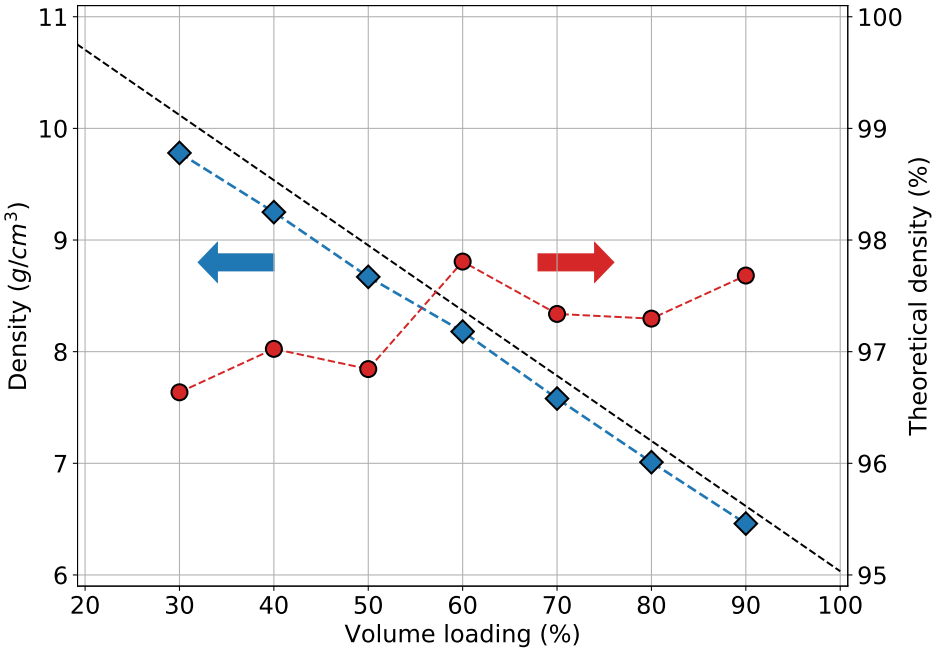


Figure 4.36: Spherical YSZ cermet density with respect to volume loading.

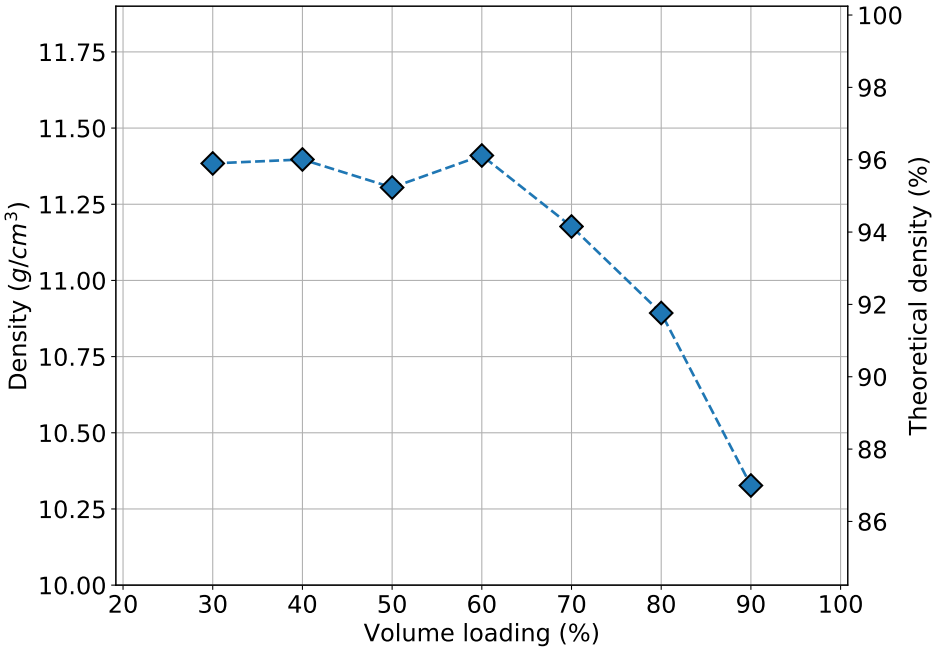


Figure 4.37: Calculated Mo30W matrix density from the spherical YSZ cermets with respect to volume loading.

however, above 70 vol%, a linear decrease in matrix density begins with increasing volume loading. The matrix density of the 90 vol% even drops below 90% TD.

The angular HfN surrogate also sintered well under the optimized conditions for the CR Mo30W. A uniform particle spacing was achieved, as seen in Figure 4.30. Additionally, an excellent particle matrix interface was achieved as seen in Figure 4.30 and 4.38. All the larger particles had an interfacial region of medium gray in between the light gray (HfN) and dark gray (Mo30W). This interfacial phase will be discussed further in Chapter 5. The EDS map shown in Figure 4.38 confirms the formation of the interfacial region. It is most apparent when looking at the Mo and Hf maps. The interfacial region was between 5 and 10 µm in length. Some areas appeared to have much larger interfacial regions, however, this was a result of polishing the particle near one of its surfaces, making the region appear much larger.

Like with the YSZ, a volume loading study was conducted for the angular HfN particle. Volume loadings from 30 to 90% were tested. The SEM microstructure of these are shown in Figures 4.39 and 4.40. Unlike with the Mo30W-YSZ cermets, as the HfN content increased, there is no increase in observable porosity in the Mo30W matrix. As HfN content increased, there appeared to be an increase in the formation of the interfacial phase. This resulted from an increased HfN surface with respect to the Mo30W matrix, allowing for more of the phase to form.

Figure 4.41 illustrates the effect of volume loading on the composite density. Unlike with the spherical YSZ cermets, there is no definitive trend in the cermet sintered density with respect to volume loading. By assuming the HfN particles did not densify during sintering, the density of the Mo30W matrix was calculated and is presented in Figure 4.42. Unlike with the YSZ, this assumption may not be as valid. Since the HfN was more porous to begin with, some porosity may have closed during sintering. However, the expected change in density would be relatively small. A minor increase in matrix density was observed for a 50 and 70 vol% loading, compared to a 30 vol% loading of the angular HfN. When the loading is raised to 90 vol%, another drop in matrix density is observed.

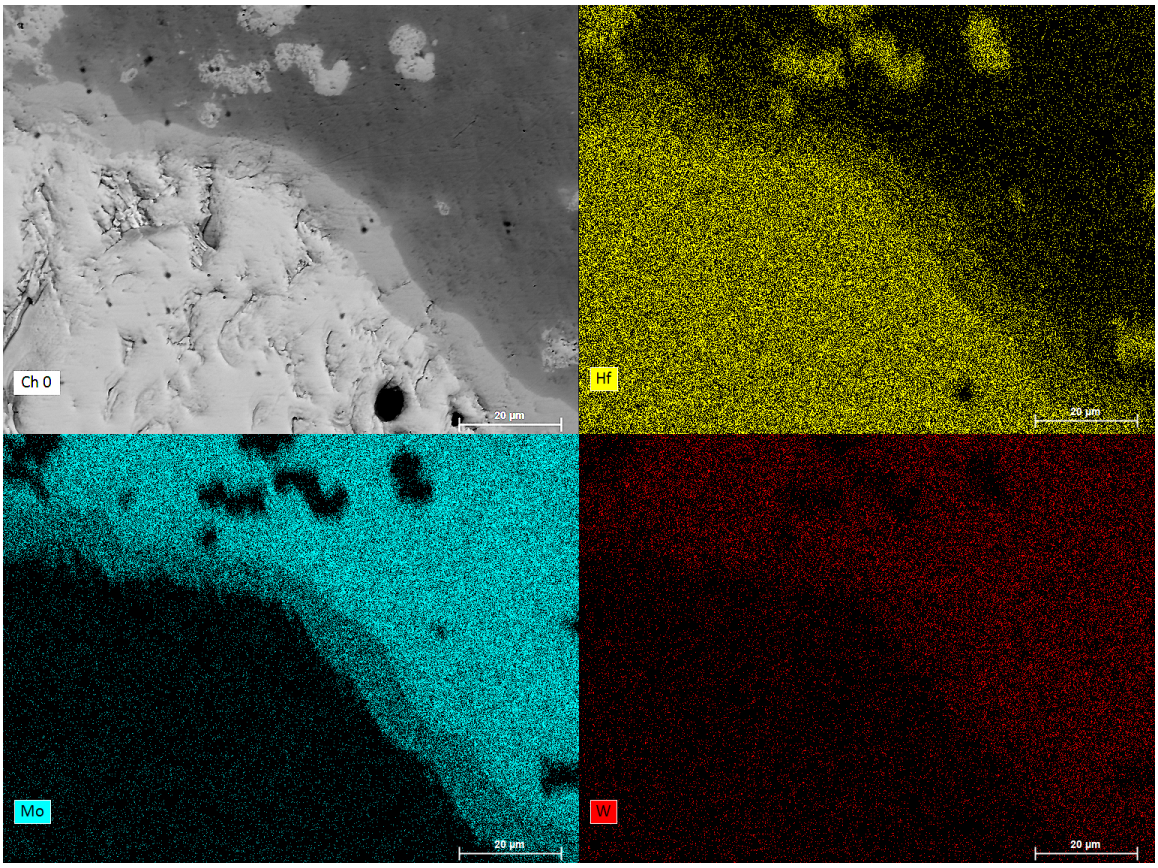


Figure 4.38: EDS map of Mo30W-50vol-HfN cermet sintered at 1600°C and 30 MPa for 15 min.

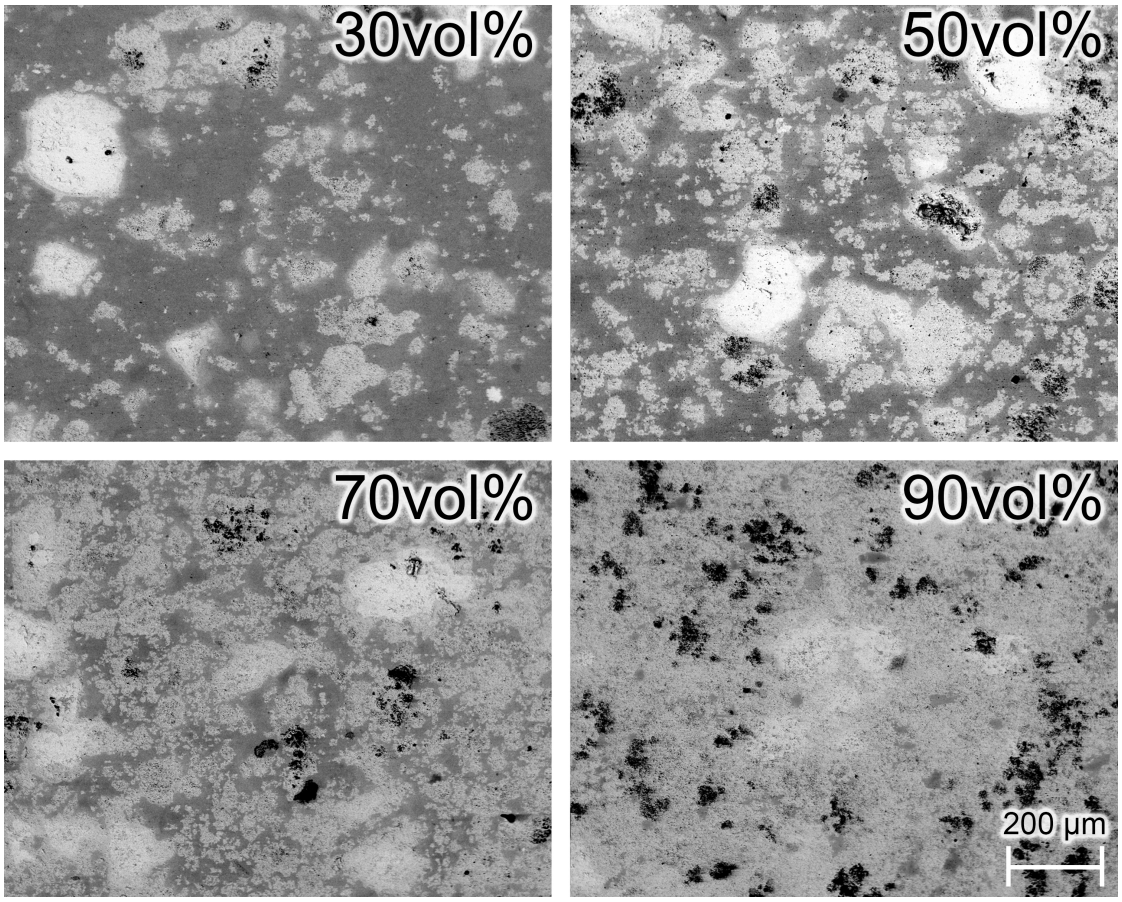


Figure 4.39: SEM images of the sintered microstructures of Mo30W-HfN cermets at volume loadings ranging from 30 to 90 % taken at 200X magnification.

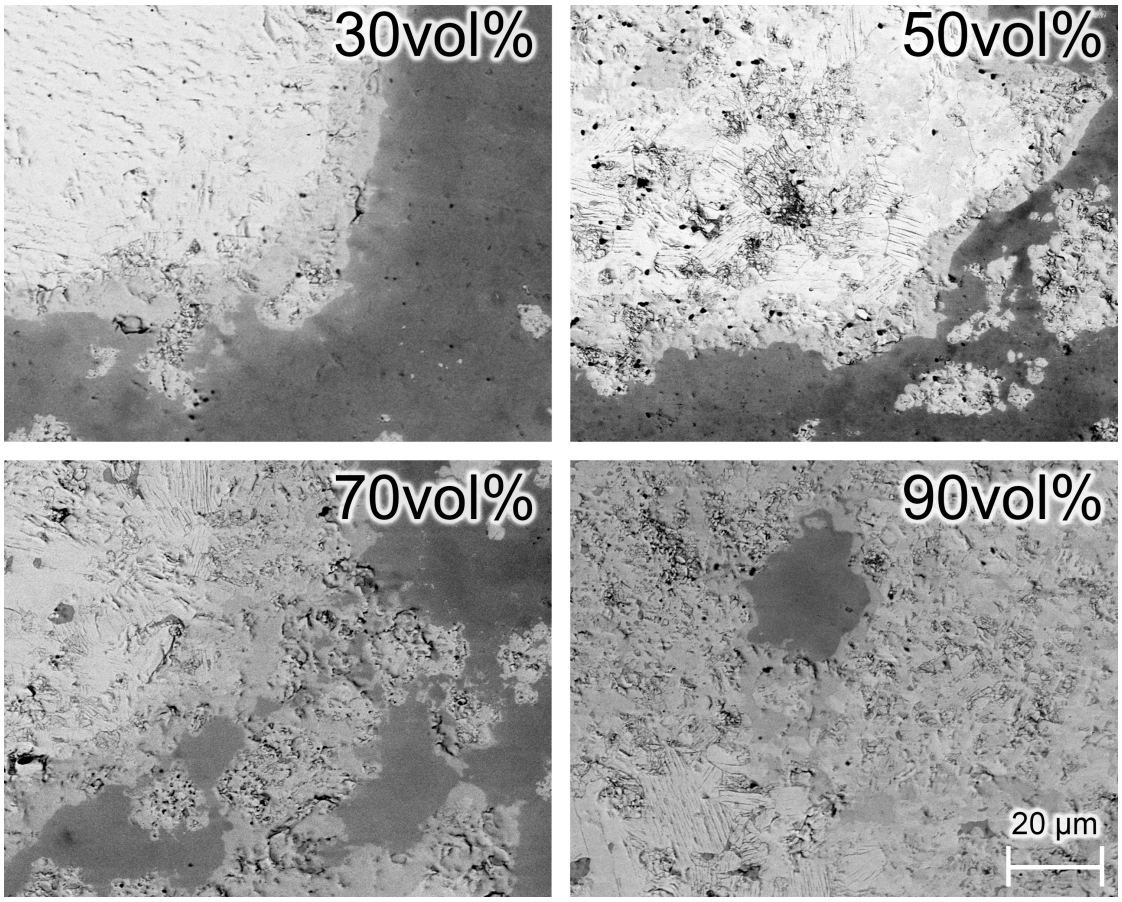


Figure 4.40: SEM images of the sintered microstructures of Mo30W-HfN cermets at volume loadings ranging from 30 to 90 % taken at 2000X magnification.

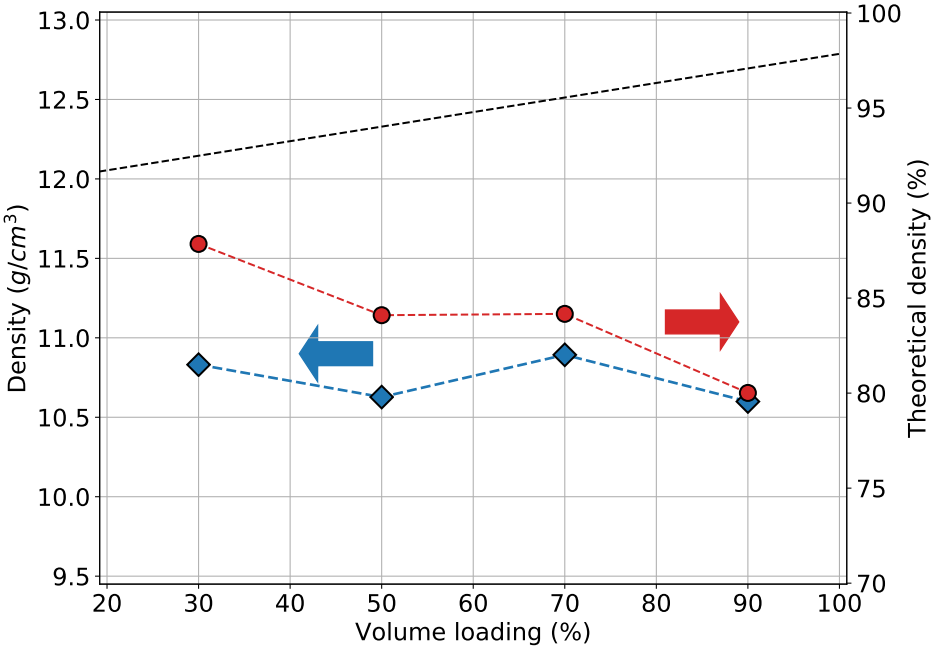


Figure 4.41: Angular HfN Cermet density with respect to volume loading.

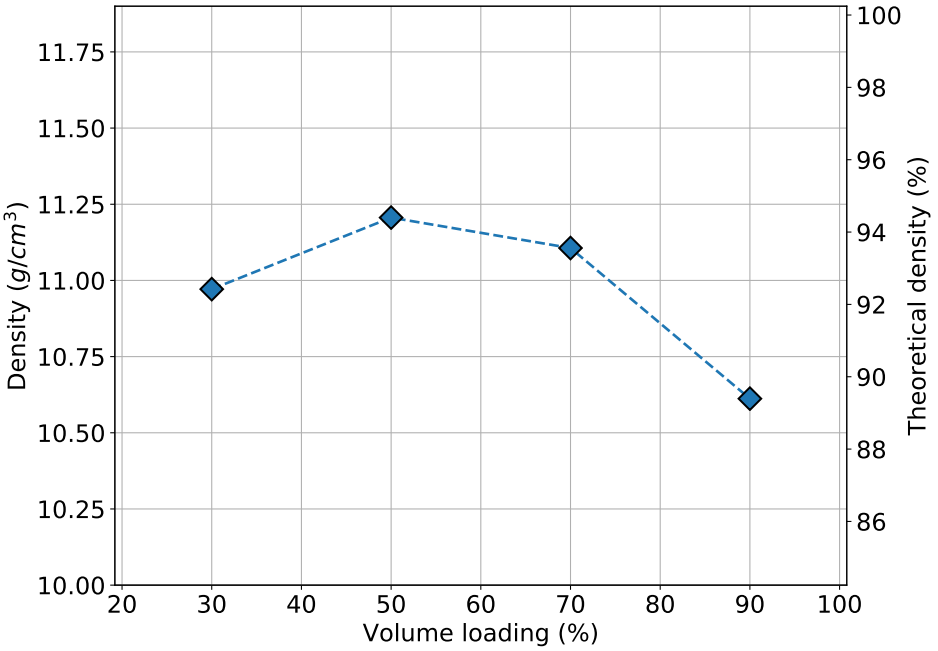


Figure 4.42: Calculated Mo30W matrix density from the angular HfN cermets with respect to volume loading.

The spherical HfN surrogate was also used with the Mo30W to produce a cermet. Sintering conditions of 1600°C and 30 MPa for 15 minutes were used. The final density of a 50 vol% cermet was 11.436, or 93.1% theoretical density. The second optimized powder coating method proved successful in evenly dispersing the spherical HfN powder, as seen in Figure 4.43. While a few particles were touching, a majority were completely encased in Mo30W. Moreover, there was excellent bonding of the particle to the matrix. Like with the angular HfN, a small interfacial region was observed in backscatter SEM images. This region was confirmed using EDS, as seen in Figure 4.44. This region was significantly smaller than the interfacial region that formed with the angular HfN material.

Because of the observed porosity in the Mo30W matrix, it was decided to raise the sintering temperature from 1600 to 1700°C. This increased the final sintered density to 12.25 g/cm^3 or 97.7% theoretical. The final optimized sintering conditions for the 3 different cermet materials are listed in Table 4.9.

4.1.7 Fabrication of Cercer Materials

While the fabrication of the cermet materials was fairly straight forward using the optimized matrix sintering conditions, the sintering of the cercer materials proved more difficult due to the more brittle ZrC matrix. Initially, a volume loading of 50 vol% with the spherical YSZ particles was used to optimize the material. Cracking in both the YSZ and the ZrC matrix was an issue at sintering temperatures above 1800 °C. When sintered above 1850°C, a loss of oxygen was observed. In Figure 4.45, carbon was observed to be present at the interface and inside the cracks. Above 1850 °C, the carbothermic reaction presented in Equation 4.2 occurs.

$$ZrO_2 + 3C <=> ZrC + 3CO \tag{4.2}$$

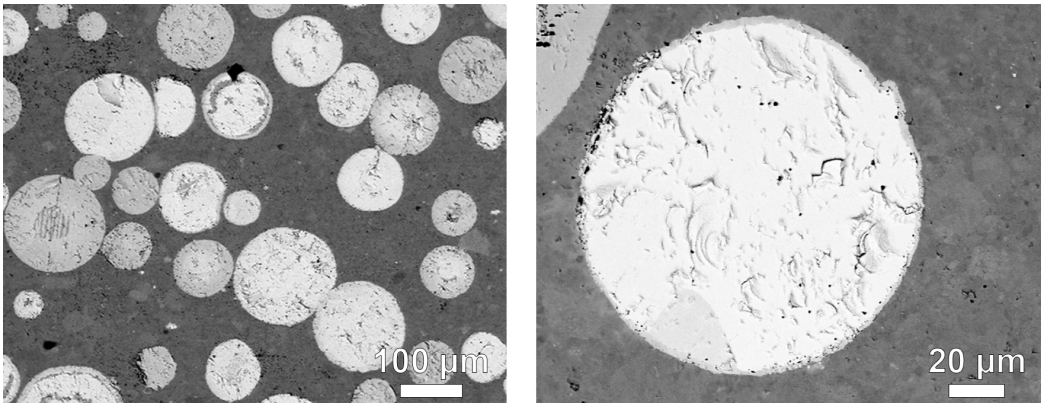


Figure 4.43: SEM images of the Mo30W-50vol-HfN (spherical cermet sintered at 1600°C and 30 MPa for 15 minutes.

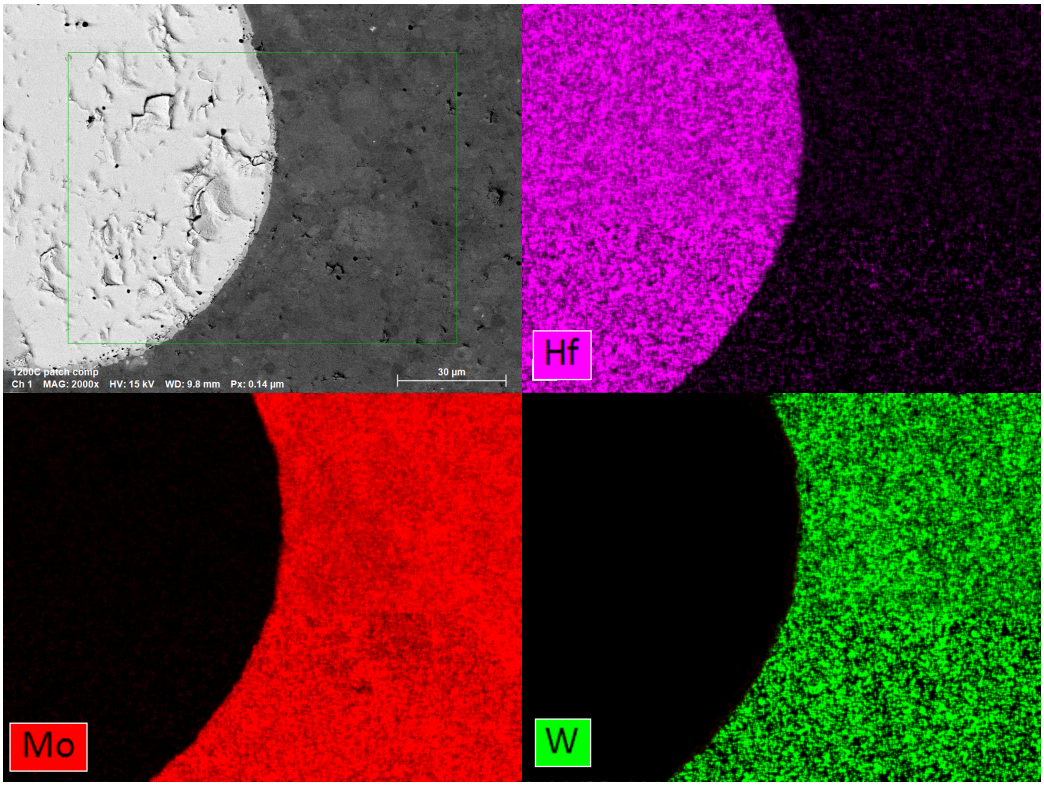


Figure 4.44: EDS map of the Mo30W-50vol-HfN (spherical cermet sintered at 1600°C and 30 MPa for 15 minutes.

Table 4.9: Determined optimum SPS sintering conditions for the Mo30W cermets.

Material	Hold Temp. (°C)	Heat rate (°C/min)	Applied press. (MPa)	Hold time (min)
YSZ (spherical)	1600	100	30	15
HfN (angular)	1600	100	30	15
HfN (spherical)	1600	100	30	15

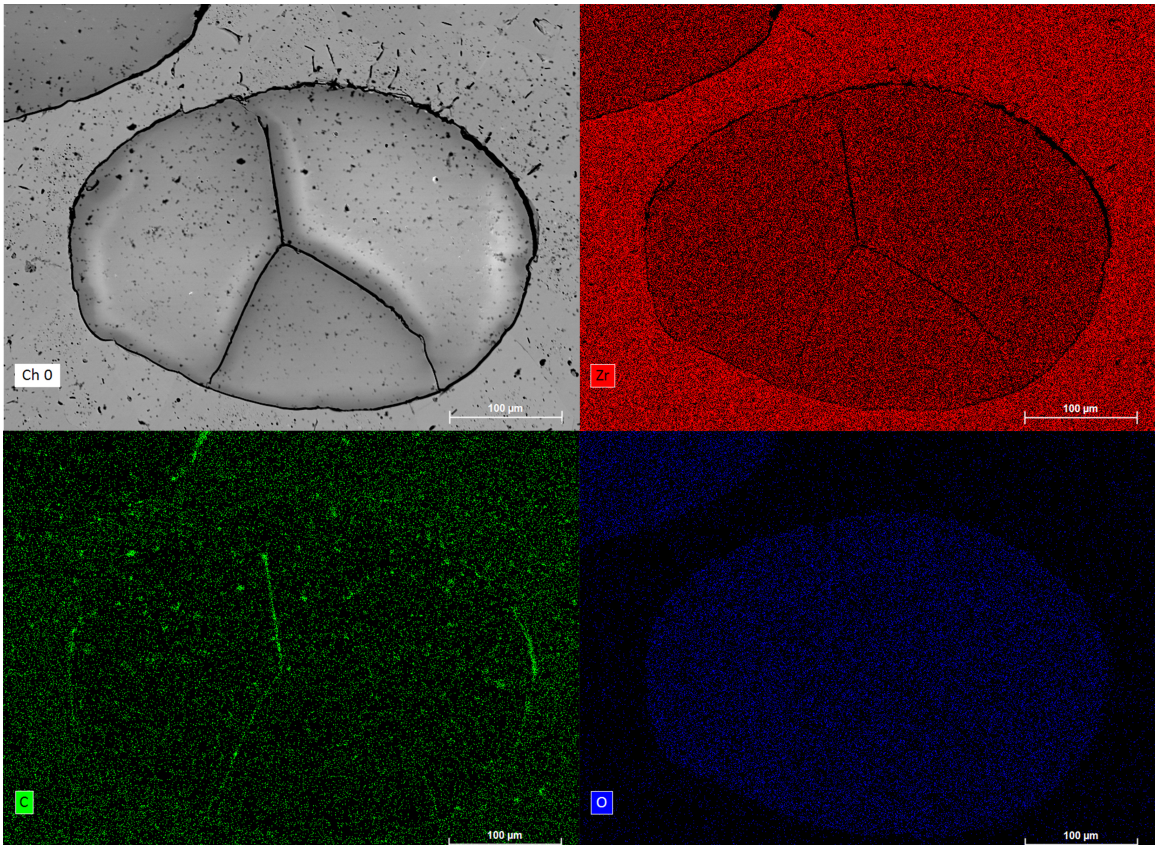


Figure 4.45: SEM image and EDS map of the polished cross-sections for ZrC-50vol-YSZ sintered at 1900°C and 30 MPa for 10 minutes. The loss of oxygen is not apparent, but carburization can be seen at the interface and the cracks.

A similar reaction occurs with the yttria. Free carbon is available in the matrix, and readily diffuses to the YSZ where this reaction occurs. The increased formation of carbide along with the release of CO exacerbates the cracking problem.

It was found that lower the sintering temperature to 1800°C was sufficient to eliminate the carburization of the YSZ. Still, sintering at 1800°C and 30 MPa for 20 minutes produced a material where nearly all YSZ particles were cracked at their grain boundaries, as seen in Figure 4.46 b). Additionally, matrix cracking was also observed in the ZrC. This cracking is attributed to the CTE mismatch between the two materials. During cooling, the ZrC matrix contracts, which increases tensile stress on the YSZ particles, causing the YSZ to crack. This was not an issue in the Mo30W, since it was more ductile and the Mo30W-YSZ composites were sintered at the lower temperature of 1600°C. Attempts to sinter below 1800°C resulted in a highly porous ZrC microstructure. Instead, After the 20-minute hold at 1800°C, the sample was cooled at a much slower rate by slowly backing off the current. The cooling rate was set to 33°C per minute. As seen in Figure 4.46 c), this was sufficient to eliminate most of the cracking in the ZrC matrix while also significantly reducing the cracking in the YSZ.

The final microstructure of the ZrC-HfN cercers depended heavily on the sintering temperature. When sintered at 1800°C and 30 MPa for 20 minutes, a distinctly two phase material formed, as seen in Figure 4.47. The HfN particles remained well dispersed throughout the ZrC matrix. The final density was measured at 9.34 g/cm^3, which is 93% theoretical density. The ZrC matrix had a relatively high porosity, at around 10 %.

The sintering temperature was increased to 2000°C, in order to try and improve the ZrC matrix density. However, the resulting microstructure revealed the formation of a new phase. This new phase occupied roughly 60 vol% of the sintered material, as seen in Figure 4.48. XRD analysis was also conducted on the sintered sample. As seen in Figure 4.49, the spectra contained peaks for ZrC and HfN, however, it was dominated with the Zr,Hf-C,N carbonitride. For this study, the two phase material

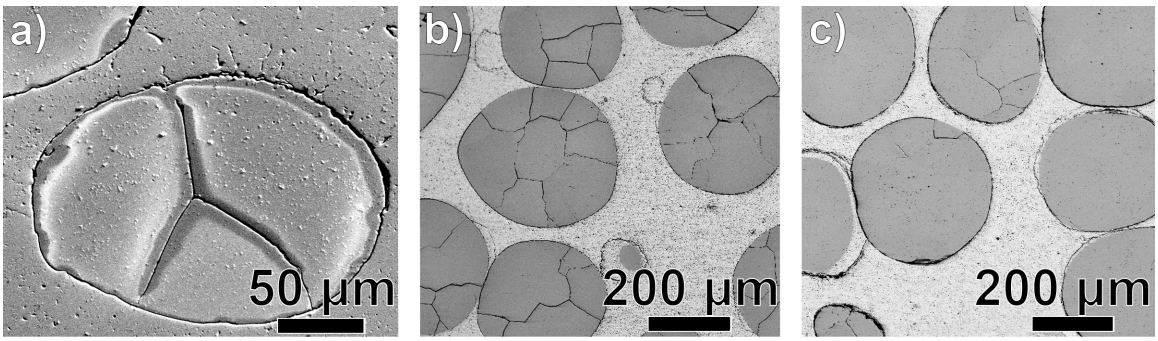


Figure 4.46: SEM images of the polished cross-sections for ZrC-50vol-YSZ sintered at a) 1900°C and 30 MPa for 10 minutes, b) 1800°C and 30 MPa for 20 minutes, and c) 1800°C and 30 MPa but with a slowed cooling rate of -33°C per minute.

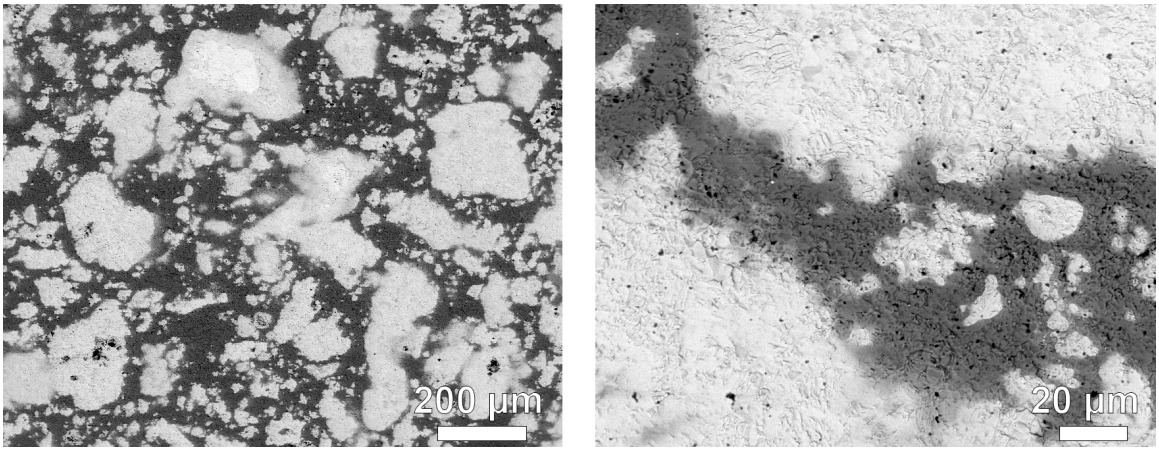


Figure 4.47: SEM images of the polished cross-sections for ZrC-50vol-HfN sintered at 1800°C and 30 MPa for 20 minutes.

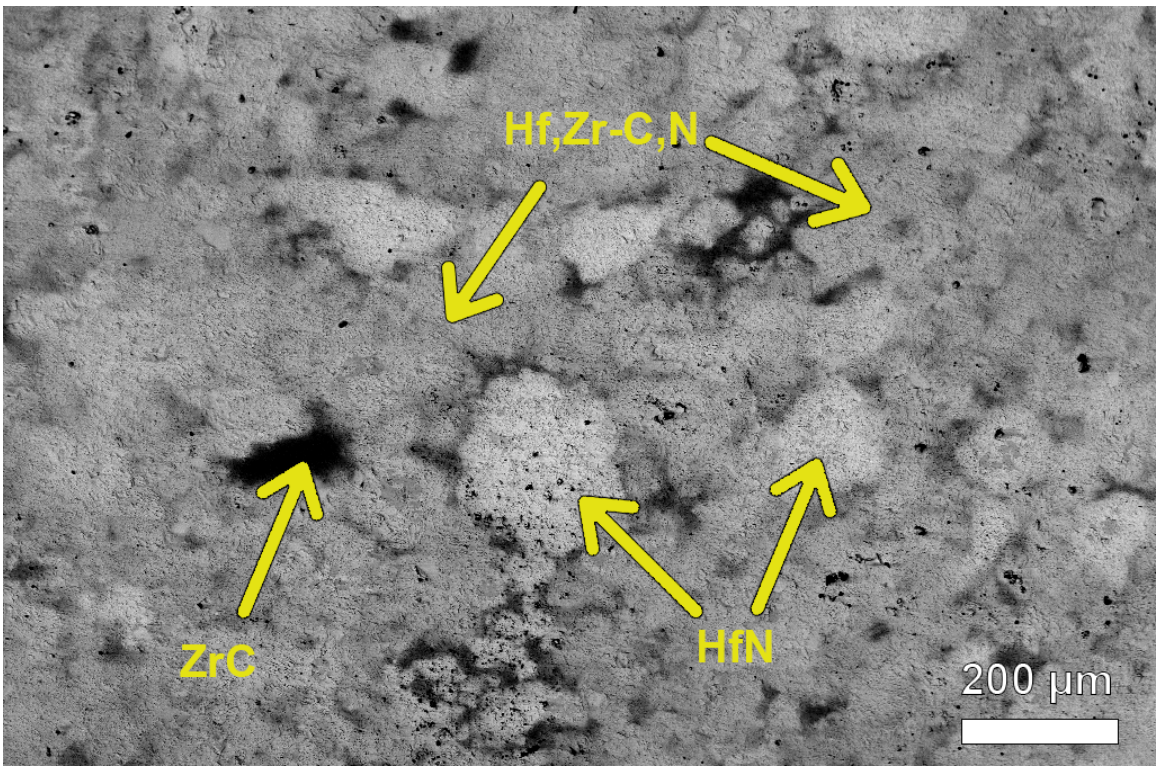


Figure 4.48: SEM images of the polished cross-sections for ZrC-70vol-HfN sintered at 2000°C and 30 MPa for 20 minutes. Three phases are visible, ZrC (darkest), HfN (lightest), and a Hf,Zr-C,N (medium tone).

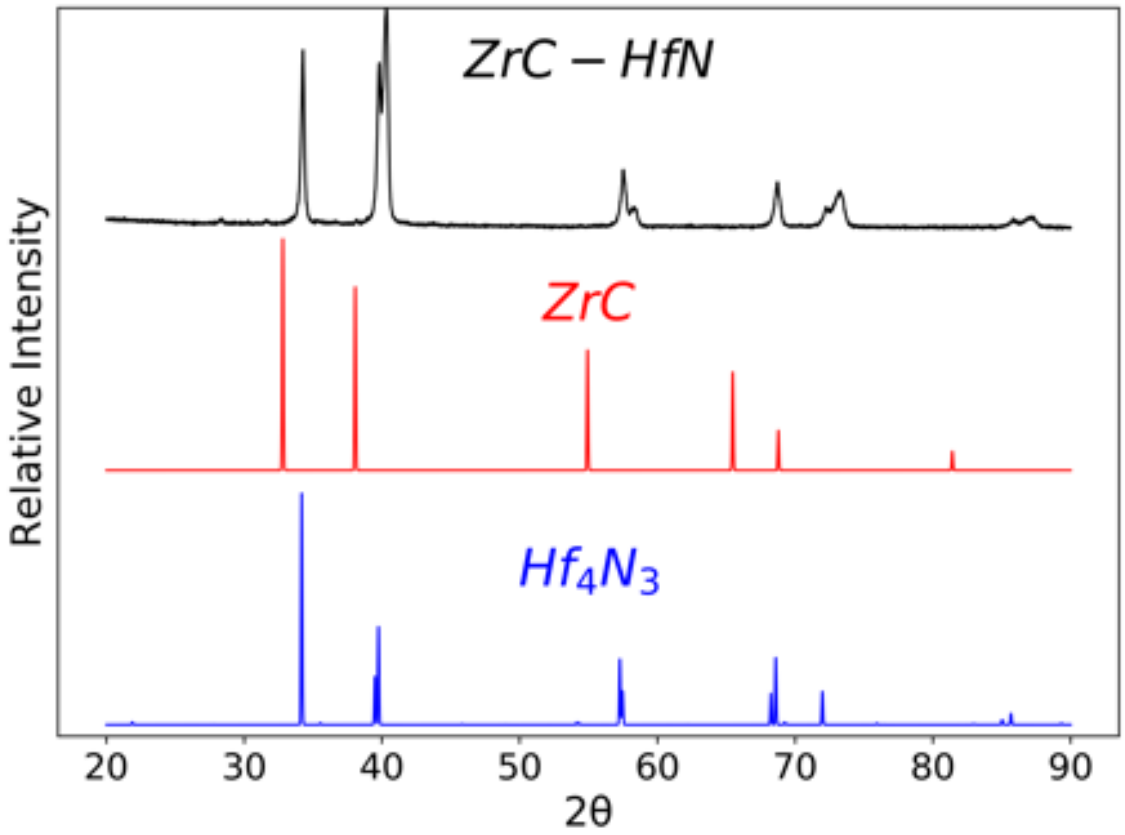


Figure 4.49: XRD spectra for the as sintered Zr,Hf-C,N carbonitride (black), ZrC (red), and HfN (blue).

was of greater interest, so the final selected sintering conditions were that of the two phase material sintered at 1800°C.

As discussed previously, using the first powder coating method, the ZrC matrix powder failed to fully coat the spherical HfN particles. When sintered, this led to significant clumping of the HfN particles and large areas that were particle free. The improved coating technique resulted in much better coating of the HfN particles with the ZrC. When sintered using SPS, the HfN particles were more evenly dispersed in the matrix, as seen in Figure 4.50. The samples were sintered at 1850°C and 30 MPa for 10 minutes. They reached a final density of 7.475 g/cm^3, which corresponds to 93% theoretical density. Like with the angular HfN, the ZrC matrix remained slightly porous, though it remained well consolidated. The particle matrix interface seen in the higher magnification SEM image in Figure 4.50 was excellent. More importantly, there was not cracking observed in either the matrix or the particles.

Once again, the goal was to produce a 2 phase material, so the sintering temperature was limited to 1850°C. EDS mapping, as seen in Figure 4.51, did not reveal any significant diffusion of Hf into the ZrC matrix.

For the thermophysical and mechanical properties testing, two volume loadings were selected (10 and 20 vol%). 40 mm diameter samples were sintered. Table 4.10 lists the different cercer materials and includes their final relative densities. All samples achieved a final density of greater than 92 % theoretical. Additionally, XRD spectra were taken for 3 representative samples, namely ZrC-20vol-YSZ, ZrC-20vol-HfN-Angular, and ZrC-20vol-HfN-Spherical, as presented in Figure 4.52.

4.2 Thermophysical Properties

Grain size analysis was conducted on a selection of the five machined pure matrix materials. The results of these are presented in Table 4.11.

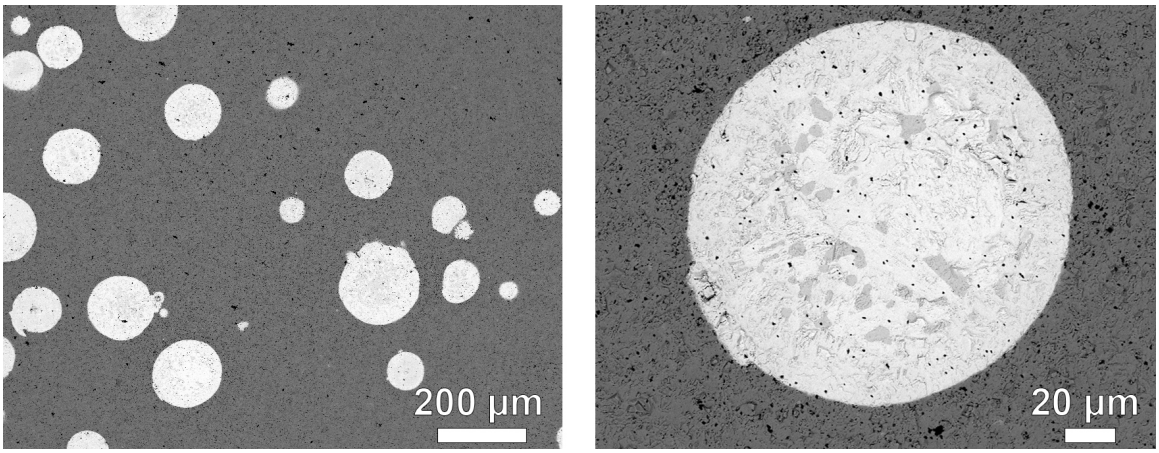


Figure 4.50: SEM images of the polished cross-sections for ZrC-20vol-HfN sintered at 1850°C and 30 MPa for 10 minutes taken at two different magnifications.

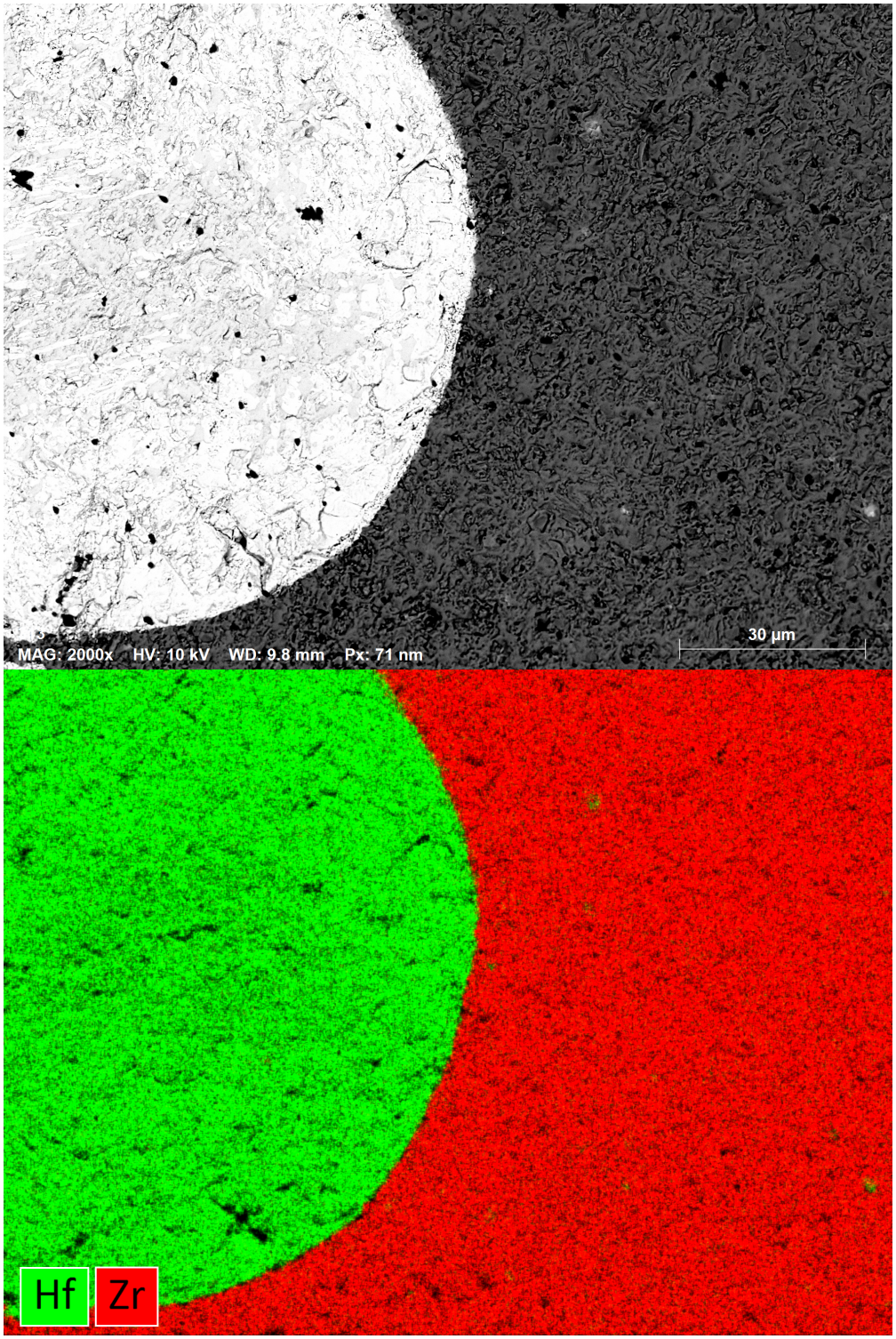


Figure 4.51: EDS map of the ZrC-20vol-HfN sintered at 1850°C and 30 MPa for 10 minutes .

Table 4.10: Ideal, envelope, and theoretical densities for the ZrC cercers fabricated using SPS.

Material	Volume loading (%)	Ideal density (g/cm^3)	Envelope density (g/cm^3)	Theoretical density (%)
ZrC-YSZ	10	6.795	6.497 ± 0.01	97
(spherical)	20	6.710	6.569 ± 0.13	98
ZrC-HfN	10	7.464	7.231 ± 0.04	97
(angular)	20	8.047	7.702 ± 0.37	96
ZrC-HfN	10	7.512	7.231 ± 0.04	96
(spherical)	20	8.144	7.502 ± 0.25	92
ZrC-WC	10	6.710	6.440 ± 0.10	96
(spherical)	20	8.911	8.309 ± 0.01	93

Table 4.11: Grain size and sample nomenclature for the pure matrix Mo30W and ZrC test samples. The grain size presented for the cermet and cercer materials is the matrix grain size.

Material Label (µm)	Grain size (µm)	Standard Deviation
Mo30W-Sm-GS	1.70	0.56
Mo30W-Md-GS	12.42	4.04
Mo30W-Lg-GS	34.9	9.24
ZrC-Small-GS	2.24	0.90
ZrC-Med-GS	9.49	5.70

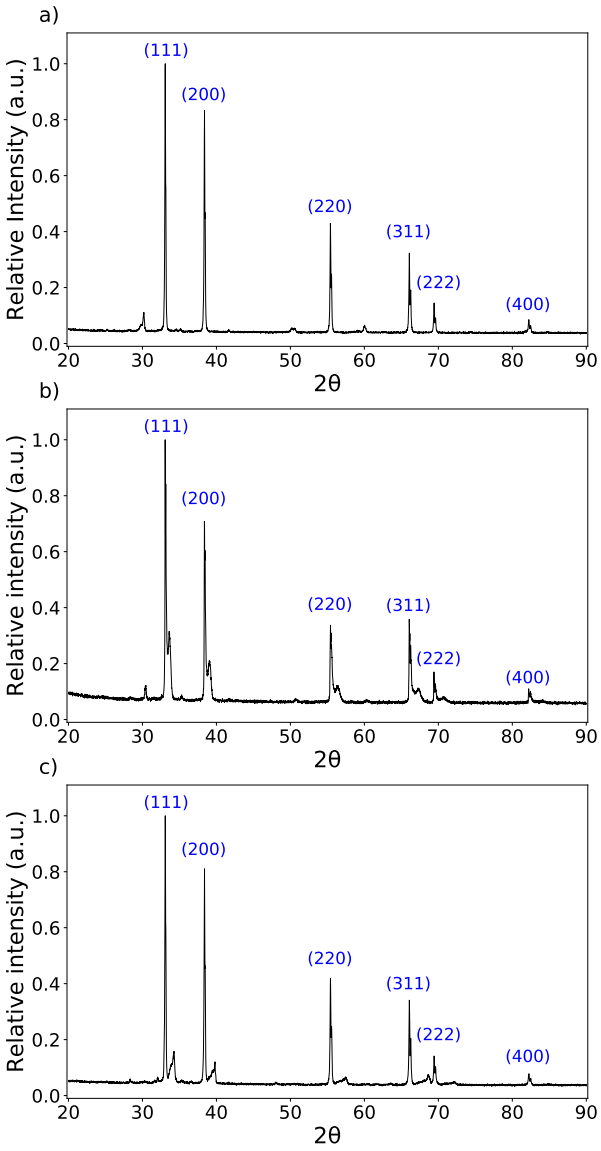


Figure 4.52: XRD spectra for a) ZrC-20vol-YSZ, b) ZrC-20vol-HfN-Angular, and c) ZrC-20vol-HfN-Spherical. ZrC crystal planes are labeled in blue.

4.2.1 Coefficient of Thermal Expansion

CTE was determined using both high temperature XRD and traditional push-rod dilatometry. XRD was only conducted on the pure matrix materials, namely, Mo30W and ZrC. The XRD spectra for Mo30W up to 1200°C are shown in Figure 4.53. Peak intensity increases with temperature and the peaks narrow. A modified Rietveld refinement was used to determine the lattice parameter for every spectrum. As seen in Figure 4.54, there was an issue with the first test. Microstrain resulting from the polishing procedure was determined to be causing issues with results. A second run was conducted where the sample was first heated to 1200°C for 30 min, then cooled prior to obtaining the spectra. This annealing, also shown in Figure 4.54, step successfully removed the microstrain and allowed for CTE data to be determined. The initial test on the non-annealed sample revealed the stress relief temperature to be between 800 and 1000°C.

The $\Delta a/a_0$ data was fit to a second order polynomial then differentiated to produce the CTE line. The calculated CTE of Mo30W (extrapolated out to 1400°C is shown in Figure 4.55, compared with that of pure Mo [57] and pure W [7]. The CTE of all the metals increase with increasing temperature. Interestingly, the CTE of Mo30W is greater than that of pure Mo and pure W, so it does not follow any rule of Mixtures.

High temperature XRD was also used to determine the CTE of ZrC. A few select X-ray spectra are presented in Figure 4.56. Due to the high oxidation potential of ZrC, even with the Ar-H_2 cover gas, the surface of the sample began to oxidize at 650°C. Because of this, CTE data from HTXRD was only determined up to 600°C. The calculated CTE compared with the CTE of ZrC of different stoichiometries from other studies is presented in Figure 4.57. Similar to the Mo30W, the CTE of ZrC increases with increasing temperatures. The CTE of ZrC starts at a higher value at room temperature and also reaches a higher value at 1200°C. As discussed in Chapter 2, the stoichiometry of ZrC heavily affects its properties. This is apparent in Figure 4.57.

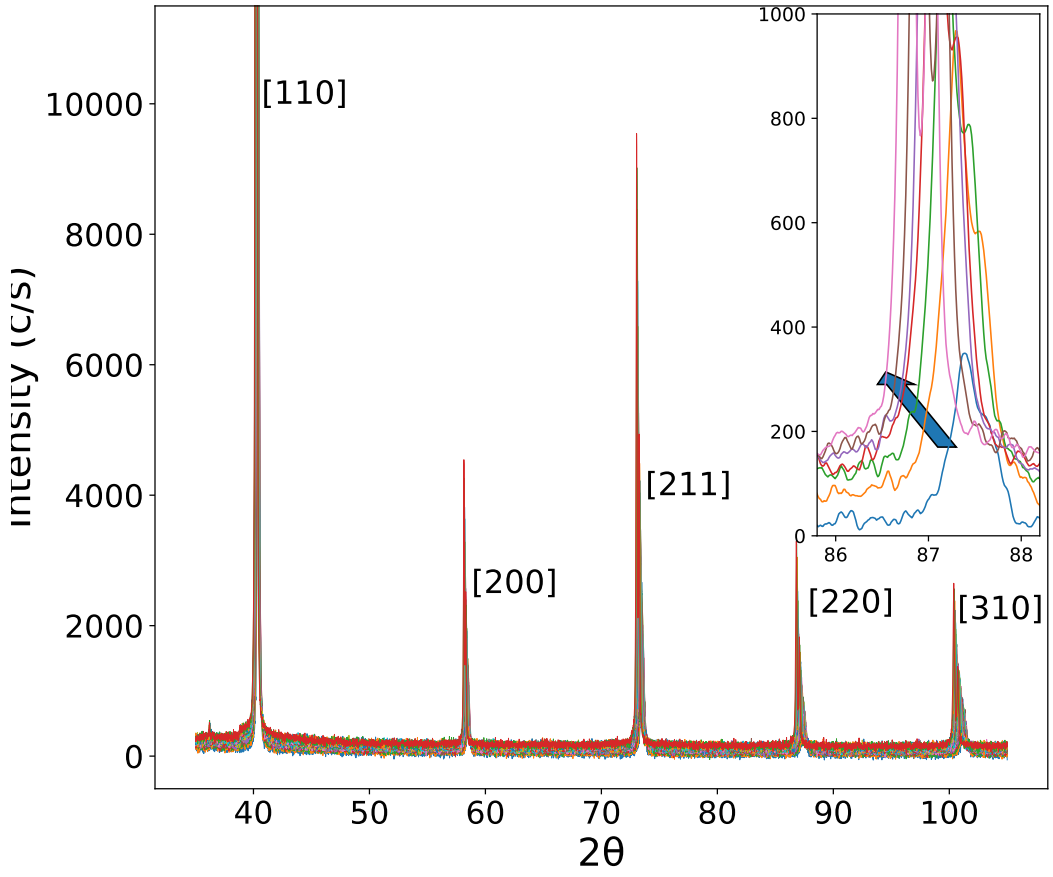


Figure 4.53: XRD spectra for Mo30W taken every 50°C up to 1200°C. An insert provides a closer look at the [220] peak. As the temperature increases, the intensity increases and the 2θ shifts decreases.

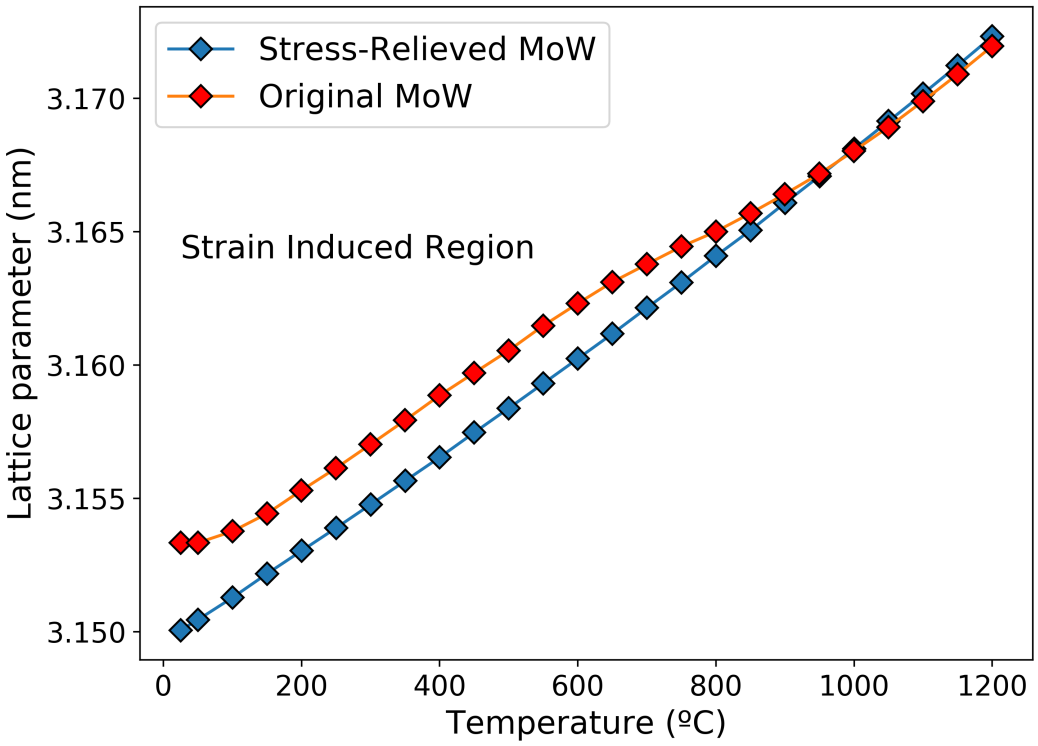


Figure 4.54: $\Delta a/a_0$ versus temperature for Mo30W for both an as polished sample and a stress-relieved sample.

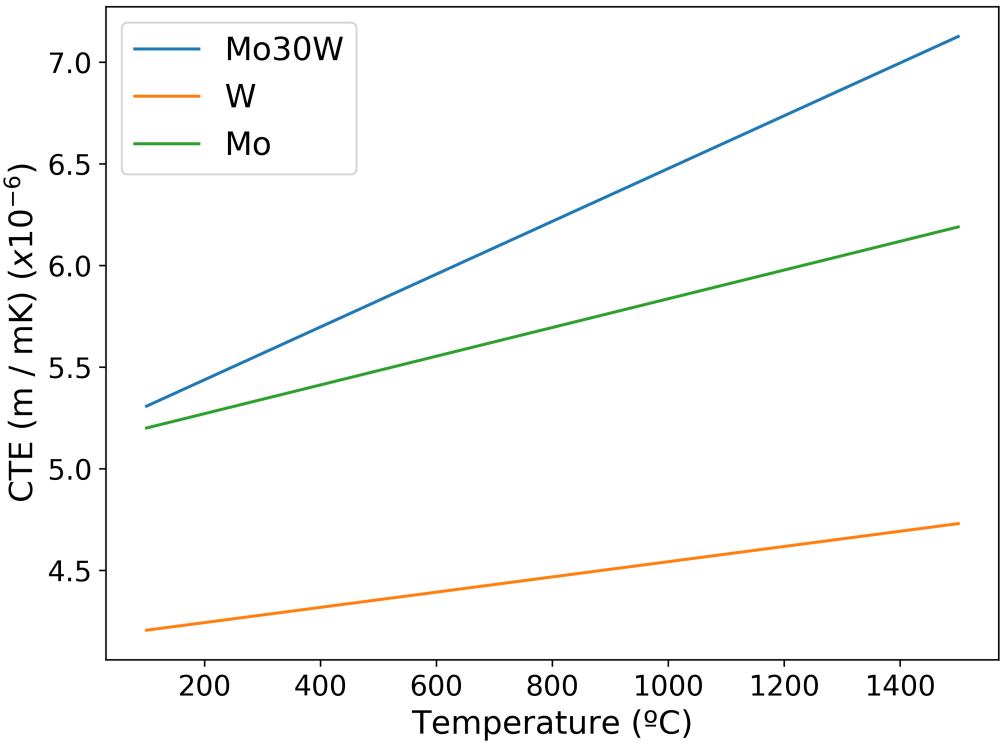


Figure 4.55: Calculated CTE of Mo30W, Mo, and W up to 1400°C.

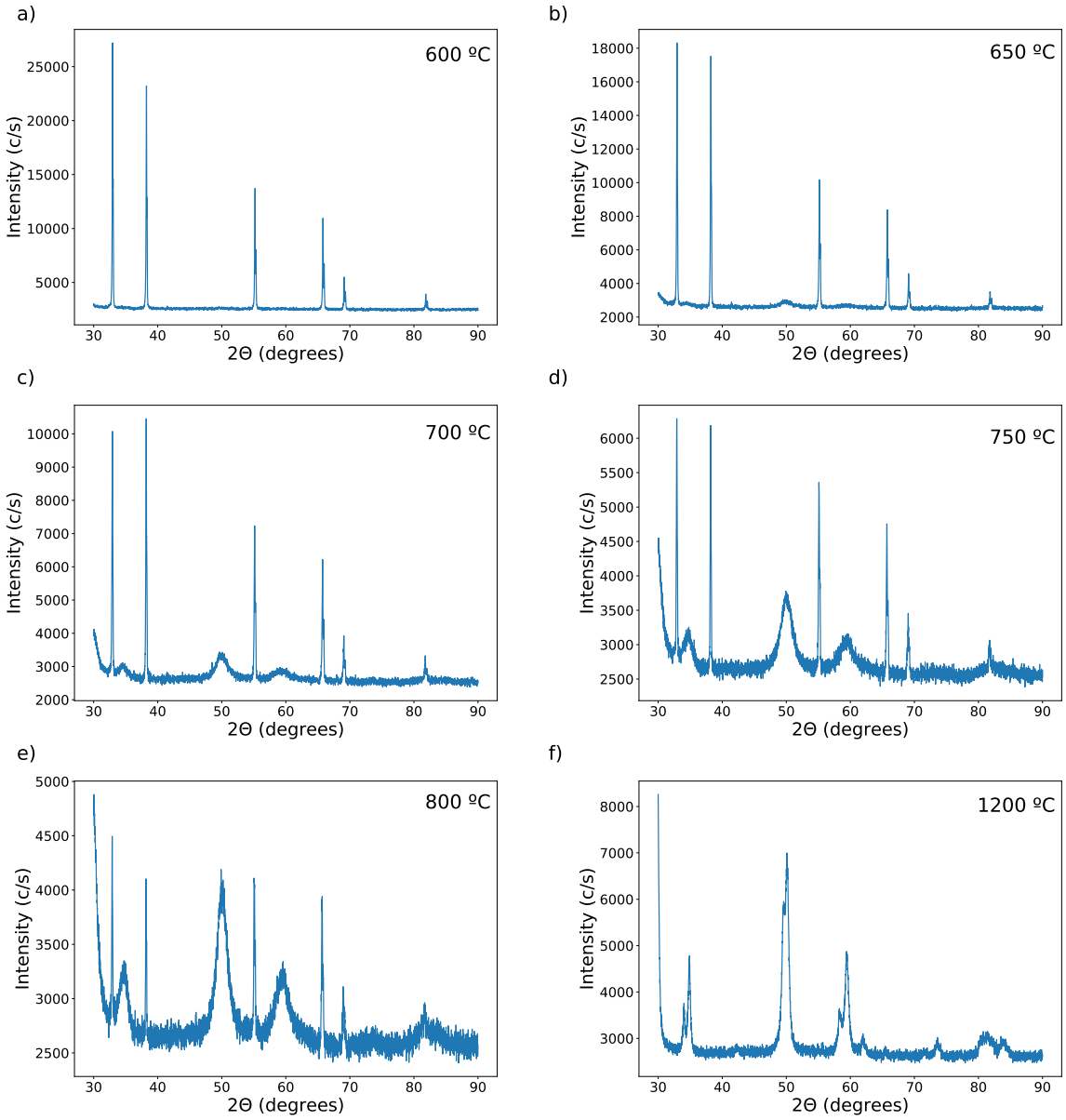


Figure 4.56: XRD spectra for ZrC taken at 600, 650, 700, 750, 800, and 1200°C.

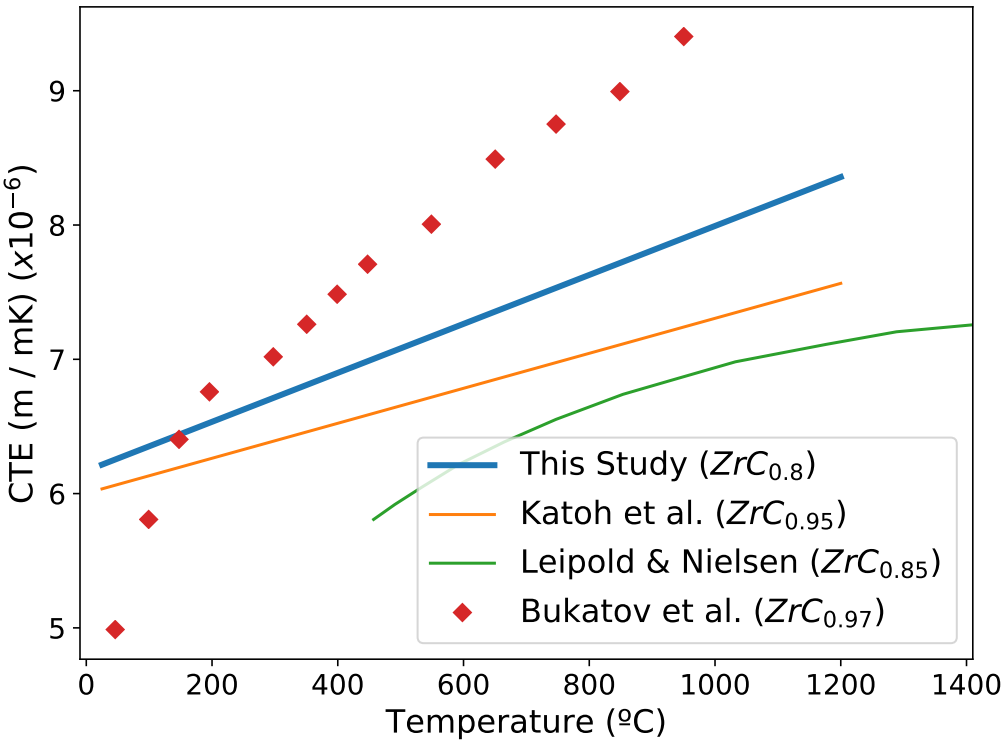


Figure 4.57: CTE of ZrC with the blue line from this study, the orange line from [74], the green line from Leipold & Nielsen, and red diamonds from Bukatov et al.

$\Delta L/L_0$ measured using dilatometry up to 700 °C is presented in Figure 4.58. The normalized expansion curves were fit to a second order equation, presented in Equation 4.3. The CTE can then be determined from the derivative of this second order equation, presented in Equation 4.4.

$$\Delta L/L_0 = A(T-25)^2 + B(T-25) + C \tag{4.3}$$

$$\alpha = 2A(T-25) + B \tag{4.4}$$

The calculated CTE data for Mo30W and its cermet composites are presented in Figure 4.59. For pure Mo30W, as the grain size decreased, the CTE increased. This is a commonly observed phenomena [202]. Moreover, the CTE for both YSZ and HfN cermet materials were higher than that of the pure Mo30W. This is due to both YSZ and HfN having a higher CTE than Mo30W over the range tested.

The calculated CTE for the ZrC and cercer is presented in Figure 4.60. As with the Mo30W, as the grain size decreases, the CTE increased. There was also good agreement with the CTE determined from HTXRD. The CTE of the ZrC-HfN cercers were less than that of pure ZrC. The CTE decreased with increasing HfN volume loading, up to 20 vol%. A summary of the calculated fitting parameters for all tested materials is preseneted in Table 4.12.

4.2.2 Specific Heat Capacity

The specific heat capacity (C_P) for the Mo30W, ZrC, HfN, Mo30W-YSZ and HfN cermets, and ZrC-HfN cercer materials were all determined using DSC. The results were all fit to Equation 2.18 in order to reduce noise and provide CP models as a function of temperature for use in calculating the thermal conductivity. The results are presented in Figure 4.61. The C_P of all the tested materials follow a second order

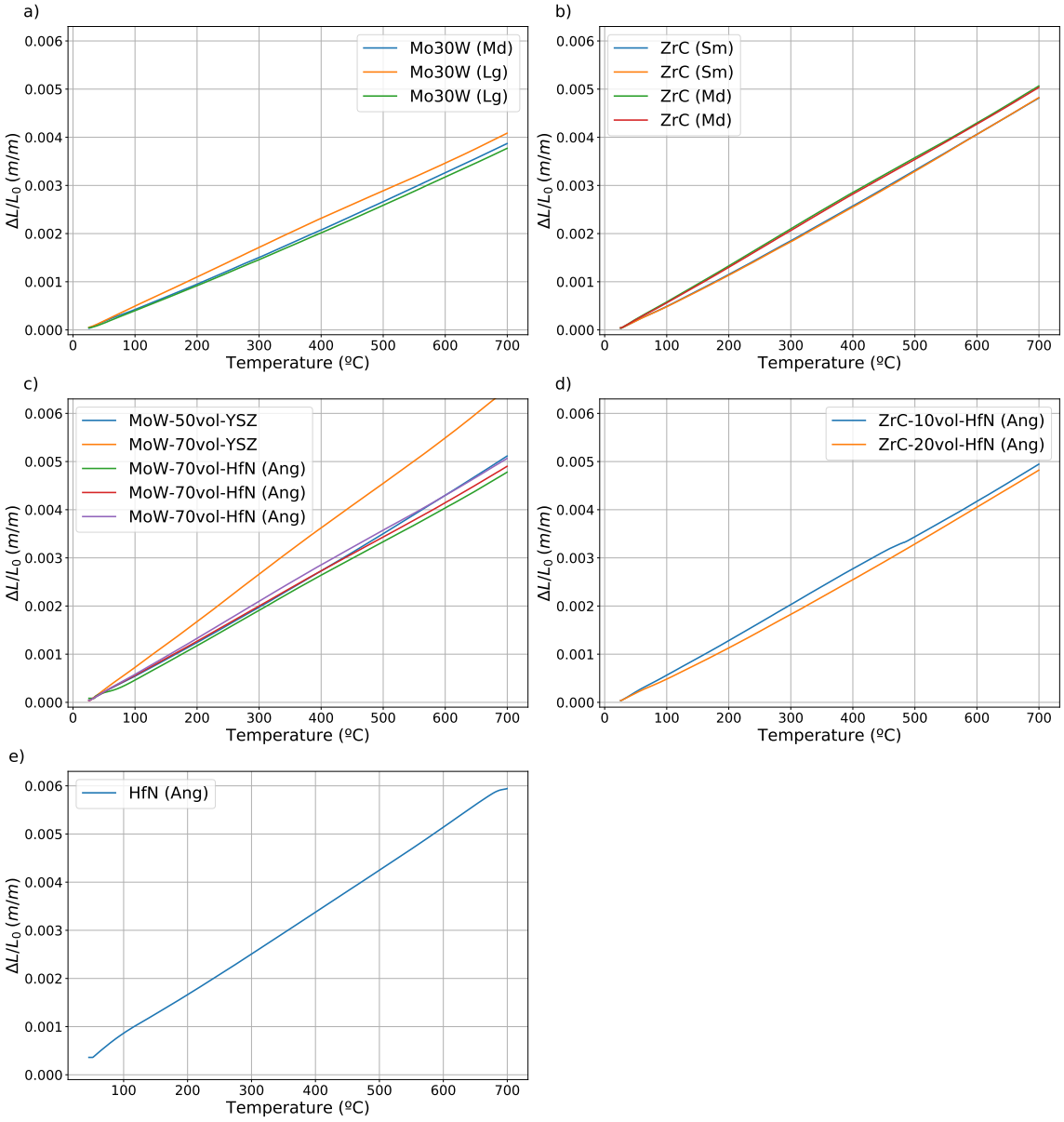


Figure 4.58: $\Delta L/L_0$ from dilatometry data for all the materials tested.

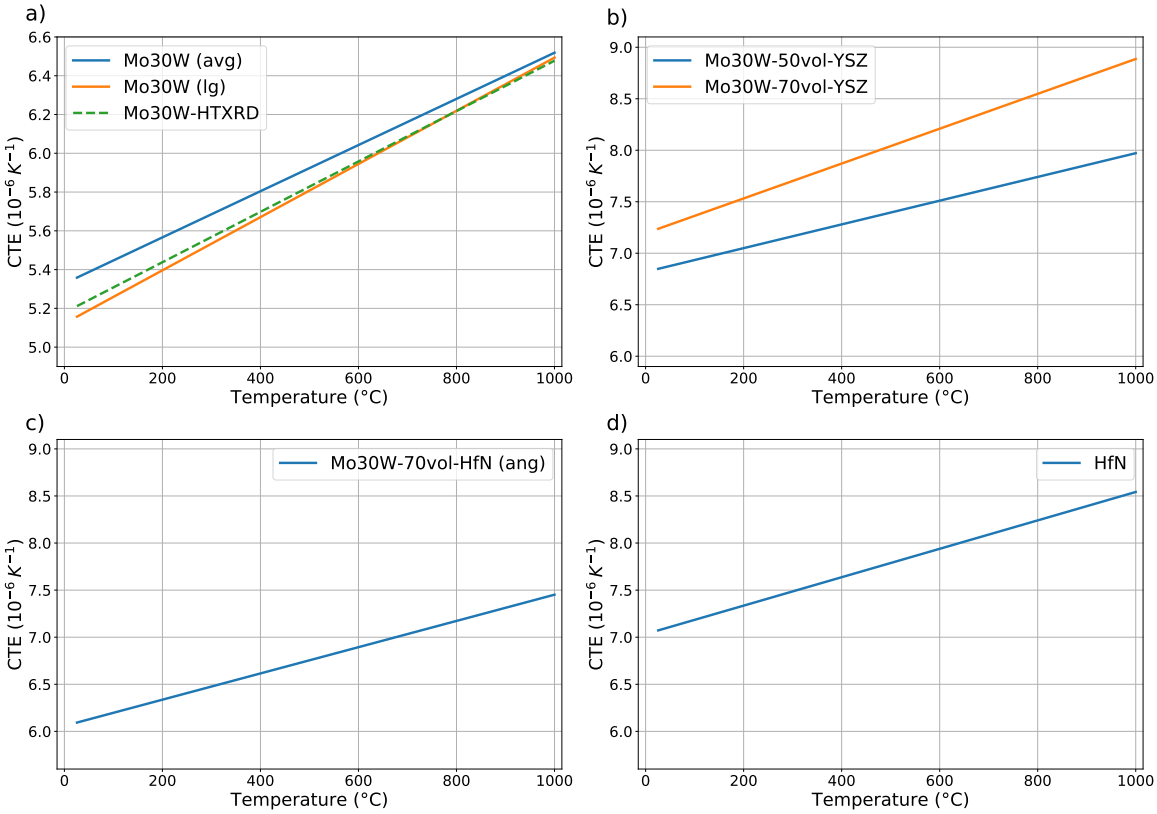


Figure 4.59: CTE for a) Mo30W and b) Mo30W-YSZ cermets, c) Mo30W-HfN cermets, and d) pure HfN determined from push rod dilatometry. The CTE results from high temperature XRD were also included for pure Mo30W.

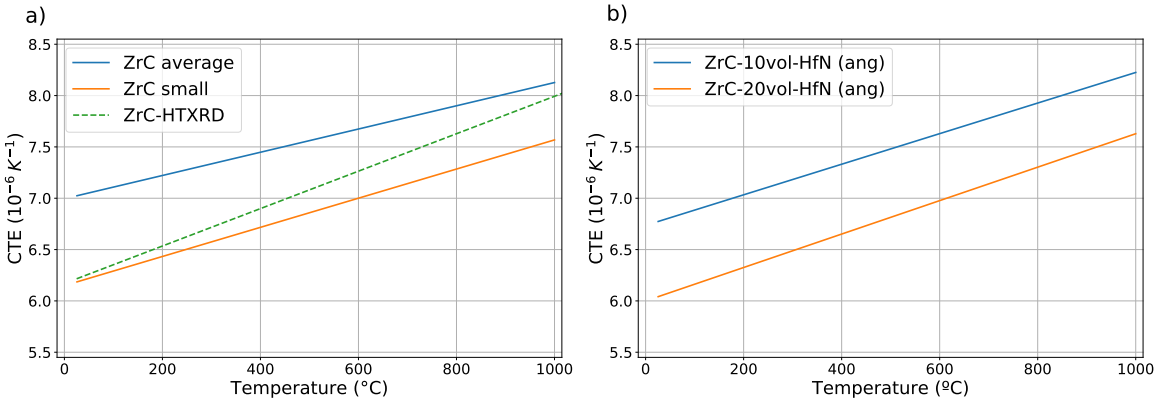


Figure 4.60: CTE for a) ZrC and b) ZrC-HfN cercers determined from push rod dilatometry. The CTE results from high temperature XRD were also included for pure ZrC.

Table 4.12: Fitting parameters for the CTE of the different cermet and cercer materials.

Material	A x 10^9	B x 10^6
Mo30W - Medium GS	1.19	5.33
Mo30W - Large GS	1.37	5.12
Mo30W-50vol-YSZ	1.15	6.82
Mo30W-70vol-YSZ	0.47	9.59
Mo30W-50vol-HfN (Ang)	N/A	N/A
Mo30W-70vol-HfN (Ang)	1.39	6.06
ZrC - Small GS	2.84	6.39
ZrC - Avg GS	2.26	7.41
ZrC-50vol-HfN (Ang)	2.98	6.74
ZrC-70vol-HfN (Ang)	2.58	6.30
HfN (ang)	1.51	7.03

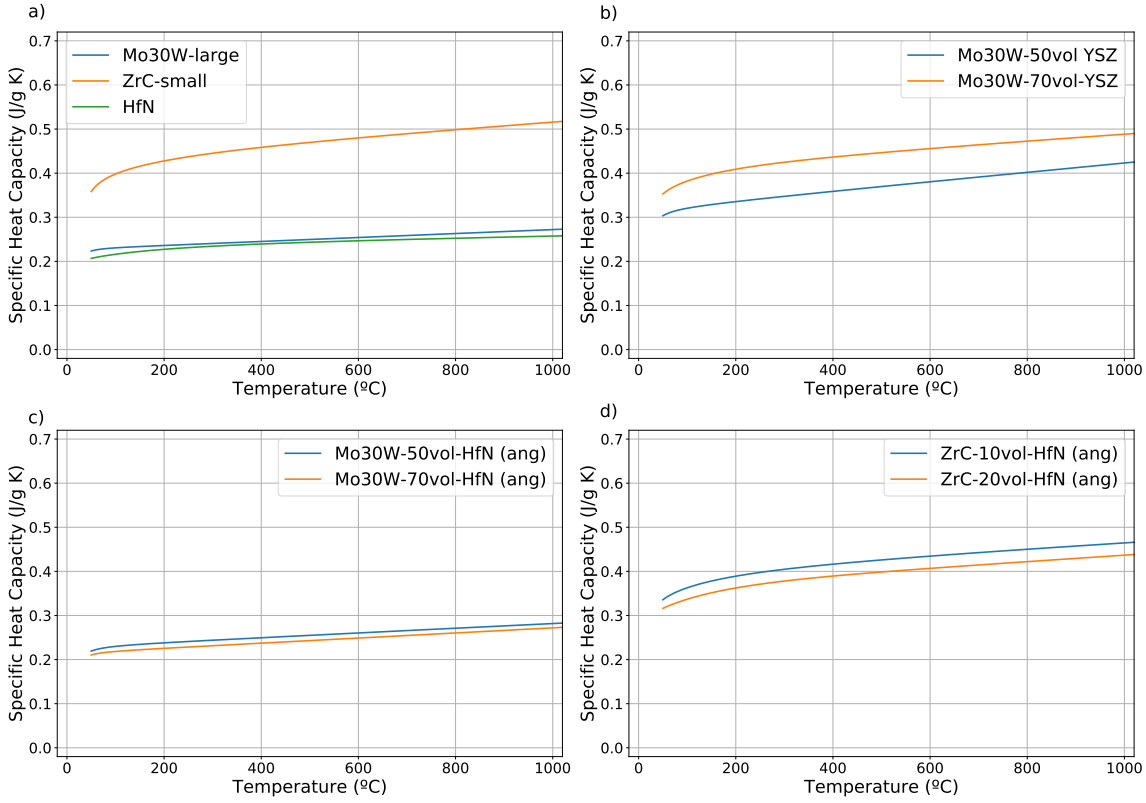


Figure 4.61: Specific heat capacity determined using calorimetry for a. Mo30W, b. ZrC, C. HfN, d. Mo30W-YSZ cermets, e. Mo30W-HfN cermets, and f. ZrC-HfN Cercer.

increase up to around 100 or 200°C, followed by a roughly linear increase up to the maximum tested temperature. The ZrC had a higher heat capacity than the Mo30W, over the range tested. This is due to the stronger covalent bond between the Zr and C atoms, allowing for higher vibrations.

Table 4.13 contains the fitted parameters for the matrix, composite materials, and HfN. Fitted parameters for YSZ were taken from [41]. Fitted values for UN [39] were also included. UO_2 was fitted to a modified version of the equation (Equation 2.15) in Chapter 2. The values for UN and UO_2 will be used for predictive models in Chapter 5. The C_P for Mo30W fit better to a linear equation. The slope was determined to be 4.515 x 10^{-5} and the intercept was determined to be 0.227.

4.2.3 Thermal Conductivity

In determination of the thermal conductivity, the thermal diffusivity was first measured using LFA. Three points were taken at each temperature. The thermal diffusivity for the Mo30W and cermets is presented in Figure 4.62. Several data points were also taken during cooling to check for hysteresis. None was observed from the Mo30W and from any of the cermet materials. For the Mo30W, there was a trend of increasing thermal diffusivity with increasing temperature. Additionally, the larger grain size (34.9 µm) material had a higher thermal diffusivity than the medium grain size (12.8 µm), as seen in Figure 4.62 a). For materials with similar material properties (i.e. density and porosity), materials with larger grain boundaries with have a higher thermal conductivity, and thus higher thermal diffusivity, with the single crystal material having the highest. This is due to the increased phonon scattering smaller grain boundaries provide versus larger ones [203]. Additionally, the larger grained Mo30W had slightly better repeatability than the average grain size, though the heating and cooling points matched quite well for each run.

The addition of the surrogate particles drastically decreased the thermal diffusivity for the different cermet materials. Once again, this is due to increased phonon

Table 4.13: Empirical Einstein temperature (θ_E) and specific heat capacity constants determined as a fit. Literature values for YSZ [41], and UN [39] are also included.

Material	θ_E (K)	a ($J/mol\ K$)	b ($J/mol\ K^2$)	c ($J/mol\ K^3$)	d (K^-1)
MoW	203.4	24.54	4.66 x 10^{-3}	-1.77 x 10^{3}	2.66 x 10^{6}
ZrC	211.5	-56.93	3.02 x 10^{-3}	-7.48 x 10^{4}	4.25 x 10^{6}
HfN	440.4	0.234	2.028 x 10^{5}	-7.98 x 10^{-9}	-6198
YSZ	545	0.597	4.45 x 10^{-5}	98.44	649.4
UN	367.5	51.14	9.49 x 10^{-3}	2.64 x 10^{11}	18081

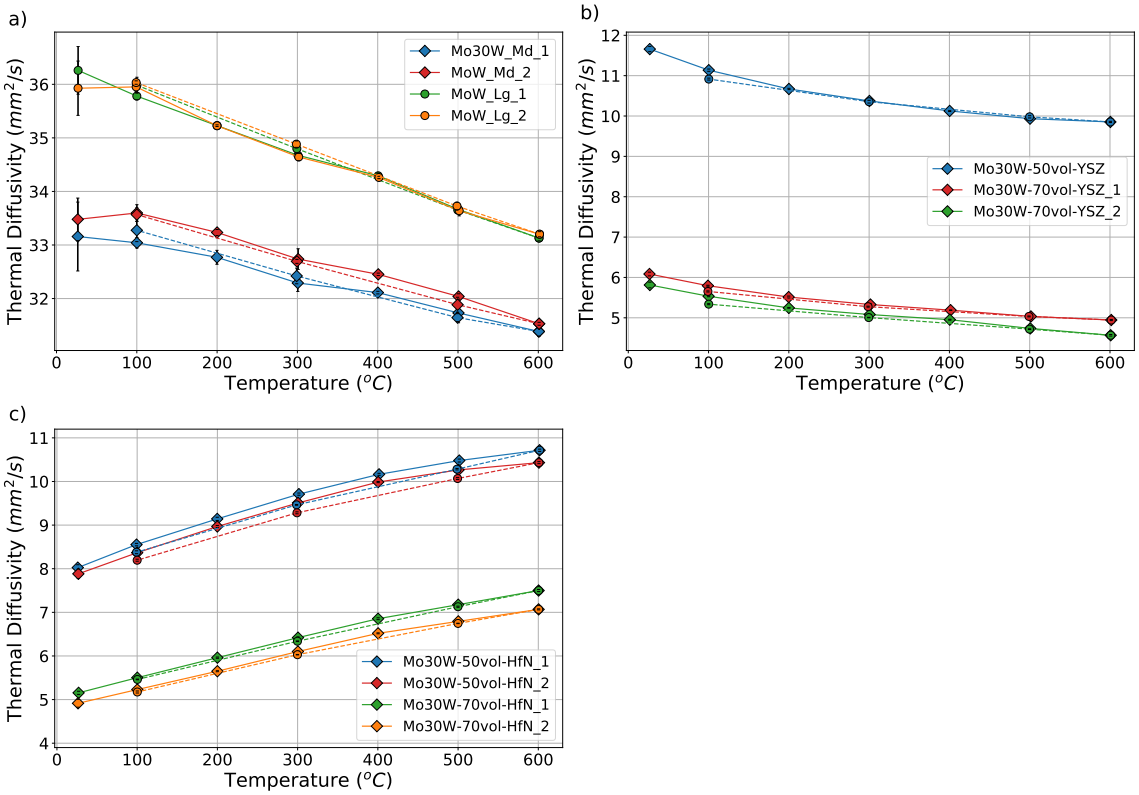


Figure 4.62: Thermal diffusivity from RT to 600°C for a) pure Mo30W for the medium and large grain sized material, b) for the Mo30W-YSZ cermets, and c) for the Mo30W-HfN (angular) cermets. The solid lines with diamond points represent the points taken during heating and the dotted lines and circles represent the points taken during cooling. The standard deviation from the three runs taken at each temperature is also included.

scattering, but this time at the matrix particle interfaces. For both materials, the 50-vol% cermet had a higher thermal diffusivity than the 70-vol% cermet. The Mo30W-YSZ cermets followed the matrix Mo30W trend of decreasing thermal diffusivity with increasing temperature. The Mo30W-HfN (angular) cermets actually experienced an increase in thermal diffusivity with increasing temperature.

The thermal diffusivity of ZrC and the ZrC-HfN angular cercers are plotted in Figure 4.63. Interestingly, the thermal diffusivity decreases initially with increasing temperature up to 100 or 200°C for both the pure ZrC and the cercer composites. After this, the diffusivity increases linearly with increasing temperature. Unlike with the Mo30W, grain size place much less of a role with the thermal diffusivity of the ZrC, likely due to the lower magnitude to begin with. The addition of the 10vol% HfN did not make much of a difference with the observed thermal diffusivity compared to the pure ZrC, but once the volume loading reached 20%, then a more noticeable decline in thermal diffusivity was observed, while still following the same general trend as the pure ZrC.

The thermal diffusivity data was converted into thermal conductivity using Equation 2.13. The density was assumed constant and the heat capacities previously measured were also used. The thermal conductivity of Mo30W was compared directly to that of pure Mo and pure W, as seen in Figure 4.64. The thermal conductivity of Mo30W, is less than that of either Mo or W. Additionally, the thermal conductivity decreases as the grain size decreases.

The electrical properties of the Mo30W and ZrC pure matrix materials were measured. The electrical resistivity up to 450°C is plotted in Figure 4.65 a). The resistivity increases linearly for both materials with increasing temperature over the range tested. The resistivity of the ZrC is almost an order of magnitude greater than that of the Mo30W. The Seebeck coefficients were also determined, as shown in Figure 4.65 b). From these results, Mo30W is a p-type conductor while ZrC is an n-type material.

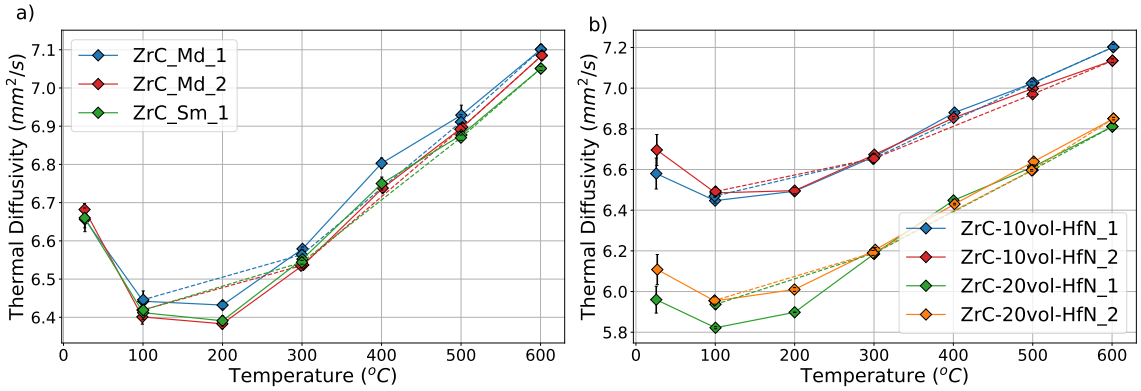


Figure 4.63: Thermal diffusivity from RT to 600°C for a) pure ZrC for the medium and small grain sized material and b) for the ZrC-HfN angular cermets. The solid lines with diamond points represent the points taken during heating and the dotted lines and circles represent the points taken during cooling. The standard deviation from the three runs taken at each temperature is also included.

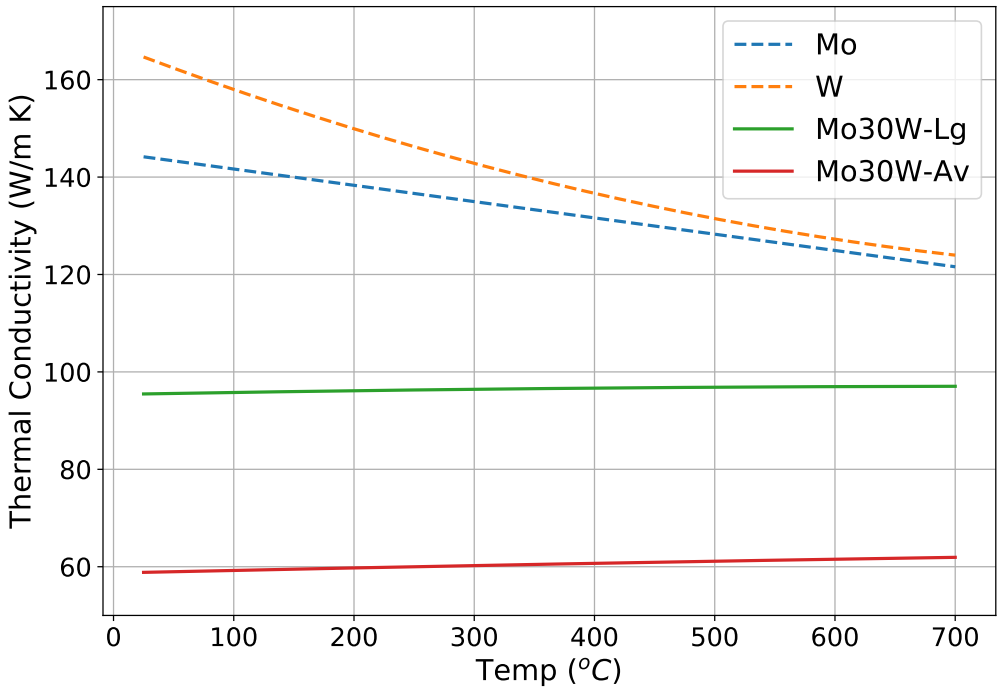


Figure 4.64: Thermal conductivity from RT to 700°C for the large grained (34.9 µm) and medium grained (12.8 µm) Mo30W, compared to that of pure Mo and W [55].

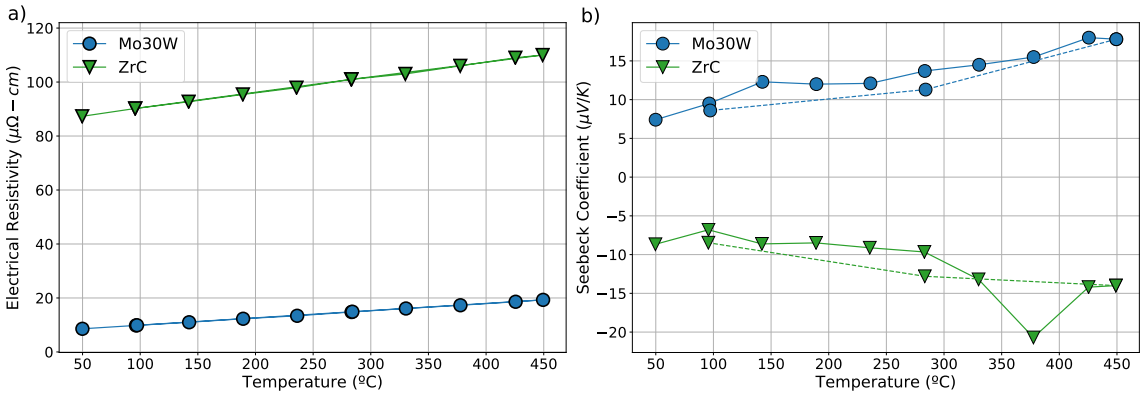


Figure 4.65: a) Electrical diffusivity and b) Seebeck coefficient for Mo30W and ZrC measured from 50 to 450°C. The dotted lines represent the measurements taken during the cooling of the specimens.

4.3 Mechanical Properties

4.3.1 Dynamic Modulus

Impulse excitation of vibration was used to determine the elastic properties of the pure ZrC and Mo30W matrix materials. Initial room temperature properties are presented in Table 4.14. Figure 4.66 contains the elastic and shear moduli for the SPS Mo30W up to 825°C. Above 825°C, the system was no longer able to generate a signal due to the limited size of the sample tested. All three properties were fit to the linear model

$$k = mx + b \tag{4.5}$$

with k representing E (GPa), G (GPa), and ν, m the slope, and b the intercept. The fitting parameters along with the fit errors are presented in Table 4.15. Both the elastic and shear moduli follow a trend of decreasing with increasing temperature, which is expected. Poisson's ratio also follows a slight trend of increasing with increasing temperature.

Figure 4.67 contains the elastic and shear moduli for the SPS ZrC up to around 500°C. Above 500°C, the ZrC began to oxidize, in spite of the flowing Ar-H_2 purge gas. The two moduli and Poisson's ratio were also fit to a linear model, with the fitting parameters presented in Table 4.15. The two moduli also decrease with increasing temperature. While the slope of the linear regression for Poisson's ratio is positive, the error is three times the magnitude of the slope, so it can be assumed that Poisson's ratio of the ZrC is constant, at least up to 500°C.

4.3.2 Tensile Properties

Both the medium and small grained samples underwent tensile testing at room temperature and 800°C. The small grained material was also tested at 400°C. Stress strain curves for the small grained material is presented in Figure 4.68 and for the

Table 4.14: Room temperature properties of ZrC and Mo30W.

Parameters	184-ZrC-Md	292-Mo30W-Md
Diameter (mm)	40.00	40.62
Thickness (mm)	4.01	4.02
Mass (g)	33.50	60.10
Density (g/cm^3)	6.648	11.537
E (GPa)	393.65	325.86
G (GPa)	163.74	125.71
ν	0.202	0.296

Table 4.15: Fitting parameters for Young's modulus, the sheer modulus, and Poisson's ratio for Mo30W and ZrC.

Material	Parameter	E (GPa)	G (GPa)	ν
Mo30W	m	-4.29E-02	-1.81E-02	1.69E-05
	m_{error}	4.81E-04	2.95E-04	1.32E-06
	b	3.29E+02	1.27E+02	2.93E-01
	b_{error}	2.22E-01	1.36E-01	6.09E-04
ZrC	m	-2.19E-02	-9.88E-03	3.23E-06
	m_{error}	3.67E-02	1.58E-02	9.97E-06
	b	3.87E+02	1.61E+02	2.03E-01
	b_{error}	8.33E+00	3.58E+00	2.26E-03

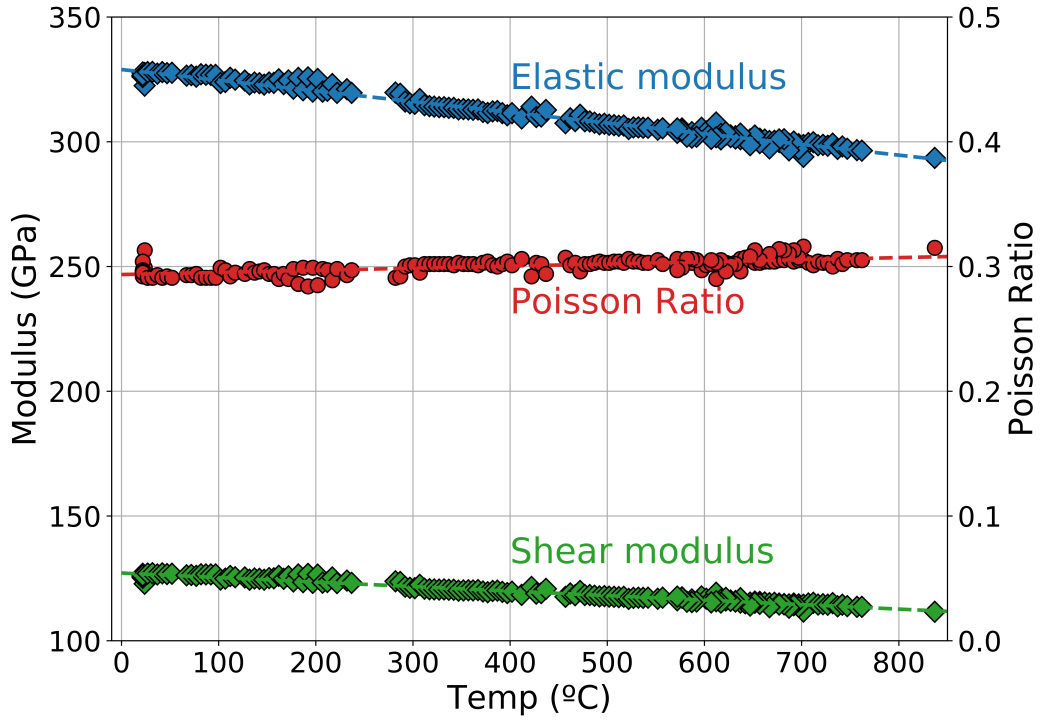


Figure 4.66: Elastic modulus, shear modulus, and Poisson's ratio for as SPS Mo30W. The dotted lines are the linear models determined from linear regression.

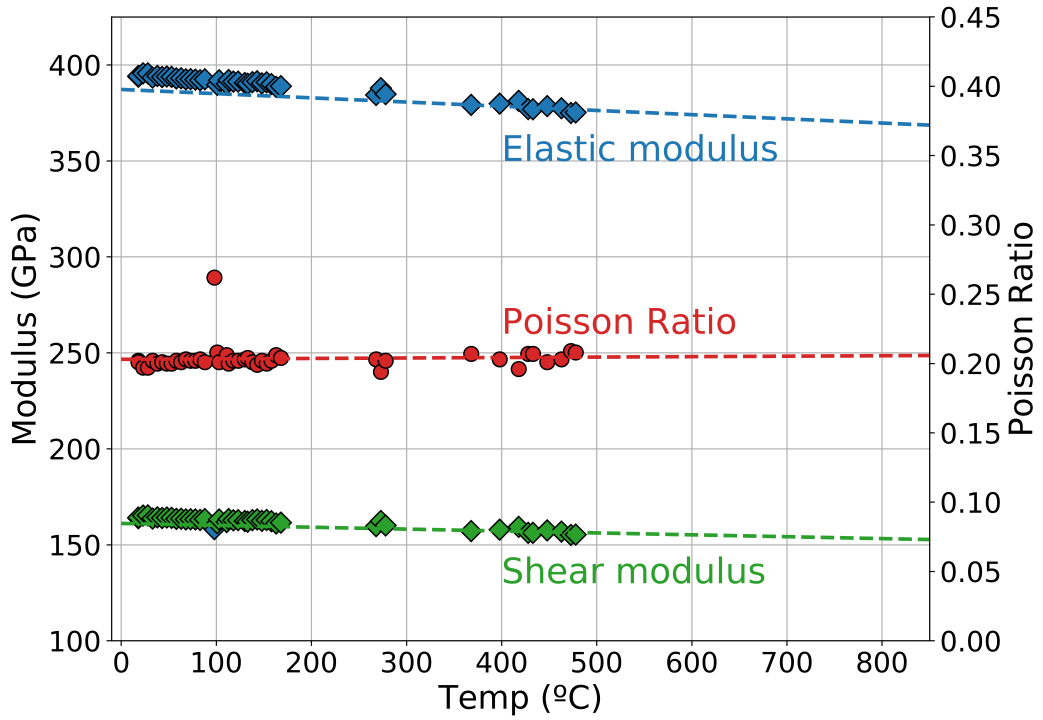


Figure 4.67: Elastic modulus, shear modulus, and Poisson's ratio for as SPS ZrC. The dotted lines are the linear models determined from linear regression.

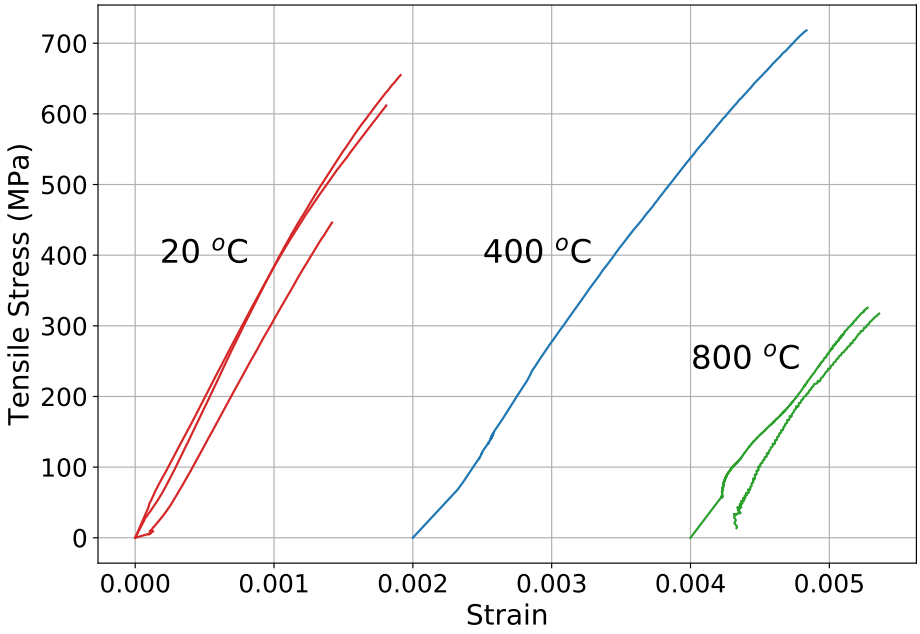


Figure 4.68: Tensile stress strain curves for the Mo30W Small grained Mo30W. The red curves are for samples tested at 20°C, the offset blue curve is for the sample tested at 400°C, and the offset green curve is for the sample tested at 800°C.

medium grained material is presented in Figure 4.69. Both materials failed at the Yield stress without undergoing any plasticity, even at 800°C. SEM images of the fracture surface for at room temperature are included in Figure 4.70. For both grain sizes, the tensile barred failed from intergranular fracture. No significant changes in UTS were observed up to 800 °C, as seen in Figure 4.71.

Wrought W was also acquired and machined into tensile specimens to compare with the Mo30W material. The wrought W exhibited much higher ductility compared with the as sintered Mo30W. The room temperature uniform elongation (e_u), total elongation (e_t), yield strength (YS) at 0.02% offset, and the ultimate tensile strength (UTS) are all presented in Table 4.16. The YS and e_u for the Mo30W were taken to be the UTS and e_t, respectively. The calculated Young's modulus (E) was also included.

4.3.3 Fracture Toughness

The results of the room temperature fracture toughness tests for the Mo30W and ZrC matrix along with the cermet and cercer composites are presented in Figure 4.72. For the pure Mo30W materials, there is a definitive grain size dependence with the fracture toughness. The finer grained materials have the highest toughness, while the large grained materials had the lowest. On the other hand, there appears to be no grain size dependence for the ZrC material. Additionally, the Mo30W is two to seven times greater than that of the ZrC, depending on its grain size.

Analysis of the fractured surfaces was done using SEM. For the pure Mo30W samples, all showed evidence of fracture along the grain boundaries, or intergranular fracture. As seen in Figure 4.73, the intergranular fracture mechanism was dominant for all three grain sizes. There was no evidence of dimpling. Since the fracture mode is intergranular, as the grain size decreases, the distance the crack needs to travel in order to fracture increases, resulting in the higher fracture toughness.

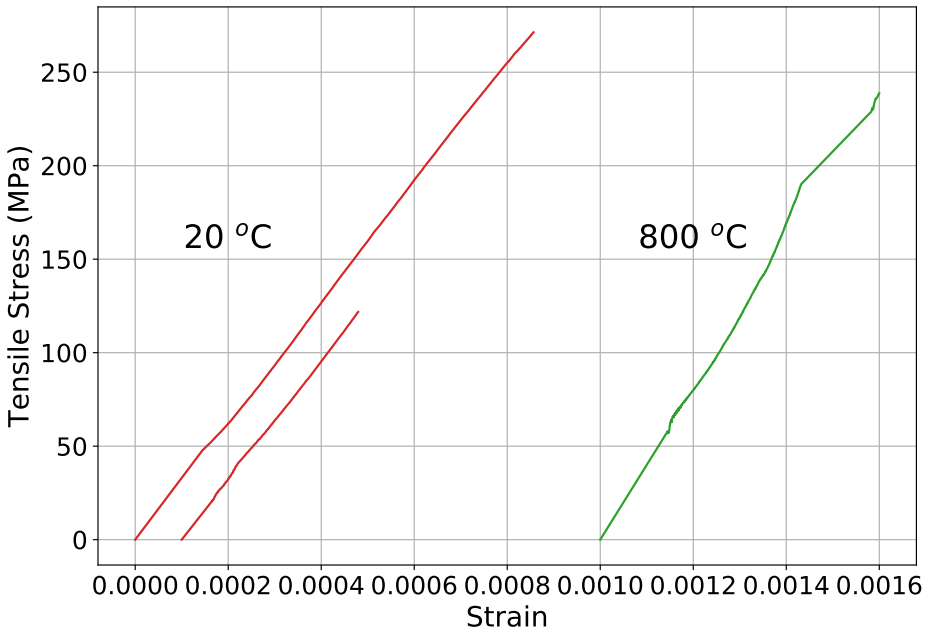


Figure 4.69: Tensile stress strain curves for the Mo30W Small grained Mo30W. The red curves are for samples tested at 20°C and the offset green curve is for the sample tested at 800°C.

Table 4.16: Room temperature tensile properties for wrought W, small grained Mo30W (Mo30W-Sm), and medium grained Mo30W (Mo30W-Md). e_u is the uniform elongation, e_t is the total elongation, YS is the yield strength at 0.02% offset, and UTS is the ultimate tensile strength.

Material	e_u (%)	e_t (%)	YS (MPa)	UTS (MPa)	E (GPa)
Wrought W	0.40 ± 0.04	4.49 ± 1.22	771 ± 55	803 ± 48	376 ± 53
Mo30W-Sm	1.51 ± 0.15	1.51 ± 0.15	571 ± 90	571 ± 90	359 ± 6
Mo30W-Md			183 ± 54	183 ± 54	

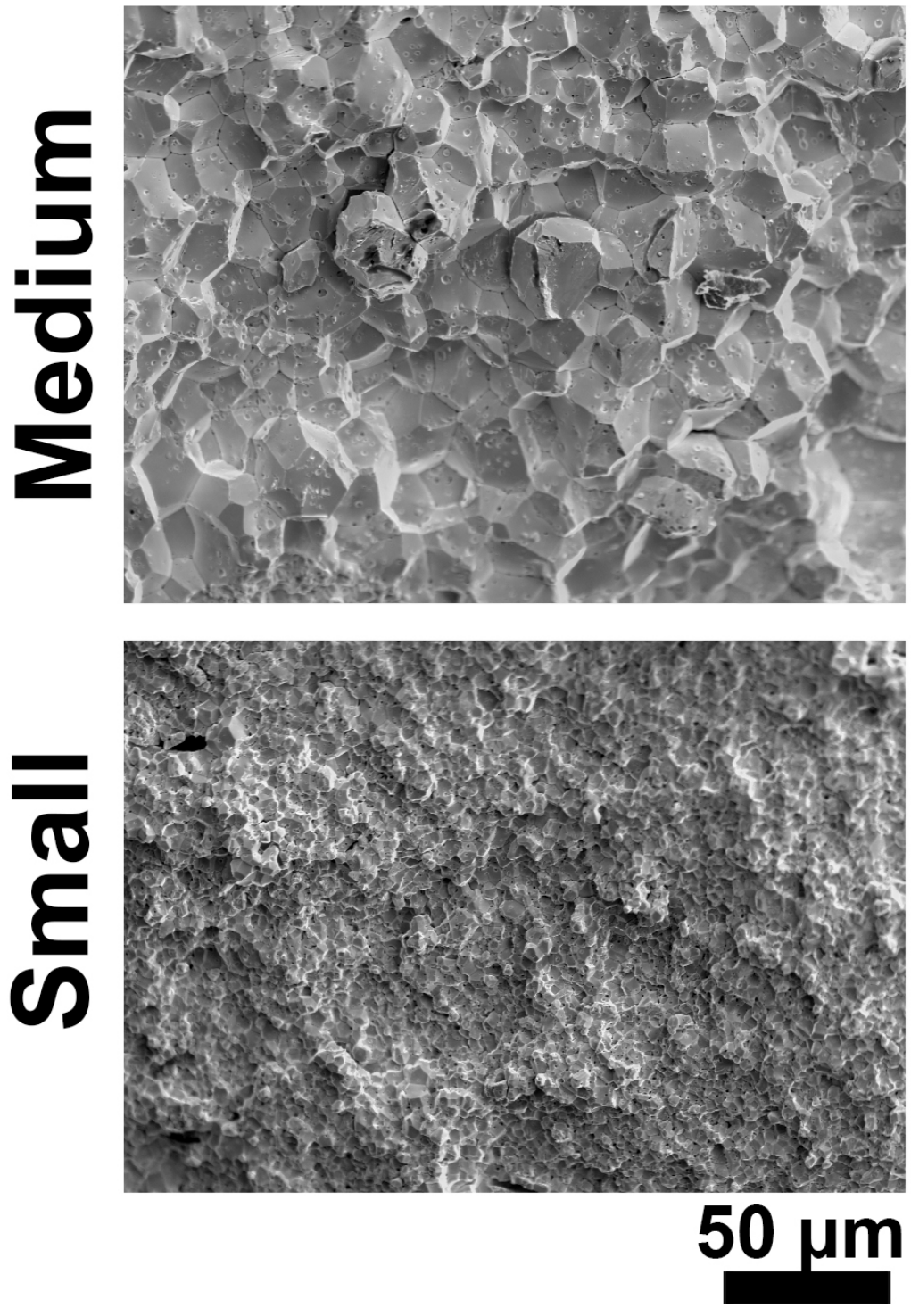


Figure 4.70: Fracture surfaces for Mo30W tensile specimens tested at room temperature.

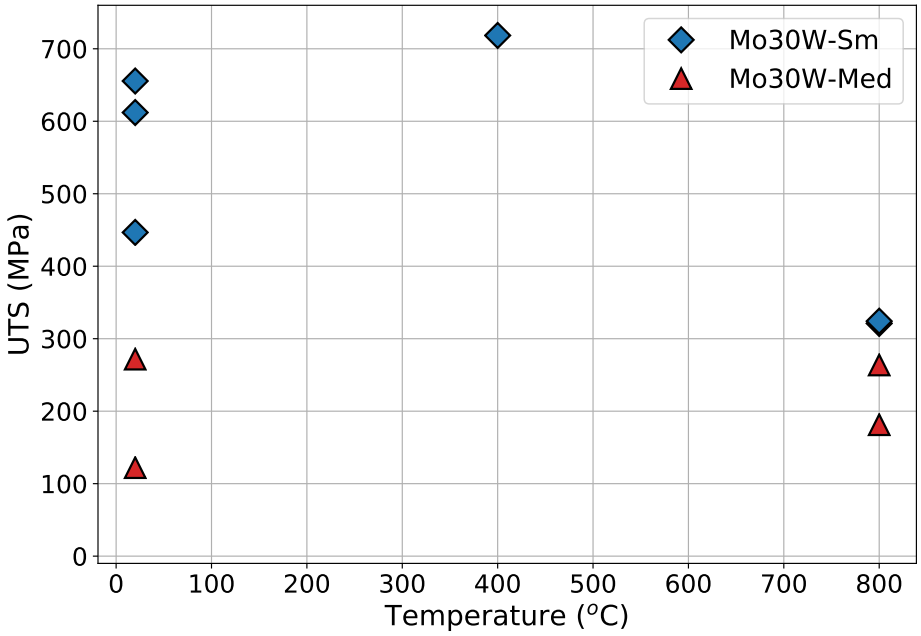


Figure 4.71: The UTS for Mo30W small grain size (blue diamonds) and medium grain size (red triangles) tested at room temperature, 400, and 800°C.

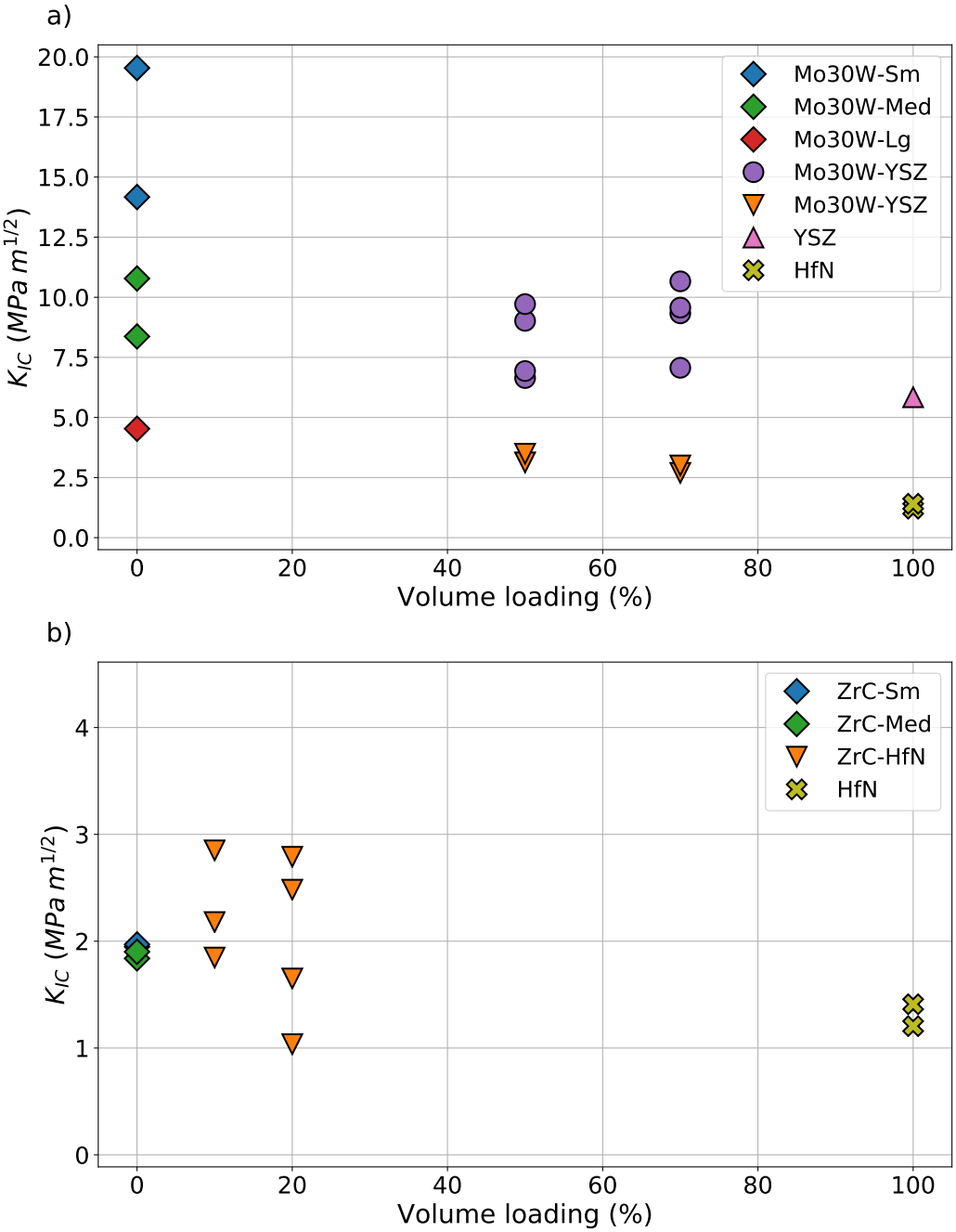


Figure 4.72: Room temperature fracture toughness determined using SENB for a) Mo30W, Mo30W-YSZ cermets, Mo30W-HfN (angular) cermets, HfN, and YSZ taken from literature and b) ZrC, ZrC-HfN cercers, and HfN.

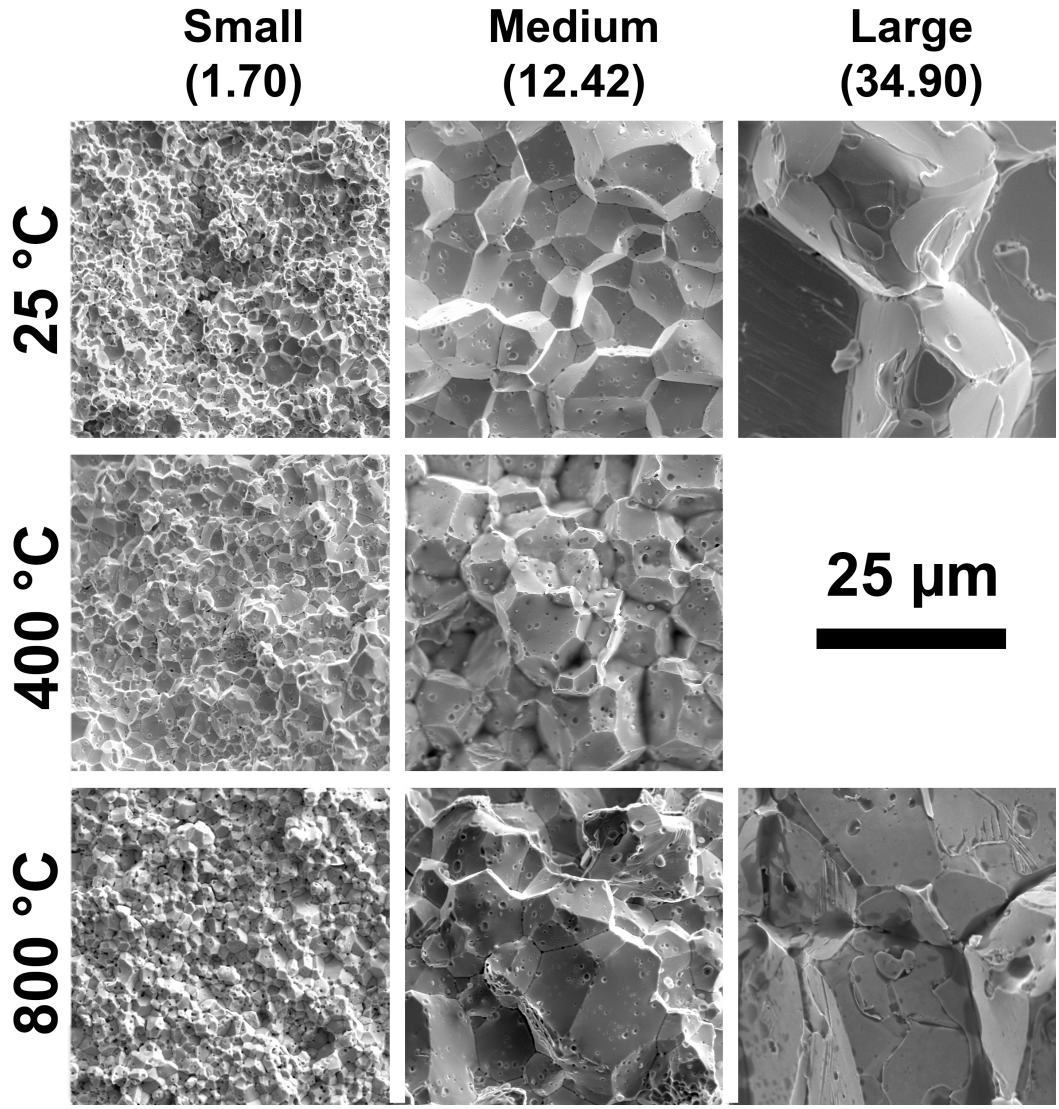


Figure 4.73: SEM fractographs of the Mo30W matrix SENB samples tested at 25, 400, and 800°C.

The ZrC is a much more brittle matrix compared with the Mo30W, since it is a carbide. Figure 4.74 contains the fractographs for the two grain sizes of the ZrC samples tested at 25, 400, and 800°C. The fracture mode is transgranular cleavage. This is why there was no grain size dependence on the fracture strength of the ZrC. As the crack propagates through the ZrC, it ignores the grain boundaries and splits through the matrix.

The room temperature fracture toughness of the Mo30W-YSZ cermet varied over a range of around 4 MPa-$m^{1/2}$. There was not a noticeable trend of either increasing or decreasing fracture toughness with increasing volume loading. Some samples had a higher fracture toughness with respect to the average fracture toughness for the medium grain size Mo30W, while others had a lower value. SEM of the fractographs revealed intergranular fracture in the Mo30W matrix and two different behaviors for the YSZ. Some YSZ particles sheared at the fracture plane and experienced transgranular cleavage, while others remained fully intact with the fracture traveling at the particle-matrix interface and debonding the entire particle, as seen in Figure 4.75.

The Mo30W-HfN cermet had a significantly lower fracture toughness compared with the average fracture toughness for the medium grain size Mo30W. The range of K_{IC} values were much lower than that of the YSZ cermets. Unlike with the YSZ, no debonded particles were observed, as seen in Figure 4.75. Instead, all HfN particles were sheared at the fracture surface with a combination of intergranular fracture and transgranular cleavage.

The ZrC-HfN cercer experienced brittle fracture for the 10 and 20 % volume loadings. As seen in Figure 4.76, the fracture mode of the HfN appeared similar to that of the HfN in the Mo30W cermet. All particles cleaved at the fracture surface with a combination of intergranular fracture and transgranular cleavage. A majority of the ZrC still experienced transgranular cleavage, similar to the fracture mode of the pure ZrC samples. However, there was some evidence of a mixture of intergranular fracture and transgranular cleavage in the ZrC at the particle-matrix interface.

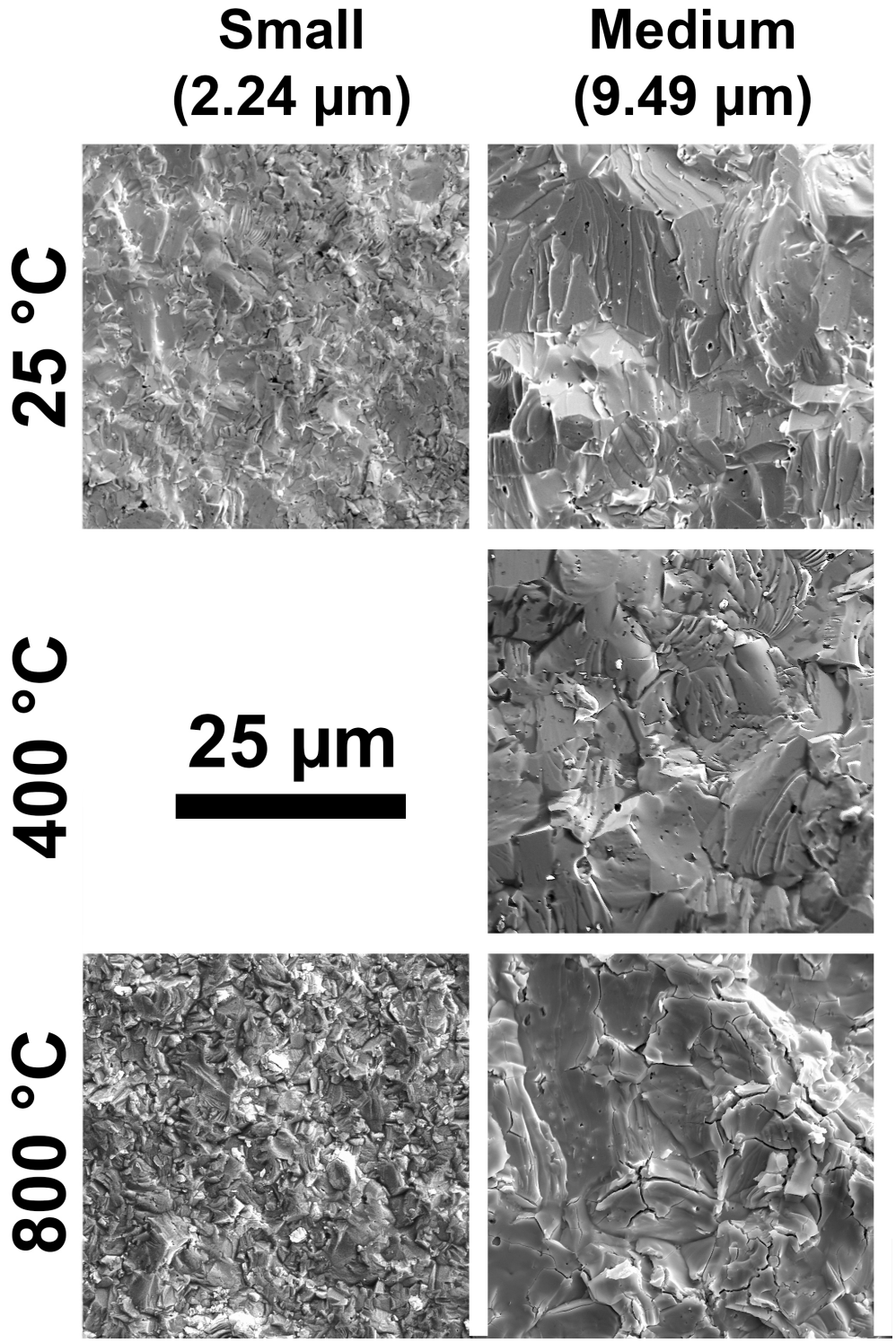


Figure 4.74: SEM fractographs of the ZrC matrix SENB samples tested at 25, 400, and 800°C.

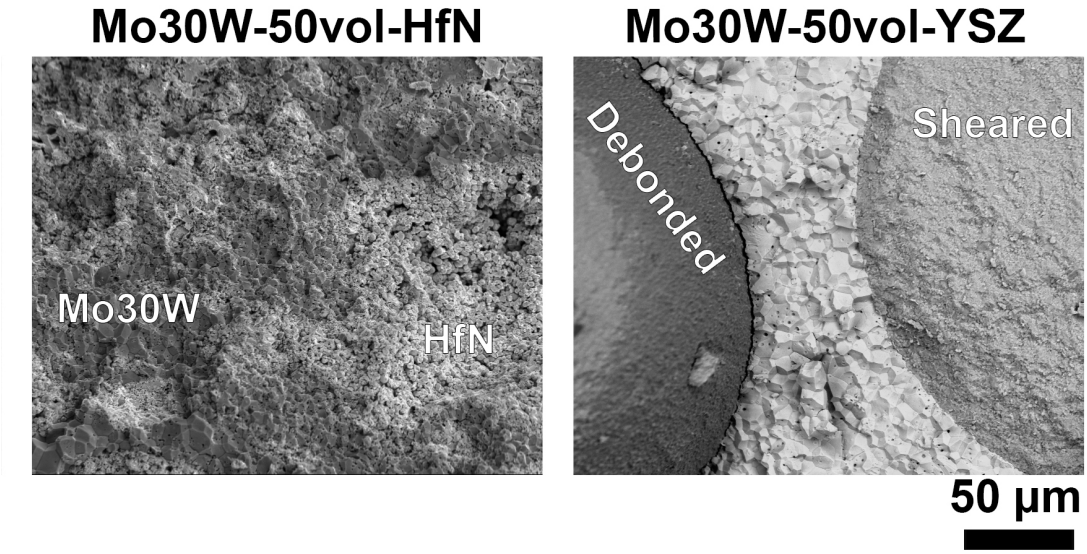


Figure 4.75: Room temperature SEM (80% secondary electron and 20% backscatter electron) fractographs of the Mo30W cermets with angular HfN and spherical YSZ particles.

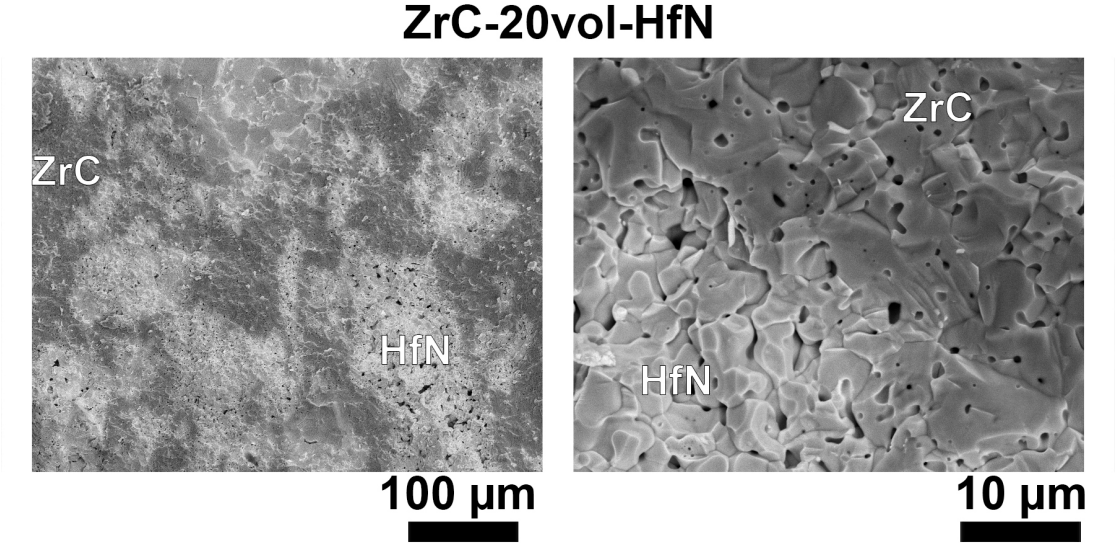


Figure 4.76: Room temperature SEM (50% secondary electron and 50% backscatter electron) fractographs of the ZrC cercer with angular HfN particles.

Fracture toughness testing was also conducted at 400 and 800°C for some select samples. The results for the pure matrix materials is presented in Figure 4.77. The small grained Mo30W only experienced a slight decrease in fracture toughness with increasing temperature up to 800°C. Looking at the fractograph in Figure 4.73, there is no difference between the fracture surfaces broken at the different temperatures. The fracture mode remains intergranular. There is also no evidence of dimpling. This suggests that 800°C is below the ductile to brittle transition temperature (DBTT) for the Mo30W, which would be expected given its alloy composition.

There was a slight increase in fracture toughness for the Mo30W medium and large grained materials. At 800°C, the fracture toughness for all grain sizes ended between 10 and 12 MPa $m^{1/2}$. At 800°C, even though the Mo30W is still experiencing brittle fracture, the grain size dependence has been removed. In the medium and large grained Mo30W, there is still no evidence of dimpling and the fracture mode remained intergranular, as seen in Figure 4.73. It is also important to not that only one test for these materials was conducted at elevated temperatures. Further tests with larger samples sizes are needed to produce definitive conclusions.

The ZrC material experienced a slight increase in toughness with increasing temperature. Several studies looking a flexural strength of ZrC did not observe an increase in strength until a temperature of at least 1600°C [75, 10]. While the fracture toughness increased with increasing temperature, the fracture mode remained transgranular. Once again, tests with larger sample sizes are needed in order to produce better statistics for these materials.

Finally, some select surrogate cermet and cercer materials were tested up to 800°C. The fracture toughness of the cermets at various temperatures is presented in Figure 4.78. The Mo30W-HfN materials experienced no change in fracture toughness. The Mo30W-70vol-YSZ seemed to experience a drop in fracture toughness at 400°C, then a significant increase at 800°C. This, however, is a result of the wide variation of the MoW-YSZ K_{IC} and not anything physical. The mechanisms for fracture toughness for the spherical YSZ cermets will be discussed in the next chapter. SEM analysis of

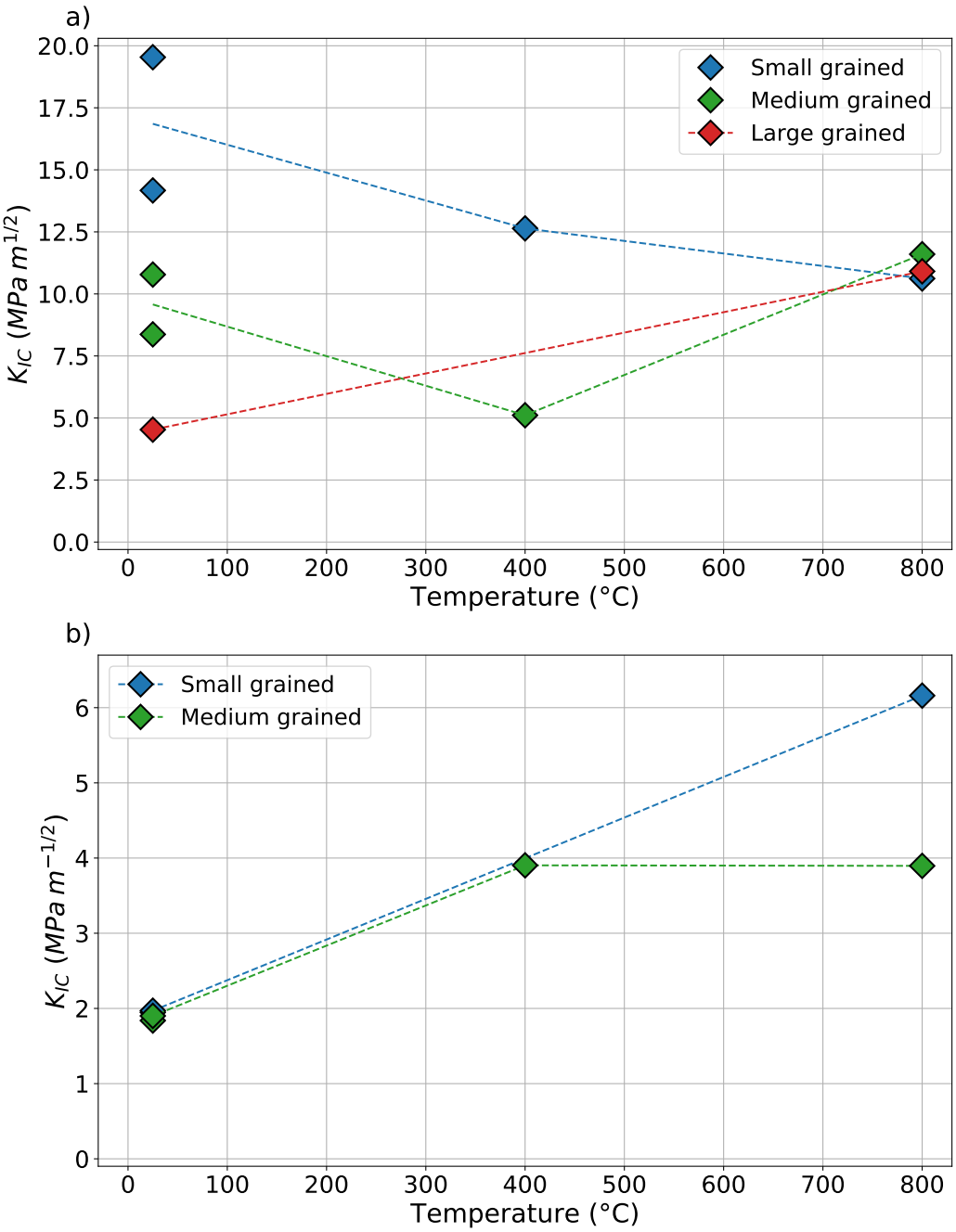


Figure 4.77: Fracture toughness determined using SENB for a) Mo30W and b) ZrC from 25 to 800°C.

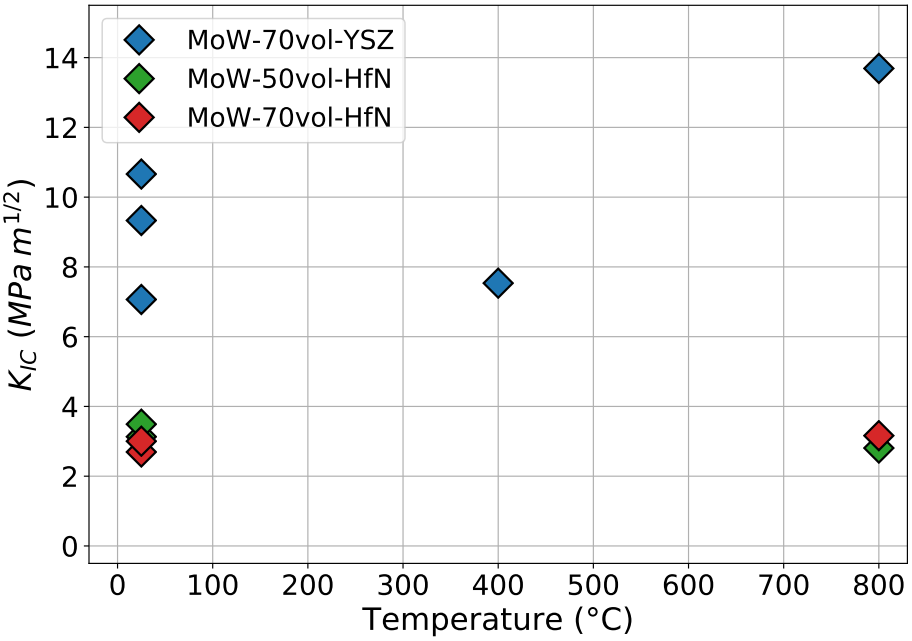


Figure 4.78: Fracture toughness determined using SENB for Mo30W surrogate cermets at 25, 400, and 800°C.

the fracture surfaces found no discernible differences between the high temperature fractured samples and the room temperature tested samples.

Chapter 5

Discussion

5.1 Fabrication

5.1.1 Mo30W Matrix

The Mo30W powder was found to sinter to a high relative density (88-98 % theoretical density) for all of the investigated SPS consolidation conditions (10-50 MPa, 1400-1700°C, 5-90 minute hold times). Comparing the microstructure with the hardness results, it was discovered that like most materials, the sintered Mo30W decreases in hardness with increasing grain size. Density can also play a role on the hardness of material, as a sample that is not fully densified will deform under lower applied stresses compared to fully densified samples of the same material. The data from this experiment was split three different density groups of 88.5 to 92%, 92% to 96%, and 96-99 % theoretical density in order to separately investigate the influence of sintered density and grain size on hardness; the data are plotted in Figure 5.1 a.

Combining the hardness data with the average grain size illustrated the well documented trend of decreasing hardness with increasing grain size for grain diameters above 5 µm. At very fine sintered grain sizes (<5 µm), there was some variability in the measured hardness for the materials with 88-96% theoretical densities). For the samples sintered to greater than 96% theoretical density, there appeared to be a

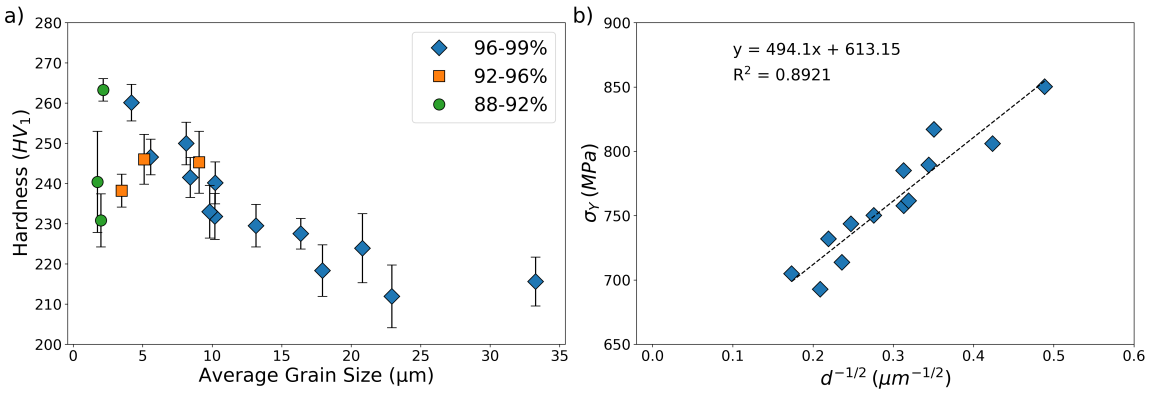


Figure 5.1: Vickers hardness a) Vickers hardness versus average grain size for various densities and b) calculated yield strength verse square root of grain size for the Hall-Petch relationship for the sintered chemical reduction powder taken from [40].

monotonic trend at all grain sizes. The Vickers hardness values were converted into equivalent metric system (MPa) hardness values using the relationship $H(MPa) = 0.0098 H_{Vickers}(HV)$. The hardness values were then converted into yield strength using the Tabor relationship for metals, $H(GPa) = 3\sigma_Y$ [131]. Once the values for yield strength were approximated using this relationship, the data were then fitted to the Hall-Petch relationship for grain boundary barriers to dislocation glide, as seen in Equation 5.1 [204, 205]:

$$\sigma_Y = \sigma_0 + \frac{k_y}{\sqrt{d}} \tag{5.1}$$

where σ_Y is the yield strength, σ_θ is a friction stress (or the stress in a single crystal of the material), d is the average grain size, and k_y is the strengthening coefficient unpinning stress. Figure 5.1 b) summarizes the results of the measured hardness of the sintered specimens with final sintered densities above 96% theoretical, plotted against the square root of the average grain size. The data fits well into a linear trend that confirms the Hall-Petch relationship. Using linear regression fitting, values for σ_θ and k_y were determined as 610 MPa and 490 MPa $\mu m^{1/2}$, respectively. These values are compared to data obtained from pure Mo of varying sources [206], pure sintered W [207], and W wire [208] in Table 5.1. The σ_θ for Mo is much smaller than for tungsten, as W is a harder material. Also, between the two W samples, there was a significant disparity in values for σ_θ. The value of σ_θ for Mo30W is in-between the values of σ_θ for pure Mo and pure W. This may be evidence of solid solution strengthening. Interestingly, the value for k_y for Mo30W is much less than that for both Mo and W (of which Mo has a lower value). This means that the hardness, or strength dependence on grain size for Mo30W alloy has a much smaller dependence on grain size than pure Mo or W. This is a favorable result, as rapid grain growth is expected to occur in NTP systems operating at full temperature, and the expected strength loss due to grain growth will be mitigated in the alloy compared to the pure materials.

Table 5.1: Results from linear regression to fit the Hall-Petch relationship for pure Mo, pure W, and Mo30W taken from [40].

Property	Mo30W [40]	Mo (Cordero et al.) [208]	W (Vashi et al. [207]	W. (Nikolić et al.) [208]
σ_θ (MPa)	610	104	880	1560
k_y (MPa µm$^{1/2}$)	490	1430	995	850

In addition to comparing the hardness and grain size, the effect of isothermal hold time on the microstructure was also examined. Samples were sintered at 1600°C and 30 MPa from 0.5 to 90 minutes and then the microstructure was analyzed. These conditions were selected due to their intermediate ranges, to give representative results for relatively few tests. The grain growth as a function of time can be seen in the SEM images in Figure 5.2. A high amount of porosity was observed for the 30 second sintering time at maximum temperature. This is likely due to the powder not having enough time to fully consolidate and close the voids between different powder particles. As the sintering time increased, the porosity decreased. Once a hold time of fifteen minutes was reached, there was a significant decline in porosity, and most of the pores were located on the grain boundaries. Increasing the hold time further decreased the porosity.

The observed grain growth fits well to the classical law following the second order power law, as shown in Equation 5.2,

$$d^2 - d_0^2 = kt \tag{5.2}$$

where d is the average grain size, d_0 is the initial grain size at that sintering condition, and k is the rate parameter. Fitting the data using a linear regression resulted in an initial grain size value of 4.19 µm. This is larger than the starting powder size, likely a result of densification occurring during the 100°C/min climb to the hold temperature of 1600°C. The k value was found to be 12.25 µm ^{2}/s. For most crewed Mars mission architectures, an NTP system is expected to run for 60 to 90 minutes [209]. Assuming a starting grain size of 13.16 µm, for a material sintered at 1600°C and 30 MPa for 15 minutes, the grains would be expected to grow to around 36 µm. This should not be of any concern. However, in the hotter regions of the reactor (>2200°C), grain growth will be much more accelerated. In order to determine how significant this grain growth would be, additional testing at multiple

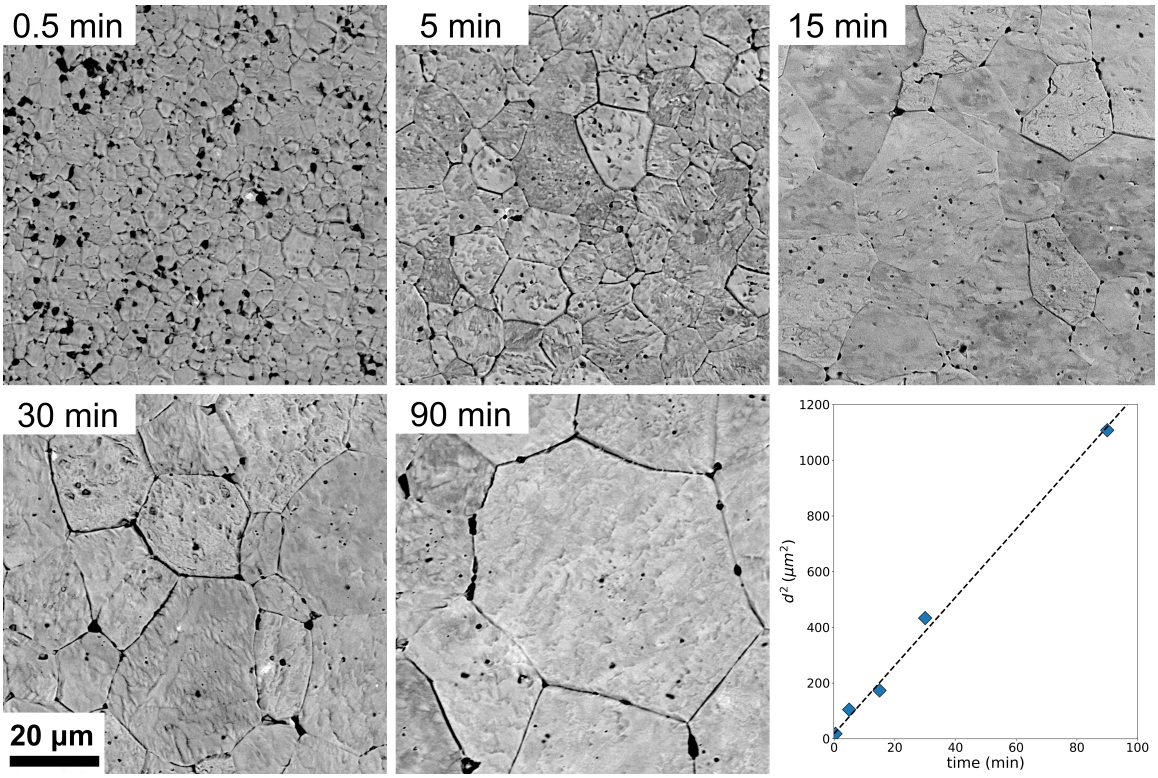


Figure 5.2: SEM micrographs and a plot of the square of grain size of the sintered Mo30W at 1600°C and 30 MPa for 0.5, 5, 30, and 90 minutes and the linear relationship between the grain size squared and time taken from [40].

high temperatures would be valuable in order to estimate high temperature grain growth, as k from the power law equation is temperature dependent.

Figure 5.3 summarizes the hardness and grain size of the sintered Mo30W samples as a function of time for samples sintered at 1600°C and 30 MPa. As the hold time increases, the grain size increases and the hardness decreases. The grain size model was fit to the previously determined second order rate law. The decrease in hardness can be associated with the increase in grain size, as discussed previously. By combining the Hall-Petch relationship (Equation 5.1) with Equation 5.2, a model for the hardness as a function of sintering time was developed. Equation 5.3 illustrates this model, which is based off of the constants determined for the other two equations. By using the previously described relationships between yield strength and hardness, this equation can be converted back into hardness values, as shown in Figure 5.3, modeling hardness as a function of time. Given enough time, the hardness will level out to the value of a single crystal.

$$\sigma_Y = \sigma_0 + \frac{k_y}{(d_0^2 + kt)^{1/4}} \tag{5.3}$$

As the average grain size increases, the range of grain sizes increases as well. Figure 5.4 shows histograms of the grain size at 1600°C for various hold times. Between 0.5 and 15 minutes, the average grain size peak broadens as well as shifts towards larger grain size. At 90 minutes hold time, there is no longer a discernible single peak and there is a wide range of grain sizes.

Pressure was found to have a significant effect at 50 MPa for all the tested hold temperatures. Analysis of SPS operations has found that pressure typically increases sintering for two primary reasons [192, 104]. The first is that the applied pressure aids in the re-arrangement of the particles and the destruction of larger agglomerates that can inhibit sintering and increase sample porosity. Pressure can also increase the driving force for sintering. Typically, there is a critical pressure where pressure becomes the dominant factor in the final density of the sintered material over a

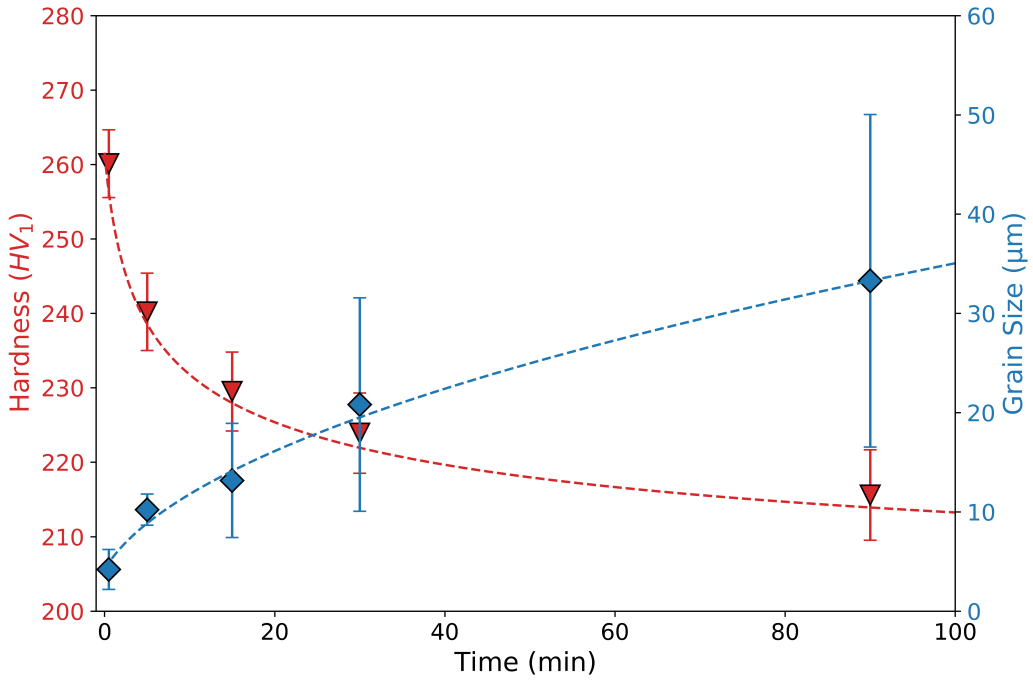


Figure 5.3: Hardness (inverted red triangles) and grain size (blue diamonds) as a function of sintering time for the chemical reduction Mo30W sintered at 1600°C and 30 MPa. The hardness and grain growth models have also been included, taken from [40].

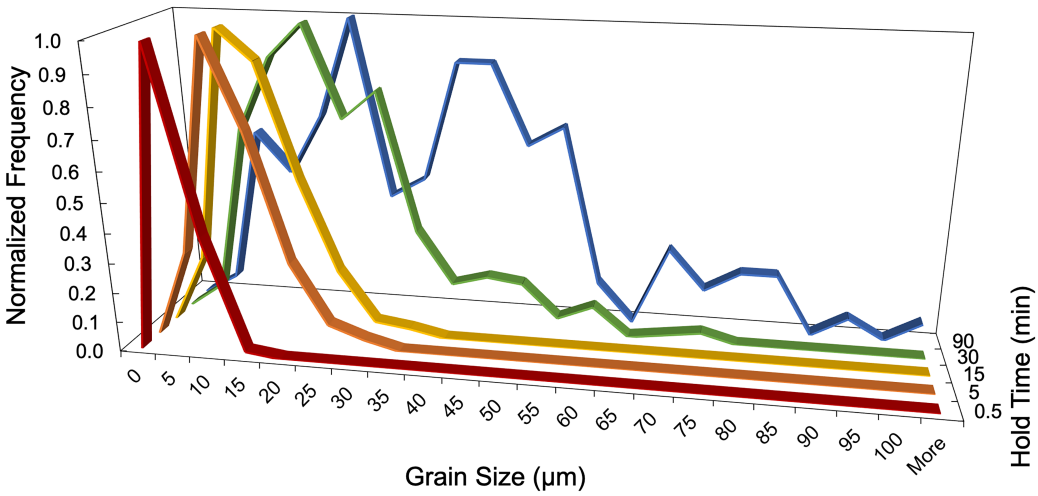


Figure 5.4: Histogram of grain size for Mo30W sintered at 1600°C and 30 MPa for 0.5, 5, 30, and 90 minutes taken from [40].

wide range of sintering temperatures [104]. It was discovered that for this powder chemical reduction powder, 50 MPa is the pressure where it becomes the dominant factor. This is a similar pressure for the sintering of pure Mo, which was found to be pressure dominant at around 57 MPa [45].

The current study attained higher theoretical density with the chemical reduction powder compared to the study conducted by Batienkov et al. which did not attain a theoretical density above 95% until sintering at 1850°C and 50 MPa [50]. This is likely due to different powder morphologies and sizes. However, since different powder morphologies were not evaluated in this study, it is unclear. While information on powder size or morphology was not provided in the study by Batienkov et al., they likely started with a larger powder than this study, as evidenced by the larger grains and increased porosity between grain boundaries compared to this study.

The highest density achieved was 11.62 g/cm^3, with the chemical reduction powder sintered at 50 MPa and at 1700°C for a dwell time of 5 minutes. While a highly dense material is important, it is not the most important factor for the NTP fuel metal matrix. The NTP cermet fuel system will have ceramic fuel (UO_2 or UN) particles dispersed throughout the matrix. These particles have significantly different thermal and mechanical properties, especially the coefficient of thermal expansion. Sintering at higher temperatures and higher pressures could cause excess strain in the matrix and fuel particles, that could result in cracking upon cooling. This study found that increasing the dwell time at a lower hold temperature and set pressure could produce similar densified material. These parameters will need to be optimized for the cermet material. In order to ensure a high sintered density of the Mo30W matrix, the materials should be sintered at or above 1600°C with an applied load of 30 MPa.

5.1.2 Comparison of the Consolidation of Different Mo30W Powders

In order to determine the apparent activation energy, the noise inherent to the piston travel data was first reduced using a zero phase linear filter with a single pass. Additionally, the derivative of the normalized change in displacement data, with respect to temperature $\frac{d(\Delta L/L_0)/L_0}{dT}$, was approximated using a finite difference centering method. Figure 5.5 shows the linearized plot of ln $\frac{(d(\Delta L/L_0)/L_0}{dT}$) versus inverse temperature. Table 5.2 contains the apparent activation energies of the four powders. Two separate runs were conducted for the CR and BM materials.

The noticeable increase in onset sintering temperature for the larger spherical powders is a result of the difference in particle surface energy. The driving force for the sintering of metallic powders is the reduction of the surface energy [186]. Particles with the highest starting surface energy will have the largest driving force, which results in the reduced onset sintering temperature. Surface energy depends on both particle shape and particle size. The angular BM powder had the lowest onset displacement temperature. Typically, spherical particles are thought to have higher surface energies due to their low surface area to volume ratio. However, the particle surface free energy is the product of the orientation-dependent surface energy parameter and the particle surface area. In general, spherical particles have the lowest surface area per unit volume, but may have higher surface energy parameters since they do not predominantly consist of low index number planes (110 planes would be expected to have the lowest surface energy parameter for BCC metals). Also, for a given particle volume fraction of similarly shaped particles, smaller particles have higher initial surface energy per unit volume than larger particles, and thus they start to sinter at lower temperatures [210, 12]. This combination of size and crystallographic effects led to the sintering of the BM powder at the lowest temperature. Conversely, although the GA particles were spherical, the larger average particle size contributed to a lower starting surface energy, requiring a higher

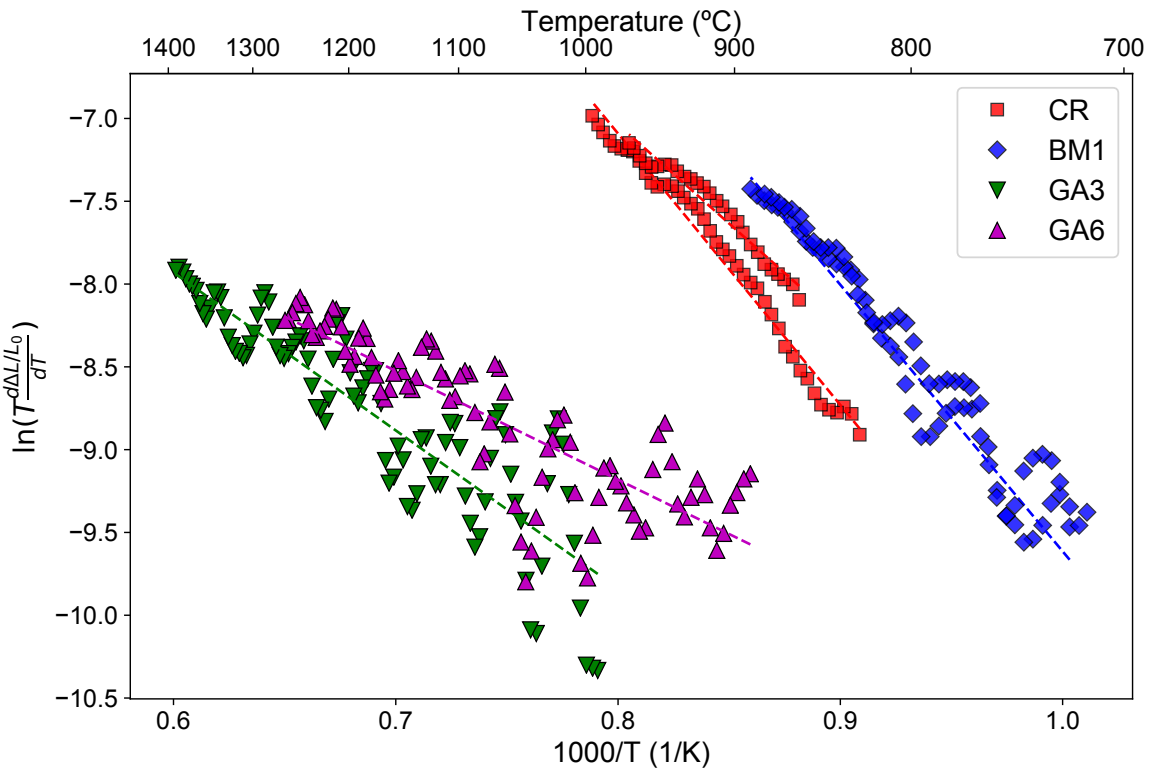


Figure 5.5: Plots of $\ln\left(\frac{d(\Delta L/L_0)/L_0}{dT}\right)$ versus inverse temperature for initial stage sintering of the Mo30W powders.

Table 5.2: Measured apparent activation energy (nQ) and calculated Q_B grain boundary activation energy and Q_v, volume diffusion limited activation energy.

Material	nQ (kJ/mol)	Q_B (kJ/mol)	Q_v (kJ/mol)
CR	131 ± 18	392 ± 55	261 ± 37
BM	139 ± 7	416 ± 22	277 ± 14
GA (-325 Mesh)	98	295	196
GA (-635 Mesh)	69	206	137

temperature for onset sintering to occur. The difference in particle size also led to an 80°C lower onset sintering temperature for the smaller GA powder compared with the larger one.

Both the CR and BM materials have similar apparent activation energies for the initial stage sintering. Chemically, the two powders are different. While the CR powder is a solid solution of Mo and W, the BM powder consists primarily of Mo and W rich particles, and also has a much higher iron and oxygen content. This suggests that chemistry does not play a significant role in the sintering of the Mo30W powders. Both also have a smaller particle size with a more angular geometry compared with the spherical GA powders. The GA spherical powders had much lower apparent activation energies. Comparing the two GA powders, the smallest powder had the lowest activation energy, once again due to smaller particles having higher starting surface energies per unit volume compared with larger particles of the same geometry.

Table 5.2 also includes the calculated values for the grain boundary and volume activation energies calculated from the determined apparent activation energies. Only one diffusion mechanism is likely dominant for this material, however the primary diffusion mechanism cannot be determined from CRH experiments. As stated previously, other studies determined that volume diffusion was the primary diffusion mechanism for the sintering of Mo and that grain boundary diffusion was the dominant mechanism for the sintering of W. Volume diffusion activation energies between 390 and 410 kJ/mol were determined for pure Mo [211, 212, 213][32-34]. The activation energies for volume diffusion of the CR and BM powders, which were between 261 and 277 kJ/mol, were significantly lower than the activation energies for volume diffusion of pure Mo. One of these studies found that adding alloying elements reduced the activation energy [212]. Additionally, it is known that mass transport is enhanced for materials in SPS due to the pulsed current [104]. This could result in the lower determined activation energy. The other option could be that the sintering of Mo30W is grain boundary diffusion dominant. The grain boundary activation energy for the CR and BM powders were 392 and 416 kJ/mol, respectively,

which is similar to the values between 410 and 465 kJ/mol determined for pure W [214, 215, 216]. In order to determine the dominant diffusion mechanism for sintering, several isothermal experiments need to be run using the Mo30W powders. Moreover, the significant difference in activation energies and sintering temperatures for the GA powders compared with the CR and BM powders could represent a change in the dominant diffusion mechanism for sintering at the higher temperature.

While this densification model gives useful insight into the consolidation mechanisms of the different powders, these experiments are also useful in determining the optimum sintering parameters. For the CR and BM materials, 1600°C is high enough that stage II consolidation can fully occur. For the GA powders, it is expected that a temperature above 1800°C would be required to achieve final densities above 95

For NTP cermet fuel applications, the Mo30W feedstock should allow for the fabrication of a high matrix density cermet with a single Mo30W phase. A high density is desired to ensure the metallic matrix is free of interconnected porosity, which can accelerate hydrogen attack and known NTP cermet failure modes. A single Mo30W phase, free of local low melting temperature phases (such as pure Mo) will allow for a high and uniform melting temperature. A reduced sintering temperature is also desired. This will reduce the stresses between the matrix and ceramic fuel particles, resulting from mismatched coefficients of thermal expansion, during sintering. Lower sintering temperatures also typically correspond to finer grain structures, which is desired for the metal matrix to exhibit good mechanical properties as the structural material for the fuel system. Additionally, reduced sintering temperatures limits the temperatures that ceramic fuel particles are exposed to prior to operation, extended high temperature exposure of the fuel form can lead to thermodynamic instability of the compound and degradation. Due to the increased homogeneity and reduced sintering temperatures, the CR feedstock is recommended for future NTP cermet applications requiring a Mo30W matrix material.

5.1.3 Comparison of Sintering Analysis Techniques

The Young and Cuttler initial stage sintering method proved effective for determining the difference in apparent activation energies for the four different Mo30W powders. The MSC method was also used on the CR Mo30W powder to compare techniques. Three different heating rates were used, namely, 50, 100, and 150°C. The mean square residuals, calculated using Equation 3.14 are shown in Figure 5.6 a). The minimum activation energy was determined to be 225 kJ/mol. The Ψ model matched well with the normalized data as for all three heating rates, as seen in Figure 5.6 b), confirming the minimized value. This activation energy matches very closely to the volume diffusion limited activation energy determined using the Young and Cuttler method of 261 $\pm$ 37 kJ/mol. By utilizing both of these techniques, we can assume that the dominant mechanism controlling diffusion for the CR Mo30W powder is volume diffusion.

Both the Young and Cuttler initial stage sintering method and the MSC methods were also to analyze the sintering of the Stanford Advanced ZrC powder. A summary of the calculated activation energies using the two methods is presented in Table 5.3.

The Young and Cuttler method is relatively easy to implement (see example code in Appendix A). It also only requires one CRH experiment at 1 heating rate (ideally at a lower heating rate). It is also useful to compare the densification of similar powders under similar conditions. Despite its usefulness, the largest downside to the Young and Cuttler method is that it does not reveal the dominant sintering mechanism. It also only provides analysis for Stage I sintering. The calculated values are dependent upon the heating rate. And finally, if multiple diffusion mechanisms are dominant, these cannot be decoupled.

The MSC model use more comprehensive, in that it models the entire sintering process (all three stages). Once determined, the MSC can then be used to a limited extent to predict the sintering of the same material under different conditions. Like with the Young and Cuttler model, it does not predict the dominant sintering

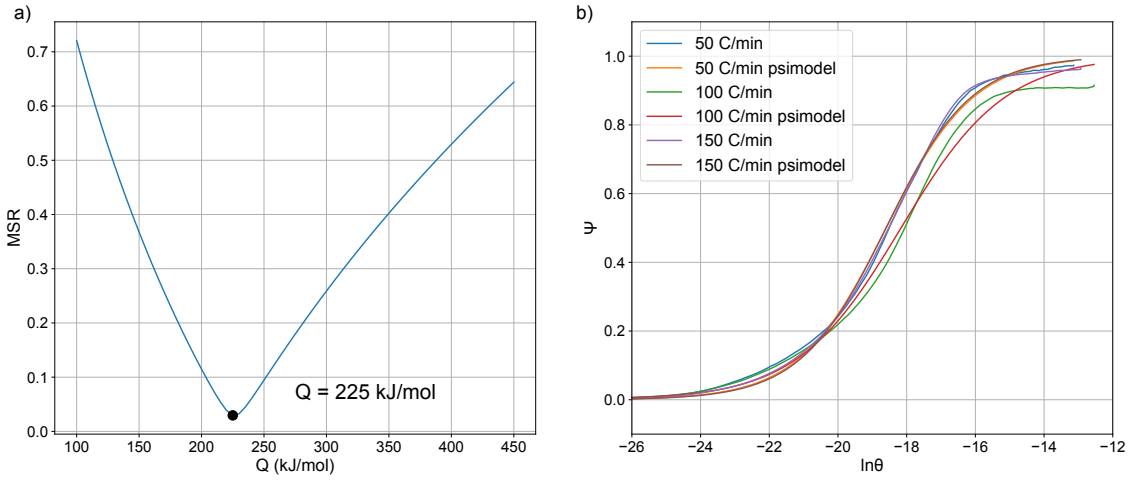


Figure 5.6: a) Mean square residuals for Mo30W and b) the collapsed normalized densification curves with Ψ models.

Table 5.3: Apparent activation energies for sintering for the Mo30W and ZrC powders using the Young and Cutler and Master Sintering Curve models.

Material	nQ (kJ/mol)	Q_B (kJ/mol)	Q_V (kJ/mol)	Q_{MSC} (kJ/mol)
Mo30W	131 ± 18	392 ± 55	261 ± 37	225
ZrC	174 ± 19	521 ± 56	347 ± 38	345

mechanism on its own. Additionally, it requires at least three CRH experiments at different heating rates in order to generate the MSC. Finally, the code is more difficult to implement (see example code in Appendix A).

By using both methods together for the same powder, the dominant sintering mechanism can be predicted, as was done for the CR Mo30W and ZrC powders.

5.1.4 Mo30W-HfN Secondary Phase Formation

The sintering of the Mo30W cermet with both the angular and spherical HfN particles produced a small interfacial region easily visible in backscatter electron imaging (as seen in Figure 4.30). An EDS line scan was performed in order to determine the concentrations of Mo, W, Hf, and N, over the interfacial region. The results of this scan are presented in Figure 5.7. The interfacial region was an order of magnitude large for the angular HfN particle cermets compared with the spherical HfN particle cermets.

There is very little diffusivity data for Hf in Mo and no easily accessible data available for Mo in HfN. Given the limited data, the MoW matrix can be treated as pure Mo to get a rough estimate as to the diffusivity of Hf in MoW. The diffusivity of Hf in pure Mo at 2080°C was determined to be 5×10^{-12} m^2/s [217]. By assuming Hf diffusion in Mo is similar to W diffusion in Mo, an activation energy of diffusion was determined for W in Mo and used for Hf in Mo [201, 191]. From this the diffusivity of Hf in Mo can be estimated to be 2.5×10^{-14} m^2/s at 1600°C, or the sintering temperature. Using a Fick's law one dimensional $\sqrt{Dt}$ approximation, the Hf can be expected to diffuse 40 µm into the metal matrix. This is larger than the observed interfacial phase, however, the addition of the W solute in the Mo matrix likely reduces the diffusivity of Hf in the matrix.

XRD was used to identify the interfacial phase, as seen in Figure 5.8. The phases were fit using a modified Rietveld refinement. In the Mo-W binary system, an Mo_2Hf laves phase forms below 1800°C as seen in the phase diagram in Figure 5.9. XRD

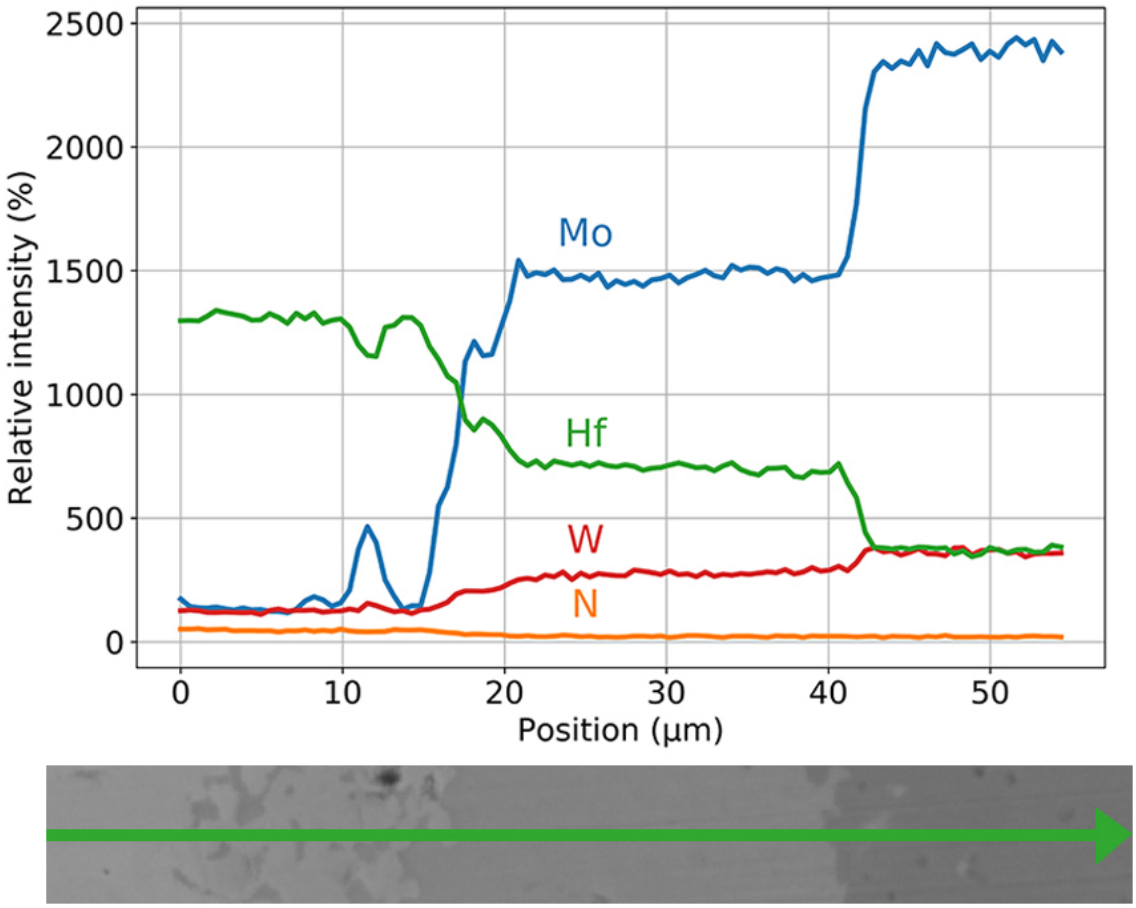


Figure 5.7: EDS line scan of the MoW-HfN cermet crossing the newly formed interfacial region.

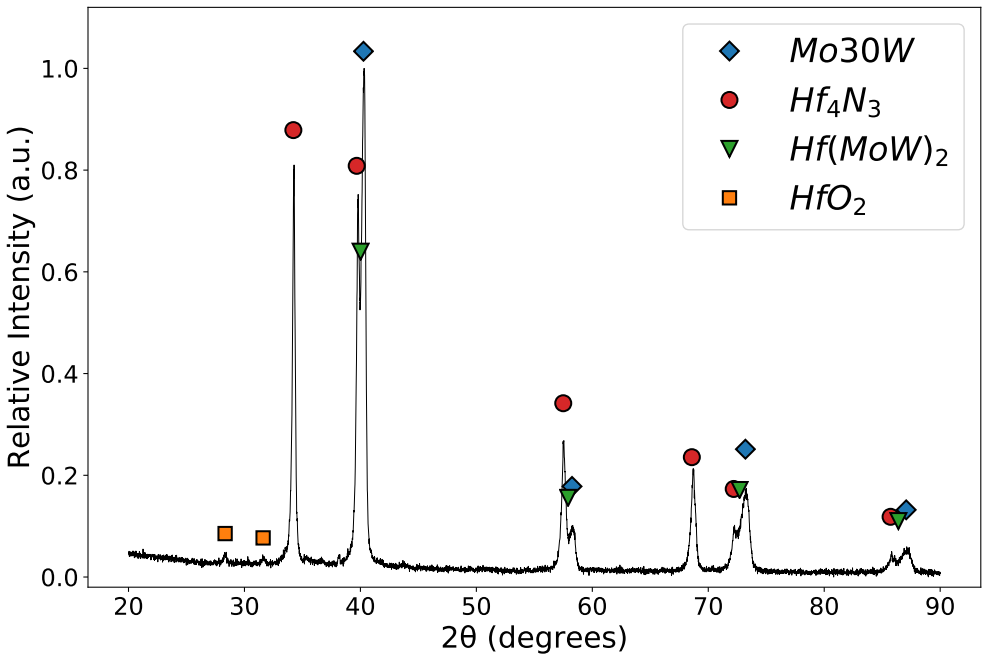


Figure 5.8: XRD Spectra for the Mo30W-50vol-HfN cermet fitted using a modified Rietveld refinement.

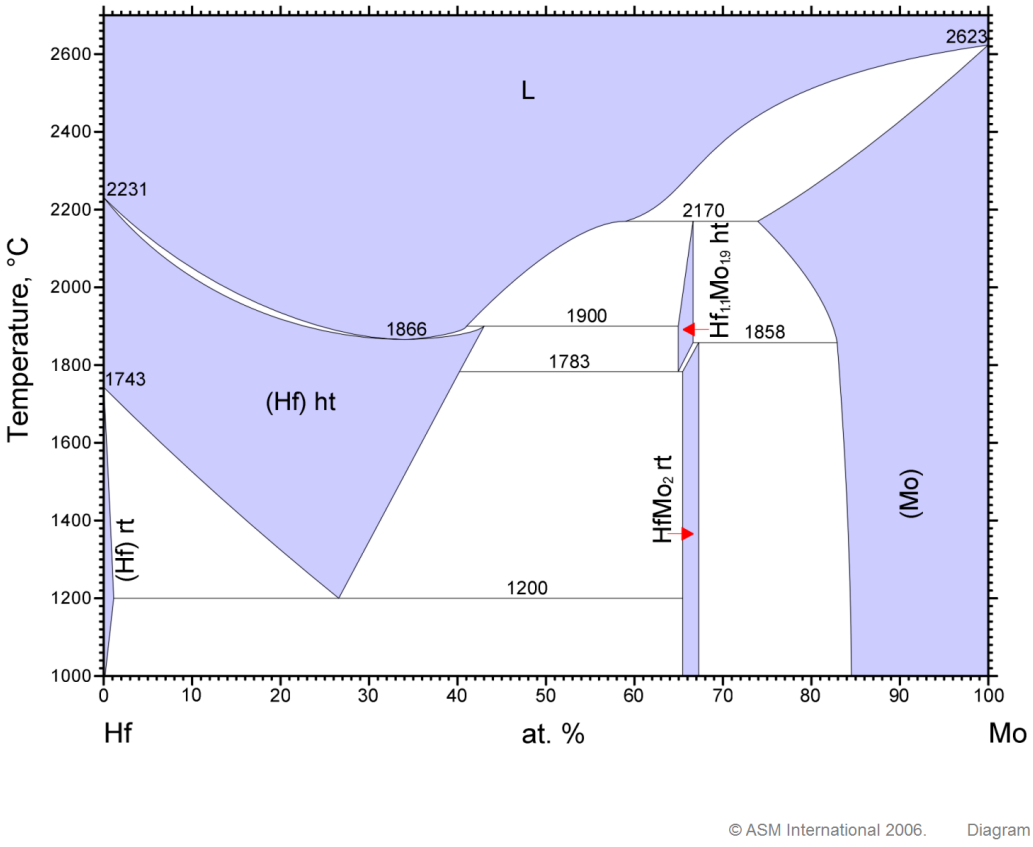


Figure 5.9: Phase diagram for the Mo-HfN system taken from [91].

found evidence of a small amount of a similar phase (less than 1 wt%). It was determined that C15 laves-like phase formed during the powder consolidation process between the Mo30W and the HfN particles. This phase is likely $(MoW)_2Hf$ + N, consisting mostly of $(MoW)_2Hf$. The amount of N is unknown exactly, but it is significantly less than the amount in the HfN phase. Also, the exact ratio of Mo and W is unknown, but the EDS line scans suggest a higher ratio of Mo to W compared with the bulk phase. The use of Thermocalc software confirmed the formation of this phase at the sintering temperature of 1600°C.

5.1.5 Sintering Analysis for Cermet and Cercer

Initial stage sintering analysis using the Young and Cutler method was conducted for both the CR-Mo30W cermets and the ZrC based cercers using all three surrogate types. Like with the final samples fabricated for material properties, a volume loading of 50 and 70% were used for the cermets and 10 and 20% for the cercers.

Corrected density data and displacement rate data are presented in Figure 5.10 for the cermet and pure Cr Mo30W. The pure matrix material began sintering at the lowest temperature, with the peak displacement occurring just above 1100°C. Each material had different displacement rate curves. Interestingly, while onset displacement temperatures varied between materials, the peak displacement temperature for HfN and YSZ spherical particles at each volume loadings were the same at around 1300°C. The cermets with angular HfN did not follow the standard parabolic displacement rates and do not have peak displacement temperatures.

Data from the CRH experiments were used to determine the apparent activation energy of sintering for all the cermet materials. Plots of $\ln\left(\frac{d(\Delta L/L_0)/L_0}{dT}\right)$T) vs $1/T$ are shown in Figure 5.11. The calculated apparent activation energies are listed in Table 5.4. For the spherical YSZ cermet materials, at 50 vol%, nQ for sintering is lower than that of the CR Mo30W. However, once the YSZ reaches 70vol%, nQ increases quite a bit. This suggests that the YSZ helps aid in sintering when at 50vol%, but

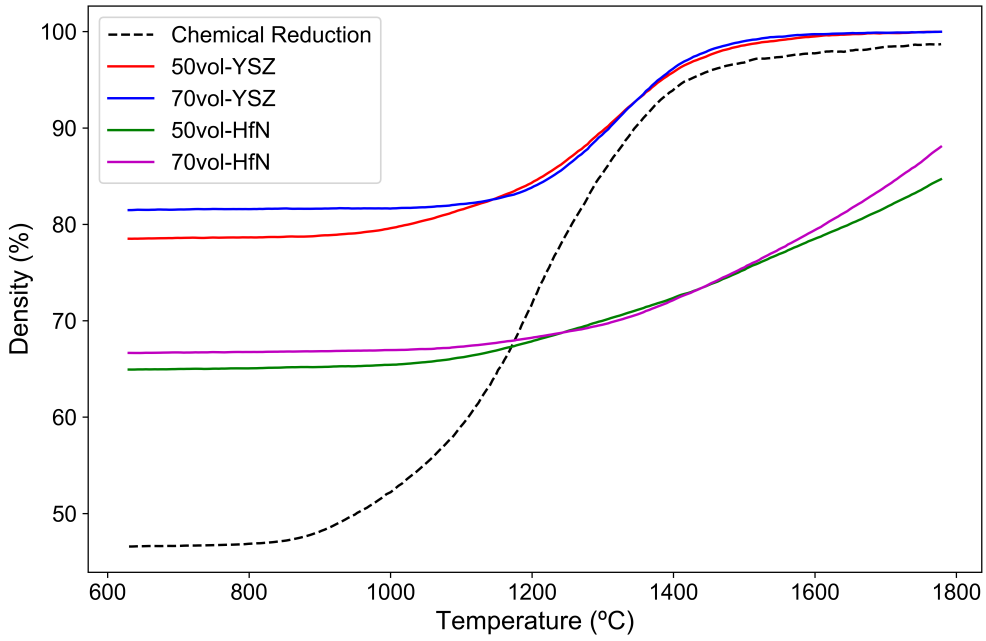


Figure 5.10: Plots of $\ln\left(\frac{d(\Delta L/L_0)/L_0}{dT}\right)$ versus inverse temperature for initial bulk sintering stage of the Mo30W powders.

Table 5.4: Apparent activation energies for the cermet materials determined from initial sintering curve analysis.

Matrix material	Surrogate particle	Surrogate geometry	Volume loading (%)	Activation energy (kJ/mol)
CR Mo30W	None	–	–	131 ± 18
CR Mo30W	YSZ	Spherical	50	105
CR Mo30W	YSZ	Spherical	70	221
CR Mo30W	HfN	Spherical	50	131
CR Mo30W	HfN	Spherical	70	92
CR Mo30W	HfN	Angular	50	117
CR Mo30W	HfN	Angular	70	96

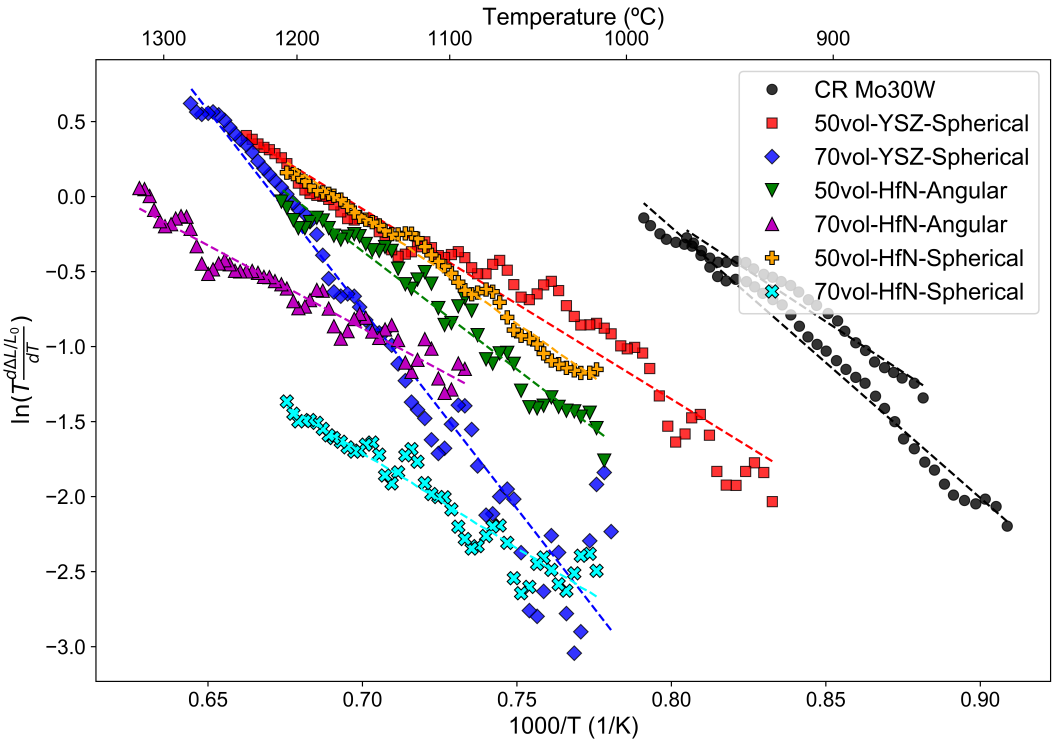


Figure 5.11: Plots of $\ln\left(\frac{d(\Delta L/L_0)/L_0}{dT}\right)$ versus inverse temperature for the initial stage sintering of the CR Mo30W and the cermet materials for volume loadings of 50 and 70%.

starts to become detrimental to the sintering process at a volume loading of 70%, likely due to the reduced amount of Mo30W matrix material available to sinter.

The HfN cermets behave differently than the YSZ cermets. For both geometries, the nQ for the 50vol% was similar to that of pure CR Mo30W. At the 70vol%, the nQ decreases quite a bit. These particles were smaller than the YSZ particles. This likely explains this discrepancy.

The same analysis was conducted for the cercer materials using similar CRH experiments. Plots of $\ln\left(\frac{d(\Delta L/L_0)/L_0}{dT}\right)$T) vs $1/T$ are shown in Figure 5.12 a). Additionally, Figure 5.12 b) contains the densification rate as a function of temperature for the different cercer composites. Pure ZrC was also included. The shift in displacement curves was much less pronounced in the cercer material compared with the cermet materials. This is primarily due to the much lower surrogate particle volume loadings of 10 and 20 %. Both powder compacts with the angular HfN powders experienced a secondary peak displacement. This secondary peak likely corresponds to the onset of the formation of the carbonitride phase discussed earlier. A small secondary peak was also observed for the 20vol% spherical HfN powder compact. The formation of the carbonitride phase is reduced in the spherical powders due to the smaller particle matrix interface compared with the angular particles.

Results from the Young and Cuttler method for the cercer particles are presented in Figure 5.13. The calculated apparent activation energies are also included in Table 5.5. The apparent activation energies for all cermet materials were less than the pure ZrC, except for the ZrC-20vol-YSZ (spherical) cercer. With both spherical powders, as the volume loading went from 10 to 20 vol%, the apparent activation energy increased. This was not true for the powder compacts with the angular HfN particles, which were almost identical.

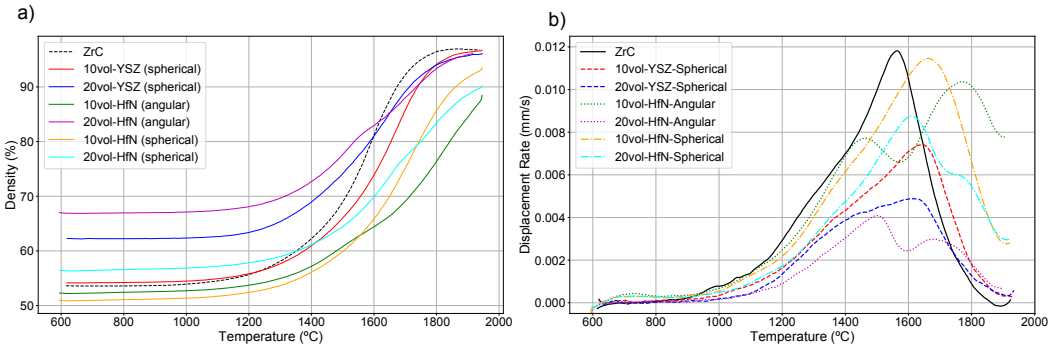


Figure 5.12: Plots of $\ln\left(\frac{d(\Delta L/L_0)/L_0}{dT}\right)$ versus inverse temperature for initial bulk sintering stage of the Mo30W powders.

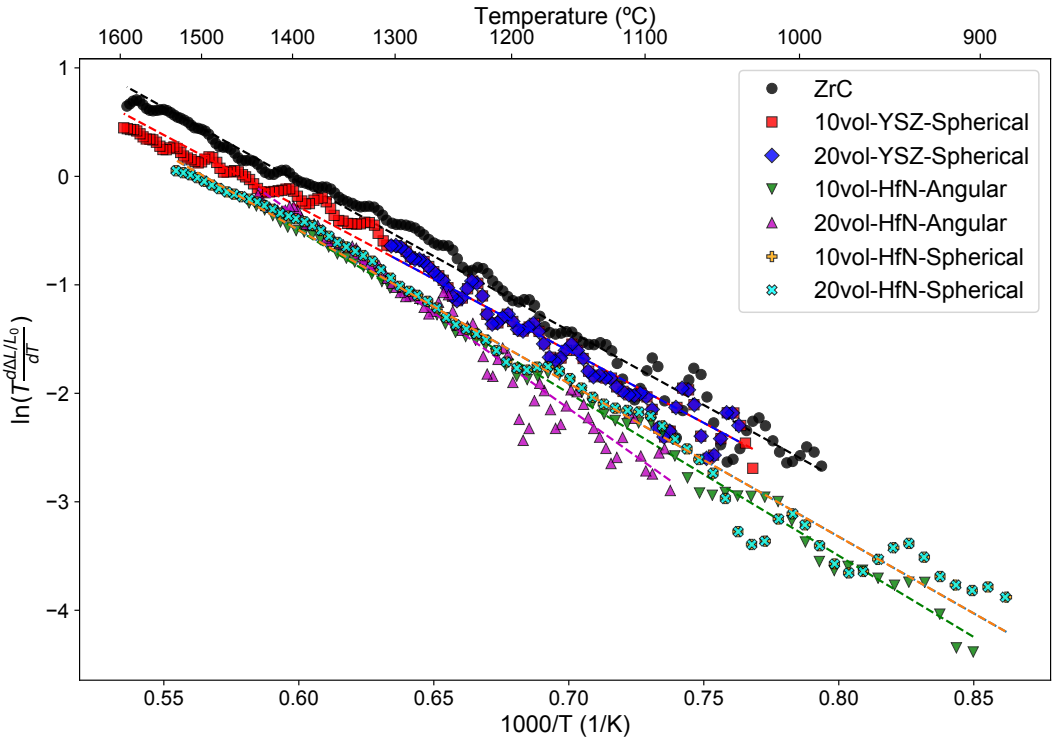


Figure 5.13: Plots of $\ln\left(\frac{d(\Delta L/L_0)/L_0}{dT}\right)$ versus inverse temperature for the initial stage sintering of the ZrC and the cercer materials for volume loadings of 10 and 20%.

Table 5.5: Apparent activation energies for the cercer materials determined from initial sintering curve analysis.

Matrix material	Surrogate particle	Surrogate geometry	Volume loading (%)	Activation energy (kJ/mol)
ZrC	None	–	–	174 ± 19
ZrC	YSZ	Spherical	10	110
ZrC	YSZ	Spherical	20	195
ZrC	HfN	Spherical	10	125
ZrC	HfN	Spherical	20	147
ZrC	HfN	Angular	10	118
ZrC	HfN	Angular	20	120

5.2 Thermophysical Properties

5.2.1 Coefficient of Thermal Expansion

As noted in Chapter 4, the CTE of Mo30W was greater than that of either Mo and W. Figure 5.14 contains the CTE of Mo30W, both large and medium grained and as determined from high temperature XRD, and pure Mo and W. Most binary alloys have a lower CTE compared with the primary material, which would by Mo for Mo30W. However, in some cases, there can be an increase in CTE compared to both alloying elements.

The Blackburn equation (Equation 2.33) is one model that predicts an increase in CTE with the addition of an alloying element [89]. This equation is also plotted in Figure 5.14. This model dramatically underpredicts the CTE value determined from the data. This deviation could be real behavior. It could also be a result of increased CTE due to smaller grain size. In order to determine the true effect of alloying Mo with W, either very large grained or preferably single crystal Mo30W should be compared directly with similar grain sized Mo and W.

The CTE of the composite materials for both the spherical YSZ and angular HfN composites fell between the CTE of the Mo30W matrix and the ceramic particle. The data was compared with the models discussed in Chapter 2. Figure 5.15 compares shows the models compared with the Mo30W-HfN cermet. Most of the models overpredicted the CTE by a wide margin. It did fit well with the model by Tummala and Friedberg (Equation 2.35), even though this model was originally developed for dilute suspensions [93]. This fit can be explained by the excellent particle matrix interface from the interfacial phase. Figure 5.16 illustrates the fit of the CTE data from RT to 1000°C. At higher temperatures, the Tummala model slightly underpredicts the CTE for Mo30W-70vol-HfN.

Unlike with the Mo30W-HfN angular cermet, the Mo30W-YSZ cermets did not fit well to any model over a large temperature range, as illustrated in Figure 5.17.

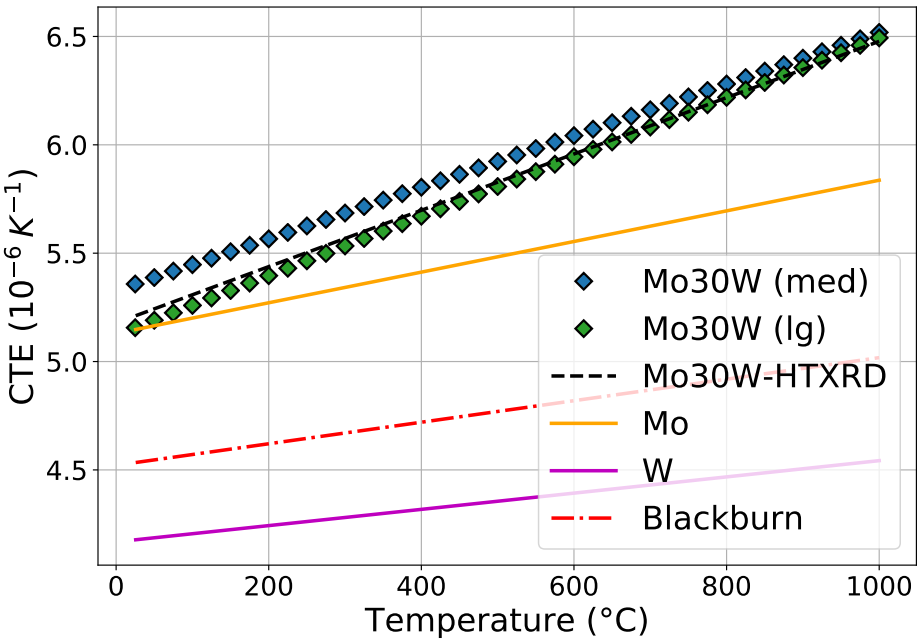


Figure 5.14: CTE of Mo30W (medium and large grain size), pure Mo and pure W, taken from Martienssen and Warlimont [55], and the predicted CTE using the Blackburn model.

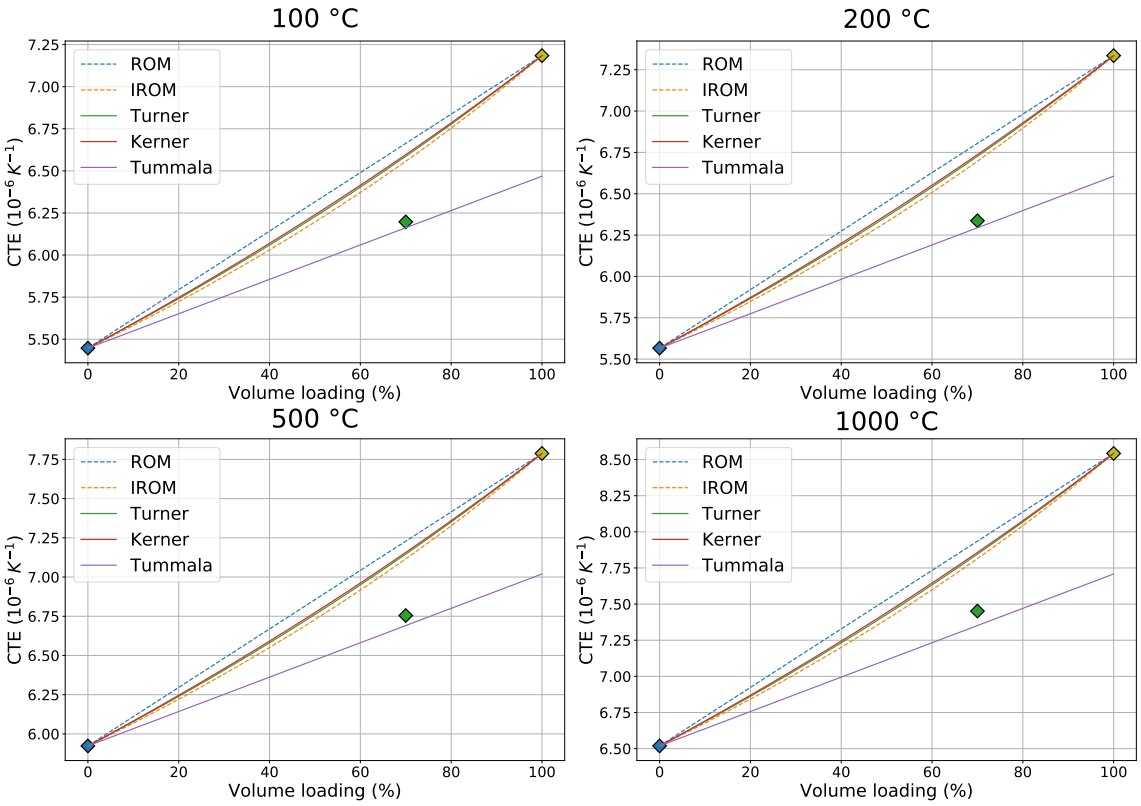


Figure 5.15: CTE model fits as a function of volume loading for Mo30W-HfN cermet at 100, 200, 500, and 1000°C.

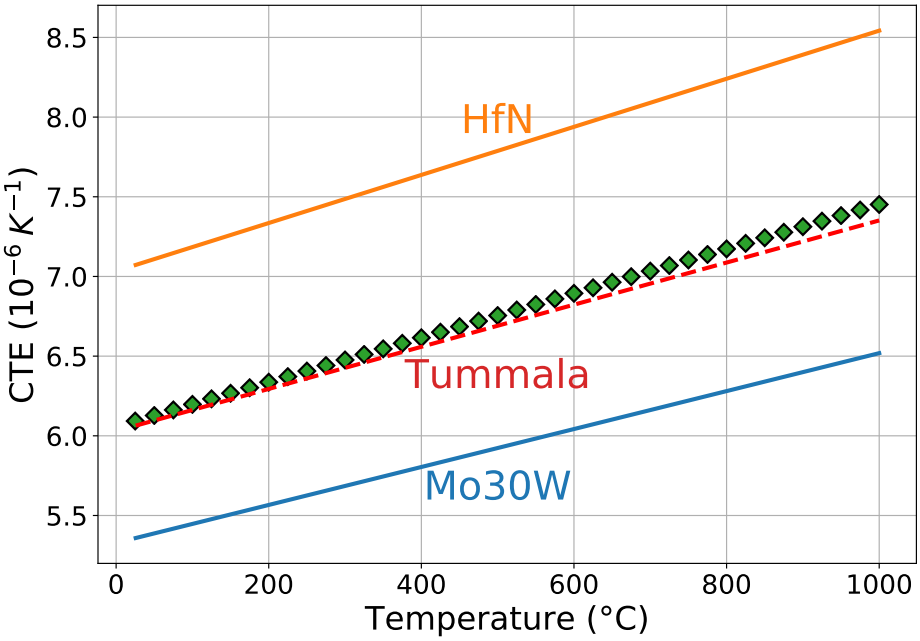


Figure 5.16: Mo30W-70vol-HfN (angular) CTE fit to the model derived by Tummalla et al.

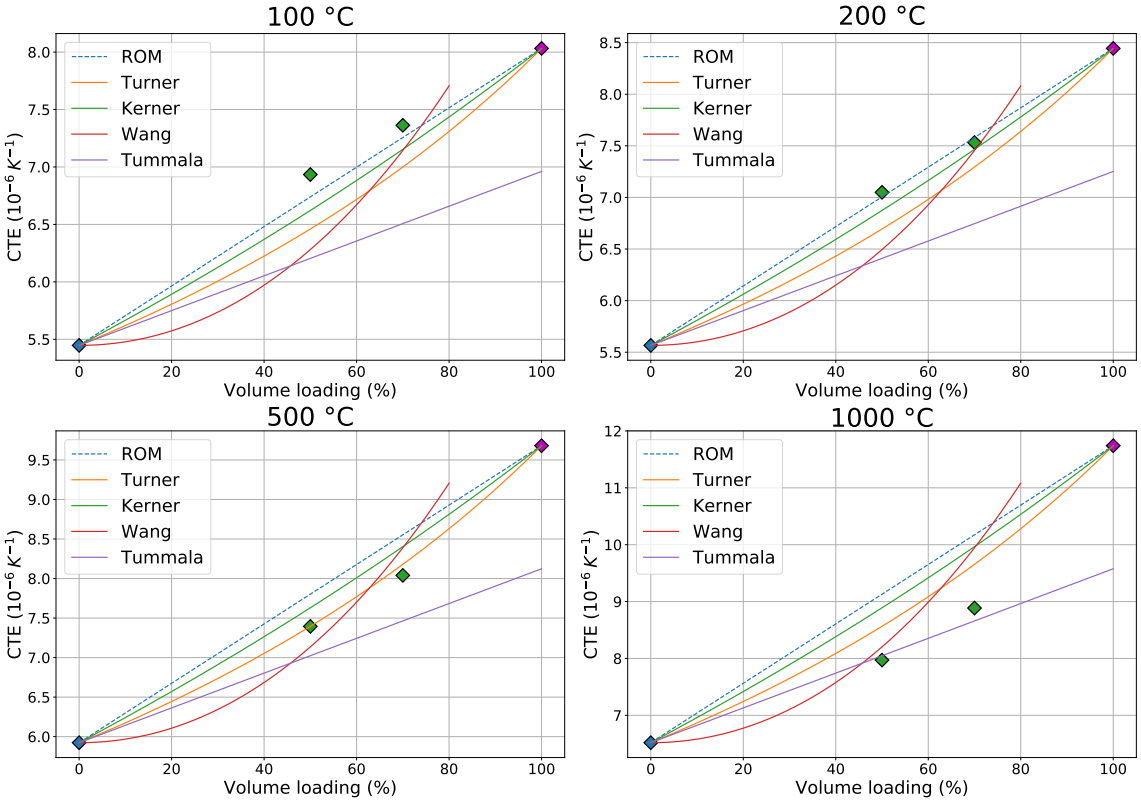


Figure 5.17: CTE model fits as a function of volume loading for Mo30W-YSZ cermet at 50 and 70 vol% at 100, 200, 500, and 1000°C.

At lower temperatures, the data fit well with the ROM model. However, as the temperature increased, the models began to overpredict the CTE. At the highest temperatures, the data fit best with the Tummala model. Instead of the fitting the MoW-YSZ CTE data to a single model, a range of expected CTE values was used, as shown in Figure 5.18. The ROM model was used as the upper limit and the Tummala model was used as the lower limit. Below 200°C the data falls above the projected range and above 800°C, it drops below the expected range.

Based on the model fit for the Mo30W-HfN and YSZ cermets, a predicted CTE was determined for 50 and 70 vol% cermets with UO_2 and UN, as presented in Figure 5.19. A range was provided for the UO_2 cermets, using the ROM as the upper bound and Tummala model as the lower bound. The UN cermets used the Tummala model. While these values can provide a general idea as to the expected CTE to the uranium containing cermets, these values have a low level of confidence. Measurement of the CTE of actual uranium containing cermets is needed to validate these results.

A similar effort was made to fit ZrC-HfN cercer CTE to a model, as shown in Figure 5.20. However, none of the models were able to predict the unique behavior of the ZrC-HfN. For the ZrC-10vol-HfN, the CTE always fell in between that of the ZrC and the HfN. If it was following ROM behavior, its CTE is that of what would be expected for a 70 vol% cercer as opposed to a 10 vol% cercer. Until around 800°C, the CTE of the ZrC-20vol-HfN cercer was lower than that of the pure ZrC and HfN. The most likely reason for this odd behavior is the formation of a new phase. Since the sintering temperature was low enough, no secondary phase should have formed according to XRD and EDS results. However, a small amount of inter diffusion into either the particle or the matrix could be enough to affect the CTE in this way. Since the CTE varies greater than the range of the individual component materials, there is no point in making a prediction for the CTE of ZrC-UN cercer, as it would need to include a wide range and would not provide useful for design of a system utilizing it.

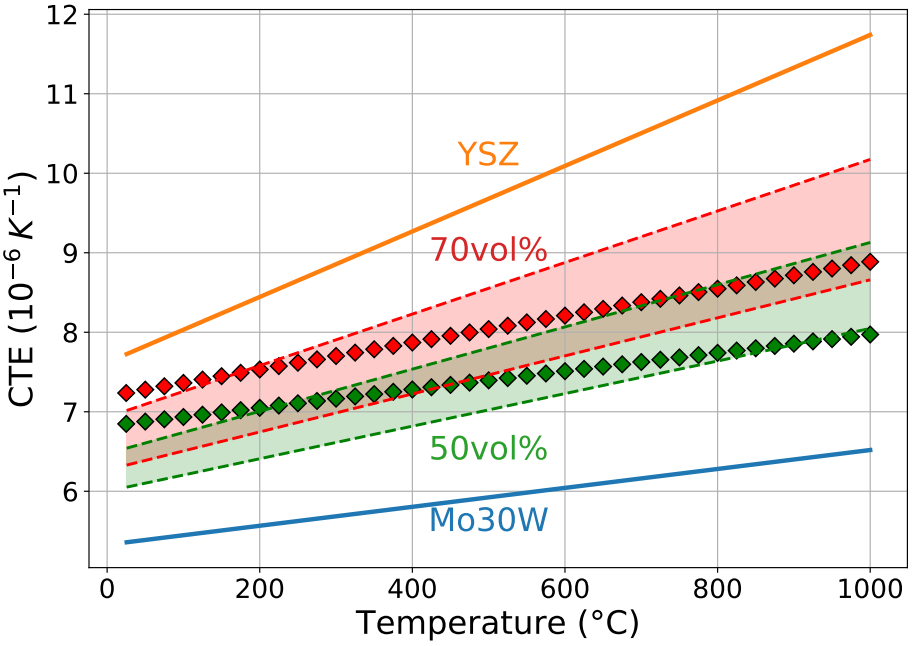


Figure 5.18: Range of predicted Mo30W-YSZ (spherical) CTE using the ROM model as an upper bound and the model derived by Tumala et al. as the lower bound.

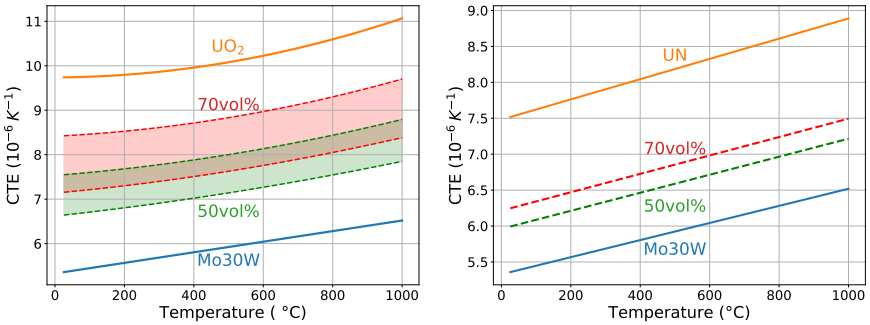


Figure 5.19: Predicted CTE for Mo30W cermets with a) 50 and 70 vol% UO_2 and b) 50 and 70vol% UN. CTE data for UO_2 and UN were taken from Fink et al. [21] and Hayes et al. [92], respectively. The range provided for the predicted UO_2 cermets were bound by the ROM and the model by Tummala et al. The value for the UN cermet was predicted by Tummala et al. [93].

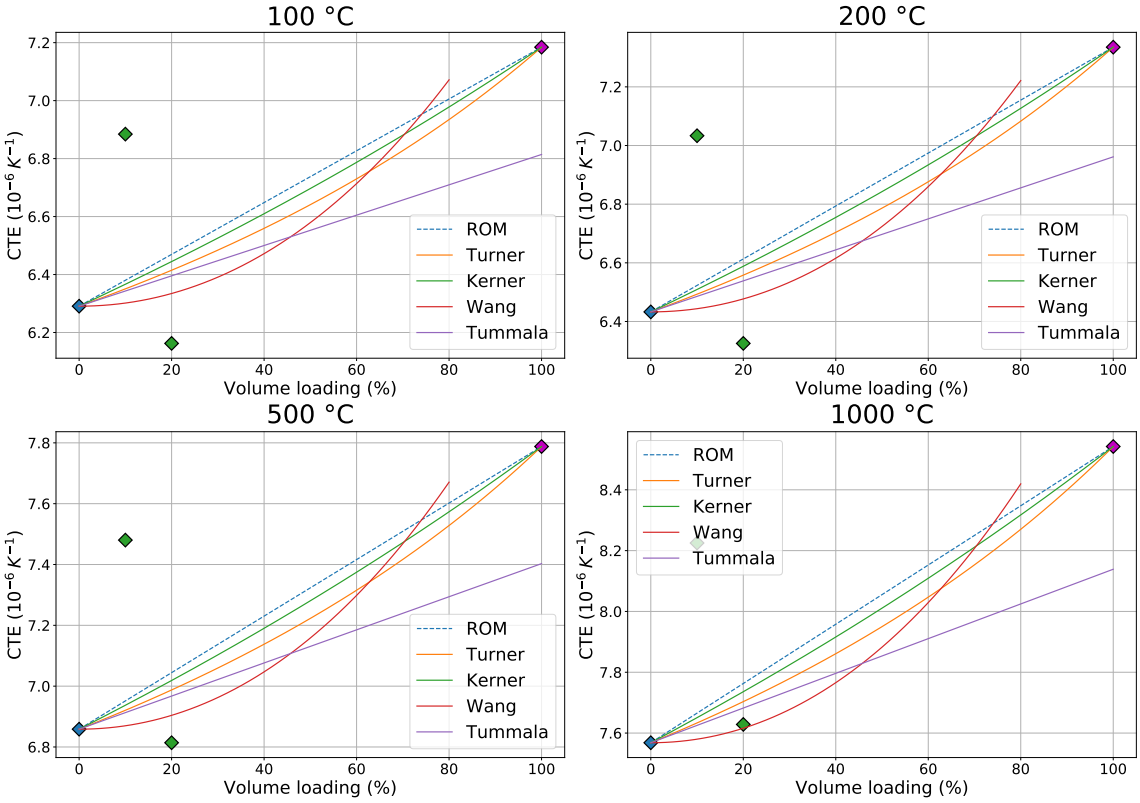


Figure 5.20: CTE model fits as a function of volume loading for ZrC-HfN cercer at 100, 200, 500, and 1000°C.

5.2.2 Specific Heat Capacity

As expected, the C_P of Mo30W falls in between that of Mo and W, as seen in Figure 5.21. The ROM model (Equation 5.4) for C_P is also plotted. The measured value is slightly higher than the predicted value. This could be a result of one of two things. First, the Mo30W alloy may not be exactly 30 wt% W. Second, the literature values are for high purity Mo and W [55], while the Mo30W material used had a lot of impurities, including a high oxygen content (as seen in Table 4.2). This could also raise the heat capacity by the small amount needed to match the ROM model.

Using the fitting parameters from Table 4.13 and the ROM models, a master model was determined for the heat capacity of cermet and cercer materials. Equation 5.4 defines the heat capacity of the composite material as a function of temperature ($C_{P,c}(T)$):

$$C_{P,c}(T) = \left[f_f \rho_f C_{P,f}(T) + (1 - f_f)\rho_m C_{P,m}(T)\right]\rho_c^{-1} \tag{5.4}$$

f_f is the volume fraction of the fuel particle, $C_{P,f}(T)$ and $C_{P,m}(T)$ are the temperature dependent heat capacity functions for the fuel and matrix, respectively, ρ_f and ρ_p are the densities for the fuel and matrix, respectively, and ρ_c is the density of the composite material defined by Equation 5.5 [149].

$$\rho_c = f_f \rho_f + (1 - f_f)\rho_m \tag{5.5}$$

First, Equation 5.4 was used to fit the data for the surrogate cermets and cercers. The fit of this model with the C_P date is presented in Figures 5.22 and 5.23 for the cermet materials, and in Figure 5.24 for the ZrC-HfN cercer. The model fits the data for the Mo30W-YSZ and ZrC-HfN composites well, with only a slight deviation observed in the Mo30W-YSZ data above 600°C. The model is less accurate with the Mo30W-HfN cermet. This could be due to a few reasons. The values of heat capacity for Mo30W and HfN are very similar. Since the heat capacity of HfN depends heavily

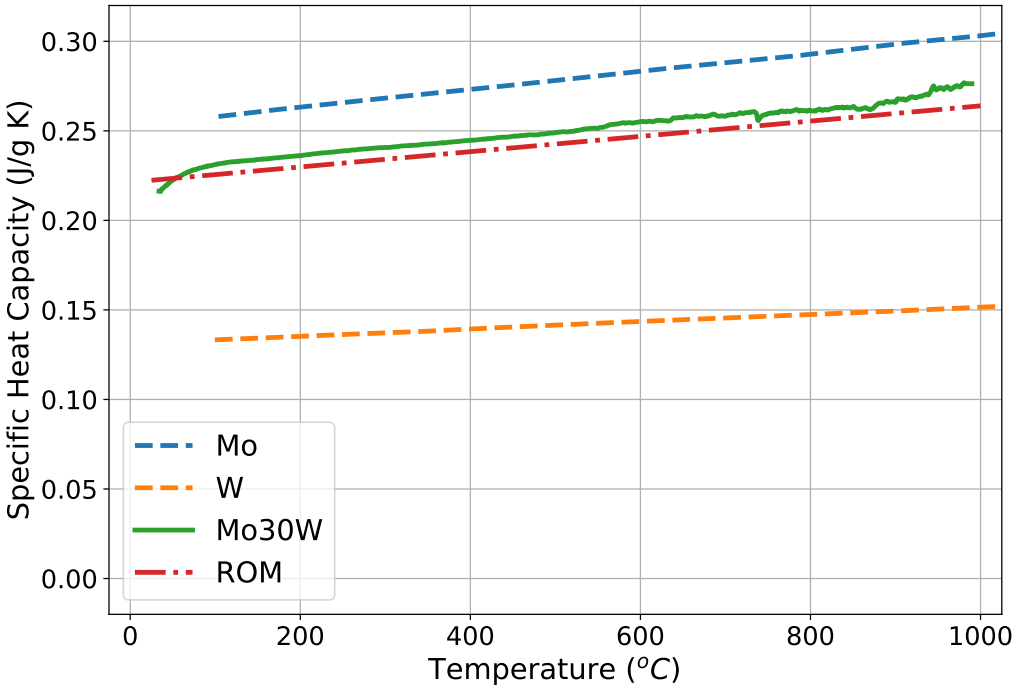


Figure 5.21: Specific heat capacity of Mo30W compared with pure Mo and W. The ROM model for heat capacity is also plotted. The data for Mo and W comes from [55].

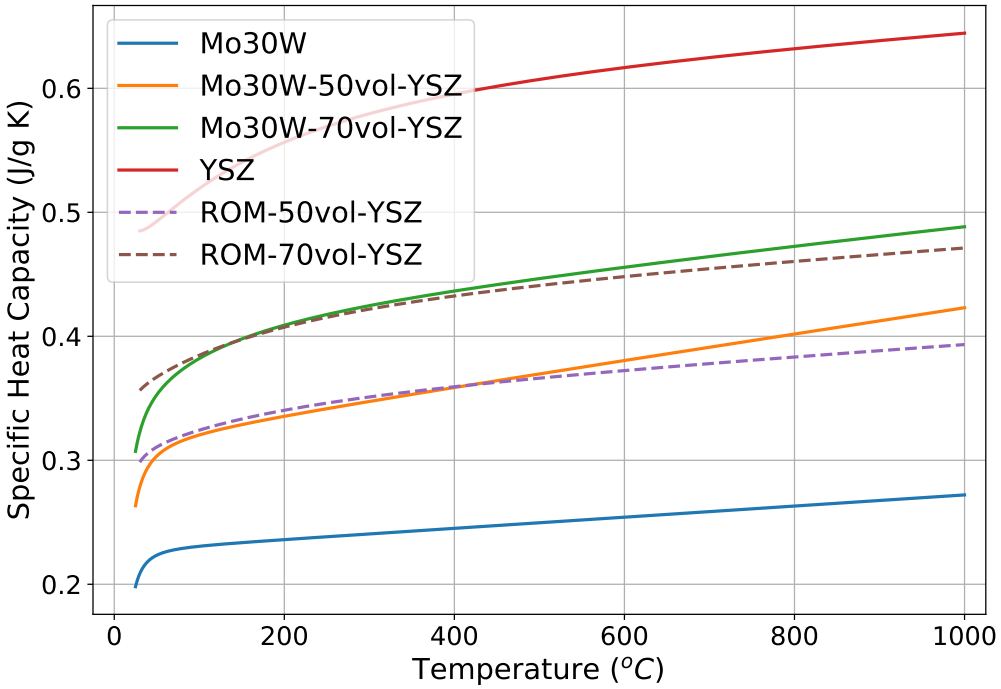


Figure 5.22: Specific heat capacity of Mo30W, Mo30W-50vol-YSZ, Mo30W-70vol-YSZ, and YSZ taken from [41]. The ROM models for 50 and 70vol% were also included.

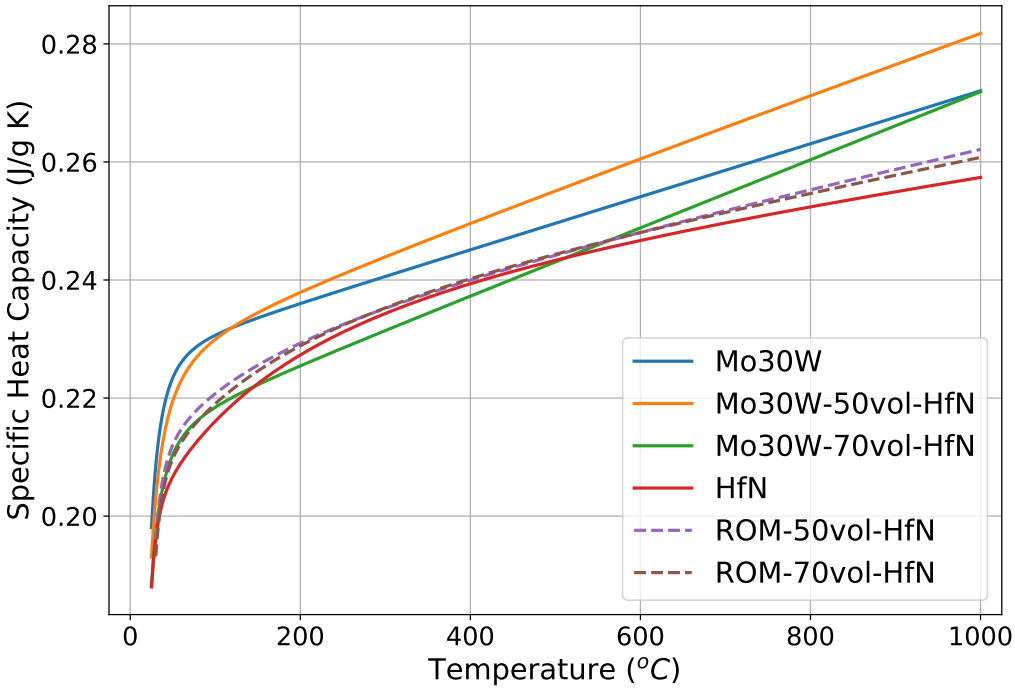


Figure 5.23: Specific heat capacity of Mo30W, Mo30W-50vol-HfN, Mo30W-70vol-HfN, and HfN. The ROM models for 50 and 70vol% were also included.

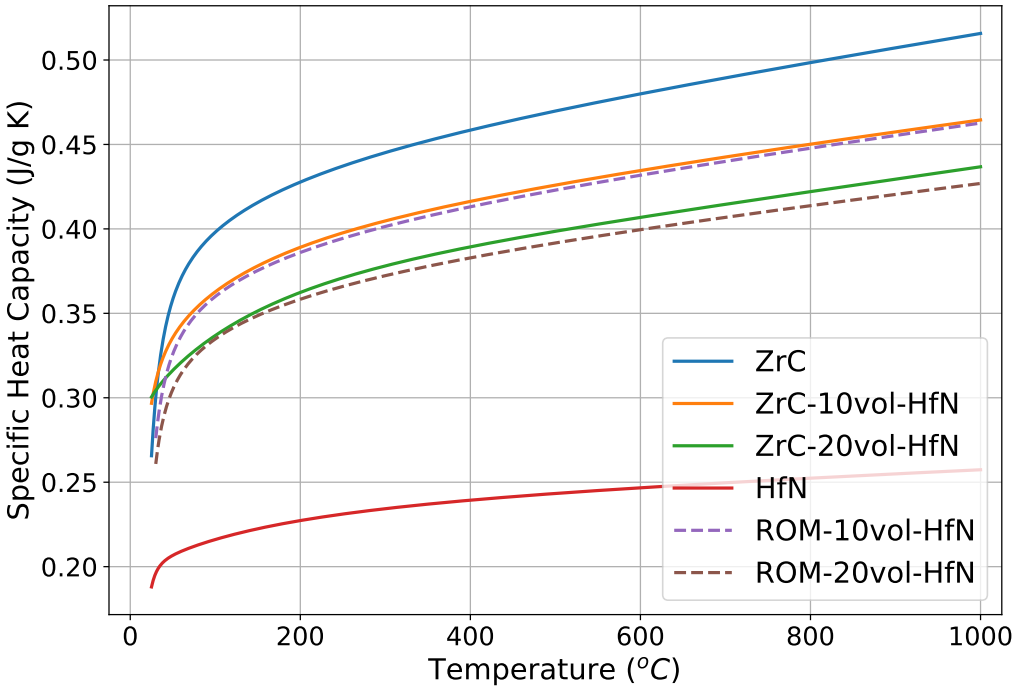


Figure 5.24: Specific heat capacity of ZrC, ZrC-10vol-HfN, ZrC-20vol-HfN, and HfN. The ROM models for 10 and 20vol% were also included.

on the stoichiometry, any variations in the feedstock material could alter the value, causing it to shift. Also, as discussed previously, during sintering the Mo30W and HfN formed an interfacial phase. This diffusion could result in a preferential loss of either Hf or N, changing the composition of the HfN phase, resulting in a higher or lower heat capacity.

Using the C_P equations discussed in Chapter 2 for UO_2 and UN and the fitted models for Mo30W and ZrC determined in Chapter 4, the models for two different volume loadings are plotted in Figure 5.25 up to 1000°C.

5.2.3 Thermal Conductivity

The thermal conductivity of a material is dependent upon both the electron and phonon contributions. For pure metals, the electrons are the dominant contribution. Because of this, the thermal conductivity can be directly related to the electrical conductivity. According to the Wiedemann-Franz law, the ratio of the thermal conductivity to the electrical conductivity is directly proportional to the temperature, as seen in Equation 5.6 [218].

$$\frac{\kappa}{\sigma} = LT \tag{5.6}$$

κ (W/mk) is the conductivity, σ is the electrical conductivity (S/m), T is the absolute temperature (K), and L is the Lorenz number ($W\Omega K^{-1}$). Ideally, L is considered to be a constant of 2.44×10^{-8}. In reality, L is only constant at lower temperatures. As the temperature increases, the value for L also increases. The calculated Lorenz numbers for Mo30W is plotted in Figure 5.26.

As discussed in Chapter 2, the thermal conductivity of binary alloys in solid solution does not follow a simple rule of mixtures. This is apparent for Mo30W in Figure 4.64, when compared directly with pure Mo and W. Using Equation 2.20, the thermal conductivity of Mo30W can be directly compared to that of pure Mo and W. The constant k can also be solved for. Figure 5.27 a) through e) contains the results of the fit to Equation 2.20, with the calculated k values from 50 to 700°C. The value

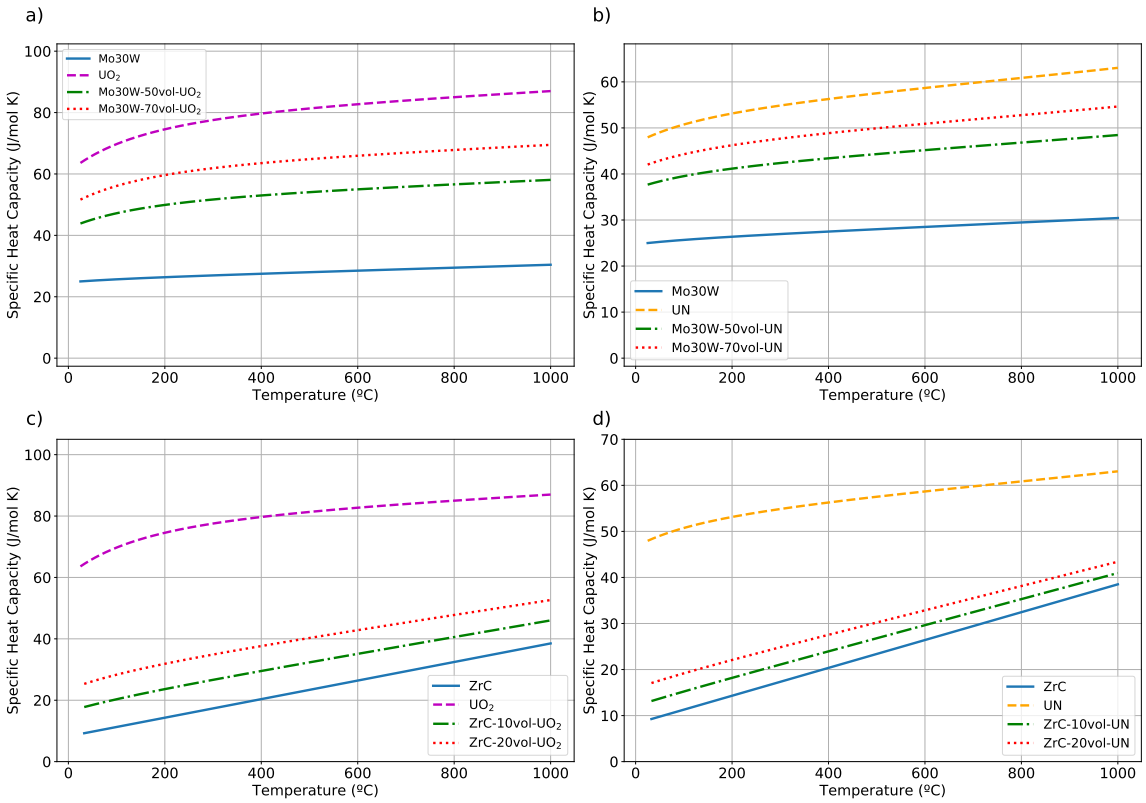


Figure 5.25: Predicted heat capacity for a) Mo30W-YSZ cermets, b) Mo30W-HfN cermets, c) ZrC-YSZ cercers, and d) ZrC-HfN cercers. The reference matrix and fuel particle heat capacities are also provided. The UO_2 and UN values were taken from [21] and [39].

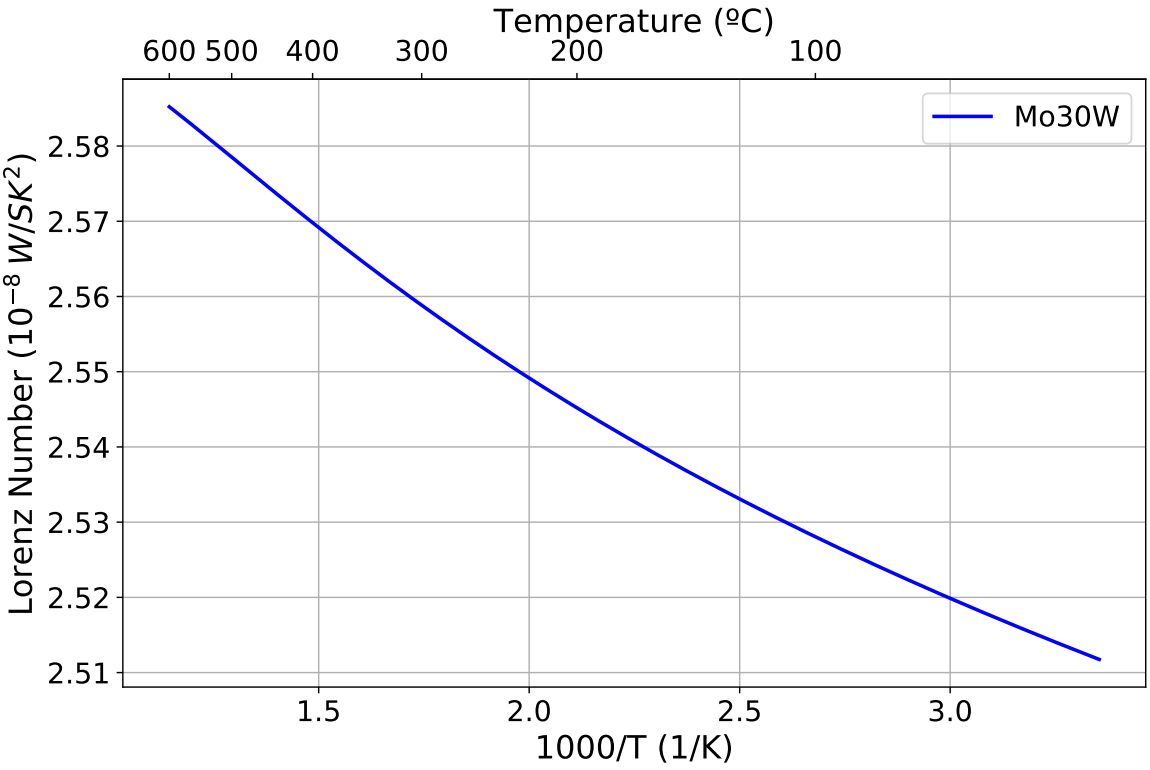


Figure 5.26: Calculated Lorenz number for Mo30W up to 600°C.

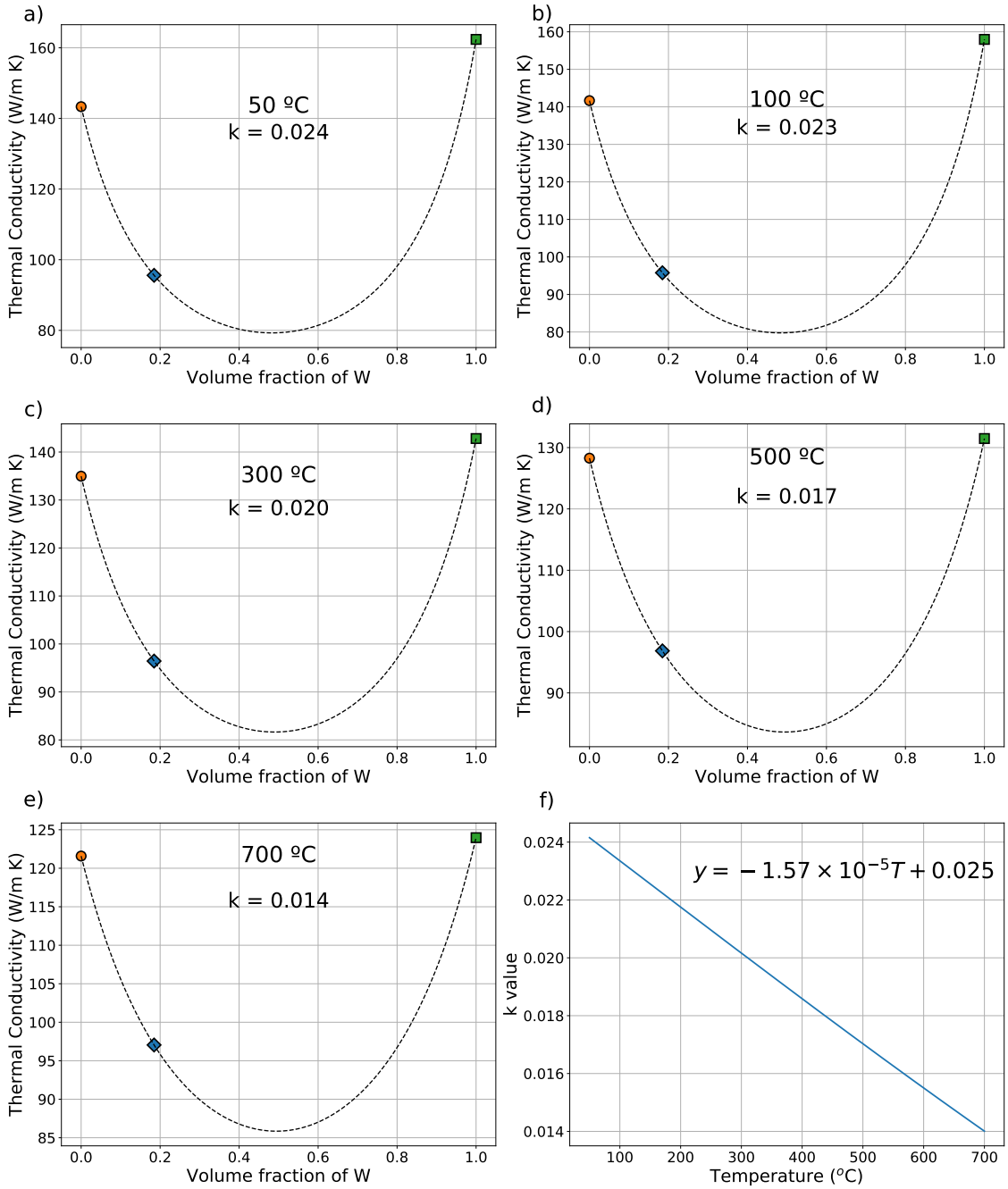


Figure 5.27: a) through e) the thermal conductivity of Mo30W fitted to Equation 2.20 from 50 to 700°C and f) the relationship between the k value and temperature.

of k is actually seen to be decreasing with increasing temperature, as shown in Figure 5.27 f). This is a result of the Lorenz number increasing with increasing temperature, as Equation 2.20 is only valid with a constant Lorenz number, since it is actually based on the electrical conductivity [145]. The k value actually follows closely to a linear relationship with respect to temperature.

The thermal conductivity can follow a variety of models depending on the particle interface, particle spacing, and particle geometry. Because of this, it was expected that the MoW-YSZ and MoW-HfN cermets would follow different models. Several models were tested for each matrix, particle combination. The ROM and IROM models provided the maximum and minimum expected values. Literature data from Schlichting et al. was used for the thermal conductivity of the YSZ [26]. Figure 5.28 contains the results to the model fits for Mo30W-YSZ cermets at four different temperatures from 100 to 600°C. While the Bruggeman theoretical model (Equation 2.28) fit closely and only overpredicted the conductivity a little, the Lewis and Nielsen semi-theoretical model (Equation 2.29) was the best fit. The Bruggeman theoretical model was derived assuming dilute suspensions and 50 and 70vol% are well above the limit. The Lewis and Nielsen semi-theoretical model had empirically derived factors for spherical particles randomly distributed in the matrix. For this reason, it was the best fit. The model is presented with the data over the entire temperature range in Figure 5.29 a).

The same models were compared with the thermal conductivity of the Mo30W 50 and 70 vol% angular HfN cermets. These results are presented in Figure 5.30. HfN literature data was used from Opeka et al. [38]. To account for the porosity of the HfN (resulting in a lower thermal conductivity) the Percolation model presented in Equation 5.7 was used to account for the lower expected thermal conductivity of the HfN feedstock [219].

$$\kappa = \kappa_0(1-\phi)^3 \tag{5.7}$$

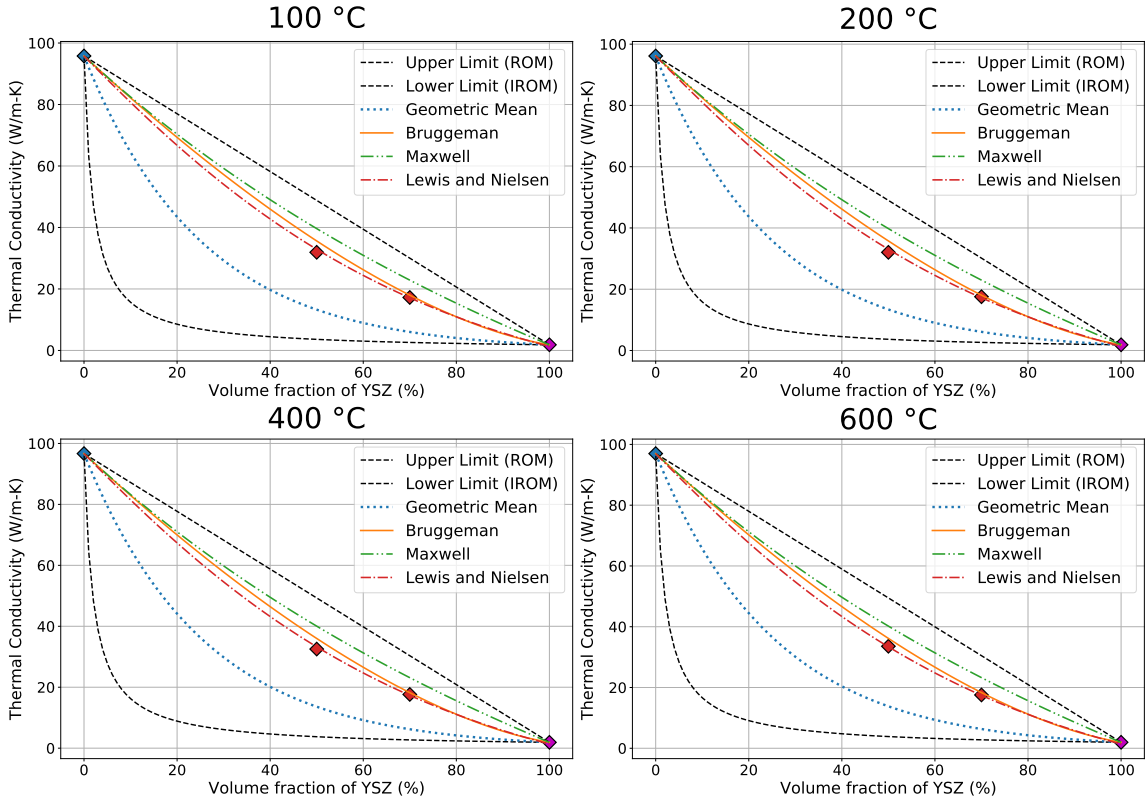


Figure 5.28: Model fits for the thermal conductivity of the Mo30W-YSZ composites at 100, 200, 400, and 600°C. The upper and lower bounds are represented by the ROM and IROM models, respectively.

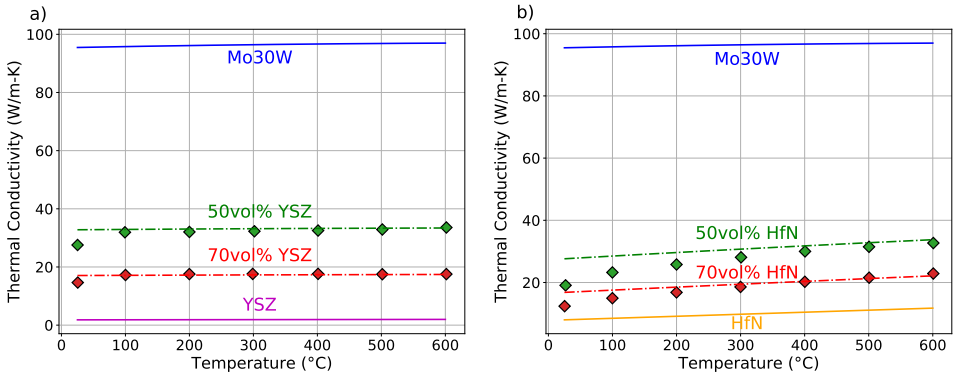


Figure 5.29: Model fits for the thermal conductivity of the a) Mo30W-YSZ and b) Mo30W-HfN cermet composites from 30 to 600°C. The Mo30W-YSZ cermets are fit to the Lewis and Nielsen semi-theoretical model and the Mo30W-HfN is fit to the geometric mean model.

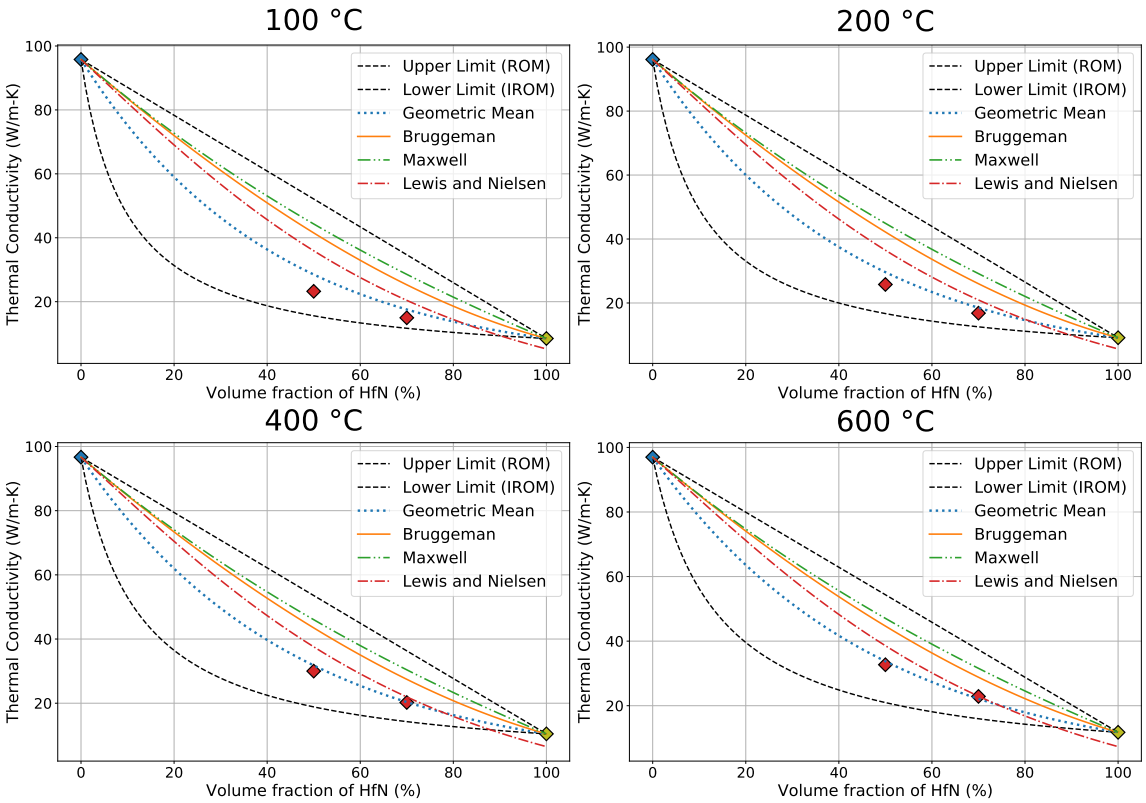


Figure 5.30: Model fits for the thermal conductivity of the Mo30W-HfN composites at 100, 200, 400, and 600°C. The upper and lower bounds are represented by the ROM and IROM models, respectively.

κ is the thermal conductivity of the porous material, κ_0 is the conductivity of the fully dense material, and ϕ is the porosity. The cermets with the angular HfN particles had a greater loss in thermal conductivity compared with the cermets containing spherical YSZ particles, relative to the particle thermal conductivity. This is due to the angular particles having a much larger interfacial area compared with the spherical particles at similar volume loadings. At higher temperatures, the geometric model (Equation 2.27 is the best fit, with the model lining up almost perfectly at 400 and 600°C. At lower temperatures, the model slightly overpredicts the results, with around a 20% error at 100°C and less than a 15% error at 200°C. The geometric model is presented with the data over the entire temperature range in Figure 5.29 b). It is interesting to note that for non-spherical particles, the Lewis and Nielsen model breaks down at high volume loadings.

Using the Lewis and Nielsen model for the oxide cermet and the geometric mean model for the nitrite cermet, predictive thermal conductivity models were made using the Mo30W thermal conductivity and literature data from Gibby et al. for UO_2 and from Ross et al. for UN [139, 37]. The results of this model are presented in Figure 5.31. It is important to note that this model is only valid for spherical UO_2 particles and for angular HfN particles, to match the surrogate models. These models could be off by as high as 20% in some areas. However, despite the shortcomings, this model proves a useful tool in predicting the thermal conductivity of the cermet materials.

Since the thermal conductivity of ZrC and HfN were much closer than that of the Mo30W and HfN, the models all predict values that are much closer together or around 8% difference. Figure 5.32 contains the thermal conductivity of the ZrC-angular HfN (10 and 20 vol%) cercer materials compared with the different thermal conductivity composite models from 100 to 600°C. The models all underpredict the thermal conductivity of the ZrC-10vol-HfN cercer at every temperature. At lower temperatures, below 200°C, both the geometric mean and Lewis and Nielsen models match well. However, above this, the simple series ROM model is the best predictor.

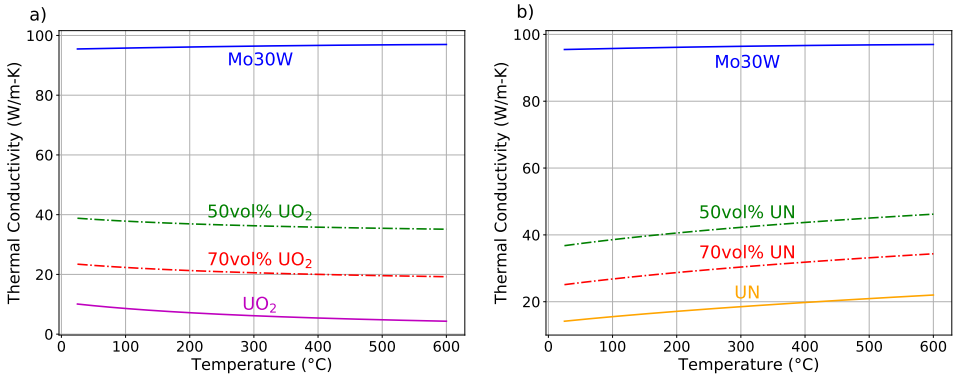


Figure 5.31: Predicted thermal conductivity for a) Mo30W-UO_2 and b) Mo30W-UN cermet composites at 50 and 70 vol% from 30 to 600°C. The Mo30W-UO_2 cermet uses Lewis and Nielsen semi-theoretical model and the Mo30W-UN cermet uses the geometric mean model.

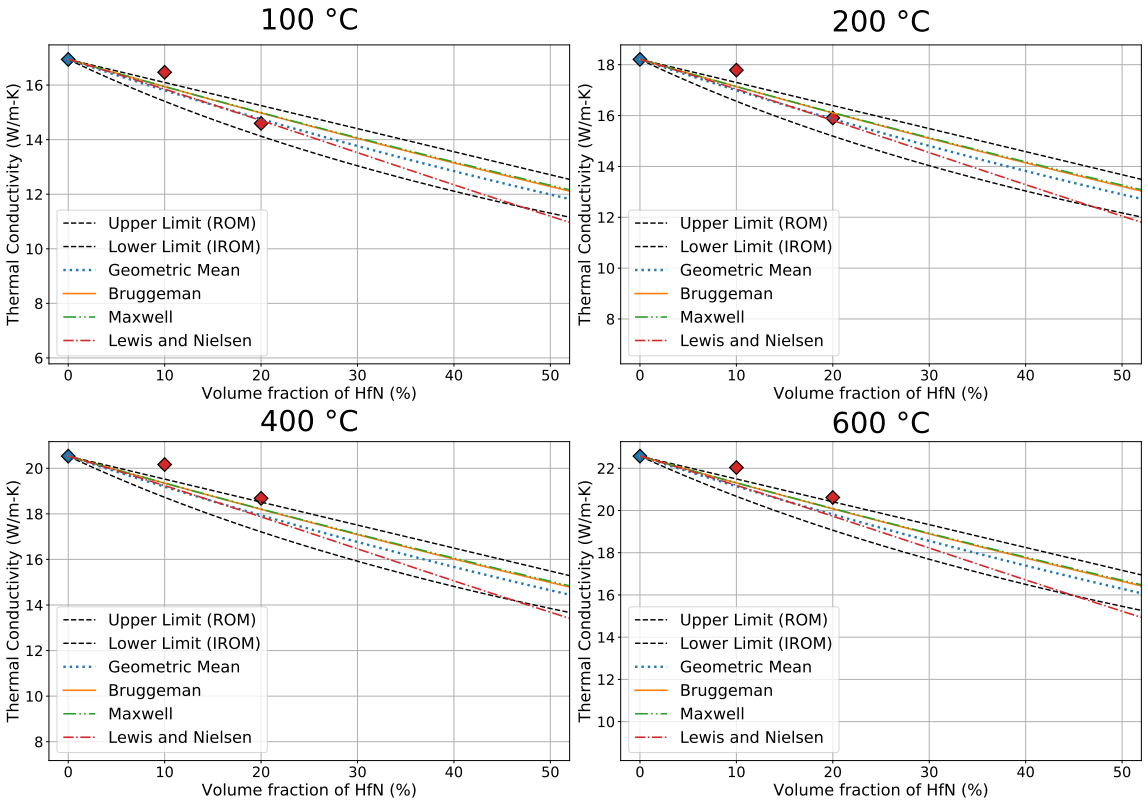


Figure 5.32: Model fits for the thermal conductivity of the ZrC-HfN composites at 100, 200, 400, and 600°C. The upper and lower bounds are represented by the ROM and IROM models, respectively.

The ROM model represents the best case scenario for the thermal conductivity of two phase composites. The thermal conductivity of the ZrC-HfN is high, likely do to excellent particle matrix interfaces, due to inter diffusion between the two phases. The lower volume loading also contributes to the higher thermal conductivity. Figure 5.33 contains the fit of the ZrC-HfN cercer to the ROM model up to 600°C. Using the ROM model, the predicted thermal conductivity for ZrC-UN cercers is presented in Figure 5.34. Since the thermal conductivity of ZrC and UN are similar over this temperature range, the model used will not make a large difference in the predicted value.

5.3 Mechanical Properties

5.3.1 Model of Modulii and Poisson's Ratio

The moduli of the composite materials were not measured. However, the maximum and minimum limits are known to follow the ROM and IROM models [149]. The upper limit is defined by the series or ROM model and the lower limit is defined by the parallel or IROM model. The predicted Young's modulus for MoW and ZrC matrix and UO_2 and UN particle composites as a function of volume loading are shown in Figure 5.35.

5.3.2 Tensile Properties

Tensile testing was used to validate the Tabor relationship discussed earlier for the Mo30W matrix material. Hardness values were converted into predicted yield stress (YS) using Tabor's relationship [131]. The results are presented in Table 5.6. Wrought W was used as a direct comparison. The predicted value for YS for the W matched well with the measured tensile YS. For the Mo30W small grain sized material, the Tabor relationship overestimated the true value by a factor of two and for the Mo30W medium grain size material, it over-predicted by a factor of four. This discrepancy

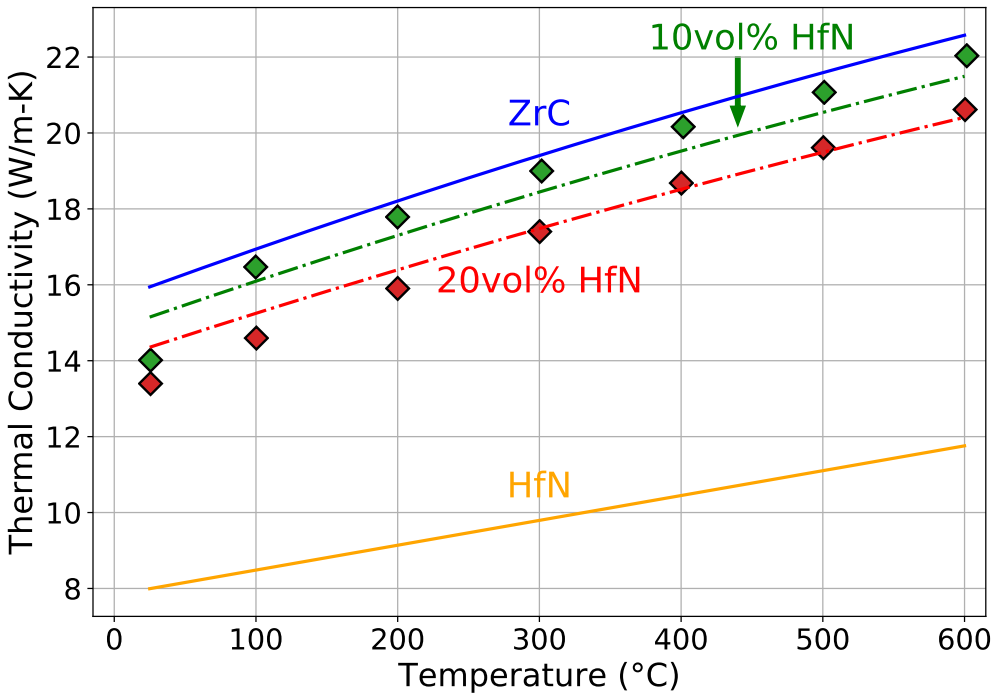


Figure 5.33: Thermal conductivity of the ZrC-HfN angular cercer fit to the ROM model for 10 and 20 % volume loadings.

Table 5.6: Calculated YS from Tabor relationship compared to tensile YS for wrought W and as sintered Mo30W small and medium grain size.

Property	W	Mo30W-Small	Mo30W-Medium
Hardness (HV_1)	253 ± 14	238 ± 4.1	230 ± 5.3
Hardness (Gpa)	2.47 ± 0.14	2.34 ± 0.40	2.25 ± 0.52
Tabor YS (MPa)	826 ± 45	779 ± 13	750 ± 17
Tensile YS (MPa)	803 ± 58	378 ± 116	183 ± 54
Fit (Tabor/tensile)	1.03	2.06	4.10

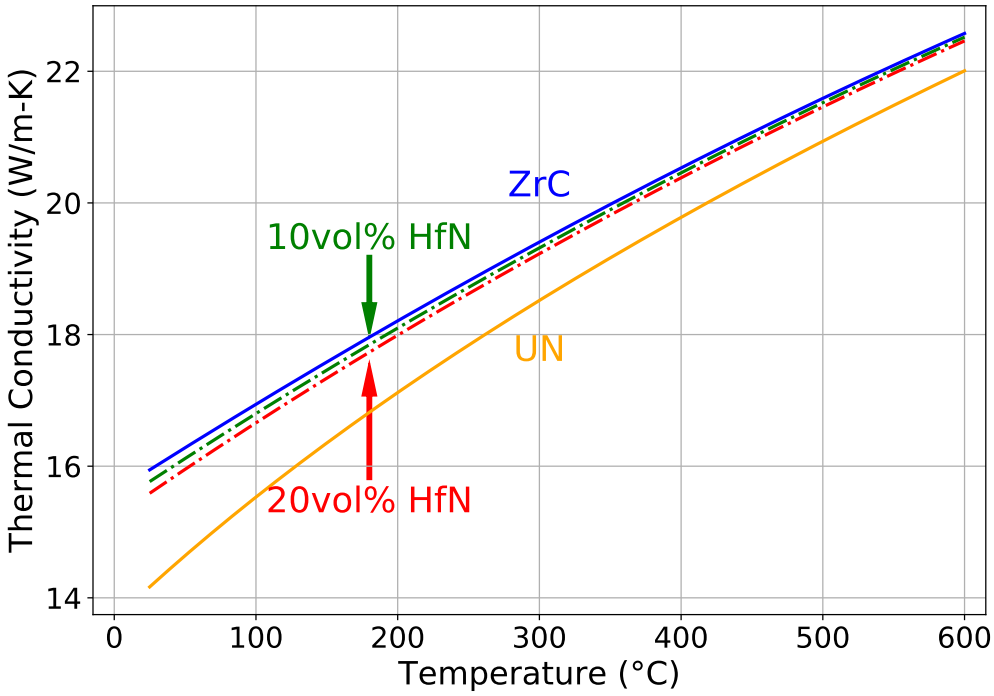


Figure 5.34: Predicted thermal conductivity for ZrC-UN cercer composites at 10 and 20 vol% from 30 to 600°C using the series ROM model.

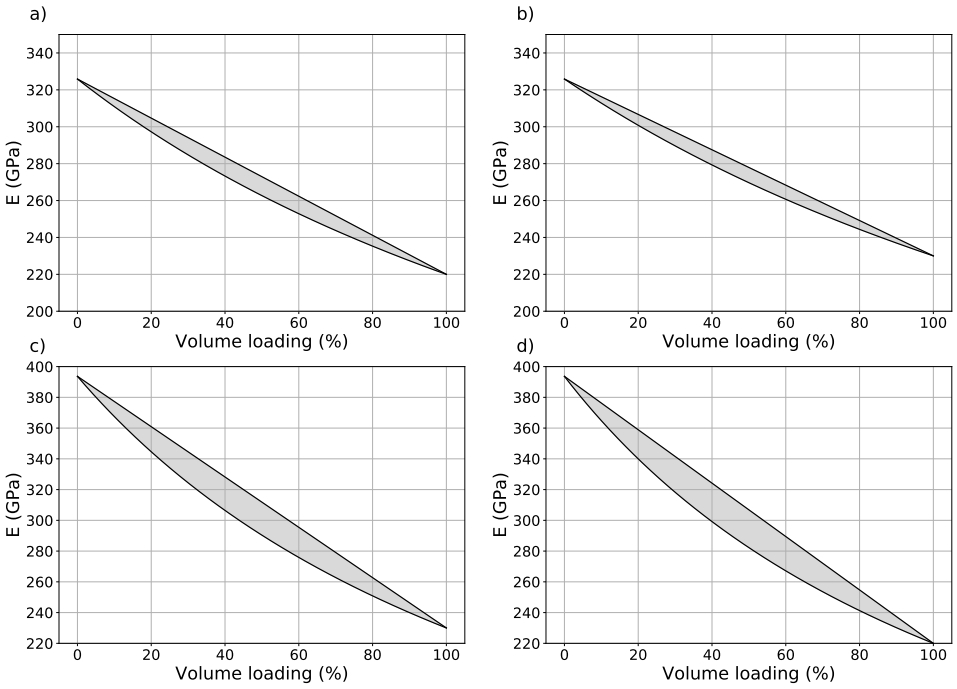


Figure 5.35: Range of Young's Modulus for a) Mo30W-UO_2, b) Mo30W-UN, and c) ZrC-UN composites as a function of volume loading. The maximum value is the series or ROM model and the minimal value is the parallel or IROM model.

is likely due to the large stresses inherent in Mo30W material from the sintering process. It was also shown that the Mo30W experienced no ductility during the tensile test, while the W did, even at room temperature. The Tabor relationship is likely predicting the true strength of the stress-relieved Mo30W. A heat treatment above the stress relief temperature would most likely result in YS values that more closely match those predicted by Tabor's relationship.

The 4 point bend-bar fixture used for fracture toughness testing was also used to determine the flexural strength of the Mo30W-medium grained material without a pre-machined notch. The flexural yield strength was determined to be 496 $\pm$ 25 MPa. This more closely relates to the predicted Tabor value, however, it still overpredicts by a factor of 1.5. Once again, a stress-relieving heat treatment is required in order to optimize the mechanical properties.

5.3.3 Fracture Toughness

The formula used to determine the fracture toughness from the SENB specimen was based off of Equation 3.2. In this equation, the fracture toughness depends on the strength at fracture, the notch depth, and Y, a geometric factor. For all samples tested, the average value for Y was 1.862 with a standard deviation of 4.23 x 10^{-3} and the average notch depth was 1.26 x 10^{-3} m with a standard deviation of 4.47 x 10^{-8} m. These errors resulted in minor differences in the machining of the samples. Using error propagation, the expected difference would be 2.27 x 10^{-3} for the K_{IC} calculation. For this reason, since all samples tested have a similar geometry, K_{IC} is directly proportional to σ_f for this batch of samples. Because of this, strength correlations can be used to help model and describe the fracture toughness behavior of the pure matrix and the cermet and cercer materials.

It was shown in Figure 4.72 that the fracture toughness for Mo30W depends on the grain size. The pure Mo30W material followed the Hall-Petch relationship, at least using Vickers hardness as a measure of strength. Since K_{IC} is directly proportional to

the yield strength, the fracture toughness of the three Mo30W were fit to the second order Hall-Petch relationship (Equation 5.1). This fit is presented in Figure 5.36. A linear dependence is observed, however the coefficient of determination was rather low at 0.82. This is likely low due to the very limited samples size. Only three grain sizes were tested with only a few samples at each grain size. Still, the value is high enough to confirm the fracture toughness dependence on grain size according to the Hall-Petch relationship.

For some composite materials, it is difficult to determine whether there is a change in the fracture toughness with respect to the pure matrix material at room temperature. According to Figure 4.72, the only apparent decrease in fracture toughness is with the Mo30W angular HfN cermets. The MoW-YSZ cermets had a large spread at both volume loadings and the ZrC-HfN cercers also had a large spread and a matrix and particle with very similar a fracture toughness. The two sample student t-test with unequal variance was used to determine whether there was a statistical difference between the fracture toughness of the matrix and the composite materials. The p-value as well as confidence probabilities are presented in Table 5.7. Ideally, a probability of 95% or higher is needed to definitively confirm whether the difference between the two data sets are statistically significant. However, given the small sample sizes and high variability of fracture toughness in brittle materials, a lower value could signify statistical significance.

The probability of a statistical significantly different fracture toughness was high (>88%) for the MoW-HfN cermets. It was much lower for the MoW-YSZ, though some interesting behavior was observed that will be discussed later. The ZrC-20vol-HfN cercer had the lowest probability (14%), which suggests there was no change in fracture toughness to the ZrC with the addition of the 20 vol% HfN. The addition of 10 vol% HfN resulted in a value of (67%). This is high enough to suggest the strengthening behavior might have some relevance. This also matches literature data that found the highest increase in fracture toughness comes at a lower volume loading,

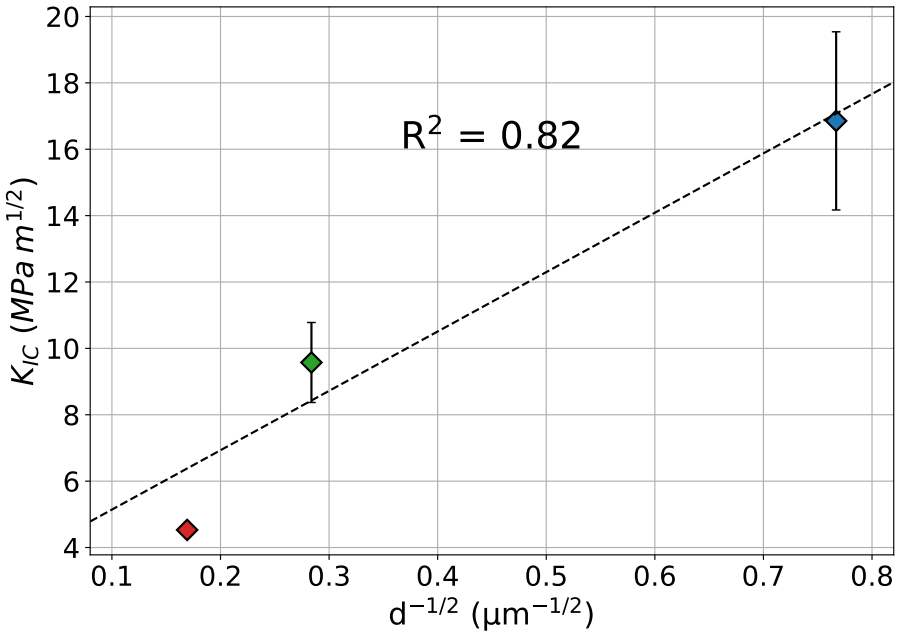


Figure 5.36: Plot of Fracture toughness versus $d^{-1/2}$ for the Mo30W samples tested at room temperature.

Table 5.7: P values and estimated probability of statistical significance that the room temperature fracture toughness of the cermet and cercer composite materials vary from the pure matrix materials, using the student t-test.

Material	P-value	Probability (%)
MoW-50vol-HfN	0.12	88
MoW-70vol-HfN	0.11	89
MoW-50vol-YSZ	0.54	45
MoW-70vol-YSZ	0.76	24
ZrC-10vol-HfN	0.33	67
ZrC-20vol-HfN	0.86	14

typically between 8 and 15 % followed by a decrease in fracture toughness back down to the matrix value for ceramic matrix ceramic particle composites [90, 220].

The strength equations outlined by Fu et al. and described in Chapter 2 were modified to fit K_{IC} instead of yield strength [167]. The simple model (Equation 2.40 and modified simple model (Equation 2.41) both assume no particle adhesion. The Leidner and Woodhams model (Equation 2.42) assumed moderate particle-matrix adhesion and the Pukanszky model (Equation 2.43) assumed a strong particle matrix adhesion. All of these models were fit to the MoW-HfN data, as presented in Figure 5.37.

The constants for the different models were determined using a least squares method. The value of a and b for the modified simple model (Equation 2.41) were found to be 0.758 and 0.212, respectively. For the Leidner and Woodhams model (Equation 2.42), p and f were lumped into a single constant A_{LW}. The value of A_{LW} and k were found to be -0.856 and 0.948, respectively. B for the Pukanszky model (Equation 2.43) was determined to be 1.14.

The modified simple model provided the best fit. This excellent fit is due to the empirical nature of the model and the limited tested volume loadings available. The negative value for A_{LW} from the Leidner and Woodhams model is a nonphysical value, since the friction and strength terms should not be negative. For this reason, the model is invalid for the MoW-HfN system. The Pukanszky model is not far off as well. Since the composite has such a low fracture toughness at the 50 and 70 vol% loadings it is hard to draw a realistic conclusion. The ROM and IROM models due make excelent bounds for a region of predicted fracture toughness.

To predict the behavior for the strength of an MoW cermet with UN particles that are similarly sized and shaped to the tested angular HfN particles, the modified simple model is the best choice. The ROM and IROM models can also act as the upper and lower expected toughness values. The K_{IC} of UN is higher than that of HfN, though it depends heavily on the stoichiometry and processing parameters. The modified simple model does not rely on the mechanical properties of the solute particle, so the

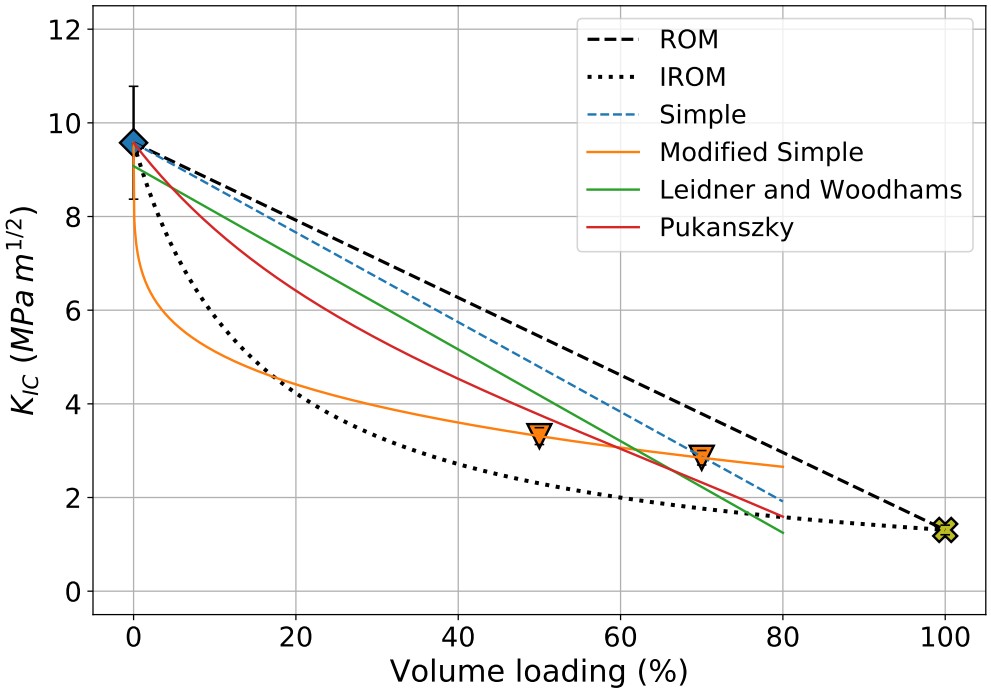


Figure 5.37: Room temperature fracture toughness of Mo30W with angular HfN cermets fit to various models.

predicted fracture toughness is the same as measured for the 50 and 70 vol% MoW-HfN cermets, as shown in Figure 5.38. The modified simple model actually predicts a lower fracture toughness than the IROM for the Mo30W-UN system. Also, this model would only be valid in the 50-70vol% range. The behavior at lower volume loadings will likely be considerably different.

The Mo30W-YSZ cermets had the largest spread for fracture toughness. Examination of the fractured surfaces led to the discovery that some particles were shearing, while others were simply debonding at the crack face. It was found that as more of the particles sheared, the fracture toughness increased. Figure 5.39 contains examples SEM images to illustrate this point.

In order to determine the effect the particles were having on the fracture toughness as a whole, the contribution to the fracture toughness from the Mo30W was first subtracted out. Using the simple model in Equation 2.40, the expected fracture toughness of the Mo30W based on the cross-sectional area was calculated for both a 50 and 70vol% loading. These were 4.78 and 2.87 MPa-m$^{1/2}$, respectively. The K_{IC} of the YSZ particle contribution was then plotted with respect to the number of sheared particles, as presented in Figure 5.40. A linear regression was then used to determine the effect the number of shear particles had on the increase in fracture toughness. A good fit was obtained with a coefficient of determination of 0.78. The fit could be improved if more samples were tested.

From this linear regression, a simple linear expression was derived to model the expected increase in K_{IC} caused by the shearing of the YSZ particles. Another linear expression was derived for the maximum number of particles that could shear in the fracture plane as a function of volume loading. This model is presented in Equation 5.8.

$$N_{max} = 150V_p \tag{5.8}$$

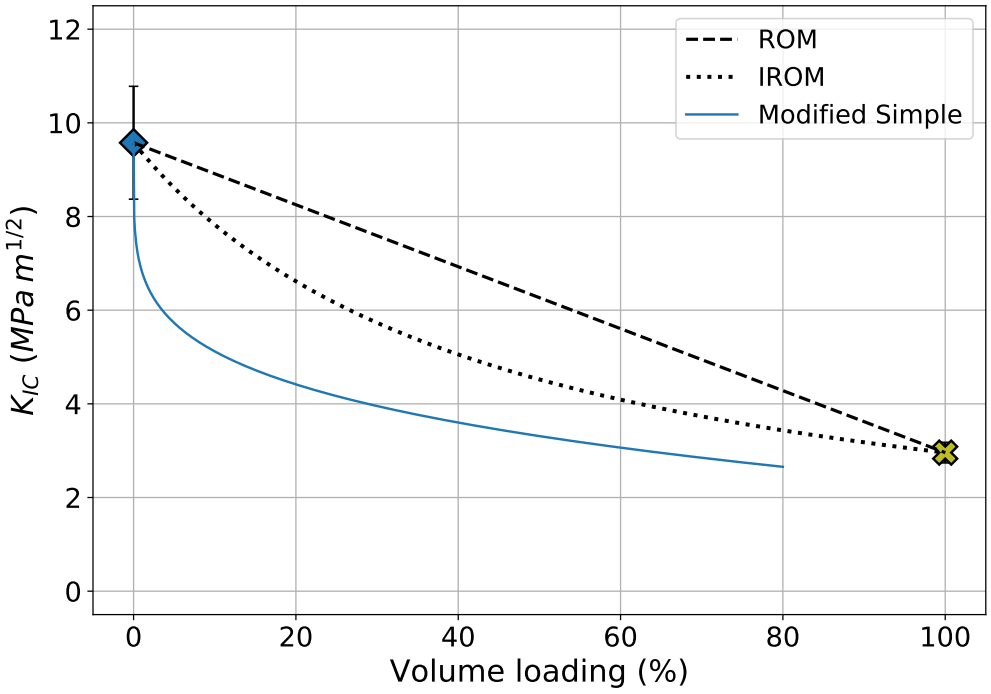


Figure 5.38: Predicted fracture toughness for Mo30W-UN cermets using the modified simple model. The ROM and IROM model is also included.

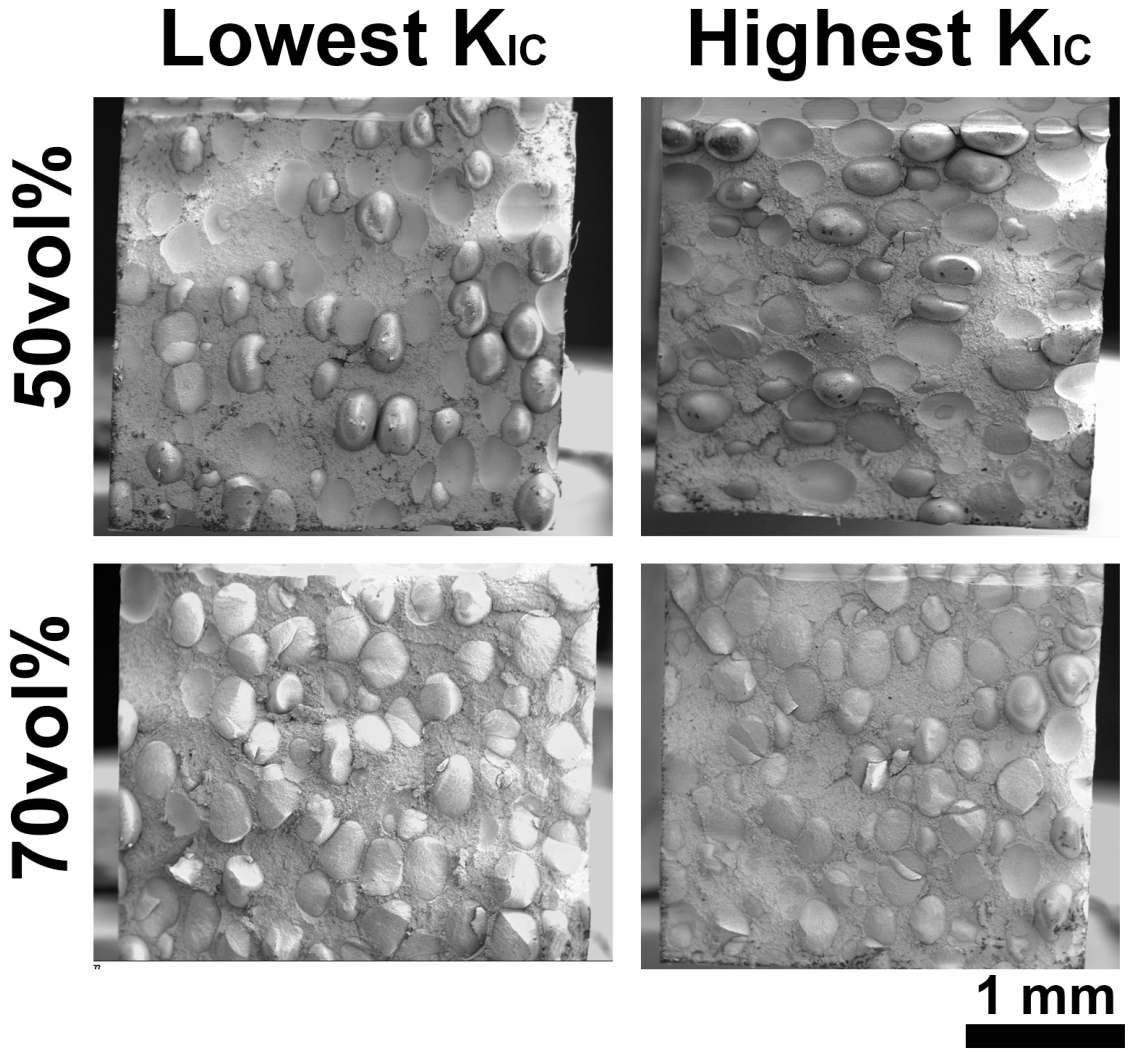


Figure 5.39: Composite backscatter (20%) and secondary electron (80%) SEM micrographs of the fracture surfaces for the Mo30W-YSZ cermet samples with the highest and lowest fracture toughness. As fracture toughness increases, more particles sheared as opposed to debonded.

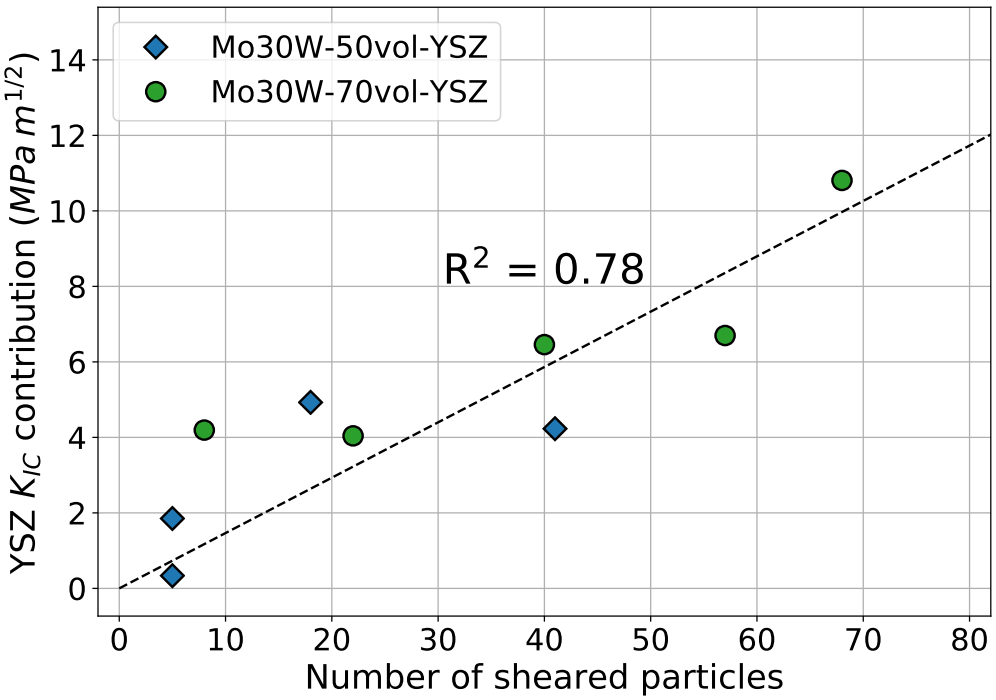


Figure 5.40: Sheared YSZ contribution to fracture toughness of Mo30W-YSZ cermets as a function of the number of sheared particles. The blue diamonds are data taken from the Mo30W-50vol-YSZ and the green circles are data taken from the Mo30W-70vol-YSZ cermets.

The upper bound for K_{IC} then becomes the sum of the K_{IC} of the cross-sectional area corrected Mo30W with the K_{IC} contribution from the sheared YSZ particles with the maximum number of shear particles for the given volume loading. The lower limit is then simply the K_{IC} of the cross-sectional area corrected Mo30W assuming no YSZ particles shear. Figure 5.41 contains these two limits plus the current data. Given the tested samples, it is unlikely that all particles will shear or debond, so these limits are likely extreme. It is also unclear the mechanism behind particle debonding and shearing, though it likely has to do with the crack path and the particle-matrix interface at the crack path.

The limits presented in Figure 5.41 also work to predict the fracture toughness of a Mo30W-UO_2 cermet. The lower limit will be the same, but the upper limit will change, since the fracture toughness of UO_2 is less than that of YSZ. This will affect the particle shearing strengthening factor. Still, the bounds provided for the YSZ cermets should contain the UO_2 cermets.

Since the fracture toughness of the ZrC and HfN are both equally low, it would be expected that the fracture toughness of the ZrC-HfN cercer be equally low. The statistical analysis using the student t-test provided a low level of confidence that there was any difference between fracture toughness of the ZrC-20vol-HfN and the pure ZrC. While there is a chance that there was only a slight increase in toughness with the addition of the 10 vol% HfN, this increase is so subtle that it would not affect any design parameters. Moreover, toughness increase in particle based ceramic composites results primarily from crack deflection and the particle matrix interface. Since the particle and matrix are well bonded, the crack simply propagates through the interface without any difficulty, as seen in toughness for the Figure 4.76. For this reason, it is expected that the ZrC-HfN composite follow a simple ROM or IROM model.

Figure 5.42 contains the K_{IC} data for the ZrC and the two volume loadings of the ZrC-HfN cercer. There is very little difference between the ROM and IROM models, due to the similarly low K_{IC} values for both ZrC and HfN. The ROM and

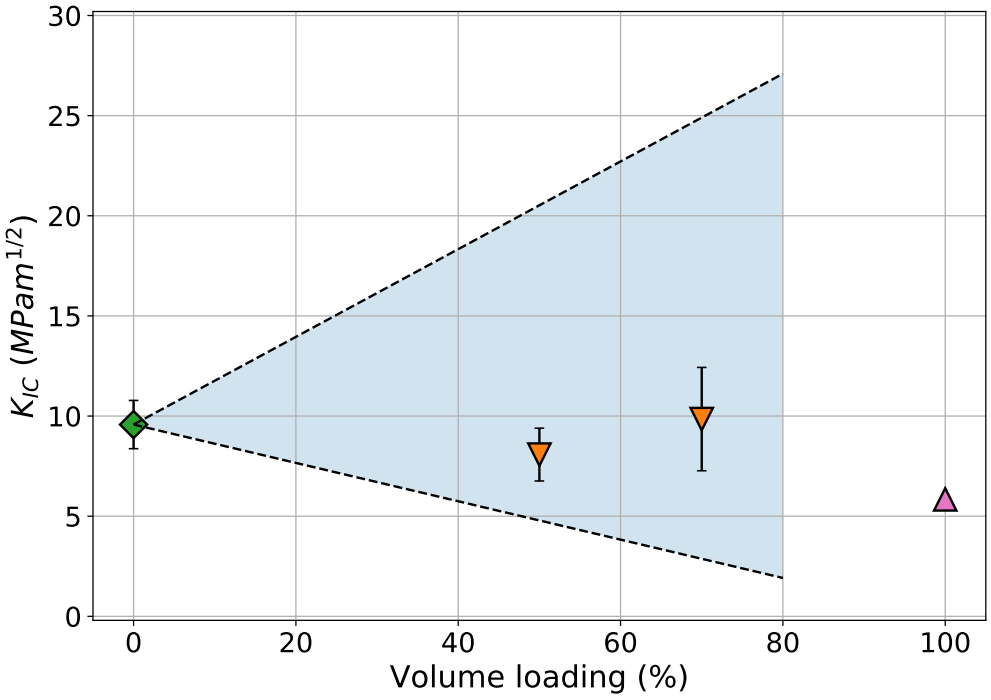


Figure 5.41: Fitted range for the room temperature fracture toughness of Mo30W-YSZ cermets as a function of volume loading. The lower limit is an area reduced model, while the upper limit takes into account the shearing of YSZ particles.

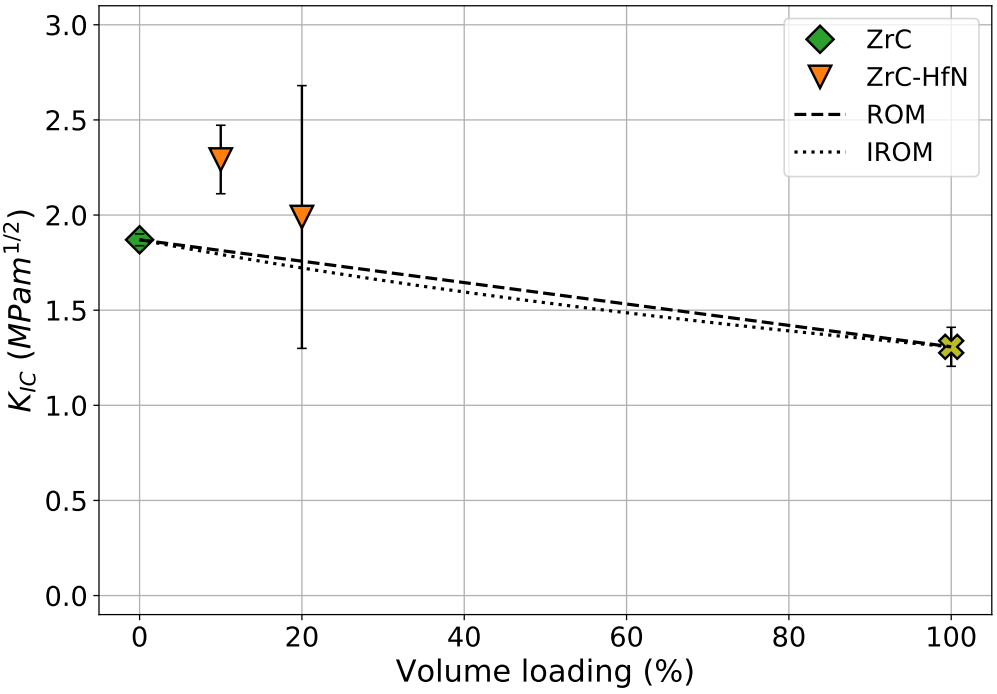


Figure 5.42: K_{IC} ROM and IROM models fit to the ZrC-HfN cercers tested at room temperature.

IROM models can also be used to predict the fracture toughness of ZrC-UN cercers as presented in Figure 5.43. This model is only valid for cercers with angular UN particles that are well bonded with the ZrC matrix. While this model may not be the most accurate, at low volume loadings and give the overall low fracture toughness for the system, it is sufficient to predict the behavior for the fueled cercer for the initial design stage of an NTP system.

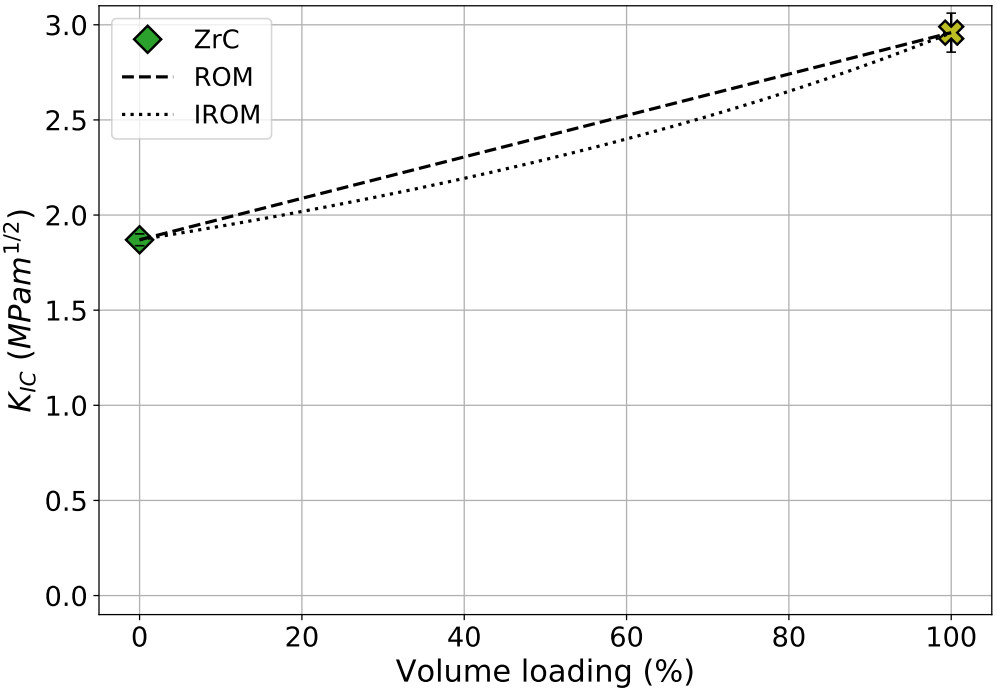


Figure 5.43: Predicted K_{IC} for ZrC-UN cercer at room temperature using the ROM and IROM models.

Chapter 6

Conclusions

6.1 Fabrication

SPS proved a viable technique in the sintering of both Mo30W and ZrC powders. By examining the chemical reduction Mo30W powder, the effect of pressure, hold time, and hold temperature on the final density and microstructure of the densified material was understood. From this, an optimized Mo30W matrix sintering condition of 1600 °C and 30 MPa for 15 minutes was determined. Additionally, the effect of powder size and geometry was analyzed by comparing four different Mo30W powders. It was determined that more angular metallic powders sinter to a high density at lower applied pressures and temperatures than larger, more spherical powders.

The sintering of ZrC using SPS had been well documented, however, most studies relied on high pressures ($\geq$ 60 MPa) in order to ensure high densification of the powder compact. Given the need to sinter at a lower applied pressure (<= 30 MPa) for the fabrication of the cercer materials, hold temperature and vacuum pressure were the dominant options to improve the ZrC matrix density. Since the densification of ZrC depends heavily on the vapor phase, it sinters better at a higher vacuum. The current SPS did not allow for a high vacuum to be pulled in the sample chamber, so instead a turbopump was used to increase the outflow of the off gasses and the vapor phase.

The turbopump lowered the absolute vacuum pressure to below 5 Pa during the initial heating and kept the peak vacuum pressure below 13 Pa. This in combination with a higher hold temperature allowed for the sintering of ZrC powder to high density at 30 MPa pressure. The optimum sintering conditions for ZrC were determined to be 1850 °C and 30 MPa for 10 minutes.

Two sintering analysis methods were used to model the densification of the matrix powder compacts during sintering. The initial stage sintering method developed by Young and Cuttler was used to determine an apparent activation energy of sintering for the ZrC and the four Mo30W powders. The master sintering curve was also used to determine an activation energy for sintering for the ZrC and CR Mo30W powder. While neither method alone provides information on the dominant diffusion mechanism for sintering, by comparing the results from the two analyses, it was determined that the dominant sintering mechanism for both powders was volume diffusion.

In order to fabricate the composite cercer and cermet samples, a new powder coating technique was developed. This technique worked well in coating the spherical YSZ and angular HfN particles in both Mo30W and ZrC up to relatively high volume loadings. By increasing the amount of binder and changing the mixing method, it also worked well in coating the spherical HfN surrogate particle. The cermets with spherical YSZ and angular HfN particles sintered well using the optimum sintering conditions for the pure Mo30W. For the spherical HfN cermet, the hold temperature was raised to 1700 °C to remove some additional matrix porosity and raise the final density from 93 to 97.7 % theoretical density. The ZrC cercers all required specialized sintering conditions due to the less forgiving and less ductile ZrC ceramic matrix. The ZrC-YSZ cercers needed to be sintered below 1850 °C to avoid reaction between the free carbon and the zirconia and yttria. Moreover, to remove the cracking in the ZrC matrix and to reduce the cracking in the YSZ particles, a controlled cooling rate was used after sintering. For the ZrC-HfN cercers, a two phase material was desired, so the sintering temperature was set as 1800 and 1850 °C for the angular and spherical

particles respectively. The resulting cercers were had very minimal matrix cracking and only minimal cracking in the YSZ paricles.

Since the mechanical properties of the surrogate materials are similar to the fuel materials (UO_2 and UN), fueled cermet and cercer composites should sinter well using the sintering conditions optimized for the surrogate composites. These sintering conditions will only be valid if the geometry and size of the uranium ceramic particles match that of the surrogate particles. If the UO_2 and UN particle geometry size or shape change, then further optimization of the sintering conditions will be needed.

The first hypothesis of this thesis was that the surrogate particles will aid in the sintering of the matrix material. For all cermets and cercers, the addition of the composite particles increased the onset sintering temperature, where stage one sintering began. This would suggest the particles actually inhibited sintering. However, for all but two particles, the calculated initial stage activation energy for sintering was lower than that of the pure Mo30W and ZrC. This suggests that the particles aid in the sintering process. For the spherical YSZ and angular HfN with the Mo30W, the matrix porosity of the cermet did not differ from the Mo30W when sintered at the same conditions. The Mo30W matrix with the spherical HfN was more porous and required an increase in sintering temperature to reduce the matrix porosity. The particles can aid in sintering, but it depends on the particle geometry, size, and volume loading. The highest volume loading tested for composites containing the YSZ particles (70 vol% for Mo30W and 20 vol% for ZrC) were the only two cases where the apparent activation energy for sintering increased compared with the sintering of the pure matrix material. All other cases either maintained or reduced the apparent activation energy.

SPS is useful in producing high density composite materials. It also allows for rapid development of materials. By rapidly optimizing sintering conditions, a wide array of composites can be quickly produced to provide samples for thermophysical and mechanical testing. However, SPS has limits with regard to scaling. Since the cermet and cercer composites are brittle and difficult to machine, ideally, near net

shape elements should be sintered. Depending on the desired size and length, SPS as it currently stands may not be able to provide near net shape NTP elements. Bonding of shorter elements can also to lead to increased points of failure. Still, despite these limitations, SPS can continue to provide a source for rapid property data acquisition.

6.2 Thermophysical Properties

The thermophysical properties for cermets of 50 and 70 vol% and for cercers of 10 and 20 vol% were determined. The specific heat capacity was found to follow a density normalized ROM model. This was true for both the cermet and cercer materials. Because of this, predictive models for fueled particles (UO_2 and UN) were created with a high level of confidence.

The coefficient of thermal expansion proved more difficult to model. The Mo30W experienced an increase in CTE compared with that of pure Mo and W. Moreover, the particle composite materials all behaved differently. The Mo30W cermet with angular HfN particles followed the model developed by Tummala. The Mo30W cermet spherical particles did not follow any existing model, so a range was determined using the ROM as the maximum expected value and the Tummala model as the lower bound. Still, even using the wide range, several values at the lower and higher ends of the tested temperature diverged from the bounded region. The ZrC cercer with angular HfN particles did not follow any particular model, which was attributed to inter-diffusion between the particle and the matrix. The behavior was so extreme that it could not even be bound by existing models. Because of this, predictive models were only created for the fueled cermet materials, and even then, the level of confidence is lower than that of the specific heat capacity models.

The thermal conductivity behaved much more predictably. The Mo30W-YSZ cermets and Mo30W-HfN cermets both fit well to different models. The Lewis and Nielsen model worked best for the cermet with spherical YSZ particles by taking into account the spherical shape and homogeneous particle distribution. This model

fit the data well over the entire temperature range tested. A simple geometric mean model worked best for predicting the thermal conductivity of the cermet with angular HfN particles. This model fit well above 200 °C, but overpredicted by as high as 12% at lower temperatures. The thermal conductivity of the ZrC-HfN cercer did not fit well to any of the models tested for the cermet materials. Instead, the best fit was the ROM model. This was less accurate at lower temperatures, however, given the similar thermal conductivity between ZrC and UN, a predictive model for the thermal conductivity of a ZrC-UN cercer was produced.

Only the specific heat capacity for the composite materials fit a single model. Given the complex dependence of CTE and thermal conductivity on the particle shape and interface, different models were used to fit each different cermet and cercer. Because of this, these models may be limited in predicting the thermophysical properties of fueled cermets and cercers. Until the properties of the fueled composites can be measured directly, they should be treated as a rough approximation by NTP core designers.

6.3 Mechanical Properties

Tensile testing of the Mo30W revealed inherent weakness in the as sintered Mo30W. Stresses from the sintering and cooling of the alloys removed all ductility and resulted in yielding and fracture well below the strength predicted using the Tabor relationship.

The matrix ZrC experienced transgranular cleavage, while the Mo30W experienced intergranular fracture. Because of this, the ZrC did not depend on the grain size, while the MoW saw an increase in toughness with decreasing grain size. The Mo30W HfN cermet caused a massive decrease in the fracture toughness, which was predicted using a strength model. The fracture toughness of the Mo30W-YSZ cermet depended on the number of YSZ particles that sheared and debonded. The greater number of particles that sheared, the higher the fracture toughness, independent of test temperature and volume loading. From this, a range of possible fracture

toughness values was predicted for a Mo30W cermet with spherical UO_2 particles. Finally, the ZrC-HfN experienced a slight increase in fracture toughness with the addition of the angular HfN particles. This was explained using models that predicted the reinforcement of the ceramic matrix from the particles.

The fracture toughness was found to have only a small dependence on test temperature up to 800 °C. Changes in strength and fracture toughness for both materials were predicted to occur at much higher temperatures (> 1000 °C).

As with the thermophysical properties, excluding specific heat capacity, the fracture toughness of the composite materials all needed to be fit to a different model. The predicted values for these materials come with a higher degree of certainty. Since all the materials were so brittle, small errors in predicted fracture toughness will not alter NTP design considerations. Instead, efforts should be made to improve the toughness of these materials.

6.4 General Conclusions

Surrogate cermet and cercer materials were successfully produced using SPS. Models were fit to the thermophysical and mechanical properties of the composite materials. The level of confidence for these properties varies with each model. While these values can provide useful values for initial design and optimization of NTP systems, the models need to be validated using fueled cermet and cercers and by testing samples to higher temperatures.

When comparing the Mo30W cermet to the ZrC cercer, they both have a variety of distinct advantages and disadvantages. The cermets have higher thermal conductivity and a lower heat capacity, compared to the cercers. The Mo30W-YSZ cermets had the highest fracture toughness as well, with the ZrC-HfN cercers having the lowest. The Mo30W-YSZ cermet had the highest CTE up to 1000°C, but was not much higher than the cercer. The cercer requires less fuel compared with the cermet material to produce a critical reactor and has a higher melting point compared to

the cermet. From these results, it is difficult to determine which material is ideal for NTP. Additional testing is also needed up to NTP relevant temperatures in order to make a more informed decision. Recommended future work will be discussed in Chapter 7.

A list of 7 desired NTP fuel element material properties was presented in Chapter 1. Some of these attributes were not tested as part of this study. All materials fabricated will be able to withstand the high required temperatures without melting. Efforts were made to reduce the neutron absorption cross-section of the cermet by using an alloy of Mo30W. All samples were fabricated to high densities over a range of volume loadings and surrogate types using SPS. Sample processing was optimized to minimize particle inter-particle conductivity, matrix microcraking, and particle cracking through the optimization of sintering parameters and development of a powder coating process. Additional work will be needed to optimize the sintering of relevant geometry fuel elements with cooling channels.

No perfect material and manufacturing process exist for producing NTP fuel elements. With some modifications and additional testing, the materials presented in this thesis could be viable options for an NTP fuel element. Moreover, SPS should continue to be used as a tool to produce high density composites for determining important material properties, even if other techniques could be used to produce full-scale fuel elements.

Chapter 7

Recommendations for Future Work

The present work successfully optimized the sintering of multiple cermet and cercer composites, as well as determined important thermophysical and mechanical properties. Additional follow-on research is recommended to further NTP fuel development.

The first recommendation is to determine the thermophysical and mechanical properties for additional cermet and cercer materials. While several surrogate particles were used to create the cermet and cercers, as described in Chapter 4 and Appendix C, thermophysical and mechanical properties were only determined for the cermets with spherical YSZ and angular HfN and for the cercers with angular HfN at two different volume loadings. The thermophysical properties should be determined for the ZrC-YSZ (spherical surrogate material). Additionally, it is important to determine the effect of particle geometry on the different physical properties of interest. Testing cermet and cercer materials with the spherical HfN and fitting these to similar models will provide useful insight into how the particle effect the different properties of the cermet and cercer composites.

Surrogate particles (YSZ and HfN) were used in place of fuel particles (UO_2 and UN) to reduce costs and facilitate fabrication and testing. Models determined for the surrogate composites when then used to predict the values for the fueled composites.

In order to validate the models, it is recommended to fabricate cermets and cercers with similar sized UO_2 and UN particles using the same conditions determined for the surrogate particles. Then, using these fueled composites, the same properties can be measured and compared with the predictive models.

One of the primary goals of this work was to determine thermophysical and mechanical properties for the NTP material handbook to be used in NTP design. Most properties were determined from room temperature up to between 800 and 1000 °C. The fuel element for NTP will reach as high as 3000 °C during operation. While some properties can be extrapolated (such as C_P), others will experience different behavior at higher temperatures. Attempts should be made to measure properties of select composites and volume loadings up to NTP relevant temperatures. In some cases, it would be beneficial to measure the values up to their melting points, in order to design for accidents.

Finally, as determined in this study, the as sintered composites were all quite brittle. While the cermets had a higher fracture toughness, it was still below what is typically accepted as a good structural material. Modeling analysis is needed to determine the extent of the thermal stresses during NTP operation in order to provide a minimum acceptable fracture toughness. Moreover, efforts should be made to improve the toughness of these materials. For the Mo30W and corresponding composites, heat treatment of the materials after sintering could relieve some of the built-up stress and help to regain ductility and toughness. Additionally, both cermets and cercer can be strengthened by the addition of small, sub-micron particles to the matrix. This could greatly improve the strength and toughness of the materials. The small particles could affect the sintering, so the process would need to be optimized. Moreover, the addition of the particles would affect the thermal properties of the composites. This effect would need to be understood and measured.

Bibliography

Bibliography

[1] C. P. Wang, J. Wang, S. H. Guo, X. J. Liu, I. Ohnuma, R. Kainuma, and K. Ishida. Experimental investigation and thermodynamic calculation of the phase equilibria in the Co-Mo-W system. *Intermetallics*, 17(8):642–650, August 2009. Section: 642. xi, xvii, 9, 67, 176

[2] SF Mughabghab. Thermal neutron capture cross sections resonance integrals and g-factors. Technical report, Brookhaven National Laboratory, Upton, NY, 2003. xi, 9

[3] SK Bhattacharyya. An assessment of fuels for nuclear thermal propulsion. Technical Report ANL/TD/TM01-22, Argonne National Lab., IL (US), 2002. Volume: ANL/TD/TM01-22. xi, xv, 6, 8, 13, 14, 15, 16, 17, 19, 20, 22, 23, 24, 25, 26, 27, 28, 29, 400

[4] T.E.R. Smith. Ablation study of tungsten-based nuclear thermal rocket fuel. *The George Washington University*, 2014. xi, 20, 21, 22

[5] S. K. Sun, G. J. Zhang, W. W. Wu, J. X. Liu, T. Suzuki, and Y. Sakka. Reactive spark plasma sintering of ZrC and HfC ceramics with fine microstructures. *Scripta Materialia*, 69(2):139–142, July 2013. Section: 139. xi, 48, 53

[6] D. S. Tucker, M. W. Barnes, L. Hone, and S. Cook. High density, uniformly distributed W/UO2 for use in Nuclear Thermal Propulsion. *Journal of Nuclear Materials*, 486:246–249, April 2017. Section: 246. xi, xvii, 62, 63, 64, 65

[7] In-Kook Suh, H Ohta, and Y Waseda. High-temperature thermal expansion of six metallic elements measured by dilatation method and X-ray diffraction. *Journal of Materials Science*, 23(2):757–760, 1988. xi, xviii, 69, 74, 76, 244

[8] GP Škoro, JRJ Bennett, TR Edgecock, and CN Booth. Yield strength of molybdenum, tantalum and tungsten at high strain rates and very high temperatures. *Journal of nuclear materials*, 426(1-3):45–51, 2012. xi, xix, 86, 87, 89

[9] Y. Wang, J. C. Gao, G. M. Chen, W. Q. Li, Y. G. Zhou, and W. Zhang. Properties at elevated temperature and recrystallization of molybdenum doped with potassium, silicon and aluminum. *International Journal of Refractory Metals & Hard Materials*, 26(1):9–13, 2008. xi, 90, 91

[10] H. F. Jackson and W. E. Lee. Properties and Characteristics of ZrC. In Rudy J. M. Konings, editor, *Comprehensive Nuclear Materials*, pages 339–372. Elsevier, Oxford, 2012. xi, xx, xxi, 94, 96, 97, 98, 101, 103, 104, 105, 107, 108, 109, 110, 111, 112, 113, 116, 117, 118, 119, 273

[11] Nicole Korklan, Gregory E Hilmas, and William G Fahrenholtz. Processing and room temperature mechanical properties of a zirconium carbide ceramic. *Journal of the American Ceramic Society*, 104(1):413–418, 2021. xi, 116, 117

[12] L. Feng, W. G. Fahrenholtz, G. E. Hilmas, J. Watts, and Y. Zhou. Densification, microstructure, and mechanical properties of ZrC-SiC ceramics. *Journal of the American Ceramic Society*, 102(10):5786–5795, October 2019. xi, 117, 121, 286

[13] B. T. Wang, P. Zhang, R. Lizarraga, I. Di Marco, and O. Eriksson. Phonon spectrum, thermodynamic properties, and pressure-temperature phase diagram of uranium dioxide. *Physical Review B*, 88(10):104107, September 2013. xi, 125

[14] Grégoire Witz, Valery Shklover, Walter Steurer, Sharath Bachegowda, and Hans-Peter Bossmann. Phase evolution in yttria-stabilized zirconia thermal

barrier coatings studied by rietveld refinement of X-ray powder diffraction patterns. *Journal of the American Ceramic Society*, 90(9):2935–2940, 2007. xi, xxi, 121, 123, 125

[15] M Idiri, T Le Bihan, S Heathman, and J Rebizant. Behavior of actinide dioxides under pressure: U o 2 and th o 2. *Physical Review B*, 70(1):014113, 2004. xi, 125

[16] M. B. Pomfret, C. Stoltz, B. Varughese, and R. A. Walker. Structural and compositional characterization of yttria-stabilized zirconia: evidence of surface-stabilized, low-valence metal species. *Anal Chem*, 77(6):1791–5, March 2005. Edition: 2005/03/15. xi, 125

[17] P. Y. Chevalier, E. Fischer, and B. Cheynet. Progress in the thermodynamic modelling of the O-U-Zr ternary system. *Calphad-Computer Coupling of Phase Diagrams and Thermochemistry*, 28(1):15–40, March 2004. xi, xxi, 122, 125

[18] I. J. Fritz. Elastic properties of UO2 at high-pressure. *Journal of Applied Physics*, 47(10):4353–4358, 1976. xi, 125

[19] N. Igata and K. Domoto. Fracture stress and elastic-modulus of uranium-dioxide Including excess oxygen. *Journal of Nuclear Materials*, 45(4):317–322, 1973. xi, 125

[20] Jane W Adams, Robert Ruh, and KS Mazdiyasni. Young's modulus, flexural strength, and fracture of yttria-stabilized zirconia versus temperature. *Journal of the American Ceramic Society*, 80(4):903–908, 1997. xi, xxi, 125

[21] J. K. Fink. Thermophysical properties of uranium dioxide. *Journal of Nuclear Materials*, 279(1):1–18, May 2000. xi, xii, xxi, xxxi, xxxii, 124, 125, 126, 128, 308, 316

[22] T. Tojo, T. Atake, T. Mori, and H. Yamamura. Heat capacity and thermodynamic functions of zirconia and yttria-stabilized zirconia. *Journal of Chemical Thermodynamics*, 31(7):831–845, July 1999. xi, xxi, 125, 126

[23] Y. Yun, D. Legut, and P. M. Oppeneer. Phonon spectrum, thermal expansion and heat capacity of UO2 from first-principles. *Journal of Nuclear Materials*, 426(1-3):109–114, July 2012. xi, xxii, 125, 134

[24] H. Hayashi, T. Saitou, N. Maruyama, H. Inaba, K. Kawamura, and M. Mori. Thermal expansion coefficient of yttria stabilized zirconia for various yttria contents. *Solid State Ionics*, 176(5-6):613–619, February 2005. xi, xxii, 125, 134, 136

[25] P. B. Weisensee, J. P. Feser, and D. G. Cahill. Effect of ion irradiation on the thermal conductivity of UO2 and U3O8 epitaxial layers. *Journal of Nuclear Materials*, 443(1-3):212–217, November 2013. xi, xxii, 125, 132

[26] K. W. Schlichting, N. P. Padture, and P. G. Klemens. Thermal conductivity of dense and porous yttria-stabilized zirconia. *Journal of Materials Science*, 36(12):3003–3010, 2001. xi, xxii, 125, 132, 319

[27] Wang Xiaofang, Hu Yin, Pan Qifa, Yang Ruilong, Long Zhong, and Liu Kezhao. Crystal structure and electronic structure of uranium nitrides. *Progress in Chemistry*, 30(12):1803, 2018. xii, 137

[28] S. V. Ushakov, A. Navrotsky, Q. J. Hong, and A. van de Walle. Carbides and nitrides of zirconium and hafnium. *Materials (Basel)*, 12(17):2728, August 2019. Edition: 2019/08/29. xii, xxii, 137, 141

[29] M. de Jong, W. Chen, T. Angsten, A. Jain, R. Notestine, A. Gamst, M. Sluiter, C. Krishna Ande, S. van der Zwaag, J. J. Plata, C. Toher, S. Curtarolo, G. Ceder, K. A. Persson, and M. Asta. Charting the complete elastic properties

of inorganic crystalline compounds. *Sci Data*, 2(1):150009, 2015. Edition: 2015/05/20. xii, 137

[30] RE Rundle, NC Baenziger, AS Wilson, and RA McDonald. The structures of the carbides, nitrides and oxides of uranium. *Journal of the American Chemical Society*, 70(1):99–105, 1948. xii, 137

[31] Andreas Zerr, Gerhard Miehe, and Ralf Riedel. Synthesis of cubic zirconium and hafnium nitride having Th 3P4 structure. *Nature materials*, 2(3):185–189, 2003. xii, 137

[32] Hugh O Pierson. *Handbook of refractory carbides and nitrides: properties, characteristics, processing and applications*. William Andrew, 1996. xii, 137

[33] U. C. Nunez, D. Prieur, R. Bohler, and D. Manara. Melting point determination of uranium nitride and uranium plutonium nitride: A laser heating study. *Journal of Nuclear Materials*, 449(1-3):1–8, June 2014. xii, 137

[34] H. Muta, K. Kurosaki, M. Uno, and S. Yamanaka. Thermal and mechanical properties of uranium nitride prepared by SPS technique. *Journal of Materials Science*, 43(19):6429–6434, October 2008. xii, xxii, 137, 143, 144, 145

[35] S. D. Gupta, S. K. Gupta, and P. K. Jha. High pressure study on the phonon spectra and thermal properties in hafnium nitride and zirconium nitride. *Journal of Thermal Analysis and Calorimetry*, 107(1):49–53, January 2012. xii, xxii, 137, 140

[36] Edward O Speidel and Donald L Keller. Fabrication and properties of hot-pressed uranium mononitride. Technical report, Battelle Memorial Inst., Columbus, Ohio, 1963. xii, 137

[37] S. B. Ross, M. S. Elgenk, and R. B. Matthews. Thermal-conductivity correlation for uranium nitride fuel between 10 and 1923 K. *Journal of Nuclear Materials*, 151(3):313–317, February 1988. xii, xxii, 137, 142, 322

[38] M. M. Opeka, I. G. Talmy, E. J. Wuchina, J. A. Zaykoski, and S. J. Causey. Mechanical, thermal, and oxidation properties of refractory hafnium and zirconium compounds. *Journal of the European Ceramic Society*, 19(13-14):2405–2414, October 1999. xii, xxii, 137, 142, 144, 319

[39] S. L. Hayes, J. K. Thomas, and K. L. Peddicord. Material property correlations for uranium mononitride: IV. Thermodynamic properties. *Journal of nuclear materials*, 171(2-3):300–318, 1990. ISBN: 0022-3115 Publisher: Elsevier. xii, xiii, xxxii, 139, 140, 254, 255, 316

[40] Neal D. Gaffin, Caen Ang, Justin L. Milner, Kelsa B. Palomares, and Steven J. Zinkle. Consolidation behavior of Mo30W alloy using spark plasma sintering. *International Journal of Refractory Metals and Hard Materials*, 104:105778, January 2022. Section: 105778. xii, xiii, xxiii, xxiv, xxx, 177, 178, 180, 181, 183, 184, 186, 278, 280, 282, 284, 398

[41] Song Xiwen, Xie Min, Zhou Fen, Jia Guixiao, Hao Xihong, and An Shengli. High-temperature thermal properties of yttria fully stabilized zirconia ceramics. *Journal of Rare Earths*, 29(2):155–159, 2011. ISBN: 1002-0721 Publisher: Elsevier. xiii, xxi, xxxii, 124, 127, 136, 254, 255, 312

[42] Daniel R Koenig. Experience gained from the space nuclear rocket program (Rover). Technical report, Los Alamos National Laboratory, 1986. xv, 3, 13, 28

[43] Anatoly Lanin. Materials of the Reactor Core. In *Nuclear Rocket Engine Reactor*, volume 170 of *Materials of the Reactor Core.*, pages 29–70. Springer, Berlin, Heidelberg, 2013. xv, 28, 30

[44] Peter M. Derlet. Sintering theory, 2017. xvi, 33, 34

[45] R. Ohser-Wiedemann, U. Martin, H. J. Seifert, and A. Muller. Densification behaviour of pure molybdenum powder by spark plasma sintering. *International*

Journal of Refractory Metals & Hard Materials, 28(4):550–557, July 2010. Section: 550. xvi, 32, 35, 36, 37, 38, 39, 285

[46] B. Mouawad, M. Soueidan, D. Fabregue, C. Buttay, V. Bley, B. Allard, and H. Morel. Full Densification of Molybdenum Powders Using Spark Plasma Sintering. *Metallurgical and Materials Transactions a-Physical Metallurgy and Materials Science*, 43a(9):3402–3409, September 2012. xvi, 32, 35, 41, 42

[47] G. Lee, J. McKittrick, E. Ivanov, and E. A. Olevsky. Densification mechanism and mechanical properties of tungsten powder consolidated by spark plasma sintering. *International Journal of Refractory Metals & Hard Materials*, 61:22–29, December 2016. Section: 22. xvi, 32, 40, 43, 44

[48] T. R. Malow and C. C. Koch. Grain growth in nanocrystalline iron prepared by mechanical attrition. *Acta Materialia*, 45(5):2177–2186, May 1997. xvi, 44, 45

[49] SP Chakraborty, S Banerjee, Gopal Sanyal, VS Bhave, Bhaskar Paul, IG Sharma, and AK Suri. Studies on the synthesis of a Mo–30 wt% W alloy by non-conventional approaches. *Journal of Alloys and Compounds*, 501(2):211–217, 2010. xvi, xvii, 44, 46, 47

[50] R. V. Batienkov, I. Y. Efimochkin, I. V. Osin, and A. A. Khudnev. Study of Molybdenum-Tungsten Powder Compaction Processes by Spark Plasma Sintering. *Metallurgist*, 63(11-12):1329–1336, March 2020. xvii, 48, 49, 50, 51, 52, 285

[51] Beatriz Núñez-González, Angel L Ortiz, Fernando Guiberteau, and Mats Nygren. Improvement of the spark-plasma-sintering kinetics of ZrC by high-energy ball-milling. *Journal of the American Ceramic Society*, 95(2):453–456, 2012. xvii, 54, 55

[52] D. Sciti, S. Guicciardi, and M. Nygren. Spark plasma sintering and mechanical behaviour of ZrC-based composites. *Scripta Materialia*, 59(6):638–641, September 2008. xvii, 54, 56

[53] X. Wei, C. Back, O. Izhvanov, C. D. Haines, and E. A. Olevsky. Zirconium carbide produced by spark plasma sintering and hot pressing: densification kinetics, grain growth, and thermal properties. *Materials (Basel)*, 9(7), July 2016. Edition: 2017/08/05. xvii, xxv, 54, 57, 58, 204, 209

[54] Dennis S Tucker, Andrew O'Connor, and Robert Hickman. A methodology for producing uniform distribution of UO2 in a tungsten matrix. *Journal of Phyisical Science*, 5(4):255–262, 2015. xvii, 59, 60, 210

[55] Werner Martienssen and Hans Warlimont. *Springer handbook of condensed matter and materials data*. Springer Science & Business Media, 2006. xviii, xix, xxviii, xxxi, 67, 75, 76, 78, 81, 82, 83, 257, 303, 310, 311

[56] N. S. Rasor and J. D. Mcclelland. Thermal properties of graphite, molybdenum and tantalum to their destruction temperatures. *Journal of Physics and Chemistry of Solids*, 15(1-2):17–26, August 1960. Section: 17. xviii, 66, 68

[57] James W Edwards, Rudolph Speiser, and Herrick L Johnston. High temperature structure and thermal expansion of some metals as determined by X-ray diffraction data. I. Platinum, tantalum, niobium, and molybdenum. *Journal of Applied Physics*, 22(4):424–428, 1951. xviii, 69, 70, 166, 244

[58] V. Y. Bodryakov. Correlation of temperature dependencies of thermal expansion and heat capacity of refractory metal up to the melting point: Molybdenum. *High Temperature*, 52(6):840–845, November 2014. Section: 840. xviii, 69, 71, 72, 75, 79

[59] L. S. Dubrovinsky and S. K. Saxena. Thermal expansion of periclase (MgO) and tungsten (W) to melting temperatures. *Physics and Chemistry of Minerals*, 24(8):547–550, October 1997. xviii, 69, 73

[60] Y Waseda, K Hirata, and M Ohtani. High-temperature thermal expansion of platinum, tantalum, molybdenum, and tungsten measured by X-ray diffraction. *High Temperatures-High Pressures*, 7(2):221–226, 1975. xviii, 74

[61] J. Demarquay. *Chaleur - Nouvelle Methode Pour Letude De La Dilation Des Corps Aux Temperatures Elevees - Dilatation Du Tungstene Et Du Molybdene. *Comptes Rendus Hebdomadaires Des Seances De L Academie Des Sciences*, 220(2):81–83, 1945. xviii, 74

[62] A. G. Worthing. Physical properties of well seasoned molybdenum and tantalum as a function of temperature. *Physical Review*, 28(1):190–201, July 1926. xviii, 74

[63] R. D. Allen, L. F. Glasier, and P. L. Jordan. Spectral emissivity, total emissivity, and thermal conductivity of molybdenum, tantalum, and tungsten above 2300-degrees-K. *Journal of Applied Physics*, 31(8):1382–1387, 1960. xviii, 75, 77

[64] V. Y. Bodryakov. Correlation of temperature dependences of thermal expansion and heat capacity of refractory metal up to the melting point: Tungsten. *High Temperature*, 53(5):643–648, September 2015. xix, 69, 75, 80

[65] Thomas Edwin Tietz and Jess W Wilson. *Behavior and properties of refractory metals*, volume 6. Stanford University Press, 1965. xix, 81, 83

[66] S. L. Robinson and O. D. Sherby. Mechanical behavior of polycrystalline tungsten at elevated temperature. *Acta Metallurgica*, 17(2):109–&, February 1969. xix, 84

[67] Y. Mutoh, K. Ichikawa, K. Nagata, and M. Takeuchi. Effect of rhenium addition on fracture-toughness of tungsten at elevated-temperatures. *Journal of Materials Science*, 30(3):770–775, February 1995. xix, xx, 81, 85, 90, 93, 95

[68] RW Burman. Molybdenum—a super superalloy. *JOM*, 29(12):12–17, 1977. xix, 86, 87

[69] E. Giorgi, S. Grasso, E. Zapata-Solvas, and W. E. Lee. Reactive carbothermal reduction of ZrC and ZrOC using Spark Plasma Sintering. *Advances in Applied Ceramics*, 117(sup1):S34–S47, October 2018. xix, 86, 88

[70] J. M. Steichen. Tensile properties of neutron-irradiated TZM and tungsten. *Journal of Nuclear Materials*, 60(1):13–19, April 1976. Section: 13. xix, 90, 91

[71] Y. Hiraoka, H. Kurishita, M. Narui, and H. Kayano. Fracture and ductile-to-brittle transition characteristics of molybdenum by impact and static bend tests. *Materials Transactions Jim*, 36(4):504–510, April 1995. xix, 90, 92

[72] B. Gludovatz, S. Wurster, A. Hoffmann, and R. Pippan. Fracture toughness of polycrystalline tungsten alloys. *International Journal of Refractory Metals & Hard Materials*, 28(6):674–678, November 2010. xx, 94, 95

[73] A. Fernández Guillermet. Analysis of thermochemical properties and phase stability in the zirconium-carbon system. *Journal of Alloys and Compounds*, 217(1):69–89, January 1995. Section: 69. xx, 96

[74] Y. Katoh, G. Vasudevamurthy, T. Nozawa, and L. L. Snead. Properties of zirconium carbide for nuclear fuel applications. *Journal of Nuclear Materials*, 441(1-3):718–742, October 2013. Section: 718. xx, xxi, xxvii, 97, 99, 100, 106, 109, 114, 115, 249

[75] D. Demirskyi, H. Borodianska, T. S. Suzuki, Y. Sakka, K. Yoshimi, and O. Vasylkiv. High-temperature flexural strength performance of ternary high-entropy carbide consolidated via spark plasma sintering of TaC, ZrC and NbC.

Scripta Materialia, 164:12–16, 2019. ISBN: 1359-6462 Publisher: Elsevier. xxi, 116, 119, 273

[76] R. Darolia and T. F. Archbold. Plastic-Deformation of Polycrystalline Zirconium Carbide. *Journal of Materials Science*, 11(2):283–290, February 1976. xxi, 116, 120

[77] K. Sasaki, T. Terai, A. Suzuki, and N. Akasaka. Effect of the Y2O3 concentration in YSZ on the thermophysical property as a thermal shielding material. *International Journal of Applied Ceramic Technology*, 7(4):518–527, 2010. xxi, 126

[78] Fredrik Grønvold, Nils Jørgen Kveseth, Arvid Sveen, and Jiři Tichý. Thermodynamics of the UO2+ x phase I. Heat capacities of UO2. 017 and UO2. 254 from 300 to 1000 K and electronic contributions. *The Journal of Chemical Thermodynamics*, 2(5):665–679, 1970. xxi, 129

[79] K. Naito. High-temperature heat-capacities of UO2 and doped UO2. *Journal of Nuclear Materials*, 167:30–35, September 1989. xxii, 130

[80] L. Vlahovic, D. Staicu, A. Kust, and R. J. M. Konings. Thermal diffusivity of UO2 up to the melting point. *Journal of Nuclear Materials*, 499:504–511, February 2018. xxii, 133

[81] D. G. Martin. The thermal-expansion of solid UO2 and (U, Pu) mixed oxides - a review and recommendations. *Journal of Nuclear Materials*, 152(2-3):94–101, May 1988. xxii, 135

[82] H Okamoto. NU (nitrogen-uranium). *Journal of phase equilibria*, 18(1), 1997. xxii, 137

[83] H Okamoto. The Hf-N (hafnium-nitrogen) system. *Bulletin of Alloy Phase Diagrams*, 11(2):146–149, 1990. xxii, 138

[84] S. L. Hayes, J. K. Thomas, and K. L. Peddicord. Material property correlations for uranium mononitride. *Journal of Nuclear Materials*, 171(2-3):289–299, May 1990. Section: 289. xxii, 144

[85] Kun Yang, Erofili Kardoulaki, Dong Zhao, Andre Broussard, Kathryn Metzger, Joshua T. White, Michael R. Sivack, Kenneth J. Mcclellan, Edward J. Lahoda, and Jie Lian. Uranium nitride (UN) pellets with controllable microstructure and phase–fabrication by spark plasma sintering and their thermal-mechanical and oxidation properties. *Journal of Nuclear Materials*, 557:153272, 2021. ISBN: 0022-3115 Publisher: Elsevier. xxii, 139, 147

[86] A. S. Pavlovic, V. Suresh Babu, and Mohindar S. Seehra. High-temperature thermal expansion of binary alloys of Ni with Cr, Mo and Re: a comparison with molecular dynamics simulations. *Journal of Physics: Condensed Matter*, 8(18):3139, 1996. ISBN: 0953-8984 Publisher: IOP Publishing. xxii, 146, 148

[87] P. Asoka-Kumar, M. Alatalo, V. J. Ghosh, A. C. Kruseman, B. Nielsen, and K. G. Lynn. Increased elemental specificity of positron annihilation spectra. *Phys Rev Lett*, 77(10):2097–2100, September 1996. Edition: 1996/09/02. xxiii, 31, 146, 149, 150

[88] M. O. Marlowe and A. I. Kaznoff. Development of low thermal expansion tungsten UO2 cermet fuel. Technical report, National Aeronautics and Space Administration, 1970. xxiii, 154, 156

[89] G. Arthur and J. A. Coulson. Physical properties of uranium dioxide-stainless steel cermets. *Journal of Nuclear Materials*, 13(2):242–253, 1964. ISBN: 0022-3115 Publisher: Elsevier. xxiii, 154, 157, 158, 302

[90] Nils Claussen. Fracture toughness of Al2O3 with an unstabilized ZrO2 dispersed phase. *Journal of the American Ceramic Society*, 59(1-2):49–51, 1976. ISBN: 0002-7820 Publisher: Wiley Online Library. xxiii, 159, 160, 331

[91] L. Brewer and R. H. Lamoreaux. Thermochemical properties. *Molybdenum: physico-chemical properties of its compounds and alloys*, 1980. xxx, 295

[92] S. L. Hayes, J. K. Thomas, and K. L. Peddicord. Material property correlations for uranium mononitride: I. Physical properties. *Journal of Nuclear materials*, 171(2-3):262–270, 1990. ISBN: 0022-3115 Publisher: Elsevier. xxxi, 308

[93] Ro R. Tummala and A. L. Friedberg. Thermal expansion of composite materials. *Journal of Applied Physics*, 41(13):5104–5107, 1970. ISBN: 0021-8979 Publisher: American Institute of Physics. xxxi, 157, 302, 308

[94] B. Predel. C-Mo (carbon-molybdenum): Datasheet from Landolt-Börnstein - group IV physical chemistry. Technical Report 5B: "B-Ba – C-Zr", Springer-Verlag Berlin Heidelberg. xxxiv, 408

[95] Sonny Mitchell and Les Johnson. STMD: nuclear thermal propulsion update. In *NIAC, Technology, Innovation and Engineering Committee Meeting*, 2019. Issue: MSFC-E-DAA-TN68083. 1, 4

[96] Stanley K Borowski, David R McCurdy, and Thomas W Packard. Nuclear thermal propulsion (NTP): A proven growth technology for human NEO/Mars exploration missions. pages 1–20. IEEE, 2012. 2

[97] Claude R Joyner, Wesley Deason, Michael Eades, Timothy Kokan, Daniel J Levack, Frederick Widman, and Tyler Jennings. NTP design sensitivities for human lunar and Mars missions. pages 1–13, 2018. 2

[98] Mark Stewart and Bruce G Schnitzler. A comparison of materials issues for cermet and graphite-based NTP fuels. In *49th AIAA/ASME/SAE/ASEE Joint PropulsionConference*, page 3999. 2013. 2, 7, 8, 13, 18, 61

[99] William J. Emrich Jr. *Principles of nuclear rocket propulsion*. Butterworth-Heinemann, 2016. 4

[100] Doyce P. Mitchell. Space technology mission directorate game changing development program-nuclear thermal propulsion (NTP) FY19 annual review. Technical report, 2019. 4, 8

[101] Stanley K Borowski, David McCurdy, and Thomas Packard. Nuclear thermal propulsion (NTP): A proven growth technology for fast transit human missions to mars. page 5354, 2013. 4, 7

[102] Christopher B Reynolds, Claude R Joyner, Timothy S Kokan, Daniel J Levack, and Brian Muzek. NTP robustness for mars conjunction and opposition class missions. page 4124, 2020. 6

[103] C. W. Watson. Nuclear rockets: high-performance propulsion for mars. Technical Report LA-12784-MS, Los Alamos National Laboratory, NM, United States., 1994. 6, 13, 17

[104] Z. A. Munir, U. Anselmi-Tamburini, and M. Ohyanagi. The effect of electric field and pressure on the synthesis and consolidation of materials: A review of the spark plasma sintering method. *Journal of Materials Science*, 41(3):763–777, February 2006. Section: 763. 7, 31, 283, 285, 288

[105] Robert Hickman, Binayak Panda, and Sandeep Shah. Fabrication of high temperature cermet materials for nuclear thermal propulsion. 2005. 7, 18

[106] Robert Hickman, Jeramie Broadway, and Omar Mireles. Fabrication and testing of CERMET fuel materials for nuclear thermal propulsion. pages 1–18, 2012. 7, 18

[107] C. Haertling and R. J. Hanrahan. Literature review of thermal and radiation performance parameters for high-temperature, uranium dioxide fueled cermet materials. *Journal of Nuclear Materials*, 366(3):317–335, July 2007. Section: 317. 7, 19

[108] J. T. Gates, A. Denig, R. Ahmed, V. K. Mehta, and D. Kotlyar. Low-enriched cermet-based fuel options for a nuclear thermal propulsion engine. *Nuclear Engineering and Design*, 331:313–330, May 2018. Section: 313. 8

[109] Taylor G Duffin, Kelsa M Benensky, Steven J Zinkle, Marvin W Barnes, and Dennis S Tucker. Production and hot hydrogen testing of subscale molybdenum cermets for nuclear thermal propulsion. pages 1–8, 2018. 8, 61, 121, 398

[110] W. F. Cureton, J. Zillinger, J. Rosales, R. P. Wilkerson, M. Lang, and M. Barnes. Microstructural evolution of Mo-UO2 cermets under high temperature hydrogen environments. *Journal of Nuclear Materials*, 538:152297, September 2020. 8, 61, 398

[111] M. Krecicki and D. Kotlyar. Low enriched nuclear thermal propulsion neutronic, thermal hydraulic, and system design space analysis. *Nuclear Engineering and Design*, 363:110605, July 2020. 8

[112] A. G. Nelson, A. A. Kasam-Griffith, M. I. Atz, and F. Heidet. Performance of HALEU and HEU-fueled nuclear thermal propulsion reactors. Technical report, Argonne National Lab.(ANL), Argonne, IL (United States), 2021. 8

[113] A. Calomino. Space nuclear power and propulsion (SNPP). *NASA STMD Nuclear Technologies Portfolio, Sept*, 2020. 8

[114] JL Finseth. Rover nuclear rocket engine program: Overview of rover engine tests. Technical report, Sverdrup Technology, Inc., Huntsville, AL (United States), 1991. Volume: N–92-15117. 13, 17, 25, 28

[115] J. M. Taub. Review of fuel element development for nuclear rocket engines. 1975. Publisher: Los Alamos Scientific Lab. 13

[116] Keith V. Davidson. Brief review of Rover fuel development at Los Alamos. In *AIP Conference Proceedings*, volume 217, pages 1015–1023. American Institute of Physics, 1991. Issue: 3. 13

[117] Luther L Lyon. Performance of (U, Zr) C-graphite (composite) and of (U, Zr) C (carbide) fuel elements in the nuclear ffurnace 1 test reactor. Technical report, Los Alamos Scientific Lab., N. Mex.(USA), 1973. 17

[118] GB Kruger. 710 high temperature gas reactor program summary report – Volume 3, fuel element development. Technical report, General Electric, Cincinnati, OH, 1973. Volume: III. 18, 19, 20, 22

[119] J. F. Marchaterre. Nuclear rocket program terminal report. *ANL-7236, Argonne National Laboratory, Argonne, IL*, 1968. 18

[120] Samim Anghaie and Paul Harris. Evaluation of cermet fuels test data. 2004. 18

[121] Robert Brengle, Richard Harty, and Samit Bhattacharyya. The promise and challenges of cermet fueled nuclear thermal propulsion reactors. page 2111, 1993. 19

[122] Samim Anghaie and Paul Harris. Evaluation of cermet fuels test data. United States, 2004. American Nuclear Society - ANS. 19

[123] J. Walton. An overview of tested and analyzed NTP concepts. page 3503, 1991. 28

[124] A. G. Lanin. Strength and thermal stress resistance of structural ceramic (111 p.). *Moscow: M. Moscow State Engineer Physical institute*, 1998. 28

[125] Rajendra K. Bordia, Suk-Joong L. Kang, and Eugene A. Olevsky. Current understanding and future research directions at the onset of the next century of sintering science and technology. *Journal of the American Ceramic Society*, 100(6):2314–2352, 2017. ISBN: 0002-7820 Publisher: Wiley Online Library. 32

[126] Wayne S Young and Ivan B Cutler. Initial sintering with constant rates of heating. *Journal of the American ceramic Society*, 53(12):659–663, 1970. 32, 172, 173

[127] Zhang Zhaohui, Wang Fuchi, Wang Lin, Li Shukui, and S Osamu. Sintering mechanism of large-scale ultrafine-grained copper prepared by SPS method. *Materials Letters*, 62(24):3987–3990, 2008. 35

[128] RC O'Brien and ND Jerred. Spark plasma sintering of W–UO2 cermets. *Journal of nuclear materials*, 433(1-3):50–54, 2013. 59

[129] L. Vegard. The constitution of the mixed crystals and the filling of space of the atoms. *Zeitschrift Fur Physik*, 5:17–26, April 1921. 66

[130] F. C. Nix and D. MacNair. The thermal expansion of pure metals II Molybdenum, palladium, silver, tantalum, tungsten, platinum, and lead. *Physical Review*, 61(1/2):74–78, January 1942. 66

[131] David Tabor. *The hardness of metals*. Oxford university press, 2000. 81, 185, 279, 324

[132] Frank J Zerilli and Ronald W Armstrong. Dislocation-mechanics-based constitutive relations for material dynamics calculations. *Journal of applied physics*, 61(5):1816–1825, 1987. 86

[133] J. J. Nickl. The refractory carbides. Von E. K. Storms. Aus der Reihe refractory materials. Vol. 2, herausgeg. von J. L. Margrave. Academic Press, New York-London 1967. 1. Aufl., XIII, 285 S., 74 Abb. und 83 Tab. $ 12.50. *Angewandte Chemie*, 81(11):436–436, 1969. Section: 436. 94

[134] C. Gasparrini, D. S. Rana, N. Le Brun, D. Horlait, C. N. Markides, I. Farnan, and W. E. Lee. On the stoichiometry of zirconium carbide. *Sci Rep*, 10(1):6347, April 2020. Edition: 2020/04/15. 94

[135] H. F. Jackson and W. E. Lee. Properties and characteristics of ZrC. 2012. Publisher: Elsevier. 97, 200

[136] Taylor G Duffin, Steven J Zinkle, and Kelsa M Benensky. Material characterization of subscale molybdenum cermets for nuclear thermal propulsion. page 3945, 2019. 121

[137] N. Gaffin, K. M. Benensky, and S.J. Zinkle. Irradiation testing of molybdenum and tungsten based cermets for use in nuclear thermal propulsion. Knoxville, TN, 2020. ORNL. 121

[138] J. K. Fink, T. Sofu, and H. Ley. International Nuclear Safety Center database on thermophysical properties of reactor materials. *International Journal of Thermophysics*, 20(1):279–287, January 1999. 131

[139] R. L. Gibby. The effect of plutonium content on the thermal conductivity of (U, Pu) O2 solid solutions. *Journal of Nuclear Materials*, 38(2):163–177, 1971. ISBN: 0022-3115 Publisher: Elsevier. 131, 322

[140] V. V. Novikov, R. B. Sivov, E. N. Mikheev, and A. V. Fedotov. Fracture toughness of vver and pwr uranium-dioxide fuel pellets with different grain size. *Atomic Energy*, 118(2):117–123, 2015. ISBN: 1573-8205 Publisher: Springer. 136

[141] Junya Kondoh, Hirohisa Shiota, Katsuhiro Kawachi, and Toshio Nakatani. Yttria concentration dependence of tensile strength in yttria-stabilized zirconia. *Journal of alloys and compounds*, 365(1-2):253–258, 2004. ISBN: 0925-8388 Publisher: Elsevier. 136

[142] V. G. Baranov, A. V. Tenishev, R. S. Kuzmin, S. A. Pokrovskiy, V. V. Mikhalchik, V. A. Astafyev, M. L. Taubin, and E. S. Solntseva. Thermal stability investigation technique for uranium nitride. *Annals of Nuclear Energy*, 87:784–792, January 2016. 136

[143] P. N. Bossart. Spectral emissivities, resistivity, and thermal expansion of tungsten-molybdenum alloys. *Physics*, 7(2):50–54, 1936. ISBN: 0148-6349 Publisher: American Institute of Physics. 146

[144] Lothar Nordheim. Zur elektronentheorie der metalle. i. *Annalen der Physik*, 401(5):607–640, 1931. ISBN: 0003-3804 Publisher: Wiley Online Library. 146

[145] A. Rudajevova, M. Staněk, and P. Lukáč. Determination of thermal diffusivity and thermal conductivity of Mg–Al alloys. *Materials Science and Engineering: A*, 341(1-2):152–157, 2003. ISBN: 0921-5093 Publisher: Elsevier. 151, 319

[146] Philip S. Turner. Thermal-expansion stresses in reinforced plastics. *J. Res. NBS.*, 37:239–250, 1946. 151

[147] Woldemar Voigt. Ueber die Beziehung zwischen den beiden Elasticitätsconstanten isotroper Körper. *Annalen der physik*, 274(12):573–587, 1889. ISBN: 0003-3804 Publisher: Wiley Online Library. 152

[148] AJZAMM Reuss. Computation of the yield point of mixed crystals due to hiring for single crystals. *Math. Phys*, 9:49–58, 1929. 152

[149] M. F. Ashby. Criteria for selecting the components of composites. *Acta metallurgica et materialia*, 41(5):1313–1335, 1993. ISBN: 0956-7151 Publisher: Elsevier. 152, 310, 324

[150] Bernard Budiansky. Thermal and thermoelastic properties of isotropic composites. *Journal of composite Materials*, 4(3):286–295, 1970. ISBN: 0021-9983 Publisher: Sage Publications Sage CA: Thousand Oaks, CA. 152

[151] B. Walter Rosen and Zvi Hashin. Effective thermal expansion coefficients and specific heats of composite materials. *International Journal of Engineering Science*, 8(2):157–173, 1970. ISBN: 0020-7225 Publisher: Elsevier. 152

[152] Hsiu-Ching Hsu, Chun-Ting Yeh, and Wei-Hsing Tuan. Heat capacity of Al2O3-NiAl composites, a key parameter for thermal management. *Ceramics International*, 43:S705–S709, 2017. ISBN: 0272-8842 Publisher: Elsevier. 152

[153] R. C. Progelhof, J. L. Throne, and R. R. Ruetsch. Methods for predicting the thermal conductivity of composite systems: a review. *Polymer Engineering & Science*, 16(9):615–625, 1976. ISBN: 0032-3888 Publisher: Wiley Online Library. 153

[154] D. A. G. Bruggeman. Dielectric constant and conductivity of mixtures of isotropic materials. *Ann. Phys.(Leipzig)*, 24:636–679, 1935. ISBN: 0003-4916. 153

[155] T. B. Lewis and L. E. Nielsen. Dynamic mechanical properties of particulate-filled composites. *Journal of applied polymer science*, 14(6):1449–1471, 1970. ISBN: 0021-8995 Publisher: Wiley Online Library. 153

[156] Lawrence E. Nielsen. Generalized equation for the elastic moduli of composite materials. *Journal of Applied Physics*, 41(11):4626–4627, 1970. ISBN: 0021-8979 Publisher: American Institute of Physics. 153

[157] Lawrence E. Nielsen. Thermal conductivity of particulate-filled polymers. *Journal of applied polymer science*, 17(12):3819–3820, 1973. ISBN: 0021-8995 Publisher: Wiley Online Library. 153

[158] James Clerk Maxwell. *Electricity and magnetism*, volume 2. Dover New York, 1954. 154

[159] E. H. Kerner. The elastic and thermo-elastic properties of composite media. *Proceedings of the physical society. Section B*, 69(8):808, 1956. ISBN: 0370-1301 Publisher: IOP Publishing. 157

[160] V. N. Kytopoulos. The elastic modulus and the thermal expansion coefficient in particulate composites by a hexaphase model. *Journal of Reinforced Plastics*

and Composites, 32(7):499–510, 2013. ISBN: 0731-6844 Publisher: SAGE Publications Sage UK: London, England. 157

[161] F. P. Knudsen. Dependence of mechanical strength of brittle polycrystalline specimens on porosity and grain size. *Journal of the American Ceramic Society*, 42(8):376–387, 1959. ISBN: 0002-7820 Publisher: Wiley Online Library. 157, 159

[162] H. S. Kim, Yu Estrin, and M. B. Bush. Plastic deformation behaviour of fine-grained materials. *Acta Materialia*, 48(2):493–504, 2000. ISBN: 1359-6454 Publisher: Elsevier. 159

[163] Hyoung Seop Kim, Sun Ig Hong, and Sun Jae Kim. On the rule of mixtures for predicting the mechanical properties of composites with homogeneously distributed soft and hard particles. *Journal of Materials Processing Technology*, 112(1):109–113, 2001. ISBN: 0924-0136 Publisher: Elsevier. 159

[164] Ning Wang, Zhirui Wang, K. T. Aust, and Uwe Erb. Effect of grain size on mechanical properties of nanocrystalline materials. *Acta Metallurgica et Materialia*, 43(2):519–528, 1995. ISBN: 0956-7151 Publisher: Elsevier. 159

[165] F. Danusso and G. Tieghi. Strength versus composition of rigid matrix particulate composites. *Polymer*, 27(9):1385–1390, 1986. ISBN: 0032-3861 Publisher: Elsevier. 161

[166] G. Levita, A. Marchetti, and Andrea Lazzeri. Fracture of ultrafine calcium carbonate/polypropylene composites. *Polymer composites*, 10(1):39–43, 1989. ISBN: 0272-8397 Publisher: Wiley Online Library. 161

[167] Shao-Yun Fu, Xi-Qiao Feng, Bernd Lauke, and Yiu-Wing Mai. Effects of particle size, particle/matrix interface adhesion and particle loading on mechanical properties of particulate–polymer composites. *Composites Part B:*

Engineering, 39(6):933–961, 2008. ISBN: 1359-8368 Publisher: Elsevier. 161, 162, 331

[168] Luigi Nicolais and Moshe Narkis. Stress-strain behavior of styrene-acrylonitrile/glass bead composites in the glassy region. *Polymer Engineering & Science*, 11(3):194–199, 1971. ISBN: 0032-3888 Publisher: Wiley Online Library. 161

[169] L. Nicolais and L. Nicodemo. The effect of particles shape on tensile properties of glassy thermoplastic composites. *International Journal of Polymeric Materials*, 3(3):229–243, 1974. ISBN: 0091-4037 Publisher: Taylor & Francis. 161

[170] J. Leidner and R. T. Woodhams. The strength of polymeric composites containing spherical fillers. *Journal of Applied Polymer Science*, 18(6):1639–1654, 1974. ISBN: 0021-8995 Publisher: Wiley Online Library. 161

[171] B. Pukanszky. Influence of interface interaction on the ultimate tensile properties of polymer composites. *Composites*, 21(3):255–262, 1990. ISBN: 0010-4361 Publisher: Elsevier. 161

[172] A. Rabiei, L. Vendra, and T. Kishi. Fracture behavior of particle reinforced metal matrix composites. *Composites Part A: Applied Science and Manufacturing*, 39(2):294–300, 2008. ISBN: 1359-835X Publisher: Elsevier. 162

[173] Joydeb Mukerji. Ceramic Matrix Composites. *Defence Science Journal*, 43(4):385, 1993. ISBN: 0011-748X Publisher: Defence Scientific Information & Documentation Centre. 162

[174] R. W. Rice. Mechanisms of toughening in ceramic matrix composites. In *Proceedings of the 5th Annual Conference on Composites and Advanced Ceramic Materials*, pages 661–701, 2009. 162

[175] Zhen-Yan Deng, Jian-Lin Shi, Yu-Feng Zhang, Dan-Yu Jiang, and Jing-Kun Guo. Pinning effect of SiC particles on mechanical properties of Al2O3–SiC ceramic matrix composites. *Journal of the European Ceramic Society*, 18(5):501–508, 1998. ISBN: 0955-2219 Publisher: Elsevier. 162

[176] Minoru Taya, Sv Hayashi, Albert S. Kobayashi, and H. S. Yoon. Toughening of a particulate-reinforced ceramic-matrix composite by thermal residual stress. *Journal of the American Ceramic Society*, 73(5):1382–1391, 1990. ISBN: 0002-7820 Publisher: Wiley Online Library. 162

[177] Sven Meister. Grain and particle analsysis with line intersection method, 2020. Publisher: MATLAB Central File Exchange. 165

[178] Gilles Orange, Hidehiko Tanaka, and Gilbert Fantozzi. Fracture toughness of pressureless sintered silicon carbide: A comparison of Klc measurement methods. *Ceramics International*, 13(3):159–165, January 1987. Section: 159. 170

[179] A. Giannattasio, Z. Yao, E. Tarleton, and S. G. Roberts. Brittle-ductile transitions in polycrystalline tungsten. *Philosophical Magazine*, 90(30):3947–3959, 2010. 170

[180] S. Mahalingam, P. E. J. Flewitt, and J. F. Knott. The ductile-brittle transition for nominally pure polycrystalline nickel. *Materials Science and Engineering a-Structural Materials Properties Microstructure and Processing*, 564:342–350, March 2013. 170

[181] J. F. Li, W. Pan, F. Sato, and R. Watanabe. Mechanical properties of polycrystalline Ti3SiC2 at ambient and elevated temperatures. *Acta Materialia*, 49(6):937–945, April 2001. 170

[182] D Munz, RT Bubsey, and JL Shannon Jr. Fracture toughness determination of A12O3 using four-point-bend specimens with straight-through and chevron notches. *Journal of the American Ceramic Society*, 63(5-6):300–305, 1980. 170

[183] Murat Bengisu. *Engineering ceramics*. Springer Science & Business Media, 2013. 170

[184] T Frueh, IO Ozer, Stephen F Poterala, H Lee, ER Kupp, C Compson, J Atria, and GL Messing. A critique of master sintering curve analysis. *Journal of the European Ceramic Society*, 38(4):1030–1037, 2018. 173

[185] Hunghai Su and D Lynn Johnson. Master sintering curve: a practical approach to sintering. *Journal of the American Ceramic Society*, 79(12):3211–3217, 1996. 173

[186] RM German. *Sintering theory and pratice*. John Willy & Sons, New York, 1996. Publisher: Inc. 175, 286

[187] Deborah C Blaine, John D Gurosik, Seong Jin Park, Randall M German, and Donald F Heaney. Master sintering curve concepts as applied to the sintering of molybdenum. *Metallurgical and materials transactions A*, 37(3):715–720, 2006. 175

[188] Seong Jin Park, Suk Hwan Chung, Debby Blaine, Pavan Suri, and Randall M German. Master sintering curve: construction software and its applications. *Advances in: Powder Metallurgy and Particulate Materials, MPIF, Princeton, NJ*, 2004. 175

[189] Eric R Jette and Frank Foote. Precision determination of lattice constants. *The Journal of Chemical Physics*, 3(10):605–616, 1935. 179

[190] VT Deshpande and Ramrao Pawar. X-ray determination of the thermal expansion of tungsten. *Current Science*, 31(12):497–499, 1962. 179

[191] W Erley and H Wagner. The diffusion coefficients in the system molybdenum–tungsten. *physica status solidi (a)*, 25(2):463–471, 1974. 179, 193, 292

[192] S. Diouf and A. Molinari. Densification mechanisms in spark plasma sintering: Effect of particle size and pressure. *Powder Technology*, 221:220–227, May 2012. 185, 283

[193] J-M Ting and RY Lin. Effect of particle-size distribution on sintering. *Journal of Materials Science*, 29(7):1867–1872, 1994. 185

[194] ZY Liu, TB Sercombe, and GB Schaffer. The effect of particle shape on the sintering of aluminum. *Metallurgical and Materials Transactions A*, 38(6):1351–1357, 2007. 185

[195] Mustafa Güden, Emrah Çelik, Alpay Hızal, Mustafa Altındiş, and Sinan Çetiner. Effects of compaction pressure and particle shape on the porosity and compression mechanical properties of sintered Ti6Al4V powder compacts for hard tissue implantation. *Journal of Biomedical Materials Research Part B: Applied Biomaterials: An Official Journal of The Society for Biomaterials, The Japanese Society for Biomaterials, and The Australian Society for Biomaterials and the Korean Society for Biomaterials*, 85(2):547–555, 2008. 185

[196] C Lemoine, A Fnidiki, D Lemarchand, and J Teillet. Grain core study of Fe1-xCrx nanograins obtained by mechanical alloying. *Journal of Physics: Condensed Matter*, 11(42):8341, 1999. 187

[197] BFO Costa, G Le Caër, and B Malaman. The effect of oxygen on ball milling of a near-equiatomic FeV sigma phase. *Journal of Applied Physics*, 104(8):084315, 2008. 187

[198] L. H. Liu, C. Yang, Y. G. Yao, F. Wang, W. W. Zhang, Y. Long, and Y. Y. Li. Densification mechanism of Ti-based metallic glass powders during spark plasma sintering process. *Intermetallics*, 66:1–7, November 2015. 189

[199] Jose Alberto Muñiz-Lerma, Amy Nommeots-Nomm, Kristian Edmund Waters, and Mathieu Brochu. A comprehensive approach to powder feedstock characterization for powder bed fusion additive manufacturing: A case study on AlSi7Mg. *Materials*, 11(12):2386, 2018. 189

[200] Annika Strondl, Ola Lyckfeldt, Håkan Brodin, and Ulf Ackelid. Characterization and control of powder properties for additive manufacturing. *Jom*, 67(3):549–554, 2015. 189

[201] J. Askill. Tracer diffusion of tungsten in molybdenum. *Physica Status Solidi*, 23(1):K21–&, 1967. 193, 292

[202] Fred J. Parker and Roy W. Rice. Correlation between grain size and thermal expansion for aluminum titanate materials. *Journal of the American Ceramic Society*, 72(12):2364–2366, 1989. ISBN: 0002-7820 Publisher: Wiley Online Library. 250

[203] Zhaojie Wang, Joseph E. Alaniz, Wanyoung Jang, Javier E. Garay, and Chris Dames. Thermal conductivity of nanocrystalline silicon: importance of grain size and frequency-dependent mean free paths. *Nano letters*, 11(6):2206–2213, 2011. ISBN: 1530-6984 Publisher: ACS Publications. 254

[204] EO Hall. The deformation and ageing of mild steel: III discussion of results. *Proceedings of the Physical Society. Section B*, 64(9):747, 1951. 279

[205] N. J. Petch. The cleavage strength of polycrystals. *Journal of the Iron and Steel Institute*, 174(1):25–28, 1953. 279

[206] Z. C. Cordero, B. E. Knight, and C. A. Schuh. Six decades of the Hall-Petch effect - a survey of grain-size strengthening studies on pure metals. *International Materials Reviews*, 61(8):495–512, 2016. 279

[207] UK Vashi, RW Armstrong, and GE Zima. The hardness and grain size of consolidated fine tungsten powder. *Metallurgical Transactions*, 1(6):1769–1771, 1970. 279, 280

[208] Vladica Nikolić, Johann Riesch, and Reinhard Pippan. The effect of heat treatments on pure and potassium doped drawn tungsten wires: Part I - Microstructural characterization. *Materials Science and Engineering: A*, 737:422–433, November 2018. Section: 422. 279, 280

[209] C. R. Joyner, M. Eades, J. Horton, T. Jennings, T. Kokan, D. J. H. Levack, B. J. Muzek, and C. B. Reynolds. LEU NTP engine system trades and mission options. *Nuclear Technology*, 206(8):1140–1154, August 2020. 281

[210] Shenghua Deng, Jianan Li, Ruidi Li, Hongjin Zhao, Tiechui Yuan, Lanbo Li, and Yingjie Zhang. The effect of particle size on the densification kinetics of tungsten powder during spark plasma sintering. *International Journal of Refractory Metals and Hard Materials*, 93:105358, 2020. 286

[211] S. Majumdar, S. Raveendra, I. Samajdar, P. Bhargava, and I. G. Sharma. Densification and grain growth during isothermal sintering of Mo and mechanically alloyed Mo-TZM. *Acta Materialia*, 57(14):4158–4168, August 2009. 288

[212] RM German and ZA Munir. Heterodiffusion model for the activated sintering of molybdenum. *Journal of the Less Common Metals*, 58(1):61–74, 1978. 288

[213] D Uskokovicj, M Risticj, and J Petkovicj. Study of kinetics and mechanism of sintering under constant heating rates. *Science of Sintering*, 8(2):129–148, 1976. 288

[214] N. C. Kothari. Sintering kinetics in tungsten powder. *Journal of the Less Common Metals*, 5(2):140–150, 1963. ISBN: 0022-5088 Publisher: Elsevier. 289

[215] T. Vasilos and J. T. Smith. Diffusion mechanism for tungsten sintering kinetics. *Journal of Applied Physics*, 35(1):215–217, 1964. ISBN: 0021-8979 Publisher: American Institute of Physics. 289

[216] Brady Butler, Eric Klier, Matt Kelly, and Micah Gallagher. Thermal stability of milled nanocrystalline tungsten powders. Technical report, Army Research Lab Aberdeen Proving Grpound MD Weapons and Materials Research Directorate, 2011. 289

[217] SP Garg and RJ Ackermann. The high temperature phase diagrams for zirconium-molybdenum and hafnium-molybdenum. *Metallurgical Transactions A*, 8(2):239–244, 1977. 292

[218] Charles Kittel, Paul McEuen, and Paul McEuen. *Introduction to solid state physics*, volume 8. Wiley New York, 1996. 315

[219] Iwan Sumirat, Y. Ando, and S. Shimamura. Theoretical consideration of the effect of porosity on thermal conductivity of porous materials. *Journal of Porous Materials*, 13(3):439–443, 2006. ISBN: 1573-4854 Publisher: Springer. 319

[220] Rocha-Rangel Enrique, A. Rodríguez-García José, Esparza-Vázquez Sergio, Cruz-Sánchez Brianda, Estrada-Guel Ivanovich, and Martínez-Sánchez Roberto. Effect of particle size and titanium content on the fracture toughness of particle-ceramic composites. *Materials Today: Proceedings*, 3(2):249–257, 2016. ISBN: 2214-7853 Publisher: Elsevier. 331

[221] Neal Gaffin, Caen Ang, Timothy Ironman, and S. J. Zinkle. Thermal shock testing of surrogate fuel materials for nuclear thermal propulsion. pages 1–8, Cleveland, Ohio, May 2022. American Nuclear Society. 395

[222] K Benensky, Marvin W Barnes, David E Bradley, C Romnes, and R Hickman. Operational characterization and testing of NASA MSFC'S compact fuel element environmental test (CFEET). 2018. 397

[223] James Werner, Sam Bhattacharyya, and Mike Houts. An overview of facilities and capabilities to support the development of nuclear thermal propulsion. 2011. 397

[224] Tyler R Steiner, Emily N Hutchins, and Richard H Howard. Steady-state in-pile nuclear thermal propulsion experimental testbed initial demonstration at The Ohio State University research reactor. *Nuclear Technology*, 208(1):100–114, 2022. 397

[225] Robert C O'BRIEN, Douglas E Burns, Nicolas E Woolstenhulme, Douglas Dempsey, Connie M Hill, and Cody Hale. The SIRIUS-1 nuclear thermal propulsion fuels transient test series in the Idaho National Laboratory TREAT reactor. *Proc. Topl. Mtg. Nuclear and Emerging Technologies for Space*, pages 25–28, 2019. 397, 398

[226] K. Palomares, R. Howard, and T. Steiner. Assessment of near-term fuel screening and qualification needs for nuclear thermal propulsion systems. *Nuclear Engineering and Design*, 367:110765, October 2020. Section: 110765. 397

[227] William Carmack and Jeff Halfinger. Current status of hot hydrogen test facilities at BWXT to support future nuclear propulsion research and development. page 3867, 2004. 397

[228] Guozheng Ma, Pengfei He, Shuying Chen, Jiajie Kang, Haidou Wang, Ming Liu, Qin Zhao, and GuoLu Li. Physicochemical properties of yttria-stabilized-zirconia in-flight particles during supersonic atmospheric plasma spray. *Coatings*, 9(7):431, 2019. 410

Appendix

Appendix A

Appendix A: Example Python Code for Sintering Analysis

Python was used to calculate the apparent activation energy using the Young and Cuttle initial stage sintering method and using the master sintering curve. Examples of the code used to determine the apparent activation energy for the ZrC powder are included in this appendix.

A.1 Young and Cuttler Initial Stage Sintering

The code used to determine the apparent activation energies for sintering using the young and Cutler method is listed below. This code was written to compare the four different Mo30W powders, but a similar code was used with the ZrC, cermet, and cercer materials.

```
# Convert data to find plot

# Initial sample height
```

```
# Temperature inverse

Tinv1  = 1/(Temp1 + 273.15)  # 50 C/min
Tinv3  = 1/(Temp3 + 273.15)  # 50 C/min
Tinvn1  = 1/(Tempn1 + 273.15) # 100 C/min
Tinvf1  = 1/(Tempf1 + 273.15) # 150 C/min

# Smooth Data

n = 4  # the larger n is, the smoother curve will be
b = [1.0 / n] * n
a = 1
Ratey1  = signal.filtfilt(b,a,Rate1, padlen=20)
Ratey3  = signal.filtfilt(b,a,Rate3, padlen=20)
Rateyn1  = signal.filtfilt(b,a,Raten1, padlen=20)
Rateyf1  = signal.filtfilt(b,a,Ratef1, padlen=20)

# Create variables for

LL01  = np.empty(np.size(Ratey1))
LL03  = np.empty(np.size(Ratey3))
LL0n1  = np.empty(np.size(Rateyn1))
LL0f1  = np.empty(np.size(Rateyf1))


for i in range(np.size(Ratey3)):
    LL03[i] = (Disp3[i])/L03
```

```
for i in range(np.size(Rateyn1)):
    LL0n1[i] = (Dispn1[i])/L0n1

for i in range(np.size(Rateyf1)):
    LL0f1[i] = (Dispf1[i])/L0f1

# Remove nonsensical data points

q = 1
o = 3
p = -4
r = 3

#Tinv3 = Tinv3[r:]
T3 = Temp3[r:]
Ratey3 = Ratey3[r:]
Tn1 = Tempn1[o:p]
#Tinvn1 = Tinvn1[o:p]
Rateyn1 = Rateyn1[o:p]
Tf1 = Tempf1[q:]
#Tinvf1 = Tinvf1[q:]
Rateyf1 = Rateyf1[q:]

### Create Variables for rate ###

grad3 = np.gradient(LL03,Temp3)
gradn1 = np.gradient(LL0n1,Tempn1)
gradf1 = np.gradient(LL0f1,Tempf1)
```

```
# Smooth Data

n = 4  # the larger n is, the smoother curve will be
b = [1.0 / n] * n
a = 1
grady3 = lfilter(b,a,grad3)
gradyn1 = lfilter(b,a,gradn1)
gradyf1 = lfilter(b,a,gradf1)

Tdiff = 1 # 5/3 for GB and 3/2 for Gv

ln3  = np.log(grady3*(Temp3**Tdiff))
lnn1  = np.log(gradyn1*(Tempn1**Tdiff))
lnf1  = np.log(gradyf1*(Tempf1**Tdiff))

### 50 C/min ###
# Plot 1/T vs. ln(TdL/L0/dT)

# Smooth Data

n = 3  # the larger n is, the smoother curve will be
b = [1.0 / n] * n
a = 1

lny3 = lfilter(b,a,ln3)

a3 = 119
```

```
b3 = 180    #98

print(Temp3[a3])
print(Temp3[b3])


plt.plot(Tinv3[a3:b3],lny3[a3:b3],'o')

# calc the trendline
z3 = np.polyfit(Tinv3[a3:b3],lny3[a3:b3], 1)
p3 = np.poly1d(z3)
plt.plot(Tinv3[a3:b3],p3(Tinv3[a3:b3]),"r--")
# the line equation:
print ("y=%.1fx+(%.1f)"%(z3[0],z3[1]))

n = 2

nQ3 = -z3[0]*R/1000
print('%2.f kJ/mol'%nQ3)

### 100 C/min ###
# Plot 1/T vs. ln(TdL/L0/dT)

# Smooth Data

n = 3  # the larger n is, the smoother curve will be
b = [1.0 / n] * n
a = 1
```

```
lnyn1 = lfilter(b,a,lnn1)

an1 = 62
bn1 = 95

print(Tempn1[an1])
print(Tempn1[bn1])



plt.plot(Tinvn1[an1:bn1],lnyn1[an1:bn1],'o')

# calc the trendline
zn1 = np.polyfit(Tinvn1[an1:bn1],lnyn1[an1:bn1], 1)
pn1 = np.poly1d(zn1)
plt.plot(Tinvn1[an1:bn1],pn1(Tinvn1[an1:bn1]),"r--")
# the line equation:
print ("y=%.1fx+(%.1f)"%(zn1[0],zn1[1]))

n = 2

nQn1 = -zn1[0]*R/1000
print('%2.f kJ/mol'%nQn1)

### 150 C/min ###
# Plot 1/T vs. ln(TdL/L0/dT)

# Smooth Data
```

```
n = 3  # the larger n is, the smoother curve will be
b = [1.0 / n] * n
a = 1

lnyf1 = lfilter(b,a,lnf1)

af1 = 37
bf1 = 60

print(Tempf1[af1])
print(Tempf1[bf1])



plt.plot(Tinvf1[af1:bf1],lnyf1[af1:bf1],'o')

# calc the trendline
zf1 = np.polyfit(Tinvf1[af1:bf1],lnyf1[af1:bf1], 1)
pf1 = np.poly1d(zf1)
plt.plot(Tinvf1[af1:bf1],pf1(Tinvf1[af1:bf1]),"r--")
# the line equation:
print ("y=%.1fx+(%.1f)"%(zf1[0],zf1[1]))

n = 2

nQf1 = -zf1[0]*R/1000
print('%2.f kJ/mol'%nQf1)
```

A.2 Master Sintering Curve

```
### Master Sintering Curve ###

Qspace = np.linspace(150,650,(650-150)/5+1)

def thetadif(Qval,Tk):
    return(1/Tk*np.exp(-Qval*1000/R/Tk))

### Find T rates ###
t50 = np.empty(len(time))
T50 = np.empty(len(time))
for i in range(len(time)):
    T50[i] = (Temp3[i])+273.15 # ((Temp1[i] + \
    Temp2[i] + Temp3[i] + Temp4[i])/4)+273.15
    t50[i] = time[i]-np.min(time)

t100 = np.empty(len(timen1))
T100 = np.empty(len(timen1))
for i in range(len(timen1)):
    T100[i] = (Tempn1[i])+273.15
    t100[i] = timen1[i]-np.min(timen1)

t150 = np.empty(len(timef1))
T150 = np.empty(len(timef1))
for i in range(len(timef1)):
    T150[i] = (Tempf1[i])+273.15
    t150[i] = timef1[i]-np.min(timef1)
```

```
### For heat rate 50 \textdegree C/min ###

theta50 = np.empty([len(time),len(Qspace)])
for j in range(len(Qspace)):
    for i in range(len(time)-1):
        theta50[i,j]  = (t50[i+1]-0)*(thetadif(Qspace[j],\
        T50[i+1])+thetadif(Qspace[j],T50[i])/2)
    theta50[-1,j] = theta50[-2,j]

RS50_1 = np.empty([len(time),len(Qspace)])
Sum50 = np.zeros(len(Qspace))
for j in range(len(Qspace)):
    for i in range(len(theta50)):
        Sum50[j] = Sum50[j] +\
        (theta50[i,j]/np.average(theta50[:,j])-1)**2

### For heat rate 100 \textdegree C/min ###

theta100 = np.empty([len(timen1),len(Qspace)])
for j in range(len(Qspace)):
    for i in range(len(timen1)-1):
        theta100[i,j]  = (t100[i+1]-0)*(thetadif(Qspace[j],\
        T100[i+1])+thetadif(Qspace[j],T100[i])/2)
    theta100[-1,j] = theta100[-2,j]

RS100_1 = np.empty([len(time),len(Qspace)])
Sum100 = np.zeros(len(Qspace))
```

```
for j in range(len(Qspace)):
    for i in range(len(theta100)):
        Sum100[j] = Sum100[j] +\
        (theta100[i,j]/np.average(theta100[:,j])-1)**2

### For heat rate of 150 \textdegree C/min ###

theta150 = np.empty([len(timef1),len(Qspace)])
for j in range(len(Qspace)):
    for i in range(len(timef1)-1):
        theta150[i,j]  = (t150[i+1]-0)*(thetadif(Qspace[j],\
        T150[i+1])+thetadif(Qspace[j],T150[i])/2)
    theta150[-1,j] = theta150[-2,j]

RS150_1 = np.empty([len(timef1),len(Qspace)])
Sum150 = np.zeros(len(Qspace))
for j in range(len(Qspace)):
    for i in range(len(theta150)):
        Sum150[j] = Sum150[j] +\
        (theta150[i,j]/np.average(theta150[:,j])-1)**2
#print(Sum150)

### Determine Fit ###

# Define psimodel

def psimodel(logtheta,b,c):
    return 1 / (1 + np.exp(-(logtheta-b)/c))
```

```
# Create arrays with guesses

aguess50 = 1
bguess50 = -30
cguess50 = 1

aguess50 = 1
bguess100 = -30
cguess100 = 1

aguess150 = 1
bguess150 = -30
cguess150 = 1

a50 = np.zeros(len(Qspace))
b50 = np.zeros(len(Qspace))
c50 = np.zeros(len(Qspace))

a100 = np.zeros(len(Qspace))
b100 = np.zeros(len(Qspace))
c100 = np.zeros(len(Qspace))

a150 = np.zeros(len(Qspace))
b150 = np.zeros(len(Qspace))
c150 = np.zeros(len(Qspace))

# Determine fit
```

```
for i in range(len(Qspace)):
    popt, pcov = curve_fit(f=psimodel,\
    xdata=np.log(theta50[:,i]),ydata=Psi3,\
    p0=(bguess50,cguess50))
    [b50[i], c50[i]] = popt
    popt, pcov = curve_fit(f=psimodel,\
    xdata=np.log(theta100[:,i]),ydata=Psin1,\
    p0=(bguess100,cguess100))
    [b100[i], c100[i]] = popt
    popt, pcov = curve_fit(f=psimodel,\
    xdata=np.log(theta150[:,i]),ydata=Psif1,\
    p0=(bguess150,cguess150))
    [b150[i], c150[i]] = popt

### Use fit to determine mean square residual

# Create new theta variable for psimodel

logthetaspace = np.linspace(-80,-5,1000)
Sum = np.zeros(len(Qspace))
MSR = np.zeros(len(Qspace))

for j in range(len(Qspace)):
    SumA = 0
    SumB = 0
    SumC = 0
    SumD = 0
```

```
    for i in range(len(logthetaspace)):
        SumA = (psimodel(logthetaspace[i],b150[j],\
        c150[j])-psimodel(logthetaspace[i],b50[j],c50[j]))
        SumB = (psimodel(logthetaspace[i],b100[j],\
        c100[j])-psimodel(logthetaspace[i],b50[j],c50[j]))
        SumC = (psimodel(logthetaspace[i],b150[j],\
        c150[j])-psimodel(logthetaspace[i],b100[j],c100[j]))
        SumD = SumD + (1/3*SumA + 1/3*SumB + 1/3*SumC)**2
    MSR[j] = np.sqrt(SumD)

### Determine Q ##

minMSR = np.amin(MSR)
print('Min MSR = %.2f'%minMSR)
min_index = np.where(MSR == np.amin(MSR))
print(min_index)

# Plot to see residuals check

print('Q = %.0f kJ/mol'%Qspace[min_index])

J = 20

plt.plot(Qspace,MSR)
```

Appendix B

Appendix B: Thermal-Shock Testing

B.1 Background

This work was taken from a conference paper presented at the ANS NETS 2022 conference [221].

B.2 Introduction

One of the biggest obstacles in designing an NTP system is the material selection, testing, and validation for the fuel element. NTP materials are uniquely challenging to test due to the combination of extreme environmental conditions, namely, high temperature operation, fast heating and cooling rates, high power density, large neutron flux, and large thermal gradients. The only way to test the combination of all environmental effects simultaneously is to build a full scale system. During material selection and evaluation, this is impractical, so different components of the extreme environment are tested separately.

Several NTP specific testbeds have been developed or adapted to test the detrimental effects high temperature operation has on the chemical and mechanical properties. These are summarized in Table B.1. Most of these systems have the ability to reach NTP operating temperatures, with some combination of hydrogen

Table B.1: Summary of existing NTP testbeds with the maximum temperature (Max T), flowing hydrogen availability (H_2), and irradiation testing (Irrad) indicated.

Testbed	Max T (°C)	H_2	Irrad
CFEET [222]	2580	Yes	No
NTREES [223]	2580	Yes	No
INSET [224]	1730	No	Yes
TREAT2,6 [225, 226]	2730	Yes	Yes
BWXT Small-scale [227]	2730	Yes	No

and irradiation exposure. CFEET, NTREES, INSET, and the BWXT small-scale system are limited to a ramp rate of around 100 °C/min and therefore cannot induce a thermal shock to the samples. TREAT has the capability to heat samples at 5500 °C/min, which can induce a thermal shock and accurately test rapid heating [225].

Pulsed electric current sintering, colloquially known as "spark plasma sintering" (SPS), has been used in increasing prevalence to fabricate materials for NTP systems [40, 109, 110]. SPS utilizes a pulsed current to heat a powder compact under an applied pressure to consolidate the material to a high final density. SPS has the capability to produce rapid heating rates especially for smaller samples. The combination of rapid heating with the large thermal transients induced will be referred to as "thermal shock" testing. This was accomplished by taking each material through two thermal cycles at relevant NTP heating rates and hold temperatures.

A significant question addressed in this study is the effect of fuel matrix to architecture. therefore, both coated particles suspended in a refractory metal and carbide matrix as well as a solid solution carbide underwent the thermal shock testing.

Four different materials, two cermet and two cercer materials, were fabricated using SPS. A molybdenum alloy of 30 weight percent tungsten (Mo30W) and zirconium carbide (ZrC), were used for the matrix materials for the cermet and cercer, respectively. In order to illustrate the paradigm, fuel surrogates were used in place of uranium containing fuel. Spherical yttria stabilized zirconia (YSZ) was used as a surrogate for uranium dioxide and angular hafnium nitride (HfN) was used as a surrogate for uranium nitride. These samples were fabricated using a powder coating technique and sintering conditions developed for the NASA SNP project task 1.10. A surrogate fuel volume loading of 40 % was selected for all materials, except for the ZrC-HfN cercer, which contained a 50 vol % loading. Two specimens of each material were fabricated to allow for the characterization of standard and thermal shock tested materials. Table B.2 contains a list of the samples fabricated for this experiment. All samples were 13 mm in diameter and between 12.5 and 13.5 mm tall.

Table B.2: Test samples and sintered densities with "C" and "TS" representing samples for characterization and thermal shock testing, respectively. The density of the sintered materials is presented as percent theoretical density (% TD).

Material	Sample ID	Purpose	Density (% TD)
Mo30W-40vol-YSZ	162	C	98.7
Mo30W-40vol-YSZ	988	TS	95.1
Mo30W-40vol-HfN	163	C	98.0
Mo30W-40vol-HfN	123	TS	94.9
ZrC-40vol-YSZ	165	C	100.0
ZrC-40vol-YSZ	164	TS	99.6
ZrC-50vol-HfN	124	C	97.2
ZrC-50vol-HfN	169	TS	97.4

The samples were characterized using X-ray diffraction (XRD), scanning electron microscopy (SEM) and Energy dispersive X-ray spectroscopy (EDS). SEM was performed on a Zeiss Evo SEM system using both secondary electron and backscatter imaging. EDS was performed using a Zeiss Evo SEM with the Bruker XFlash 6 360 EDS system and ESPIRIT software. XRD was performed on a Malvern PANalytical Empyrean diffractometer using a PIXcel3D area detector using a Cu-K αradiation source from 20 to 90°.

Thermal shock testing was conducted using the SPS on manual power control. A LABOX-675-FC, NJS Co. Ltd SPS was used in pulsed electric current sintering (PECS) mode with the default 40:7 on:off DC pulse. A pyrometer was used to monitor and record the temperature. A specialized graphite crucible was manufactured for this testing. The test specimens sit vertically inside the crucible, completely sealed in graphite. A small hole was drilled into the center of the crucible to allow for a more accurate temperature reading from the pyrometer. The system was then insulated using graphite felt, as seen in Figure B.1. Before conducting the thermal shock testing, an empty crucible was used to determine the power requirements to achieve the desired heating rates.

A summary of the tested thermocycles is presented in Table B.3. Previous materials for NTP have been tested with heating rates between 400 to 16,000 °C/min [3]. Each thermal cycle nominally consisted of a high rate of heating followed by a one minute hold at 2227 °C (2500 K) and then an unpowered rapid cool back to room temperature.

B.3 Results

All samples were sintered to a high theoretical density, as presented in Table B.2. Figure B.2 contains SEM micrographs and EDS maps of all four surrogate materials. A high matrix density and uniform particle spacing was observed in all four materials. XRD of both cermet materials and the ZrC-50vol-YSZ revealed two distinct phases

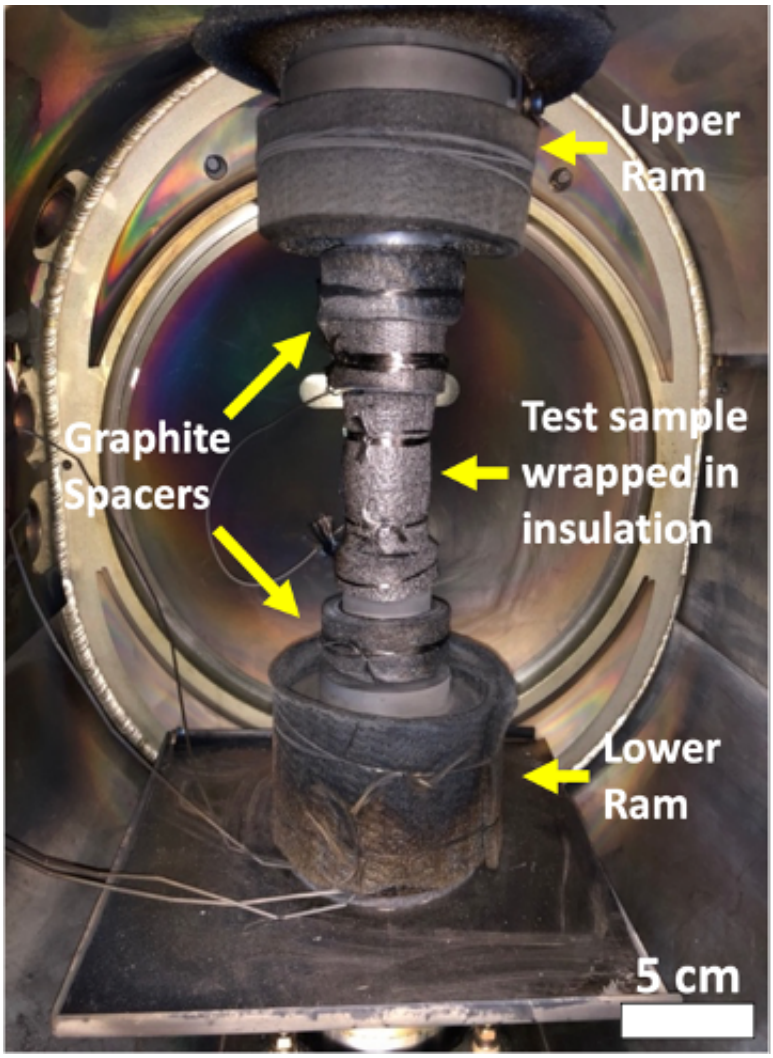


Figure B.1: Thermal shock test setup with graphite insulation.

Table B.3: Summary of thermal shock testing using SPS.

	Thermocycle 1				Thermocycle 2			
Material	Max. heat rate (°C/min)	Avg. heat. rate. (°C/min)	Max. hold temp. (°C)	Cool rate to 600 °C (°C/min)	Max. heat rate (°C/min)	Avg. heat. rate. (°C/min)	Max. hold temp. (°C)	Cool rate to 600 °C (°C/min)
Mo30W-40vol-YSZ	1600	500	2160	-557	System Failure (Melting of Material)			
Mo30W-40vol-HfN	1690	474	2120	-574	Contact Failure (Buckling of Graphite Crucible)			
ZrC-40vol-YSZ	1930	543	2230	-638	2070	593	2240	-566
ZrC-50vol-HfN	1440	459	2240	-507	1880	233	2240	-474
Mo30W-57vol-YSZ	1790	538	2230	-550	1990	737	2240	-479

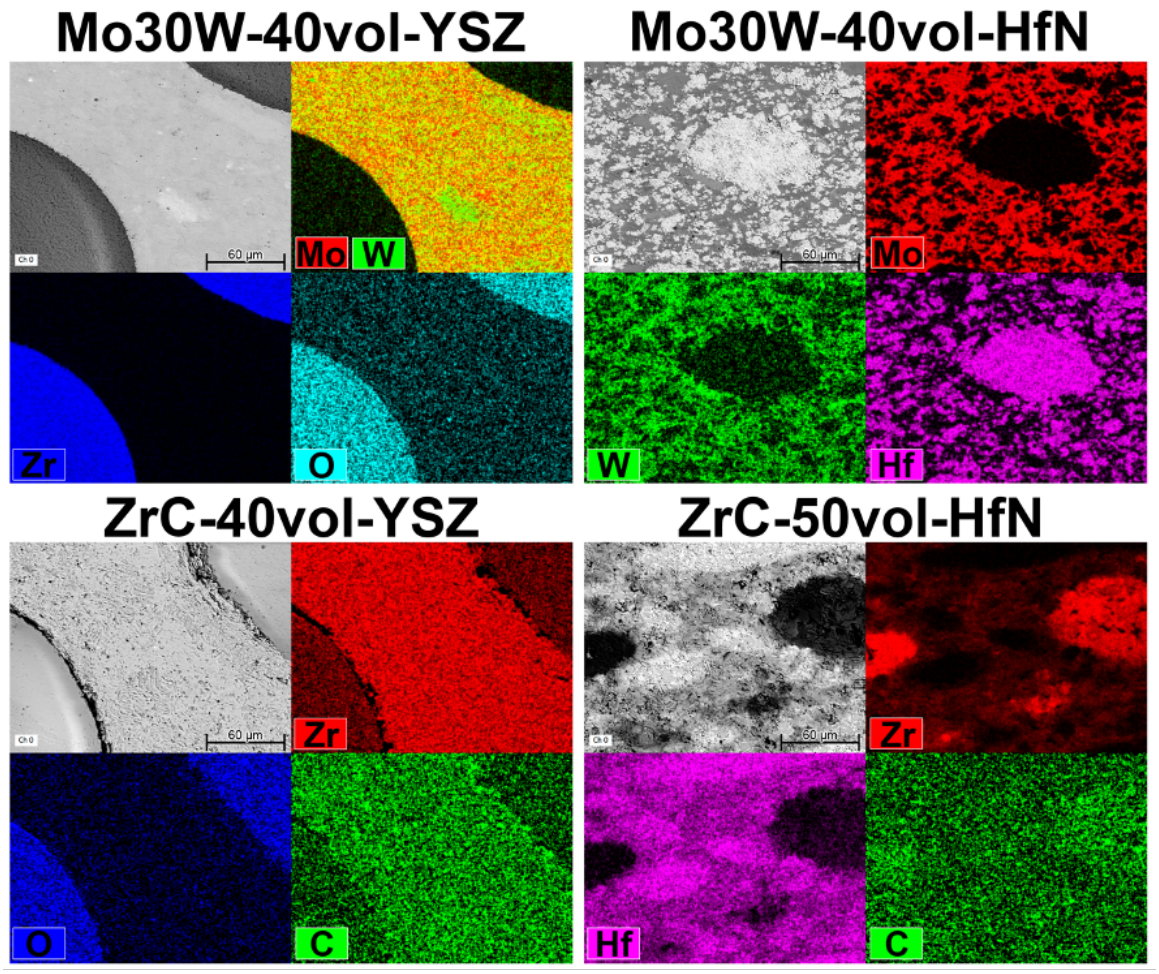


Figure B.2: Backscatter SEM image and EDS maps of the Mo30W-40vol-YSZ, Mo30W-40vol-HfN ZrC-40vol-YSZ, and ZrC-50vol-HfN cross-sections prior to testing.

for the matrix and the surrogate fuel particles, as presented in Figure B.3. The XRD spectra for the solid solution carbide suggested only a single phase was present. EDS analysis showed that while significant interdiffusion occurred between the ZrC and HfN, three phases were present. These are a ZrC rich phase, a HfN rich phase, and a true solid solution Zr,Hf carbonitride phase. This suggests that the fabrication parameters (either sintering temperature or hold time) were not enough to fully solutionize the material. However, the prevalence of the carbonitride phase still allowed for testing of the single phase region of that material.

Five thermal shock tests were conducted. An extra sample of Mo30W-57vol-YSZ was used to test the difference in required power between an empty crucible and a sample containing crucible. At least one thermal cycle was completed for each material. As summarized in Table B.3, both cermet materials experienced issues preventing a second thermal cycle. The Mo30W-40vol-YSZ experienced a critical failure when molten material began flowing out of the crucible. The Mo30W-40vol-HfN experienced buckling of the graphite crucible that prevented the second thermal cycle. Both cermet materials endured maximum heating rates between 1600 and 1700 °C/min. The average heating rates were between 474 and 500 °C/min. Figure B.4 contains the temperature and pressure profiles for the thermal shock testing. A spike in vacuum pressure was associated with the melting event in the Mo30W-40vol-YSZ.

The ZrC-40vol-YSZ performed the best with regard to testing. The first thermal cycle achieved a maximum heating rate of 1927 °C/min with the second achieving the highest rate of 2073 °C. Both cercer materials reached the desired maximum hold temperatures and were able to hold for one minute. No major spikes in vacuum pressure were observed.

B.4 Discussion

All samples experienced some amount of macroscopic deformation after thermal cycling. The Mo30W-40vol-YSZ cermet experienced the most drastic change as a

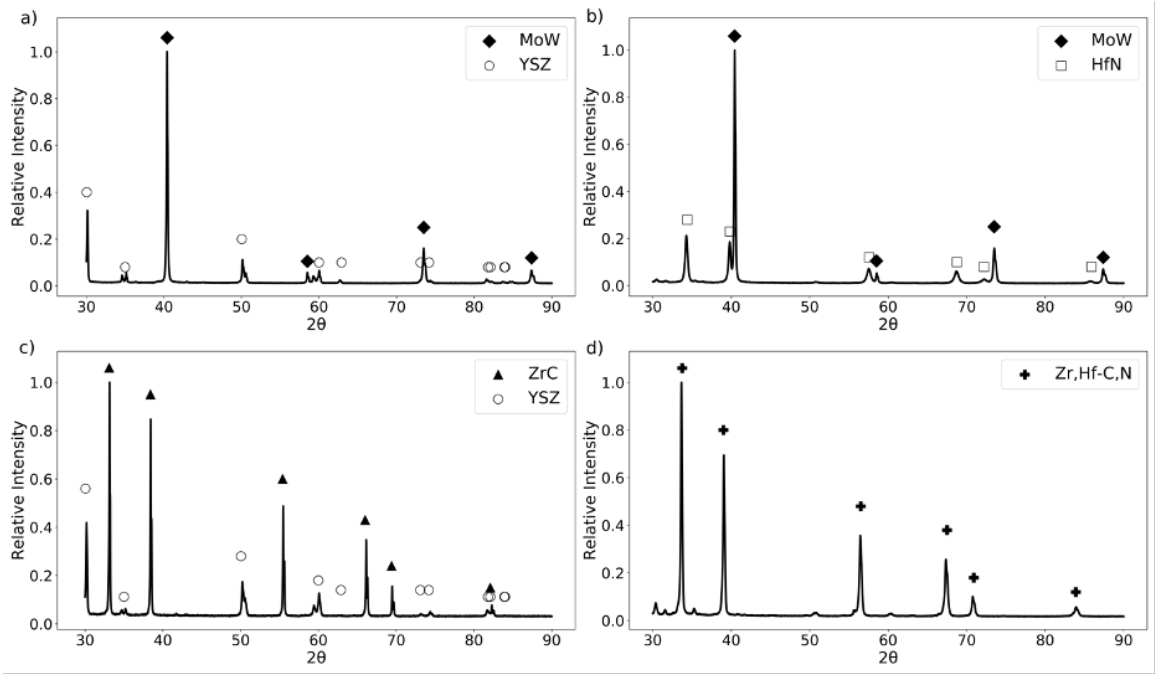


Figure B.3: Diffraction patterns for a) Mo30W-40vol-YSZ, b) Mo30W-40vol-HfN, c) ZrC-40vol-YSZ, and d) ZrC-50vol-HfN.

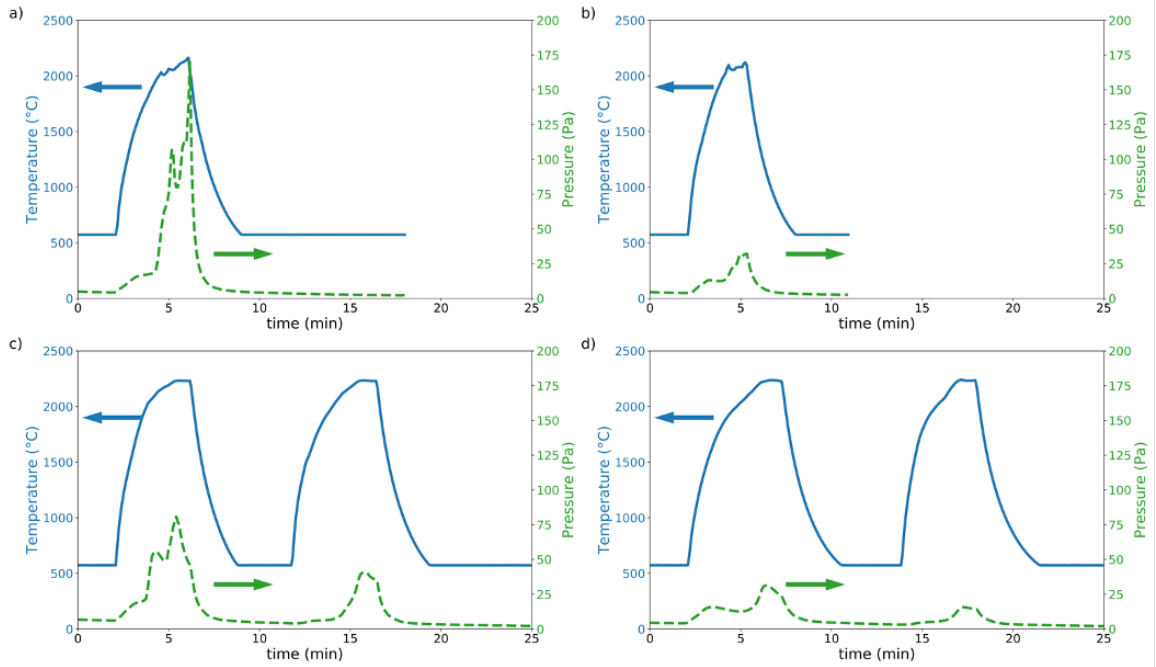


Figure B.4: Temperature (left) and pressure (right) profiles for a) Mo30W-40vol-YSZ, b) Mo30W-40vol-HfN, c) ZrC-40vol-YSZ, and d) ZrC-50vol-HfN.

significant portion of the material melted and flowed out of the pyrometer hole, as seen in Figure B.5. The pressure profile shown in Figure B.4 a) shows a spike in pressure up to 175 Pa prior to melting. The sample was extracted from the crucible and cross-sectioned, also shown in Figure B.5. The center of the material was found to be relatively undamaged, with the edges experiencing the most material loss from melting.

According to the pyrometer, the test did not reach the melting point of either Mo30W, or pure Mo (2896 K), so no melting should have occurred. XRD analysis was conducted on the solidified material that melted and leaked out of the graphite crucible. As seen in Figure B.6, the spectra showed evidence of carbide formation of either a Mo2C or $(MoW)_2C$. Most likely, this carbide formed prior to melting. As seen in the phase diagram for Mo and carbon (Figure B.7), there is a eutectic point at around 17 atom% carbon, where the melting point drops to 2200 °C.

At these elevated temperatures, carbon readily diffuses into refractory metals. So, for this run, a significant amount of carbon began diffusing into the matrix material, forming the carbide phase. Once the composition reached 17 atom %, the material began melting. The maximum recorded temperature for this run was 2164 °C, which is below the melting point. This illustrates another issue with this test setup. There is likely not a uniform temperature distribution among the entire test specimen. Some areas are obviously reaching higher temperatures, which was enough to form and consequently melt the carbide material.

The Mo30W-40vol-HfN fared better than the YSZ filled cermet. There was additional evidence of melting resulting from material loss (as seen in Figure 8), and based on small amounts of material residue fused to the graphite die. Once again, this is likely due to C diffusion into the MoW, lowering the melting point. The buckling of the graphite crucible once again suggests that the temperature being read by the pyrometer is lower than the actual maximum temperature of the sample-graphite die system. Experiencing a higher temperature at the graphite crucible interface could result in yielding. The cross-sections, shown in Figure B.8, compare the as sintered

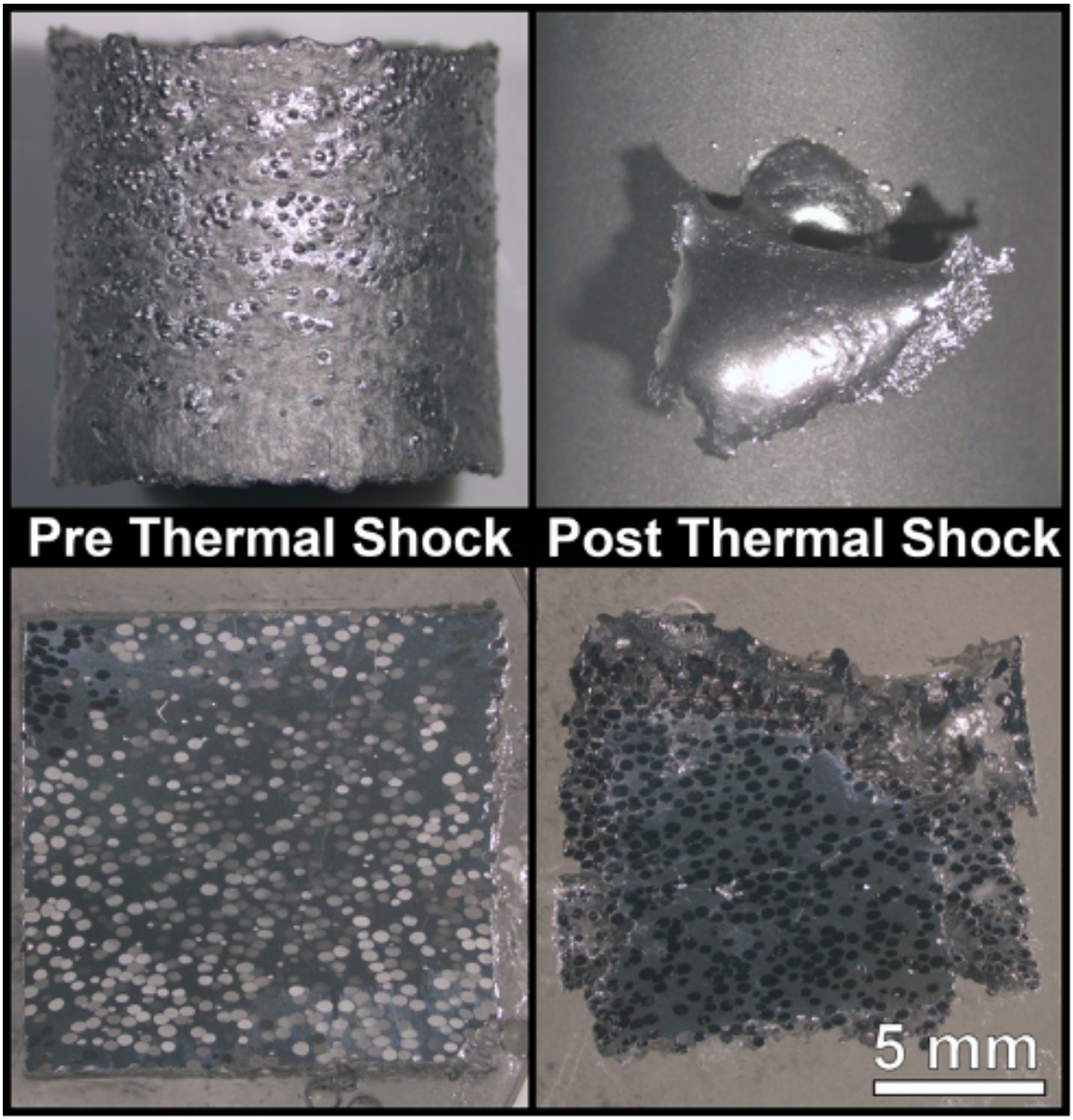


Figure B.5: Images of Mo30W-40vol-YSZ before (left) and after (right) thermal shock testing.

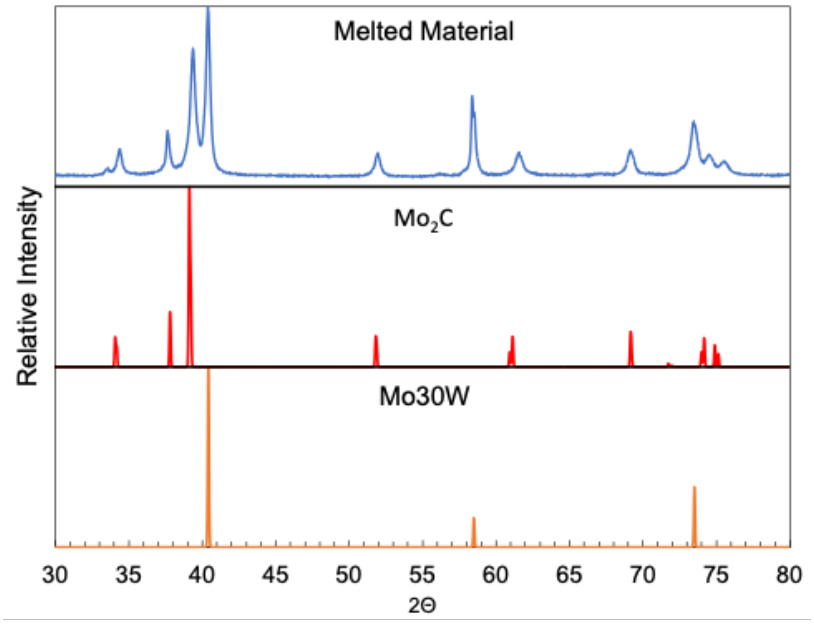


Figure B.6: XRD spectra of melted material (blue), Mo2C (red), and Mo30W (orange).

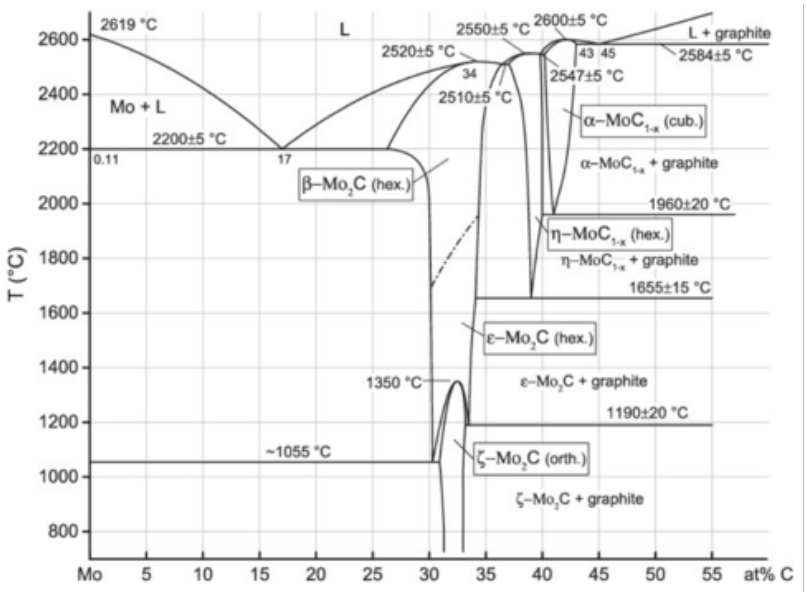


Figure B.7: Phase diagram of the Mo-C binary system [94].

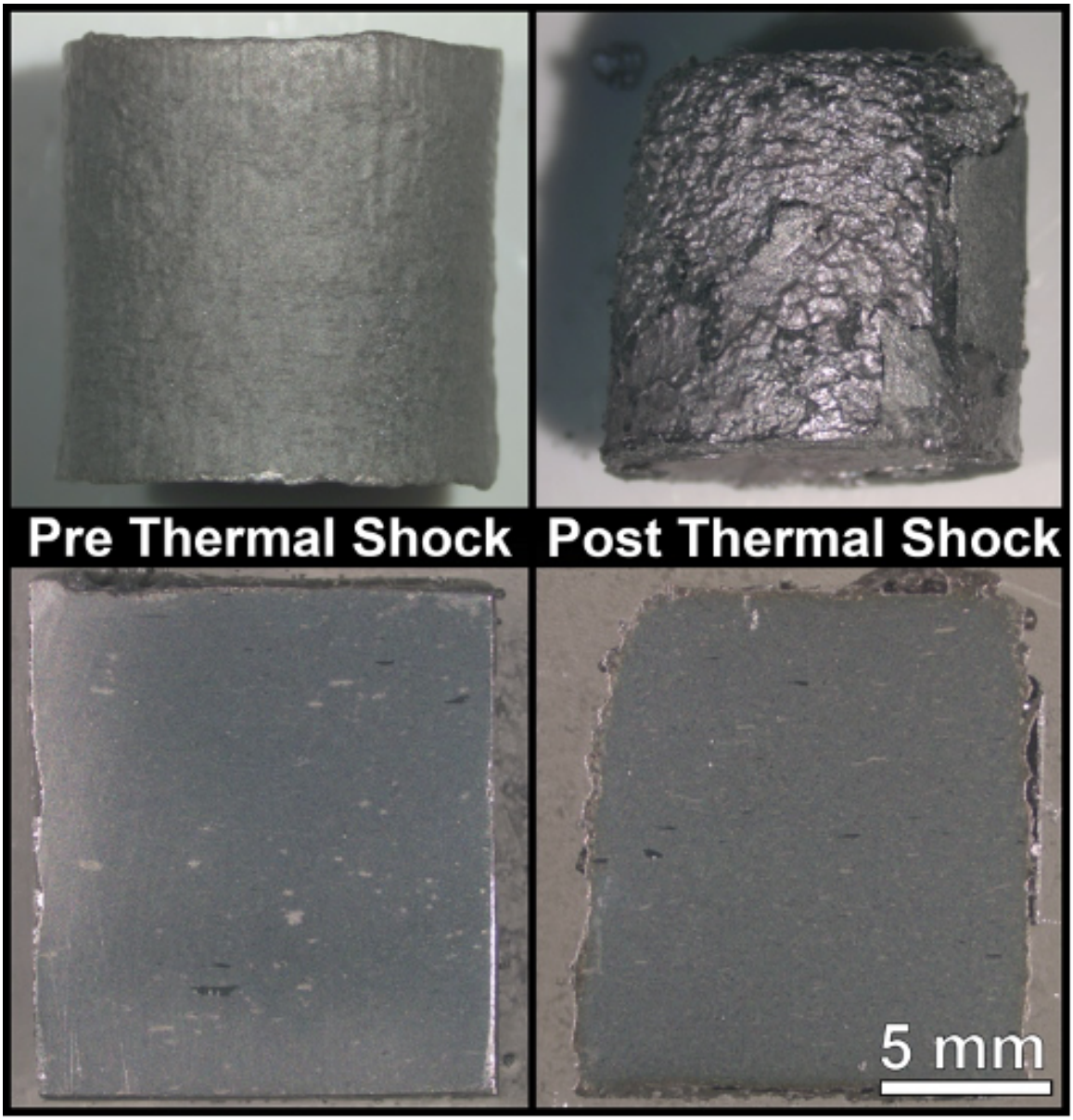


Figure B.8: Images of Mo30W-40vol-HfN before (left) and after (right) thermal shock testing.

material with the thermal shock tested sample. Except for material loss at one edge, the interior appeared relatively preserved. SEM analysis found no cracking in either the MoW matrix of HfN particles. Increased HfN diffusion into the MoW was observed as the HfN particle size decreased and the particle interface expanded.

Both ZrC materials survived two thermal cycles. The ZrC-40vol-YSZ material appeared to have very little deformation, except for the top surface which was quite shiny. The polished cross-sections presented in Figure B.9 revealed the loss of a significant amount of YSZ. At the maximum hold temperature of 2233 °C, the vapor pressure of Y_2O_3 and ZrO_2 (the primary molecules in YSZ) are 2.4×10^{-1} and 1.3×10^{-1} Pa, respectively [228]. The vapor pressure of ZrC at the same temperature is an order of magnitude lower, at 1.5×10^{-2} Pa. This difference in vapor pressure explains the preferential loss of YSZ.

The ZrC-50vol-HfN cercer experienced the least amount of deformation. The only noticeable change was the formation of a small void near the top of the sample, shown in Figure B.10. Further characterization of the microstructure revealed increased interdiffusion between the ZrC and HfN, forming a greater volume percent of the Zr-Hf carbonitride.

B.5 Conclusions

SPS has been successfully used to perform "thermal shock" testing of NTP surrogate samples. Instantaneous heating rates as high as 2000 °C/min and average heating rates around 500 °C/min were achieved. Several samples also experienced two complete thermal cycles up to the desired 2225 °C. Four different materials were tested. The MoW cermets with YSZ and HfN surrogate particles both experienced loss of the matrix material as a result of carbon ingress and a non-uniform temperature distribution. This resulted in chemical contamination and led to the unexpected melting of the matrix material. The two ZrC cercers with YSZ particles experienced loss of YSZ and minor deformation, while the ZrC-HfN cercer fared the best.

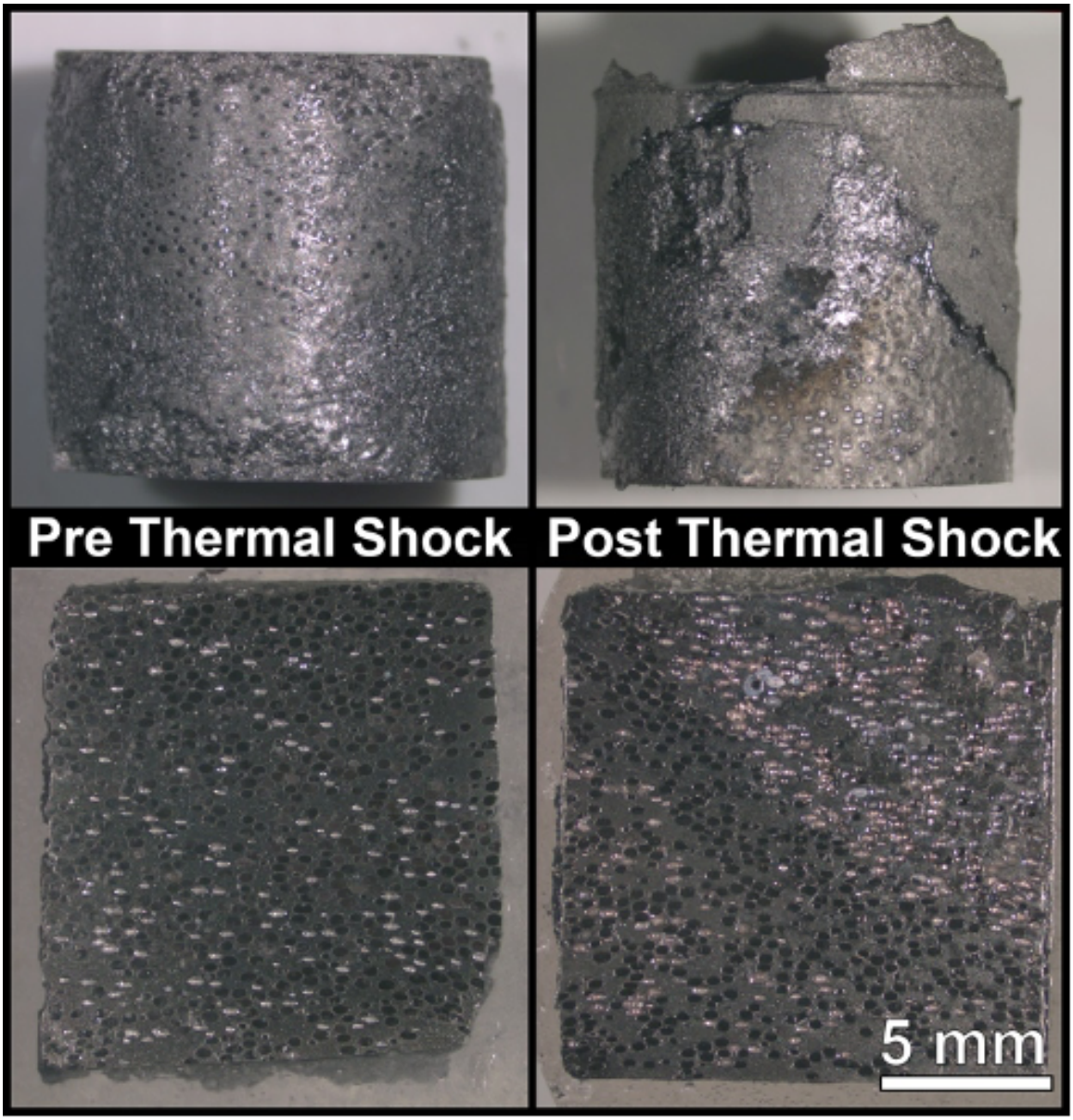


Figure B.9: Images of ZrC-40vol-YSZ before (left) and after (right) thermal shock testing.

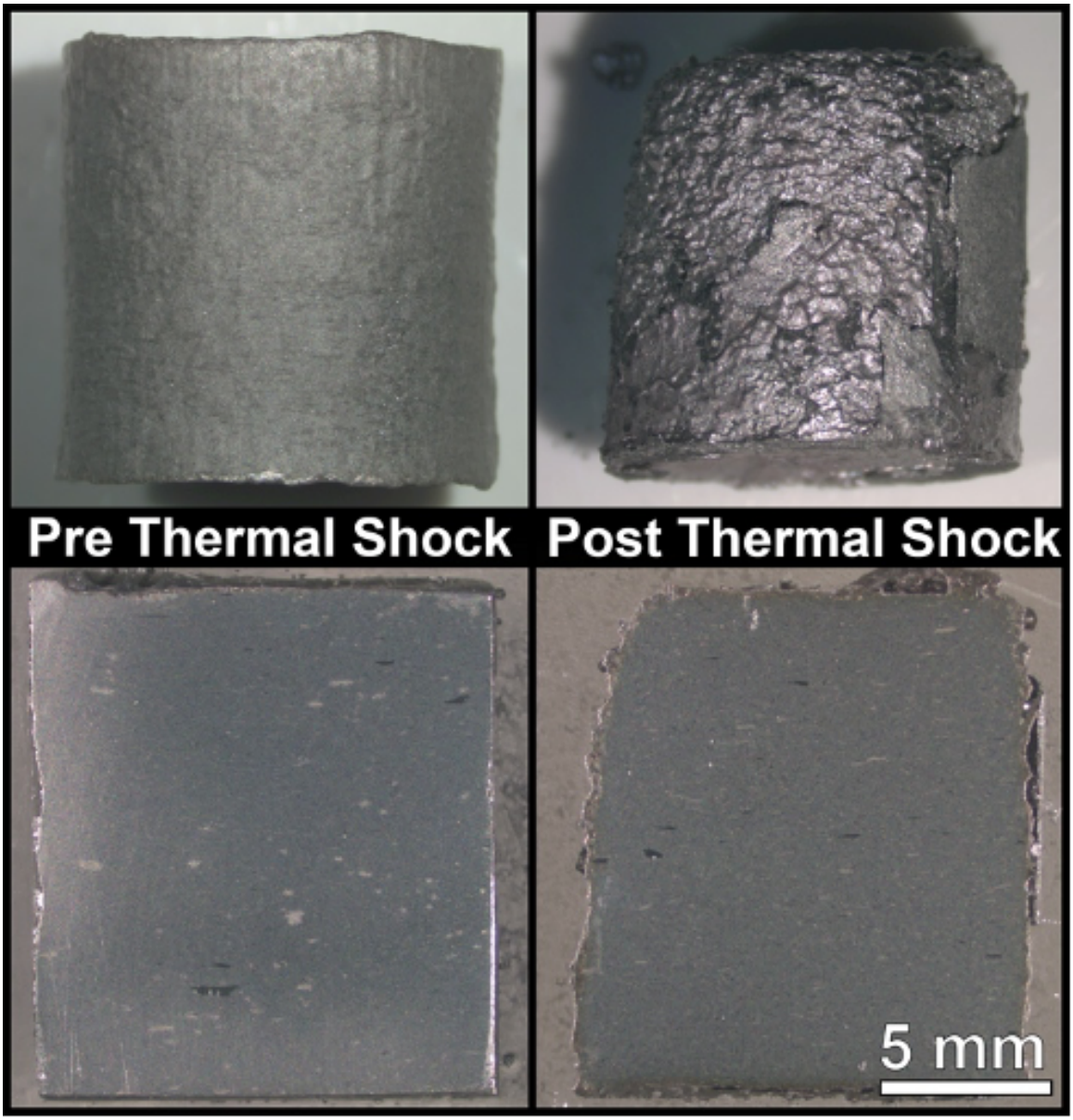


Figure B.10: Images of ZrC-50vol-HfN before (left) and after (right) thermal shock testing.

SPS appears to be viable in imposing thermal transients although modelling is required to quantify the imposed "thermal shock". The test system could be improved by addressing the following issues. First, especially for the cermet materials, a non-carbon liner (such as a refractory metal foil) could be added to the graphite crucibles to prevent carbon diffusion into the samples. This would suppress carbide formation and subsequent melting. Second, a larger hole could be drilled into the graphite crucible to give the pyrometer a clearer view of the sample. Additionally, modeling of the thermal gradient would provide insight into the extent of any thermal gradients induce in the material during heating and at the maximum hold temperature. Finally, to prevent the formation of local hot spots exceeding the melting point of the test materials, using a slower heating rate will allow for the samples to reach thermal equilibrium. A rapid heating rate up to 2000 °C or so could then be followed by a slow climb (10-20 °C/min) to the desired maximum test temperature of 2225 °C (2500 K). The shock can be simulated from rapid cooling by quenching the material in either an inert gas or using a chiller. Despite the limitations, SPS has proven its capability to simulate the rapid heating and cooling of NTP conditions, and should be considered for use in future testing.

Appendix C

Appendix C: Additional Cermet and Cercer Composites

In addition to the cermet and cercer composites fabricated using the YSZ and HfN surrogates, several other surrogates were characterized and considered with the Mo30W and ZrC.

C.1 Tungsten Coated YSZ

A batch of 200 µm YSZ spherical particles coated in W using chemical vapor deposition was obtained from an external vendor. These particles are shown in Figure C.1. The particles had a uniform coating, with no YSZ exposed. Cross-section examination of the particles found alumina contamination in the YSZ and also determined the coating thickness to be between 1 and 2 µm.

The W coated YSZ particles were initially sintered without the addition of any additional matrix material. The coated particles were sintered at 1750 °C using a heating rate of 100 °C for 20 min with an uniaxial pressure of 30 MPa. The final sintered density was determined to be 6.047 g/cm^3 which corresponded to 94.1% of

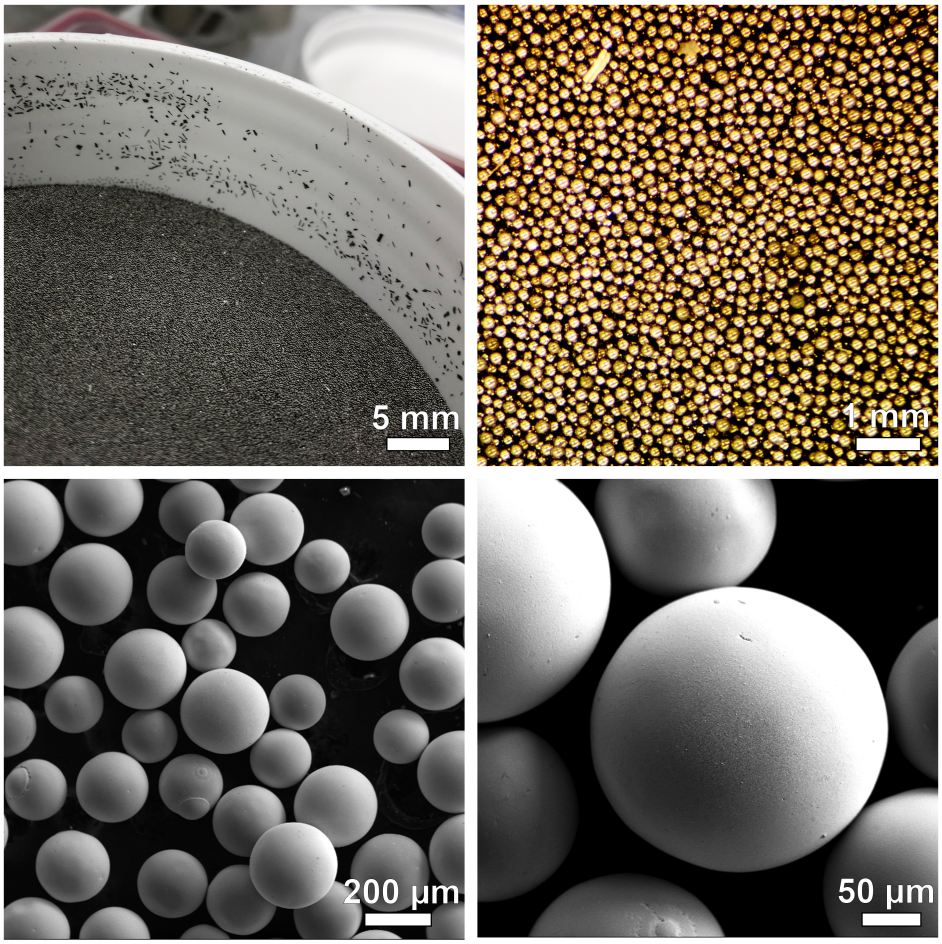


Figure C.1: Optical images (top) and SEM images (bottom) of the W coated YSZ.

the starting powder density. Figure C.2 contains SEM images of the polished cross-sections of the materials. Significant deformation was observed in the YSZ, however, the W coating appeared to hold after sintering, preventing any YSZ particles from touching.

A mixture of Mo30W with 70 vol% W-coated YSZ was also sintered at 1700 °C using a heating rate of 100 °C for 15 min with an uniaxial pressure of 30 MPa. These samples were also pre-compacted at 50 MPa prior to sintering. The final density for two runs were 7.678 g/cm^3 and 7.669 g/cm^3, corresponding to 94.4% and 94.3% theoretical density. Optical images of these materials are presented in Figure C.3.

C.2 Tungsten Carbide

Tungsten carbide (WC) was examined as a possible surrogate for uranium carbide (UC). WC was initially investigated once it was discovered ZrC was incompatible with YSZ under high temperature sintering conditions. A 200 µm spherical WC powder was obtained from Stanford Advanced Materials. The density of 17.037 g/cm^3 was measured using gas pycnometry. SEM images of the spherical WC particles are presented in Figure C.4. The particles were mostly spherical with a few containing minor deformations. The grain structure was also visible.

Table C.1 summarizes the initial set of sintering conditions. When sintered at 1850 °C for 10 minutes, a relative density above 98.2 % was achieved. However, SEM examination of the sintered material, as seen in Figure C.5, revealed high porosity in the ZrC matrix. A small interfacial layer also formed at the particle matrix interface. By increasing the sintering temperature and time to 1900 °C and 20 min, the measured density was increased to 99.9 % theoretical. SEM examination of this material, as seen in Figure C.6 revealed a significant reduction in the ZrC porosity. While some macroscopic cracking was observed, no microscopic cracking was visible in the SEM analysis.

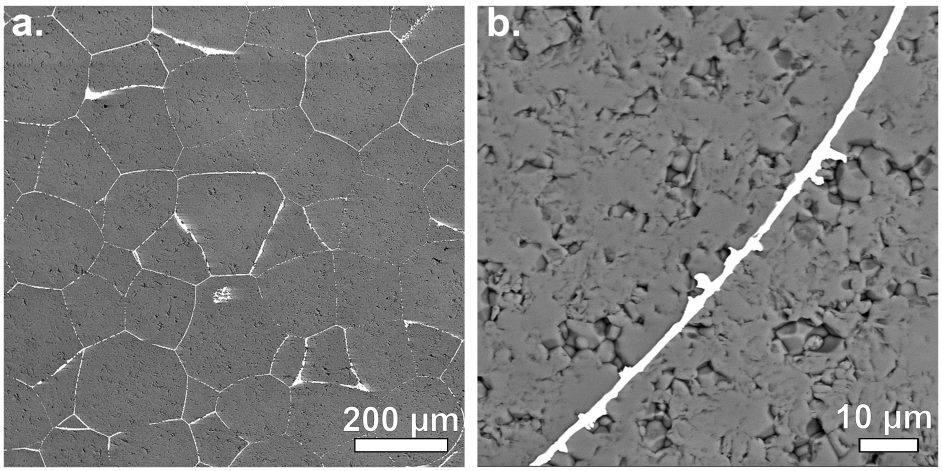


Figure C.2: SEM images of the W coated YSZ.

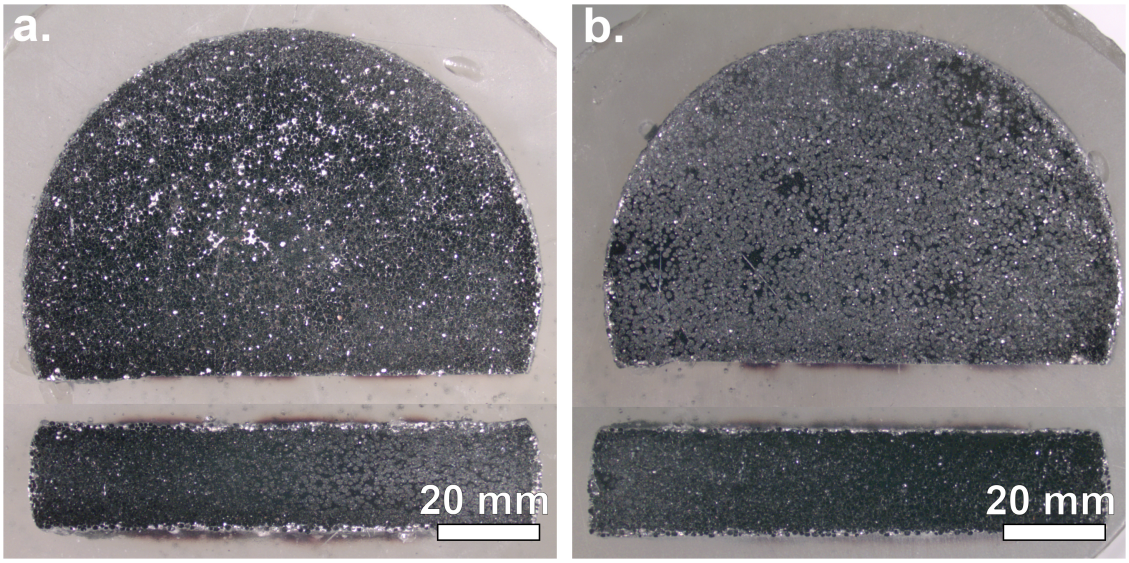


Figure C.3: Mo30W cermets with 70 vol% W coated YSZ particles.

Table C.1: Sintering conditions and density of the ZrC-WC cercer composites.

ID Num	Vol. load (%)	Hold temp. (°C)	Heat rate (°C/min)	Hold time (min)	Pre compact (MPa)	Hold press (MPa)	Final dens. (g/cm^3)	Theor. dens. (%)
204	50	1850	100	10	50	30	11.305	98.2
222	50	1900	100	20	50	20	11.51	99.9
303	20	1850	100	5	50	20	8.315	93.3

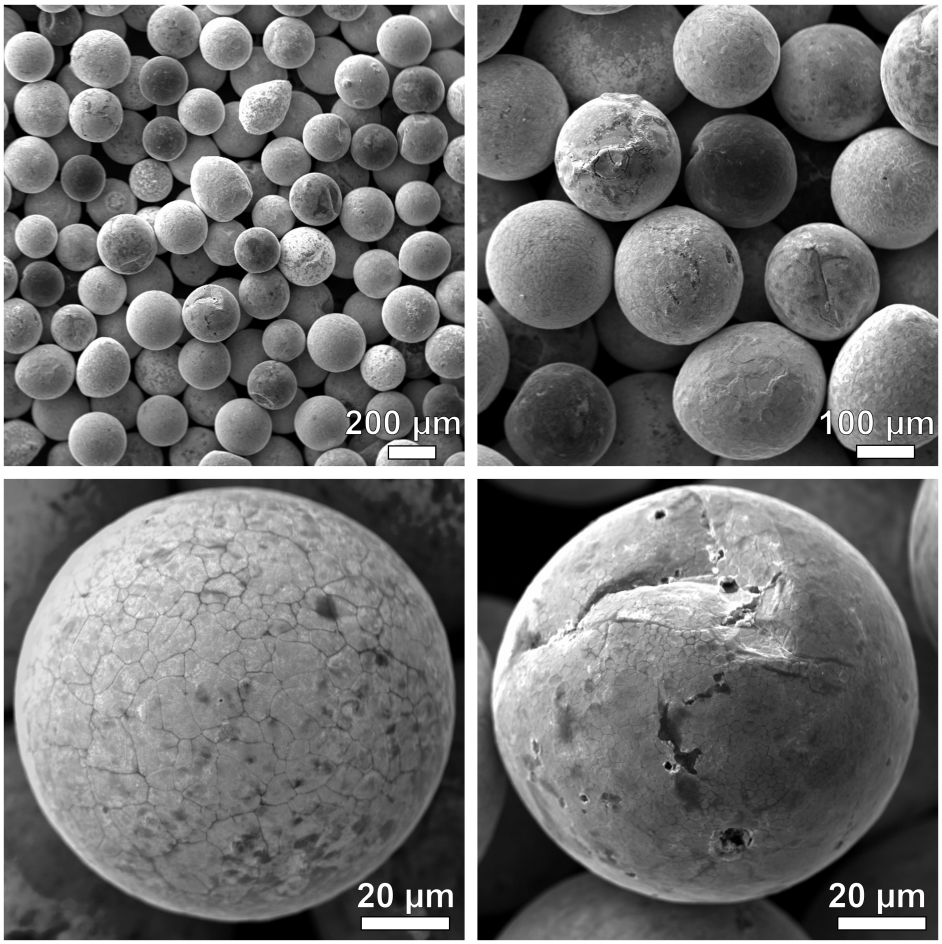


Figure C.4: SEM images of the as received spherical WC powder.

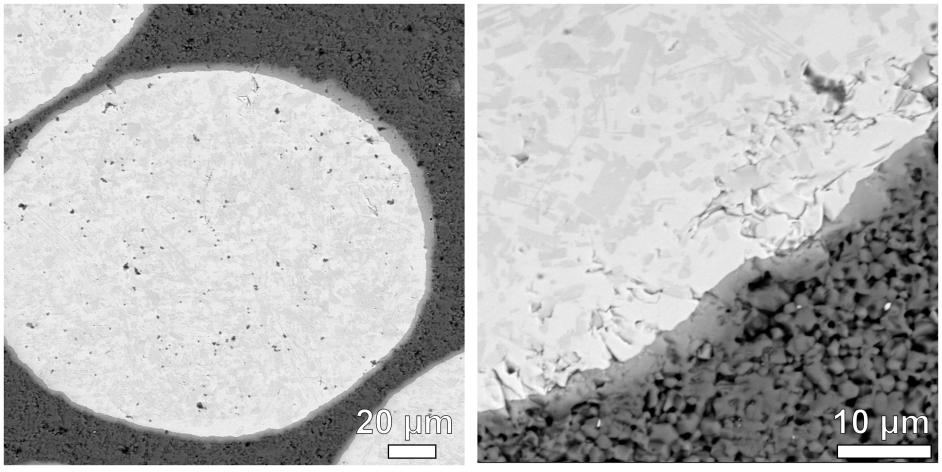


Figure C.5: SEM image of ZrC-50vol-WC sintered at 1850 °C for 10 min.

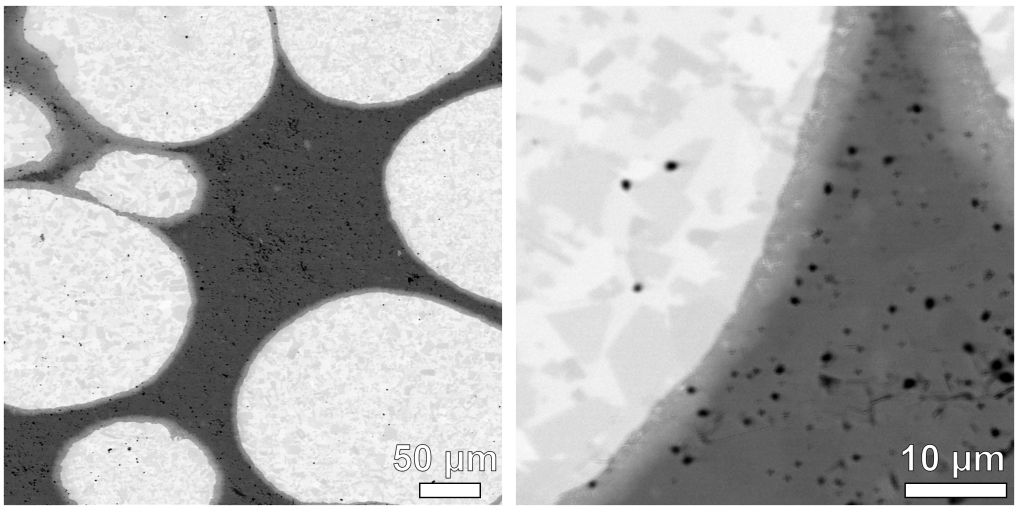


Figure C.6: SEM image of ZrC-50vol-WC sintered at 1900 °C for 20 min.

Another sample was sintered at 1850 °C for 5 minutes. This sample had a lowered volume loading of 20 vol%. The density of this sample was much lower, at 93.3 %. As seen in Figure C.7, the porosity in the ZrC was quite low. However, significant cracking was observed in the matrix material. Moreover, an interesting microstructure formed in the WC. This decay of the WC was determined to have resulted from the use of colloidal silica as a final polishing step.

Multiple attempts were made to reduce both microscopic and macroscopic cracking in the ZrC matrix at the lower volume loadings. Macroscopic cracking was especially prevalent in the sintered 40 mm samples. For this reason, the ZrC-YSZ material was selected for further analysis as opposed to the ZrC-WC material.

C.3 Surrogate BISO

A BISO surrogate particle was provided by an external vendor. A spherical YSZ was coated in two layers of carbon. The particles were characterized using SEM and EDS. Some particles were mounted an polished to reveal their cross-sections. Figure C.8 shows a sectioned particle. An EDS point scan was conducted using this particle. The results are presented in Table C.2.

The BISO particles (50vol%) were coated with Mo30W then sintered at 1600 °C for 15 minutes with an applied pressure of 30 MPa. Figure C.9 contains the optical image of the polished sample. The sintered density was measured at 6.95 g/cm^3, which equates to 96.4 % theoretical density. While a few particles were touching, relatively uniform dispersion was obtained. SEM analysis of the sintered Mo30W-50vol-BISO was also conducted, as seen in Figure C.10. Most particles experienced significant cracking in one or both of the outer layers of carbon. Moreover, significant porosity was observed in the Mo30W matrix near the outermost layer of the BISO. Further sintering optimization is needed to preserve the BISO particles during sintering and to reduce the Mo30W porosity at the particle-matrix interface.

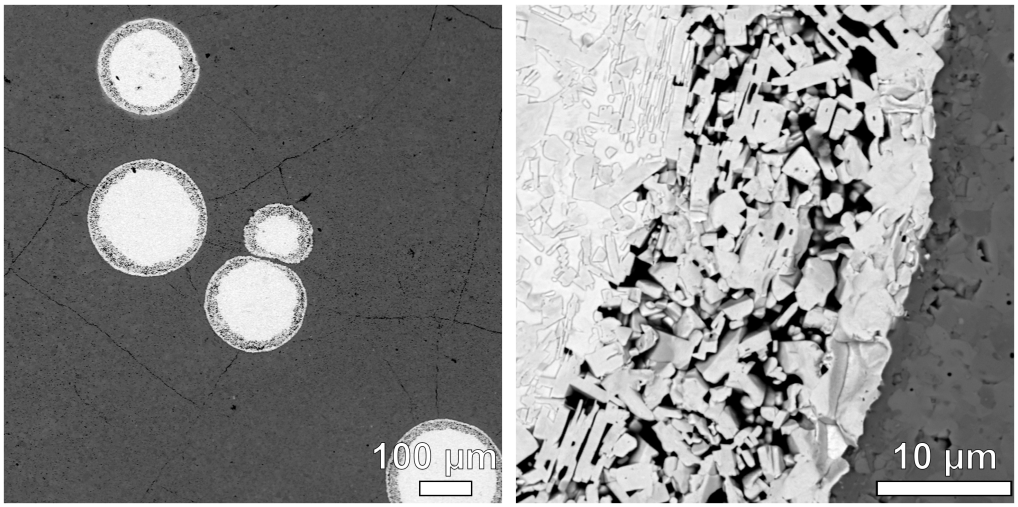


Figure C.7: SEM image of ZrC-20vol-WC sintered at 1850 °C for 5 min.

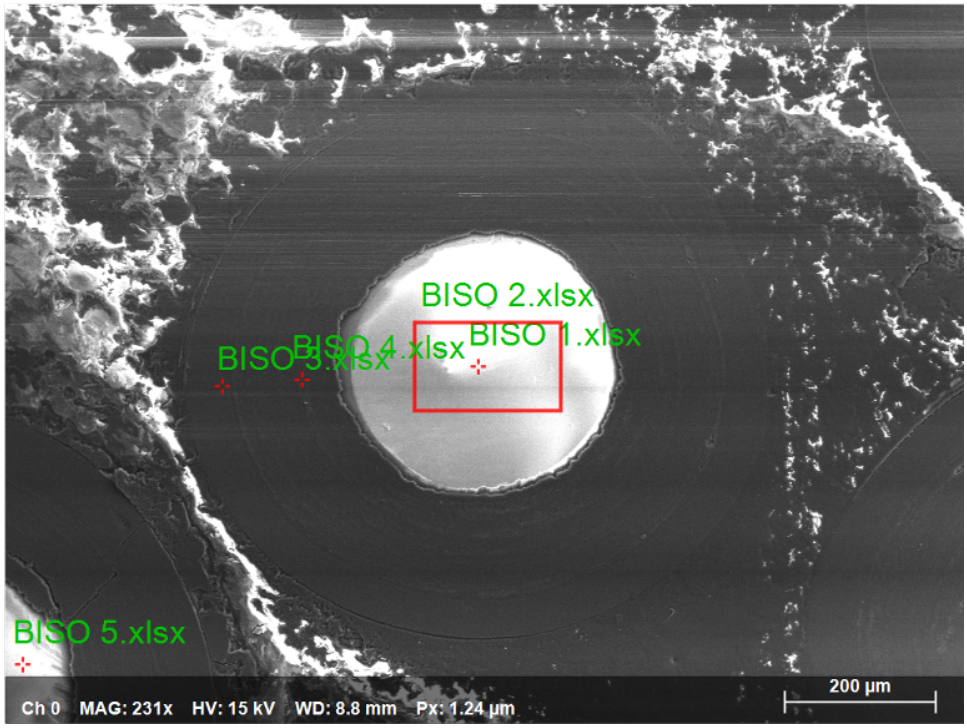


Figure C.8: SEM image of a sectioned BISO particle used for the EDS point scan.

Table C.2: Results of EDS point scan of the BISO paricle.

Spectra	C	Zr	O	N
1	21.02	54.66	24.32	0
2	23.28	59.69	17.03	0
3	93.46	0	0	6.54
4	92.22	0.7	1.38	5.7
5	10.91	66.86	22.23	0

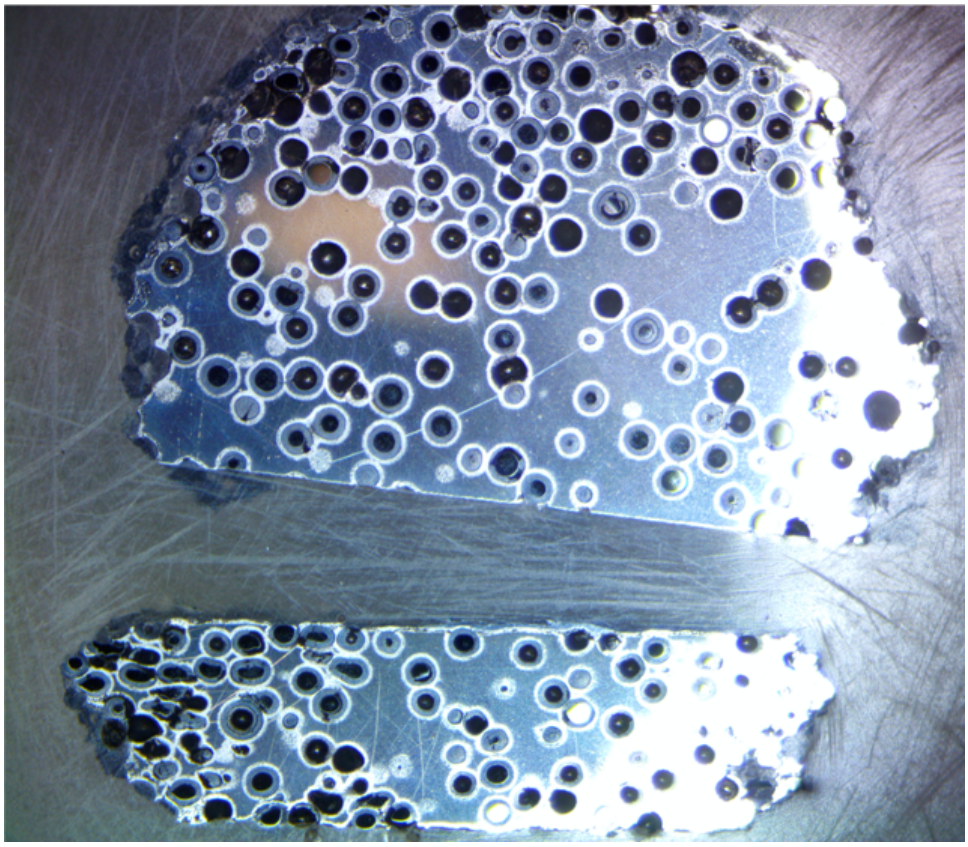


Figure C.9: Optical image of the polished Mo30W-50vol-BISO.

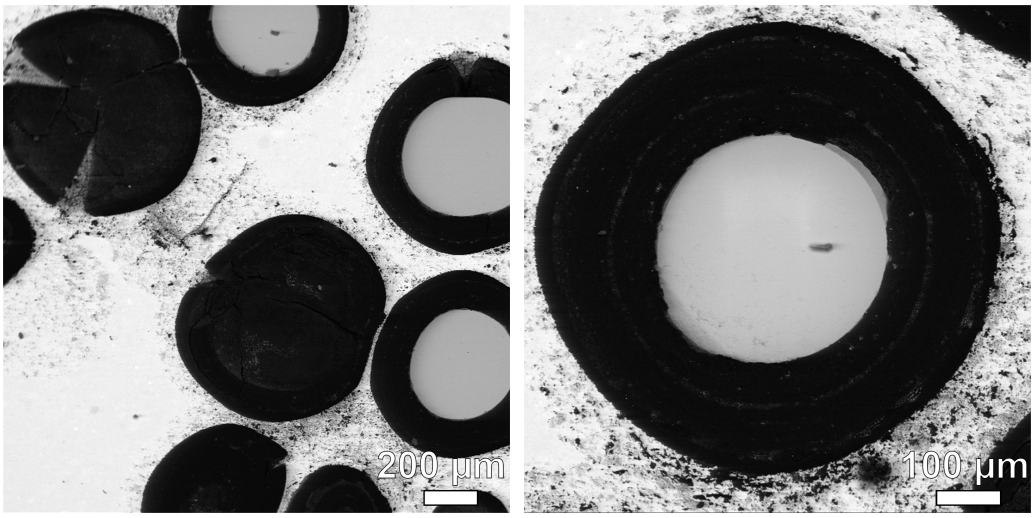


Figure C.10: SEM images of the polished cross-section of Mo30W-50vol-BISO.

The BISO particles were also sintered using ZrC as a matrix material. A ZrC cercer with 50 vol% BISO was sintered at 1900 °C for 10 minutes with an applied pressure of 30 MPa 10 minutes. A sintered density of 4.456 g/cm^3 (96.8 % theoretical) was measured. Figure C.11 contains an optical image of this material. While sectioning, the material shattered into two additional pieces, illustrating the highly brittle nature of this composite. Still, relatively uniform particle dispersion was obtained.

The sample was also examined using SEM, as seen in Figure C.12. The ZrC at the particle-matrix interface had much lower porosity compared with the Mo30W composite discussed previously. Still, most BISO particles experienced at least one significant crack during sintering.

Modifications were made to improve the sintered ZrC-BISO composites. First, the volume loading was reduced to 30 vol%. Next, the sintering conditions were modified. The applied pressure remained constant at 30 MPa. A pulsed method was used for the heating of the powder compact. The sample was heated to 1700 °C at the standard heating rate of 100 °C/min, then the powder compact was heated to 1900 °C at a heat rate of 200 °C. The sample was then cooled back to 1700 °C using a powder cooling rate of 200 °C/min. The temperature was then held at 1700 °C, after which the sample was allowed to cool without any current back to room temperature.

The results of the pulse method can be seen in Figure C.13. The density of the sintered composite was measured at 98.8 % (5.353 g/cm^3), which was an improvement compared with the 50vol% BISO discussed previously. The particles were dispersed uniformly in the ZrC and no cracking was observed in the matrix. SEM was used to examine the BISO particles, as seen in Figure C.14. Minor cracking was observed in a few particles, but the vast majority remained intact using the pulsed sintering method. XRD spectra for the ZrC-30vol-BISO is also included in Figure C.15.

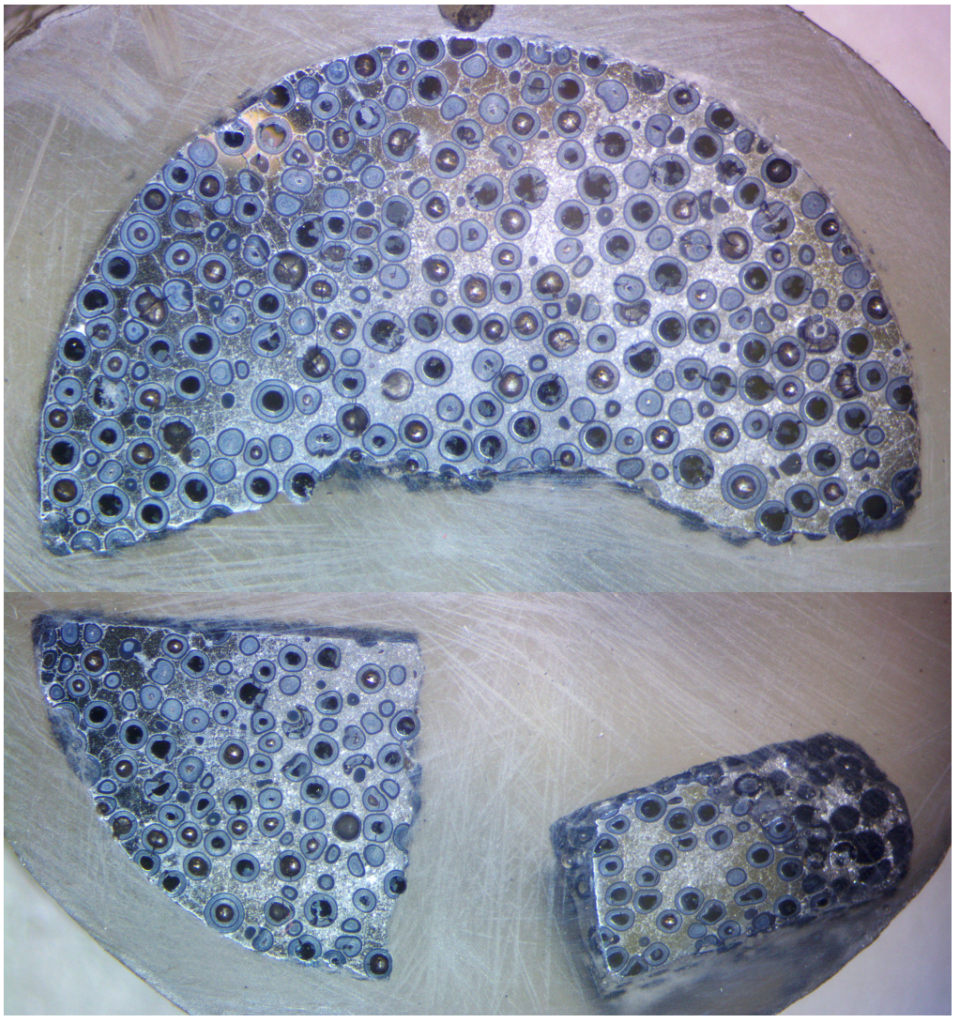


Figure C.11: Optical image of the polished ZrC-50vol-BISO.

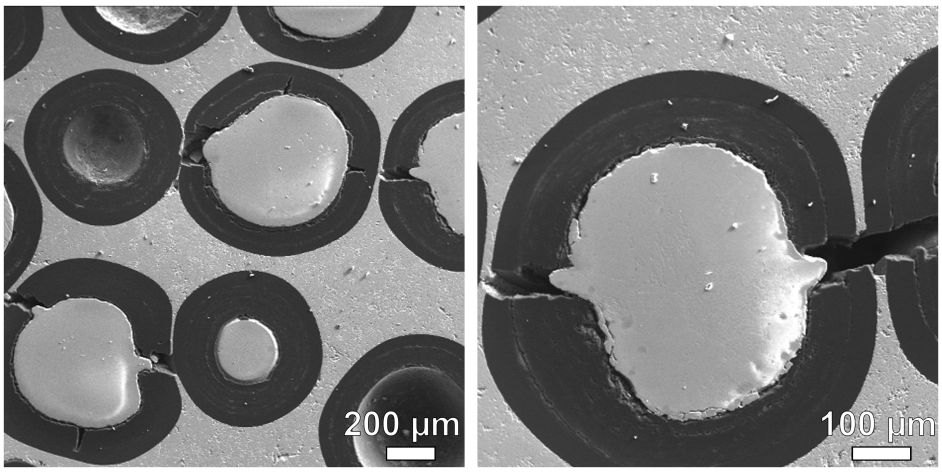


Figure C.12: Optical image of the polished ZrC-50vol-BISO.

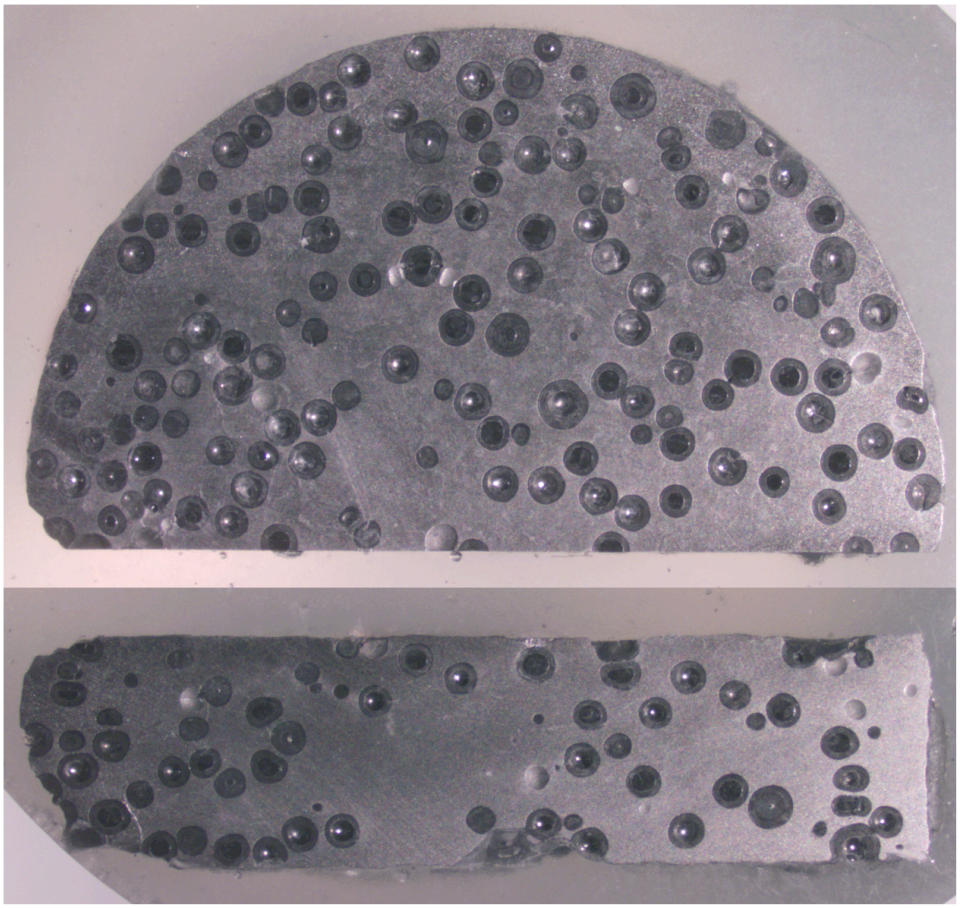


Figure C.13: SEM images of the polished cross-section of ZrC-30vol-BISO.

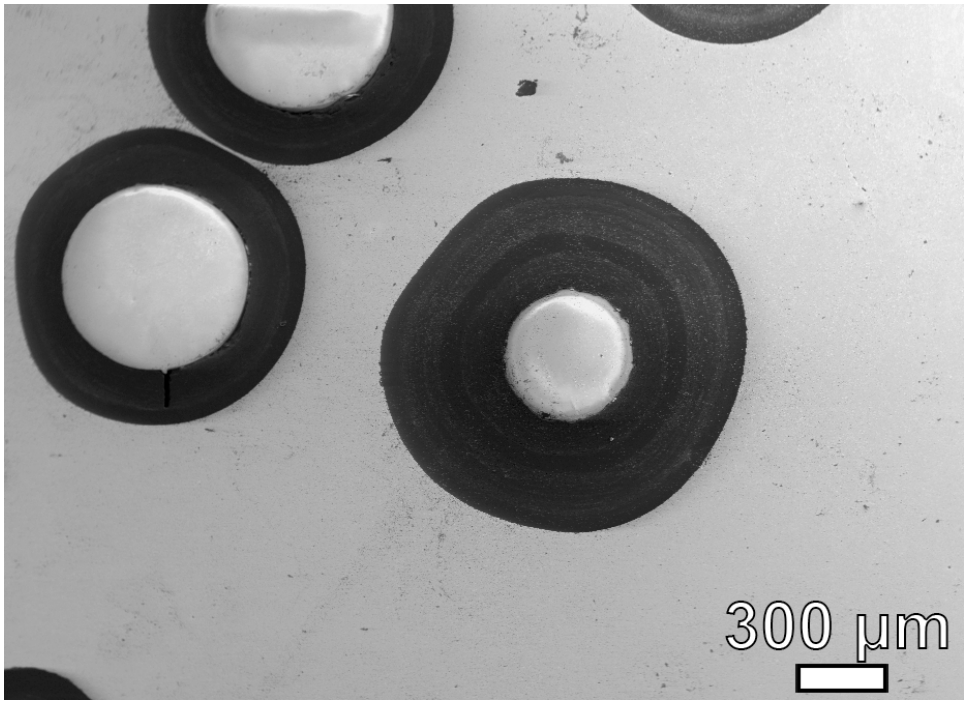


Figure C.14: SEM images of the polished cross-section of ZrC-30vol-BISO.

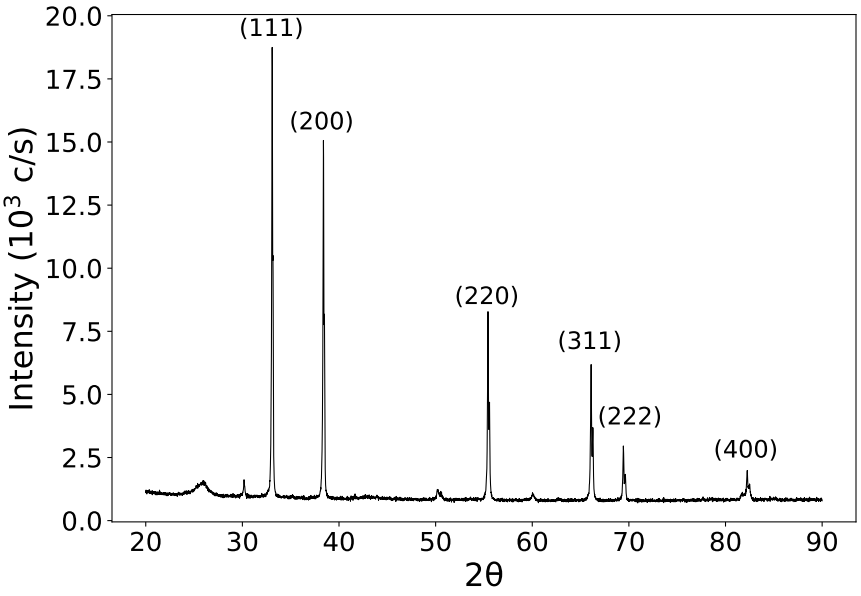


Figure C.15: XRD spectra of the ZrC-30vol-BISO.

C.4 Power T

As a demonstration for manufacturing complex geometries, a technique was developed to sinter a two phase composite, with one phase being in the shape of the University of Tennessee "Power T" logo. ZrC was selected as the matrix material and the angular HfN was selected as the "T" material. ZrC powder was first loaded into a graphite die. Then, using a custom 3-D printed punch, the outline of the "Power T" was pressed into the ZrC powder. Next, HfN powder was gently added to the ZrC powder. The material was sintered at 1850 °C and 30 MPa for 15 minutes. Figure C.16 contains examples of six of these materials. Figure C.17 contains a colorized SEM image of one of the ZrC-HfN "Power T" composites. Minor cracking resulted from the polishing of the material.



Figure C.16: Optical image of 6 different ZrC-HfN "T" composites.

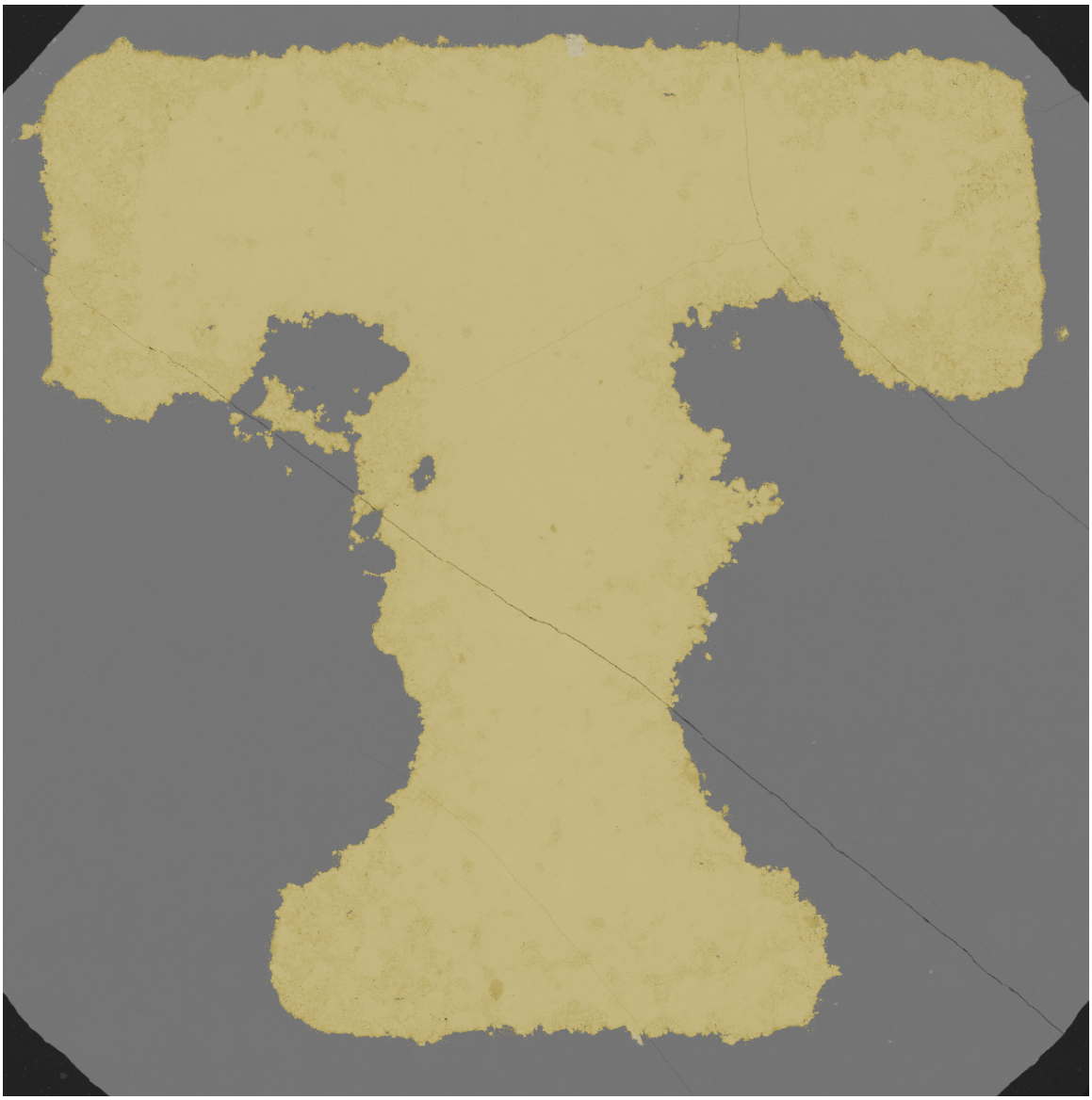


Figure C.17: Colorized SEM image of a ZrC-HfN "Power T" composite.

Vita

Neal Gaffin was born in Las Vegas, Nevada. He received a Bachelor of Science degree in Chemical Engineering at Brigham Young University in 2018. As an undergraduate and graduate research assistant at Los Alamos National Laboratory, he worked on a variety of projects including groundwater remediation, cosmic-ray muon tomography, and radioisotope thermal electric generator production. He attended the University of Tennessee to obtain a doctorate degree in nuclear engineering. Concurrently, he obtained a Master's of Science in Materials Science and Engineering in May 2021. His Master's thesis evaluated the irradiation resistance of molybdenum and tungsten cermet composites below 1100 °C for nuclear thermal propulsion. This included the design of an ion irradiation experiment to simulate the effects of neutron irradiation.

His doctoral research focused on the development of novel cermet and cercer composite fuel forms for nuclear thermal propulsion. His research has included fabrication optimization using spark plasma sintering, material testing in a flowing hot hydrogen up to 3000 °C, thermal transient testing utilizing SPS, thermophysical property measurements, and mechanical testing up to 800 °C. As part of his fabrication studies, he was awarded the U.S. Department of Energy, Office of Nuclear Energy, Office of Nuclear Fuel Cycle and Supply Chain Innovations in Nuclear Technology R&D Award for work related to a journal article analyzing the consolidation of a molybdenum tungsten alloy for nuclear thermal propulsion. He also earned the University of Tennessee Office of the Provost Professional Promise Award.